UNCLASSIFIED

AD NUMBER

AD894578

LIMITATION CHANGES

TO:

Approved for public release; distribution is unlimited.

FROM:

Distribution authorized to U.S. Gov't. agencies only; Administrative/Operational Use; 31 MAY 1972. Other requests shall be referred to Directorate, Army Air Mobility Research and Development Lab., Fort Eustis, VA 23604.

AUTHORITY

USAAMRDL ltr 19 Jul 1972

THIS PAGE IS UNCLASSIFIED

Best Available
Copy
for all Pictures

See 1473

AD

USAAMRDL TECHNICAL REPORT 71-59

AN INVESTIGATION OF AIR BEARINGS FOR GAS TURBINE ENGINES

AD No. AD894578
DDC FILE COPY

By

W. D. Waldron
W. E. Young
P. W. Curwen

December 1971

EUSTIS DIRECTORATE
U. S. ARMY AIR MOBILITY RESEARCH AND DEVELOPMENT LABORATORY
FORT EUSTIS, VIRGINIA

CONTRACT DAAJ02-69-C-0062
MECHANICAL TECHNOLOGY INCORPORATED
LATHAM, NEW YORK

[redacted]

U S ARMY MATERIEL COMMAND

DDC
RECEIVED
MAY 31 1972
B

Statement B TAE
per Mrs Horn 8/927-3002
Controlling Office: USAAMRDL
Eustis Dir
Ft. Eustis, Va. 23604

RNewton
5-31-77

DISCLAIMERS

The findings in this report are not to be construed as an official Department of the Army position unless so designated by other authorized documents.

When Government drawings, specifications, or other data are used for any purpose other than in connection with a definitely related Government procurement operation, the US Government thereby incurs no responsibility nor any obligation whatsoever; and the fact that the Government may have formulated, furnished, or in any way supplied the said drawings, specifications, or other data is not to be regarded by implication or otherwise as in any manner licensing the holder or any other person or corporation, or conveying any rights or permission, to manufacture, use, or sell any patented invention that may in any way be related thereto.

Trade names cited in this report do not constitute an official endorsement or approval of the use of such commercial hardware or software.

DISPOSITION INSTRUCTIONS

Destroy this report when no longer needed. Do not return it to the originator.



DEPARTMENT OF THE ARMY
U. S. ARMY AIR MOBILITY RESEARCH & DEVELOPMENT LABORATORY
EUSTIS DIRECTORATE
FORT EUSTIS, VIRGINIA 23604

The research work described herein was performed by Mechanical Technology Incorporated under U. S. Army Contract DAAJ02-69-C-0062. The work was conducted under the technical management of Mr. R. G. Furgurson, Propulsion Division, Eustis Directorate, USAAMRDL. Appropriate technical personnel of this Directorate have reviewed this report and concur with the findings and conclusions contained herein.

The recommendations set forth in this report will be considered in planning any future programs of advanced turbine engine/bearing development.

Task 1G162203D14413
Contract DAAJ02-69-C-0062
USAAMRDL Technical Report 71-59
December 1971

AN INVESTIGATION OF AIR BEARINGS FOR GAS TURBINE ENGINES

Phase I Summary Report

By

W. D. Waldron
W. E. Young
P. W. Curwen

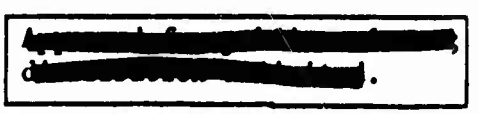
Distribution limited to U.S. Gov't. agencies only; Test and Evaluation; 31 MAY 1972. Other requests for this document must be referred to

Prepared by

Mechanical Technology Incorporated
Latham, New York

for

EUSTIS DIRECTORATE
U. S. ARMY AIR MOBILITY RESEARCH AND DEVELOPMENT LABORATORY
FORT EUSTIS, VIRGINIA



ABSTRACT

This report presents a summary of the results of work performed during Phase I of an investigation of air bearings for gas turbine engines.

A study was made to identify the significant effects of engine size on the design feasibility of air bearings. The results show that engine size per se, over the range of interest (2 to 5 lb/sec design-point air flow), is not a significant factor with respect to air-bearing feasibility. However, feasibility is strongly influenced by the types of compressor and turbine components selected, as well as by the arrangement of these components in the overall rotor assembly.

A 3.5 lb/sec engine size was selected for the balance of the Phase I and II investigations. The air-bearing-supported gas-generator spool uses a two-stage centrifugal compressor and a single-stage radial inflow turbine. The gas generator rated-power conditions are: turbine inlet temperature, 2550°F; compressor pressure ratio, 17.5 to 1; and speed, 60,000 rpm.

Two experimental efforts were also undertaken during Phase I. One effort involved evaluation tests of candidate air-bearing material combinations (substrate and coatings). The best material combination for the compressor-end journal and thrust bearings was found to be a plasma-sprayed Cr_2O_3 coating on a titanium-alloy substrate; for the turbine-end journal bearing, the best combination is a plasma-sprayed coating of 25% NiCr + 75% Cr_2O_3 on a high-temperature nickel-based alloy. Testing has demonstrated that these material combinations can satisfactorily sustain the required number of engine start-stop sliding cycles (15,000), and the large surface strains associated with overspeed conditions of engine operation (to 72,000 rpm) at elevated temperatures (to 1000°F). Current coatings, however, will not survive continuous sliding (of the order of a few seconds) at engine operating speeds. Air bearings must therefore be designed to maintain gas-film lubrication under all conditions of aircraft maneuver loads.

The second series of tests involved experimental verification of the load-carrying capability of the key journal and thrust bearing components. The tests have demonstrated that the components can carry the required maximum operating loads under the most severe conditions of bearing operation; namely, engine idle at 25,000 feet altitude. A problem of hydrodynamic instability was encountered with the initial thrust bearing design, but was subsequently corrected by modification of the design.

A full-scale rotor-bearing system simulator for the 3.5-lb/sec gas generator was designed, and will be built and tested during Phase II. The simulator accurately duplicates the mass and inertia distribution of the gas generator rotor, will use the detailed air-bearing designs evolved during Phase I, and will incorporate the actual bearing cooling schemes and engine seal arrangements likewise developed during Phase I.

The Phase I effort has resulted in a significant advancement in the overall assessment of the feasibility of air bearings for small aircraft gas-turbine engines.

"PRECEDING PAGE BLANK-NOT FILMED."

FOREWORD

The Phase I study reported herein was performed in fulfillment of Contract DAAJ02-69-C-0062 for the Eustis Directorate of the U. S. Army Air Mobility Research and Development Laboratory, Fort Eustic, Virginia. Mr. Roger Furgurson of the Eustis Directorate was the technical monitor. The work was authorized by DA Task 1G162203D14413.

The authors gratefully acknowledge the significant contributions to this program made by the following members of MTI's and P&WA's engineering staffs:

Mr. A. Frost (MTI), who led the initial part of the program

Mr. S.B. Malanoski (MTI), who performed the bearing analyses and conducted the bearing component tests

Mr. S. Calabrese (MTI), who conducted the materials test evaluation

Mr. W.A. Geiger (MTI), the lead design engineer

Mr. W.E. Young (P&WA), who led the P&WA activities and prepared the sections of this report covering the P&WA efforts.

PRECEDING PAGE BLANK-NOT FILMED.

TABLE OF CONTENTS

	Page
ABSTRACT	iii
FOREWORD	v
LIST OF ILLUSTRATIONS	ix
LIST OF TABLES	xxii
INTRODUCTION	1
Program Plan	3
PRELIMINARY ENGINE SIZING AND CONCEPT STUDIES	7
Engine Design Goals	8
Thermodynamic Analysis	9
Configuration Efficiency	32
Flow-Path Layouts	40
Thrust Loads	49
Critical Speeds of Rotor Configurations	63
Effects of Flow Rate on Engine Rotor Dimensions	68
Journal Bearing Loads	73
Journal Bearing Performance	82
Thrust Bearing Loads	90
Thrust Bearing Performance	91
Relative Performance, Cost, and Durability	93
SELECTION OF ENGINE SIZE AND CONFIGURATION	99
DESIGN OF 3.5 LB/SEC ENGINE	105
Final Component Sizing	105
Integrated Engine Design	117
Starter and Accessory Drive Evaluation	118
DESIGN AND ANALYSIS OF ROTOR-BEARING SYSTEM	127
Design of the Journal Bearings for the Engine	127
Journal Bearing Thermal Studies	149
Journal Bearing Stress and Centrifugal Growth	164
Design of the Double-Acting Thrust Bearing for the Engine	170
Thrust Bearing Mounting System	187
Thrust Bearing Stability	196
Engine Critical Speeds	200
Rotor-Bearing Dynamic Simulator	205

TABLE OF CONTENTS (cont'd)

	Page
EVALUATION OF BEARING MATERIALS	220
Preliminary Selection of Bearing Coating Materials	221
Preliminary Test Evaluation	243
Endurance Test Evaluations	264
Conclusions from Materials Evaluation Tests	281
EXPERIMENTAL EVALUATION OF BEARING COMPONENTS	290
Bearing Element Component Test Rig	291
Results of Journal Bearing Single-Pad Tests	292
Results of Thrust Bearing Tests	306
CONCLUSIONS AND RECOMMENDATIONS	330
Conclusions	330
Recommendations	334
LITERATURE CITED	336
APPENDIXES	337
I. Stability Analsyis of Gimbaled Thrust Bearing System	337
II. Computer Program for Stability Analysis of Gimbaled Thrust Bearings	346
DISTRIBUTION	369

LIST OF ILLUSTRATIONS

Figure		Page
1	Investigation of Air Bearings for Gas Turbine Engines; Phase I - Design and Component Testing------	5
2	Effect of Specific Speed on Compressor Efficiency----	12
3	Present and Projected Centrifugal Compressor Efficiency Levels----------	13
4	Single-Stage Axial Compressor Efficiency Variation With Fressure Ratio----------	15
5	Two-Stage Axial Compressor Efficiency Variation With Pressure Ratio----------	16
6	Effect of Pressure Ratio Split on Efficiency; Two Stage Centrifugal Compressor; 2 lb/sec----------	17
7	Effect of Pressure Ratio Split on Efficiency; Two-Stage Centrifugal Compressor; 3.5 lb/sec----------	18
8	Effect of Pressure Ratio Split on Efficiency; Two-Stage Centrifugal Compressor; 5 lb/sec----------	19
9	Effect of Pressure Ratio Split on Efficiency; One-Stage Axial/One-Stage Centrifugal Compressor; 2 lb/sec----------	20
10	Effect of Pressure Ratio Split on Efficiency; One-Stage Axial/One-Stage Centrifugal Compressor; 3.5 lb/sec----------	21
11	Effect of Pressure Ratio Split on Efficiency; One-Stage Axial/One-Stage Centrifugal Compressor; 5 lb/sec----------	22
12	Effect of Pressure Ratio Split on Efficiency; Two-Stage Axial/One-Stage Centrifugal Compressor; 2 lb/sec----------	23
13	Effect of Pressure Ratio Split on Efficiency; Two-Stage Axial/One-Stage Centrifugal Compressor; 3.5 lb/sec----------	24
14	Effect of Pressure Ratio Split on Efficiency; Two-Stage Axial/One-Stage Centrifugal Compressor; 5 lb/sec----------	25

LIST OF ILLUSTRATIONS (cont'd)

Figure		Page
15	Variation in Compressor Efficiency With Speed; 2 lb/sec	27
16	Variation in Compressor Efficiency With Speed; 3.5 lb/sec	28
17	Variation in Compressor Efficiency With Speed; 5 lb/sec	29
18	Turbine Axial Exit Velocity Required for Peak Efficiency as a Function of Velocity Ratio	31
19	Variation in Turbine Relative Effective Efficiency With Speed; 2 lb/sec	33
20	Variation in Turbine Relative Effective Efficiency With Speed; 3.5 lb/sec	34
21	Variation in Turbine Relative Effective Efficiency With Speed; 5 lb/sec	35
22	Variation in Turbocompressor Efficiency With Speed; 2 lb/sec	36
23	Variation in Turbocompressor Efficiency With Speed; 3.5 lb/sec	37
24	Variation in Turbocompressor Efficiency With Speed; 5 lb/sec	38
25	Air Bearing Engine Study Flow-Path Arrangements; 5 lb/sec	43
26	Air Bearing Engine Study Flow-Path Arrangements; 5 lb/sec	44
27	Alternate Combustor - Turbine Flow-Path Arrangements; 5 lb/sec	45
28	Air Bearing Engine Study Flow-Path Arrangement; 2 lb/sec	46
29	Schematic of Two-Stage Centrifugal Compressor Thrust Forces	50
30	Parameter Effect on Compressor Stage Thrust Forces	52

LIST OF ILLUSTRATIONS (cont'd)

Figure		Page
31	Compressor Modifications Evaluated in Thrust Balance Study	53
32	Effect of Rotor Scalloping on Centrifugal Compressor Thrust and Efficiency	54
33	Effect of Rotor Backface Venting on Centrifugal Compressor Thrust and Efficiency	54
34	Effect of Rotor Front Shroud on Centrifugal Compressor Thrust and Efficiency	56
35	Effect of Rotor Exit Mach No. Variation on Centrifugal Compressor Thrust and Efficiency	56
36	Effect of Rotor Pressure Ratio Split on Centrifugal Compressor Thrust and Efficiency	58
37	Thrust Balancing Scheme for Axial Turbines	59
38	Effect of Efficiency of Back-Pressurizing to Control Axial Thrust	60
39	Effect of Backface Cutback on Radial Turbine Axial Thrust	62
40	Ratio of Rotor Critical Speed to Engine Overspeed Versus Engine Flow Rate	66
41	Engine Speed Versus Engine Flow Rate	69
42	Total Weight of Compressor and Turbine Wheels Versus Engine Flow Rate	70
43	Total Rotor Weight Versus Engine Flow Rate	71
44	Journal Bearing and Wheel Hub Diameter Versus Engine Flow Rate	72
45	Polar Moment of Inertia of Rotor Versus Engine Flow Rate	74
46	Rotor Length and Bearing Span Versus Engine Flow Rate	75
47	Operating Load Diagrams for the Gas Generator	76

LIST OF ILLUSTRATIONS (cont'd)

Figure		Page
48	Maximum Journal Bearing Load Conditions for a 2 lb/sec C_o-T_o Engine With Equally Loaded Bearings	78
49	Maximum Journal Bearing Load Conditions for a 3.5 lb/sec C_o-T_o Engine With Equally Loaded Bearings	79
50	Maximum Journal Bearing Load Conditions for a 5 lb/sec C_o-T_o Engine With Equally Loaded Bearings	80
51	Maximum Resultant Journal Bearing Maneuver Load Versus Engine Flow Rate	81
52	Effect of C_p/R and Ambient Pressure on Journal Bearing Pad Film Thickness at Flight Idle Conditions - 2 lb/sec Engine	83
53	Effect of C_p/R and Ambient Pressure on Journal Bearing Pad Film Thickness at Flight Idle Conditions - 3.5 lb/sec Engine	84
54	Effect of C_p/R and Ambient Pressure on Journal Bearing Pad Film Thickness at Flight Idle Conditions - 5 lb/sec Engine	85
55	Effect of Ambient Pressure on Journal Bearing Pad Film Thickness at Flight Idle Conditions - 2 lb/sec Engine	86
56	Effect of Ambient Pressure on Journal Bearing Pad Film Thickness at Flight Idle Conditions - 3.5 lb/sec Engine	87
57	Effect of Ambient Pressure on Journal Bearing Pad Film Thickness at Flight Idle Conditions - 5 lb/sec Engine	88
58	Journal Bearing Pad Data for 2, 3.5, and 5 lb/sec Flow Rate Engines (C_o-T_o Configuration)	89
59	Thrust Bearing Load Versus Engine Flow Rate	92
60	Load-Carrying Capacity of Thrust Bearing for 2 lb/sec Engine	94

LIST OF ILLUSTRATIONS (cont'd)

Figure		Page
61	Load-Carrying Capacity of Thrust Bearing for 3.5 lb/sec Engine	95
62	Load-Carrying Capacity of Thrust Bearing for 5 lb/sec Engine	96
63	Product Efficiency Versus Engine Flow Rate for Nine Compressor and Turbine Configurations	100
64	Schematic of Engine Internal Leakage Paths	107
65	Off-Design Performance and Flow Parameter Curves for Engine Cycle Balancing Program	111
66	Air Bearing Engine Station Designations	113
67	Summary of 3.5 lb/sec C_o-T_o Engine Rotor Thrust Forces	116
68	3.5 lb/sec C_o-T_o Engine Layout With Air Bearings	119
69	Geared Accessory Drive System for Air Bearing Engine-	122
70	Schematic of All-Electric Accessory Drive System	123
71	Schematic of Air Turbine Accessory Drive System	125
72	Air Viscosity-Temperature Chart Used for Journal Bearing Calculations	130
73	Conceptual Design of a Pivoted Pad Journal Air Bearing for a 3.5 lb/sec Flow Rate Gas Turbine	132
74	Bearing Diametral Clearance at 80°F and Zero Speed as a Function of Unloaded Pad's Stiffness and Design-Speed Clearance for the Turbine-End and Compressor-End Three-Pad, Tilting-Pad Bearings	134
75	Turbine-End Bearing Non-Isothermal Performance as a Function of Bearing Clearance at 45,000 rpm and 25,000 Feet Altitude. (Unloaded Pad Flexure Stiffness Indicated Dictates Zero Speed Steup Clearance of Zero.)	136

LIST OF ILLUSTRATIONS (cont'd)

Figure		Page
76	Compressor-End Bearing Non-Isothermal Performance as a Function of Bearing Clearance at 45,000 rpm and 25,000 Feet Altitude. (Unloaded Pad Flexure Stiffness Indicated Dictates Zero Speed Setup Clearance of Zero.)----------	137
77	Three-Pad Bearing Schematic and Geometric Data-------	139
78	Performance of Turbine-End Pivoted-Pad Journal Bearing at Sea Level Under Isothermal Temperatures and Normal Load Conditions----------	140
79	Performance of Turbine-End Pivoted-Pad Journal Bearing at 25,000 Feet Under Isothermal Temperatures and Normal Load Conditions----------	141
80	Performance of Turbine-End Pivoted-Pad Journal Bearing at Sea Level Under Isothermal Temperatures and Maximum Load Conditions----------	142
81	Performance of Turbine-End Pivoted-Pad Journal Bearing at 25,000 Feet Under Isothermal Temperatures and Maximum Load Conditions----------	143
82	Performance of Compressor-End Pivoted-Pad Journal Bearing at Sea Level Under Isothermal Temperatures and Normal Load Conditions----------	144
83	Performance of Compressor-End Pivoted-Pad Journal Bearing 25,000 Feet Under Isothermal Temperatures and Normal Load Conditions----------	145
84	Performance of Compressor-End Pivoted-Pad Journal Bearing at Sea Level Under Isothermal Temperatures and Maximum Load Conditions----------	146
85	Performance of Compressor-End Pivoted-Pad Journal Bearing at 25,000 Feet Under Isothermal Temperatures and Maximum Load Conditions----------	147
86	Variation of Axial Temperature Profile With Cooling Passage Heat Transfer Coefficient - Compressor-End Journal Bearing----------	150
87	Axial Temperature Profile for Compressor-End Journal Bearing Using High-Conductivity Thermal Shunt to Compressor Wheel Hub----------	151

LIST OF ILLUSTRATIONS (cont'd)

Figure		Page
88	Thermal Model and Temperature Map (Sea Level, 100-Percent Power, and Maximum Maneuver Load) for the Compressor-End Journal Bearing----------	153
89	Thermal Distortion for the Compressor-End Journal Bearing at Sea Level, 100-Percent Power, and Maximum Maneuver Load Conditions----------	155
90	Thermal Distortion for the Compressor-End Journal Bearing at 25,000 Feet Altitude, Flight Idle, and Maximum Maneuver Load Conditions----------	156
91	Variation of Axial Temperature Profile With Cooling Passage Heat Transfer Coefficient - Turbine-End Journal Bearing at Sea Level, 100-Percent Power, and Maximum Maneuver Load Conditions----------	158
92	Thermal Model and Temperature Map (25,000 Feet Altitude, Flight Idle, and Maximum Maneuver Load) for the Turbine-End Journal Bearing----------	160
93	Thermal Model and Temperature Map (Sea Level, 100-Percent Power, and Maximum Maneuver Load) for the Turbine-End Journal Bearing----------	162
94	Thermal Distortion for the Turbine-End Journal Bearing at 25,000 Feet Altitude, Flight Idle, and Maximum Maneuver Load Conditions----------	163
95	Variation of Axial Temperature Profile With Cooling Passage Heat Transfer Coefficient - Turbine-End Journal Bearing at 25,000 Feet Altitude, Flight Idle, and Maximum Maneuver Load Conditions----------	165
96	0.2-Percent Yield Stress Versus Temperature for Three Candidate Bearing Materials----------	167
97	Ultimate Stress Versus Temperature for Three Candidate Bearing Materials----------	167
98	Effect of Speed on Stress and Centrifugal Growth of the Turbine Bearing Journal----------	168
99	Effect of Speed on Stress of the Compressor Journal Bearing----------	169
100	Effect of Speed on Centrifugal Growth of the Compressor Journal Bearing----------	169

LIST OF ILLUSTRATIONS (cont'd)

Figure		Page
101	Thrust Bearing Types----------	172
102	Performance of an Undistorted Hydrostatic Thrust Bearing----------	173
103	Performance of an Undistorted Hydrodynamic Thrust Bearing----------	174
104	Performance of an Undistorted Hybrid Thrust Bearing--	175
105	Comparison of Hybrid and Hydrodynamic Thrust Bearing Load Capacity With and Without Distorted Film--------	178
106	Hybrid Thrust Bearing Friction Loss (Nondistorted Film)----------	179
107	Geometry of the Thrust-Bearing Heat Exchanger Involute Cooling Pattern----------	181
108	Thrust Bearing With Radial Outflow Cooling----------	182
109	Thrust Bearing With Radial Inflow Cooling----------	183
110	Effect of Flow Direction on Thrust Bearing Surface Temperature----------	185
111	Effect of Bearing Film Thickness and Cooling Flow Direction on the Thrust Bearing Surface Temperature--	186
112	Temperature Distribution in Thrust Bearing at Zero Load (2-Mil Film Thickness); Speed 60,000 rpm; Cooling Flow 0.050 lb/sec Each Side----------	188
113	Thermal Distortion in Thrust Bearing at Zero Load (2-Mil Film Thickness); Speed 60,000 rpm; Cooling Flow 0.050 lb/sec Each Side----------	189
114	Temperature Distribution in Thrust Bearing at Continuous Maximum Load (10g - 1 Mil Film Thickness); Speed 60,000 rpm; Cooling Flow 0.050 lb/sec Each Side	190
115	Thermal Distortion in Thrust Bearing at Continuous Maximum Load (10g - 1-Mil Film Thickness); Speed 60,000 rpm; Cooling Flow 0.050 lb/sec Each Side------	191
116	Temperature Distribution in Thrust Bearing at Zero Load (2-Mil Film Thickness); Speed 45,000 rpm; Cooling Flow 0.025 lb/sec Each Side----------	192

LIST OF ILLUSTRATIONS (cont'd)

Figure		Page
117	Thermal Distortion in Thrust Bearing at Zero Load (2-Mil Film Thickness); Speed 45,000 rpm; Cooling Flow 0.025 lb/sec Each Side	193
118	Temperature Distribution in Thrust Bearing at Continuous Maximum Load (10g - 1-Mil Film Thickness); Speed 45,000 rpm; Cooling Flow 0.025 lb/sec Each Side	194
119	Thermal Distortion in Thrust Bearing at Continuous Maximum Load (10g - 1-Mil Film Thickness); Speed 45,000 rpm; Cooling Flow 0.025 lb/sec Each Side	195
120	Thrust Bearing Support Flexure With Tangential Spokes	197
121	Thrust Bearing Stability Map for Sea-Level, Flight-Idle Condition	201
122	Thrust Bearing Stability Map for Sea-Level, 100-Percent Power Condition	202
123	Thrust Bearing Stability Map for 25,000 Feet, Flight-Idle Condition	203
124	Thrust Bearing Stability Map for 25,000 Feet, 100-Percent Power Condition	204
125	Critical Speeds of Gas Generator Rotor for a 3.5-lb/sec Flow-Rate Engine	206
126	Rotor-Bearing Dynamic Simulator	209
127	Undamped Critical Speed Map of the 3.5-lb/sec C_o-T_o Engine and Rotor Dynamic Simulator	211
128	Undamped Critical Speed Mode Shapes of the 3.5-lb/sec C_o-T_o Engine and Rotor Dynamic Simulator	212
129	Thrust Bearing Layout Design	215
130	Journal Bearing Layout Design	217
131	MT-6 Thrust Washer Test Machine	224
132	Cross-Section Photomicrograph of Cr_2O_3 Coated Titanium Specimens	229

LIST OF ILLUSTRATIONS (cont'd)

Figure		Page
133	Photographs of the Titanium Alloy Specimen Coated With Cr_2O_3	231
134	Typical Surface Structure of Dense Cr_2O_3 Coating Before Testing	232
135	Typical Surface Structure of Normal Density Cr_2O_3 Coating Before Testing	233
136	Typical Surface Structure of 25-Percent Nickel-Chrome and 75-Percent Chrome-Oxide Coating Before Test	234
137	Typical Surface Structure of 25-Percent Nickel-Chrome and 75-Percent Chrome-Oxide Coating After Test	235
138	Typical Surface Structure of 50-Percent NiCr Bonded Cr_3C_2 + 50-Percent Cr_2O_3 Before Test	236
139	Typical Surface Structure of 50-Percent NiCr Bonded Cr_3C_2 + 50-Percent Cr_2O_3 After Test	237
140	Typical Surface Structure of 40-Percent Chrome and 60-Percent Cr_2O_3 Before Test	238
141	Typical Surface Structure of 40-Percent Chrome and 60-Percent Cr_2O_3 After Test	239
142	Typical Surface Structure of NiCr Bonded Cr_3C_2 Before Test	241
143	Typical Surface Structure of NiCr Bonded Cr_3C_2 After Test	242
144	Test Rig Setup for Start-Stop Tests to Demonstrate Coating Sliding Compatibility	244
145	Results of Preliminary Start-Stop Sliding Tests for Cr_2O_3 Plasma Sprayed on Titanium Substrate at 4-psi Loading	249
146	Results of Preliminary Start-Stop Sliding Tests for 25-Percent NiCr + 75-Percent Cr_2O_3 Plasma Sprayed on Titanium Substrate at 4-psi Loading	251

LIST OF ILLUSTRATIONS (cont'd)

Figure		Page
147	Results of Preliminary Start-Stop Sliding Tests for 50-Percent NiCr Bonded Cr_3C_2 + 50-Percent Cr_2O_3 Plasma Sprayed on Titanium Substrate at 4-psi Loading	253
148	Results of Preliminary Start-Stop Sliding Tests for 25-Percent NiCr + 75-Percent Cr_2O_3 Plasma Sprayed on Waspaloy Substrate at 4-psi Loading	255
149	Results of Preliminary Start-Stop Sliding Tests for 50-Percent NiCr Bonded Cr_3C_2 + 50-Percent Cr_2O_3 Plasma Sprayed on Waspaloy Substrate at 4-psi Loading	257
150	Results of Preliminary Start-Stop Sliding Tests for NiCr Bonded Cr_3C_2 Plasma Sprayed on Waspaloy Substrate at 4-psi Loading	259
151	HSD Elevated Temperature Spin Test Facility (Pit Closed)	262
152	Spin Test Components - Arbor and Test Cylinder	263
153	Cylinder-Arbor Assembly Mounted for Test	263
154	General Appearance of Coatings at End of Test-Cylinder No. 1	268
155	Appearance of Coating Edges After Test-Cylinder No. 2	269
156	Surface Finish of Cr_2O_3 Coating During 15,000-Cycle Start-Stop Test	271
157	Surface Appearance of Cr_2O_3 Coating During 15,000-Cycle Start-Stop Test	273
158	Surface Finish of 25-Percent NiCr + 75-Percent Cr_2O_3 Coating During 15,000-Cycle Start-Stop Test	275
159	Surface Appearance of 25-Percent NiCr + 75-Percent Cr_2O_3 Coating During 15,000-Cycle Start-Stop Test at 1000°F	277
160	Surface Finish of 25-Percent NiCr + 75-Percent Cr_2O_3 Coating During 1000-Cycle Start-Stop Test at 1000°F	279

LIST OF ILLUSTRATIONS (cont'd)

Figure		Page
161	Surface Appearance of 25-Percent NiCr + 75-Percent Cr_2O_3 Coating During 1000-Cycle Start-Stop Test at 1000°F	280
162	Coating Boundary and Surface Appearance at Start of Endurance Spin Test	283
163	Coating Boundary and Surface Appearance After 249 Hours of Endurance Spin Test	284
164	Coating Boundary and Surface Appearance After 751 Hours of Endurance Spin Test	285
165	Test Rig Shaft and Pads After Sustained Sliding Seizure at 50,000 rpm	288
166	Cr_2O_3 Coated Pad Surface After Thrust Bearing Instability Induced Shaft Seizure at 45,000 rpm	289
167	Assembly of Bearing Element Test Rig	292
168	Bearing Element Test Rig (Schematic of Rig Supply System)	294
169	Bearing Element Test Rig (Schematic of Instrument Locations)	295
170	Components for Bearing Element Test Rig	296
171	Rotor and Turbine Wheel for Bearing Element Test Rig	297
172	Three-Pad Bearing for Bearing Element Test Rig	297
173	Single Test Pad Attached to Loading Mechanism	298
174	Assembled Test Rig	299
175	Control Panel and Instrumentation for Bearing Element Test Rig	299
176	Surface of Journal Bearing Pad Showing Instrumentation for Measurement of Film Thickness	300
177	Pivot Seat and Reverse Side of Journal Bearing Pad	300

LIST OF ILLUSTRATIONS (cont'd)

Figure		Page
178	Single Journal Pad Test Results at 25,000 Feet, Flight-Idle Conditions	301
179	Single Journal Pad Test Results at 25,000 Feet, 50-Percent Power Conditions	302
180	Single Journal Pad Test Results at 25,000 Feet, 75-Percent Power Conditions	303
181	Surface of Hybrid Thrust Bearing Showing Instrumentation for the Measurement of Film Thickness	307
182	Examples of Hydrodynamic Thrust Bearing Instability	308
183	Schematic of Stability Analysis Model	309
184	Calculated Thrust Bearing Stability Map - Original Test-Rig Configuration	311
185	Calculated Load Capacity of Various Thrust Bearing Groove Geometries	314
186	Calculated Thrust Bearing Stability Map Showing Effect of Groove Geometry on Range of Stable Operation	315
187	Calculated Thrust Bearing Stability Map for Final Modified Thrust Stator at Sea Level, 100-Percent Power Conditions	315
188	Test Rig Thrust Bearing Flexible Mount	318
189	Surface of Modified Thrust Bearing	320
190	Thrust Bearing Load Capacity at Zero Speed	321
191	Thrust Bearing Load Capacity at 40,000 rpm	323
192	Thrust Bearing Load Capacity at 45,000 rpm	323
193	Thrust Bearing Load Capacity at 48,200 rpm	323
194	Effect of Speed on Bearing Load Capacity	324
195	Thrust Bearing Load Capacity at 45,000 rpm	325
196	Thrust Bearing Pressure - Speed Envelope	327
197	Program Structure	346

LIST OF TABLES

Table		Page
I	Efficiency Correlation - Small Centrifugal Compressors	11
II	Configuration Design Speeds	39
III	Estimated Engine Weights	47
IV	Estimated Polar Moments of Inertia	48
V	Critical Speeds and Static Bearing Loads of Various Configurations of a 5.0 lb/sec Engine	64
VI	Critical Speeds and Static Bearing Loads of Various Configurations of 3.5 and 2.0 lb/sec Engines	67
VII	Maneuver-Induced Thrust Bearing Loads	91
VIII	Rating of Component Combinations	98
IX	Values of Product Efficiency for the Four Configurations With Best Performance	101
X	Maximum Resulting Bearing Loads for C_o-T_2 and C_o-T_o Configurations at Flight Idle Conditions	102
XI	Air Bearing Engine Leakage and Bleed Summary	108-109
XII	Engine Design Point Values - 3.5 lb/sec	110
XIII	Air Bearing Engine Design Table	114-115
XIV	Effect of Journal Bearing Supply Control on Leakage Rates	117
XV	Accessory Drive System Effect on Engine Performance	126
XVI	Schedule of Ambient Pressures and Temperatures Used for Journal Bearing Calculations	129
XVII	Schedule of Maximum and Steady-State Loads for Journal Bearing Calculations	130
XVIII	Properties of 3 Candidate Bearing Materials	166
XIX	Aerodynamic Thrust Loads	170

LIST OF TABLES (cont'd)

Table		Page
XX	Temperature of Bearing Regions----------	221
XXI	Effects of Stress on Friction and Surface Damage Characteristics of Various Coating Combinations------	225
XXII	Thermal Cycle Test Results (in Air)----------	228
XXIII	Results of Screening Start-Stop Sliding Tests (Titanium Substrate)----------	247
XXIV	Results of Screening Start-Stop Sliding Tests (Waspaloy Substrate)----------	248
XXV	High-Speed Coating Bond Strength Test Inspection Log-	265
XXVI	High-Speed Coating Bond Strength Test Inspection Log-	266
XXVII	High-Speed Coating Bond Strength Test Inspection Log-	267
XXVIII	750-Hour Endurance Test Inspection Log----------	282
XXIX	Effect of Journal Bearing Design Changes on Pad Film Thickness at Engine Idle, 25,000 Feet Altitude, and Maximum Maneuver Load Conditions----------	305
XXX	Influence of Grooving on Critical Inertia----------	313
XXXI	Final Modified Thrust Stator Design----------	317
XXXII	Operating Conditions for Sample Case----------	352
XXXIII	Surface Pattern----------	352
XXXIV	Complete Program Input----------	354
XXXV	Input Bearing Film Characteristics----------	355
XXXVI	Dynamic Stability Analysis Results----------	356

INTRODUCTION

Future small gas-turbine power plants for the U.S. armed services will require improved performance in terms of higher power-to-weight ratio, smaller size, lower specific fuel consumption, improved reliability, and decreased vulnerability. The numerous end-item applications for these power plants will include turboshaft engines for turboprop aircraft and helicopters, jet and fan-jet aircraft engines, aircraft APU's, ground vehicle engines, electrical power generating sets, engines for small boats, pipeline pumps, and ground effect machines.

To attain the desired performance improvements for these power plants, simultaneous increases in engine operating pressures and temperatures will be required. These ascending performance conditions, with accompanying high rotational speeds, will impose increasingly severe operating requirements on main-engine bearings and seals — – to the point where conventional, oil-lubricated bearing systems may not be practical. If this should be the case, new lubrication methods will be required. One such method is the air-lubricated (gas) bearing. This report presents the Phase I results of a comprehensive investigation to determine the applicability of air bearings to small (2 to 5 lb/sec air flow) gas-turbine engines.

One of the major problems confronting the use of mainshaft rolling-element bearings in future small engines is cooling of the lubricating oil. In many current and past engine designs, the engine fuel has been effectively used as the coolant for the oil. However, as engine pressure ratios and turbine inlet temperatures continue to increase, the attendant reductions in specific fuel consumption (SFC) will reduce the availability of fuel flow for heat sink purposes. To further aggravate the situation, the heat load on the oil cooler will increase as a consequence of increased heat transfer into the bearing cavities due to the higher cycle temperatures, and increased bearing and seal losses resulting from the higher operating speeds (higher DN values). The effect of both reduced SFC and increased heat load will be an increase in the temperature of the fuel leaving the fuel/oil cooler. Higher cooler-exit fuel temperatures, however, will result in fuel coking problems. In small engines where the propensity for fuel coking currently exists, air/oil coolers are being used to supplement the fuel/oil coolers. This leads to additional complexity, weight, and vulnerability.

An additional effect of reduced SFC and increased heat load will be an increase in lube oil temperatures unless both the flow rate of the oil and the size of the cooler are greatly increased. Current aircraft engine oils are limited to bulk temperatures of 350°F to 400°F for continuous recirculating duty. New lube oils have been developed for limited recirculating service up to 600°F in an oxidizing environment. Further development may extend the capability of these oils to 700°F. However, problems of cost, logistics, and noninterchangeability with existing oils would have to be resolved before these special oils could be used on a widespread basis.

"PRECEDING PAGE BLANK-NOT FILMED."

Several other problems associated with lube-oil systems can be cited. In recent years, considerable attention has been paid to the vulnerability of aircraft systems to small-arms fire. Lubrication systems for gas-turbine engines are particularly vulnerable to this threat. The lines, fittings, coolers, and sheet-metal reservoirs can be easily damaged by small arms or fragment hits, and may cause engine failure within minutes.

Design of an "all-attitude" lube-oil system is likewise a difficult task. If operation of the engine is required in an inverted or a noseup or nose-down attitude, a complex reservoir and scavenge system is dictated.

Finally, the weight and volume of current small engine lubrication systems represents a substantial proportion of the engines' auxiliary components. Cost of development, manufacture, and field servicing of this equipment is also far from insignificant.

In contrast to oil-lubricated bearings, air bearings have the intrinsic capability of being able to use high-temperature engine air as the lubricating fluid. Accordingly, if mainshaft rolling-element bearings, with their associated seals and lube-oil system, could be successfully replaced by air bearings, all of the above-mentioned problems would be substantially eliminated. Air bearings, of course, will have their own set of development and operational problems relative to aircraft gas-turbines. However, if these problems can be solved, air bearings offer an inherent simplicity and high reliability which would be a major improvement over present bearing systems.

Since the early 1960's, gas-lubricated bearings have been successfully applied to various types of high-speed machinery: turbocompressors, turbo-alternators, turbocompressor-alternators, motor-driven compressors, air-cycle machines, and cryogenic expanders. With the exception of the air-cycle application, all of these machines are being used in special closed-loop installations where the cycle working fluid is also used to lubricate the bearings. However, the environmental conditions under which these machines operate are much less severe than those encountered in open-cycle military engine applications. For example, an aircraft engine must be able to operate during aircraft maneuver conditions specified in MIL-E-5007C. These maneuver conditions result in much greater unit bearing loads than encountered in previous gas-bearing applications. Furthermore, the load-carrying capability of the air bearings is strongly affected by the wide range of engine speeds and pressures associated with engine operation from flight-idle to maximum power, and from sea-level to maximum altitude. Not only are the engine bearing loads and operating ranges greater than exist for present-day gas-bearing machinery, the air-bearing surface velocities and operating temperatures projected for the 1975 (and later) time-frame aircraft engines will be significantly higher.

In 1968, a study entitled "Feasibility of Gas Bearings for Small High-Performance Aircraft Gas Turbines" was reported in USAAVLABS Technical

Report 68-87 [1].* To the extent that a quantitative analytical assessment could be made, the study showed that air lubrication of small high-performance engines was potentially feasible. There were, however, several areas where feasibility could not be fully assessed due to lack of advanced analytical techniques and lack of sufficient test data. These areas were: (1) rotor-bearing system stability, (2) durability of the bearing structural and coating materials, and (3) experimental verification of the ability of air-bearing components to carry the high operating loads imposed by aircraft maneuver conditions.

The objective of the current investigation is to complete the basic air-bearing feasibility assessment in the three areas mentioned above. In addition, a more detailed understanding of the design and performance characteristics of small air-lubricated gas-turbine engines is being obtained. The investigation is being conducted in two major phases; this report presents the results of the Phase I effort. The emphasis in Phase I was the identification of design and performance characteristics of air-bearing engines in the 2 to 5 lb/sec air-flow range, experimental testing of candidate bearing strucutral and coating materials, and load capacity testing of the key bearing elements.

During Phase II of the investigation, a full-scale rotor-bearing system test rig will be built and tested to experimentally evaluate rotor-bearing system dynamics, heat transfer and thermal distortion control, and bearing system performance under gyroscopic and dynamic load conditions.

PROGRAM PLAN

Figure 1 shows the network diagram for the Phase I effort of the investigation. Phase I consisted of 17 tasks which were grouped into three major activity areas as denoted below, and also on Figure 1:

1. Tasks 1 through 6: Design effort (identification of viable rotor system arrangements and bearing system design concepts for 2 to 5 lb/sec flow-rate engines; detailed rotor-bearing system design for one selected engine size; design of a full-scale rotor-bearing system dynamic simulator)

2. Tasks 7 through 12: Test evaluation of candidate bearing materials

3. Tasks 13 through 16: Test-rig evaluation of the load capacity of key bearing components.

During the Phase I effort, Pratt and Whitney Aircraft (Florida Research and Development Center) made major contributions to, or had primary

*Numbers in brackets refer to similarly numbered references listed in the LITERATURE CITED section at the end of this report.

responsibility for, eight of the Phase I tasks as identified below:

Task 1: Initial Sizing Studies

Task 2: Selection of Engine Size

Task 3: Final Component Sizing

Task 4: Integrated Engine Design

Task 7: Selection of Candidate Bearing Materials

Task 9: Cyclic Coating Bond Strength Tests

Task 12: Endurance Coating Bond Strength Test

Task 17: Phase I Report

The significant contributions and involvement of P&WA give assurance that the air-bearing investigation is being conducted within the proper constraints of aircraft engine design and application. Furthermore, P&WA is highly qualified to provide the aerodynamic flow-path and engine performance data, and to make overall judgments as to the desirability and practicability of the air-bearing approach. These judgments will be provided in the Phase II report at the conclusion of the investigation.

This report is organized much along the line of the Program Plan shown in Figure 1. The first four major report sections cover the first six tasks of the "Rotor System Arrangements and Bearing System Design" effort. The fifth major section, entitled "Evaluation of Bearing Materials", covers Tasks 7 through 12, all of which were concerned with materials tests. The final section, concerning bearing component tests, covers the work performed under Tasks 13 through 16. Final conclusions and recommendations are presented in the last section of the report.

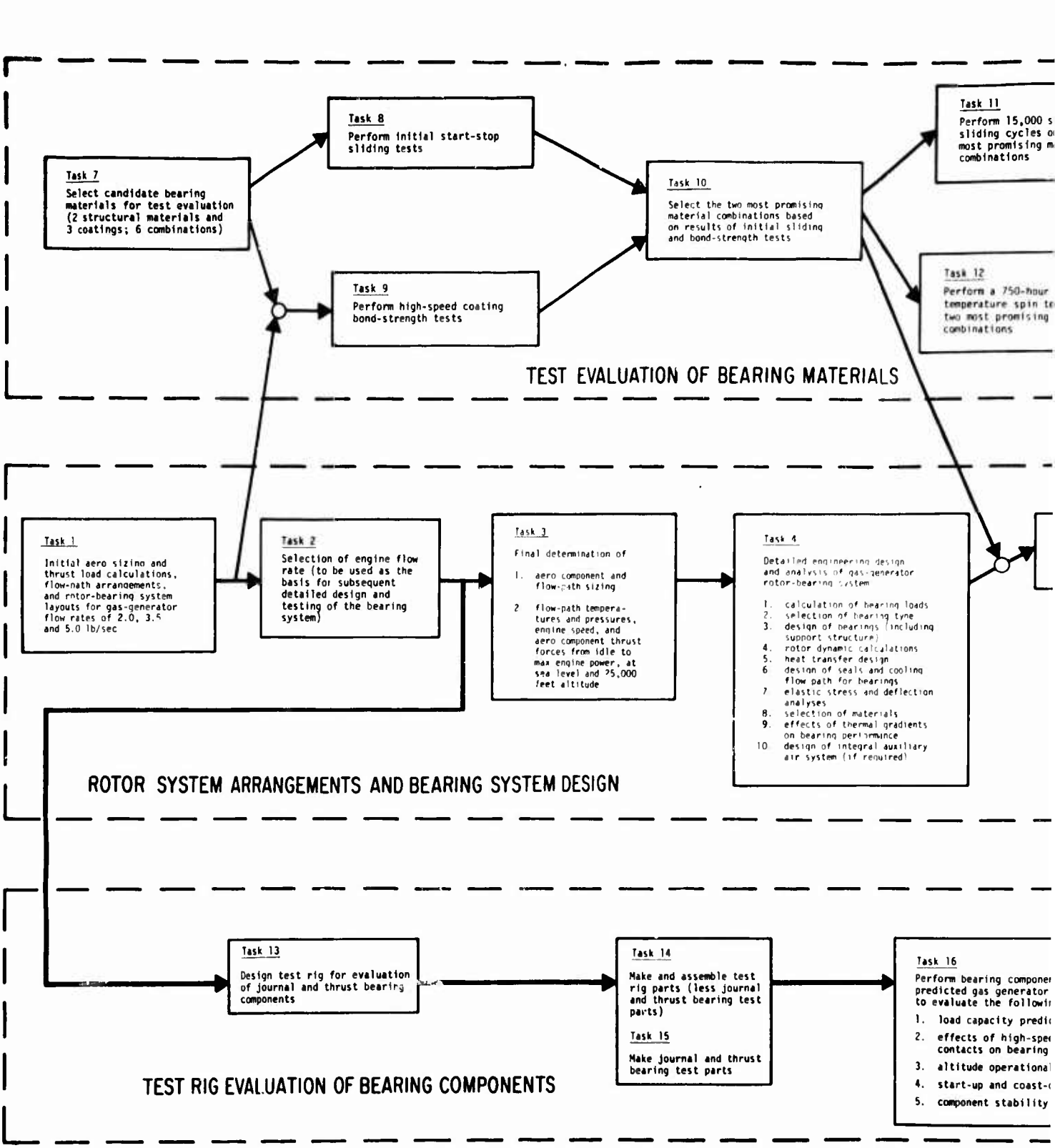
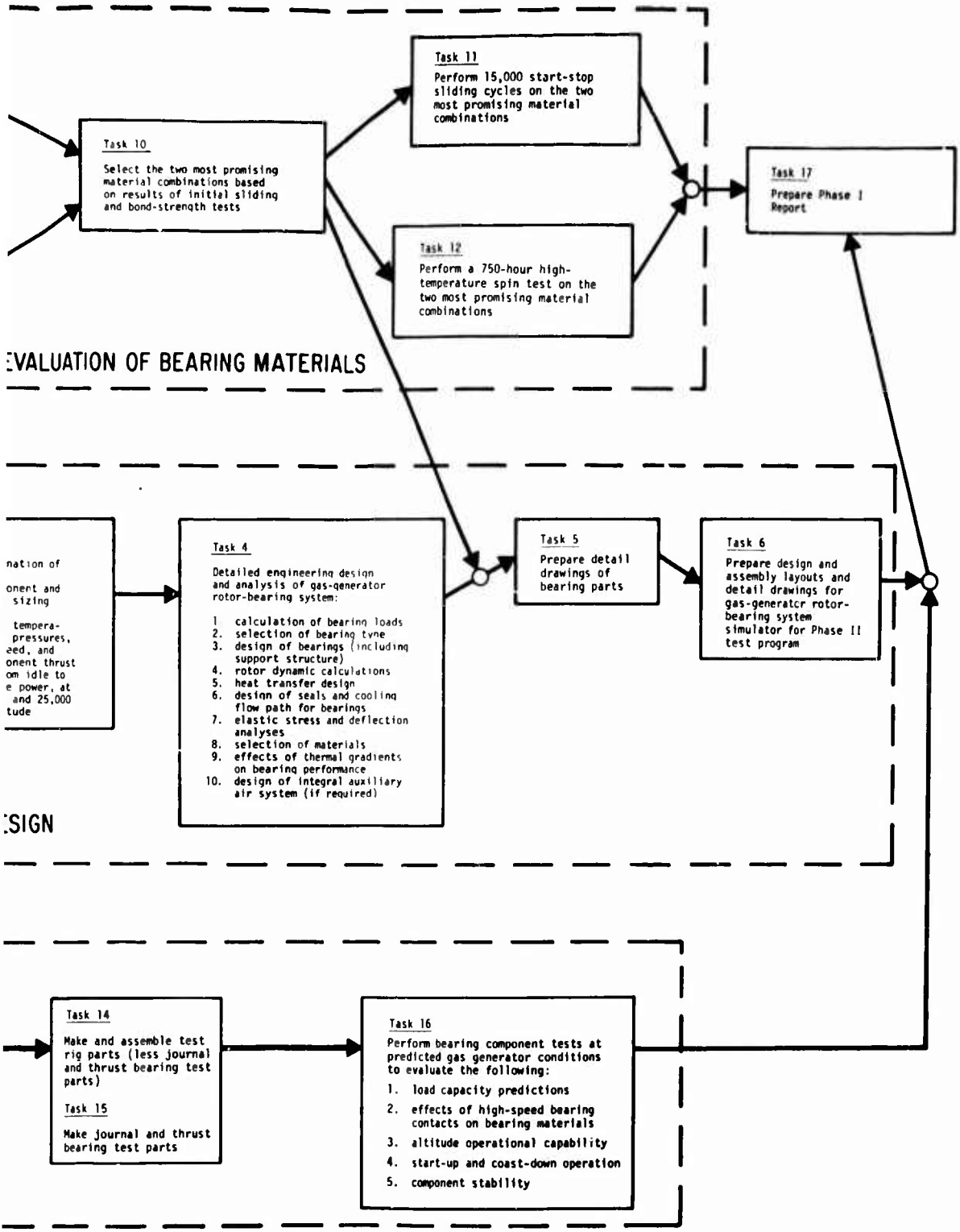


Figure 1. Investigation of Air Bearings for Gas Turbine Engines; Phase I — Design and Component Testing.



ngs for
I – Design

PRELIMINARY ENGINE SIZING AND CONCEPT STUDIES

The initial effort in the investigation of air bearings for gas-turbine engines was a quantitative evaluation of the effects of engine size and configuration on the performance of the bearings. In order to accomplish this end, Pratt and Whitney Aircraft (FRDC) provided data which described the performance and the physical dimensions for three engine sizes: 2.0, 3.5, and 5.0 lb/sec flow rate. The other cycle parameters, common to all three sizes, were compressor pressure ratio 17.5 to 1, turbine inlet temperature 2550°F, and engine speed 50,000-75,000 rpm. Nine combinations of axial and radial flow compressors and turbines were evaluated for each engine size. The abbreviated terminology used to describe these combinations is listed below. These abbreviations are used throughout this report.

Component	Abbreviation Used	Component Type and Number of Stages	
		Axial Flow	Radial Flow
Compressor	C_o	0	2
Compressor	C_1	1	1
Compressor	C_2	2	1
Turbine	T_o	0	1
Turbine	T_1	1	0
Turbine	T_2	2	0

Thus, the configuration described by the abbreviation C_o-T_o consists of a two-stage radial-flow compressor and a single-stage radial-flow turbine.

Based on the flow-path layouts, estimates of component weights and inertias, and estimates of rotor thrust loads provided by P&WA, rotor-bearing concept drawings were prepared. These drawings showed the relative positions of compressors, turbines, and bearings for each of the three engine sizes and for many of the most promising arrangements of the various component types under consideration. These concept drawings provided the basis for calculations of critical speed and bearing loads necessary for the quantitative evaluation of the effects of size and configuration on bearing performance.

During the period when performance was being evaluated, P&WA prepared a number of concept drawings showing the various engine flow-path configurations. Also prepared were concept drawings showing suitable combustors. Throughout the engine sizing studies, consideration was given to the feasibility of using a front-drive power turbine. To conclude the initial effort, P&WA performed an evaluation of the relative cost, durability, and performance of the various configurations. The results of this evaluation, and the data describing the effects of engine size and configuration on the performance of air bearings, were used as a basis

"PRECEDING PAGE BLANK-NOT FILMED."

for selecting the engine size and configuration for further study. The results of the preliminary engine sizing and concept studies (basically the Task 1 effort) are presented in this section.

ENGINE DESIGN GOALS

The design goals for the single-shaft gas generator incorporating air bearings are as follows:

a. Flow Rate — 2 to 5 lb/sec*

b. Cycle parameters at sea level, 100-percent power

Compressor pressure ratio	17.5:1
Turbine inlet temperature	2550°F
Rotor speed	50,000-75,000 rpm

c. Operating environment — MIL-E-5007 C
(Altitude limited to 25,000 feet)
(Dusty environment to be considered)

d. Lubrication system — Air only
(Any required air pressurization system to be integral with the engine)

e. Design life of bearing system — 5000 hours

f. Operating life schedule

Total life (percent)	Power Setting (percent)
15	100
45	75
25	55
10	35
5	Idle

g. Start-up requirements — Three per hour of total life; half of these will be cold starts.

*Task 1 study covered a size range from 2 to 5 lb/sec for the gas generator. Based on this study, a particular flow value was selected for the balance of the study, as is discussed later.

h. Overload conditions (speed, temperature and load)	Safe operation at 120 percent power for 1 minute
i. Overspeed conditions	Safe operation at 120 percent speed

THERMODYNAMIC ANALYSIS

The purpose of the thermodynamic analysis of the engine components (compressor and turbine) was to establish predicted component performance levels for the 1975 time period and to define the relationship between component efficiency and speed. This data was used to determine, strictly from a performance standpoint, the optimum speed for each candidate engine configuration. That is, the performance study was not constrained by bearing or shaft critical speed considerations.

The predicted performance levels (efficiency, stage loading, cooled turbine) were obtained by establishing current state of the art for each component and extrapolating to the 1975 time period using goals of present technology programs and the rate of growth in recent years as guides.

Compressor Performance

The compressor requirements for this study were:

Flow rate - 2.0, 3.5, and 5.0 lb/sec
Overall pressure ratio - 17.5:1

The required compression ratio could be obtained with several combinations of axial and centrifugal stages. In general, these combinations can be grouped into three broad categories: all centrifugal stages, all axial stages, or combinations of axial and centrifugal stages. For the required pressure ratio, a single-stage centrifugal is not feasible even with the most advanced technology foreseeable.

A two-stage centrifugal compressor is considered feasible for a pressure ratio of 17.5, even with present-day technology. All that is required is the selection of rotor speed and the work split between stages to maximize overall efficiency. A three-stage centrifugal compressor could be used. However, there is little if any gain in overall efficiency (at the selected pressure ratio) over a two-stage configuration because additional inter-stage losses, weight, cost and complexity disadvantages more than offset any performance gain. Thus, for an all-centrifugal compressor at a pressure ratio of 17.5, the only practical number of stages is two.

It follows from the above discussion that the axial-centrifugal combination involves only one centrifugal stage preceded by one or more axial stages. The exact number of axial stages depends on the optimum trade-off of centrifugal and axial stage performance as influenced by stage pressure ratio (Mach number), specific speed (disc friction), Reynolds number and

other size effects. These influences depend on the technology levels assumed in the optimization study. However, even with current technology, no more than two axial stages are required.

The third category, the all-axial configuration, was not considered competitive with the other two, particularly for the lower flow sizes. The volumetric flow rate at the exit of an all-axial compressor would be so low that passage heights on the order of 0.1 to 0.2 inch would be required for a flow rate of 2 lb/sec. Even the highest flow rate of 5 lb/sec would require airfoil heights of less than 0.5 inch. Performance would be degraded significantly by tip clearance and airfoil losses caused by manufacturing tolerances and deterioration due to erosion and impact damages.

In summary, three compressor configurations were selected for evaluation in this study:

1. Two-stage centrifugal (C_0)
2. One-stage axial/one-stage centrifugal (C_1)
3. Two-stage axial/one-stage centrifugal (C_2)

The first objective of the compressor thermodynamic study was to determine the pressure ratio split between stages in each configuration that yields the maximum overall compressor efficiency as a function of flow rate and rotor speed. Flow and speed, the two independent variables, were varied over a range of 2-5 lb/sec and 50,000-90,000 rpm respectively.

State-of-the-art efficiency levels of small centrifugal compressors, as a function of pressure ratio, were established by correlating available P&WA, UACL, and Boeing/AMRDL [2,3] test data. All data were corrected to a common total-to-static basis, a specific speed of 90, and a minimum loss diffuser Mach number. Table I shows the compressor data, corrections, and final efficiency values. The correction for specific speeds less than 90 was taken from previous P&WA analytic studies and is shown in Figure 2. Corrections were not made for specific speeds greater than 90 as will be discussed later. An optimum diffuser exit Mach number of 0.25 was set based on P&WA diffuser test data which correlated diffuser pressure loss with diffuser area ratio. For the compressor data where the exit Mach number was less than 0.25, no alterations were made. The results of this correlation are presented in Figure 3 as state-of-the-art (S-O-A) total-to-static adiabatic efficiency as a function of pressure ratio at a specific speed of 90. The projected technology curve of Figure 3 was generated based on a Boeing/AMRDL [2,3] efficiency goal of 80 percent for a 2 lb/sec, 10:1 pressure ratio impeller plus an assumed five-point improvement in S-O-A efficiency at a pressure ratio of 2.5:1. The projected technology curve was used in this study in addition to the curves in Figure 2 which provide corrections for centrifugal compressors having specific speeds less than 90. An additional correction factor was applied to account for Reynolds number and leakage effects as a function of size. Zero correction was applied to the 2.0 lb/sec size, since Figure 3 was generated from data at that approximate flow rate; the efficiencies for 3.5 and 5.0 lb/sec sizes were increased by 1 percent and 2 percent, respectively.

TABLE I. EFFICIENCY CORRELATION - SMALL CENTRIFUGAL COMPRESSORS

Typical Existing Compressors	Flow Rate = 2.0 lb/sec										
	N_{cor} rpm	lb/sec	PR_{T-T}	Mach No. Exit (T-T)	η_{T-T} %	PR_{T-S}	Mach Nc.* Exit (T-S)	η_{T-S} %	Specific Speed N_S	$\Delta\eta$ %	η_{T-S} at N_S = 90
UACL	79,200	1.56	6.0	0.35	82.0	5.81	0.25	80.0	80.0	0.5	80.5
UACL	80,300	1.56	10.0	0.14	72.0	9.864	0.14	71.4	69.9	4.4	75.8
UACL	86,000	1.69	12.0	0.14	69.0	11.84	0.14	68.5	72.3	4.3	72.8
Boeing	50,000	2.20	-	-	-	8.6	Collector Static	69.6	68.2	4.6	74.2
P&WA	25,700	1.95	-	-	-	2.5	0.15	80.0	58.6	3.9	83.9
P&WA	25,240	2.20	2.8	0.15	80.4	2.75	0.15	79.0	54.6	5.0	84.0
P&WA	23,000	2.53	2.13	0.31	83.6	2.038	0.25	78.4	73.2	1.6	80.0

*Total-to-static performance assumed to be constant for exit Mach numbers less than 0.25.

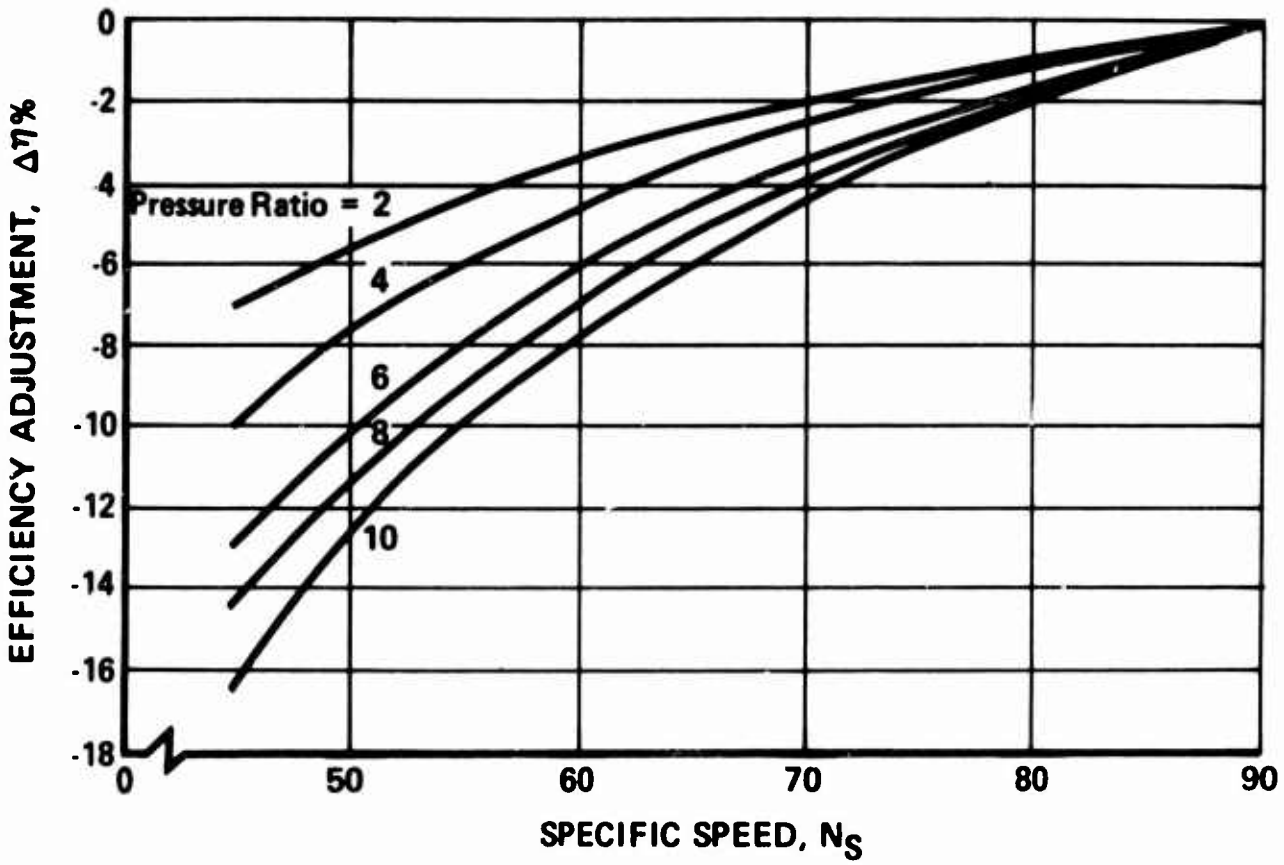


Figure 2. Effect of Specific Speed on Compressor Efficiency.

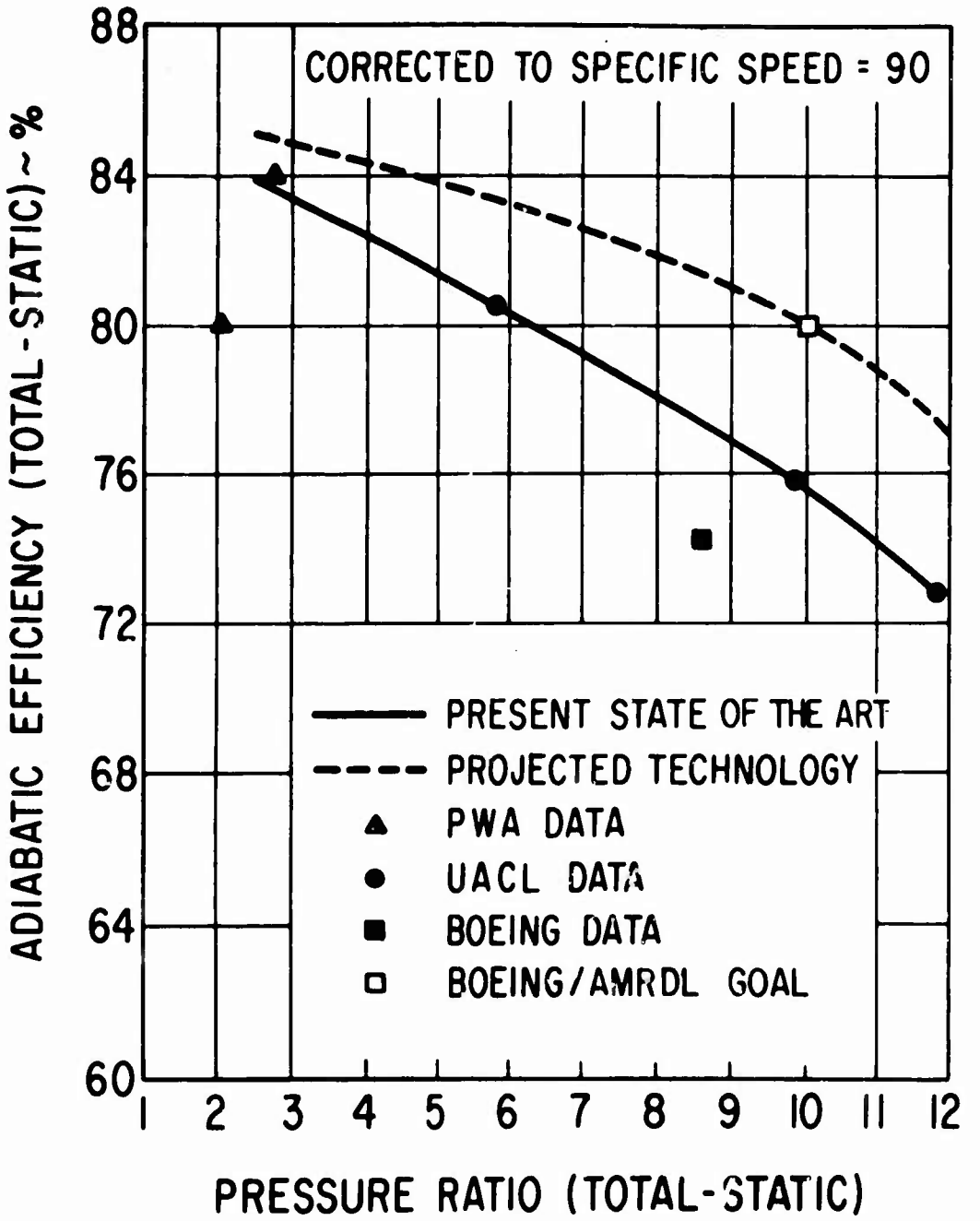


Figure 3. Present and Projected Centrifugal Compressor Efficiency Levels.

The efficiency curves for the axial compressor stages used in this study are shown in Figures 4 and 5. Figure 4 shows adiabatic efficiency as a function of pressure ratio at an air flow size of 3.5 lb/sec. This curve was generated using a constant polytropic efficiency of 88.5 percent up to a pressure ratio of 1.4. Curtiss-Wright data (Ref. 4) were used to establish representative efficiency values for stage pressure ratios around 2.0. The efficiency for intermediate stage pressure ratios, between 1.4 and 2.0, was obtained from a "best estimate" curve between the low and high pressure ratio end points. The curves for 2.0 lb/sec and 5.0 lb/sec shown on Figure 4 are corrected from the 3.5 lb/sec size by minus and plus 1 percent respectively, to account for compressor size effects.

The analysis of the three compressor configurations, at an overall pressure ratio of 17.5, was completed using the stage efficiencies generated in Figures 3 and 5. The analysis involved establishing the effects of pressure ratio split between stages and rotor speed on efficiency for each configuration. The results of the study are presented below.

Two-Stage Centrifugal (C_o)

Overall compressor efficiency as a function of first-stage pressure ratio and rotor speed for flow rates of 2.0, 3.5, and 5.0 lb/sec is plotted in Figures 6, 7 and 8 respectively. For this configuration, an efficiency correction of plus 1 percent was added to the first centrifugal stage. This correction adjusts the first-stage total-to-static efficiency to account for velocity head recovery between stages. Optimum stage-pressure-ratio split as a function of flow rate and rotor speed can be determined from Figures 6, 7 and 8 for the two-stage centrifugal configuration. The dashed lines on Figures 6, 7 and 8 indicate first-stage specific speed values of 90, which has been used as the limit for radial flow impellers. For points to the left of this line at which specific speeds are greater than 90, the first-stage compressors are no longer radial but become mixed flow.

One-Stage Axial/One-Stage Centrifugal (C_1)

Overall compressor efficiency as a function of the pressure ratio across the single-axial stage and rotor speed for flow rates of 2.0, 3.5, and 5.0 lb/sec are shown in Figures 9, 10, and 11 respectively. For this configuration, the optimum pressure ratio split is about 1.85 across the axial stage and 9.46 across the centrifugal stage regardless of the flow rate or rotor speed.

Two-Stage Axial/One-Stage Centrifugal (C_2)

Overall compressor efficiency as a function of pressure ratio across the two axial stages and rotor speed for flow rates of 2.0, 3.5 and 5.0 lb/sec are shown in Figures 12, 13 and 14, respectively. Optimum pressure ratio split as a function of flow rate and rpm can be determined from this curve for the two-stage axial/one-stage centrifugal configuration.

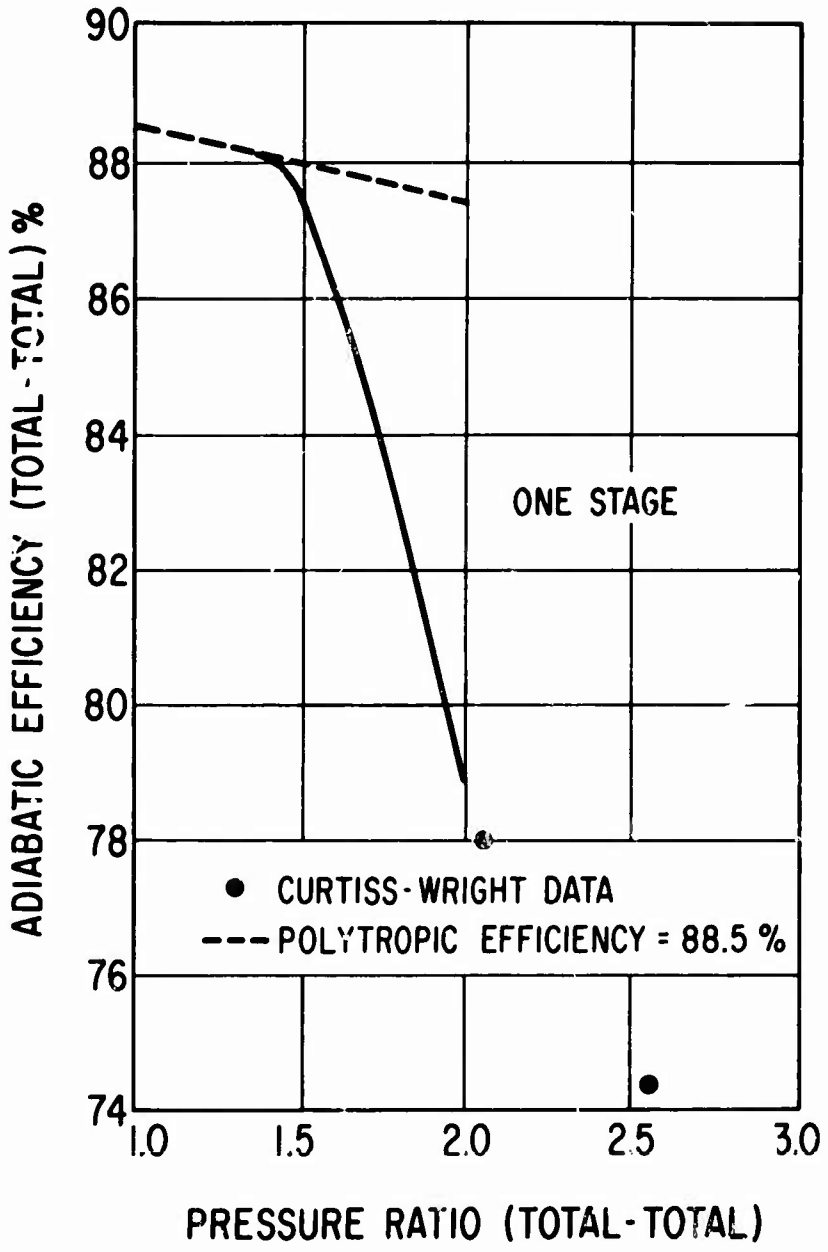


Figure 4. Single-Stage Axial Compressor Efficiency Variation With Pressure Ratio.

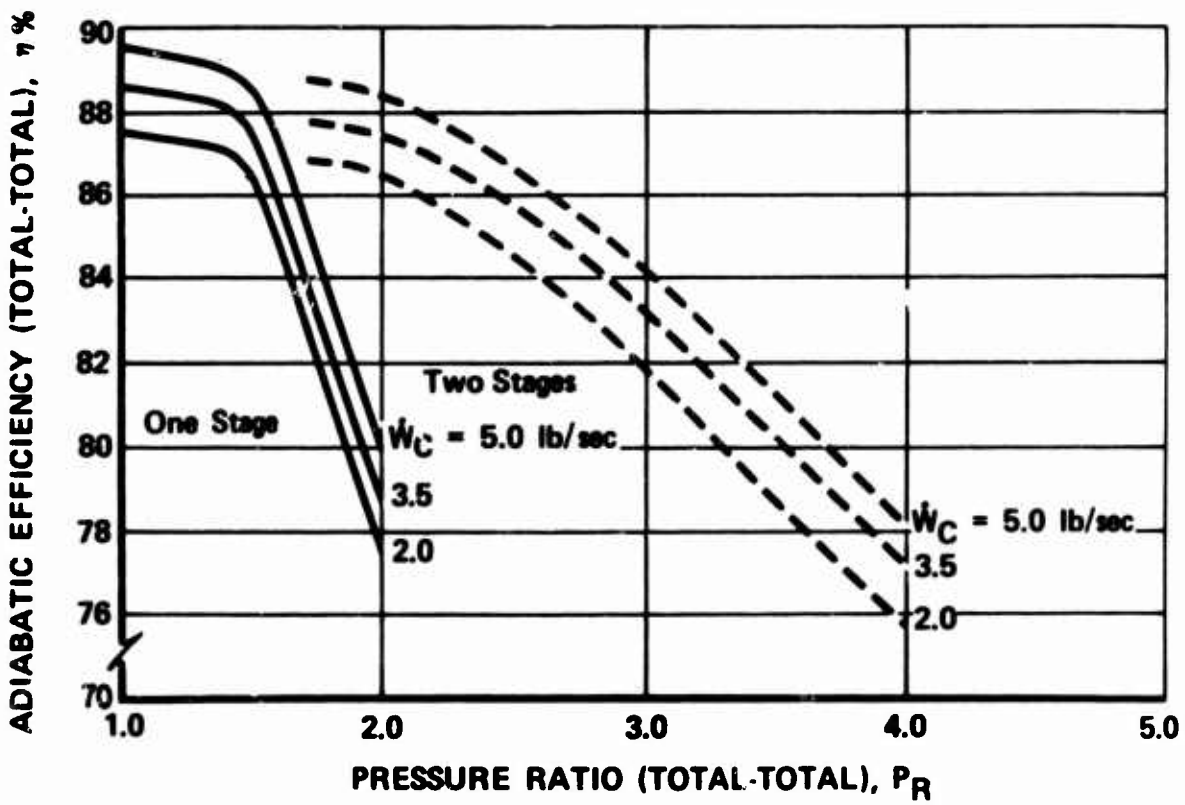


Figure 5. Two-Stage Axial Compressor Efficiency Variation With Pressure Ratio.

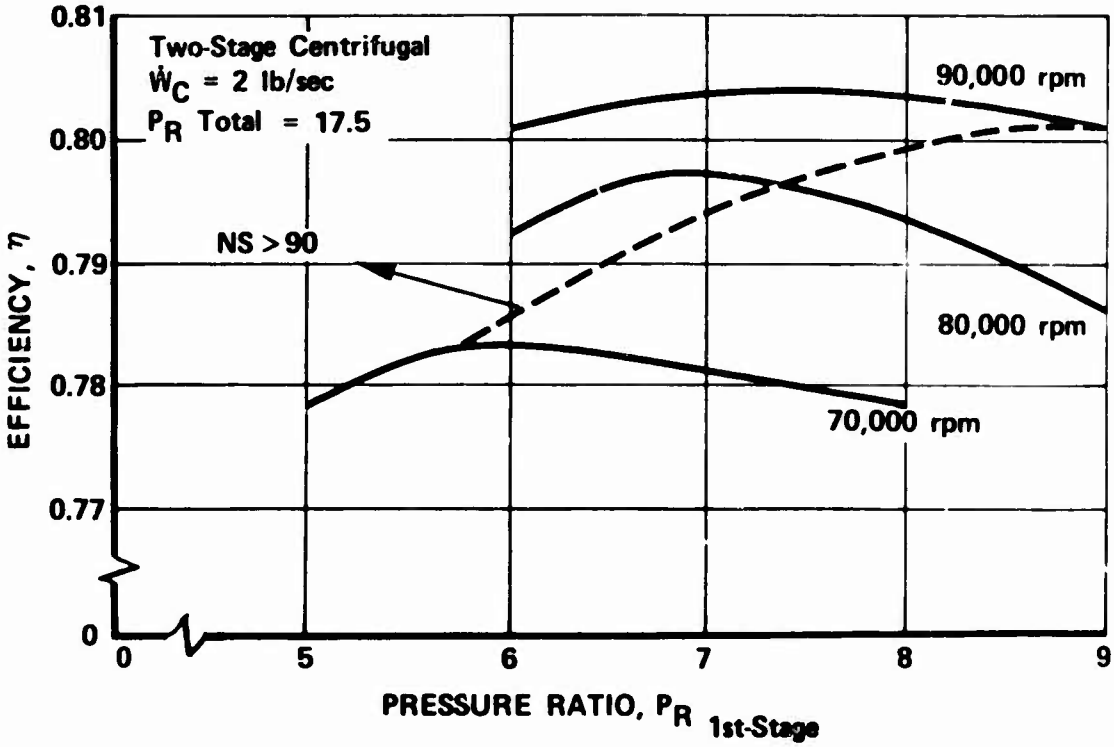


Figure 6. Effect of Pressure Ratio Split on Efficiency; Two-Stage Centrifugal Compressor; 2 lb/sec.

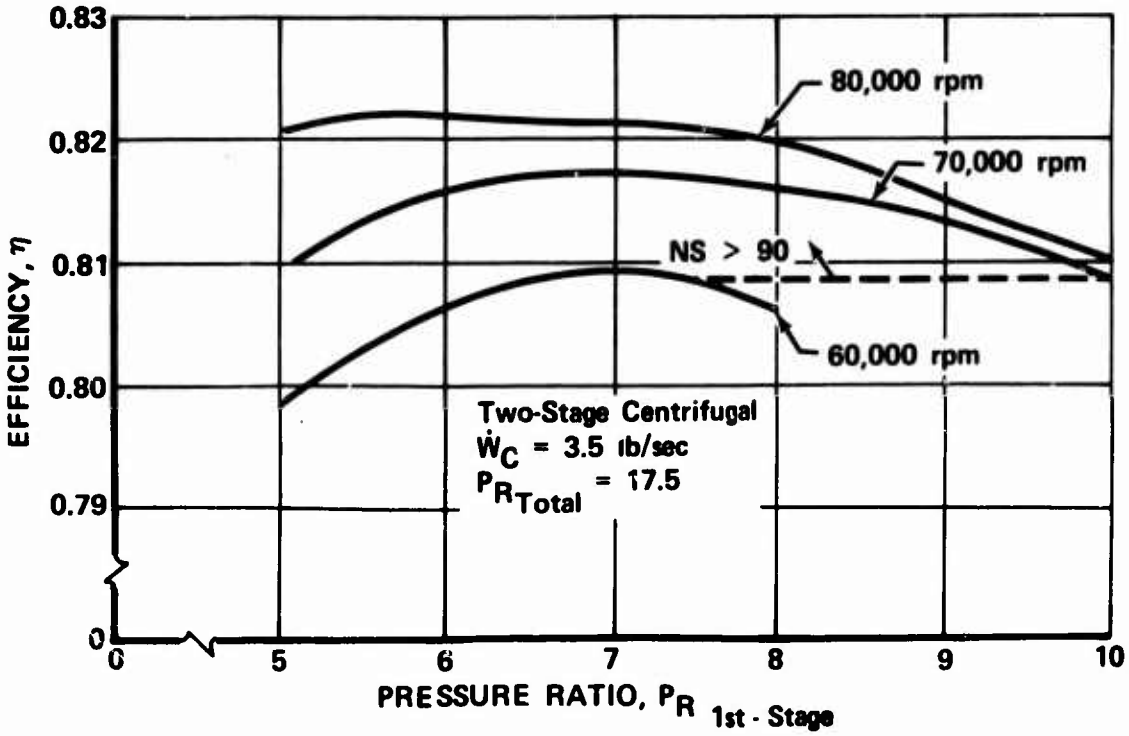


Figure 7. Effect of Pressure Ratio Split on Efficiency; Two-Stage Centrifugal Compressor; 3.5 lb/sec.

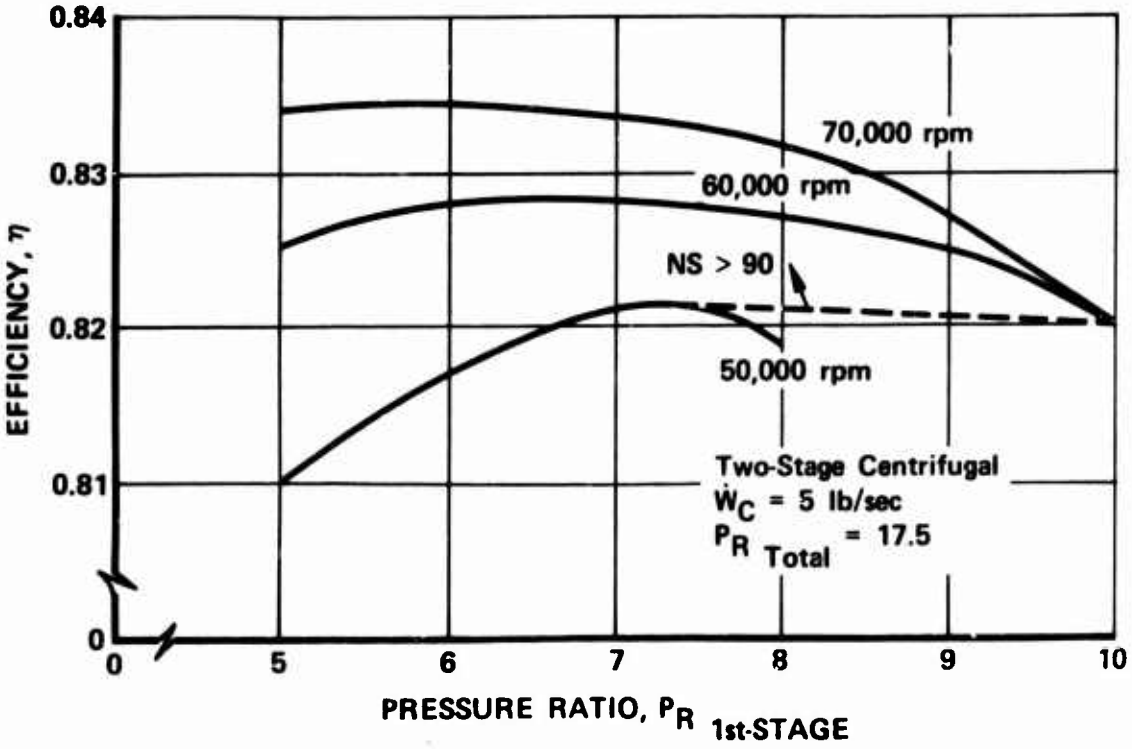


Figure 8. Effect of Pressure Ratio Split on Efficiency; Two-Stage Centrifugal Compressor; 5 lb/sec.

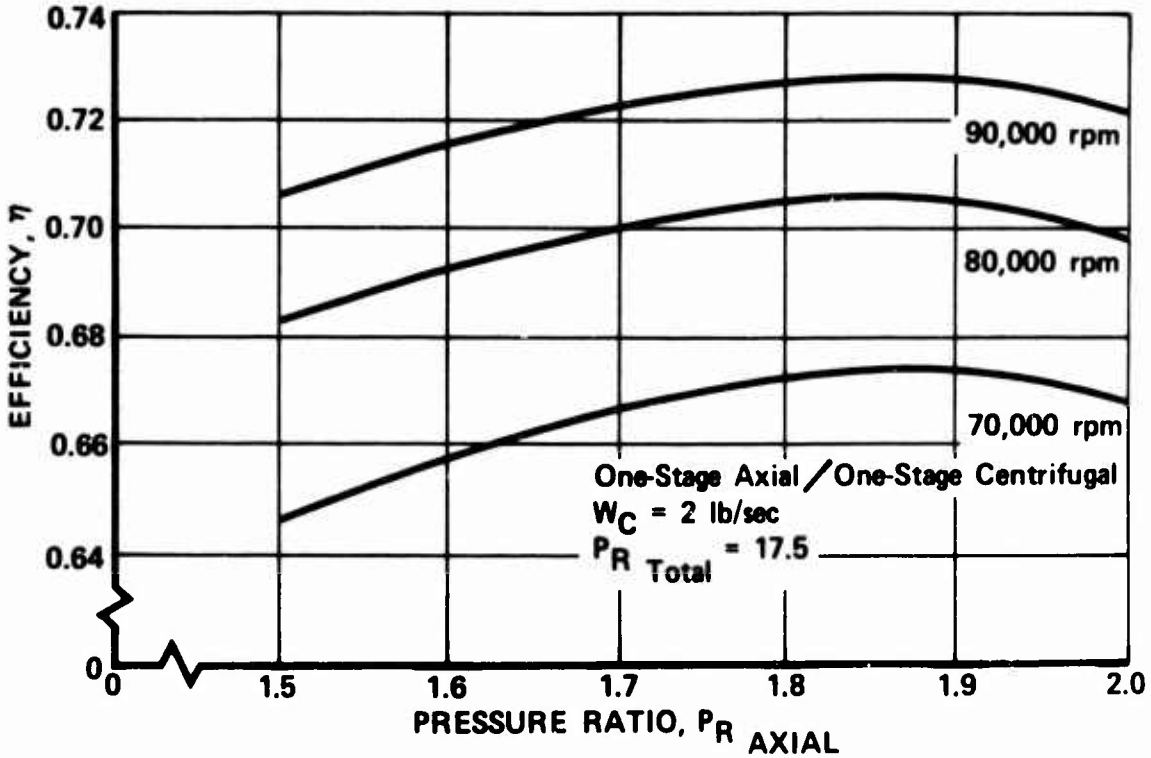


Figure 9. Effect of Pressure Ratio Split on Efficiency; One-Stage Axial/One-Stage Centrifugal Compressor; 2 lb/sec.

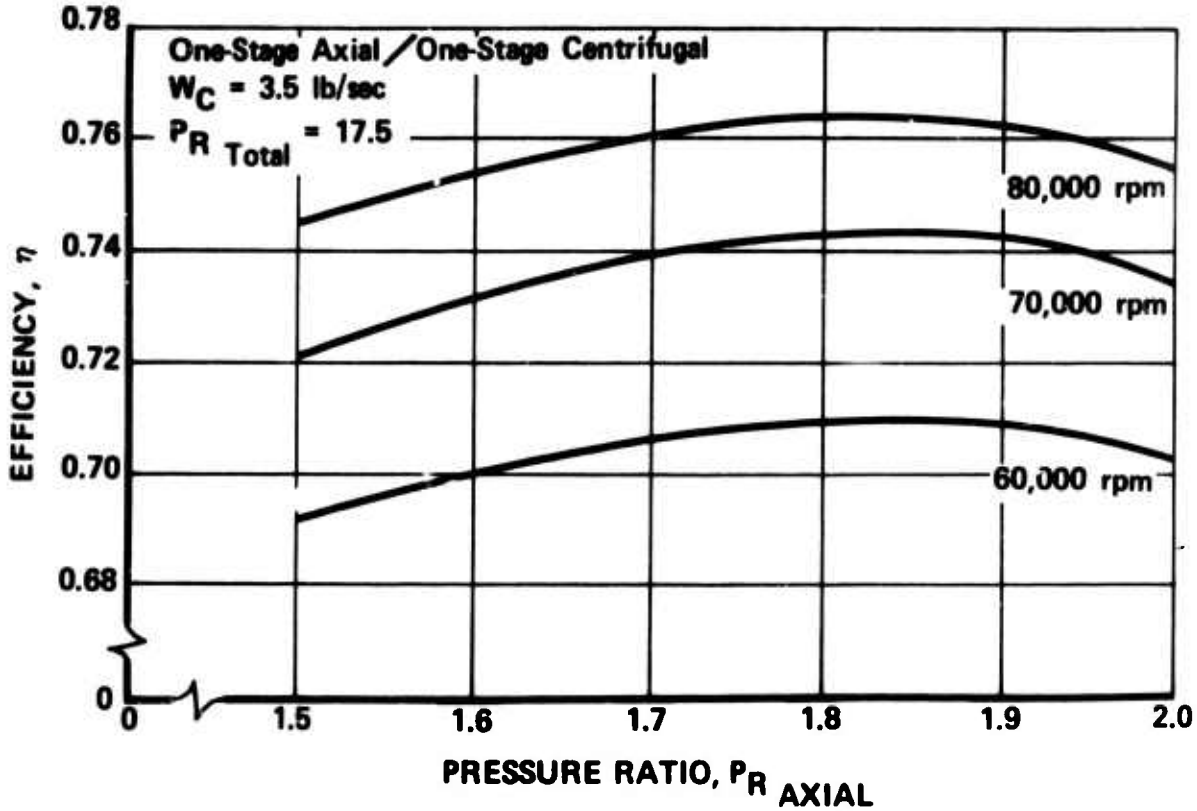


Figure 10. Effect of Pressure Ratio Split on Efficiency; One-Stage Axial/One-Stage Centrifugal Compressor; 3.5 lb/sec.

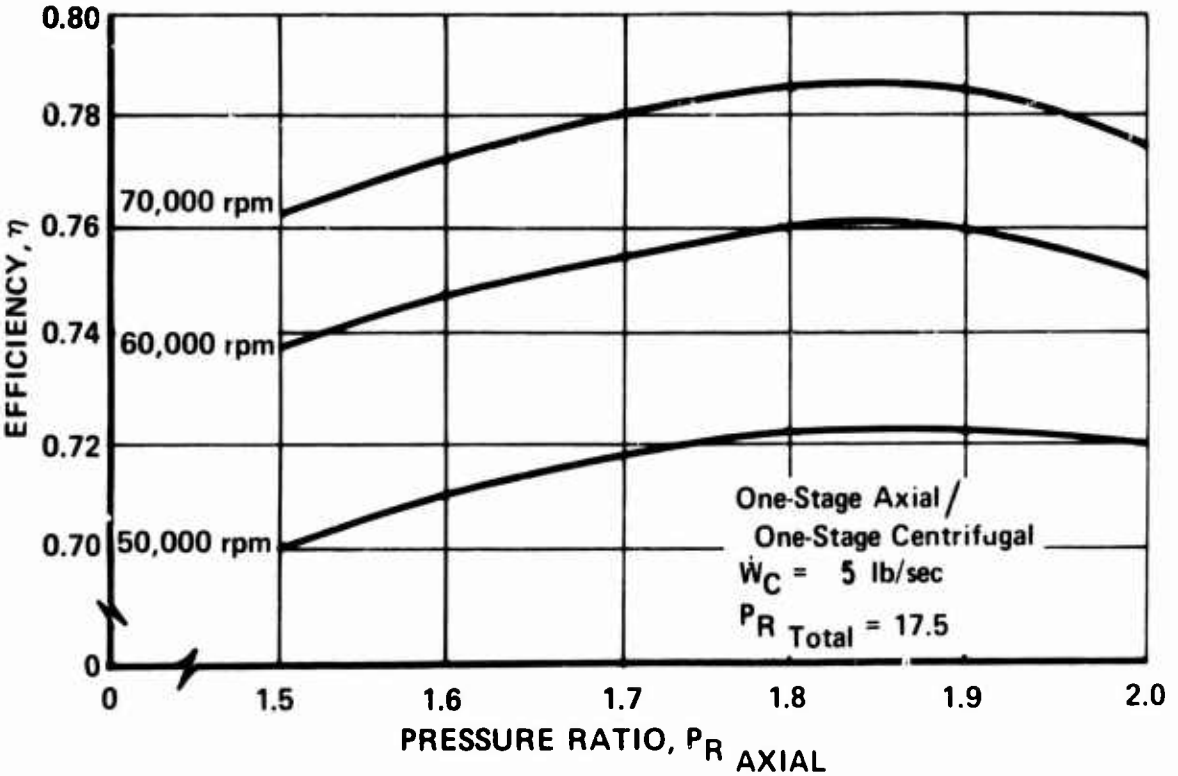


Figure 11. Effect of Pressure Ratio Split on Efficiency; One-Stage Axial/One-Stage Centrifugal Compressor; 5 lb/sec.

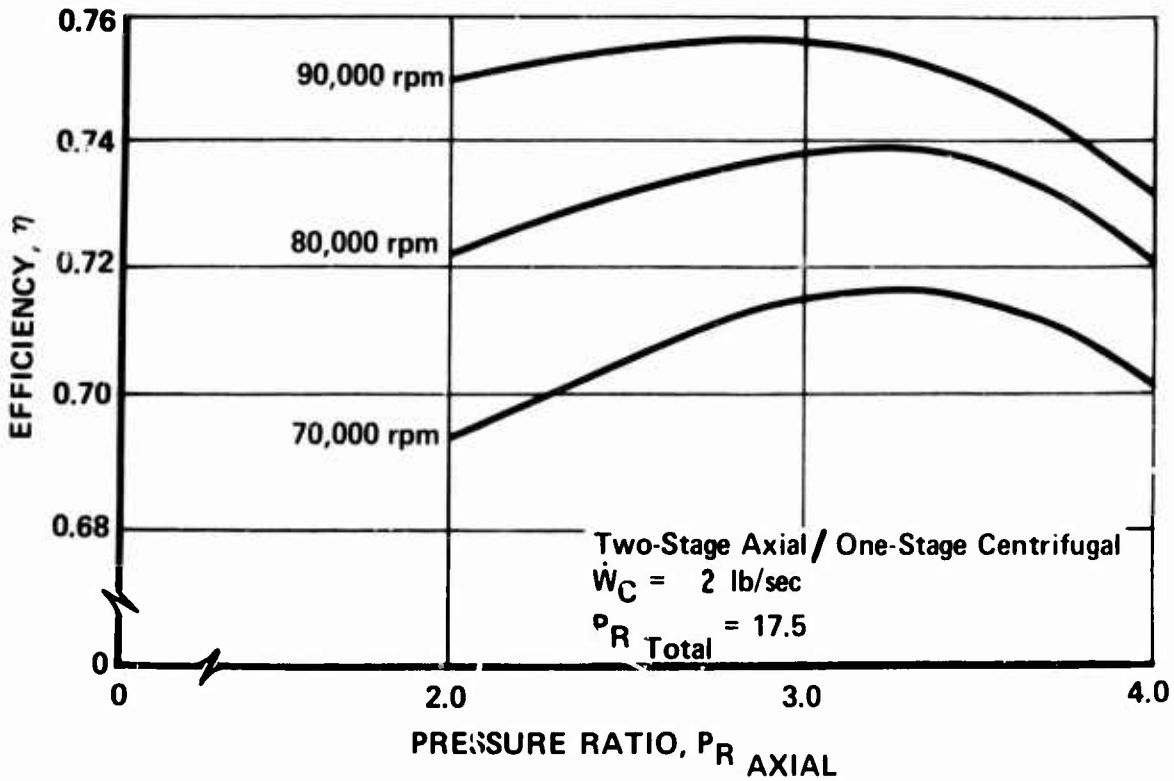


Figure 12. Effect of Pressure Ratio Split on Efficiency; Two-Stage Axial/One-Stage Centrifugal Compressor; 2 lb/sec.

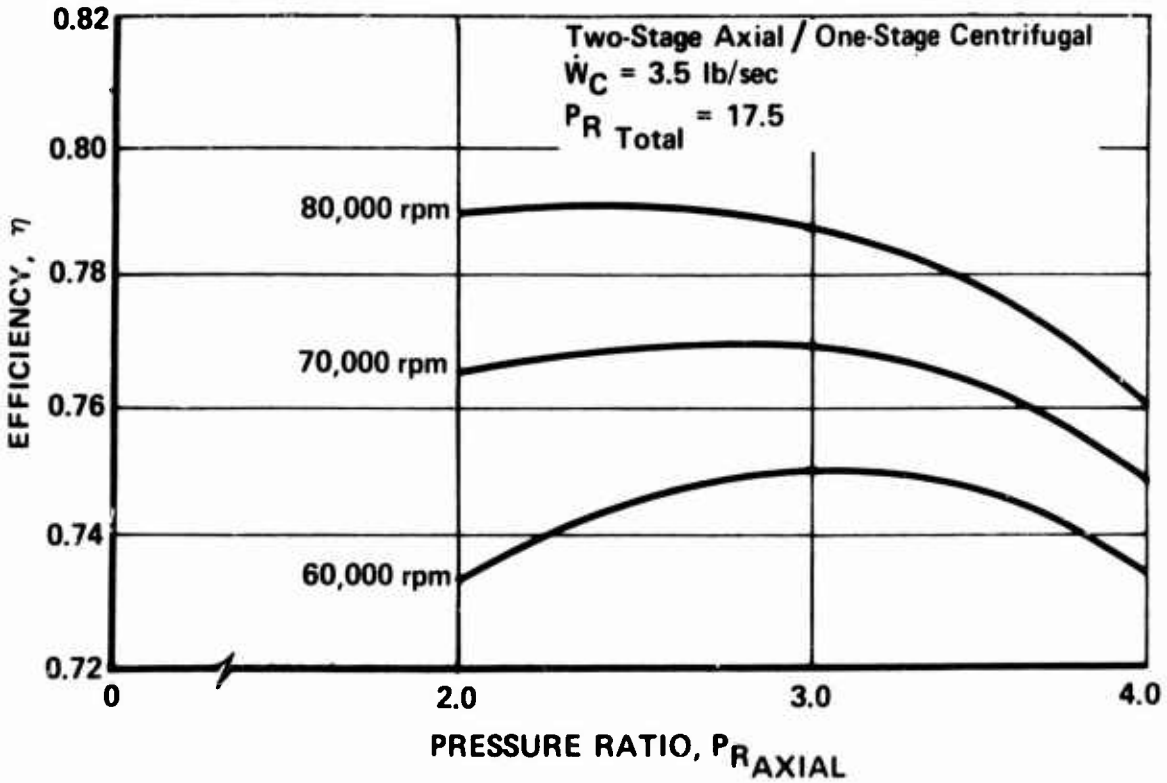


Figure 13. Effect of Pressure Ratio Split on Efficiency; Two-Stage Axial/One-Stage Centrifugal Compressor; 3.5 lb/sec.

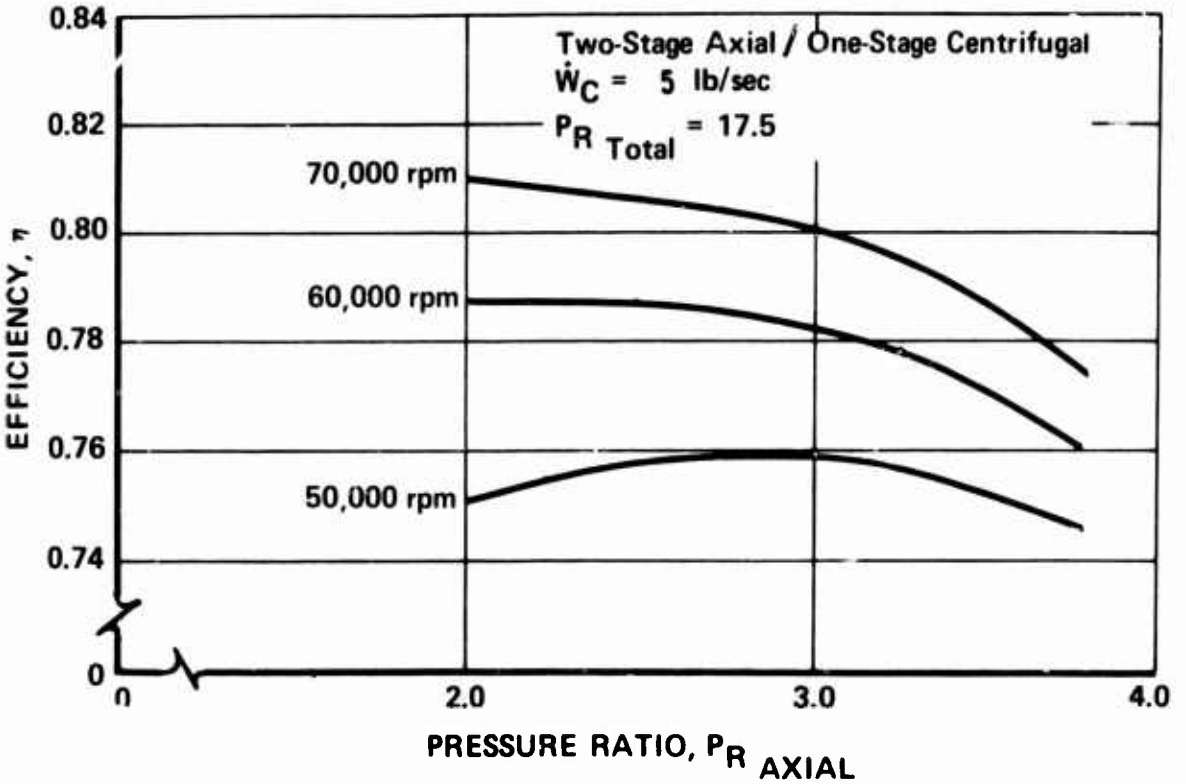


Figure 14. Effect of Pressure Ratio Split on Efficiency; Two-Stage Axial/One-Stage Centrifugal Compressor; 5 lb/sec.

Peak Efficiency vs. RPM

Peak overall compressor efficiency as a function of rotor speed for the three compressor configurations is shown in Figures 15, 16, and 17 for the 2.0, 3.5, and 5.0 lb/sec flow rate sizes, respectively. These curves were generated by cross-plotting the speed, flow rate, and optimum pressure ratio split data from Figures 6 through 14.

The peak efficiency for the two-stage centrifugal configuration occurs in a region, for certain values of rotor speed, in which the first-stage impeller is the mixed flow type. The C_o compressor configuration was limited in rotor speed in this study to avoid mixed flow impellers (specific speed greater than 90) because (a) there was no basic efficiency data available for advanced mixed-flow impellers with pipe diffusers, (b) there is some question whether the level of efficiency shown in Figure 2, and based on radial impellers, could be obtained with mixed-flow impellers due to the pressure gradient (hub to shroud) inherent in their exit flow and the effect of this gradient on collection system performance, and (c) no advanced programs for advanced technology mixed-flow impellers have been reported in the open literature. Analyzing Figures 6, 7, and 8 on the basis of efficiency, rotor speed, and a specific speed limit of 90, it is seen that at 2.0 lb/sec flow rate the limiting speed is 79,000 rpm, at 3.5 lb/sec the limiting speed is 60,000 rpm, and at 5.0 lb/sec the limiting speed is 50,000 rpm. Thus the turbocompressors incorporating the C_o configuration were limited to the above values of rotor speed.

Turbine

The turbine study requirements also included a flow rate range of 2.0 to 5.0 lb/sec and a power output typical of an average compressor efficiency for a pressure ratio of 17.5. The candidate turbine configurations considered were as follows: (designations similar to those used for the compressors were assigned to the turbine configurations)

1. Single-Stage Axial (T_1)
2. Two-Stage Axial (T_2)
3. Single-Stage Radial Inflow (T_o)

The parametric efficiency evaluation consisted of developing a basic component efficiency level and then correcting it, as necessary, to account for airfoil cooling flow and flow-path leakage losses.

Cooling flow losses were particularly significant because, at the level of turbine inlet temperature considered (2550°F), advanced cooling methods must be employed. For the axial turbines, airfoil cooling technology currently being applied in other high-temperature engine designs was assumed. This involved the consideration of impingement cooling, multi-pass convective cooling and film cooling, where necessary, for the various

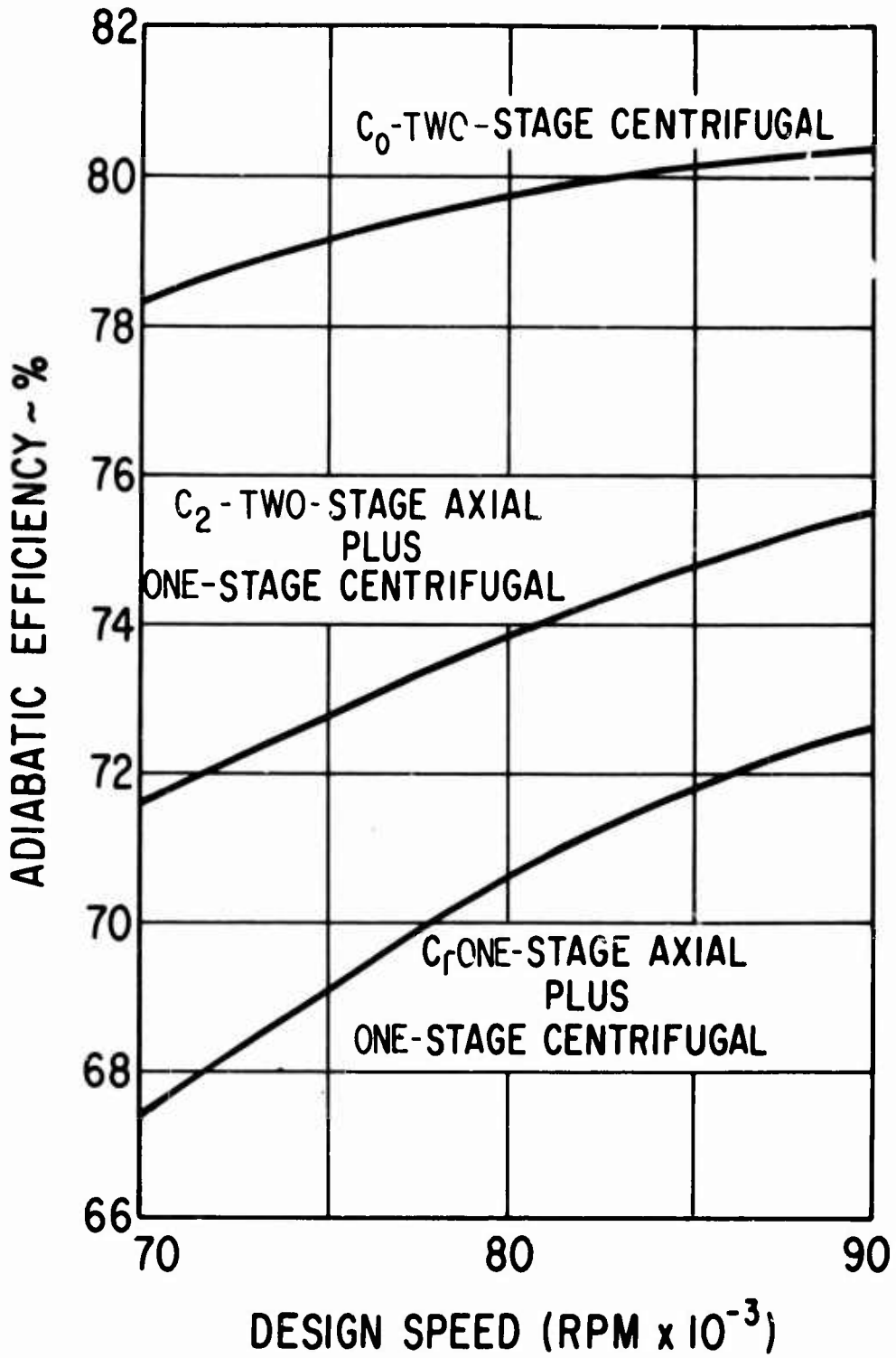


Figure 15. Variation in Compressor Efficiency With Speed; 2 lb/sec.

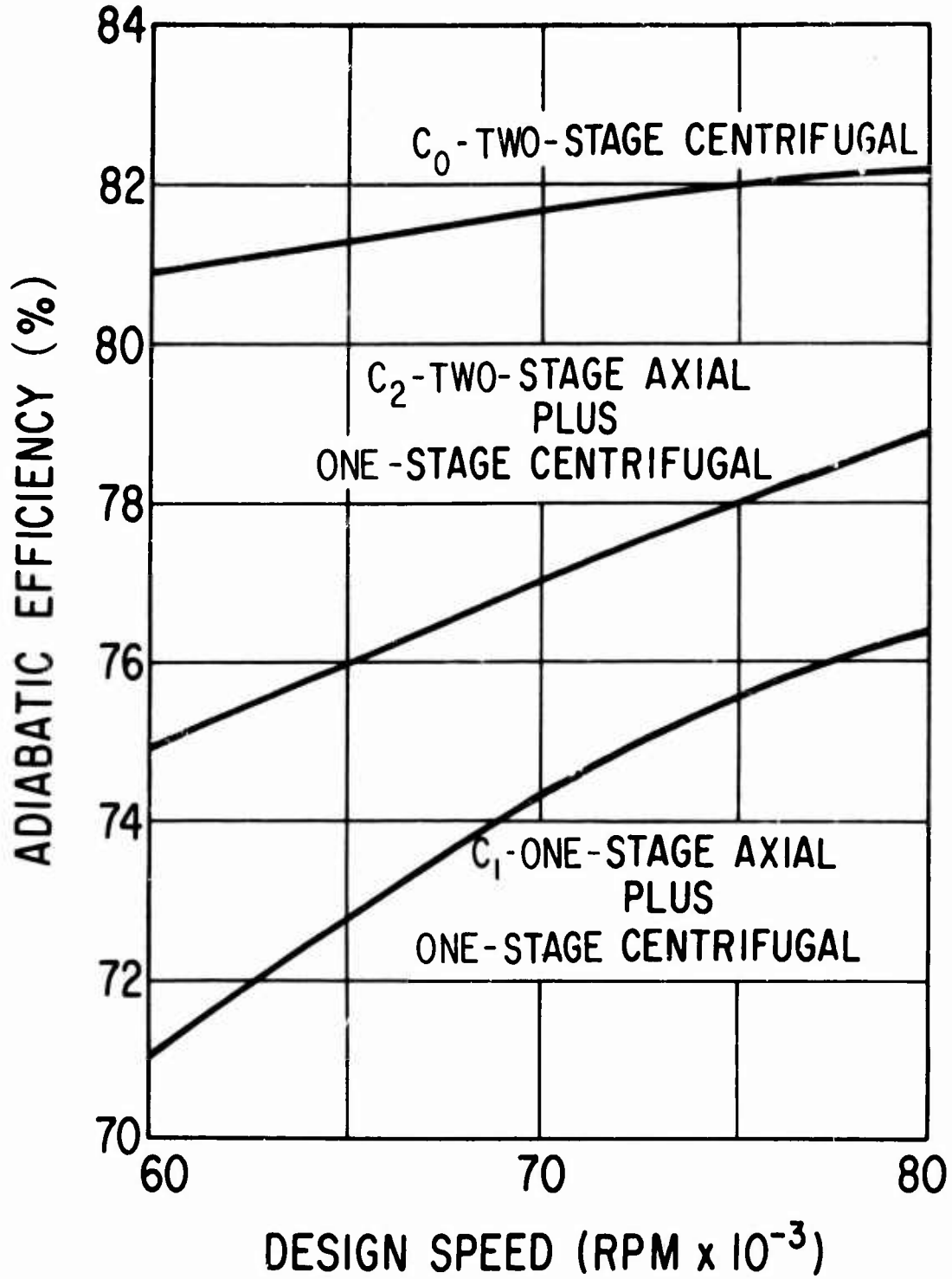


Figure 16. Variation in Compressor Efficiency With Speed; 3.5 lb/sec.

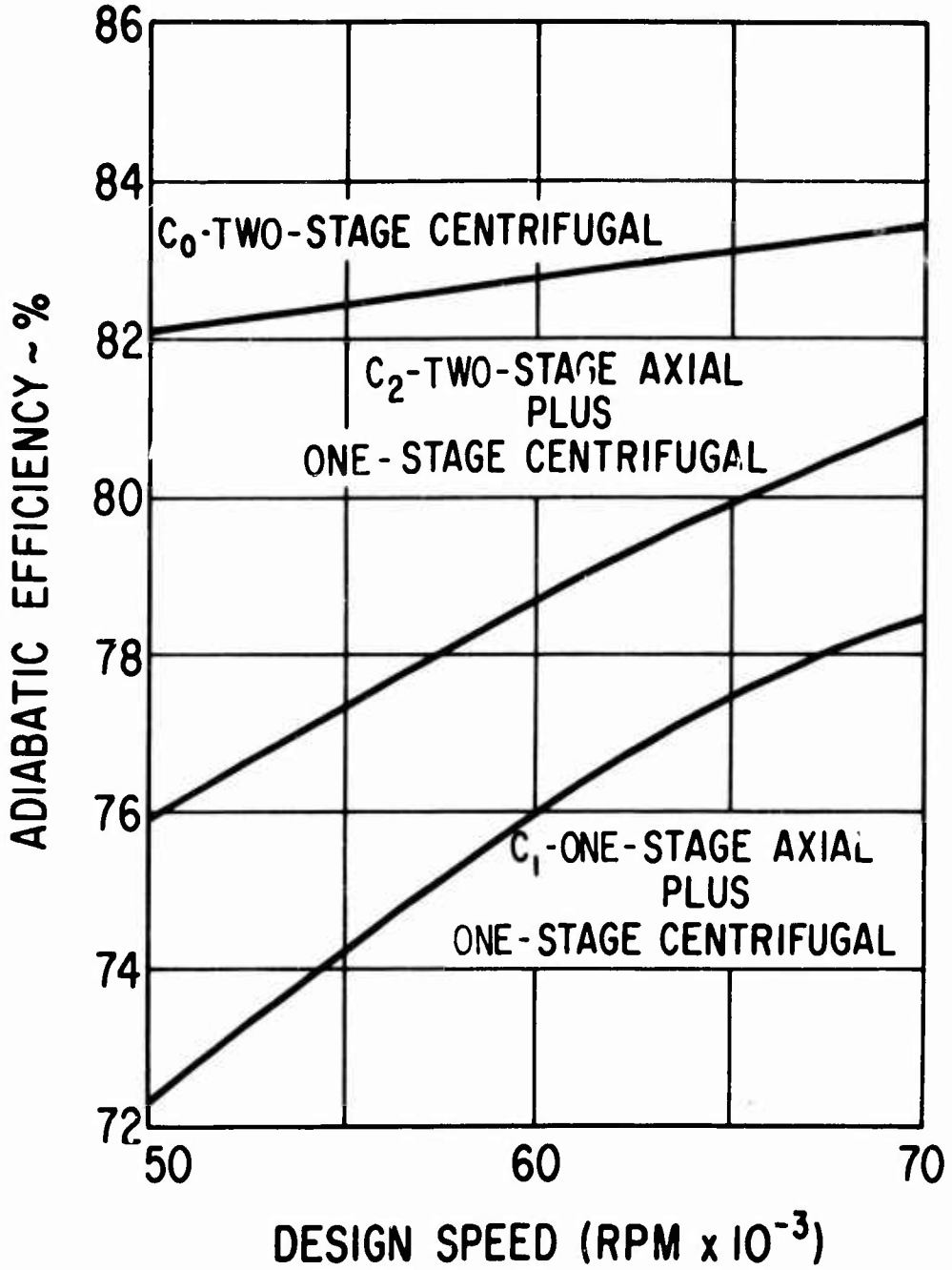


Figure 17. Variation in Compressor Efficiency With Speed; 5 lb/sec.

vanes and blades. The radial turbine cooling analysis was ratioed from information generated for a similar size, high-inlet-temperature, radial-inflow turbine now being evaluated at P&WA for the U.S. Army under Contract DAAJ02-68-C-0003 (Reference 5).

The cooling flow was considered to influence the "effective" turbine efficiency in two ways: (1) through the change in turbine inlet throughflow, and (2) through the disruption of the normal turbine streamlines and heat balance due to the cooling flows being injected into the primary flow after its use.

Leakage flow losses were considered to be those which resulted from leakage past the airfoil flow path through the blade tip clearances. These leakages were estimated, and their effects on performance approximated, using test data from similar low-flow-configuration operating experience.

Axial Turbines (T_1 and T_2)

The basic efficiency relationships for the axial turbines were determined using preliminary turbine parametric design data generated by P&WA. These data were used, without leakage corrections, for the 5 lb/sec designs.

The lower flow designs employed leakage losses relative to the 5 lb/sec flow rate. Cooling losses were included for all flow rates. Basically, the data are presented as curves of stage efficiency expressed parametrically in terms of U_m/C, C_x/U_m, hub/tip ratio and stage work level.

Initial ground rules were established that included an upper limit on mean wheel speed (U_m) of 1500 ft/sec and a maximum exit Mach number (M_x) of 0.5. Compressor average work requirements were established, and the work per stage for one- and two-stage designs was estimated.

A review of the preliminary turbine design data indicated that a single band depicting the optimum C_x/U_m required to produce the maximum efficiency for various values of U_m/C could be generated to include the range of the other variables (see Figure 18). For each one- and two-stage turbine, the U_m/C could be estimated. The turbines were evaluated at the optimum C_x/U_m, or at the C_x/U_m resulting from an exit M_N of 0.5, whichever was lower. Using these approximate design parameters, the turbines were sized and the basic, uncooled efficiency was estimated. It was found that, for the single-stage design, the efficiency penalty imposed by limiting the exit velocity to $M_N = 0.5$, rather than by optimizing the exit velocity, was less than 0.5 point. For the two-stage design, optimum C_x/U_m occurs at an exit $M_N < 0.5$.

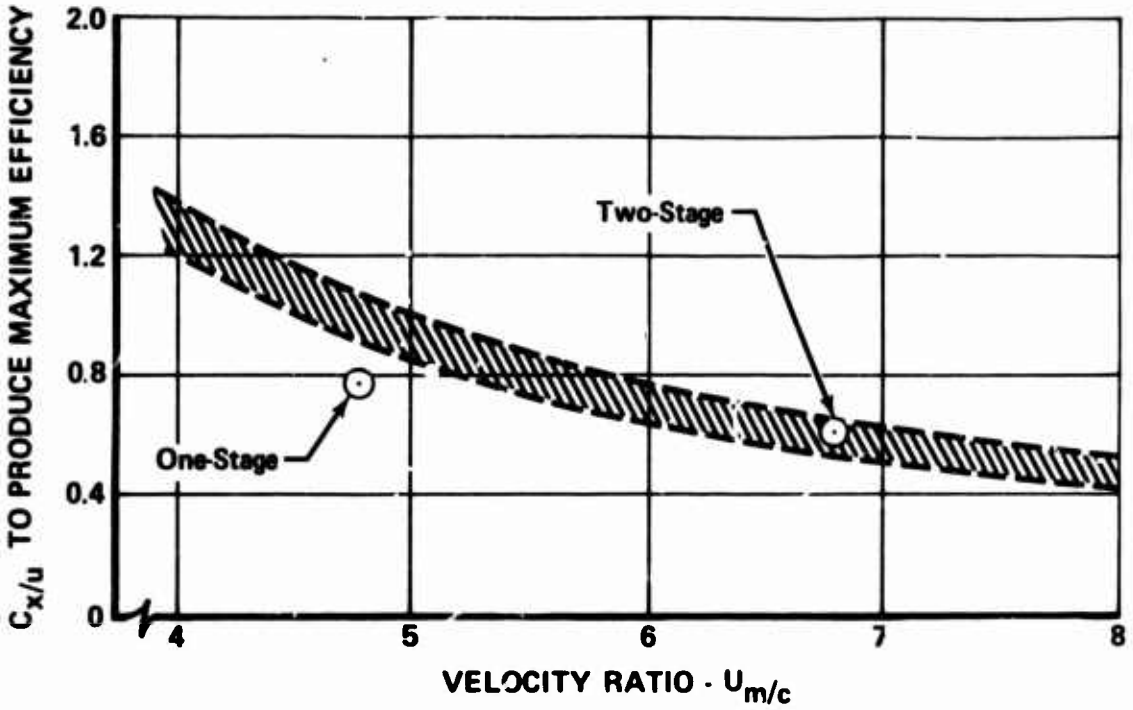


Figure 18. Turbine Axial Exit Velocity Required for Peak Efficiency as a Function of Velocity Ratio.

Radial Turbines - (T_o)

The basic efficiency levels for the radial turbine were approximated using a specific speed/specific diameter diagram for single-stage radial turbines as presented in Reference (6). These curves were modified using leakage and cooling effects to obtain net relative effective efficiency values.

It should be pointed out that, inasmuch as the studies reflect variations in turbine cooling flow (and therefore turbine through-flow) as a degradation to overall efficiency, the resulting curves depict an "effective" efficiency for comparison purposes rather than an absolute level of obtainable efficiency.

The above procedures were followed in evaluating the various turbines over a speed range from 50,000 to 90,000 rpm and at flow rates of 2.0, 3.5 and 5.0 lb/sec. The resultant component configuration efficiency curves are shown in Figures 19 through 21 for the three flow rates, respectively.

CONFIGURATION EFFICIENCY

The overall system efficiency for the nine turbocompressor combinations (three compressor configurations times three turbine configurations) was determined as the product of the individual turbine and compressor efficiencies. The system efficiency as a function of rotor speed for the 2.0, 3.5 and 5.0 lb/sec size machines is shown in Figures 22, 23, and 24, respectively. The designations used for these plots are:

Compressor	Turbine
C_o - Two centrifugal stages	T_o - One radial stage
C_1 - One axial/one centrifugal stage	T_1 - One axial stage
C_2 - Two axial/one centrifugal stage	T_2 - Two axial stages

Thus, a C_1T_2 turbocompressor would be one having a one-stage axial/one-stage centrifugal compressor and a two-stage axial turbine.

From these curves, the optimum speed for each turbocompressor combination was selected, keeping in mind the specific speed limit (N_s = 90) for the combinations incorporating the C_o compressor. The resultant design speed selected for each combination is listed in Table II.

Speeds for the combinations with axial compressor stages were limited to the values shown in the table even though in some cases their peak efficiencies occur at higher speeds. These values were selected as practical upper limits inasmuch as a further increase in speed would provide only a slight increase in efficiency while magnifying the stress and critical speed problems.

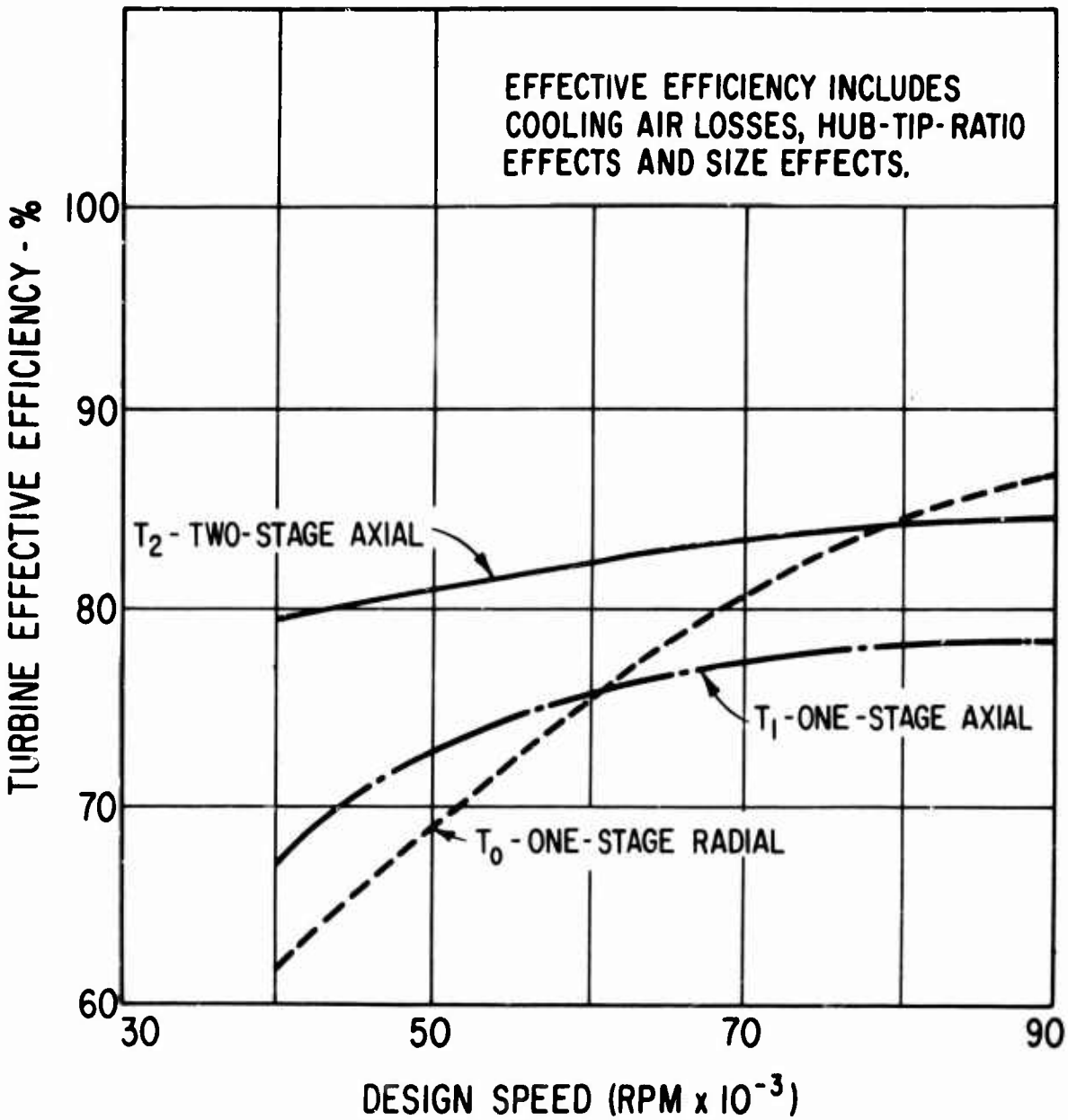


Figure 19. Variation in Turbine Relative Effective Efficiency With Speed; 2 lb/sec.

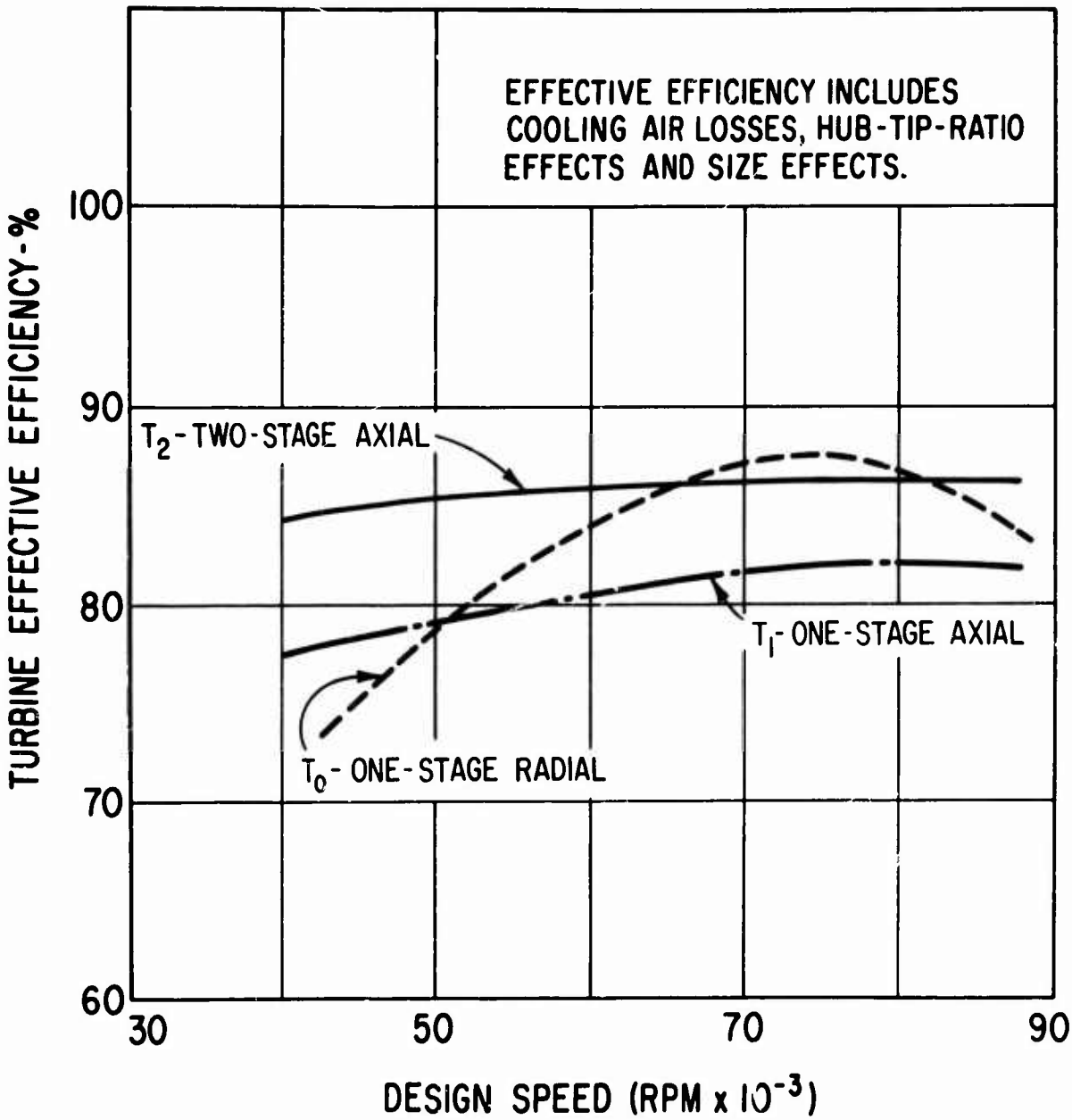


Figure 20. Variation in Turbine Relative Effective Efficiency With Speed; 3.5 lb/sec.

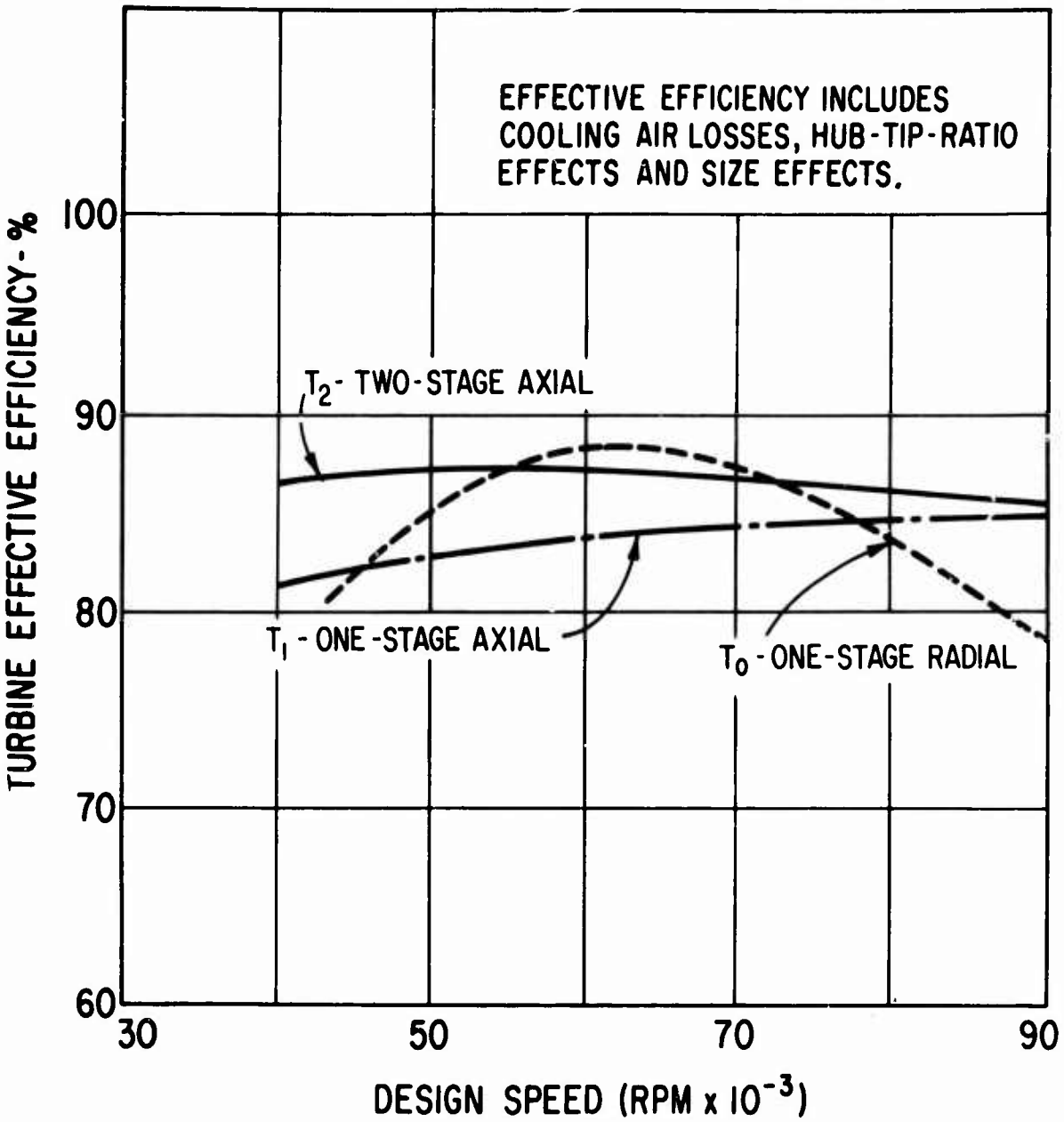


Figure 21. Variation in Turbine Relative Effective Efficiency With Speed; 5 lb/sec.

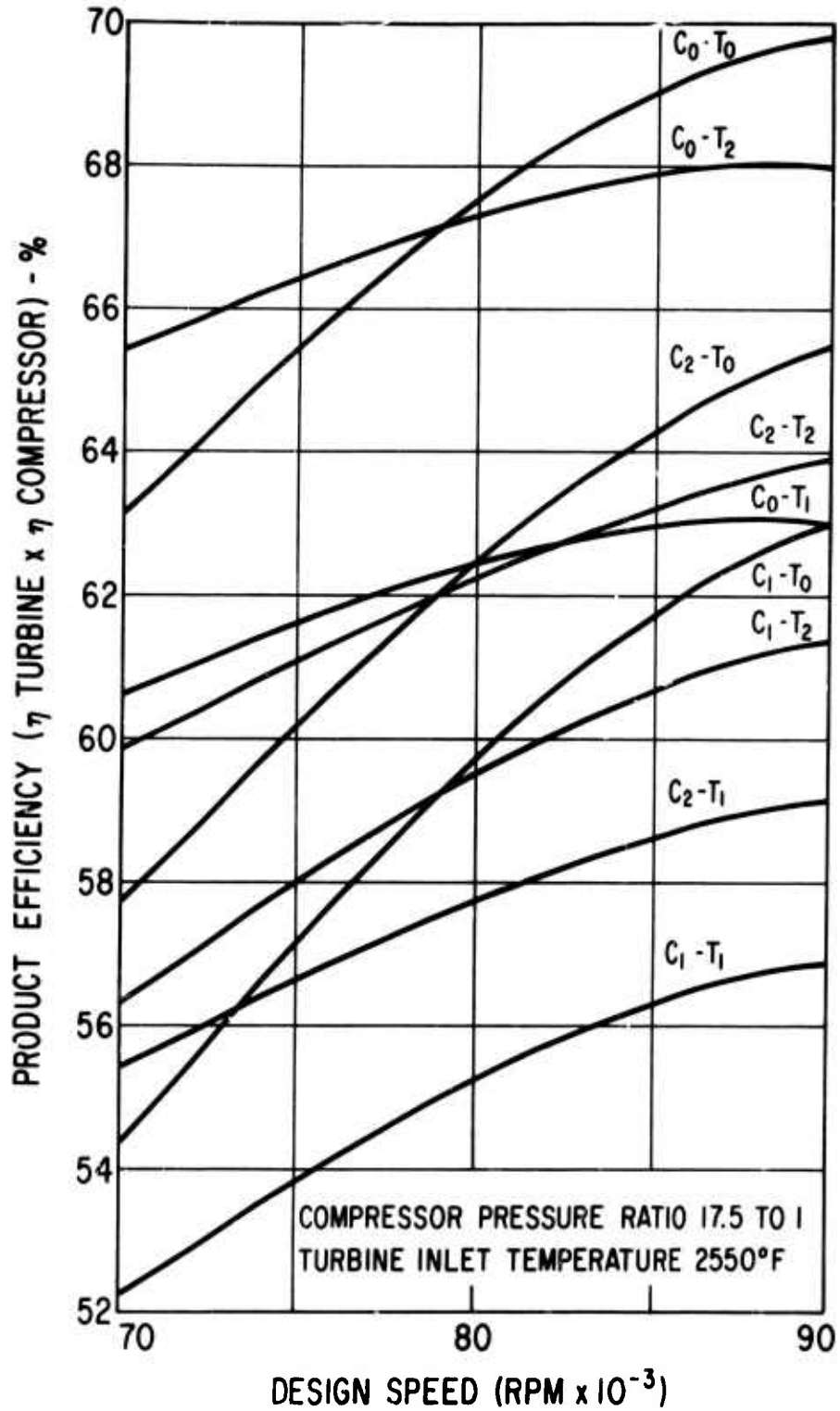


Figure 22. Variation in Turbocompressor Efficiency With Speed; 2 lb/sec.

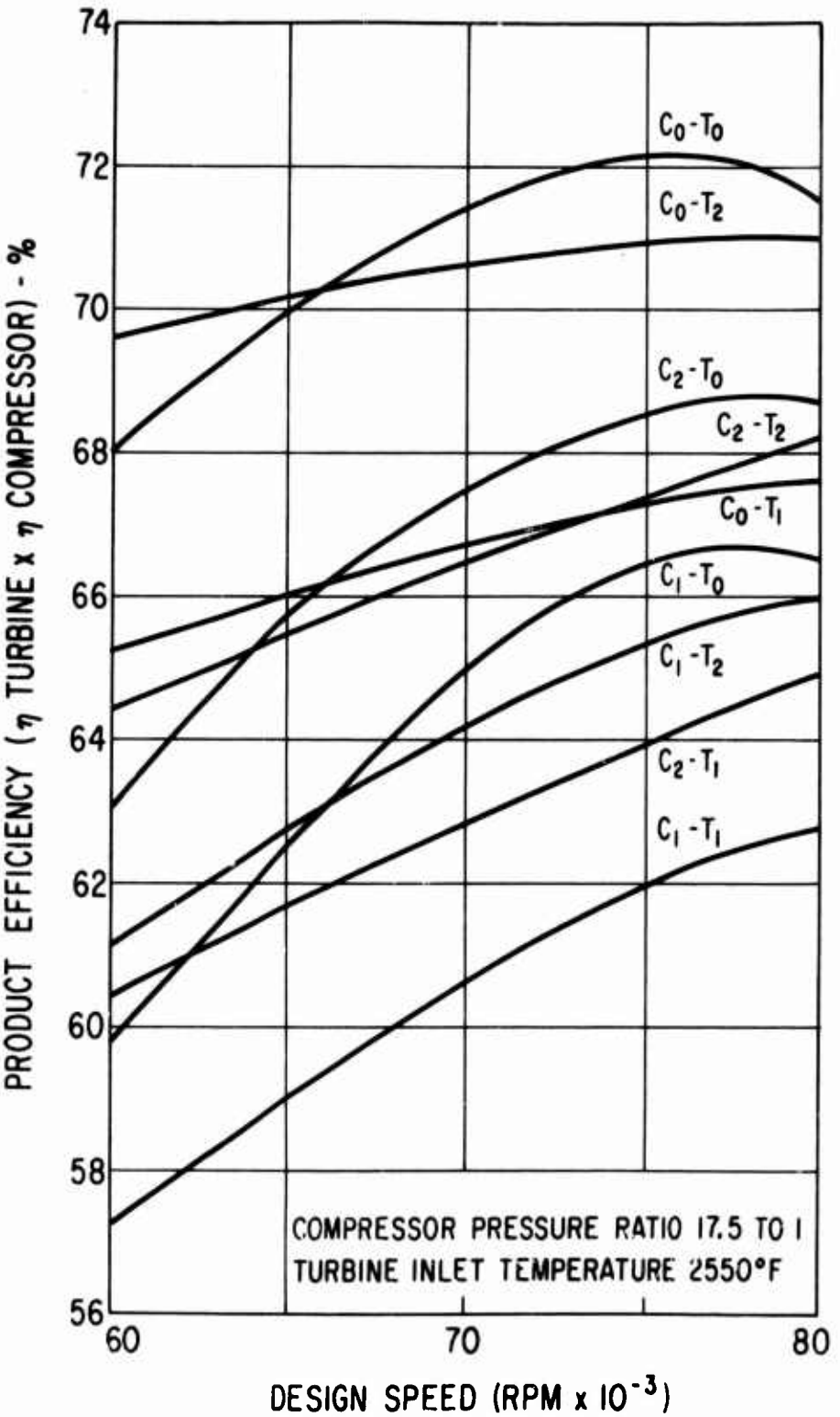


Figure 23. Variation in Turbocompressor Efficiency With Speed; 3.5 lb/sec.

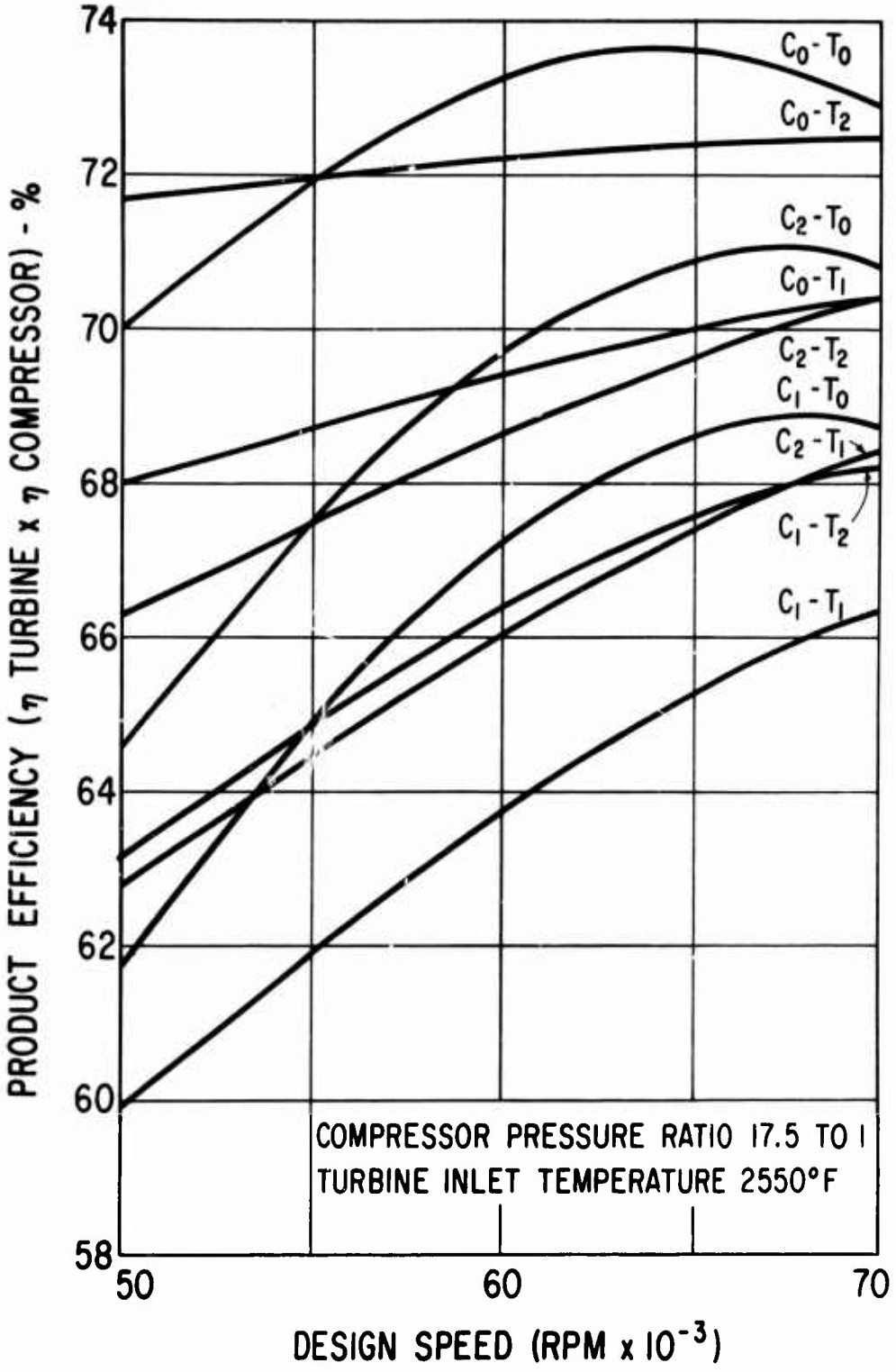


Figure 24. Variation in Turbocompressor Efficiency With Speed; 5 lb/sec.

TABLE II. CONFIGURATION DESIGN SPEEDS

Turbocompressor Configuration	Airflow Size, lb/sec		
	2.0	3.5	5.0
C_oT_o	79,000	60,000	50,000
C_oT_1	79,000	60,000	50,000
C_oT_2	79,000	60,000	50,000
C_1T_o	90,000	78,000	68,000
C_1T_1	90,000	78,000	68,000
C_1T_2	90,000	78,000	68,000
C_2T_o	90,000	78,000	68,000
C_2T_1	90,000	78,000	68,000
C_2T_2	90,000	78,000	68,000

FLOW-PATH LAYOUTS

Flow-path layouts were generated for each of the various component combinations in the 5 lb/sec engine size and for selected combinations in the 2 lb/sec size.

The layouts were made by first sizing the flow paths for each component configuration at the speed or speeds at which the components must operate (Table II). The component flow paths were assembled using combustors and compressor collection systems based on projected 1975 technology.

The procedures followed in establishing component flow-paths for the 5 lb/sec engine size are outlined in the following sections.

Compressor (5 lb/sec)

Two-Stage Centrifugal (C_0)

As stated earlier, the rotor speed for this configuration was limited to 50,000 rpm in order not to exceed a specific speed of 90 on the first stage. The optimum pressure ratio split from Figure 7 was used (7.4 across the first stage and 2.37 across the second stage). An inlet Mach number of 0.6 was used for the first stage and an inlet axial Mach number of 0.3 was used for the second stage. A prewhirl of 25 degrees was used for both stages. The first stage inlet hub diameter was set at 3.2 inches based on preliminary estimates of required bearing sizes. Impeller tip diameters were determined as a function of stage pressure ratio, rotor speed, and an aerodynamic slip factor taken from the P&WA ST9* compressor test data. Spacing, area ratios, and impeller length-to-diameter ratios were scaled from the ST9.

One-Stage Axial/One-Stage Centrifugal (C_1)

The rotor speed selected for the one-stage axial/one-stage centrifugal compressor at 5.0 lb/sec airflow was 68,000 rpm, based on system performance criteria. Pressure ratio split for this configuration was selected to be 1.75 across the axial stage and 10 across the centrifugal stage. The selected pressure ratio split is slightly different from the optimum split of 1.85 across the axial stage and 9.45 across the centrifugal stage as indicated by Figure 10. This split was selected to make use of data from a development program on a 10:1 centrifugal compressor being initiated at that time by AMRDL. An inlet specific flow of 40 and an exit Mach number of 0.4 were selected for the axial stage. The relative inlet blade tip Mach number was 1.7. Aspect ratios for the axial stage were taken from

*A small gas-turbine engine built by P&WA under AMRDL contract having a two-stage centrifugal compressor and two-stage axial turbine.

the TX-10* compressor stage, which has similar high stage pressure ratio. The centrifugal stage length-to-diameter ratio and area ratio were scaled from the ST-9 first stage. The hub diameter was set at 3.2 inches based on estimated bearing requirements.

Two-Stage Axial/One-Stage Centrifugal (C_2)

The rotor speed selected for the two-stage axial/one-stage centrifugal compressor at 5.0 lb/sec was 68,000 rpm based on system performance criteria. The optimum pressure ratio split from Figure 13 was used. This split requires a pressure ratio of 2.0 across the two-axial stages and a pressure ratio of 8.75 across the centrifugal stage. An inlet specific flow of 40 for the first axial stage and an exit Mach number of 0.4 from the second axial stage were selected. The blade inlet relative tip Mach number was 1.7. Aspect ratios for the axial stages were taken from an existing engine design which incorporates a low-flow-rate (11.1 lb/sec), conventionally loaded axial compressor. The centrifugal compressor area ratio and length-to-diameter ratio were scaled from the ST-9 first stage. Compressor hub diameter was held at 3.2 inches to meet estimated bearing size requirements.

Turbines

Flow paths were generated for each turbine configuration (T_o, T_1 and T_2) at two speeds, 50,000 rpm and 68,000 rpm, for use with the all centrifugal and axial/centrifugal compressors, respectively.

Axial Turbines (T_1 and T_2)

For the axial turbines, with the rotor speed and mean wheel speed (1500 ft/sec) fixed, mean diameter was determined and exit blade height for the specified flow rate and axial exit Mach number (M_x = 0.5) was established. The axial flow-path contour consisted of a constant I.D., with tip divergence of 12 degrees or less for the multistage designs. Blade axial chords were set at 0.65 inch, approximately the same as the ST-9 turbine blade chords, which were sized to provide sufficient axial space for internal cooling and adequate wall thicknesses. Vane axial chords also were approximately the same as ST-9 dimensions: first vanes approximately 1.0 inch and second vanes 0.65 inch. The vane-blade gap was set at 0.25 inch.

Radial Turbine (T_o)

For the radial turbine, the tip diameter was determined from the specific diameter/specific speed curve of Reference 2 for the specified flow, speed and stage work. Blade heights and impeller length were ratioed from the high-temperature, radial turbine program

*Transonic compressor stage, pressure ratio = 2.75, Reference 7.

currently under way at FRDC for AMRDL [5]. Exit blade diameters were established to give an axial exit Mach number (M_x) of approximately 0.5, and the flow-path curvature was approximated.

Engine Flow-Path Layouts

Overall engine flow-path layouts were produced for each combination of component configurations in the 5 lb/sec engine size. These layouts were generated by assembling the various compressor and turbine configurations with suitable interstage passages and combustors. The layouts show essentially the minimum spacing between components as dictated by aerodynamic considerations without regard to bearing and seal requirements.

Figures 25-27 present some of the flow-path arrangements that were produced. Figure 25 shows the C_o compressors with T_o and T_2 turbines, and Figure 26 shows the T_o turbine with C_1 and C_2 compressors. Similar layouts were made for the C_oT_1, C_1T_1, C_1T_2 and C_2T_2 combinations. All of these arrangements use the reverse-flow or "folded" type of burner to achieve minimum rotor length. To provide added flexibility in selecting bearing locations, alternative burner-turbine arrangements were prepared using through-flow burners, as shown in Figure 27.

Analysis of the results of the component and turbocompressor efficiency study indicated that engine size, in the 2-5 lb/sec flow range, had no effect on the relative performance levels of the various engine configurations. A preliminary sizing of the components indicated, however, that a structural limit was reached as size was reduced in some configurations. The structural limit was encountered due to excessive disc bore stresses that negated the possibility of using a front-drive power turbine in the higher speed configurations, i.e., those configurations with one or more axial compressor stages. Preliminary critical speed estimates also revealed that the higher speed configurations would not have the desired 160 percent (of design speed) third critical speed margin.

For these reasons, flow-path layouts for only the C_oT_o, C_oT_1 and C_oT_2 configurations in the 2 lb/sec size were subjected to detailed rotor dynamic and bearing feasibility studies. The layout of the C_oT_o arrangement is shown in Figure 28.

Sizing of Component Discs

Using flow-path layouts and design speeds of each engine, the compressor and turbine discs were sized. Using titanium in the compressors, IN-100 for the radial and INCO 718 for the axial turbines disc, bore sizes and axial lengths were established based on maximum allowable stress limits.

Weights were estimated for each of the components as shown in Table III, and polar moments of inertia are listed in Table IV.

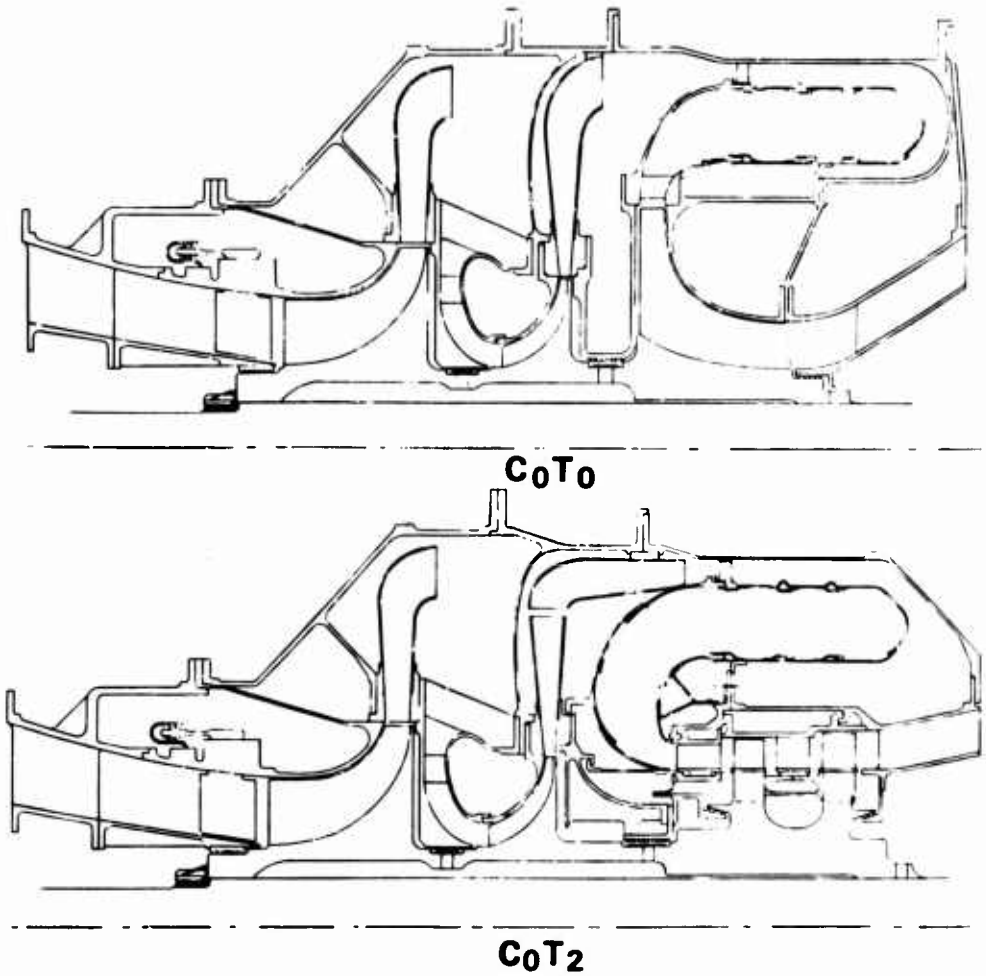


Figure 25. Air Bearing Engine Study Flow-Path Arrangements; 5 lb/sec.

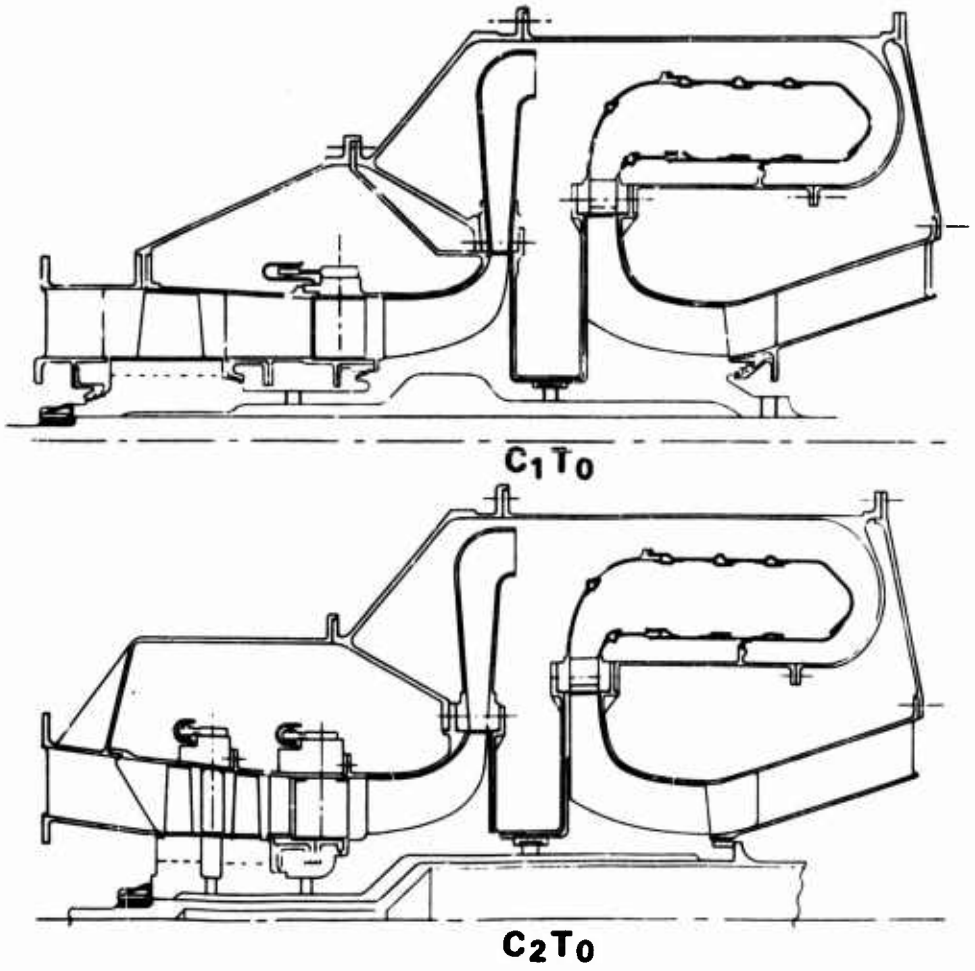


Figure 26. Air Bearing Engine Study Flow-Path Arrangements; 5 lb/sec.

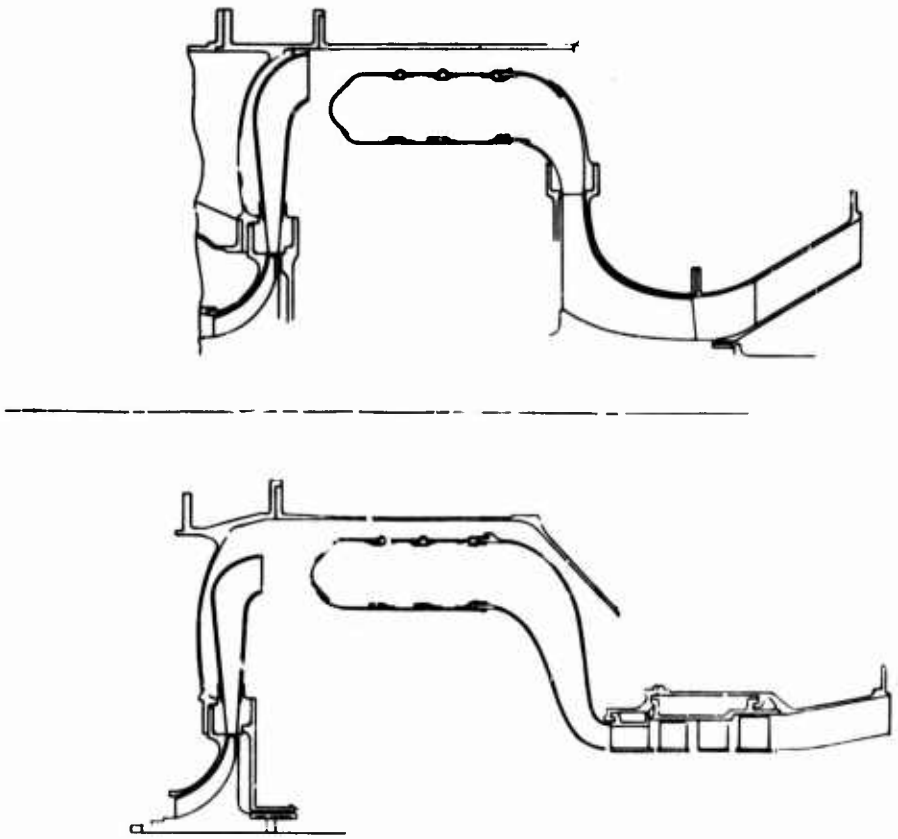


Figure 27. Alternate Combustor - Turbine Flow-Path Arrangements; 5 lb/sec.

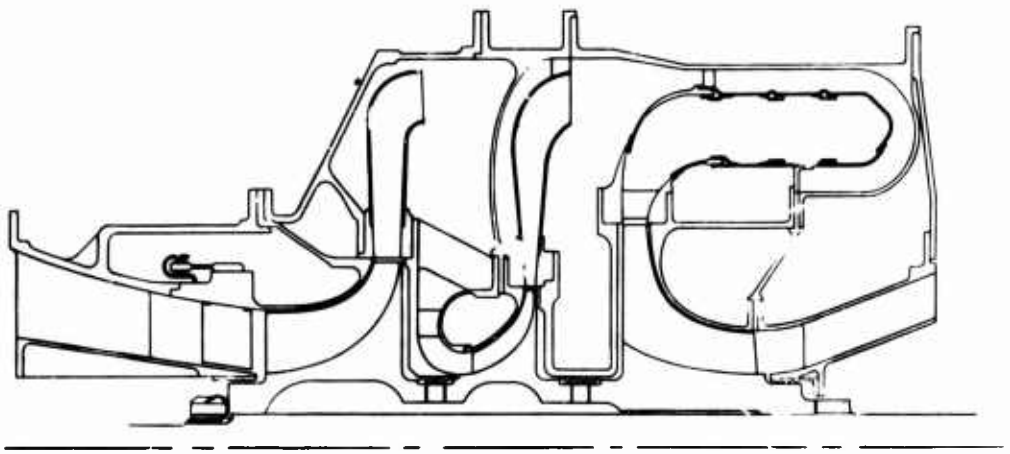


Figure 28. Air Bearing Engine Study Flow-Path Arrangement; 2 lb/sec.

TABLE III. ESTIMATED ENGINE WEIGHTS			
Configuration	Compressor Weight	Turbine Weight	Total Weight
	5.0 lb/sec		
C_oT_o	11.0	6.0	17.0
C_oT_1	11.0	8.8	19.8
C_oT_2	11.0	17.2	28.2
C_1T_1	10.0	6.5	16.5
C_1T_2	10.0	12.7	22.7
C_2T_o	8.6	6.5	15.1
C_2T_1	8.6	6.9	15.5
C_2T_2	8.6	12.7	21.3
	3.5 lb/sec		
C_oT_o	7.1	4.9	12.0
C_oT_1	7.1	4.65	11.75
C_oT_2	7.1	6.45	13.55
	2.0 lb/sec		
C_oT_o	2.8	3.2	6.0
C_oT_1	2.8	2.0	4.8
C_oT_2	2.8	4.0	6.8

TABLE IV. ESTIMATED POLAR MOMENTS OF INERTIA

Combination	Size - in. lb/sec^2		
	5.0	3.5	2.0
C_oT_o	0.182	0.0775	0.023
C_oT_1	0.23	-	-
C_oT_2	0.34	-	-

THRUST LOADS

An initial estimate was made of the unbalanced rotor thrust to establish generalized requirements for the thrust bearings in each engine combination. The first configuration evaluated was the C_oT_2, which was selected because the thrust forces could be estimated accurately by scaling values calculated from measured pressures in the P&WA ST-9 engine, a C_oT_2 configuration. The estimated values were:

100% Power - 1028 pounds rearward
Idle - 199 pounds forward

The 1000-pound aerodynamic thrust load, in addition to maneuver loads, would require greater capacity than the thrust bearing could provide. The full power load could be reduced, but only at the expense of the idle load, which would increase proportionately. Furthermore, the load capacity of the externally pressurized hybrid thrust bearing is dependent upon compressor discharge pressure and speed, and is significantly reduced at engine idle condition.

To establish thrust levels on the other configurations and determine what modifications, if any, could be made to reduce the unbalanced forces, a limited thrust balance study was conducted. In the study, methods of reducing net thrust on the rotor by lowering the thrust load of each component were investigated and the effect of each method on engine performance was determined. The results of the study, which was conducted on the 5 lb/sec engine size, are presented in the following paragraphs by component.

Axial Compressors

The thrust loads on either the single- or two-stage axial compressors were considerably smaller than on any of the other components principally due to the low pressure differential across the stage and the small projected area. As a result, no special modifications were investigated for the axial compressors.

Centrifugal Compressors

To effectively control the net compressor thrust, an initial thrust load analysis was performed for the basic design to determine which areas are the most critical. The resultant thrust breakdown for maximum power conditions is shown in Figure 29. It is seen that by far the largest single load is the rotor backface load.

The methods considered to reduce thrust were as follows:

a. Rotor disc scalloping (rim cutback)
b. Rotor disc backface venting
c. Rotor shrouding with variable front seal location
d. Rotor exit Mach number variation (reaction)
e. Change in compressor stage pressure ratio split

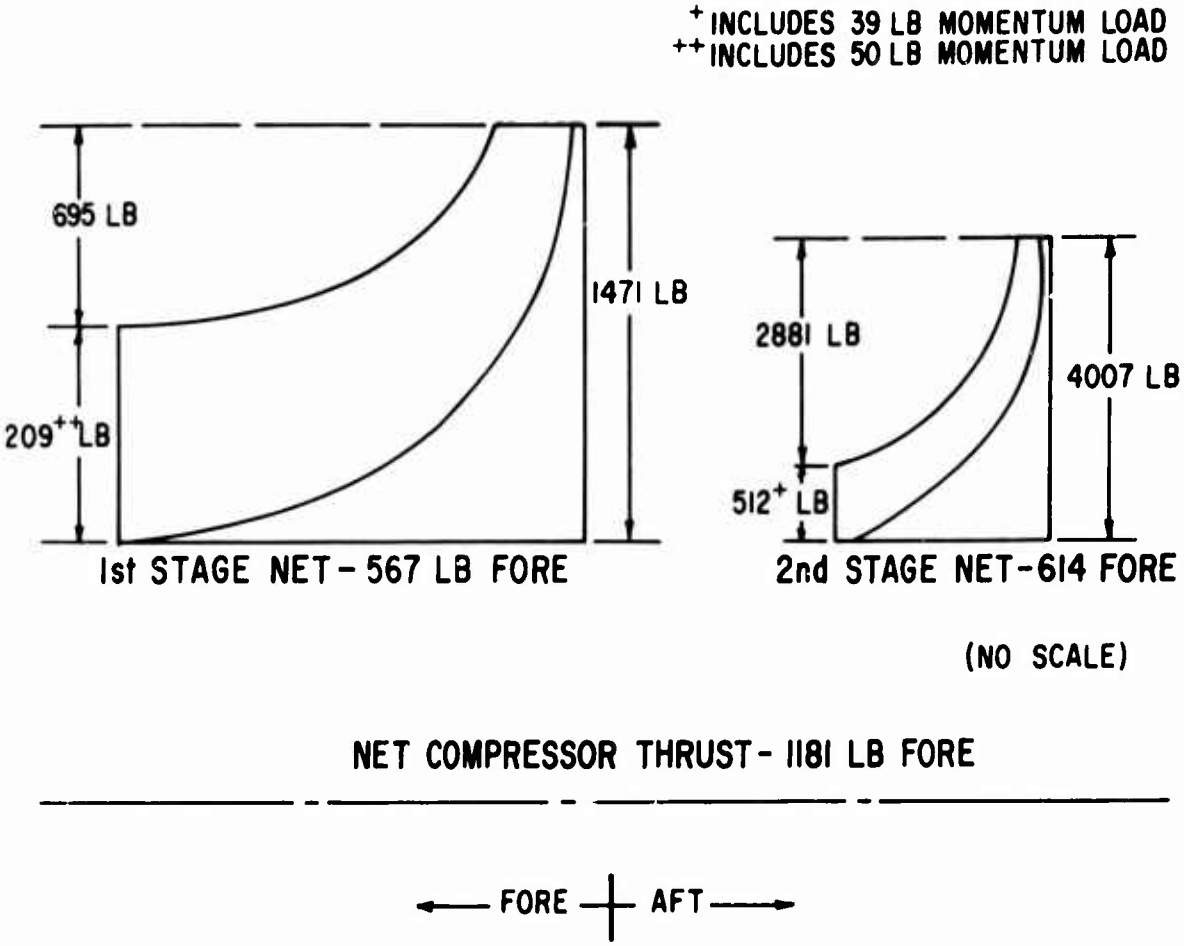


Figure 29. Schematic of Two-Stage Centrifugal Compressor Thrust Forces.

Each of the methods of controlling compressor thrust unbalance was found to result in efficiency changes of varying degrees. The proper system selection must be made with regard to its influence on both of these factors. A composite plot (Figure 30) has been developed to show the comparative thrust/efficiency trade-off for each of the methods considered.

Rotor Disc Scalloping (rim cutback)

Figure 29 shows that the thrust unbalance of the basic design results from the extremely large force acting over the backface of each of the discs. The pressure felt in this cavity is approximately equal to the rotor exit static pressure. One method of effectively reducing this backface pressure, and thus the stage and whole compressor rotor unbalance, is by scalloping the disc. This involves cutting back the outer radius of the disc between the blades. Figure 31a shows this location, schematically. If no other corrective procedures are employed, there is effectively no thrust load on the impeller in the area of cutback. Below this radius, the pressure which is felt behind the disc is essentially the static pressure within the impeller passage at the point of cutback (P_{sx} and P_{sy} of Figure 31a), rather than the blade exit static pressure, as was the case previously. Static pressure rise increases through the rotor approximately as the square of the radius; therefore, since the static pressure at the point of cutback is lower than the rotor exit static pressure, it results in significantly reduced backface loads. Figure 32 shows how these backface load changes result in net reductions to stage overall thrust for various degrees of cutback.

Net efficiency effects for various cutbacks are also presented. Based on limited test experience and analysis available, the presence, or complete absence, of a full back shroud was felt to result in a net efficiency change or approximately 8 points. Inefficiencies for various degrees of disc cutback were ratioed from this by the square of the cutback disc tip radius.

Rotor Disc Backface Venting

Another means of controlling disc backface pressure is by venting each impeller backface cavity to the stage inlet. This is accomplished by sealing the rear of the rotor from the blade exit static pressure by means of a labyrinth seal at the outer tip of the impeller. The basic design of the system is modified to provide two cavities, one under each disc, as indicated in Figure 31b. This disc backface is vented through this cavity to the inlet. The pressure maintained in the backface cavity will be dictated by a flow/pressure balance between the rotor tip seal area, the vent passage areas, the stage exit inner seal area (near the shaft), the rotor exit static pressure, the rotor inlet static pressure, and the inner seal driving pressure (second-stage inlet static or turbine inlet static for first and second stages, respectively). The resultant pressure will be higher than stage inlet pressure, yet lower than either of the other two pressures. Figure 33 shows that backface venting provides a large capability for moderating stage thrust. Its disadvantage is that stage recirculation results, penalizing system efficiency greatly.

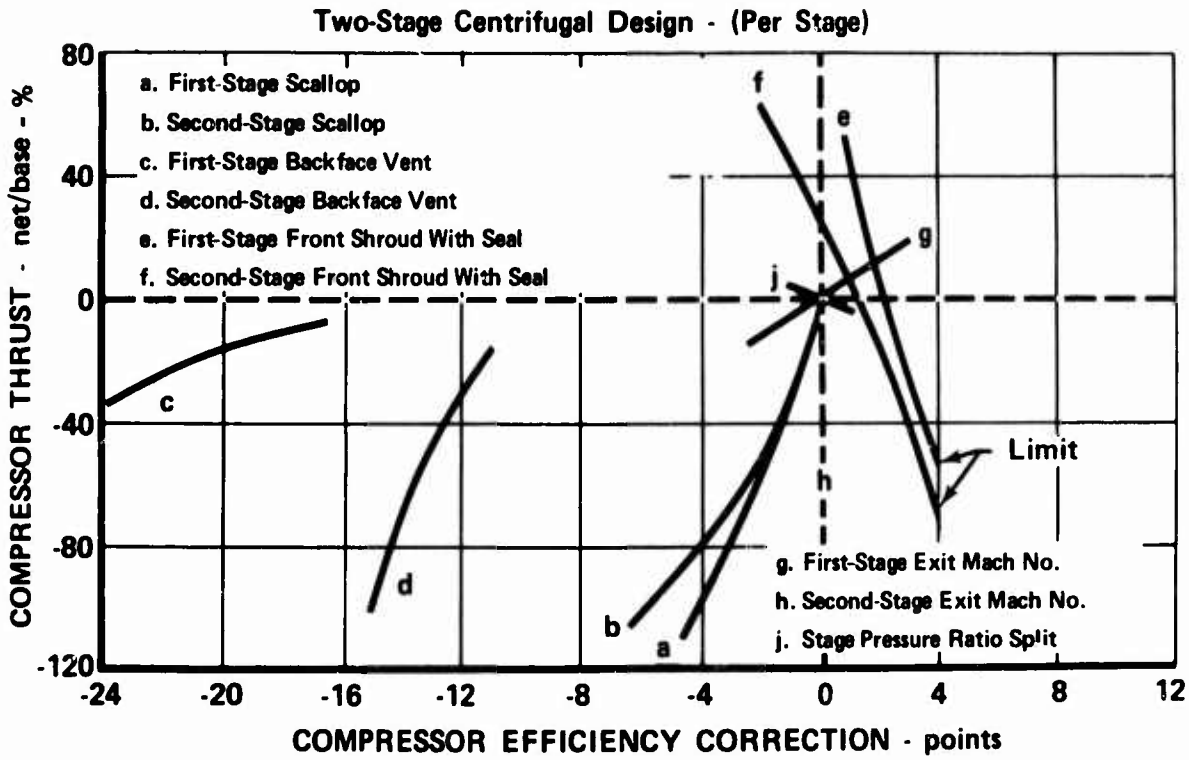


Figure 30. Parameter Effect on Compressor Stage Thrust Forces.

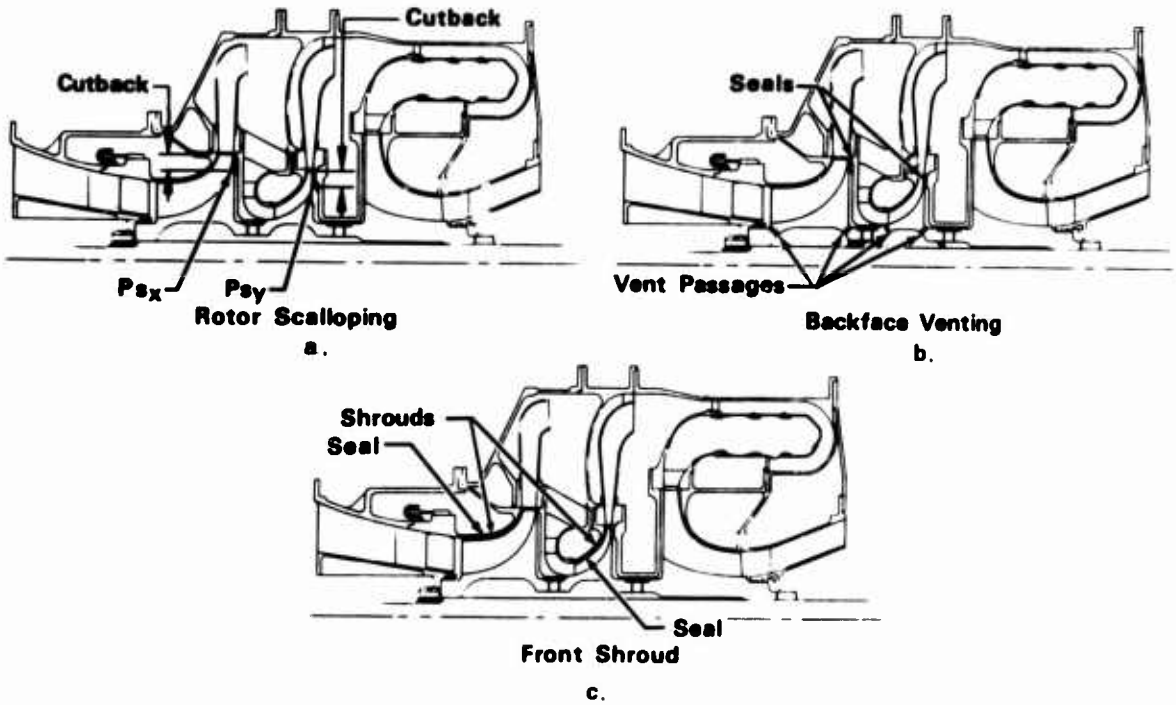


Figure 31. Compressor Modifications Evaluated in Thrust Balance Study.

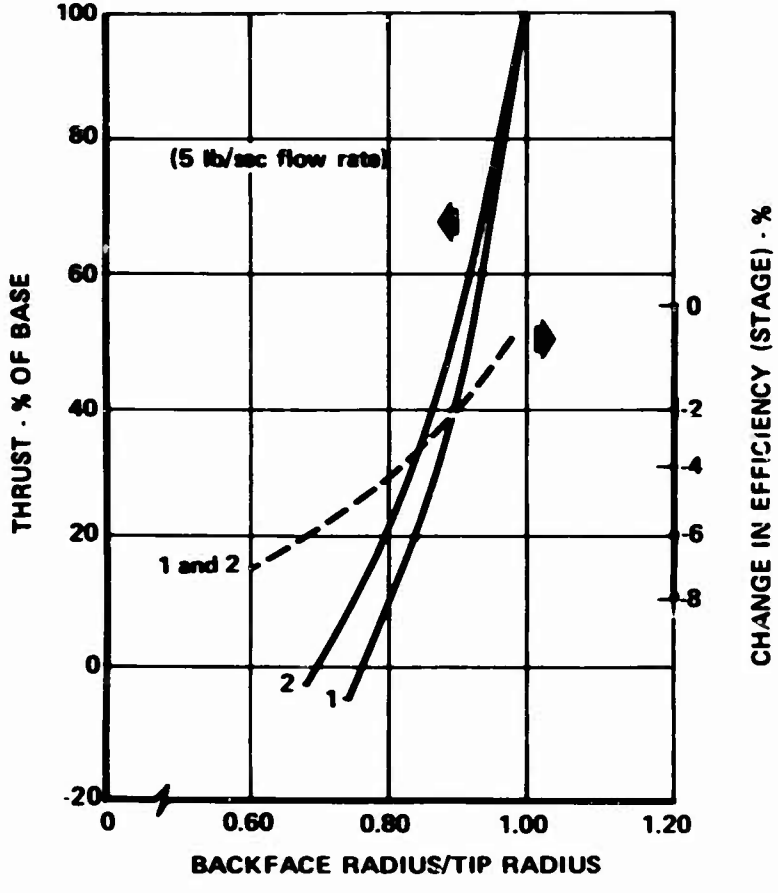


Figure 32. Effect of Rotor Scalloping on Centrifugal Compressor Thrust and Efficiency.

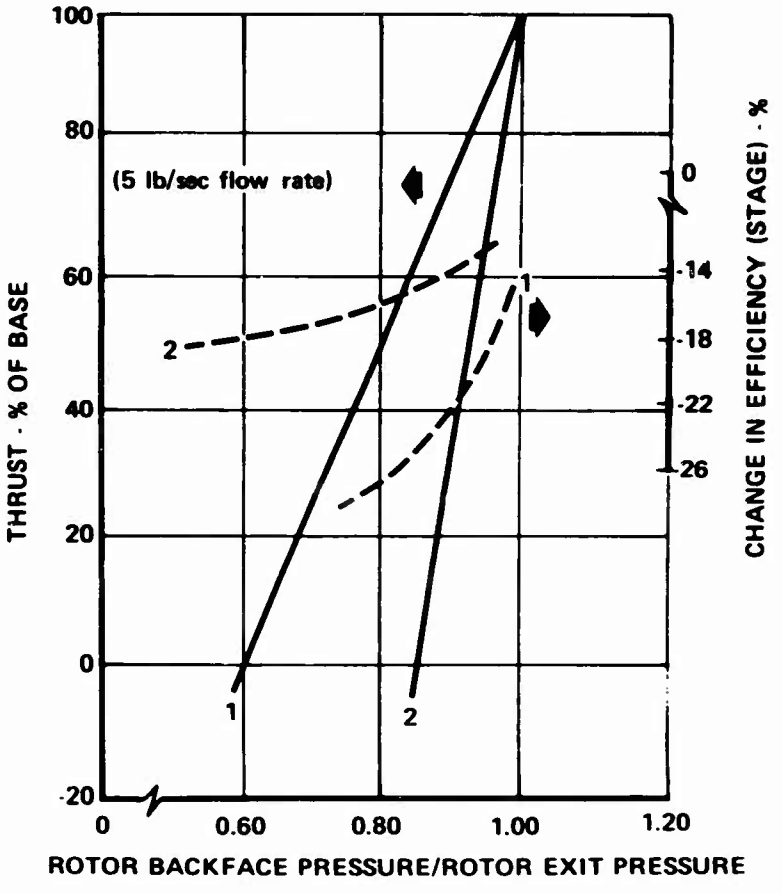


Figure 33. Effect of Rotor Backface Venting on Centrifugal Compressor Thrust and Efficiency.

The system efficiency penalties were calculated by estimating the disc recirculation flows and considering that every percentage of total flow that recirculates through a stage reduces the efficiency of that stage by 1.5 points.

Rotor Shrouding With Variable Front Seal Location

The basic radial compressor designs employed open-faced rotors. As a result, the rotor thrust component in the aft direction represents, in part, the inlet-to-exit static pressure variation integrated over the projected rotor frontal area. Control of this pressure load, while not as significant in the net thrust as back-face load, exercises a significant degree of control over net rotor thrust. This control can be accomplished by shrouding the impeller and providing a rotor front seal (Figure 31). When this is done, exit static pressure is felt from the inlet up to the seal. Then, by varying the seal position, the relative amounts of high and low loads are adjusted, varying the net frontal loads. The optimum position for minimum thrust unbalance, however, has the seal as close to the inlet as possible, maximizing rotor aft load.

In addition to the above, shrouding the impeller increases efficiency. A rotor with a full front shroud, sealed at the inlet, was considered to be 4 points in efficiency better than an unshrouded impeller due to reductions in windage and disc friction losses. Further efficiency variations result from leakage flow changes due to variations in the seal radial position. Changes in leakage were considered to change efficiency at the rate of 1.5 points in efficiency for each percentage of total flow leaking past the seal. Figure 34 shows, however, that as the front seal radial location is reduced, relative to the rotor tip, the entire thrust unbalance cannot be removed. This is because rotor exit static pressure acts over the entire backface, while it is felt on the front only between the inlet outer radius and the rotor tip, a smaller projected area, resulting in a smaller load.

It should be noted that structural analyses for this particular design have not been made. Depending on the size and design of the shroud and disc, consideration must be given to possible stress problems when operating at the design tip speed and stage exit temperature (1780 f/s and 950^{o}R, total, and 1480 f/s and 1300^{o}R, total, for the first and second stages, respectively).

Rotor Exit Mach Number Variation (reaction)

Increases in rotor exit Mach number result in decreases in the static pressure at that point through the increase in the velocity head. Conversely, decreases in Mach number increase static pressure. Changes in system Mach numbers, therefore, control, to a degree, rotor loads and the resultant net thrust.

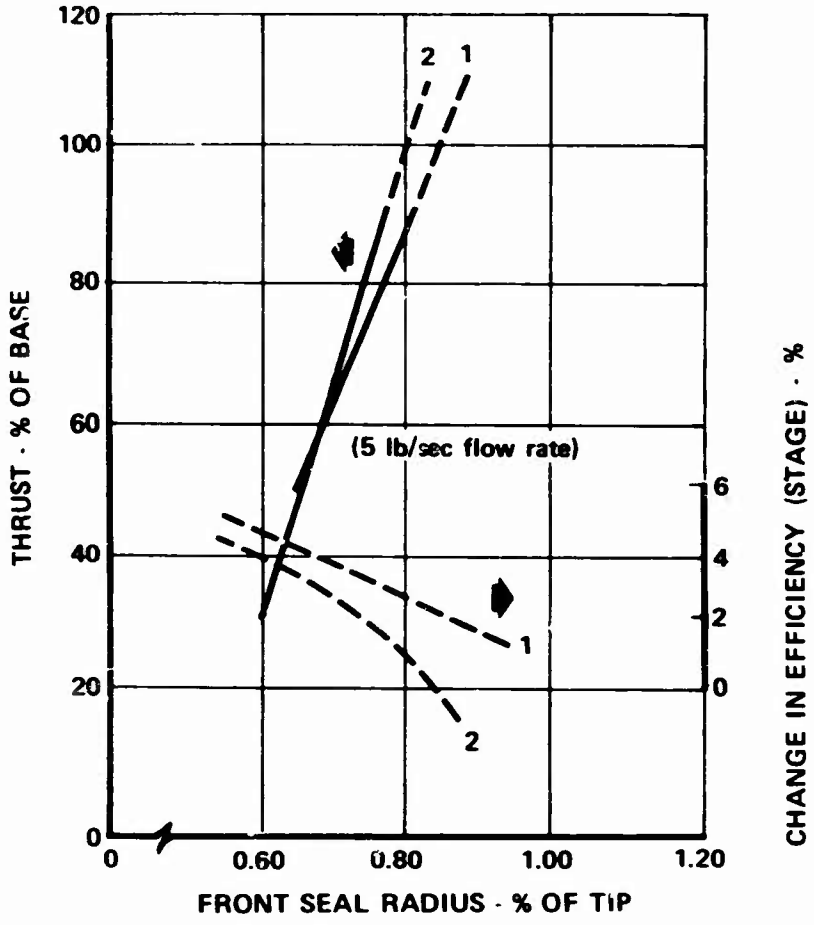


Figure 34. Effect of Rotor Front Shroud on Centrifugal Compressor Thrust and Efficiency.

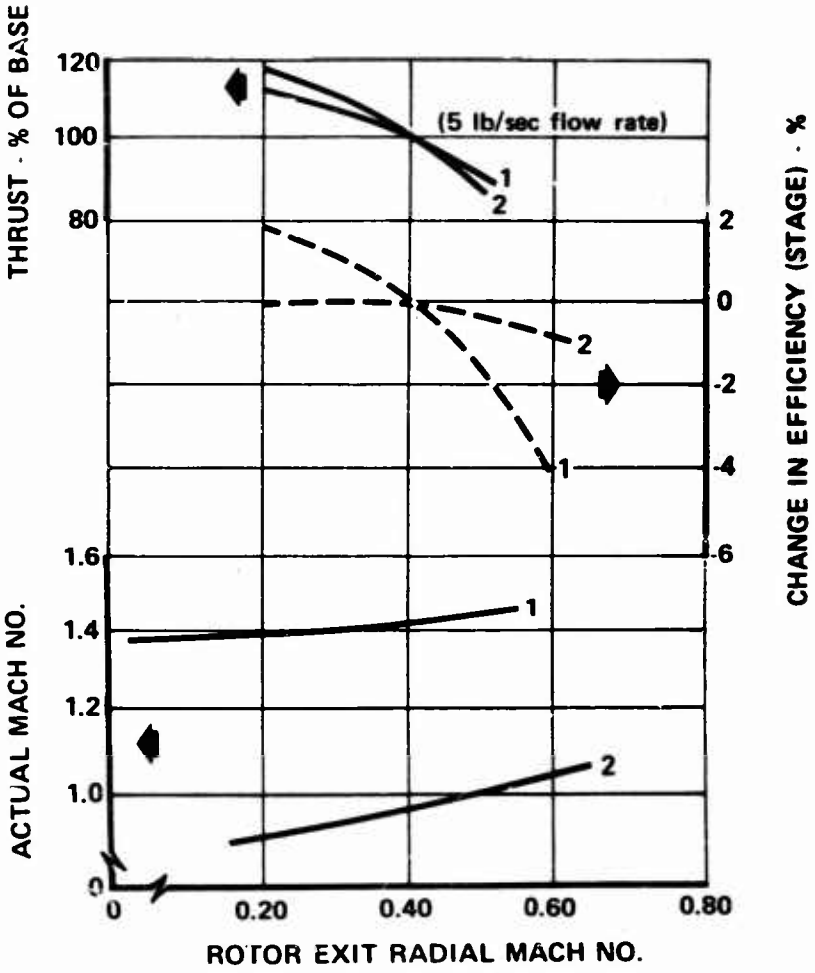


Figure 35. Effect of Rotor Exit Mach No. Variation on Centrifugal Compressor Thrust and Efficiency.

Figure 35 shows the approximate effect of changing first- and second-stage impeller exit Mach number. Increases in rotor exit Mach number improve thrust balance by lowering rotor exit static pressure and, thus, the rotor backface pressure. The difficulty incurred in raising rotor exit Mach number is that, since the existing actual Mach numbers are already high, further increases tend to be met with reduced efficiencies due to increased diffuser velocity ratios and increased shock losses and blockage at diffuser inlet. Estimates of these efficiency losses are also shown in Figure 35. These efficiency data are based on numerous compressor/diffuser configurations tested at varying impeller exit Mach numbers.

Change in Compressor Stage Pressure Ratio Split

Changes in pressure ratio split between the two compressor stages result in different first-stage exit and second-stage inlet static pressures.

Reductions to first-stage pressure ratio result in lower first-stage backface pressure and, therefore, improved thrust balance for that stage. However, the lower inlet static pressure for the second stage increases the thrust unbalance for that stage. The converse is true regarding increases in first-stage pressure ratio.

Figure 36 indicates the approximate individual stage effects and the net effect on overall compressor rotor thrust. It is observed that, for the base design being considered, changes in stage pressure ratio split result in minimal thrust improvements.

Figure 36 also presents the variation in stage, and overall, efficiencies resulting from these pressure ratio changes. The efficiency determinations were made using data generated in the compressor performance study described earlier in this report.

Axial Turbine

The axial thrust on the two-stage axial turbine is composed, almost totally, of the static pressure drop between first blade inlet and second blade exit, acting over the projected disc/blade frontal area, plus the net momentum loads which are comparatively small. For the basic two-stage axial turbine being considered (50 percent reaction, 0.50 exit axial Mach number), an assumption of this type results in a calculated net turbine load of approximately 4700 pounds. This is unacceptably high for the present gas bearing capabilities.

A significant reduction in thrust load may be achieved by lowering the exit Mach number and reaction levels. No optimum values were determined, but preliminary studies indicate that for reactions of 20 percent and exit axial Mach numbers of 0.20, a thrust load of approximately 2700 pounds can be achieved - still an excessive value.

Another method of reducing thrust on the axial turbine is by back-pressuring the rear rotor disc with high-pressure gas (possibly from compressor discharge, as shown in Figure 37). Figure 38 shows the effect

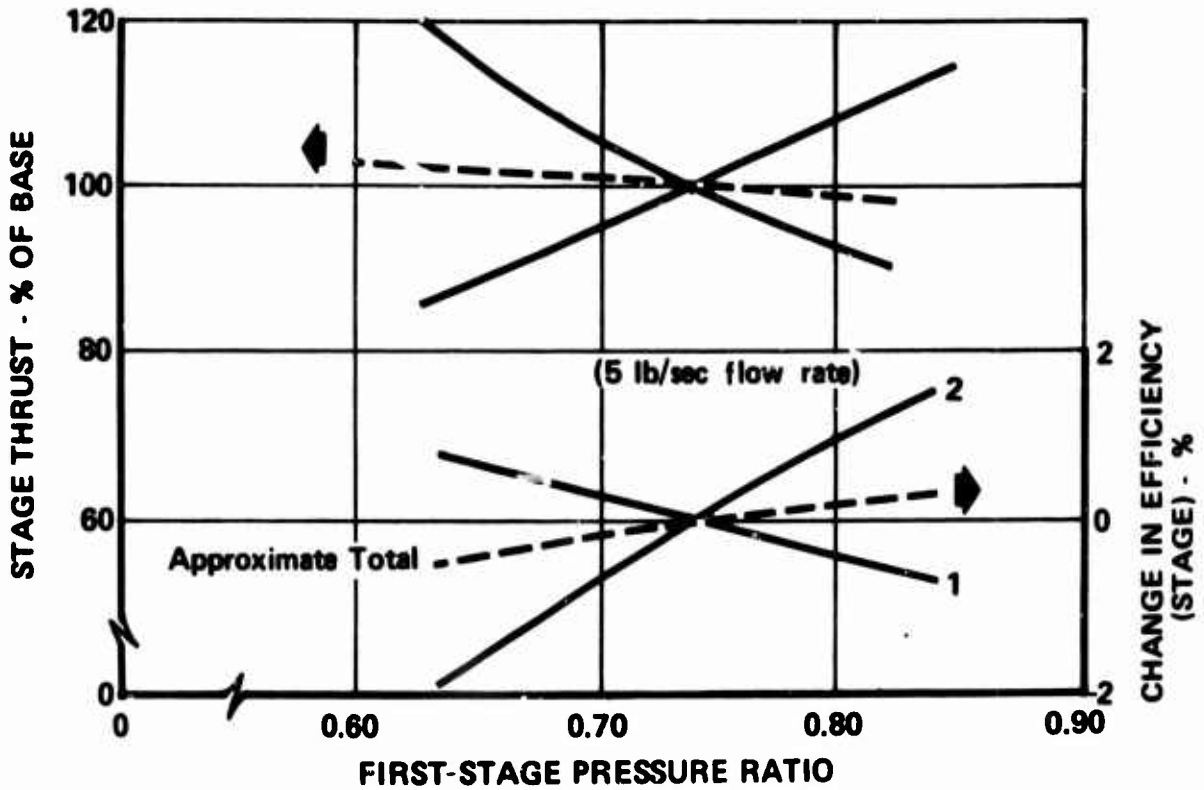


Figure 36. Effect of Rotor Pressure Ratio Split on Centrifugal Compressor Thrust and Efficiency.

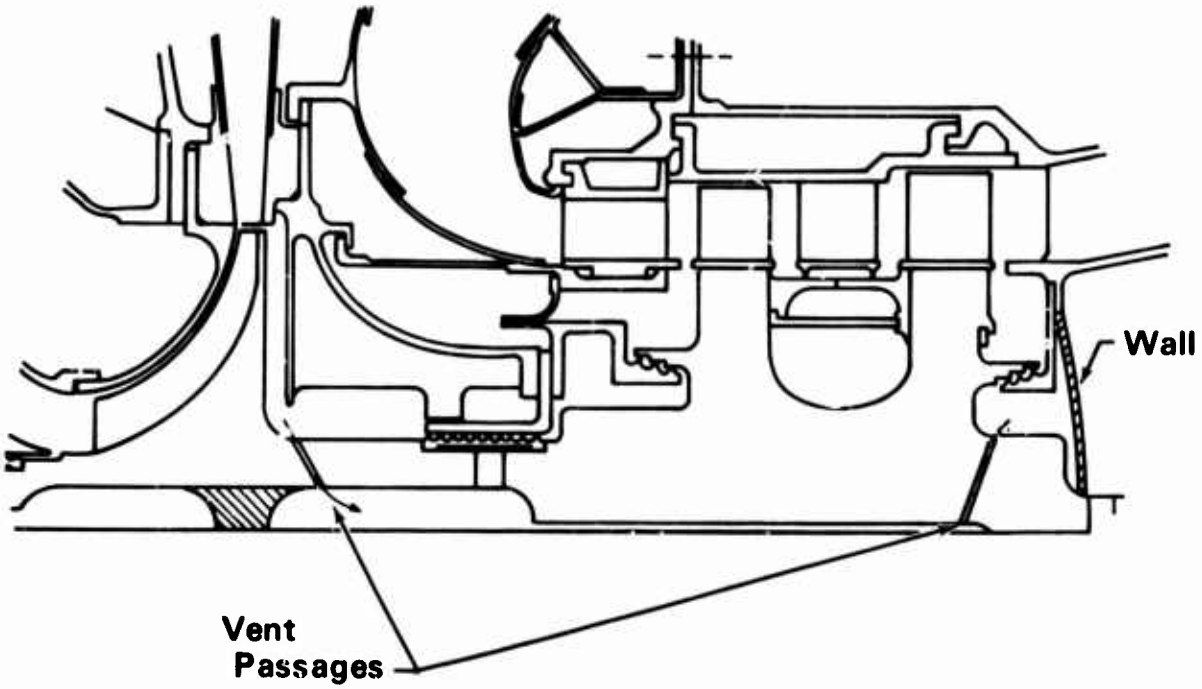


Figure 37. Thrust Balancing Scheme for Axial Turbines.

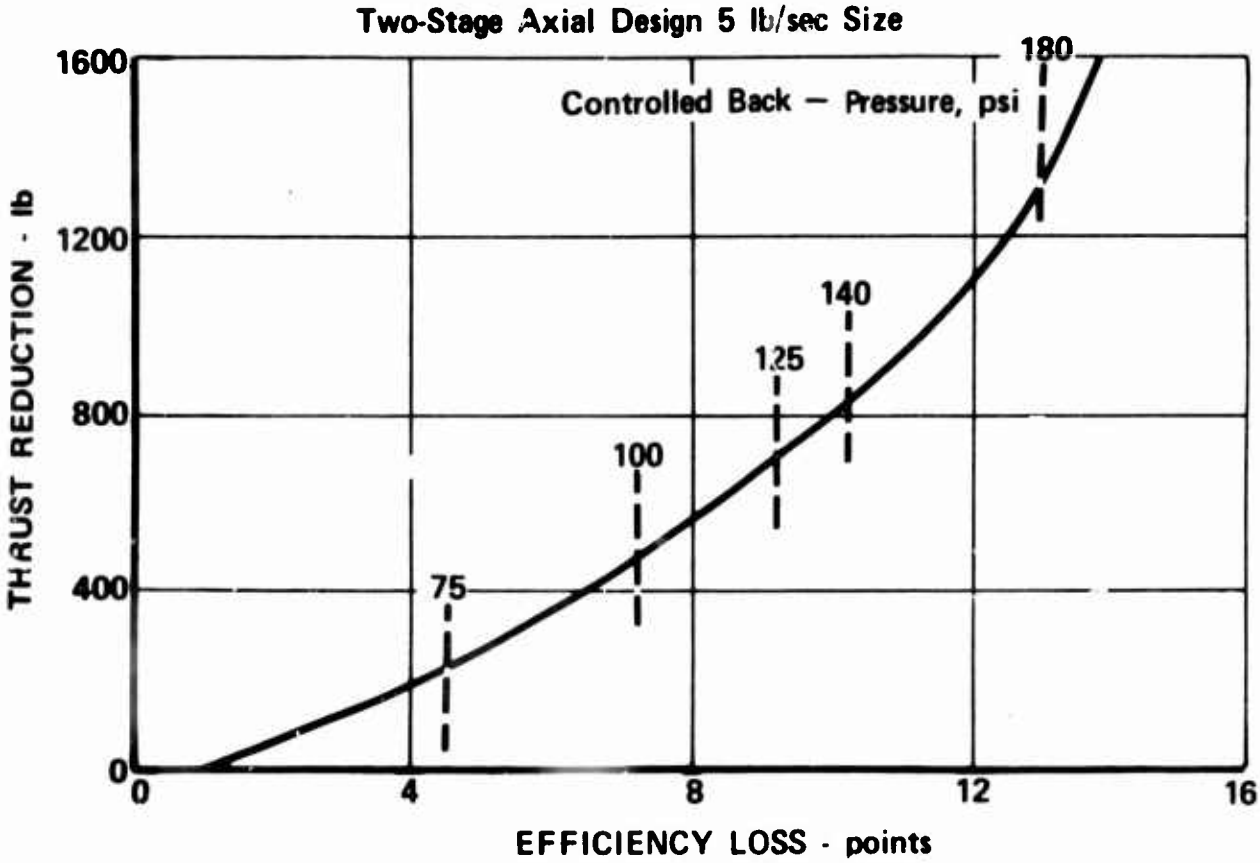


Figure 38. Effect of Efficiency of Back-Pressurizing to Control Axial Thrust.

on thrust and efficiency. It is obvious that back-pressuring the rotor to achieve thrust balance is accompanied by heavy efficiency penalties and is not a practical solution to the problem.

Further reduction in thrust by reducing reaction levels even more was not evaluated, but it is expected that the loss in turbine efficiency would be significant.

Radial Turbine

The radial turbine was investigated to determine the net thrust load resulting from varying degrees of rotor backface cutback. The results are presented in Figure [illegible]. The base thrust load, for no cutback, is approximately 3100 pounds forward. As can be seen in Figure 39, the net turbine thrust is virtually zero at approximately 40-45 percent of rotor cutback.

FRDC is currently involved in a research program, sponsored by AMRDL, to design and test a high-temperature, radial-inflow turbine which is very similar to the design considered in this study. The FRDC/AMRDL design includes a rotor backface radial cutback to approximately 45 percent of blade inlet radius. This was predicated primarily on a stress requirement. Since the operating conditions under consideration are likely to produce stress conditions at least as severe as those of the referenced design, the current design probably will have to be cut back a similar amount. Therefore, the resultant net turbine thrust will be negligible and has not been considered in preliminary turbocompressor rotor thrust estimates.

Because the turbine flow is expanding and a favorable pressure gradient exists, the influence of rotor cutback on efficiency is negligible.

In summary, the following conclusions were reached in regard to the thrust balancing of the engine components:

1. The axial compressor has an acceptable-inherent thrust unbalance and does not require special modification.

2. The centrifugal compressor thrust, while moderately high, can be reduced to much lower and more reasonable values through many methods. Shrouding of the impeller front face is preferred because it affords significant thrust reduction capabilities and, at the same time, increases stage efficiency. This method, however, does not completely eliminate the thrust but could be combined with backface cutback to achieve increased rear thrust with little or no performance penalty.

3. The axial turbine has a very high net thrust unbalance for its base design. This can be significantly reduced by lowering design exit Mach numbers and reaction levels, and/or back-pressuring the turbine at the expense of lower efficiency due to high seal leakage.

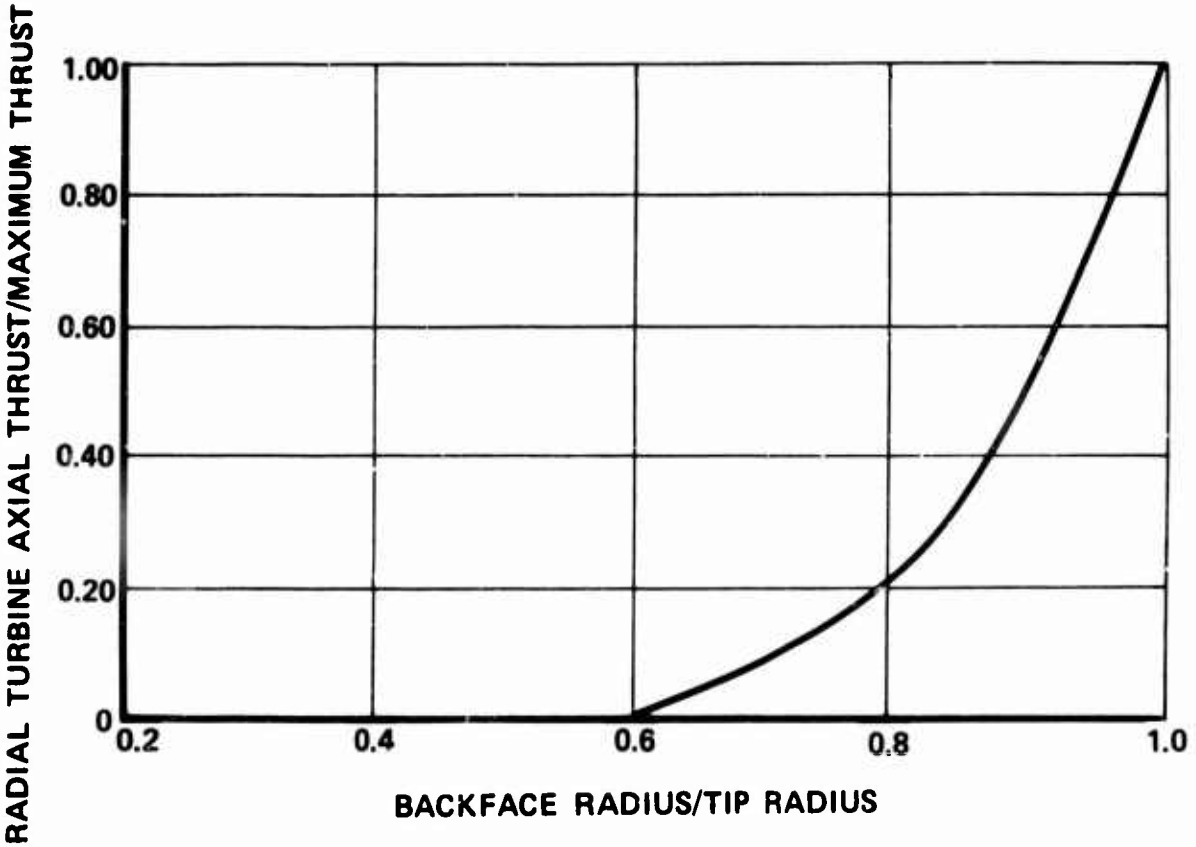


Figure 39. Effect of Backface Cutback on Radial Turbine Axial Thrust.

4. The radial turbine, with a rotor backface cutback necessitated by stress criteria, has a very small resultant net thrust.

It is obvious from the results of the study that an engine configuration consisting of centrifugal compressors and radial turbine, C_oT_o, can be balanced theoretically to zero net thrust. When mated with an axial turbine, the C_o compressor would have to be unbalanced to offset the axial turbine thrust load.

CRITICAL SPEEDS OF ROTOR CONFIGURATIONS

Since air bearings have very low inherent damping capacity relative to oil-film bearings, a rotor with air-lubricated bearings is generally more prone to exhibit resonant unbalance response amplitudes at rotor critical speeds. Because of the absence of boundary lubrication in air bearings, any conditions which could result in repeated bearing contacts, whether induced by resonant unbalance response or by externally applied vibration and shock, must be avoided. It follows that the rotor-bearing system should be designed to avoid operation at or near the rotor critical speeds. The avoidance of operation near the third critical speed is probably the most important; for this reason, a criterion for design acceptability has been established which requires that the third critical should not occur at a speed below 133 percent of engine overspeed (160 percent of design speed).

Based on the flow paths, wheel weights, and wheel inertias discussed previously, rotor layouts were drawn for various configurations of axial and radial flow compressors and turbine for the 5 lb/sec flow rate engine. Most attention was given to the configurations having both high spool (product) efficiency and low rotational speed. No rotor layouts were prepared for the configurations using C_1 compressors because of the very low product efficiency.

Each layout included journal and thrust bearings sized to accommodate the anticipated loads and to fit within the proposed aerodynamic flow-path. With the dimensions obtained from the rotor layouts, critical speed studies were performed. These studies included computation of rotor-system undamped transverse natural frequencies (critical speeds) and corresponding more shapes, taking into account the stiffness and mass characteristics of both the rotor and the bearings.

The calculated values of the third critical speed for the 5.0 lb/sec engine rotors are given in the last column of Table V. This column is entitled "Free-Free Critical Speed at a Bearing Stiffness of 1×10^5 lb/in.". Strictly speaking, the use of the term "free-free" indicates that the bearing stiffness is so small that it does not affect the critical speed. This is not necessarily the case for all of the rotors evaluated. In those cases where the rotor is not very stiff, increasing values of bearing stiffness result in increasing values of critical speed:

TABLE V. CRITICAL SPEEDS AND STATIC BEARING LOADS OF VARIOUS CONFIGURATIONS OF A 5 LB/SEC ENGINE

Configuration	Remarks	Weight of Compressor and Turbine Wheels (lb)	Weight of Complete Rotor (lb)	Bearing Span (in.)	Static Load on Compressor End Bearing (lb)	Static Load on Turbine End Bearing (lb)	Design Speed (rpm)	Free-Free Critical Speed at Bearing Stiffness of 1×10^5 lb/in. (rpm)
Co-To	Titanium 1st and 2nd Stage Compressor Wheels	17.0	25.9	11.94	6.3	19.5	50,000	104,100
As Above	Titanium 1st Stage, Steel 2nd Stage Compressor Wheels	20.6	30.6	11.94	7.6	23.0	50,000	110,600
	Titanium 1st Stage, Steel 2nd Stage Compressor Wheels	20.6	32.0	17.37	16.0	16.0	50,000	90,540
	Titanium 1st Stage, Steel 2nd Stage Compressor Wheels	20.6	33.0	16.37	19.4	13.6	50,000	62,360
	Titanium 1st Stage, Steel 2nd Stage Compressor Wheels	20.6	32.6	12.0	8.1	24.5	50,000	97,900
Co-T1	Titanium 1st and 2nd Stage Compressor Wheels	19.8	28.7	11.94	6.1	22.6	50,000	103,800
As Above	As above but with Increased Bearing Span	19.8	30.0	14.0	7.5	22.5	50,000	89,200
	Titanium 1st and 2nd Stage Compressor Wheels	19.8	29.3	15.25	11.1	18.2	50,000	111,300
	Titanium 1st Stage, Steel 2nd Stage Compressor Wheels	22.8	35.7	14.25	12.1	23.6	50,000	87,150
Co-T2	Titanium 1st and 2nd Stage Compressor Wheels	28.2	37.9	11.94	2.9	35.0	50,000	91,100
	Titanium 1st and 2nd Stage Compressor Wheels	28.2	39.1	17.5	7.9	31.2	50,000	86,900
C2-To	Titanium Compressor Wheels	15.1	24.1	11.94	4.3	19.8	68,000	97,500
As Above	As Above with Ip-It Effect	15.1	24.1	11.94	4.3	19.8	68,000	94,100

Key:

Compressors
- Co - 2 Stage Centrifugal
- C2 - 2 Stage Axial + 1 Stage Centrifugal

Turbines
- To - Radial Inflow
- T1 - Single Stage Axial
- T2 - 2 Stage Axial

Bearings
- Journals
- Thrust

An examination of the data given in Table V reveals the following:

a. All of the 5.0 lb/sec flow-rate engine configurations using a centrifugal compressor (C_0), except the C_0-T_0 configuration which has a thrust runner mounted outboard of the compressor-end journal bearing, meet the critical speed criteria of 160 percent design speed, i.e., 1.6 x 50,000 = 80,000 rpm.

b. The 5.0 lb/sec flow-rate engine configuration using two axial stages (C_2) in the compressor does not meet the critical speed criteria, i.e., 1.6 x 68,000 = 108,000 rpm.

c. The use of the two-stage axial turbine results in the heaviest rotor design and the most unequal distribution of static load between the journal bearings.

From examination of the critical speed data in Table V, it would appear that the C_0-T_0, C_0-T_1, and C_0-T_2 rotors would be suitable for inclusion in an air bearing engine. Furthermore, it would appear that some freedom of choice exists in the relative positions of bearings, compressors and turbines. However, two other rotor parameters strongly influence the performance of a rotor-bearing system, and these must, therefore, be considered when evaluating the critical speed behavior. These two parameters are the bearing span, which should be as large as possible; and the static journal bearing loads, which should be nearly equal as possible. Additional discussion of these parameters is contained in the section of this report devoted to "journal bearing loads". The rotor found to best meet the critical speed criteria, to have large bearing span, and to have equally loaded journal bearings is the C_0-T_0 configuration supported between journal bearings. It will be recalled from the discussion of compressor and turbine performance that the product efficiency of this configuration is also very good.

Based on the results of the critical speed evaluation of the 5.0 lb/sec flow-rate engine, critical speed studies of the 3.5 and 2.0 lb/sec flow-rate engines were limited to configurations with two-stage centrifugal compressors with the bearings located at the rotor extremities. The results of these studies are given in Table VI. From this table it can be seen that each configuration studied has a critical speed in excess of the critical speed criteria (96,000 rpm for the 3.5 lb/sec engine and 126,400 rpm for the 2.0 lb/sec engine). It can also be seen that the static loads to be supported by each journal bearing are approximately equal.

The results of the evaluation to ascertain the effects of engine size on rotor critical speed are shown in Figure 40. In this figure the ratio of the calculated rotor critical speed (third) divided by the engine overspeed is plotted against engine flow rate. It can be clearly seen from this figure that the critical speed criterion can be satisfied by a number of attractive engine configurations throughout the 2- to 5-lb/sec flow range. As flow rate decreases, the critical speed criterion becomes easier to satisfy.

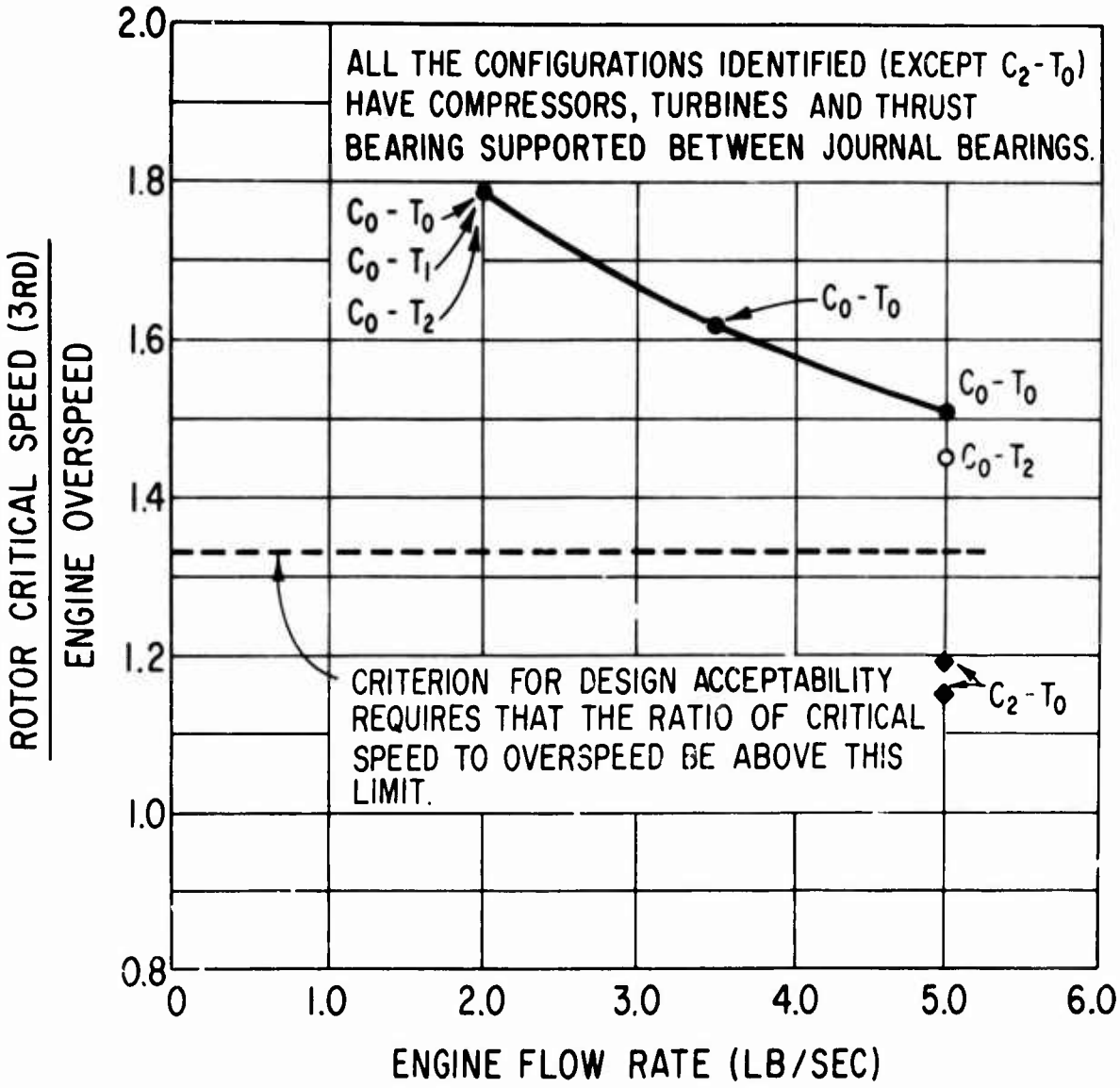
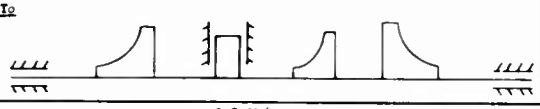
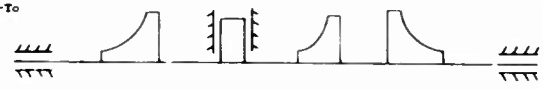
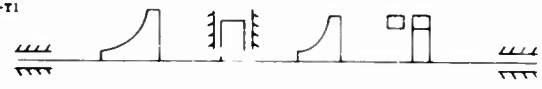
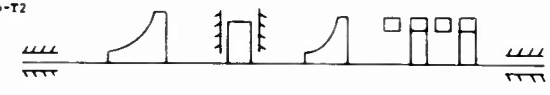


Figure 40. Ratio of Rotor Critical Speed to Engine Overspeed Versus Engine Flow Rate.

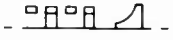
TABLE VI. CRITICAL SPEEDS AND STATIC BEARING LOADS OF VARIOUS CONFIGURATIONS OF 3.5 AND 5 LB/SEC ENGINES

Configuration	Remarks	Weight of Compressor and Turbine Wheels (lb)	Weight of Complete Rotor (lb)	Bearing Span (in.)	Static Load on Compressor End Bearing (lb)	Static Load on Turbine End Bearing (lb)	Design Speed rpm	Free-Free Critical Speed at Bearing Stiffness of 1×10^3 lb/in. rpm
3.5 lb/sec								
Co-To 	Titanium 1st and 2nd Stage Compressors Wheels	12.06	20.9	14.85	10.4	10.5	60,000	116,300
2.0 lb/sec								
Co-To 	Titanium 1st and 2nd Stage Compressor Wheels	6.0	9.7	12.3	4.4	5.3	79,000	170,000 +
Co-T1 	Titanium 1st and 2nd Stage Compressor Wheels	4.8	8.95	11.9	4.0	4.95	79,000	170,000 +
Co-T2 	Titanium 1st and 2nd Stage Compressor Wheels	6.8	11.0	13.06	4.7	6.3	79,000	170,000 +

Key:

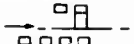
Compressors

Co - 2 Stage Centrifugal 

C2 - 2 Stage Axial + 1 Stage Centrifugal 

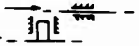
Turbines

To - Radial Inflow 

T1 - Single-Stage Axial 

T2 - Two-Stage Axial 

Bearings

Journals 

Thrust

EFFECTS OF FLOW RATE ON ENGINE ROTOR DIMENSIONS

The most promising engine configuration to emerge from the evaluation of turbine and compressor performance and the evaluation of rotor critical speeds was the C_o-T_o. However, no predominant effects of engine size on the performance of the air bearing rotor system were identified by the evaluation. At most, the critical speed to overspeed ratio, which was satisfactory for all C_o-T_o engine sizes, favored the smaller engines (Figure 40).

The effects of engine flow rate on the dimensions and design speeds of the C_o-T_o configuration are presented in the following paragraphs. For purposes of comparison, the effects of using a single- or two-stage axial turbine instead of the radial inflow turbine (T_o), in conjunction with the two-stage centrifugal compressor, are shown in Tables V and VI showing rotor weights.

Figure 41 shows a curve of engine speed versus engine flow rate for the C_o-T_o configuration. Design point occurs at 100 percent power, at which point the compressor specific speed is 90 for each engine flow rate. The pressure ratio and turbine inlet temperature at design point are 17.5:1 and 2550°F respectively for each engine flow rate. It should be noted here that the selected design speeds for the three engine flow rates coincide closely with the speed range specified in the design objectives, i.e., 50,000 to 75 000 rpm. At the 2.0 lb/sec flow rate, design is slightly in excess of the objective at 79,000 rpm.

Figure 42 shows the weights of the compressor and turbine wheels plotted against engine flow rate, while Figure 43 shows total rotor weight plotted against engine flow rate. Rotor weights and wheel weights used in these figures are based on the use of a titanium alloy for both centrifugal compressor wheels and a nickel-based alloy for the turbine wheel.

Estimates of total rotor weight (Figure 43) are based on the compressors, turbine and thrust bearing being supported between journal bearings located at the rotor extremities. The lightest rotor (later found impractical for critical speed reasons) designed for the 5.0 lb/sec engine was for the C_2-T_o configuration. The weight of this rotor is shown on Figure 43 to provide a benchmark when considering the weights of the rotors used in other configurations. Figure 43 shows the C_o-T_1 to be the lightest practical configuration, with the C_o-T_1 approximately 10 percent heavier. The C_o-T_2 configuration is approximately 25 percent heavier than the C_o-T_1.

Figure 44 shows both hub diameter and journal diameter plotted against engine flow rate. The hub diameters are the inlet diameters of the C_o compressors and the exit diameter of the T_o turbine. The preferred engine configuration locates the bearings at the rotor extremities, i.e., at the inlet to the first-stage compressor and at the exit from the turbine. Therefore, in order to avoid undesirable distortion of the air flow path, the journal bearings must be smaller in diameter than the hub diameter. The extent of this difference in diameter is shown in Figure 44.

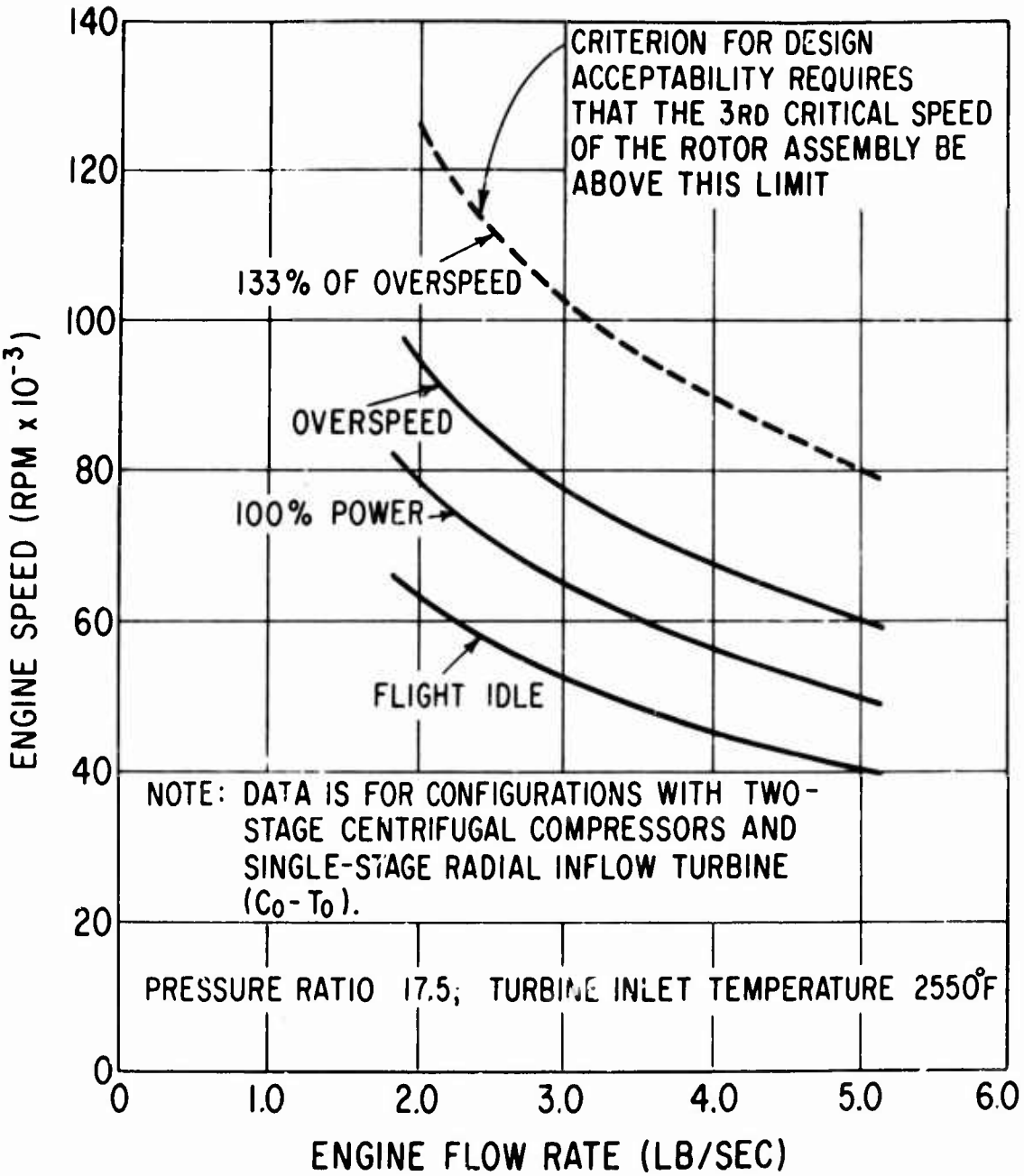


Figure 41. Engine Speed Versus Engine Flow Rate.

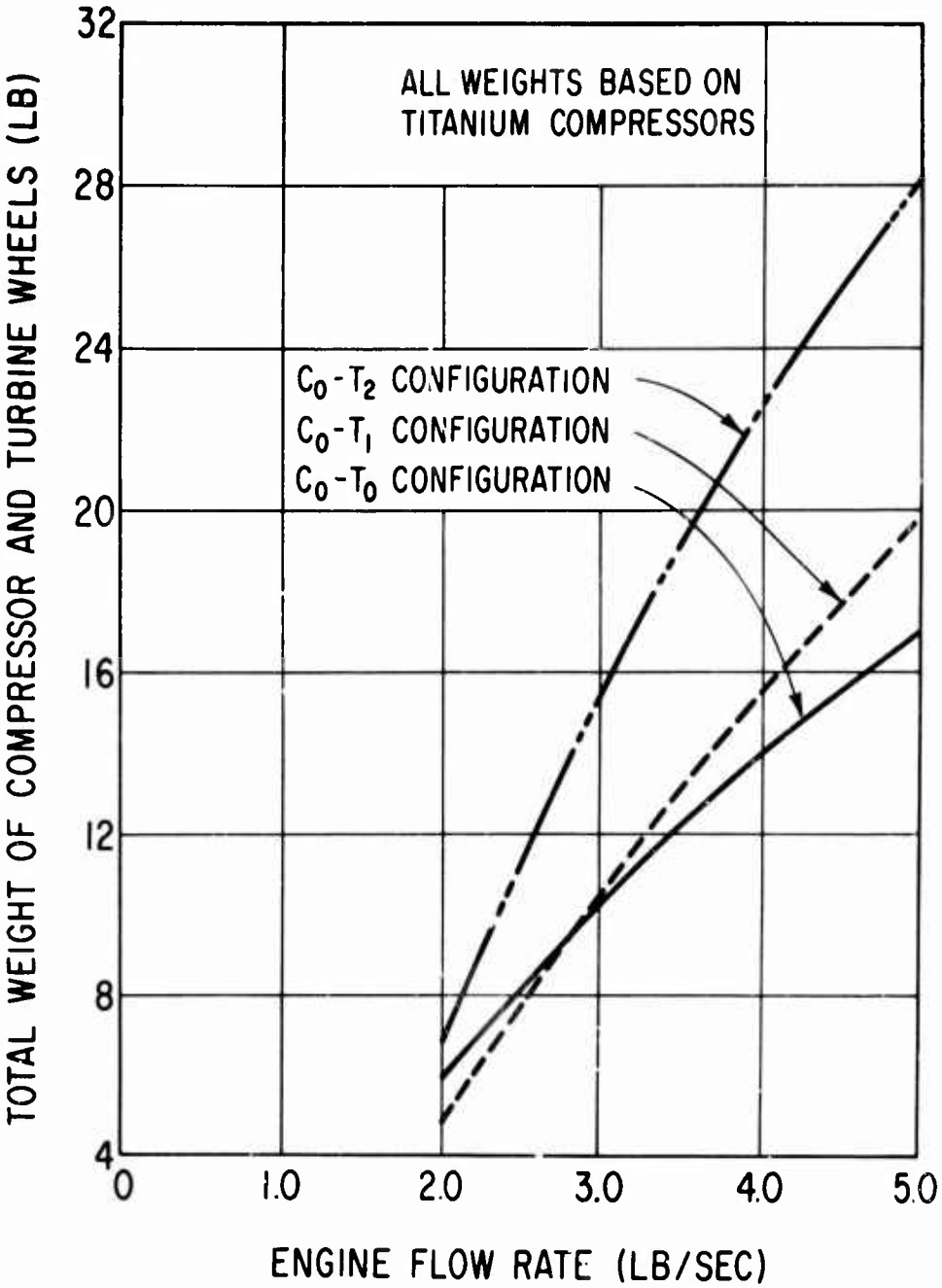


Figure 42. Total Weight of Compressor and Turbine Wheels Versus Engine Flow Rate.

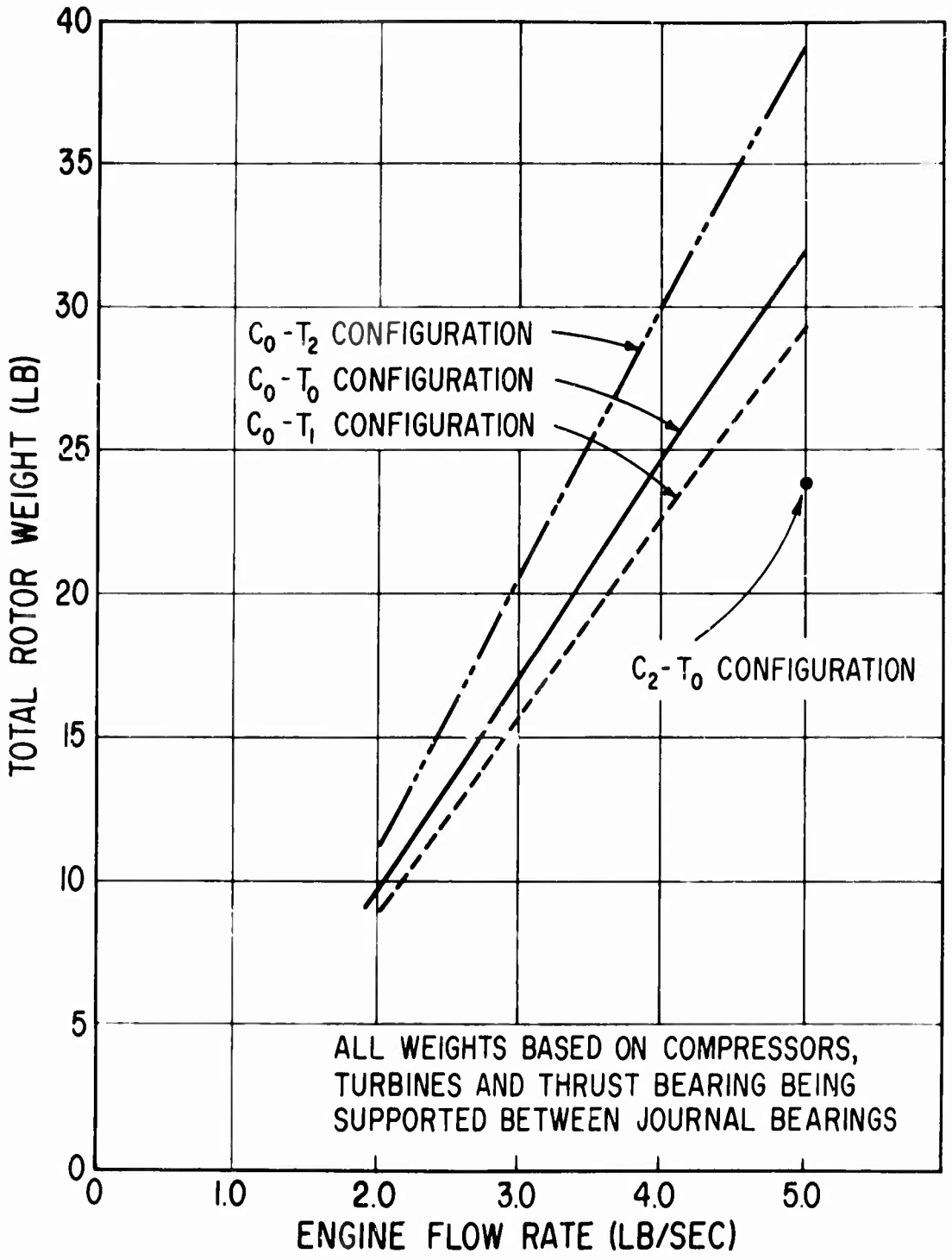


Figure 43. Total Rotor Weight Versus Engine Flow Rate.

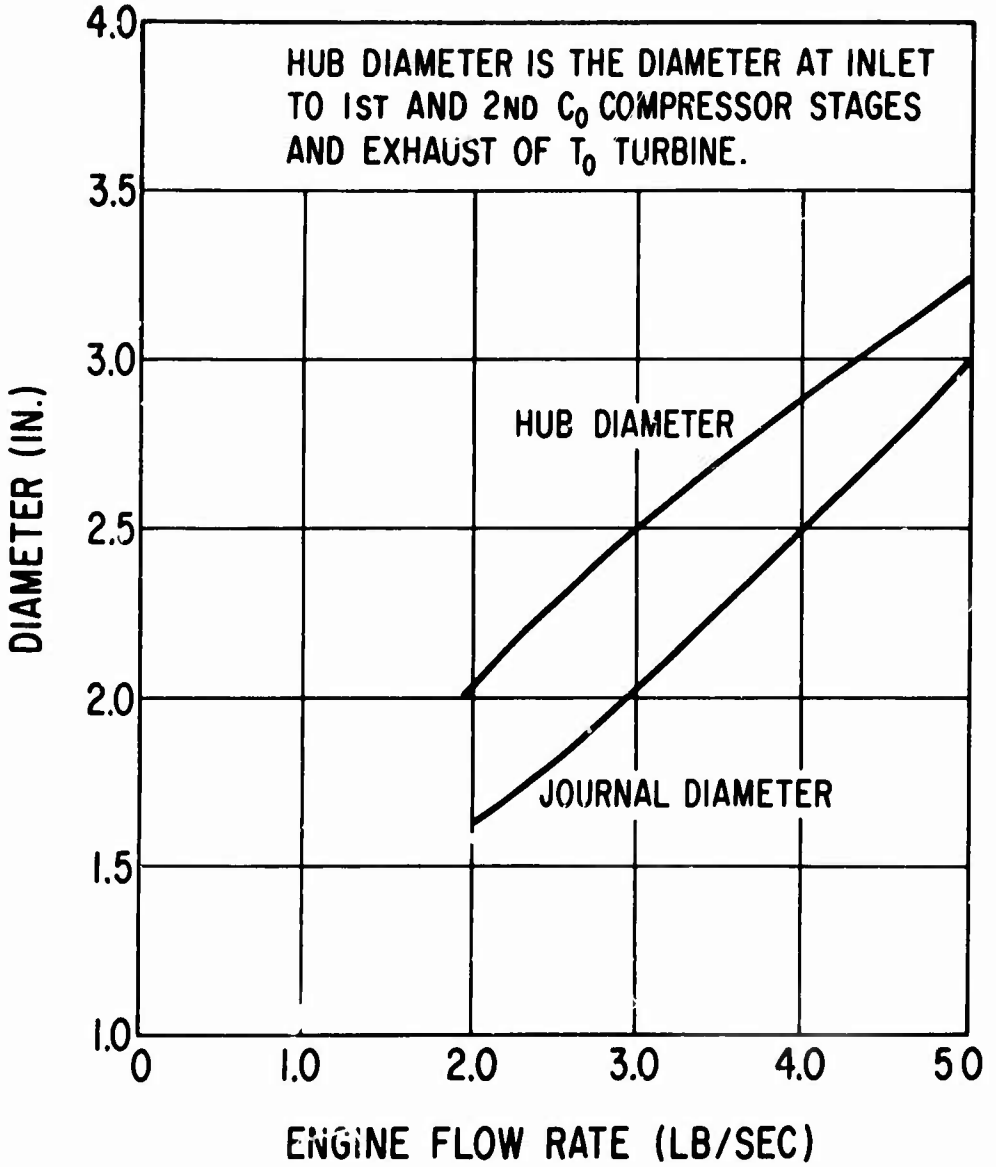


Figure 44. Journal Bearing and Wheel Hub Diameter Versus Engine Flow Rate.

Figures 45 and 46 show dimensions that are of primary importance in calculating the gyroscopic loads on the journal bearings induced by aircraft maneuver conditions (2 radians/sec pitch). Plots of polar moment of inertia and length between journal bearing versus engine flow rate are given in Figures 45 and 46, respectively. Each of these plots is for the C_o-T_o configuration with the compressor wheels, turbine, and thrust runner located between journal bearings. The rotor dimensions and materials used to determine the polar moment of inertia are consistent with those used to determine the total rotor weight given in Figure 43. A curve showing total rotor length is also given in Figure 46.

It can be seen from the Figures 41 through 46, in which the most significant rotor dimensions are plotted against engine flow rate, that no one parameter is found to vary in a manner likely to dictate the selection of a particular engine size for the application of air bearings. However, some variations in dimensions of secondary importance are detectable in the C_o-T_o configurations as follows:

a. Increasing the flow rate by 150 percent (2.0 to 5.0 lb/sec) results in a 220 percent increase in rotor weight (Figure 43). This effect favors the lower flow rate engine.

b. Increasing flow rate by 150 percent (2.0 to 5.0 lb/sec) results in a 635 percent increase in rotor polar mement of inertia and a 41 percent increase in bearing span. The journal bearing gyroscopic loads are directly proportional to inertia and inversely proportional to length. Thus from a gyroscopic load standpoint, the greater increase in inertia with flow rate would tend to favor the lower flow rate engines.

The rotor dimensions affected by engine size are seen to be those that influence the maneuver load capacity of both the journal and thrust bearings. Discussion of the importance of these influences will, therefore, be deferred until the sections of this report in which bearing load and bearing performance are described.

JOURNAL BEARING LOADS

The loads to be supported by the air-lubricated journal bearings arise from two sources. The first of these is the static load, the magnitude of which depends on rotor weight and the position of the rotor center of gravity. The second, and by far the most important, is the load resulting from the aircraft maneuver conditions specified in MIL-E-5007C. The operating load diagrams from this specification are given in Figure 47.

While in flight, at any altitude between sea level and 25,000 feet, and any power level between 0 and 100 percent, the major loads imposed on the journal bearings are the result of velocities and accelerations of the magnitude and direction given as follows:

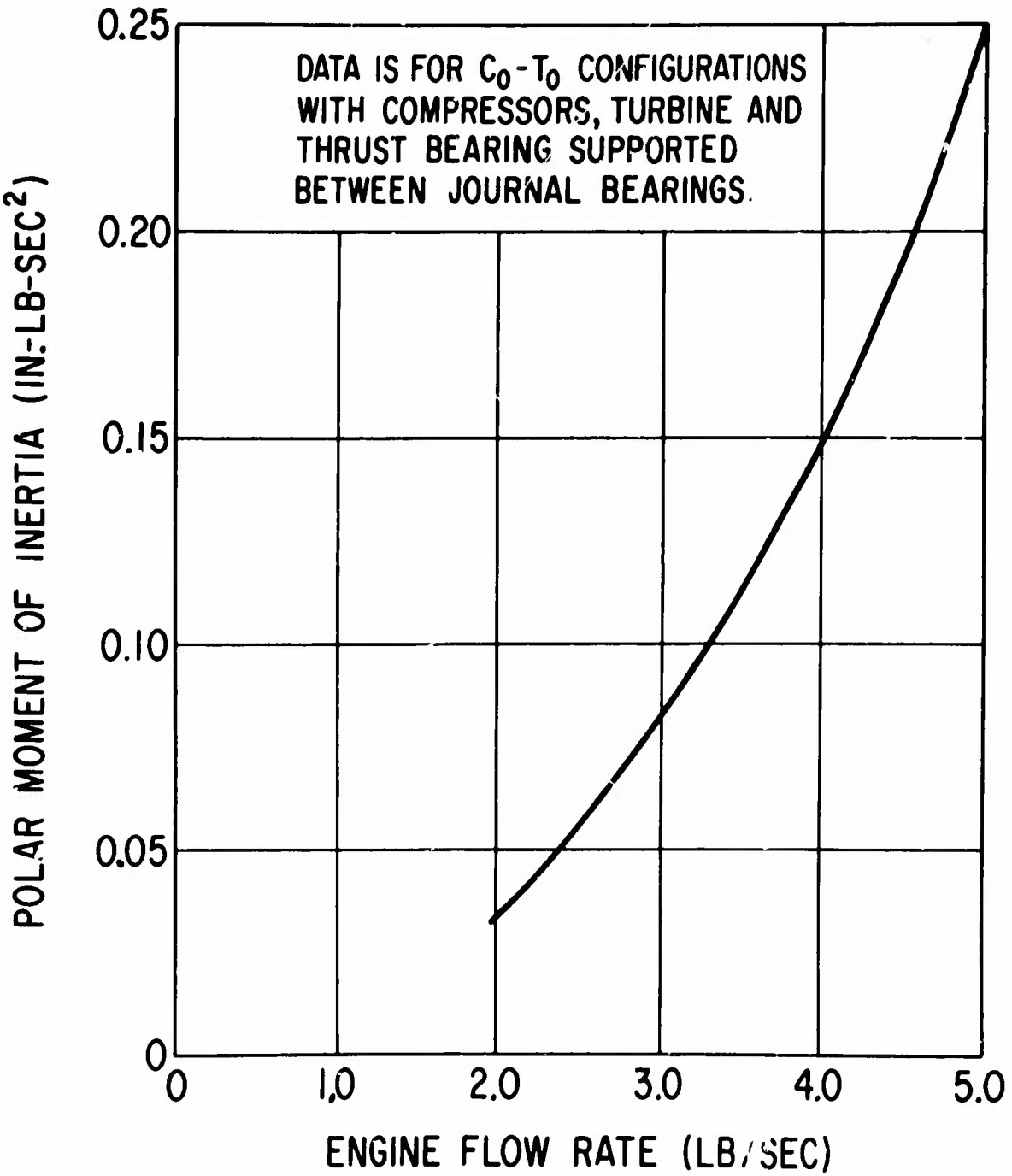


Figure 45. Polar Moment of Inertia of Rotor Versus Engine Flow Rate.

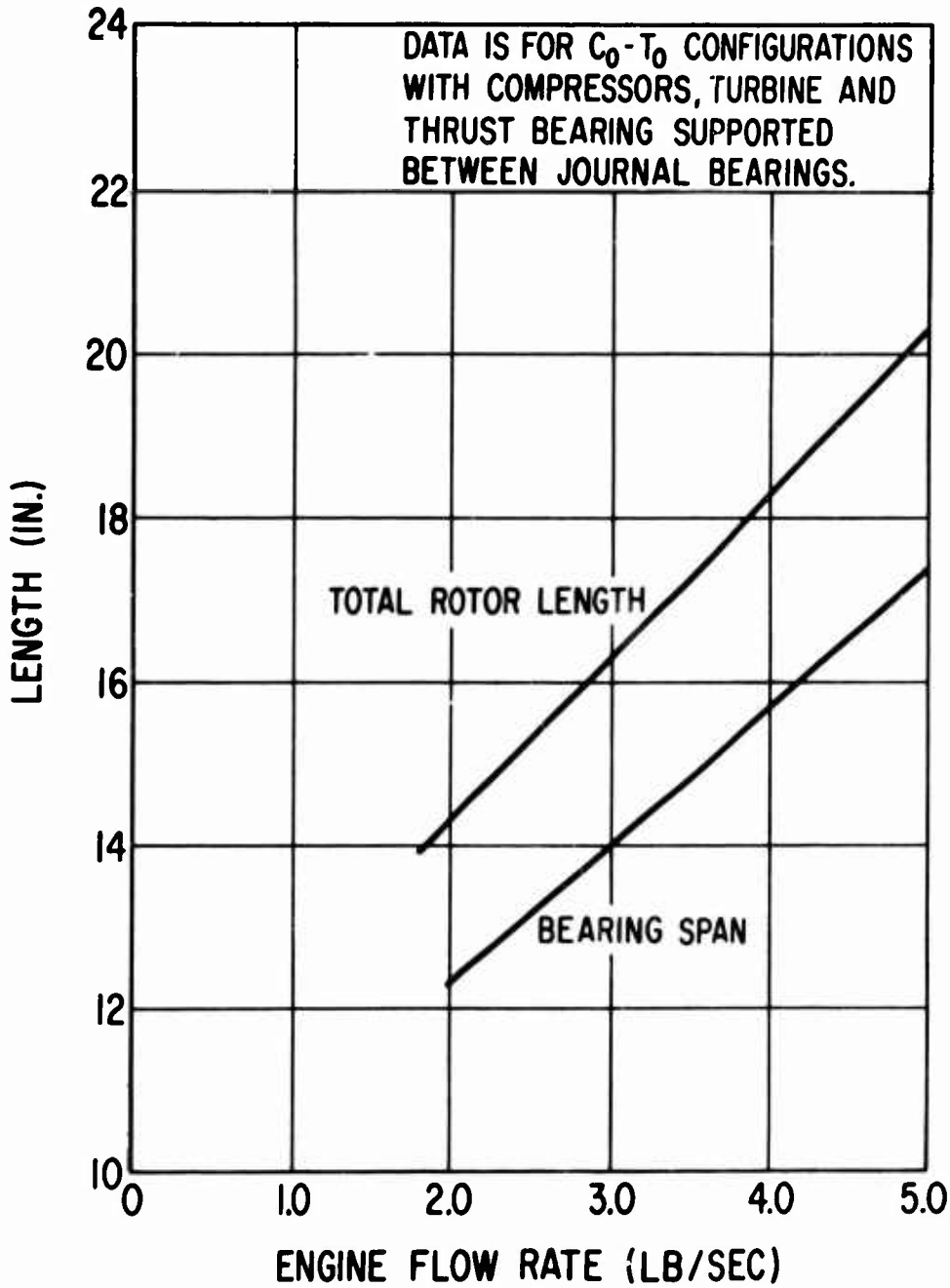


Figure 46. Rotor Length and Bearing Span Versus Engine Flow Rate.

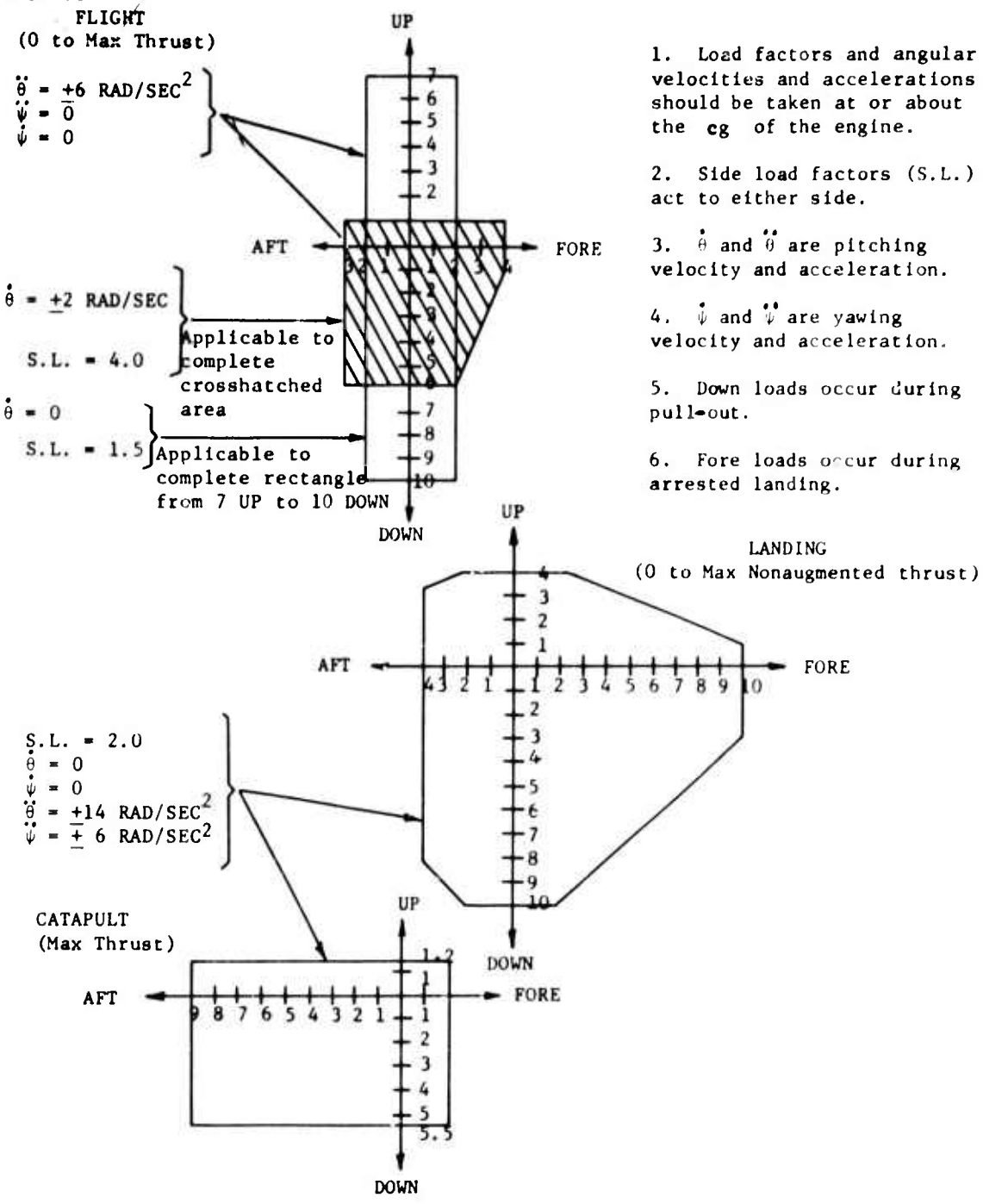


Figure 47. Operating Load Diagrams for the Gas Generator.

a. 2 rad/sec pitch
b. The resultant of 6g down and 4g side
c. The resultant of 10g down and 2g side

Also, when landing at any power level between zero and 100 percent, the maximum loads on the journal bearings result from accelerations of the magnitude and direction given in c, above. Catapult conditions, at 100-percent power, cause resultant accelerations of a magnitude approximately equal to those in c, above.

Based on these velocities and accelerations, maximum journal bearing loads have been calculated for each of the 2.0, 3.5, and 5.0 lb/sec engines at various rotor speeds. In all cases, total bearing load was calculated as the vector sum of the simultaneously acting vertical and side force components. The maximum value of total vector load obtained has been retained for use when evaluating journal bearing performance. Maximum journal bearing loads versus engine rotor speed are shown for the 2.0, 3.5, and 5.0 lb/sec, C_o-T_o engines in Figures 48, 49, and 50 respectively. It is seen from these figures that a significant proportion of the total load on each journal bearing is caused by the gyroscopic forces associated with the 2 rad/sec pitch maneuver.

The gyroscopic force is given by

$$F_{gyro} = \frac{I_P \dot{\theta} \omega}{\ell}$$

where F_{gyro} = gyroscopic force acting on the bearing, lb

I_P = polar mass moment of inertia of the rotor, in.-lb-sec^2

θ = pitch velocity, rad/sec

ω = rotor speed, rad/sec

ℓ = bearing span, in.

It is possible at this point to evaluate some of the effects of engine size on journal bearing performance. The total bearing load is seen to be determined from consideration of the following rotor parameters:

a. Rotor weight
b. Static load on each journal
c. Polar mass moment of inertia
d. Rotor speed
e. Bearing span

A plot of the maximum resultant journal bearing maneuver loads versus engine flow rate is shown in Figure 51. From this figure it can be seen that increasing the flow rate by 150 percent (2.0 to 5.0 lb/sec) results in an increase in maximum journal bearing load (at design speed) of 200 percent. The effect on journal bearing load on the operating speed range,

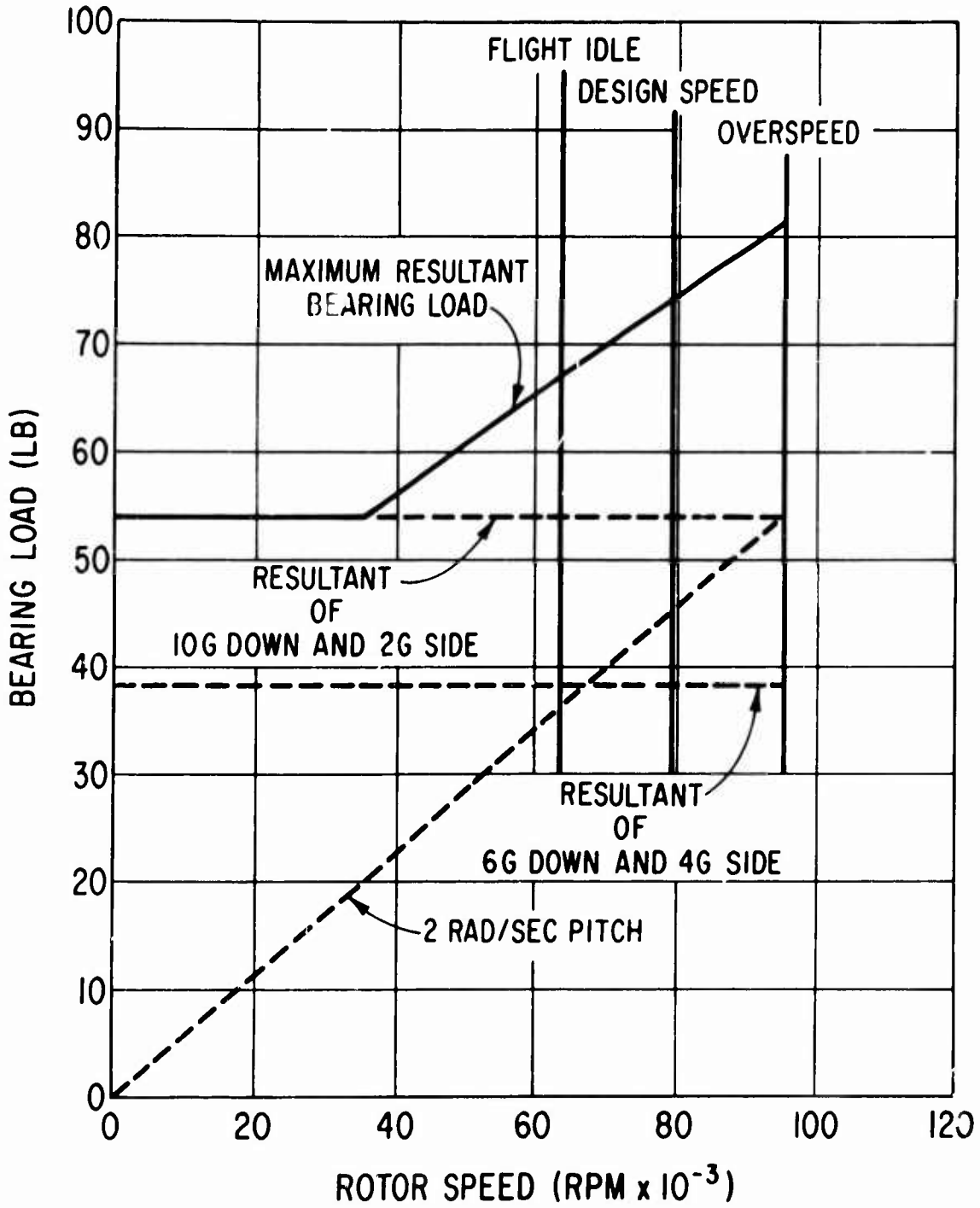


Figure 48. Maximum Journal Bearing Load Conditions for a 2 lb/sec C_o-T_o Engine With Equally Loaded Bearings.

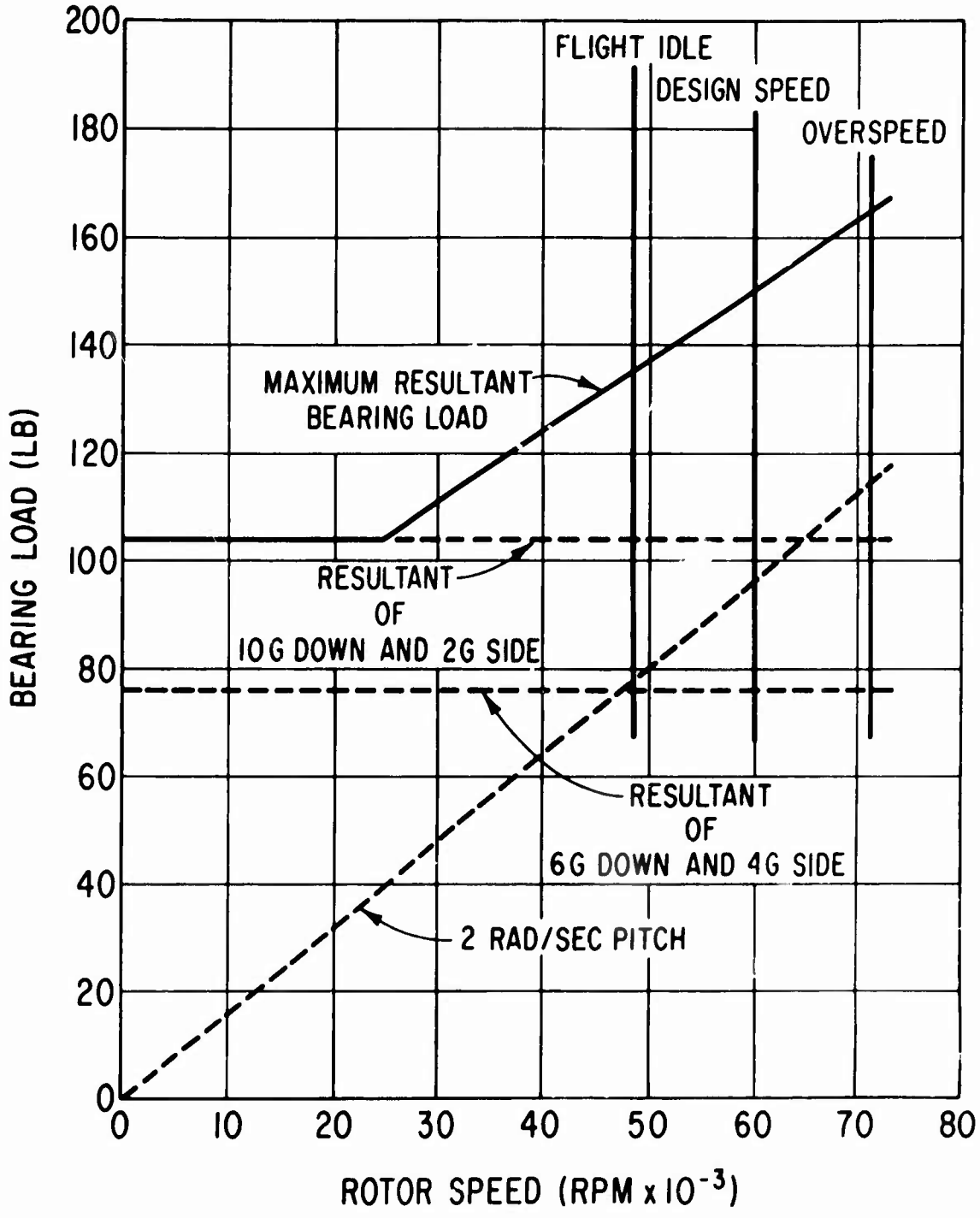


Figure 49. Maximum Journal Bearing Load Conditions for a 3.5 lb/sec C_o-T_o Engine With Equally Loaded Bearings.

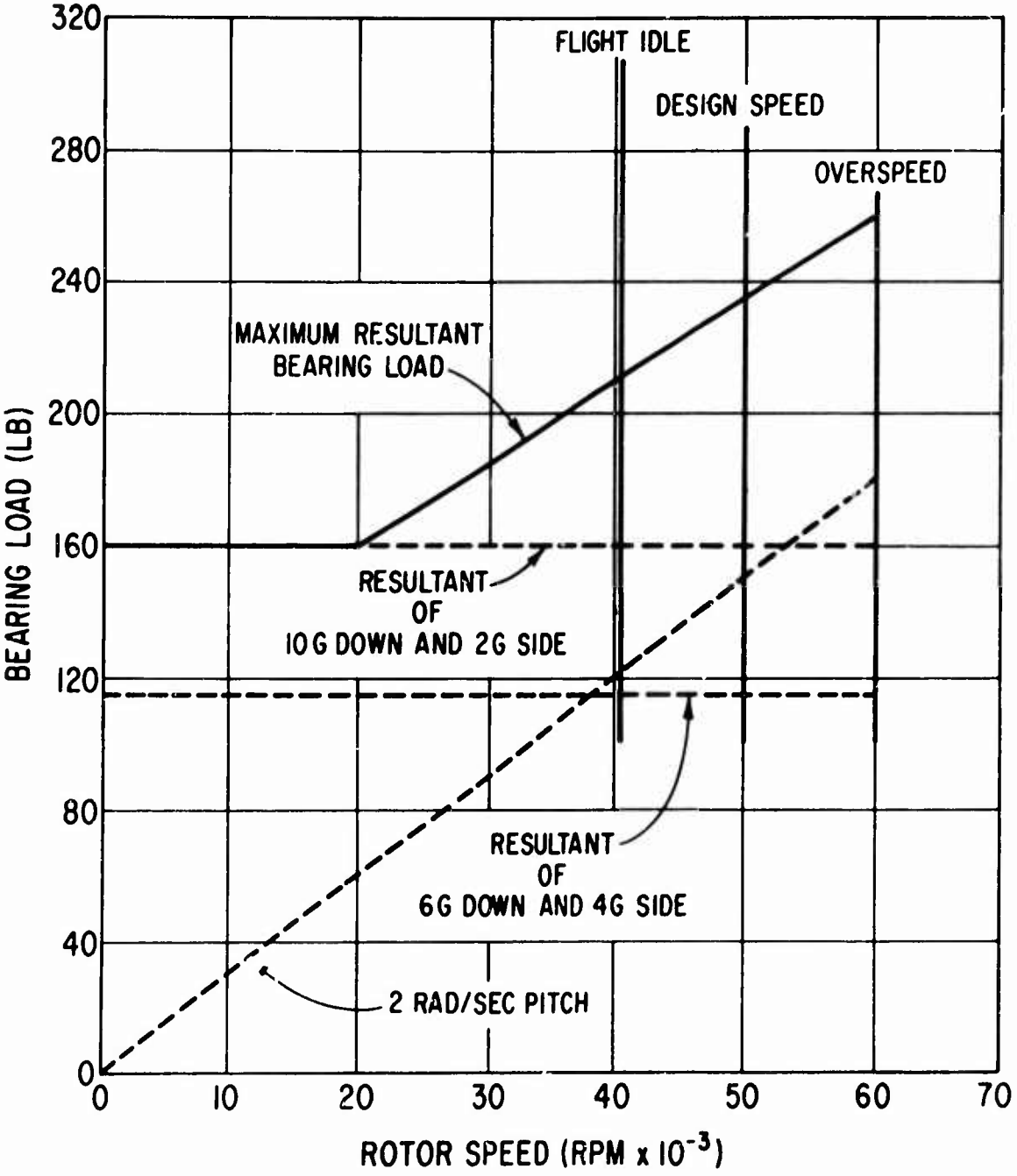


Figure 50. Maximum Journal Bearing Load Conditions for a 5 lb/sec C_o-T_o Engine With Equally Loaded Bearings.

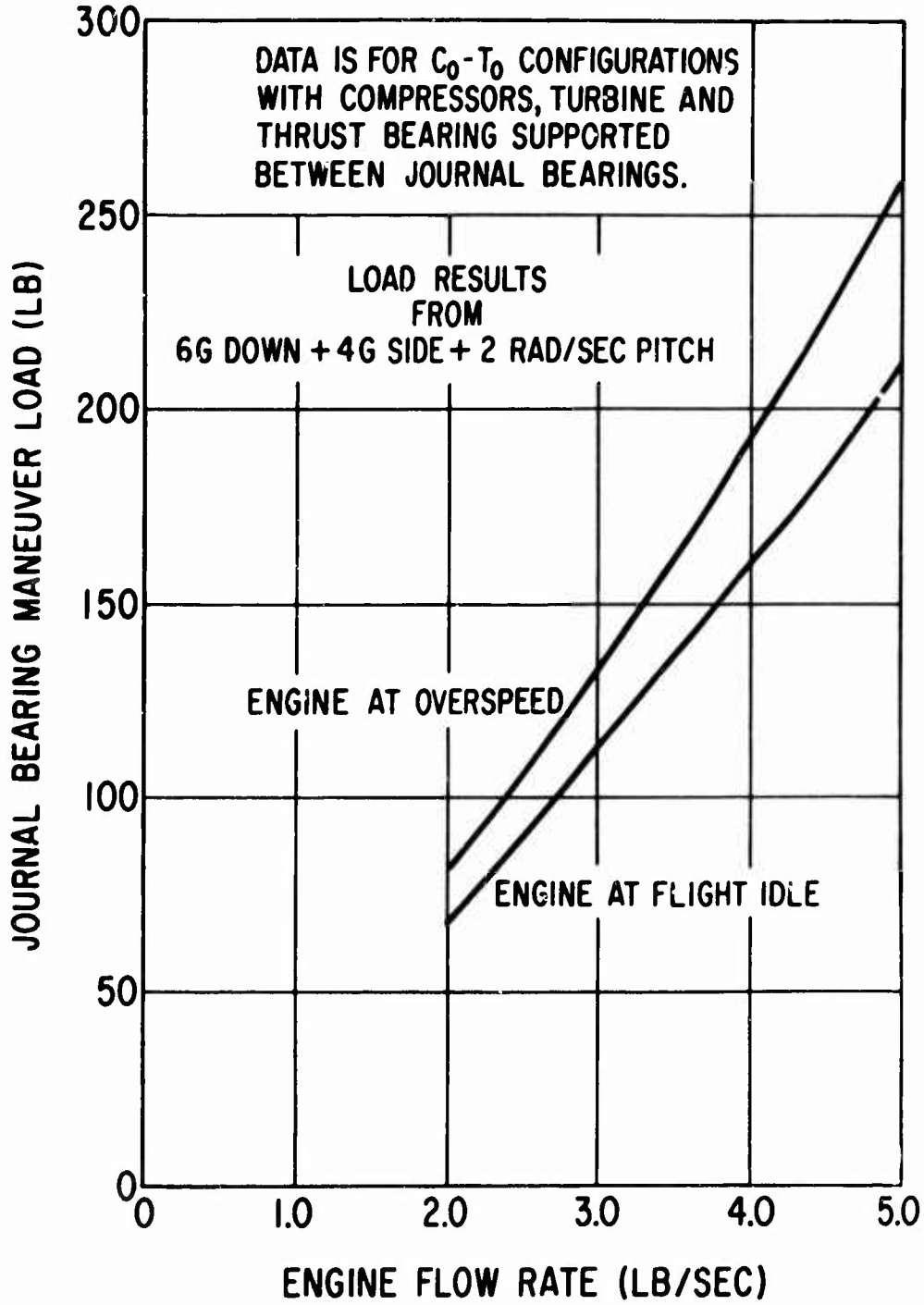


Figure 51. Maximum Resultant Journal Bearing Maneuver Load Versus Engine Flow Rate.

i.e., flight idle to 120 percent overspeed, can also be determined from this figure.

JOURNAL BEARING PERFORMANCE

A previous study [1] has shown that pivoted-pad hydrodynamic journal bearings would be the most suitable type of bearing for use in a small gas turbine. This same study also identified the most severe operating condition for the journal bearings to be engine idle at 25,000 feet altitude with maximum loads imposed. The severity of this operating condition occurs because of the association of low speeds of rotation and low pressures in the bearing cavities (bearing cavity pressure is obtained from compressor discharge), when the bearing load is large. As would be expected, the load-carrying capacity of a hydrodynamic bearing is strongly affected by both rotational speed and ambient pressure. Bearing studies have, therefore, been carried out for each engine size (only the C_o-T_o configuration was considered) at flight-idle speeds of rotation and the associated maximum loads. The first task performed was to ascertain the effects of both clearance ratio and ambient pressure on bearing performance. Clearance ratio is defined as the difference between the radius of the bearing pad and the radius of the journal divided by the radius of the journal. Although each journal bearing will consist of three pivoted pads, the study of bearing performance was based on the maximum load being supported by one pad, which, depending upon bearing orientation relative to load direction, is a potential worst-case situation.

Bearing diameter for each engine size was determined from concept drawings which showed the maximum journal diameter that could reasonably fit within the hub diameters given in Figure 44. A bearing length-to-diameter ratio of one (1.0) was selected based on previous experience. The film thickness between the bearing pad and the journal is shown plotted versus clearance ratio in Figures 52, 53, and 54 for the 2.0, 3.5, and 5.0 lb/sec engines respectively. These curves show that the film thickness at flight idle and maximum load increases with increasing ambient pressure. The curves also show that the optimum clearance ratio reduces as ambient pressure is increased. Values of ambient pressure starting at 40 psia were used, 40 psia being the lowest value of compressor discharge pressure within the operating range of the engine (40 psia pressure available from second-stage compressor corresponds to an altitude of 25,000 feet and flight-idle speed). The higher values of 80 and 120 psia were selected arbitrarily. Figures 55, 56, and 57 show the pad load-carrying capacity versus film thickness at flight idle conditions for the 2.0, 3.5, and 5.0 lb/sec flow-rate engines respectively. These curves are based on a clearance ratio of 2.0×10^{-3}, this being the optimum ratio at low ambient pressures (see Figures 52, 53, and 54). The effects of increasing ambient pressure from 40 to 120 psia can be clearly seen in each of these three figures. Figure 58 shows pad load versus film thickness at both flight idle and design speed for all three engine sizes. These curves are based on an ambient pressure of 40 psia and a clearance ratio of 2.0×10^{-3}. Maximum values of journal load at flight idle conditions have been identified on Figure 58 for each engine size, and it is seen that minimum film thickness increases with increasing engine size.

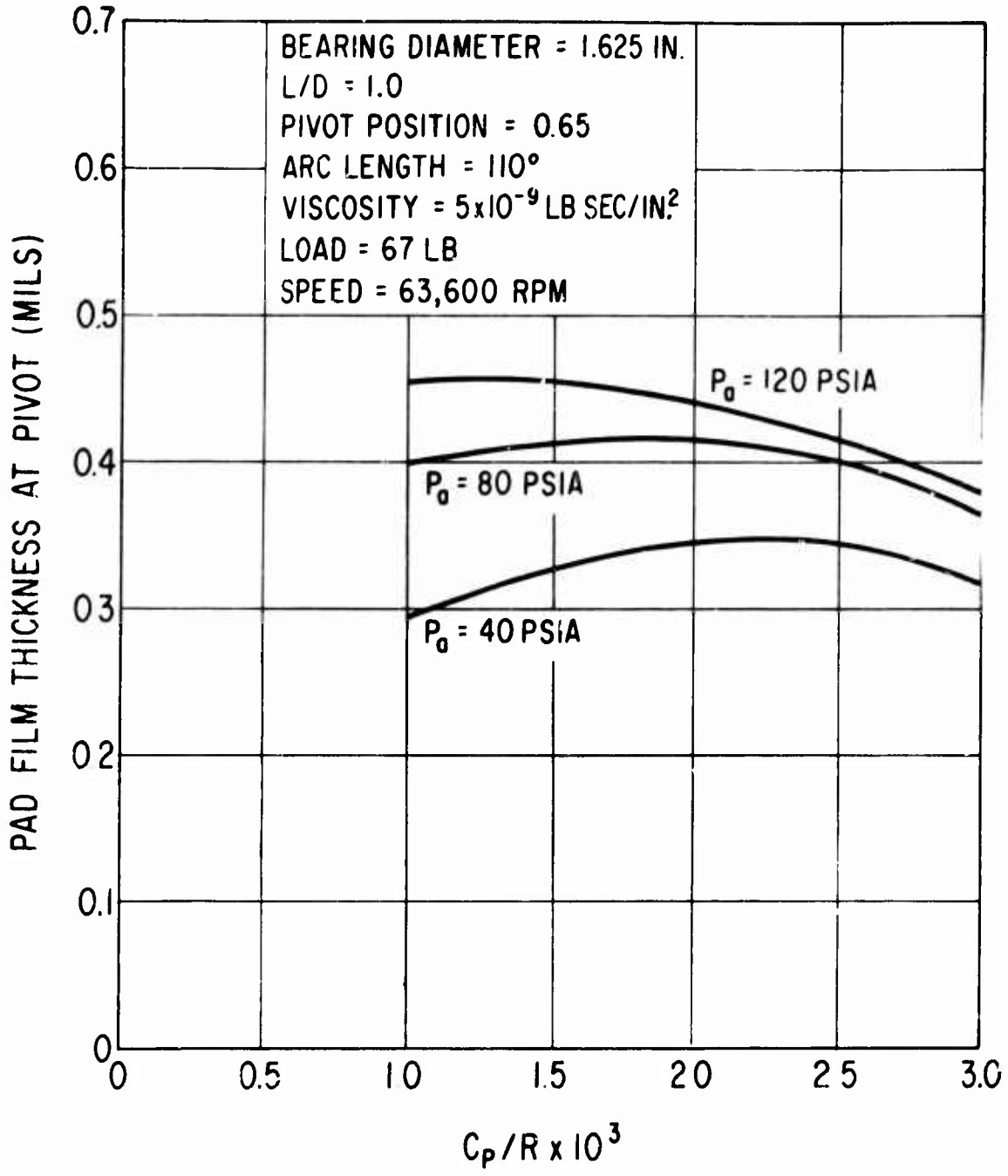


Figure 52. Effect of C_p/R and Ambient Pressure on Journal Bearing Pad Film Thickness at Flight Idle Conditions – 2 lb/sec Engine.

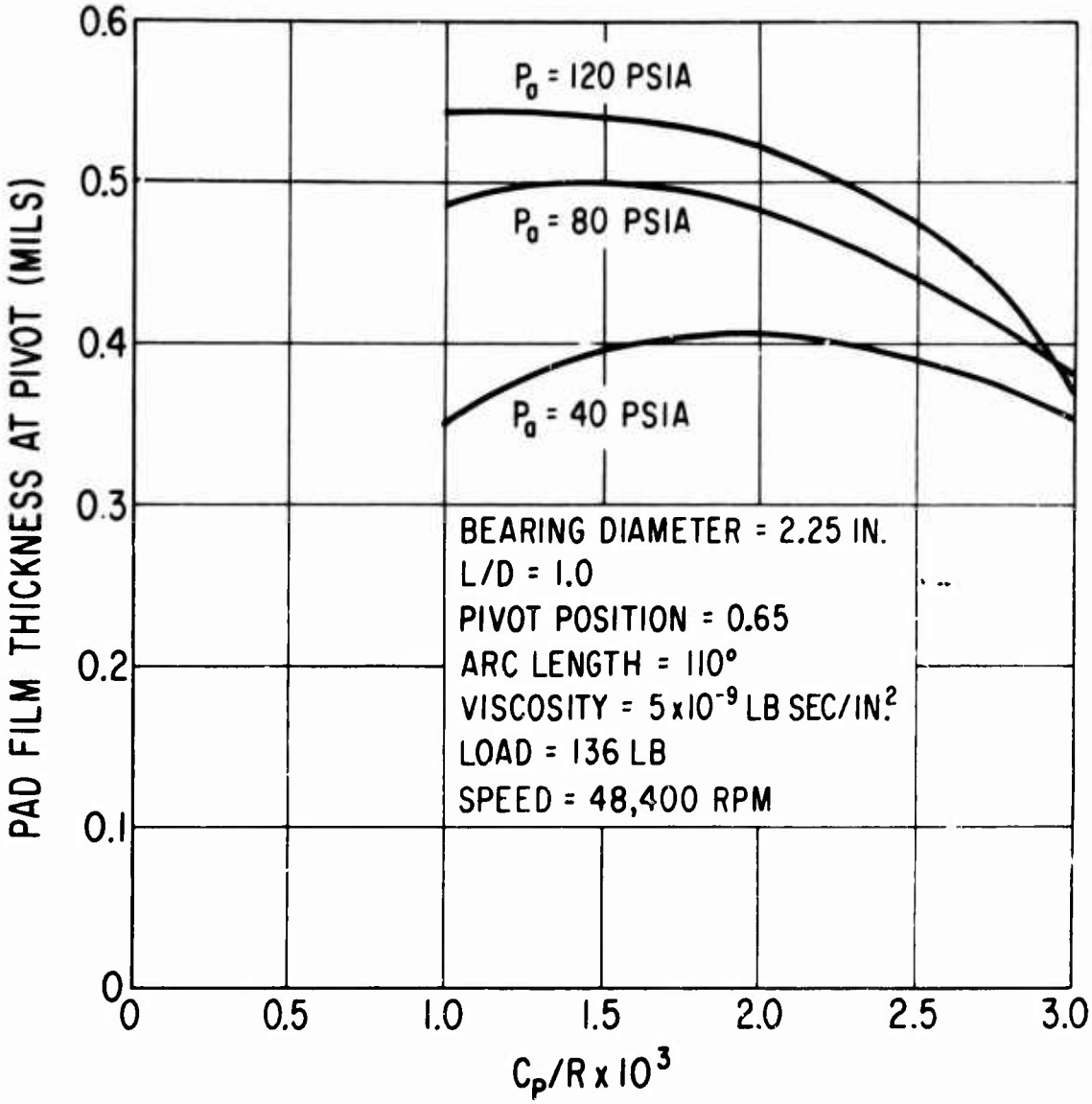


Figure 53. Effect of C_p/R and Ambient Pressure on Journal Bearing Pad Film Thickness at Flight Idle Conditions – 3.5 lb/sec Engine.

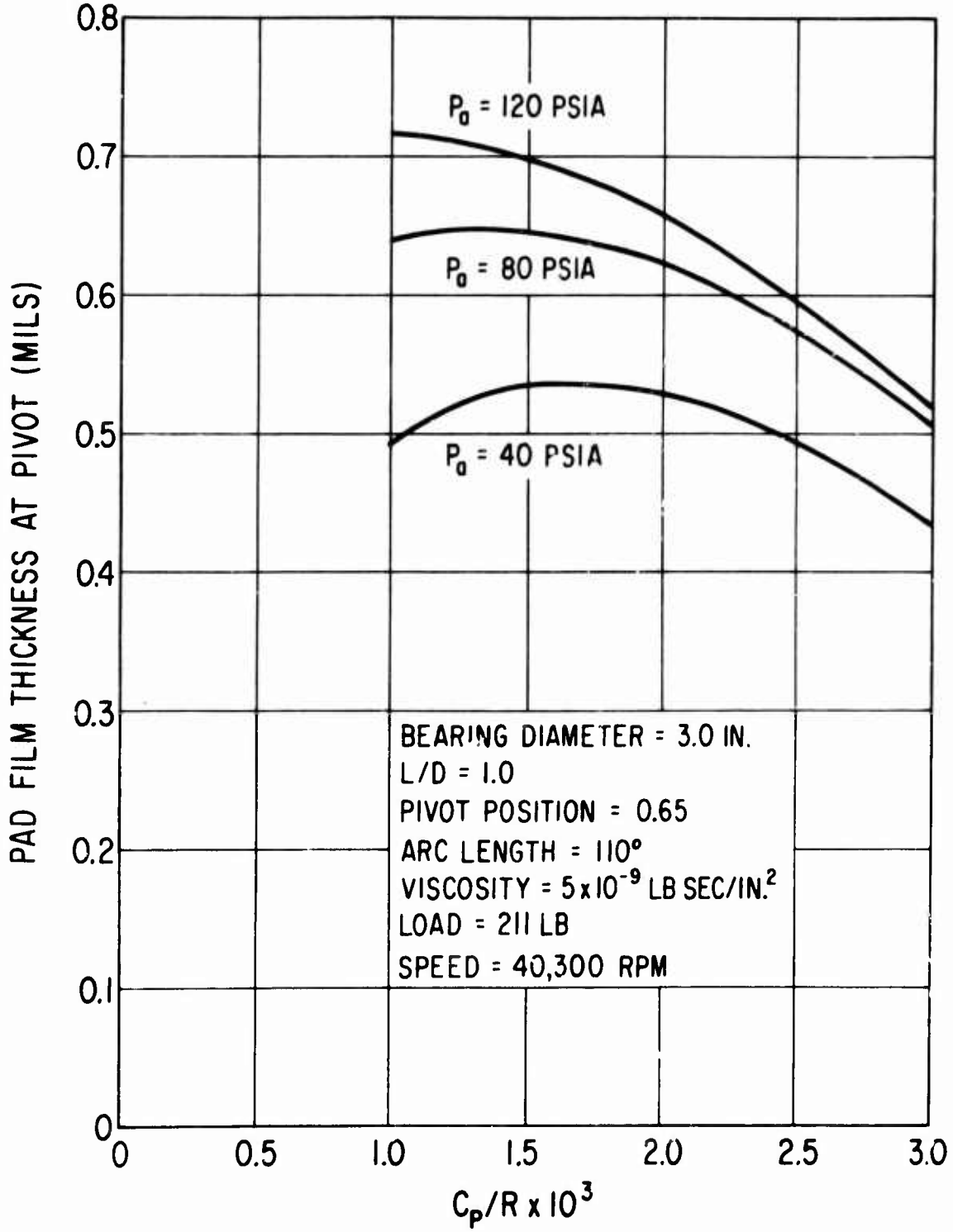


Figure 54. Effect of C_p/R and Ambient Pressure on Journal Bearing Pad Film Thickness at Flight Idle Conditions – 5 lb/sec Engine.

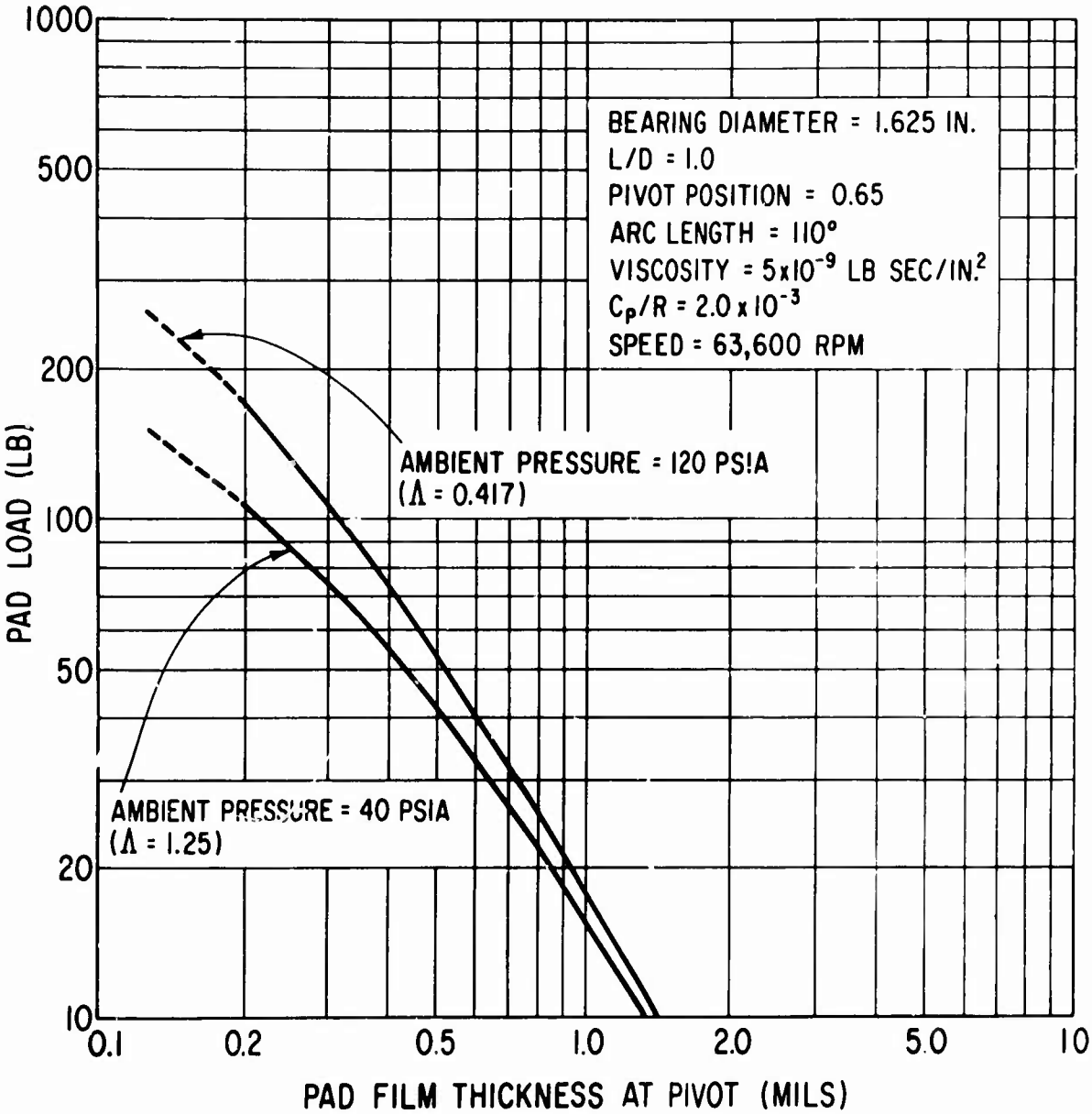


Figure 55. Effect of Ambient Pressure on Journal Bearing Pad Film Thickness at Flight Idle Conditions — 2 lb/sec Engine

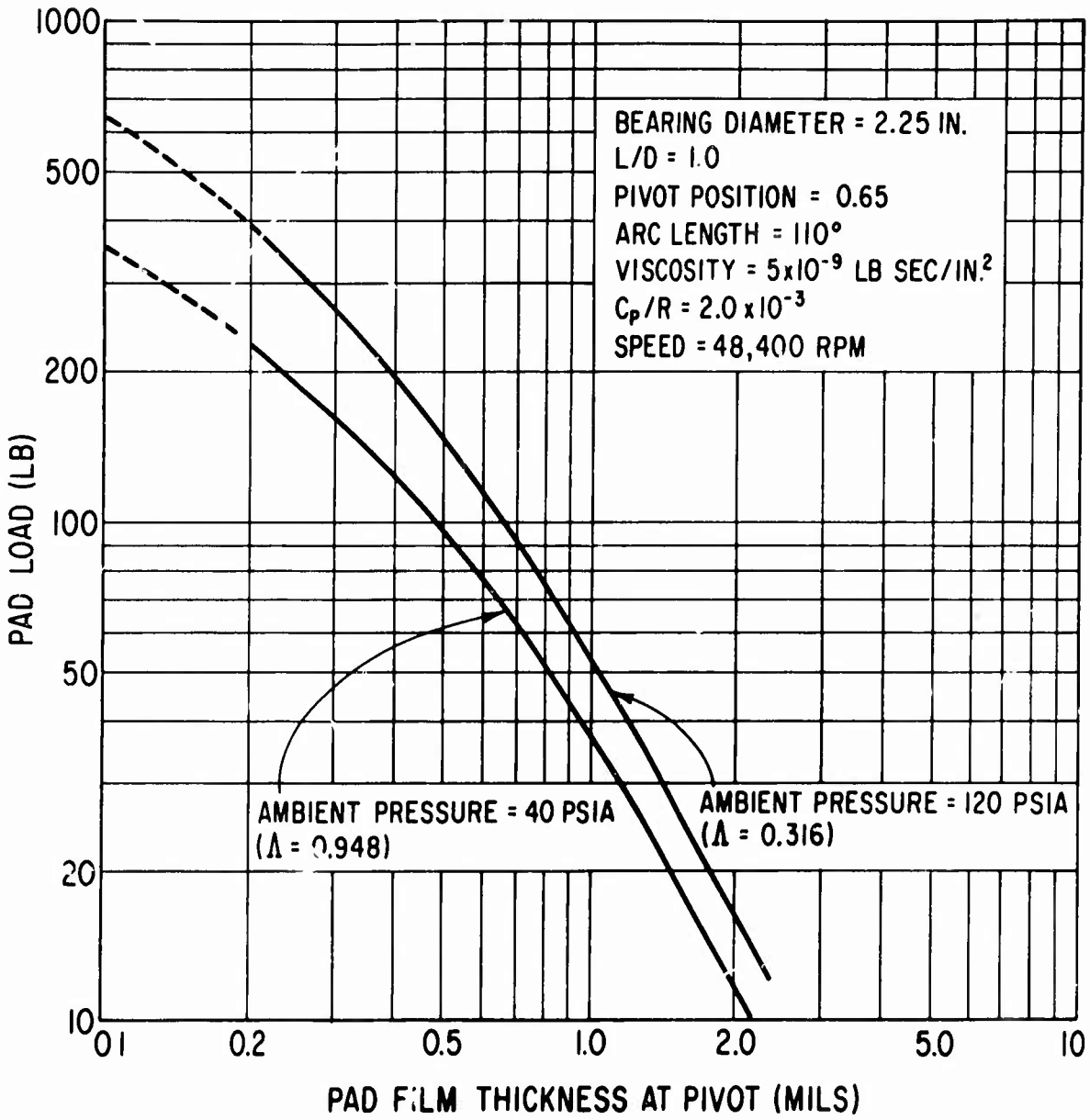


Figure 56. Effect of Ambient Pressure on Journal Bearing Pad Film Thickness at Flight Idle Conditions — 3.5 lb/sec Engine.

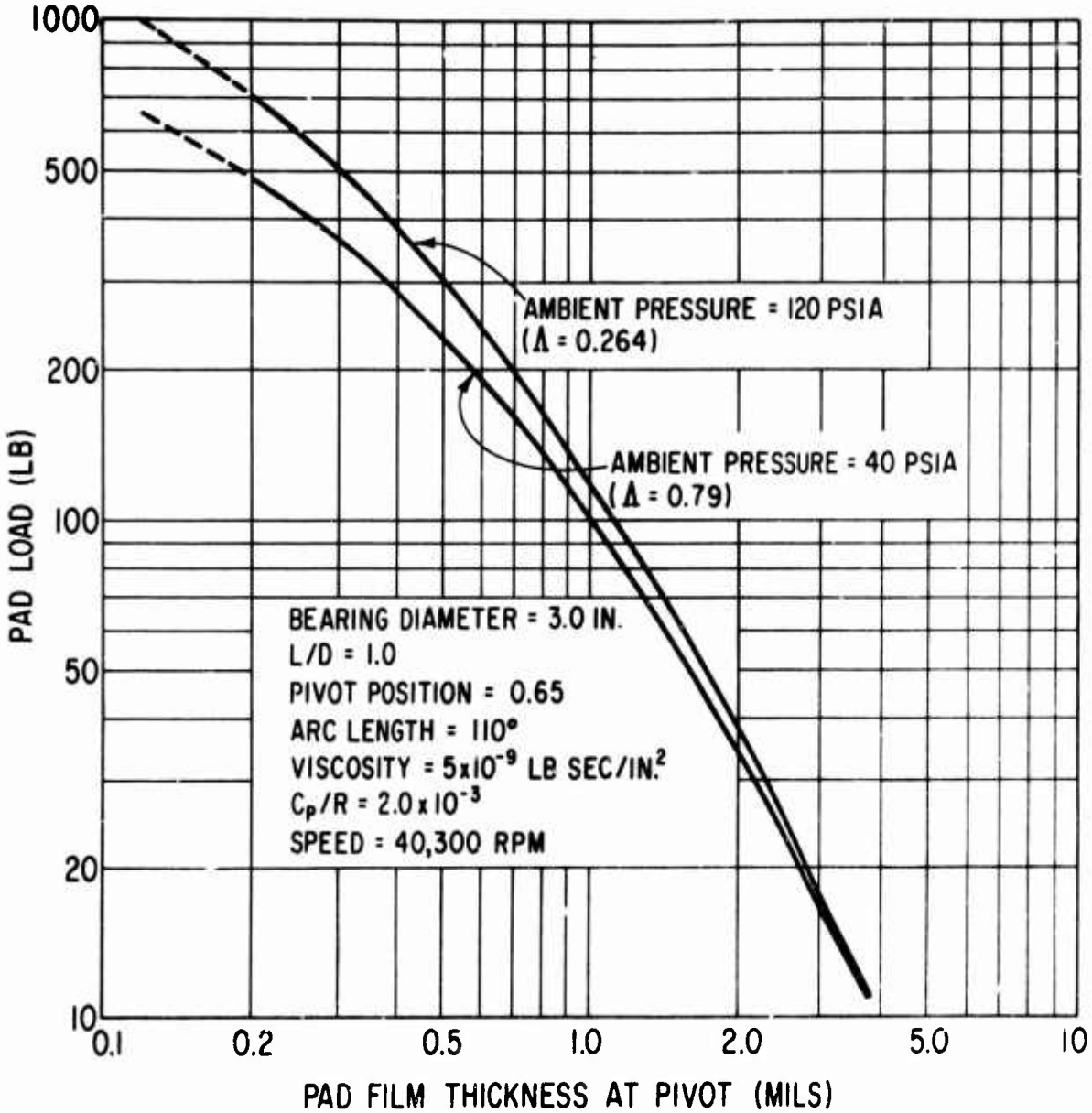


Figure 57. Effect of Ambient Pressure on Journal Bearing Pad Film Thickness at Flight Idle Conditions — 5 lb/sec Engine.

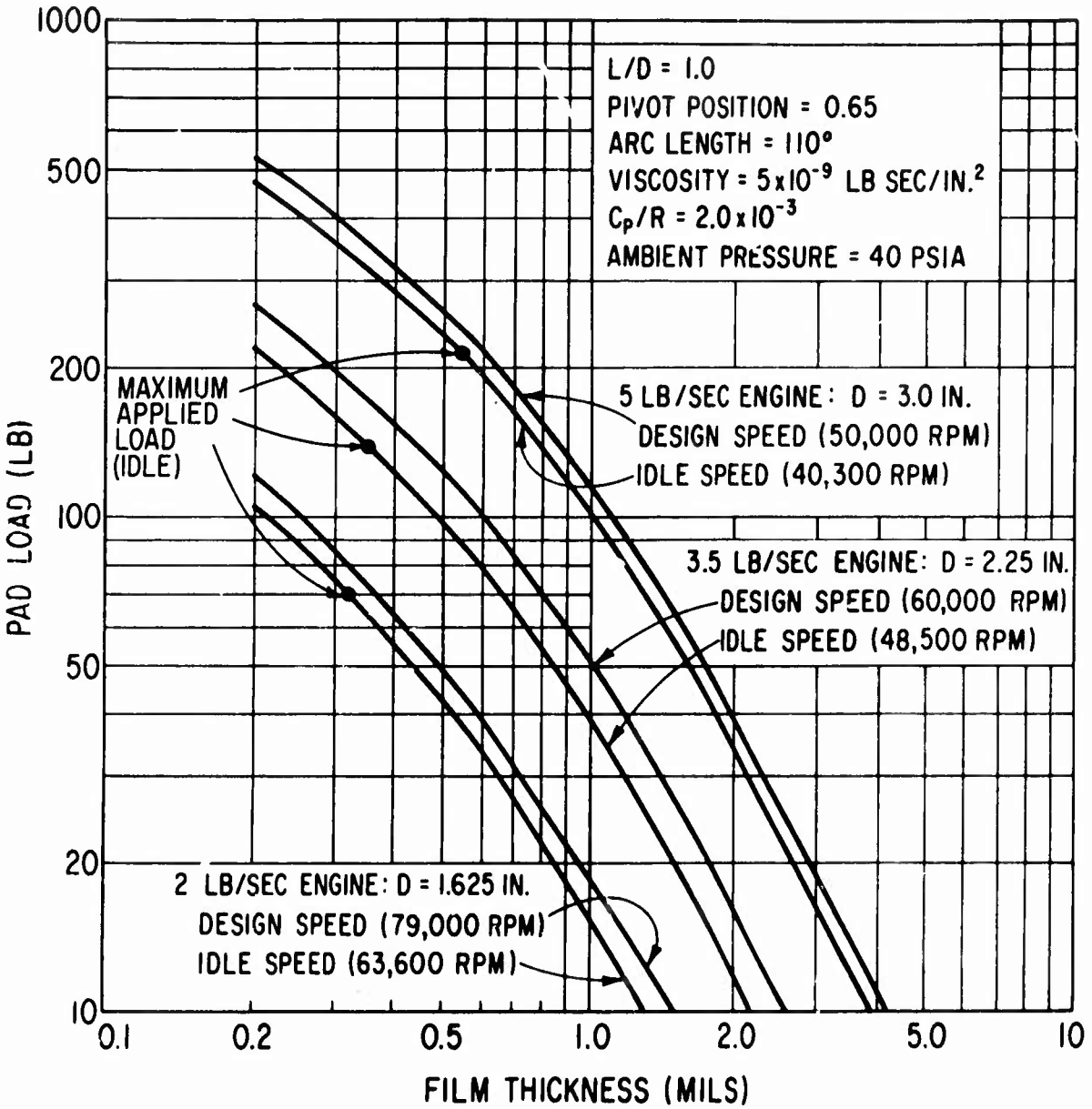


Figure 58. Journal Bearing Pad Data for 2, 3.5, and 5 lb/sec Flow Rate Engines (C_o-T_o Configuration).

Calculations of hydrodynamic journal bearing performance show that air bearings are suitable for use in C_o-T_o engines with flow rates in the range 2.0 to 5.0 lb/sec. The calculations also show the minimum film thicknesses to be small. This will necessitate careful design to ensure that thermal distortion does not cause any significant reduction in minimum film thickness, particularly in the case of the smaller engines. Generally, the calculated values of minimum film thickness favor the use of air bearings in the larger engines, thereby allowing more freedom in designs to control thermal distortion.

THRUST BEARING LOADS

Air-lubricated thrust bearings in general have a relatively low specific load-carrying capacity. It is necessary, therefore, to consider, at an early stage in the evaluation, the effects of engine size, configuration, and type of component on the performance of the air-lubricated thrust bearings.

The major axial loads imposed on the rotor of the gas turbine engine arise from two independent sources. Like the journal bearings, inertia force reaction to the aircraft maneuver conditions specified in MIL-E-5007C (Figure 47) is one such source of load. Control over the magnitude of these maneuver-induced loads is, therefore, confined to reducing rotor mass within the limitations of practical rotor design. The second source of axial load, of course, is a result of the pressure distributions on either side of the compressor and turbine wheels, as has already been discussed.

As was indicated previously under the discussion on "THRUST LOADS", the combination of turbine backface scalloping and compressor front shrouding will balance the aerodynamic thrust forces. Inertia forces, therefore, become the major proportion of thrust forces to be accommodated by the air bearing.

An examination of MIL-E-5007C (Figure 47) shows that an engine, suitable for either horizontal or vertical installation, will be subjected to 10g accelerations in both the aircraft fore and aft directions, i.e., along the engine axis. This level of acceleration applies to all flight conditions (from sea level to 25,000 feet altitude and all power levels from zero to 100 percent) and landing conditions. Catapult-assisted takeoff involves 9g at 100 percent power. For design purposes, then, the maximum maneuver-induced axial acceleration has been taken as 10g. Using the rotor weights from Tables IV and V, the maneuver loads to be supported by the thrust bearing are as given in Table VII.

TABLE VII. MANEUVER-INDUCED THRUST BEARING LOADS

	Axial Load Resulting From 10g Acceleration (lb)		
Engine Flow Rate, lb/sec	2.0	3.5	5.0
Configuration			
C_o-T_o	97	209	308*
C_o-T_1	89	—	309*
C_o-T_2	110	—	385*
C_2-T_o	—	—	241*

*The load given for the 5.0 lb/sec flow-rate rotors was determined using the average weight of several rotor layouts of each configuration. For example, six layouts were prepared for the C_o-T_o configuration.

Figure 59 shows a plot of thrust bearing maneuver load versus engine flow rate for the C_o-T_o engine configurations. As can be seen, an increase of 220 percent in load results from a 150-percent increase in engine size (2.0 to 5.0 lb/sec flow-rate).

THRUST BEARING PERFORMANCE

Studies to determine thrust bearing characteristics were conducted in parallel with the other component studies necessary to evaluate the effect of engine size on the performance of an air-bearing-supported rotor system. At the onset of the study, the magnitude of the axial load to be supported by the thrust bearing for each size of engine (2.0, 3.5, and 5.0 lb/sec flow-rate) was not known. A previous study [1], however, showed that axial loads should be expected of a magnitude that necessitated the use of hydrostatic thrust bearings. Hydrodynamic thrust bearings were thought to be inadequate with respect to load-carrying capacity.

In order to evaluate the performance of the three sizes of thrust bearings, the load-carrying capacity of each size was calculated at an operating film thickness of 1 mil. Bearing size was determined from the assumption that stress levels in the thrust runner resulting from a tip speed of 1500 ft/sec could be accommodated by good design practice and the proper choice of materials. An assumption was also made that the location of the thrust bearing relative to the turbine and compressor would be such that

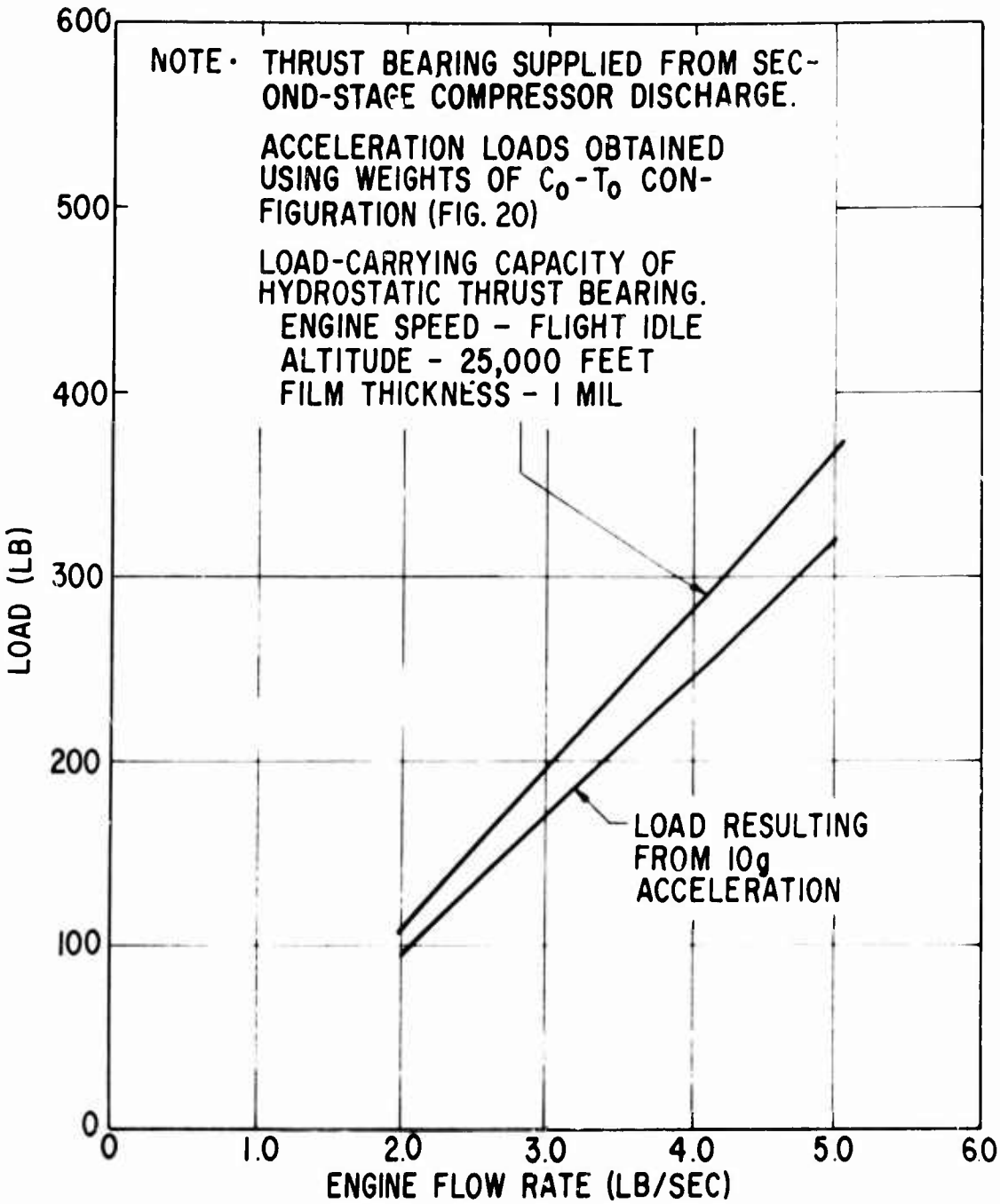


Figure 59. Thrust Bearing Load Versus Engine Flow Rate.

acceptable values of temperature could be obtained. Hydrostatic bearing load-carrying capacity is strongly influenced by the differential pressure across the bearing, i.e., supply pressure minus ambient pressure. The highest supply pressure in the engine was taken to be at compressor discharge, the lowest pressure at compressor inlet.

Using these values of pressure for bearing supply and ambient pressure respectively, the bearing performance was calculated. The worst case for bearing operation was found to be flight idle at an altitude of 25,000 feet. At this condition the compressor pressure ratio has fallen to 7.3:1; therefore, the differential pressure available to the bearing is only 34.5 psi. Bearing design was optimized for the conditions prevailing at this point. At sea level and 100-percent power, the bearing will not be optimized. However, the differential pressure available has increased to 243 psi, with an attendant increase in load-carrying capacity. Curves showing load-carrying capacity versus altitude for the 2.0, 3.5, and 5.0 lb/sec engines are given in Figures 60, 61, and 62 respectively. From these curves, which show bearing performance at 100-percent, 50-percent, and flight-idle power levels, it is seen that increasing engine size by 150 percent (2.0 to 5.0 lb/sec flow rate) results in a 220-percent increase in load-carrying capacity (constant 1-mil film thickness) at flight idle and 25,000 feet altitude. The same percentage increase in load-carrying capacity is also seen at sea level because of the assumption that flight-idle engine speed is independent of altitude.

Inserting the maneuver-induced loads (10g) from Figure 59 into the curves of bearing capacity in Figures 60, 61, and 62 shows the thrust bearings for each engine size to be capable of supporting the required load. These curves also show the significant excess of load capacity at lower altitudes and increased power levels.

RELATIVE PERFORMANCE, COST, AND DURABILITY

To aid in the selection of an engine size and configuration for use in the balance of the Phase I program, each flow-path arrangement was evaluated and rated based on criteria without regard to bearing or critical speed considerations. The factors included in the evaluation were: performance, weight, durability, cost, and thrust balance. The nine combinations (C_oT_o, C_oT_1, etc.) were ranked under each factor from 1 through 9, with 1 being the highest ranking.

Each combination was given a relative rating within each factor. For example, under "Performance", the arrangement having the highest turbo-compressor efficiency (C_oT_2) at its design speed was given a rating of 1.00. The efficiency for each of the other arrangements was then divided by the efficiency of the C_oT_2 combination to arrive at the relative rating. Under the "Weight" factor, the weight of the lightest combination (C_2-T_o) was divided by the weights of the other combinations. Durability, cost, and thrust balance factors were handled in a different manner inasmuch as absolute values of each factor could not readily be established. Therefore, based on previous experience and engineering judgment, relative ratings were assigned each combination. For durability, the radial flow components

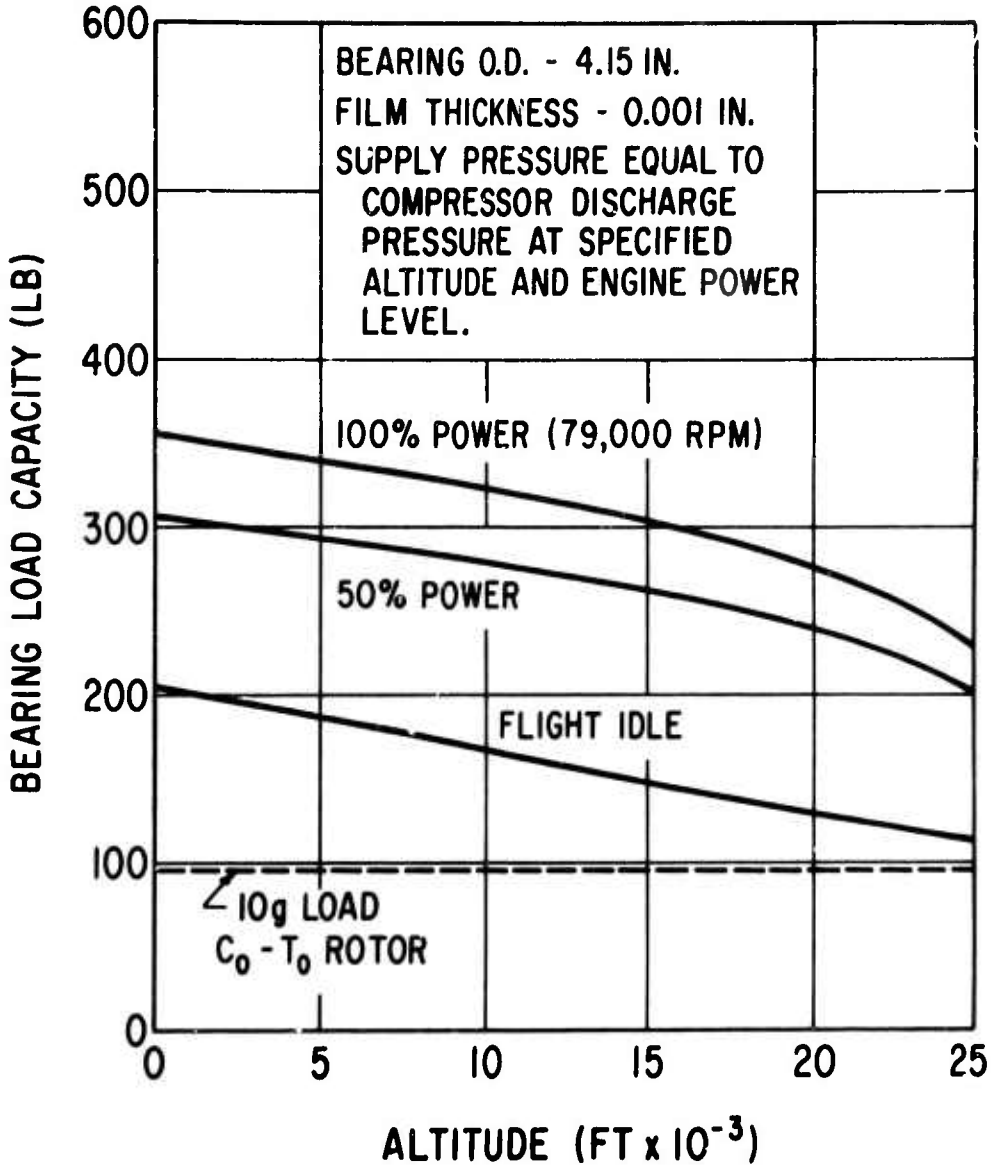


Figure 60. Load-Carrying Capacity of Thrust Bearing for 2 lb/sec Engine.

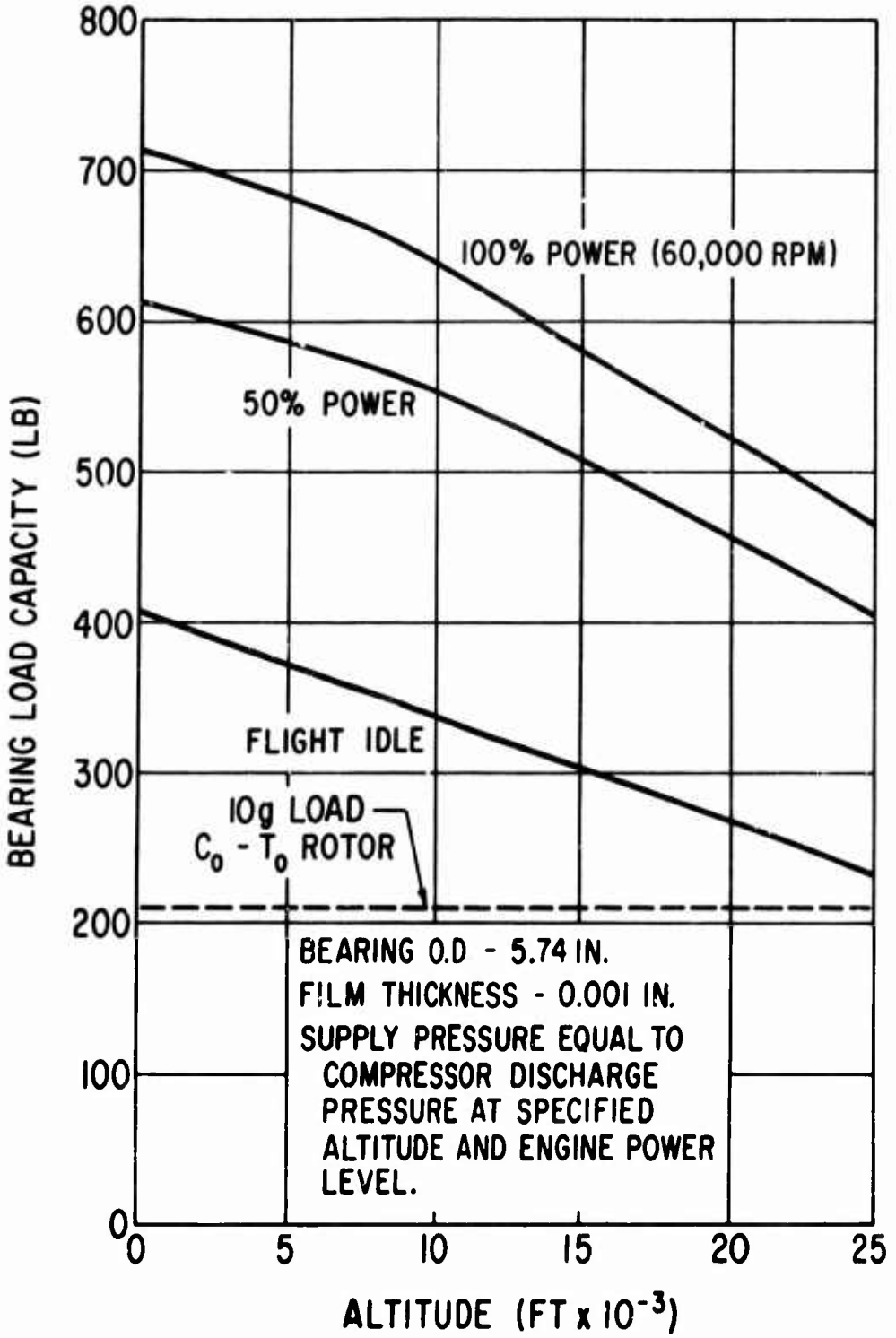


Figure 61. Load-Carrying Capacity of Thrust Bearing for 3.5 lb/sec Engine.

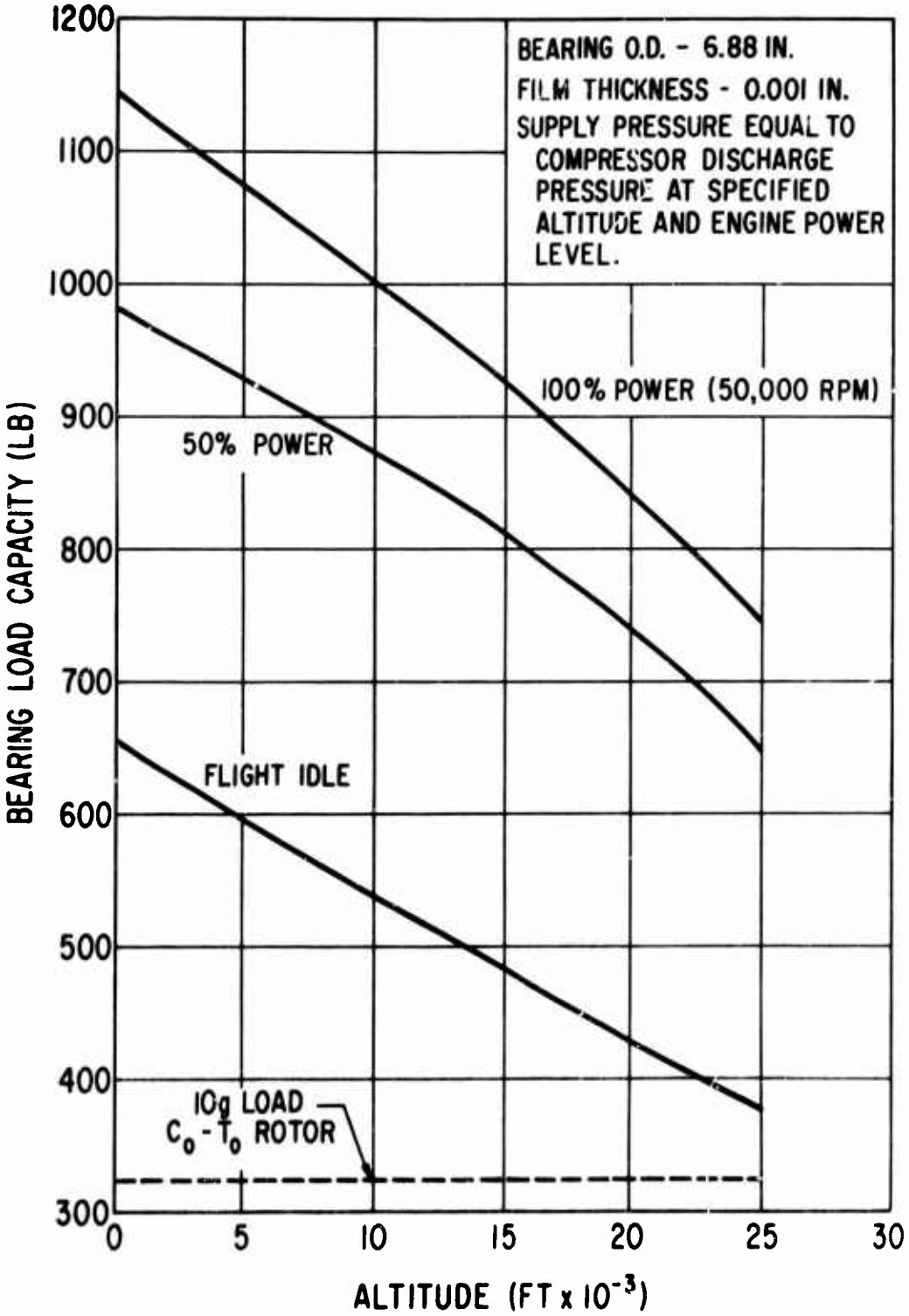


Figure 62. Load-Carrying Capacity of Thrust Bearing for 5 lb/sec Engine.

were assumed to be much less susceptible to foreign object damage and, therefore, were rated higher. As a result, the all-radial combination, C_oT_o, was rated first and the combination with the greatest number of axial stages, C_2T_2, was rated last.

Under the cost factor, again based on previous experience, relative cost values were applied to each component and the relative rating of the combinations established. Relative ratings were assigned under the thrust balance factor based on the degree to which each combination can be balanced. Thus the more radial components a combination had, the higher its relative rating.

Each factor was then given a "weight" from 0 to 1 that reflects the importance of each factor to the overall engine design. These factors are arbitrary and can vary with engine application, but for the purposes of this study were selected to emphasize performance and durability, with weight, cost, and thrust balance having less influence. By multiplying the rating in each factor by the weight of the factor and summing the results for each combination, a weighted relative rating was established, as shown in Table VIII.

In this performance, cost and durability evaluation, the C_oT_o and C_1T_o arrangements achieved the highest ratings and, neglecting for the moment bearing and rotor dynamic aspects, would be recommended for selection for further study.

TABLE VIII. RATING OF COMPONENT COMBINATIONS

Combination	Performance 1.0*		Weight 0.5		Durability 0.75		Cost 0.5		Thrust Balance 0.5		Weighted Relative Rating
	Rank	Rating	Rank	Rating	Rank	Rating	Rank	Rating	Rank	Rating	
C_oT_o	3	0.976	5	0.89	1	1.00	6	0.875	1	1.00	3.16
C_oT_1	7	0.950	6	0.76	2	0.95	7	0.78	4	0.90	2.88
C_oT_2	1	1.00	9	0.535	3	0.90	9	0.695	5	0.90	2.74
C_1T_o	5	0.96	3	0.915	4	0.80	1	1.00	2	0.95	3.00
C_1T_1	9	0.92	4	0.895	5	0.75	2	0.95	6	0.85	2.84
C_1T_2	6	0.95	8	0.665	6	0.70	4	0.825	7	0.85	2.65
C_2T_o	2	0.992	1	1.00	7	0.70	3	0.87	3	0.94	2.92
C_2T_1	8	0.95	2	0.975	8	0.65	4	0.83	8	0.84	2.77
C_2T_2	4	0.978	7	0.71	9	0.60	8	0.73	9	0.84	2.58

*Weights

SELECTION OF ENGINE SIZE AND CONFIGURATION

The objective of the engine sizing and concept studies discussed in the previous section was to provide data that described the effect of engine size and configuration on the performance of an air-bearing-supported aircraft gas-turbine engine rotor. Having identified the significant effects of both size and configuration, then an engine size and configuration could be selected that would provide the most meaningful basis for subsequent rotor-bearing system investigation.

As part of this effort, the following elements of the performance and design of an aircraft gas turbine engine were studied:

1. The performance of nine combinations of axial and radial flow compressors and turbines for each of three engine flow rates (2.0, 3.5, and 5.0 lb/sec)

2. Rotor dynamics (critical speeds) of the most promising configurations of compressor and turbine components

3. Journal bearing load-carrying capacity for each of the three engine sizes

4. Rotor thrust load balancing

5. Thrust-bearing load-carrying capacity for each of the three engine sizes

6. Engine concept drawings

In addition, a brief study was conducted to determine the relative cost and durability of the configurations examined.

The effect of engine size and configuration on spool efficiency can be seen from Figure 63. From consideration of performance only, the best spool efficiencies can be obtained from the configurations using:

a. The two-stage centrifugal compressor and two-stage axial flow turbine (C_o-T_2)

b. The compressor with two axial stages preceding one stage of radial flow and a single-stage radial flow turbine (C_2-T_o)

c. The compressor with two axial stages preceding one stage of radial flow and a two-stage axial flow turbine (C_2-T_2)

d. The two-stage centrifugal compressor and a single-stage radial flow turbine (C_o-T_o)

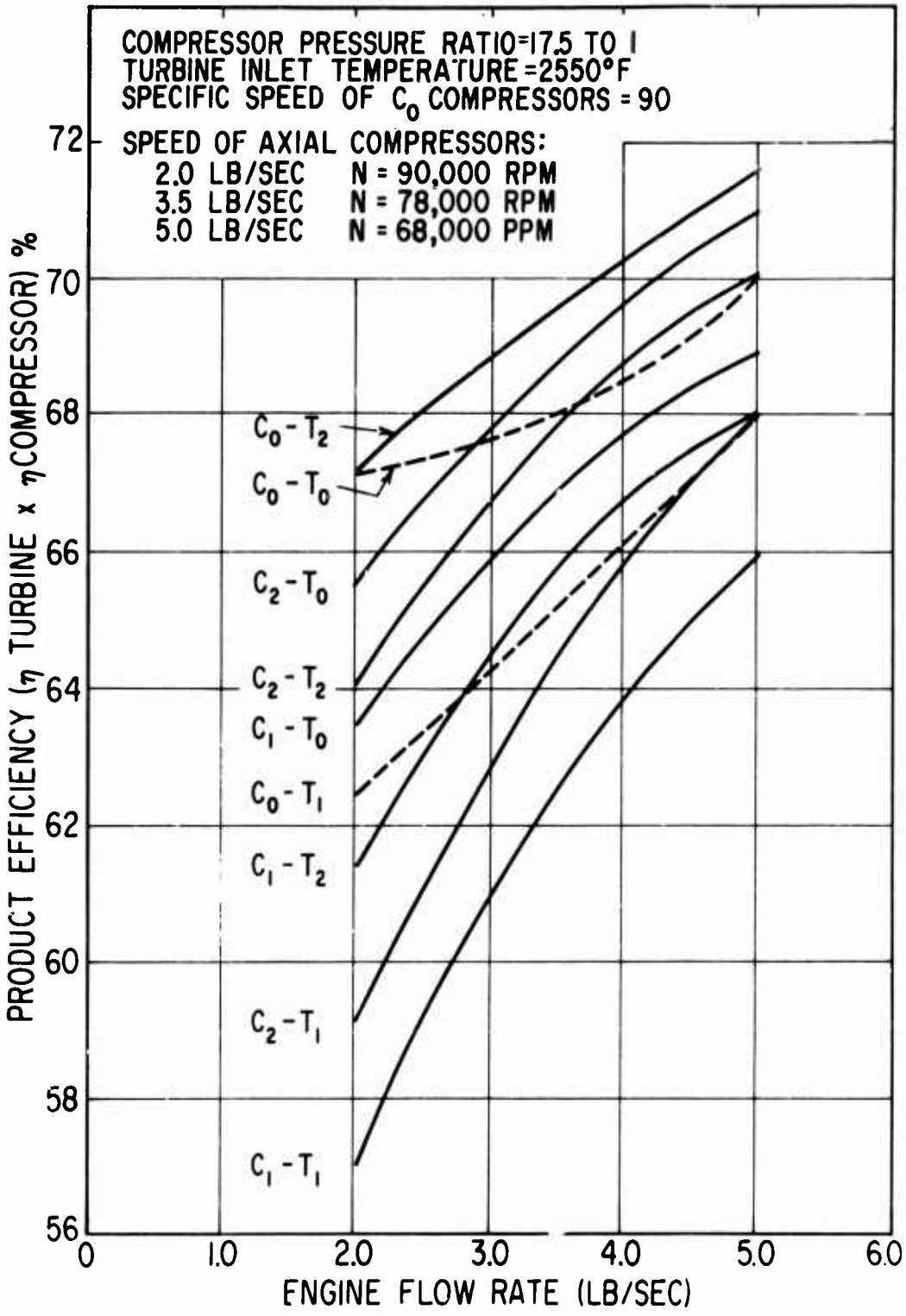


Figure 63. Product Efficiency Versus Engine Flow Rate for Nine Compressor and Turbine Configurations.

This last configuration (C_o-T_o) is particularly noticeable because the spool efficiency is seen to be the least sensitive to reductions in the design value of engine flow rate. In fact, at the 2.0 lb/sec flow rate, the efficiency is equal to that of the C_o-T_2 configuration. Values of product efficiency are given in Table IX for the four configurations with the highest efficiency.

TABLE IX. VALUES OF PRODUCT EFFICIENCY FOR THE FOUR CONFIGURATIONS WITH BEST PERFORMANCE

Engine Flow Rate (lb/sec) / Configuration	Product Efficiency (percent) 2.0	3.5	5.0
C_o-T_2	67.2	69.6	71.7
C_2-T_o	65.5	68.7	71.1
C_2-T_2	63.9	67.9	70.1
C_o-T_o	67.2	68.0	70.0

Table IX shows the spread in efficiency between the four best configurations to be 1.7 percent for both the 5.0 and 3.5 lb/sec flow-rate engines, but increasing to 3.3 percent for the 2.0 lb/sec engine. Because of the relatively low values of product efficiency, no further consideration was given to the C_1-T_o, C_o-T_1, C_1-T_2, C_2-T_1, and C_1-T_1 configurations.

The effect of engine size and configuration on the rotor dynamic performance of an air-bearing-supported rotor system is shown in Tables IX and X and Figure 17. From this data, it is seen that the configuration using axial flow stages in the compressor do not meet the minimum critical speed criteria of 1.33 times the engine overspeed. The C_o-T_2 and C_o-T_o configurations, both of which have good spool efficiencies, have critical speeds in excess of the minimum criteria and, therefore, are suitable candidates for the application of air bearings. Figure 17 indicates that the smaller engine sizes have the largest critical speed margins, thereby allowing more freedom in rotor design and rotor balancing than would be possible for the larger engines.

The selection process has, after examination of engine spool efficiency and rotor critical speed, shown that engine sizes in the range 2.0 to 5.0 lb/sec flow rate, and in either the C_o-T_2 or C_o-T_o configuration, are candidates for the application of gas bearings. Before the final selection is made, the effects of engine size and configuration on journal and thrust bearing load and performance must be considered.

It has been shown that journal bearing loads are, primarily, the results of maneuver conditions of aircraft operation, and that the maximum load to be carried by each of the journal bearings in a given engine is dependent on the rotor mass, distribution of mass, polar mass moment of inertia, and bearing span. Each of these parameters is affected by engine size and configuration. To minimize, as far as practical, the bearing loads resulting from maneuver-induced gyroscopic forces, requires a rotor design with minimum mass and inertia in conjunction with a maximum bearing span. If, in addition, the rotor mass can be equally distributed between the two journal bearings, then the acceleration-induced bearing loads can also be reduced to a minimum. Designs with the journal bearings located at the rotor extremities (maximum bearing span) have been achieved while retaining acceptable rotor critical speed characteristics for both the C_o-T_2 and C_o-T_o configurations of each engine size. Because of the relatively heavy T_2 turbine, the C_o-T_2 rotors are heavier, have higher polar mass moment of inertia, and have more unequally loaded journal bearings than the C_o-T_o configuration. The important differences between the C_o-T_2 and C_o-T_o rotors and the resulting maximum maneuver-induced loads on the journal bearings at flight idle are given in Table X.

TABLE X. MAXIMUM RESULTANT BEARING LOADS FOR C_o-T_2 AND C_o-T_o CONFIGURATIONS AT FLIGHT IDLE CONDITIONS (5.0 lb/sec flow rate)

Configuration	Polar Mass Moment of Inertia ($in.\text{-}lb\text{-}sec^2$)	Static Load on Bearing (lb)		Maximum Resultant Bearing Load (lb)	
		Compressor End	Turbine End	Compressor End	Turbine End
C_o-T_o	0.25	16	16	210	210
C_o-T_2	0.41	7.9	31.2	209	380

Table X presents data only for the 5.0 lb/sec flow rate engine because at this flow rate the effect of using the T_2 turbine is clearly noticeable. However, the same trend persists to a less noticeable degree in the smaller engines.

The minimum journal bearing film thickness, previously shown in Figure 58 for all three engine sizes in the C_o-T_o configuration, would be reduced by the larger loads resulting from use of the T_2 turbine. In the one case for which calculations have been performed (5.0 lb/sec flow rate), the reduction would be from 0.55 mil to 0.275 mil, a decrease of 50 percent. The same trend, but not so severe, should be expected in the 3.5 and 2.0 lb/sec engines.

From consideration of journal bearing loads and journal bearing performance, the most suitable configuration is clearly the C_o-T_o; and using minimum film thickness as the deciding criteria, the 5.0 lb/sec engine is the most suitable size for the application of gas bearings.

Without the use of thrust balancing, the pressure distribution throughout each of the engine configurations studied (independent of size) results in an axial load in excess of the load-carrying capacity of air-lubricated thrust bearings. In the case of the C_o-T_o configurations, it has been shown that the aerodynamic thrust load can be reduced to essentially zero by the addition of compressor front shrouds in combination with scalloping of the rear shrouds. Because thrust balance of each component has been achieved, changes in operating conditions will have little effect on the thrust load. Therefore, the primary axial load to be supported by the thrust bearing in the C_o-T_o configurations results from the acceleration force of 10 g's. Spool efficiency is unaffected by this method of thrust-balancing.

In the C_o-T_2 configuration, partial aerodynamic thrust balance can be achieved by offsetting the rearward-directed turbine load with the forward-directed compressor load, augmented by additional forward-directed load obtained by pressurizing the rear face of the turbine wheel. To obtain the total thrust load, the resultant load from this scheme must then be added to the acceleration load. For the C_o-T_2 configuration of the 5.0 lb/sec engine, the total load amounts to approximately 1000 pounds rearward at 100 percent power and sea level conditions of operation. At sea level and flight idle, the thrust is reversed in direction and the total load is reduced to approximately 500 pounds. Engine efficiency penalties will be incurred by this scheme if leakage from the turbine wheel pressurization system occurs. Leakage past an appropriately sized labyrinth seal would result in an efficiency loss of about 7.7 percent. The use of a face type seal, if practical in this application, would significantly reduce this leakage loss.

From consideration of the axial load to be supported by the thrust bearing, the most suitable configuration is the C_o-T_o. Figure 59 shows that the hydrostatic thrust bearing, taking its air supply directly from second-stage compressor discharge, can support the total thrust load with a 1-mil film thickness under the worst condition of engine operation, i.e., flight idle at an altitude of 25,000 feet. The effect of engine size is not significant, as the increase in load associated with increasing engine size is matched by increasing thrust bearing capacity. For example, increasing the C_o-T_o engine size by 150 percent (2.0 to 5.0 lb/sec) increases both total thrust load and thrust bearing load capacity by 220 percent.

Some evaluation of the engine configuration and size was attempted from consideration of general design suitability, fabrication of parts, assembly, etc. The configurations considered were the C_o-T_o and C_o-T_2 engines in the 2.0, 3.5, and 5.0 lb/sec flow-rate sizes. The basic difference, therefore, is between the turbine arrangements, the thrust balancing systems, and the size of engine components. It is generally

felt that decreasing size results in increased difficulty in the areas of design, fabrication and assembly. A review of "to scale" concept drawings, however, did not reveal any areas in which significant difficulties would arise in the size range of 2.0 to 5.0 lb/sec, for either engine configuration.

When examining the C_o-T_o and C_o-T_2 configurations from the general design point of view, there appears to be a trade-off between the shrouded compressor wheels required for balancing the C_o-T_o configuration, and the two-stage axial turbine with a properly sealed thrust balancing cavity, for the C_o-T_2 configuration. Without a more detailed evaluation, it is not possible to select one configuration rather than another. However, it is considered that the feasibility of compressor shrouding should be evaluated at the earliest opportunity. Cooling of the T_o and T_2 turbines would seem to be equally difficult.

In concluding the discussion on the selection of the most suitable engine size and configuration for the application of air-lubricated bearings, all that remains is the final selection. Size has been found to be a relatively unimportant parameter. The effect of size on rotor-bearing system critical speeds favors small engines, while large engines are favored from consideration of journal bearing film thickness. Given the freedom of choice, the most advantageous size for the applications of air bearings is, therefore, the middle-sized engine which has a flow rate of 3.5 lb/sec. The successful development of this engine will permit scaling up or scaling down, for any particular application, with considerably more certainty than scaling from one extreme end of the flow range to the other end.

The effects of configuration on the selection of an engine for the application of gas bearings are more obvious. Either high rotor speed (inadequate critical speed margin) or poor spool efficiency eliminates those configurations using either C_1 or C_2 compressors and T_1 turbines. The remaining contenders are, therefore, the C_o-T_2 and C_o-T_o configurations. Overall efficiency favors the C_o-T_2 configuration if the thrust balancing cavity can be sealed; otherwise, the result of using standard seals is a loss of 7.7 percent in spool efficiency. The C_o-T_2 configuration, however, would not require the development of shrouded compressor wheels.

The C_o-T_o configuration is very clearly the best from consideration of both journal and thrust bearing performance as well as cost and durability. The performance penalty, if the T_2 turbine thrust balance cavity could be completely sealed, would be 1.7 percent. Development of the necessary shrouded compressor wheels is felt to be both reasonable and of general use in the development of high-efficiency centrifugals.

The final recommendation for the size and configuration of the gas generator model which should be used for the balance of this air bearing investigation was the 3.5 lb/sec flow-rate engine with a two-stage centrifugal compressor and a single-stage radial inflow turbine, i.e., the 3.5 lb/sec C_o-T_o engine.

DESIGN OF 3.5 LB/SEC ENGINE

The preceding sections described the data and preliminary designs that were generated to accomplish three major objectives of the program:

1. Establish the effect of engine flow rate (between 2.0 and 5.0 lb/sec) on the performance of air bearing engines.

2. Establish the effect of engine configuration on the performance of air bearing engines.

3. Select a particular flow rate and configuration for further design evaluation such that an in-depth study of air bearing feasibility as applied to advanced aircraft engines could be accomplished.

As has previously been discussed, flow rate per se had no significant effect on either performance or the factors that affect the feasibility aspects of applying air bearings to aircraft engines. Engine configuration, on the other hand, did have a significant influence on both performance and air bearing feasibility aspects. Accordingly, the 3.5 lb/sec configuration consisting of a two-stage radial compressor and a single-stage radial turbine was selected for further evaluation and detail design of the bearing and rotor components.

The discussion in this section addresses itself to the finalization of the aerodynamic design aspects and consideration of starting and accessory drive systems. This portion of work conducted under Task 3 provided, in addition to the finalized performance data, the design and parametric data (pressures, temperatures, speeds, etc.) required for the detailed bearing design study. The latter was conducted under Task 4 and is discussed later in the report.

FINAL COMPONENT SIZING

In the initial engine sizing performed in Task 1 discussed earlier in this report, each component was sized for approximately 3.5 lb/sec air flow, with only the turbine size being reduced to account for removal of turbine cooling flow.

In Task 3, possible sources of significant engine leakage were identified, and these leakage rates were input, along with bearing flow rates and component performance curves, into an engine cycle analysis computer program. With a fixed inlet airflow (3.5 lb/sec), the computer program balances the engine cycle and determines the exact flow rate through each component, based on leakage, cooling flows, and recirculation values. The same program provides schedules of temperatures and pressures at pertinent engine locations and overall engine performance in terms of output power and specific fuel consumption.

To assist in the study, a sketch layout of the 3.5 lb/sec C_o-T_o combination was made with the two journal bearings outboard of the compressors and turbine, and with space provided between the two compressor stages for the thrust bearing. The layout, shown in Figure 64, was used to:

1. Locate leakage paths

2. Select supply sources for bearing pressurization and cooling

3. Establish seal locations, based on minimum leakage and thrust balance requirements

The estimated leakage and bleed flows corresponding to the numbered location on the engine sketch layout are shown in Table XI. It should be noted that front shrouds were included on both compressor stages to thrust balance the rotor. Leakages were calculated using an assumed radial seal clearance of 0.0035 inch.

The input to the computer program includes the following data in addition to the leakage and bleed flow:

1. Design point values of all engine operating parameters, as listed in Table XII.

2. Off-design flow parameters and efficiency curves for each component. These curves, which relate speed, flow rate, pressure ratio, and efficiency, were generated for the compressors, using ST9 engine compressor data scaled to the 3.5 lb/sec air flow size. Pressure ratio scaling at the engine design point was at constant map polytropic efficiency. The adiabatic efficiency levels used in performance calculations were linearly adjusted to the specified design point level. The radial turbine curves, shown in Figure 65, were developed from design data published by Benstein and Wood [8]. The two-stage power turbine characteristics were consistent with ST9 data. Power turbine wheel speed was scaled to achieve the same corrected tip velocity as the ST9.

3. Other parasitic losses, air bearing and seal friction, accessory power, case heat losses, etc.

4. Values of the selected parameter at which the cycle is to be balanced. The off-design points at which engine performance is checked are selected, for fixed nozzle areas, using one of three parameters: air flow, fuel flow, or turbine inlet temperature. Estimated values of the desired parameter are plotted versus engine power. From this curve, values of the parameter can then be determined and input to the computer program for each power setting at which a check of the engine performance is desired. For this study, turbine inlet temperature (TIT) was selected as the governing parameter and a curve of TIT vs. power was generated.

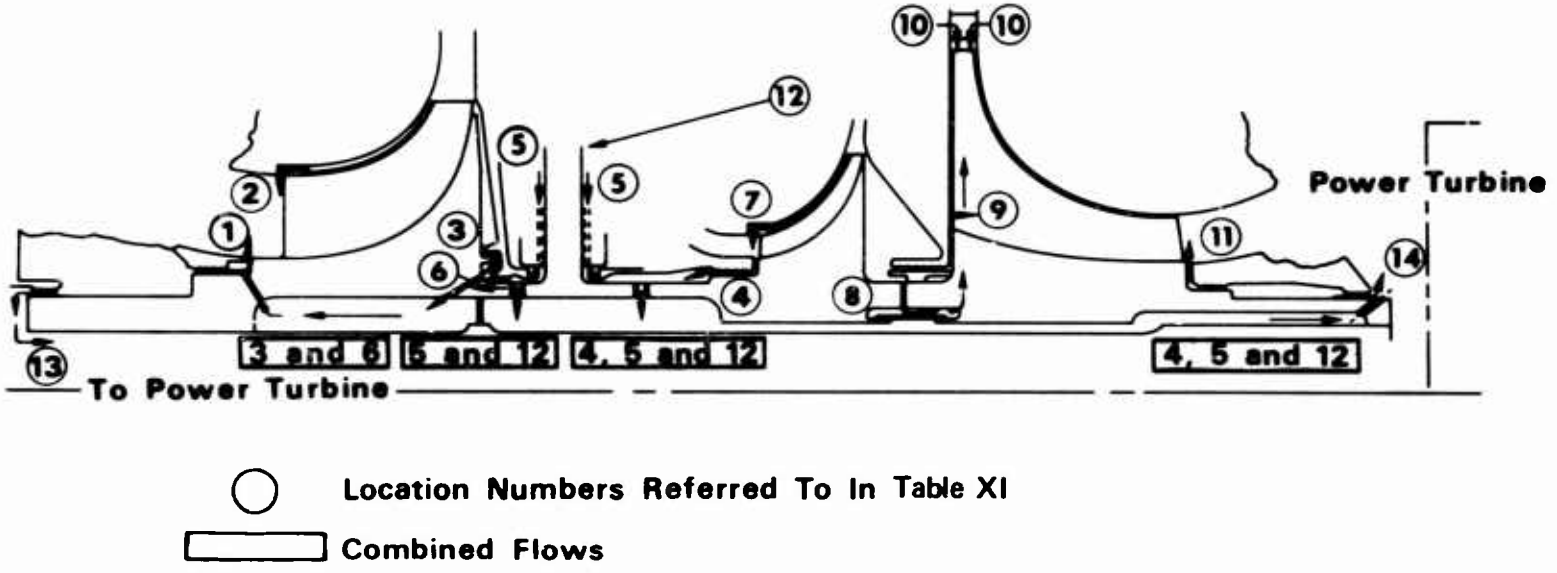


Figure 64. Schematic of Engine Internal Leakage Paths.

TABLE XI. AIR BEARING ENGINE LEAKAGE AND BLEED SUMMARY

Loc	Description	lb/sec at SLTO
1	Leakage into compressor inlet from cavity surrounding front air bearing. This cavity is supplied from second-stage compressor discharge total conditions.	0.0357
2	Leakage into first-stage compressor inlet around rotating shroud seal, from rotor exit static conditions. (Recirculation)	0.0155
3	First-stage backface flow recirculation to inlet.	0.0048
4	Second-stage inlet leakage to thrust bearing cavity - also used for cooling rear bearing and power turbine.	0.0169
5	Cooling flow for thrust bearing plates - also used to cool rear bearing and power turbine.	0.1000
6	Thrust bearing discharge cavity to first-stage inlet.	0.0134
7	Leakage into second-stage compressor inlet around rotating shroud seal, from rotor exit static conditions. (Recirculation)	0.0379
8	Turbine rotor (disc and blade) cooling flow exiting at second-stage rotor exit static conditions - 16.7% assumed to enter at turbine rotor inlet and 83.3% at turbine rotor exit.	0.1050
9	Leakage from second-stage rotor exit static into turbine. Assumed to enter at turbine exit.	0.0272
10	Turbine vane and housing coolant. Taken from second-stage compressor total conditions, by-passing burner and entering rotor inlet.	0.2100
11	Leakage into gas generator turbine exit from cavity surrounding rear air bearing. This cavity is supplied from second-stage compressor discharge total conditions.	0.0341
12	Thrust bearing operating flow - taken from second compressor total discharge conditions and also used for cooling rear bearing and power turbine.	0.036

TABLE XI - Continued

Loc	Description	lb/sec at SLTO
13	Leakage into power turbine cavity from front journal bearing supplied from second-stage compressor discharge.	0.0321
14	Leakage into power turbine cavity from rear journal bearing compartment supplied from second-stage compressor discharge.	0.0358

TABLE XII. ENGINE DESIGN POINT VALUES - 3.5 LB/SEC			
Altitude	0 ft	$\Delta P/P$ (C_2 Diffuser)	0% (*)
Velocity	0 kt	η (Burner)	99.9%
Day	Standard	$\Delta P/P$ (Burner)	2.0%
Power Setting	Max (TIT= 2550°F)	LHV	18,500 Btu/lb
Inlet Airflow	3.5 pps	η_{HT}	81.7%
η_{RAM}	100%	η_{PT}	89.0%
Inlet P/P	0%	N_2 (Power Turbine)	24,483 rpm
P/P (Comp 1)	7.40	$\Delta P/P$ (Exhaust Diff)	4.0%
η(Comp 1)	84.2%	Air Bearing Power Loss	1.0 hp
$\Delta P/P$ (C_1 Diffuser)	0% (*)	Thrust Bearing Power Loss	2.0 hp
N_1	60,000 rpm	PT Parasitic Friction	2.0 hp
P/P (Comp 2)	2.365	Accessory Power	2.21 hp
η (Comp 2)	82.2%	Case Heat Loss	0.73 Btu/sec
(*) Included in the efficiency			

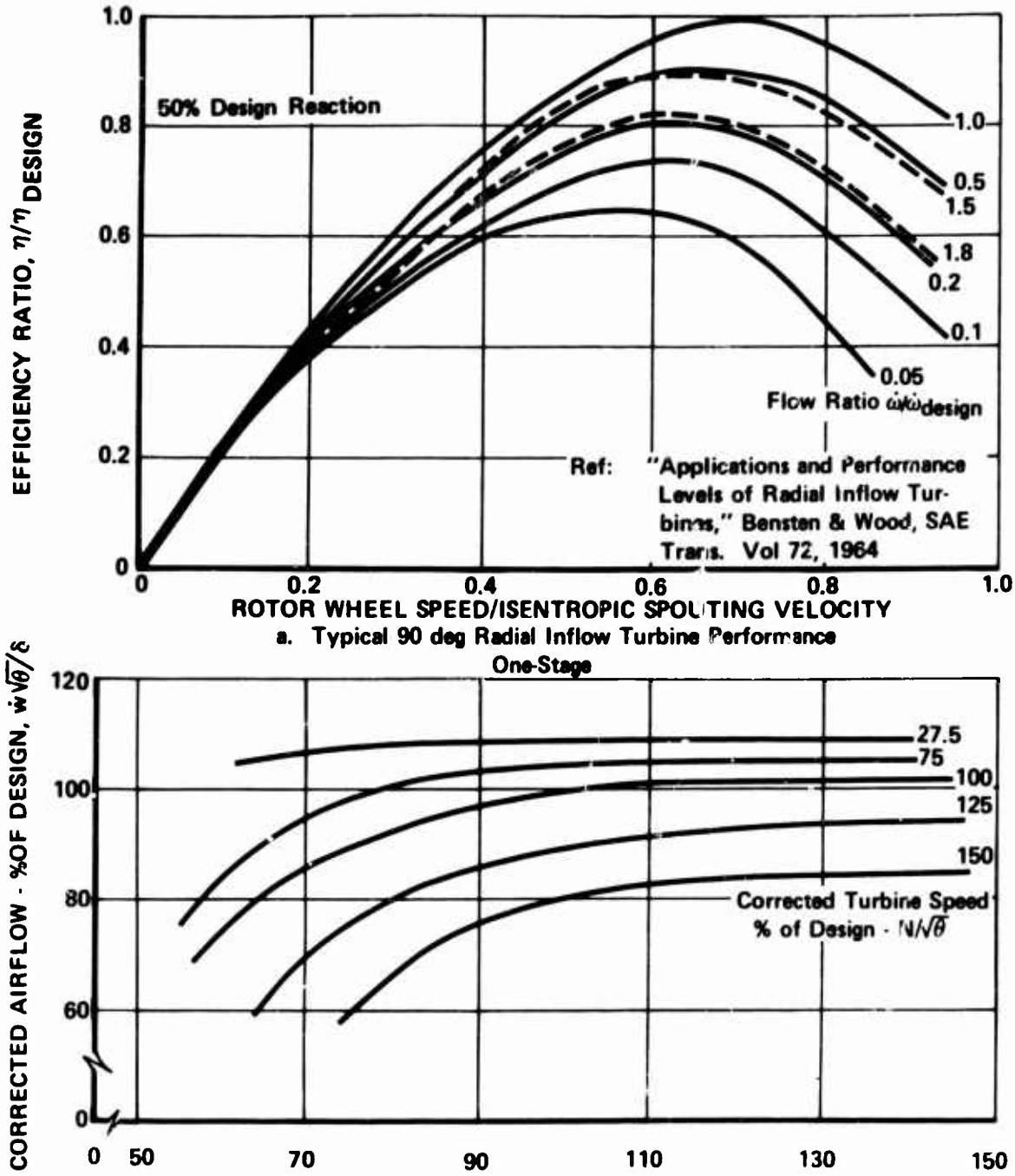


Figure 65. Off-Design Performance and Flow Parameter Curves for Engire Cycle Balancing Program.

The engine matching or cycle balancing involves an iterative process in which the engine cycle is balanced for optimum performance at the design power setting, and performance is then determined at off-design conditions from idle to full power. If off-design performance is not satisfactory, changes are made at the design point and the process is repeated.

Output from the computer program includes the airflow, temperature, and pressure at eleven critical locations in the engine flow path (shown in Figure 66), in addition to engine performance parameters such as fuel flow, rotor speed, specific fuel consumption, and output horsepower. Values for each are given at 100%, 75%, and 25% engine power and flight idle at both sea level and 25,000 feet altitude, as shown in Table XIII a and b, respectively.

The air flows, temperatures, and pressures at 100% power are used to check the seal leakages and rotor thrust loads estimated originally. If the values do not agree, new seal ΔP's are assumed, leakage estimates are made, and the rotor thrust balance is achieved. The new leakage numbers are input to the engine cycle deck, and revised design tables are generated. This iterative process is repeated until the leakage values calculated using the engine cycle deck output agree with the estimates used as input. In this case the leakage estimates used as input agreed very well with the program output. Rotor thrust, which was initially balanced to within approximately 40 lb at 100% power, as shown in Figure 67, was checked at flight idle and found to be less than 10 lb.

The data in these design tables were used to determine bearing environmental conditions and cooling flow-rate requirements.

The overall performance of the air-bearing-equipped, 3.5 lb/sec engine was very satisfactory at 658 shaft horsepower (shp) and 0.448 specific fuel consumption (sfc), as shown in Table XIII a. However, a review of the engine internal leakages listed in Table XI revealed several sources of significant leakage that could possibly be reduced. Of particular interest were the leakages at the front and rear seals of the compressor and turbine end journal bearing compartments. These locations (No. 1, 11, 13 and 14 on Figure 64) are subjected to very high ΔP's as a result of the need to pressurize the compartments under certain operating conditions. Because the bearings' load capacity is dependent on its ambient air pressure, the bearing compartments must be pressurized from the highest available source at the 25,000-ft, idle-power condition, to provide the load capacity required by MIL-E-5007. The highest pressure source in the engine is second-stage compressor discharge.

Unfortunately, using second-stage discharge to supply the bearing compartments results in much higher compartment pressures, therefore seal ΔP's, than are required at sea level and 100% power. However, it may be feasible to use a pressure-operated, flow control valve in the bearing supply lines to provide only the flow necessary to maintain the minimum ambient pressure required around the bearing (the pressure prevailing at the 25,000-ft, idle-power condition). In this manner the leakage rates out of the bearing compartment could be greatly reduced, as shown in Table XIV, which presents

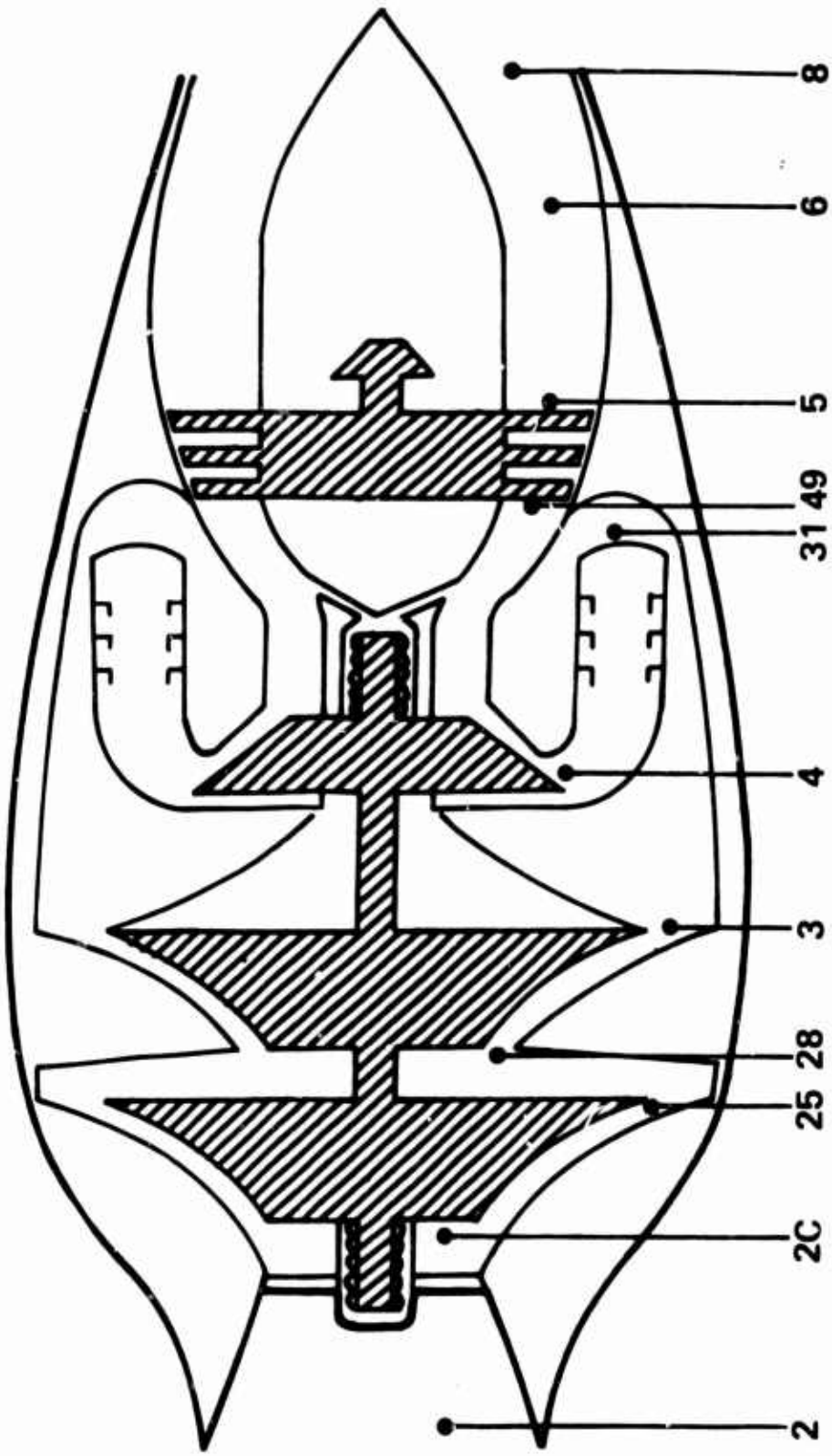


Figure 66. Air Bearing Engine Station Designations.

TABLE XIIIa. AIR BEARING ENGINE DESIGN TABLE

Flight Conditions: PAM - 14.7 psi Altitude - 0.0 ft Velocity - 0 knots TAM - 59°F

Station	100% Power			75% Power			50% Power			25% Power			Flight Idle		
	Flow (pps)	Temp. (°R)	Press.* (psia)	Flow (pps)	Temp. (°R)	Press.* (psia)	Flow (pps)	Temp. (°R)	Press.* (psia)	Flow (pps)	Temp. (°R)	Press.* (psia)	Flow (pps)	Temp. (°R)	Press.* (psia)
2	3.50	519	14.7	3.23	519	14.7	2.79	519	14.7	2.21	519	14.7	1.91	519	14.7
2C	3.50	519	14.7	3.23	519	14.7	2.79	519	14.7	2.21	519	14.7	1.91	519	14.7
25	3.50	1000	124	3.23	948	114	2.79	910	100	2.21	855	82	1.91	801	65
28	3.38	1000	109	3.13	948	100	2.69	910	87.7	2.14	855	71..	1.66	801	56.7
3	2.90	1330	293	2.68	1240	252	2.31	1170	208	1.83	1080	156	1.39	995	118
31	2.90	1330	258	2.68	1240	225	2.31	1170	184	1.83	1080	138	1.39	995	104.0
4	2.98	3010	252	2.75	2720	220	2.36	2490	180	1.87	2220	135	1.42	2190	102.0
49	3.58	2100	52.1	3.30	1890	45.7	2.84	1740	38.2	2.24	1560	2..8	1.74	1540	24.3
5	3.58	1640	16.2	3.30	1510	15.9	2.84	1430	15.6	2.24	1350	15.2	1.74	1400	15.0
6	3.58	1640	16.2	3.30	1510	15.9	2.84	1430	15.6	2.24	1350	15.2	1.74	1400	15.0
8	3.58	1640	15.6	3.30	1510	15.4	2.84	1430	15.2	2.24	1350	15.0	1.74	1400	14.9
Engine Performance:															
Fuel Flow lb/hr		295			232			175			116			91.9	
W_{a2c} θ_{t2c}/ θ_{t2c} lb/sec		3.50			3.23			2.79			2.21			1.91	
N_1, rpm		60,000			56,400			52,800			49,100			45,000	
N_2, rpm		24,500			24,500			24,500			24,500			24,500	
SFC, lb/hr/hp		0.448			0.469			0.525			0.672			1.0	
SHP, hp		658			496			333			173			92.1	
FNT, lb		62.5			48.9			34.4			20.4			12.8	
Parasitic Losses and Extractions:															
Air Bearing Power Loss, hp		1.01			0.87			0.77			0.68			0.56	
Thrust Bearing Power Loss, hp		2.00			1.76			1.56			1.34			?.13	
Power Turbine Disc Friction, Bearings and Seals		2.01			1.94			1.82			1.66			1.54	
Accessory Power, hp		2.21			2.21			2.21			2.21			2.21	
Case Heat Loss, Btu/sec		0.73			0.73			0.73			0.73			0.73	
Compressor Interstage Bleed, %		0.0			0.0			0.0			0.0			10.0	

*Total Pressure

TABLE XIIIb. AIR BEARING ENGINE DESIGN TABLE

Flight Conditions: PAM - 5.45 psi Altitude - 25,000 ft Velocity - 0 knots TAM - 59°F

Station	100% Power			75% Power			50% Power			Flight Idle		
	Flow (pps)	Temp. (°R)	Press.* (psia)	Flow (pps)	Temp. (°R)	Press.* (psia)	Flow (pps)	Temp. (°R)	Press.* (psia)	Flow (pps)	Temp. (°R)	Press.* (psia)
2	1.43	430	5.45	1.32	430	5.45	1.14	430	5.45	1.01	430	5.45
2C	1.43	430	5.45	1.32	430	5.45	1.14	430	5.45	1.01	430	5.45
25	1.43	833	46.7	1.32	790	43.1	1.14	757	37.5	1.01	716	30.7
28	1.38	833	40.8	1.28	790	37.6	1.10	757	32.8	0.87	716	26.9
3	1.18	1110	108	1.10	1040	953	0.94	979	78.4	0.73	911	61.4
31	1.18	1110	96.0	1.10	1040	84.2	0.94	979	69.1	0.73	911	53.8
4	1.21	2550	94.0	1.12	2310	82.4	0.96	2130	67.6	0.75	2140	52.7
49	1.46	1760	19.30	1.34	1590	17.0	1.15	1470	14.2	0.92	1480	11.8
5	1.46	1370	6.02	1.34	1260	5.90	1.15	1210	5.77	0.92	1270	5.67
6	1.46	1370	6.02	1.34	1260	5.90	1.15	1210	5.77	0.92	1270	5.67
8	1.46	1370	5.78	1.34	1260	5.71	1.15	1210	5.63	0.92	1270	5.57
Engine Performance:												
Fuel Flow, lb/hr		98.0			77.9			59.5			49.4	
$W_{a2c}\ \theta_{t2c}/\ \theta_{t2c}$ lb/sec		3.50			3.24			2.78			2.47	
N_1, rpm		54,600			51,400			48,200			45,000	
N_2, rpm		24,500			24,500			24,500			24,500	
SFC, lb/hr/hp		0.444			0.468			0.531			0.682	
SHP, hp		221.0			166.0			112.0			72.5	
FNT, lb		23.2			18.3			12.9			8.66	
Parasitic Losses and Extractions:												
Air Bearing Power Loss, hp		0.83			0.74			0.65			0.57	
Thrust Bearing Power Loss, hp		1.66			1.47			1.29			1.13	
Power Turbine Disc Friction, Bearings and Seals		1.45			1.42			1.37			1.31	
Accessory Power, hp		2.21			2.21			2.21			2.21	
Case Heat Loss, Btu/sec		0.73			0.73			0.73			0.73	
Compressor Interstage Bleed		0.0			0.0			0.0			10.0	

*Total Pressure

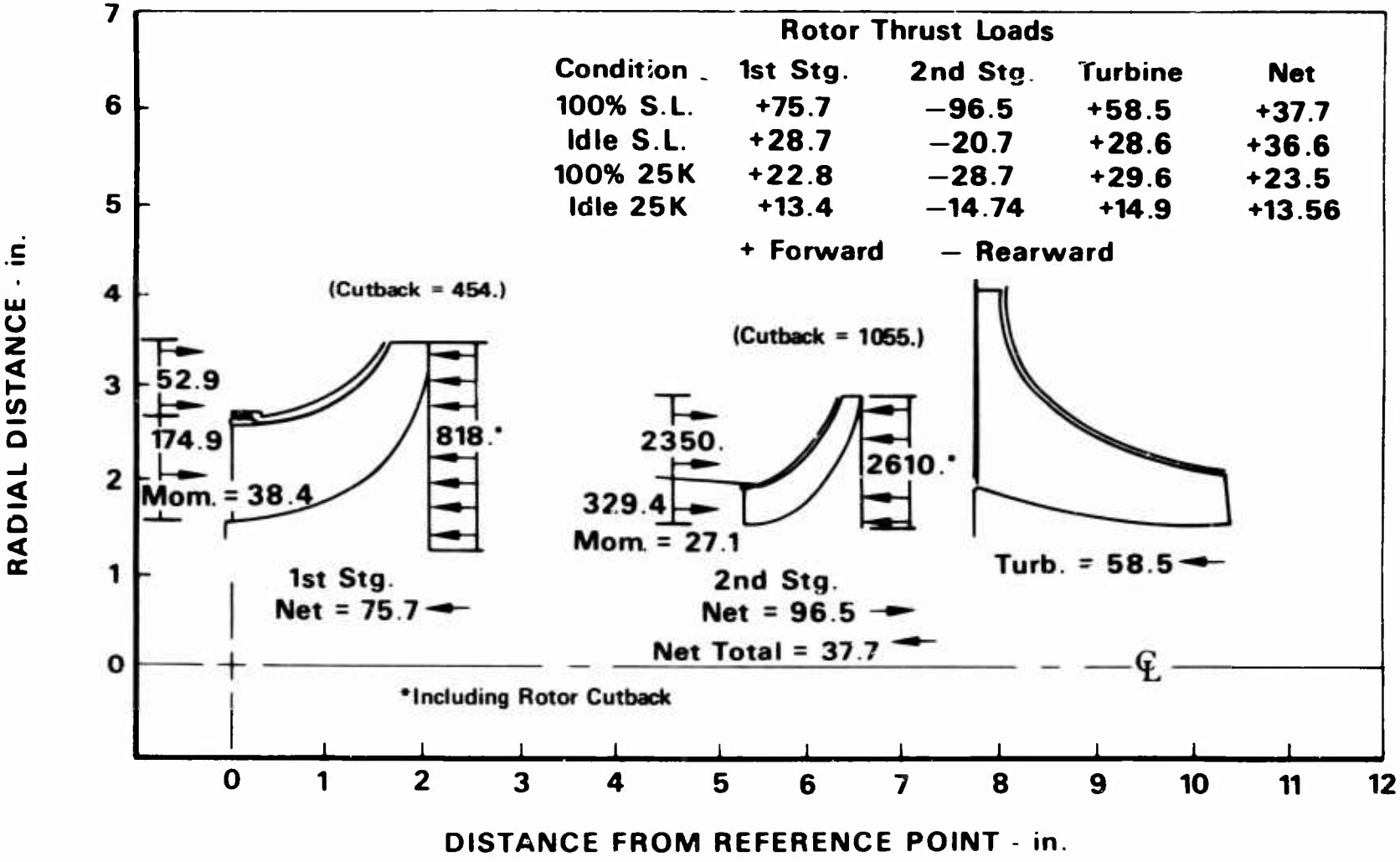


Figure 67. Summary of 3.0 lb/sec C_o-T_o Engine Rotor Thrust Forces.

the leakage at locations 1, 11, 13 and 14, both with and without a flow control device. Table XIV also shows the effect of the leakage reduction on engine performance in terms of shaft horsepower and specific fuel consumption.

TABLE XIV. EFFECT OF JOURNAL BEARING SUPPLY CONTROL ON LEAKAGE RATES (in.-lb/sec)

Location	Leakage Without Control	With Control
1	0.0357	0.0084
11	0.0341	0.0080
13	0.0321	0.0077
14	0.0358	0.0084
	Engine Performance	
Output Horsepower	658	705
Specific Fuel Consumption lb/hr/hp	0.448	0.435

The gains to be realized by controlling bearing compartment pressures would seem to warrant the time and expense required to develop a reliable, fail-safe flow or pressure regulator.

Without any bleed flow for bearing purposes, approximately 785 horsepower could be developed with an SFC of about 0.414. For direct comparison to a rolling element bearing supported engine rotor, bearing, seal, and lube system losses, along with any required bleed flow losses would have to be deducted from the aforementioned output power.

INTEGRATED ENGINE DESIGN

A preliminary design layout of the 3.5 lb/sec C_o-T_o engine incorporating the air bearing rotor support system was prepared in sufficient detail to ensure that the engine could be assembled and disassembled without difficulty, and that the bearings and supports could be aligned and alignment maintained. This layout is shown in Figure 68.

As previously indicated, the journal bearing compartments are pressurized from second-stage compressor discharge to obtain maximum bearing capacity at low power conditions. The hydrostatic supply to the thrust bearing is also taken from second-stage discharge, while the cooling flow for the thrust plates is taken from first-stage discharge. These two flows, after

exiting from the thrust bearing, are routed down the shaft and are used to cool the rear journal bearing and the power turbine.

The design incorporates a beryllium shunt to carry heat from the front bearing into the first-stage impeller. As the layout shows, the power turbine is supported by an air bearing in the rear and a rolling element type thrust bearing in front. With this arrangement, the only location in the engine requiring oil, the power turbine thrust bearing, is situated in the cool portion of the engine, thereby minimizing heat rejection.

Front shrouds are incorporated on both compressor stages to balance rotor thrust. The vented cavity at the base of the first-stage impeller prevents flow from recirculating up the backface of the impeller and into the diffusers. Leakage in that direction can adversely affect collection system performance. The vented cavity also assists in controlling backface pressure necessary in balancing first-stage thrust loads. Variable inlet geometry is shown on both compressor stages, even though it is unlikely that it will be needed on both stages.

As stated earlier, the two compressor stages and the thrust bearing runner are made of titanium (either 8-1-1 or 6-2-4-2) and the turbine is made of IN-100. Curvic couplings are used between components to transmit torque and for alignment with the assembly clamped together by a center-tube tiebolt.

Primarily engine flow and some of the more critical cooling and leakage flows are indicated by arrows on the figure.

STARTER AND ACCESSORY DRIVE EVALUATION

As may be noted on the layout, there are no provisions for accessory drives or starting. As part of this study, the problems associated with starting and driving accessories on an air-bearing engine were investigated. The basic requirements for the starter/accessory drive system include those features desirable for any type of engine: efficient, lightweight, durable, reliable, and if possible, self-contained for operation in remote areas. The air bearing system imposes some additional requirements, such as: does not require oil lubrication or, if so, lubrication system is self-contained; does not impose excessive loads on gas generator rotor, particularly during start and shutdown. An additional requirement, specified in the contract, was that the starter/accessory system must be compatible with a front-drive power turbine.

The following assumptions were made to facilitate the accessory study:

1. Lightweight, high-speed (40,000 to 60,000 rpm) accessories will be developed in time for use in air-bearing engines (programs are currently in progress on most accessories: alternators, fuel pumps, controls).

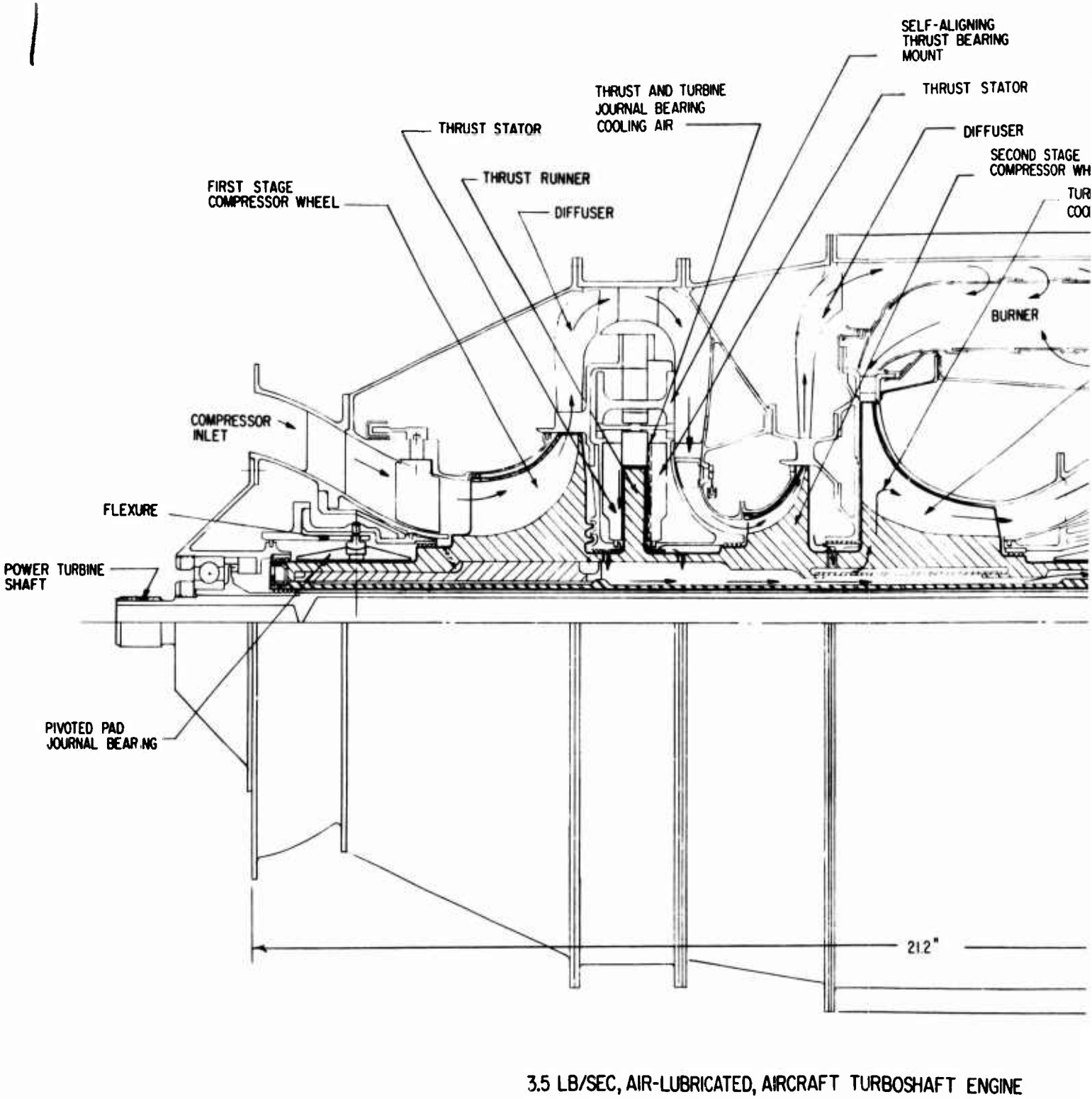
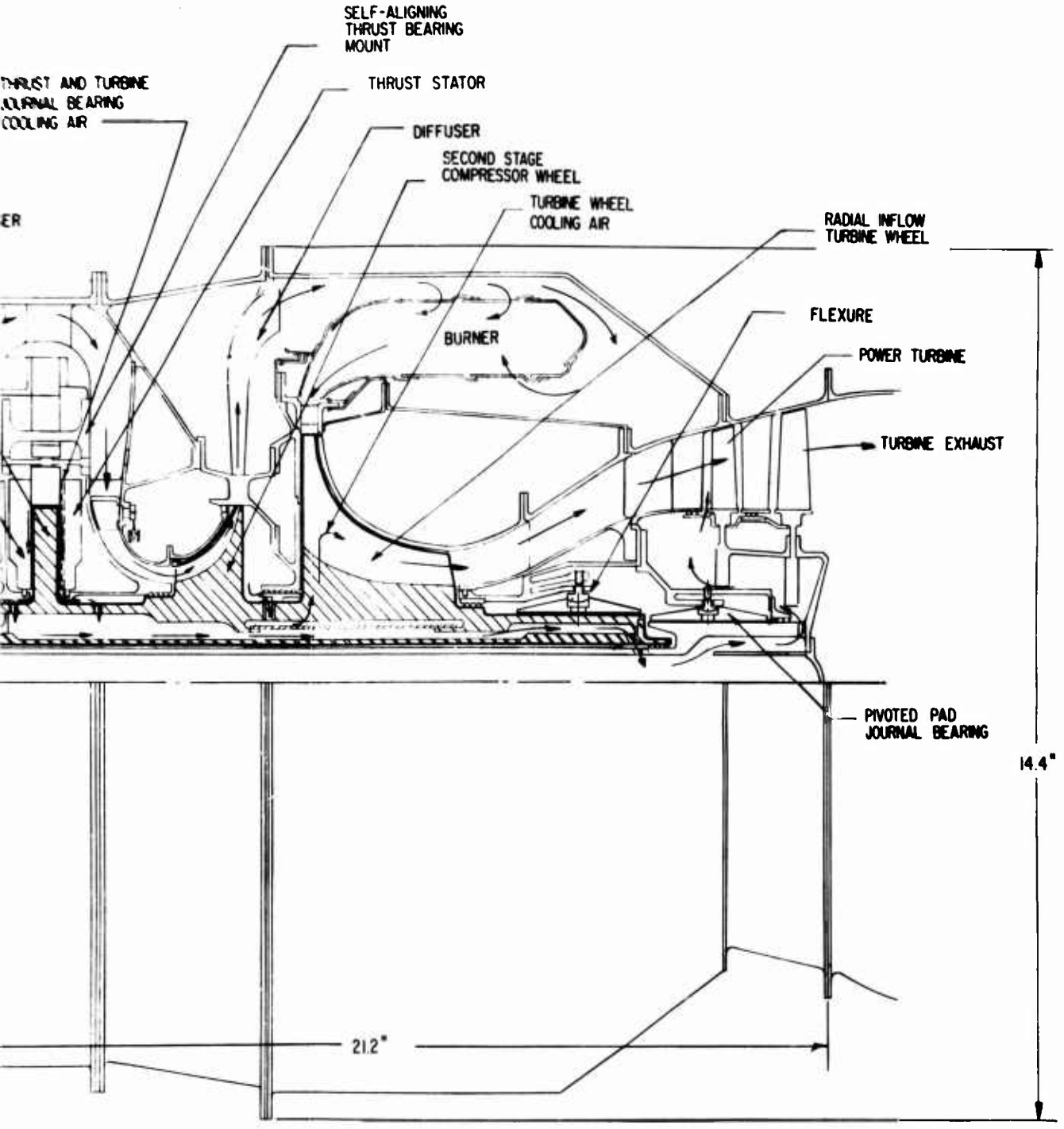


Figure 68. 3.5 lb/sec C_o-T_o Engine Layout With Air Bearings.



EC, AIR-LUBRICATED, AIRCRAFT TURBOSHAFT ENGINE

yout

2. Gear development will follow technology growth in other areas through the mid-1970's (i.e., pitch line velocities of 25,000 to 30,000 fpm will be feasible for spur gears).

The accessory drive systems evaluated in the study can be divided into three broad categories: geared, electrical, and turbine driven.

Geared Drive

The geared system has as its main advantages:

1. Reliable - direct mechanical connection
2. Efficient - only loss is in gears, seals, and bearings
3. Starting capability is inherent - any type of starter may be used
4. Lightweight

Disadvantages of the geared drive system include:

1. Oil lubrication required
2. Imposes loads on gas generator rotor
3. Magnifies critical speed problems on power turbine shaft by increasing distance between bearings

The most attractive geared arrangement minimizes most of these disadvantages. This scheme, shown in Figure 69, is a front-mounted, doughnut-shaped gearbox that also contains the front thrust bearing for the power turbine. By combining functions, all oil requirements for the engine are isolated in one compartment. The lubrication for the gearbox could be self-contained with a small pump, a finned heat exchanger around the OD, and an adequate sump volume.

The use of three equally spaced spur gears greatly reduces the radial loads imposed on the gas generator shaft. This type drive (spur gear) as opposed to a tower shaft, imparts no axial load on the shaft and requires less axial length so that the power turbine front bearing does not have to be moved as far forward. The use of spur gears does pose a problem in that, because of the limited space available inside the inlet duct, only a small speed reduction is possible. In the scheme shown, the accessory speed is 50,000 rpm compared to the gas generator speed of 60,000 rpm.

Location of the accessories inside the inlet fairing provides additional protection. However, it also restricts accessibility in most small engine installations.

Electric Drive

The all-electric drive system, shown schematically in Figure 70, consists of a shaft-mounted generator that supplies power to electric-motor-driven fuel pumps, fuel control, and variable-geometry vane actuators. The generator could be a rotating rectifier type modified to provide starting motor capabilities. With an external power input, the generator would respond as a synchronous motor. At a preset speed, the control circuits

PRECEDING PAGE BLANK-NOT FILMED.

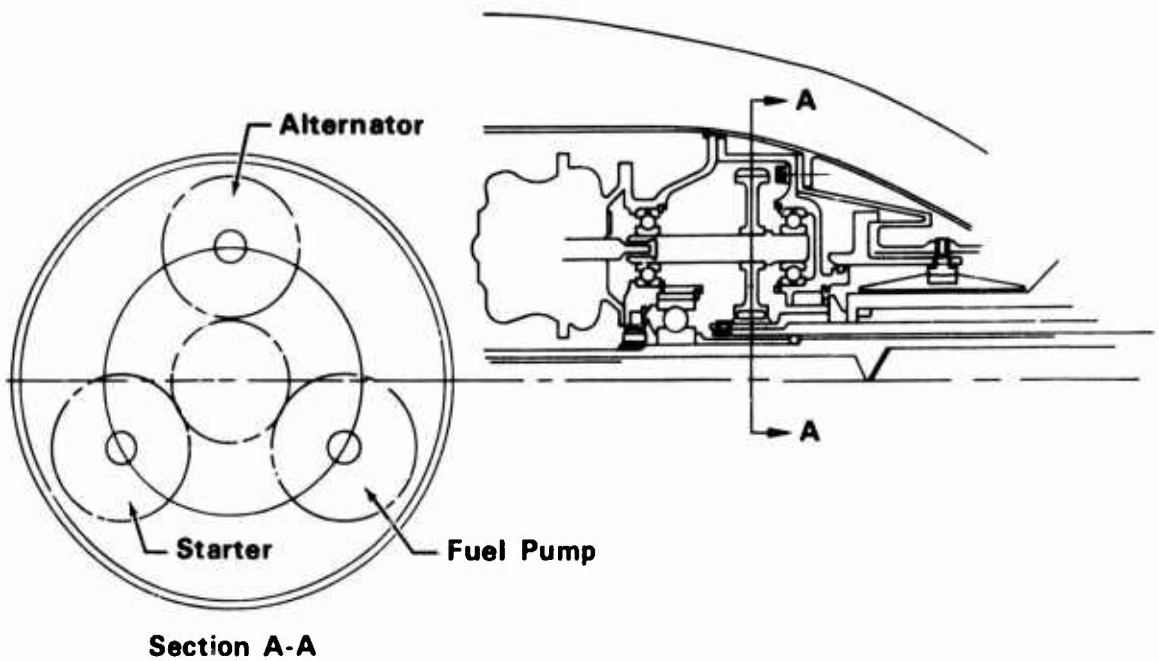


Figure 69. Geared Accessory Drive System for Air Bearing Engine.

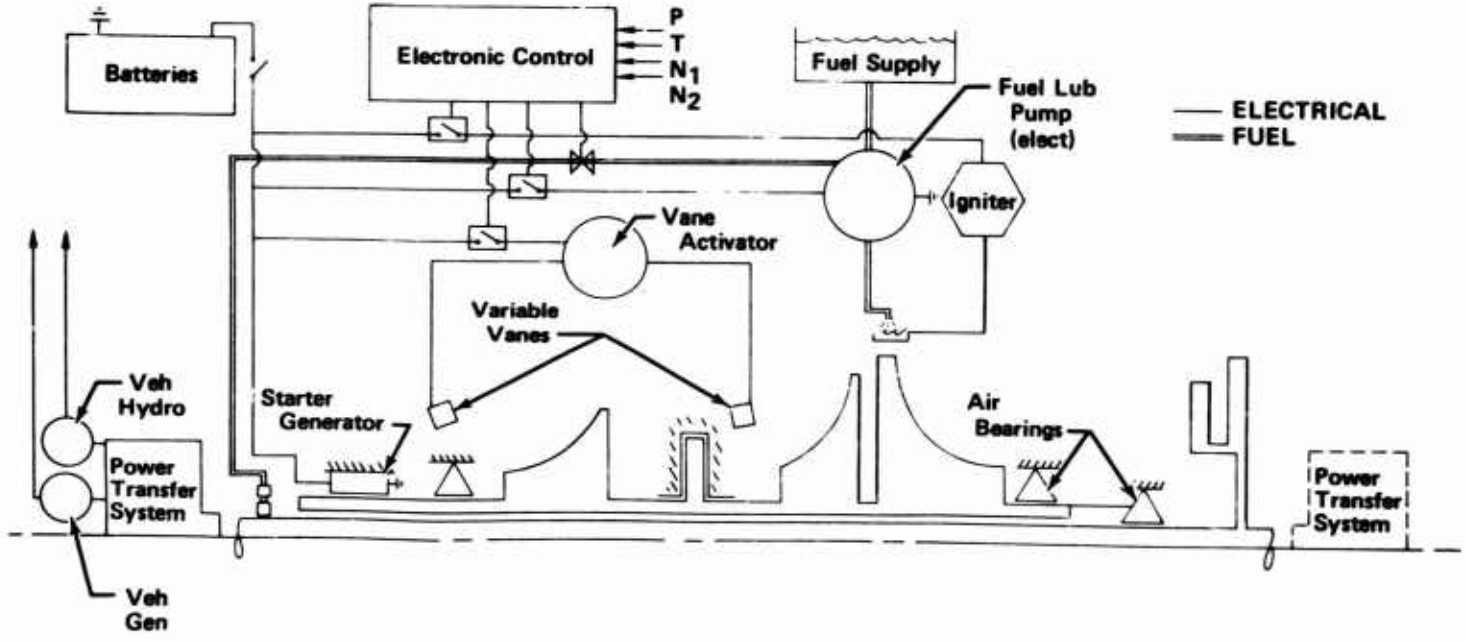


Figure 70. Schematic of All-Electric Accessory Drive System.

would automatically change the system operation to a variable-speed constant-frequency generating mode. The advantages of this system include:

1. Accessories can be remotely mounted, providing added flexibility in engine packaging
2. Minimum complexity of overall system - control functions reduced
3. Starting capability included at little extra weight and cost

Disadvantages are:

1. Lower reliability than other systems due to reliance on electrical components
2. Heavier than other systems
3. Long development time will be required for the high-speed (60,000 rpm) starter/generator. Some work is presently being done on high-speed, solid-core generators, but little if any effort has been devoted to hollow-core generators.

Turbine Drive

The bleed air turbine accessory drive scheme is shown schematically in Figure 71. In this scheme, the main fuel pump is driven by a bleed air turbine, and electrical power is supplied by an engine-shaft-mounted generator. The generator could be mounted in line with the fuel pump on the turbine shaft and could be switched with control circuits to drive the pump for starting. The schematic shows two possible starting systems; one uses an impingement starter, like a Terry turbine, located on the first-stage impeller shroud and supplied by an air storage bottle, which in turn can be recharged by a small electric-motor-driven compressor or hand pump. Unfortunately, because of the low efficiency of the Terry turbine, large quantities of air are required. For example, if the storage bottle is limited to 250 psia, 16 cubic feet of volume is required for a single start (maximum starter running time - 30 sec). If the volume of the storage bottle is reduced to fit within the engine envelope, it would have to be charged to 2500 psia -- an unacceptably high level.

The alternative starting scheme employs a retractable tower shaft through which a hydraulic starter powers the gas generator shaft. Inasmuch as the tower shaft is used only intermittently and then at low speeds, lubrication of the gears should not be necessary. With grease-packed bearings, the entire starting system could operate without an external source of lubrication.

The air supply to the accessory turbine could be taken from any one of several locations, such as first-stage compressor discharge or gas generator turbine discharge. The use of first-stage discharge results in a severe performance penalty: 5 engine horsepower for each accessory horsepower. In contrast, the trade-off when using gas generator discharge air is 1.28 engine horsepower for 1 accessory horsepower. A comparison of the effect of bleed air turbines and other drive systems on engine performance is given in Table XV.

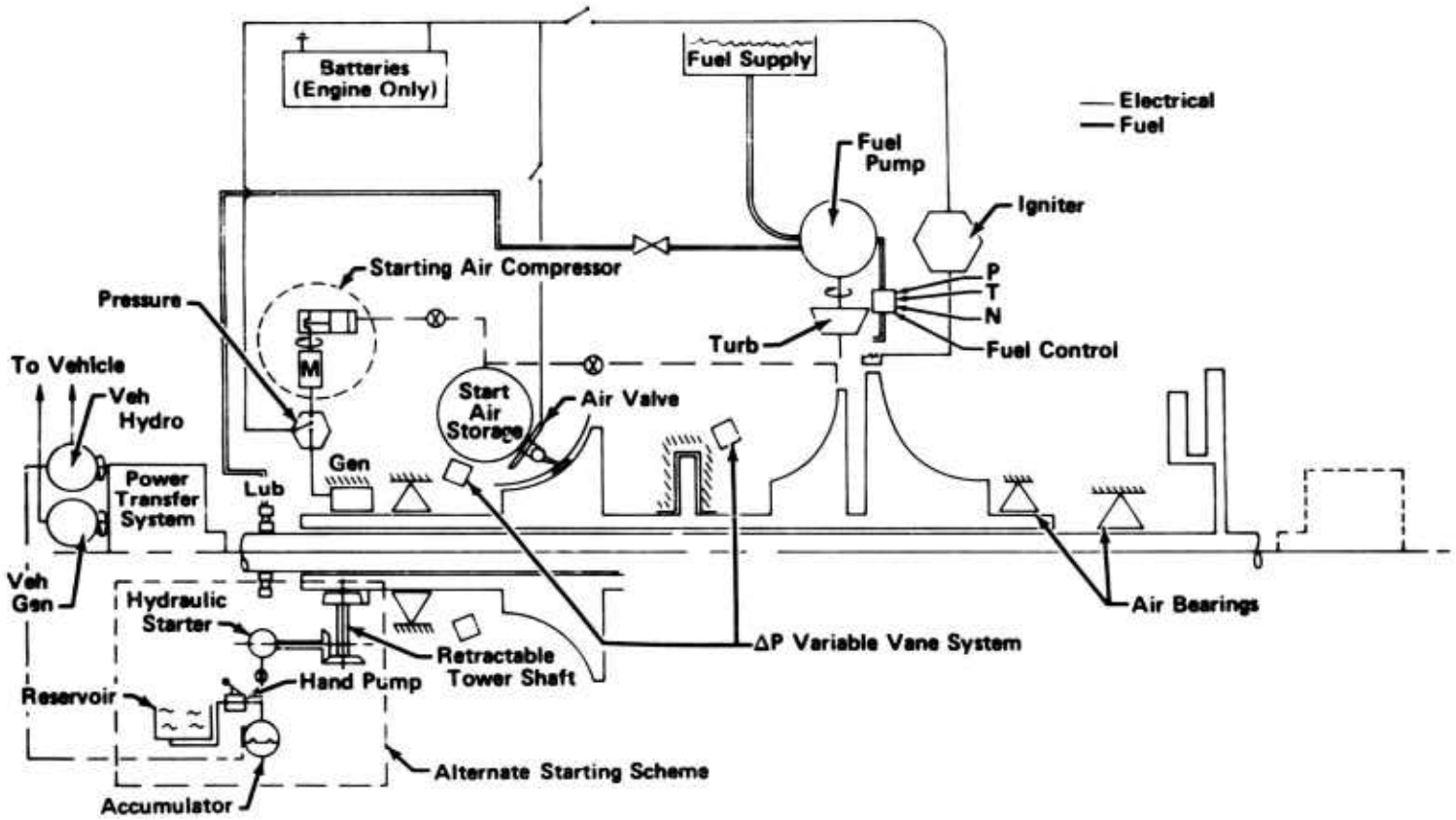


Figure 71. Schematic of Air Turbine Accessory Drive System.

In summary, the accessory drive/starter system study has indicated that a geared system could be adapted to the air bearing engine within state-of-the-art technology. However, development in the area of high-speed accessories will be required. If the accessory technology is not available, a system employing a bleed air turbine-driven fuel pump and generator and a shaft-mounted starter could be used.

TABLE XV. ACCESSORY DRIVE SYSTEM EFFECT ON ENGINE PERFORMANCE

Method	Loss of Engine Power Accessory Power	% Increase of SFC
Direct Drive	1.24	0.44
Electric Drive	1.93	0.69
Geared Drive	1.26	0.44
Bleed Turbine		
From 1st Comp. Overboard	5.4	1.3
From GG Exit Overboard or P.T. Exit	1.28	0.48

DESIGN AND ANALYSIS OF ROTOR BEARING SYSTEM

To fully identify the problem areas associated with the application of air bearings to small, advanced gas-turbine engines, it is necessary to perform a detailed engineering design and analysis on the engine rotor-bearing system. This work was accomplished under Task 4 of the program on the conceptual engine design described in the preceding section. The engine parametric and design data described in the preceding section were used in the detailed rotor-bearing design analysis discussed in this section.

The following factors established during the preliminary sizing and concept studies were used as starting points for establishing air temperature and pressure values in the design of the rotor-bearing system:

a. To ensure that the journal bearings have an adequate film thickness under the most severe conditions of operation (flight idle at 25,000 feet altitude with maximum maneuver loads imposed), it is necessary to pressurize the cavities in which the bearings are located. This pressure is obtained from second-stage compressor discharge, i.e., the pressure given at station 31. (Table XIII)

b. The hydrostatic air supplied to the thrust bearing should be at the highest pressure available from the cycle. The required air, therefore, is also taken from station 31. (Table XIII)

c. The thrust bearing is located between the first and second compressor stages; thus, it will operate in an ambient pressure environment equal to first-stage discharge, i.e., conditions prevailing at station 28 minus the pressure drop required by the thrust bearing heat exchanger. A pressure drop of 15 psi was assumed.

d. The air used to cool both the thrust bearing and the turbine-end journal bearing is not subject to a large pressure drop. Therefore, in order to minimize parasitic losses, the required cooling air should be taken from first-stage compressor discharge (station 28). Having performed the cooling function, this air may be returned to the cycle at the inlet (after the nozzle ring) to the power turbine.

DESIGN OF THE JOURNAL BEARINGS FOR THE ENGINE

A previous study [1] had shown that pivoted-pad hydrodynamic journal bearings would be the most suitable type of air bearing for use in small gas turbine engines. This same study also identified the most severe operating condition for the journal bearings to be engine idle at 25,000 feet altitude with maximum loads imposed. The severity of this operating condition occurs because of the low speed of rotation, and the low pressures and temperatures in the bearing cavities (bearing cavity pressure is obtained from compressor discharge), in association with the large bearing loads resulting from maximum maneuver conditions of aircraft operation. As would be expected, the load-carrying capacity of a hydrodynamic bearing is strongly affected

by rotational speed, ambient pressure, and gas viscosity. Preliminary bearing studies were made during the preliminary engine sizing phase as was discussed earlier in this report. With the load supported by one pad, the effect of ambient pressure and clearance ratio on the bearing pivotal film thickness under maximum load was determined. These studies indicated that a clearance ratio of 2×10^{-3} at the low ambient pressure was optimum, thus providing the largest film thickness under maximum load. Also, the required journal diameter was determined to be 2.25 inches and the bearing length-to-diameter ratio equal to one (1.0).

The following subsections describe the three-pad tilting-pad journal bearing studies that were conducted to establish the details of the journal bearings. These studies were directed toward the determination of the pad flexure stiffnesses and the design-point operating clearance, as influenced by bearing performance under isothermal and non-isothermal conditions with normal applied load, and isothermal conditions under maximum load. Isothermal bearing performance charts, for both turbine-end and compressor-end bearings, as a function of speed (dictated by engine power output) and altitude are presented as results of these studies.

Bearing Ambient Conditions and Applied Loads

The ambient temperatures, pressures, and applied loads, as a function of rotor speed and altitude for both the turbine-end and compressor-end journal bearings, were determined during the course of the final engine sizing tasks described in the preceding section. The pressures and temperatures are tabulated in Table XVI, the loads are tabulated in Table XVII, and the air viscosity-temperature relationship is illustrated by Figure 72. The data presented in Table XVI, which was used for bearing design purposes, differs slightly from that shown in Tables XIIIa and XIIIb. The latter data is a result of the engine cycle balancing iteration process. Since the bearing design effort was conducted concurrently with the final engine sizing effort, the bearing design data does not reflect the results of the final engine iteration. The differances, however, are slight and do not affect the results of the bearing design effort.

In general, the bearing ambient temperature, air viscosity, ambient pressure, and maximum maneuver load increase with increasing engine speed (power). Maximum load is slightly reduced at 100-percent power and an altitude of 25,000 feet because engine speed at this power is lower at altitude than at sea level.

It has been indicated previously that the least favorable condition for a hydrodynamic journal bearing is low speed, low ambient pressure, and low ambient temperature in combination with high load. Tables XVI and XVII and Figure 72 show that this least-favorable condition of operation occurs at an engine speed of 45,000 rpm and an altitude of 25,000 feet. The turbine-end bearing must carry a 12-pound load under normal steady-state operation. The maximum maneuver load that must be carried by this bearing with these same ambient gas conditions is 157 pounds. The compressor-end bearing operates under the same loads as the turbine-end bearing and has the same ambient pressure conditions, but it operates in an ambient temperature

TABLE XVI. SCHEDULE OF AMBIENT PRESSURES AND TEMPERATURES USED FOR JOURNAL BEARING CALCULATIONS

Power Setting	Sea Level			25,000 ft Altitude		
	Speed (rpm)	Pressure (psia)	Temperature (°F)	Speed (rpm)	Pressure (psia)	Temperature (°F)
Turbine End Journal						
Idle	45,000	103	540	45,000	52.7	450
50 percent	52,660	183	714	48,080	68.6	523
75 percent	56,370	224	790	51,360	84.0	585
100 percent	60,000	257	875	54,600	95.9	658
Overspeed	72,000	370	1000	65,600	138.0	800
Compressor End Journal						
Idle	45,000	103	308	45,000	52.7	250
50 percent	52,600	183	408	48.080	68.6	299
75 percent	56,370	224	451	51,360	84.0	334
100 percent	60,000	257	500	54,600	95.9	376
Overspeed	72,000	370	572	65,600	138.0	457

Notes: Under all conditions of engine operation, the ambient pressure surrounding both journal bearings is equal to second-stage compressor discharge pressure. Similarly, the temperature of the air used for pressurizing the journal bearing cavities is equal to second-stage compressor discharge temperature for the turbine end bearing and 57 percent of this value for the compressor end bearing.

The pressures at overspeed conditions are proportional to speed squared.

The temperatures at overspeed conditions have been assumed.

TABLE XVII. SCHEDULE OF MAXIMUM AND STEADY-STATE LOADS FOR JOURNAL BEARING CALCULATIONS

POWER SETTING	MAXIMUM MANEUVER CONDITIONS JOURNAL LOAD (LB)		STEADY-STATE CONDITIONS JOURNAL LOAD (LB)
	SEA LEVEL	25,000 FT ALTITUDE	
Idle	157	157	12
25%	164	160	12
50%	168	162	12
75%	175	168	12
100%	180	172	12
Overspeed	200	190	12

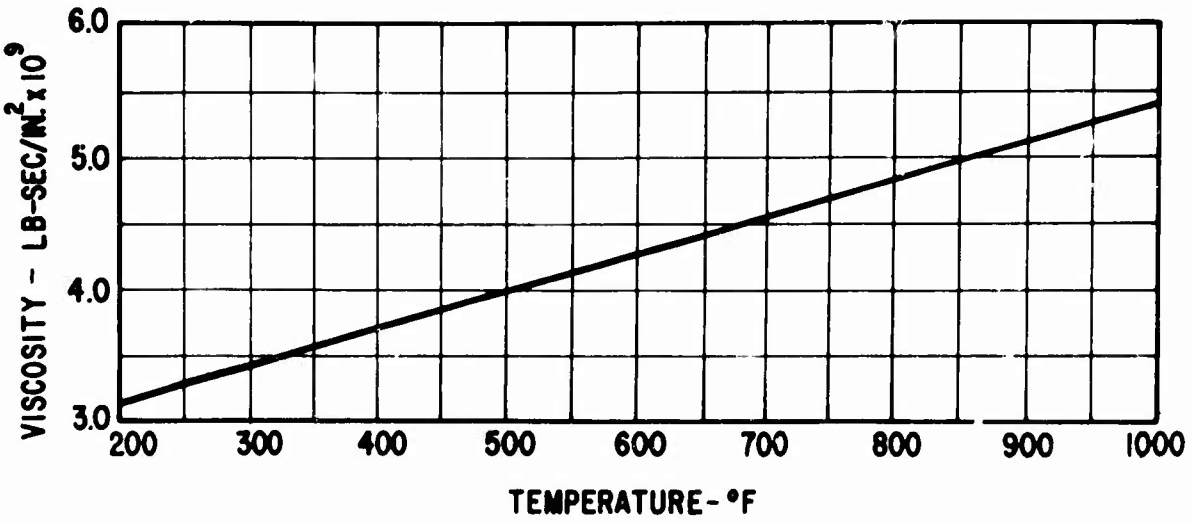


Figure 72. Air Viscosity-Temperature Chart Used for Journal Bearing Calculations.

which is lower by 200° to 400°F depending on power level and altitude. Thus the compressor-end bearing is the more severe case from a minimum film thickness standpoint.

Journal Bearing Arrangement

The conceptual arrangement of the components making up the journal bearing assembly are shown in Figure 73. This figure shows all of the principal requirements for the bearings under consideration. These are:

1. Three pivoted pads in each bearing
2. Flexible pad mounts
3. Stops to limit pad and pivot motion during maneuver conditions of aircraft operation
4. A pressurized cavity (labyrinth seals at each end) to maintain the ambient pressure required for acceptable bearing performance
5. A flexible type mounting between the bearing housing and the bearing assembly mounting flange. Flexibility in this region is required to thermally and mechanically decouple the bearing from the engine casing.

The final mechanical design details of the journal bearing assembly are discussed later in the description of the engine simulator.

Determination of Bearing Flexure Stiffness

Because of the large amount of journal centrifugal growth and the relatively high bearing temperatures (and hence thermal expansions), it is recognized that a number of pads in the bearings have to be mounted on relatively soft flexures. However, while in principle the flexure should be made as soft as possible, there are practical limitations. First, the flexure deflections must be limited to values consistent with both labyrinth clearances and safe flexure stress levels. Second, if the flexure is made too soft, it will preload the pad against the journal at low and zero speeds, thus causing rubbing during startup and shutdown, as well as increasing startup breakaway torque. The use of soft flexures can be accommodated either by providing externally pressurized lift-off orifices within the pad, or by assembling the flexure in a preloaded condition against a mechanical stop which prevents the flexure from preloading the pad against the journal. The first of these solutions entails undesirable mechanical and engine system complexity. The latter introduces some complexity which, if possible, would be desirable to eliminate. Consequently, a study was made of the bearings to determine if a flexure stiffness value could be obtained which would accommodate the effects of both centrifugal growth and thermal expansion but not involve clamping (preloading) between the pads and journal at the zero-speed room-temperature condition.

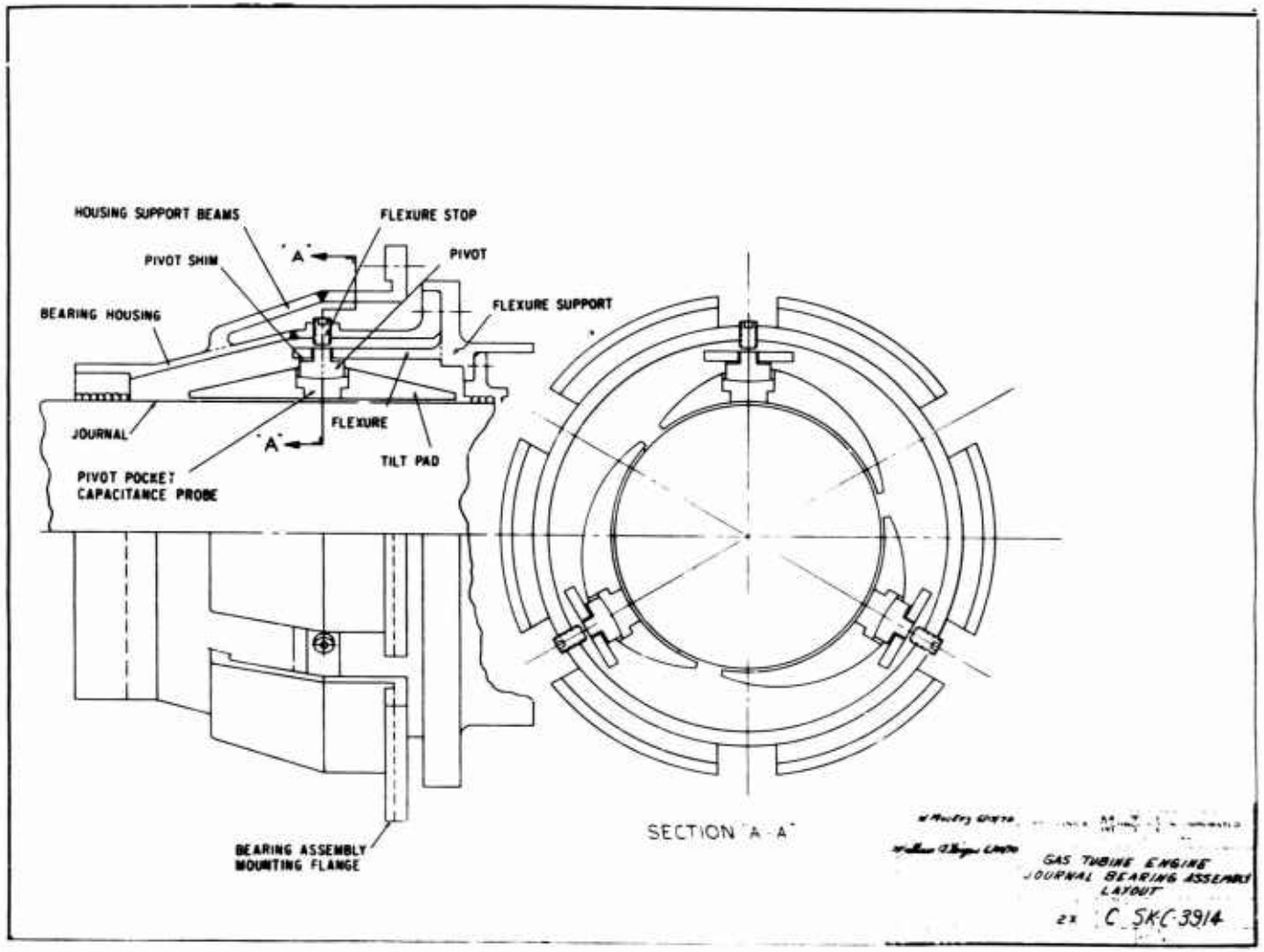


Figure 73. Conceptual Design of a Pivoted Pad Journal Air Bearing for a 3.5 lb/sec Flow Rate Gas Turbine.

The study was made using a design point of 45,000 rpm, 25,000 feet, and 12-pound steady-state bearing load. The clearance ratio (C/R) at this design point is 0.002, as has been previously discussed. The flexure stiffness of the loaded pad was set at a constant value of 2×10^5 lb/in. (considered as a reasonable, practical rigid flexure).

Figure 74 shows the results of the flexure stiffness study for both the turbine and compressor end bearings. Flexure stiffness for the two flexibly mounted pads is plotted against bearing diametral clearance at 80°F and zero speed for three values of bearing radial clearance at the 25,000-foot, flight-idle condition of operation, this being the condition for which the bearing has been optimized, henceforth called the design point. The calculations were made using a computer program which includes effects of centrifugal growth and thermal expansion. Design point journal, pad, and bearing-support temperatures were specified to be 450° and 250°F for the turbine-end bearing and compressor-end bearing respectively. Bearing load was 12 pounds (gravity load) acting through a pivot.

It is seen from Figure 74 that for a given value of flexure stiffness, zero-speed bearing clearance is strongly affected by the selected design point clearance. In satisfying the criteria that no clamping is allowed at setup (zero rpm) conditions, the following results can be obtained from Figure 74.

Bearing Radial Clearance at 45,000 RPM (mils)	Soft Pad Flexure Stiffness, (lb/in. x 10^{-3})	
	Turbine-End	Compressor-End
1.125	5.5	6.5
0.75	15.0	23.0
0.50	40.0	100.0

These data provide the information necessary to determine the optimum stiffness versus design clearance combination for the soft flexures.

Determination of Bearing Clearance at Design Point

Using the data established above, a bearing performance study was made to determine the optimum flexure stiffness versus design-point bearing clearance combination. Both isothermal and non-isothermal conditions with a 12-pound steady-state bearing load, and isothermal conditions with the maximum maneuver load of 157 pounds, were considered in the study. The non-isothermal conditions chosen were a $\pm$ 100°F difference between bearing housing and journal.

The performance parameters studied were the pivot film thickness of the loaded pad and the frequency ratio of the loaded and unloaded pads. Frequency ratio is defined as the ratio of the pad frequency in one of four modes (radial, pitch, roll or yaw) to the rotor speed. In all cases the pitch frequency was the lowest of the usual three motions (radial, pitch and roll) considered in a two-bearing system.

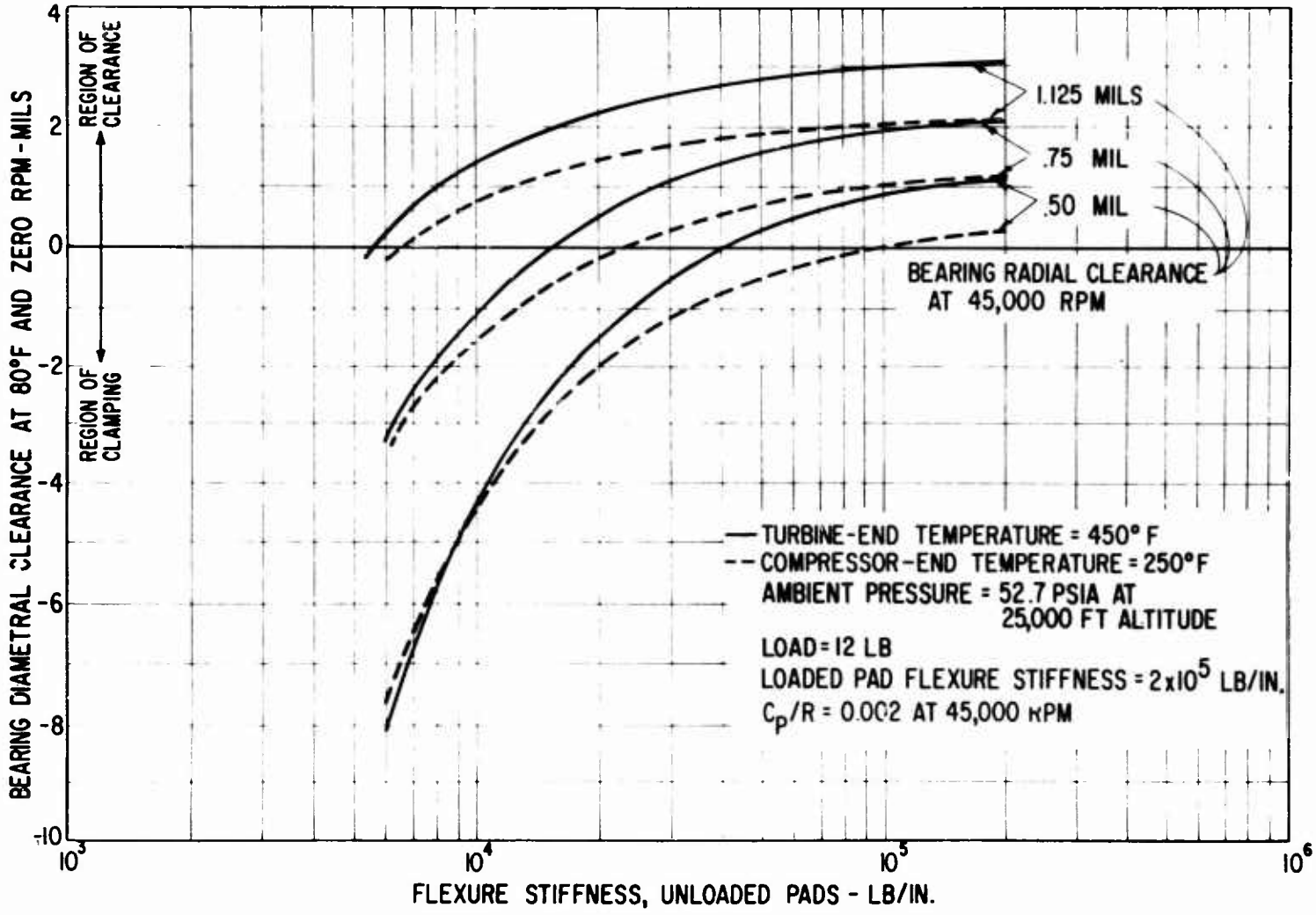


Figure 74. Bearing Diametral Clearance at 80°F and Zero Speed as a Function of Unloaded Pad's Stiffness and Design-Speed Clearance for the Turbine-End and Compressor-End Three-Pad, Tilting-Pad Bearings.

The results of the study are shown in Figure 75 for the turbine-end bearing and in Figure 76 for the compressor-end bearing. The resulting loaded-pad pivot film thickness, for the 12-pound steady-state load, is indicated by a high and a low value for a range of radial clearances. These high and low values of pivot film thickness correspond to non-isothermal conditions where the design point bearing housing temperature is either increased by 100°F or decreased by 100°F respectively. The pivot film thickness under isothermal conditions, i.e., design point, is close to the average of these non-isothermal results. The frequency ratio results also reflect the effects of non-isothermal conditions for a range of radial clearances. The highest frequency ratio corresponds to the condition in which the bearing housing is cooler than design point by 100°F, and the lowest value corresponds to the condition in which the bearing housing is above design point by 100°F. Under isothermal conditions, the frequency ratio at any load between 12 and 157 pounds lies within the bounds of these curves for the loaded and unloaded pads.

In general, the results indicate that the softest flexure is the most tolerant of the non-isothermal conditions, in that the range (spread) of each parameter for a given clearance is smallest. The pivot film thickness is also largest when using the softest flexure. However, the value of the frequency ratio is smallest, and approaches a value of unity as the flexure stiffness is reduced. Thus, the optimum combination of flexure stiffness and selected bearing clearance at design point conditions is a compromise.* Using a criterion that the minimum frequency ratio of the unloaded pads is to be equal to, or greater than, a value of 1.2, the following design data can be obtained from Figures 75 and 76:

PARAMETER	TURBINE-END	COMPRESSOR-END
Soft Pad Flexure Stiffness (lb/in.)	9,000	21,000
Bearing Radial Clearance at 45,000 rpm, 25,000 Feet Altitude and W = 12 lb (mils)	0.900	0.775
Loaded Pad Pivot Film Thickness at 157 lb Load (mils)	0.25	0.22
Loaded Pad Pivot Film Thickness at 12 lb Load (mils)	0.66	0.5
Minimum Frequency Ratio of Unloaded Pad	1.2	1.2
Minimum Frequency Ratio of Loaded Pad	1.75	1.75

*The reader is again reminded that the bearing design point is actually the 25,000-foot-altitude, engine-idle condition. All data in the following tabulation pertains to this condition.

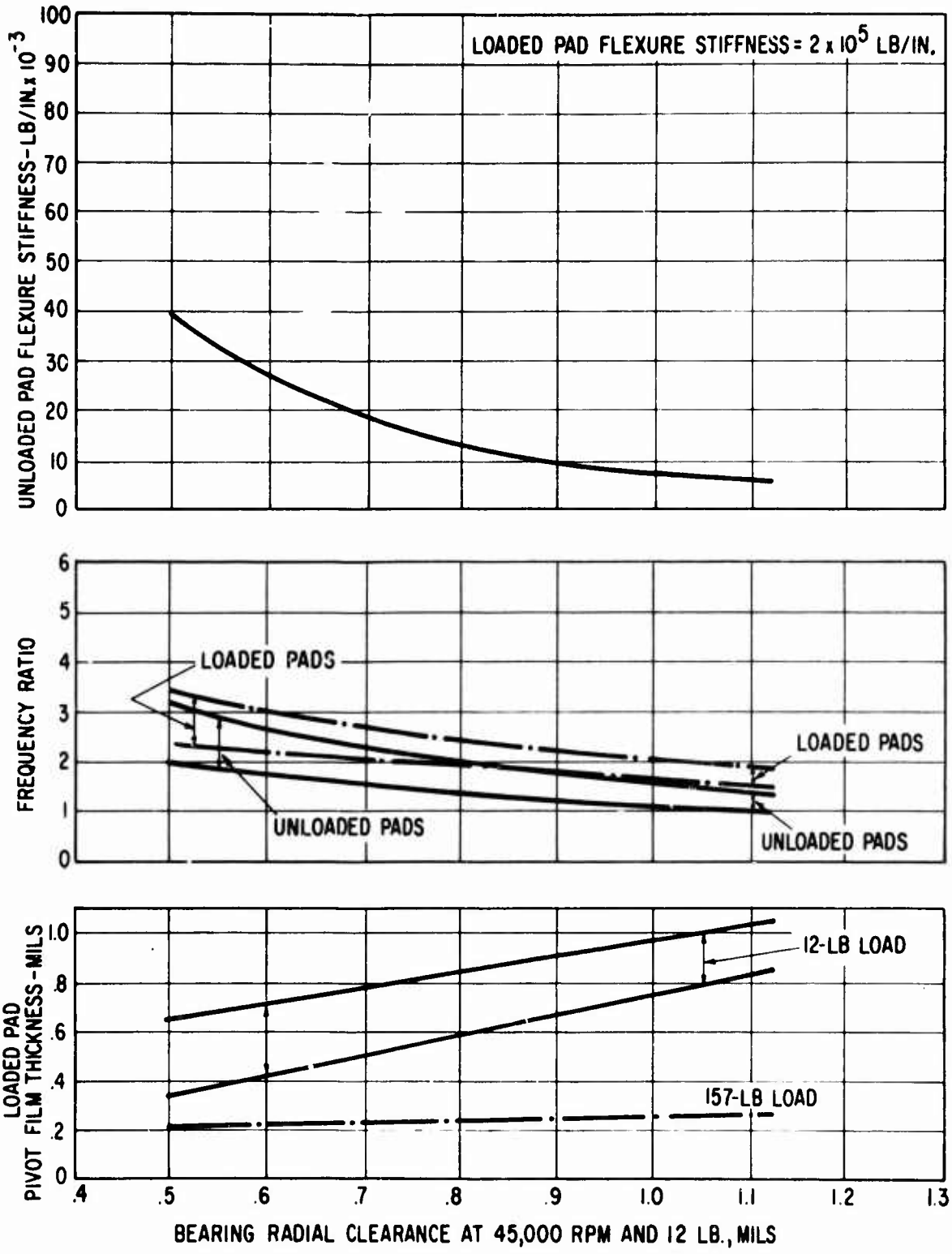


Figure 75. Turbine-End Bearing Non-Isothermal Performance as a Function of Bearing Clearance at 45,000 rpm and 25,000 Feet Altitude. (Unloaded Pad Flexure Stiffness Indicated Dictates Zero Speed Setup Clearance of Zero.)

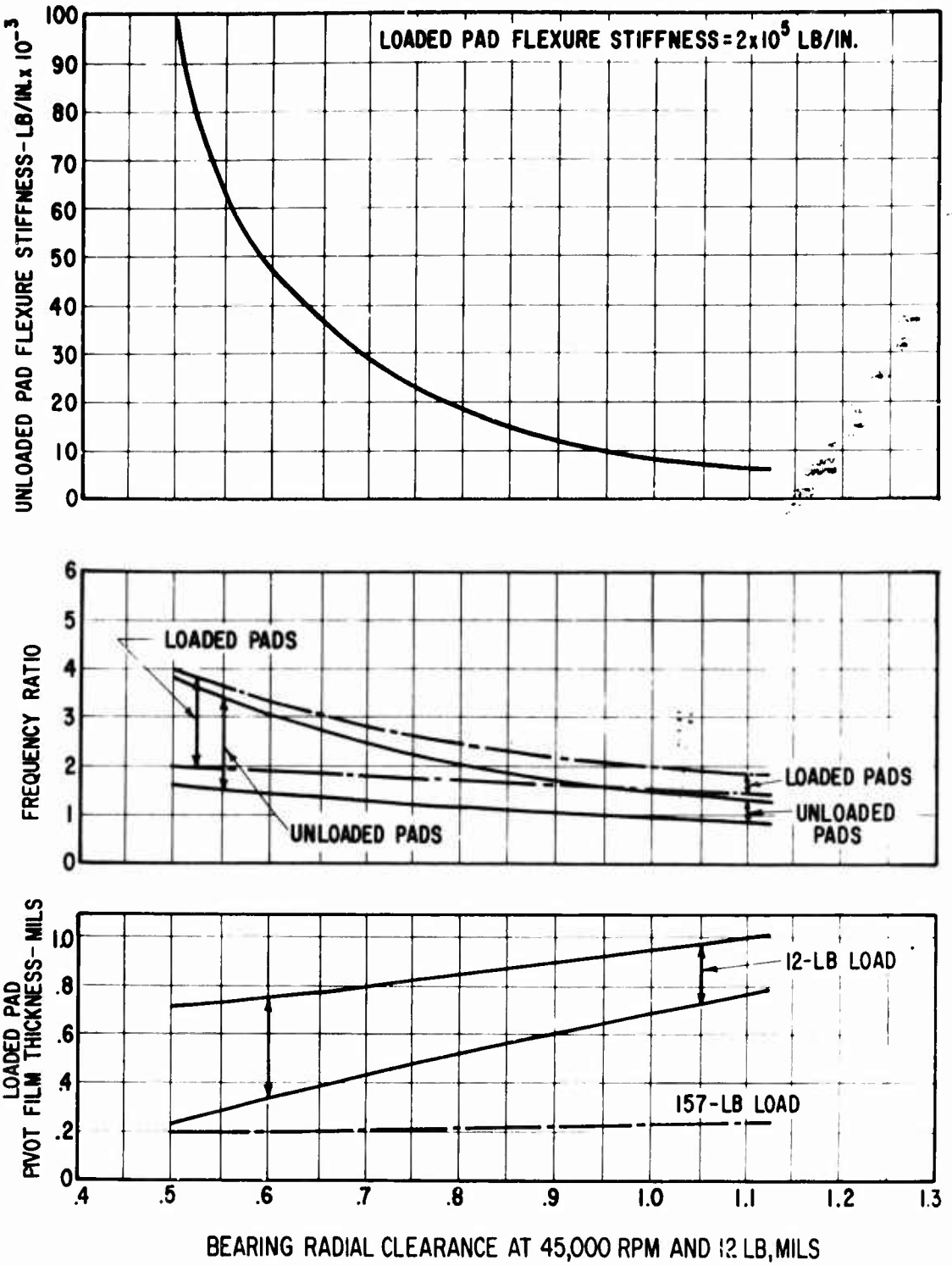


Figure 76. Compressor-End Bearing Non-Isothermal Performance as a Function of Bearing Clearance at 45,000 rpm and 25,000 Feet Altitude. (Unloaded Pad Flexure Stiffness Indicated Dictates Zero Speed Setup Clearance of Zero.)

A summary of pertinent geometric data follows. A schematic of the three-pad bearing design concept is shown in Figure 77.

TURBINE BEARING	COMPRESSOR BEARING
K_{fu} = 9,000 lb/in.	K_{fu} = 21,000 lb/in.
K_{fl} = 200,000 lb/in.	K_{fl} = 200,000 lb/in.
Machined Journal Diameter = 2.2438 in.	Machined Journal Diameter = 2.2475 in.
Pad Machined Clearance = 0.002856 in.	Pad Machined Clearance = 0.002358 in.
Radius to Pivot at Setup = 1.4338 in.	Radius to Pivot at Setup = 1.4355 in.

When assembling the journal bearings at an ambient temperature of 80°F, each of the pads should (theoretically) just contact the shaft without causing deflection of the soft flexures.

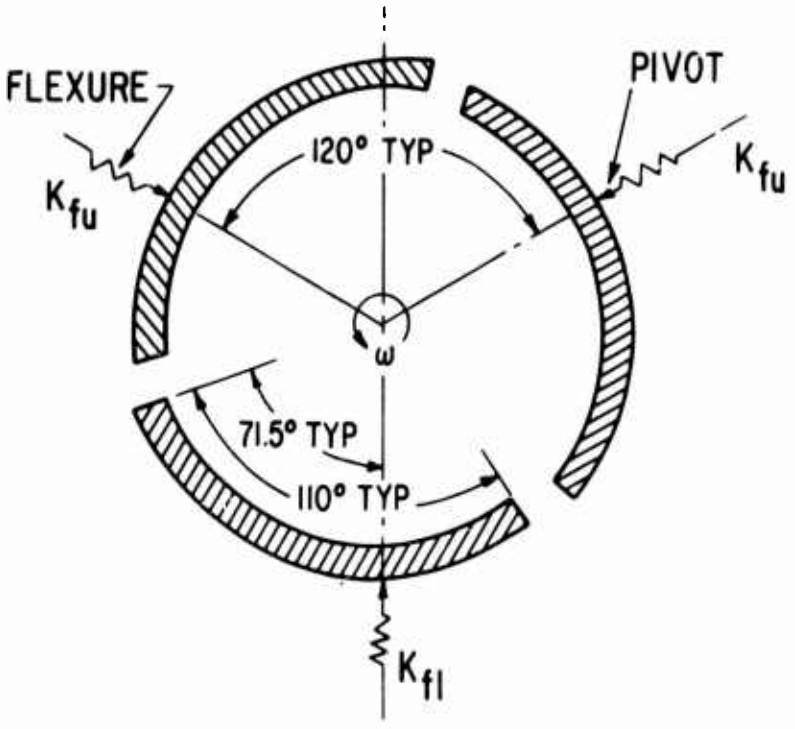
Performance of a Nondistorted Journal Bearing at Various Speeds (Engine Power Output) and Altitudes

This section presents performance charts of the turbine-end and compressor-end bearings at speeds corresponding to idle through 100-percent power to 20-percent overspeed. Operation at both sea level and 25,000 feet is covered. The performance data given in Figures 78-85 include bearing friction loss, bearing stiffness, pivot film thickness of the loaded and unloaded pads, and the lowest frequency ratio (corresponds to the pitch mode) of the loaded and unloaded pads.

In general, the compressor-end bearing has approximately 10-percent less bearing friction loss and a bearing stiffness approximately equal to the turbine-end bearing. There is little difference in bearing friction loss and bearing stiffness when comparing sea-level and 25,000-foot performance data. However, the bearing friction loss is increased by approximately 33 percent and the bearing stiffness is essentially doubled as the engine changes from steady-state operation to a maximum maneuver load situation. Bearing friction loss increases with the speed squared, but there is little variation in bearing stiffness with speed. At the journal bearing design-point of 25,000 feet altitude, engine idle, and a 12-pound steady-state load, the turbine-end bearing has a friction loss of 0.258 horsepower and a stiffness of 60,000 lb/in.; the compressor-end bearing under the same conditions has a friction loss of 0.242 horsepower and a stiffness of 72,000 lb/in.

Turbine-End Bearing

Under all conditions, the pivotal film thickness of the nondistorted unloaded pads is larger than 0.9 mil. Under a 12-pound steady-state load, the pivotal film thickness of the loaded pad is larger than 0.75 mil. As shown in Figures 8 and 9, this allows sufficient margin for non-isothermal operating effects. Under the maximum maneuver load condition, the pivotal



JOURNAL NOMINAL DIAMETER = 2.25 IN.
BEARING LENGTH-TO-DIAMETER RATIO = 1
PAD CLEARANCE RATIO = 2 MIL/IN. AT DESIGN POINT
PIVOT RATIO = 0.65
PAD AVERAGE THICKNESS = 0.15 IN.
PAD WEIGHT = 0.22 LB
PAD THICKNESS AT PIVOT = 0.312 IN.
RADIUS TO PIVOT = 1.437 IN.
PAD MOMENTS OF INERTIA:
PITCH DIRECTION = 0.151 LB-IN.^{2}
ROLL DIRECTION = 0.150 LB-IN.^{2}
YAW DIRECTION = 0.186 LB-IN.^{2}

Figure 77. Three-Pad Bearing Schematic and Geometric Data.

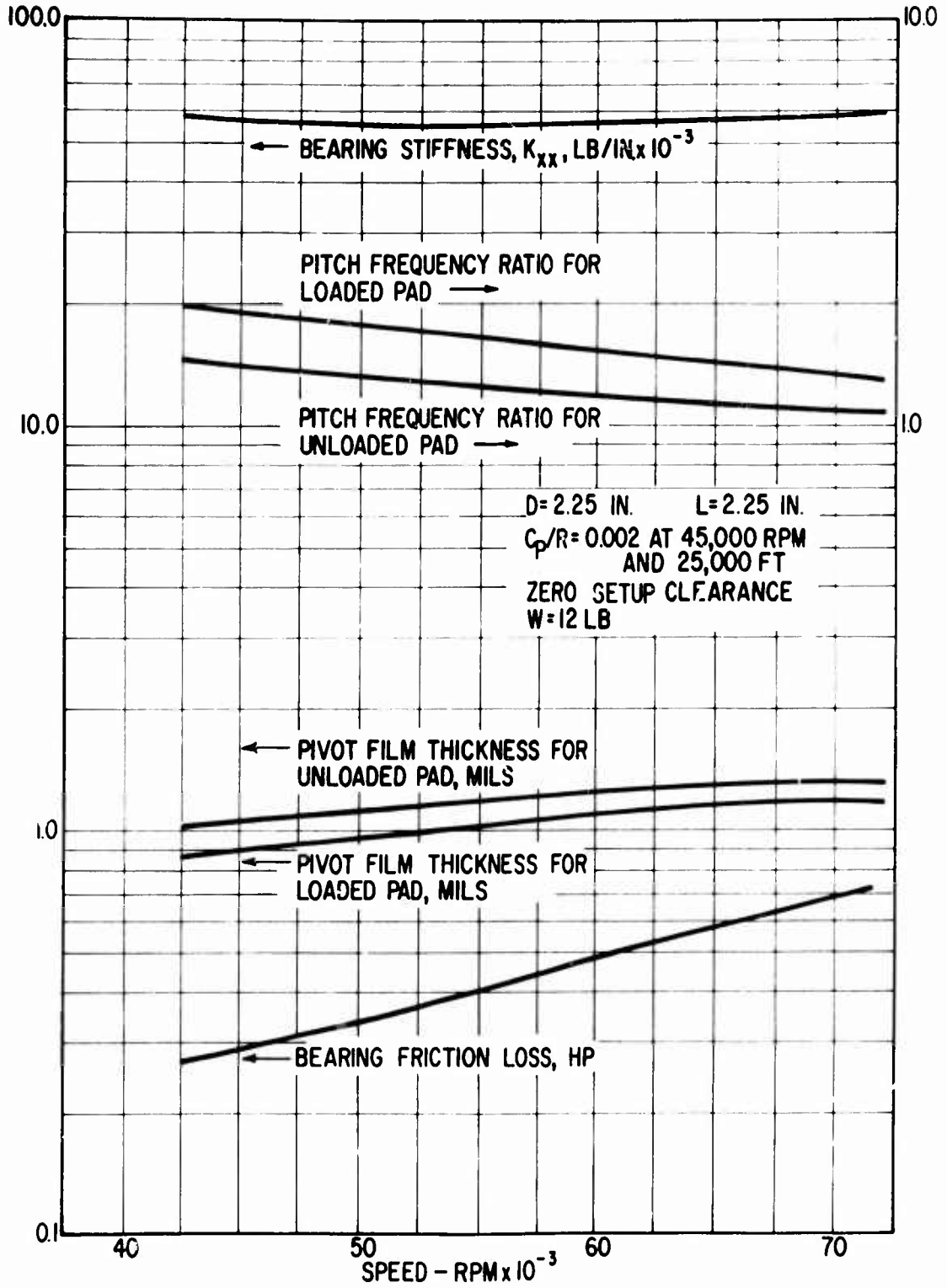


Figure 78. Performance of Turbine-End Pivoted-Pad Journal Bearing at Sea Level Under Isothermal Temperatures and Normal Load Conditions.

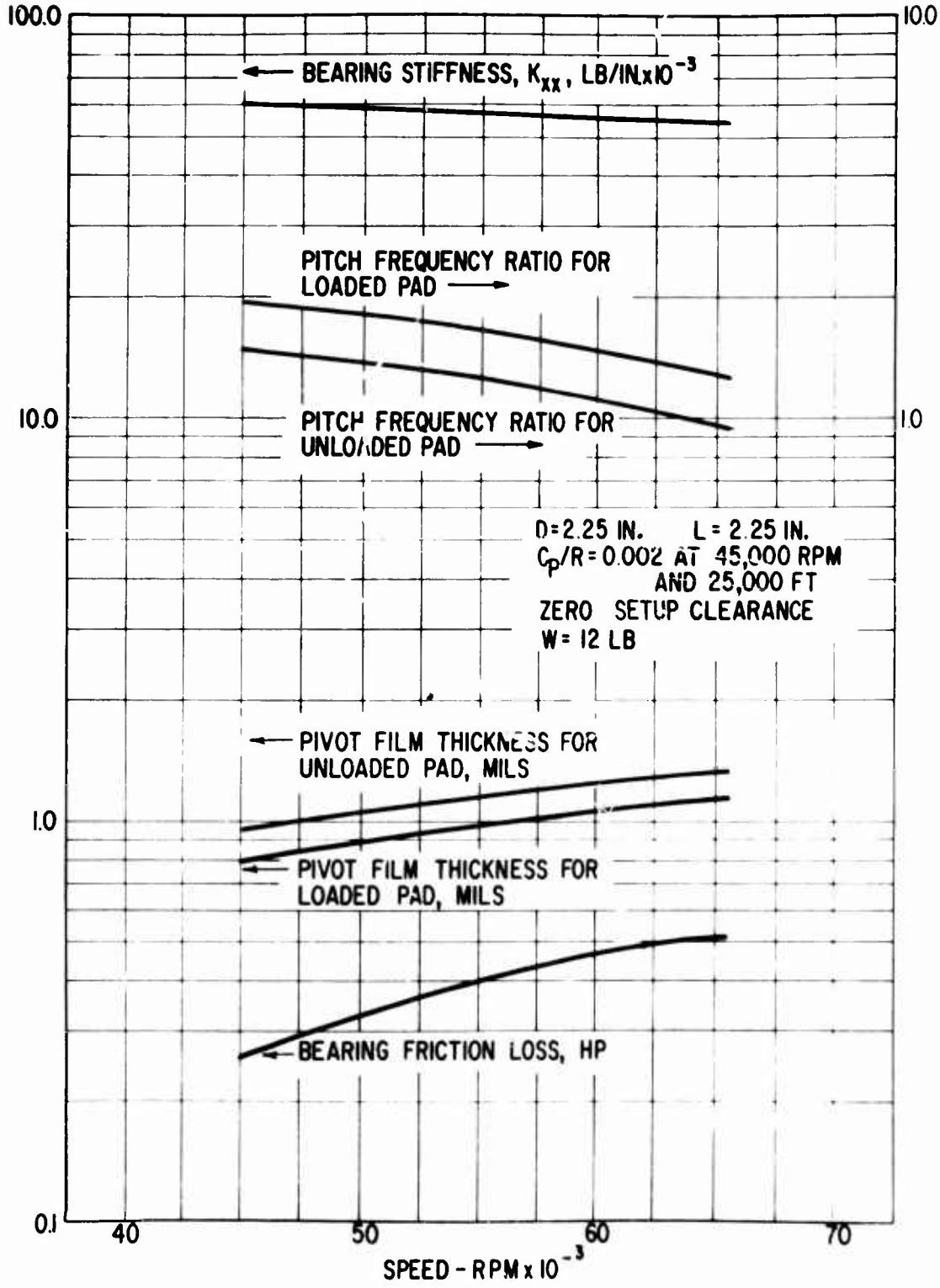


Figure 79. Performance of Turbine-End Pivoted-Pad Journal Bearing at 25,000 Feet Under Isothermal Temperatures and Normal Load Conditions.

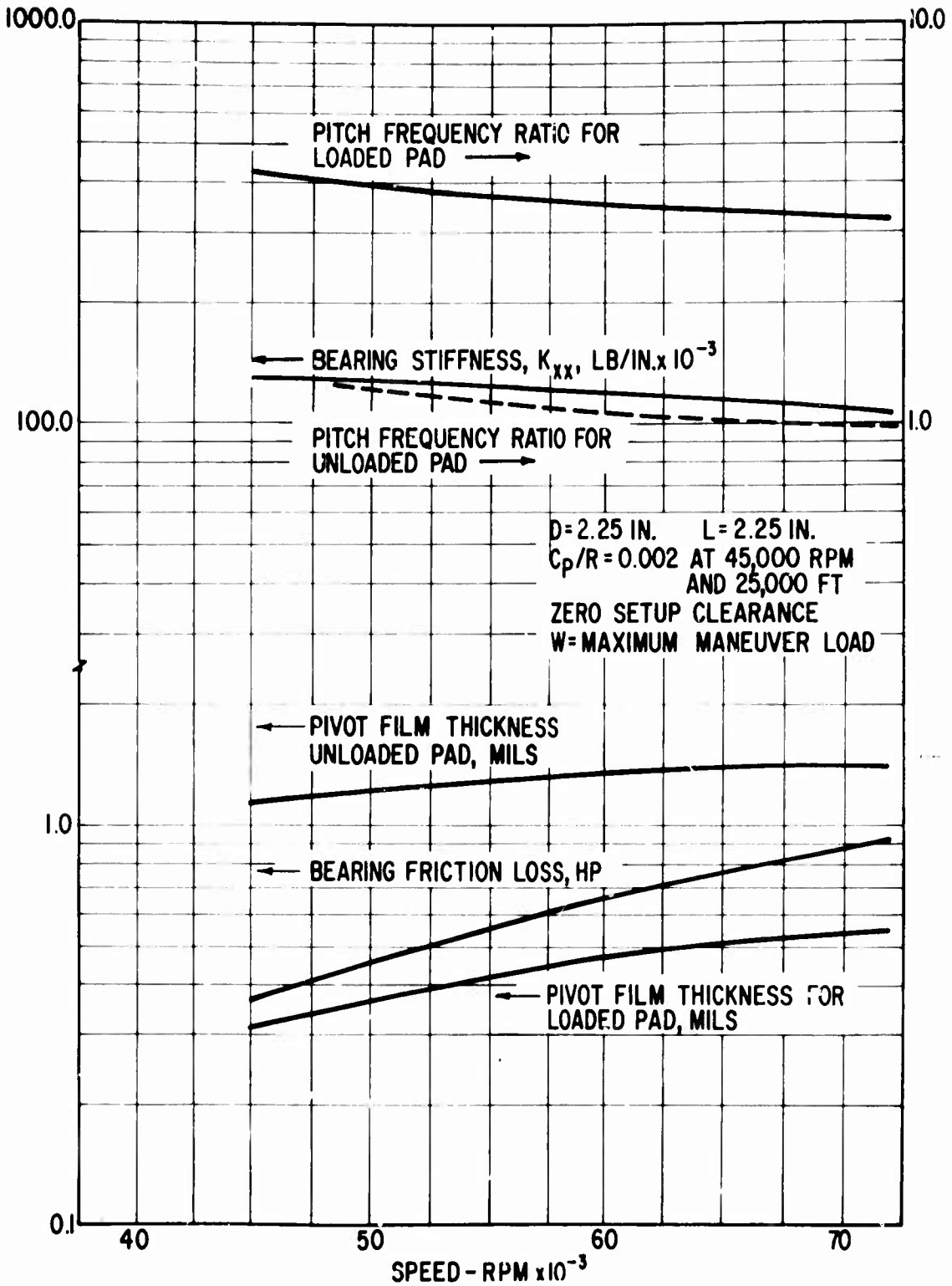


Figure 80. Performance of Turbine-End Pivoted-Pad Journal Bearing at Sea Level Under Isothermal Temperatures and Maximum Load Conditions.

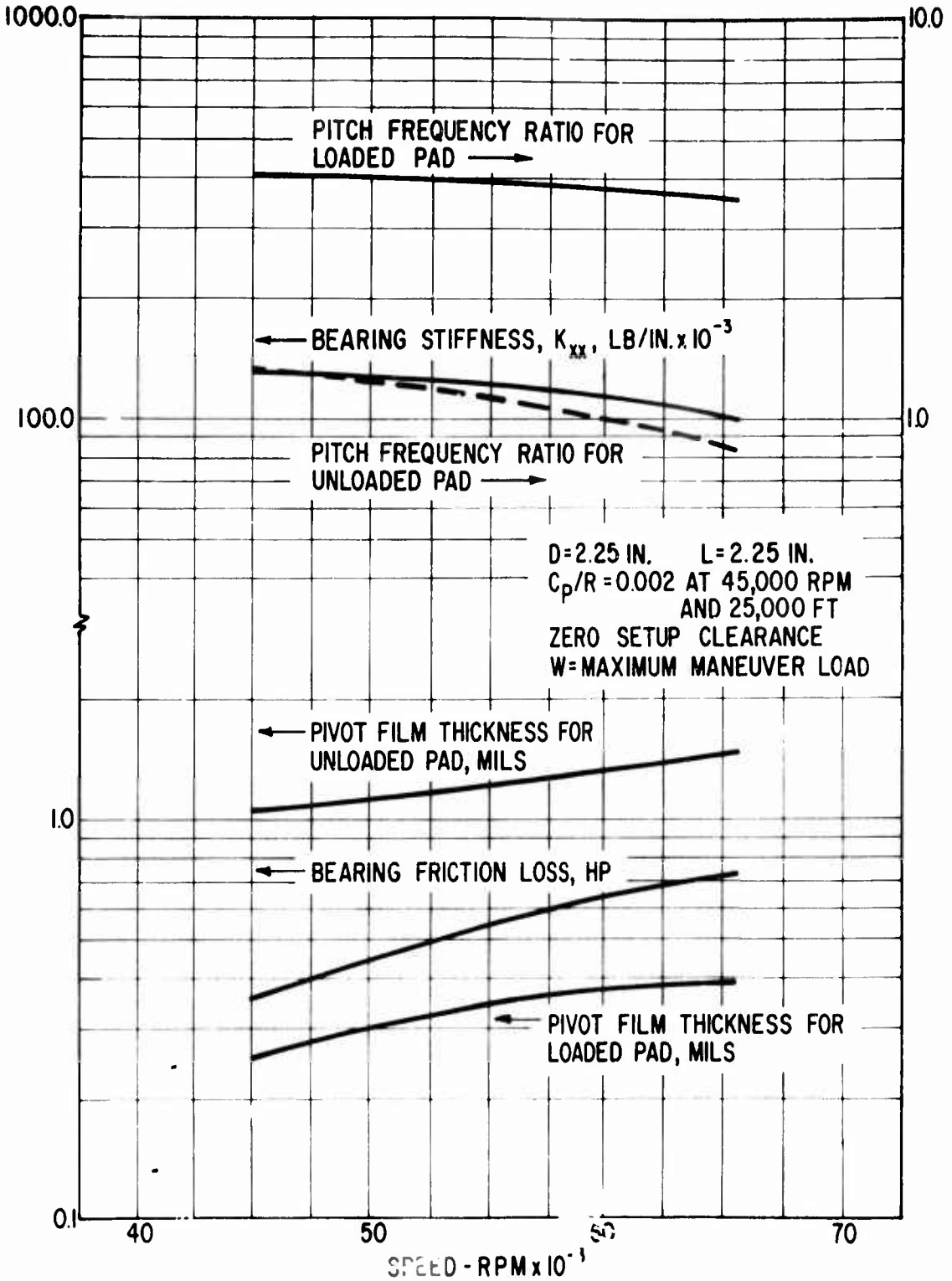


Figure 81. Performance of Turbine-End Pivoted-Pad Journal Bearing at 25,000 Feet Under Isothermal Temperatures and Maximum Load Conditions.

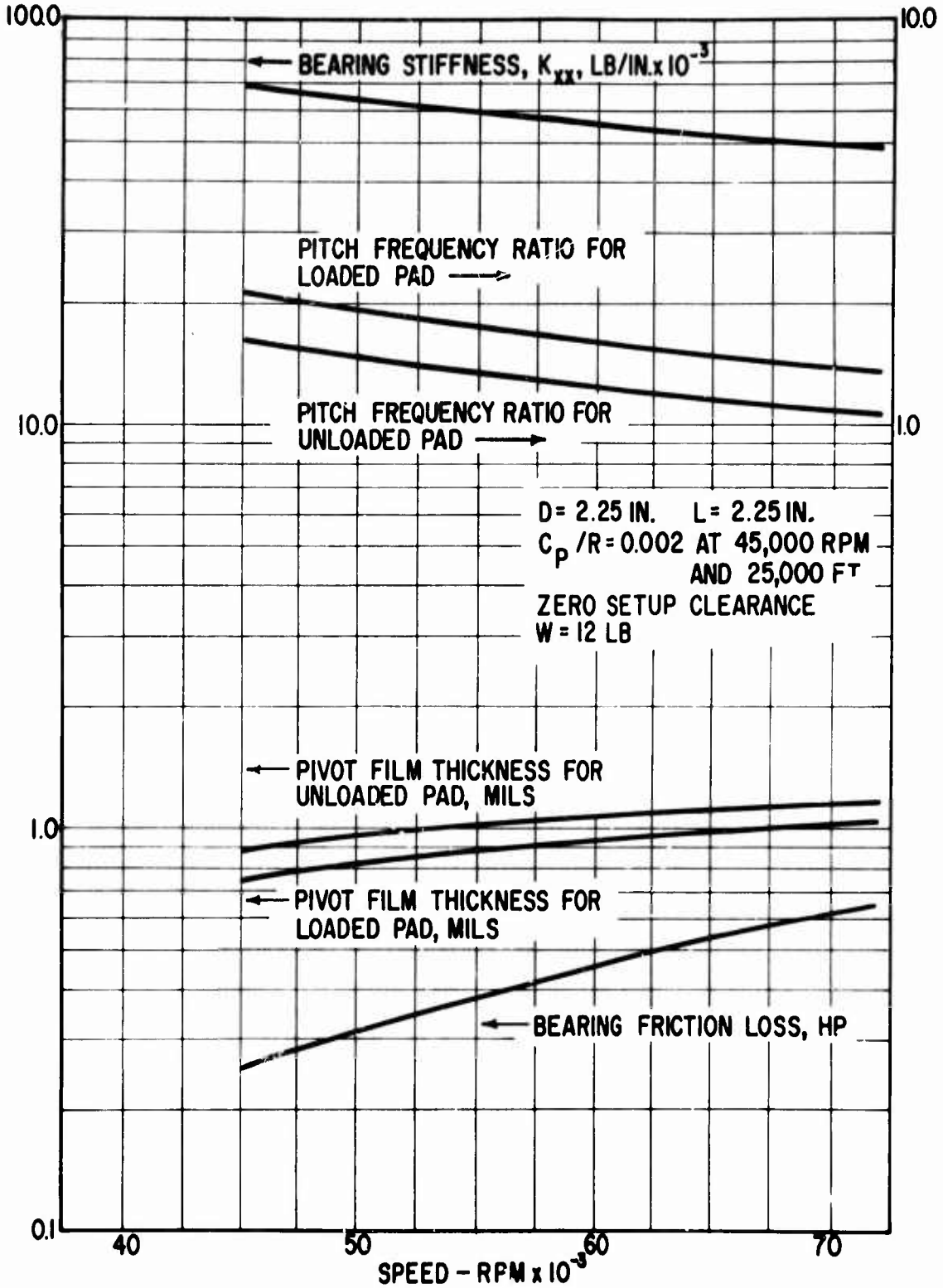
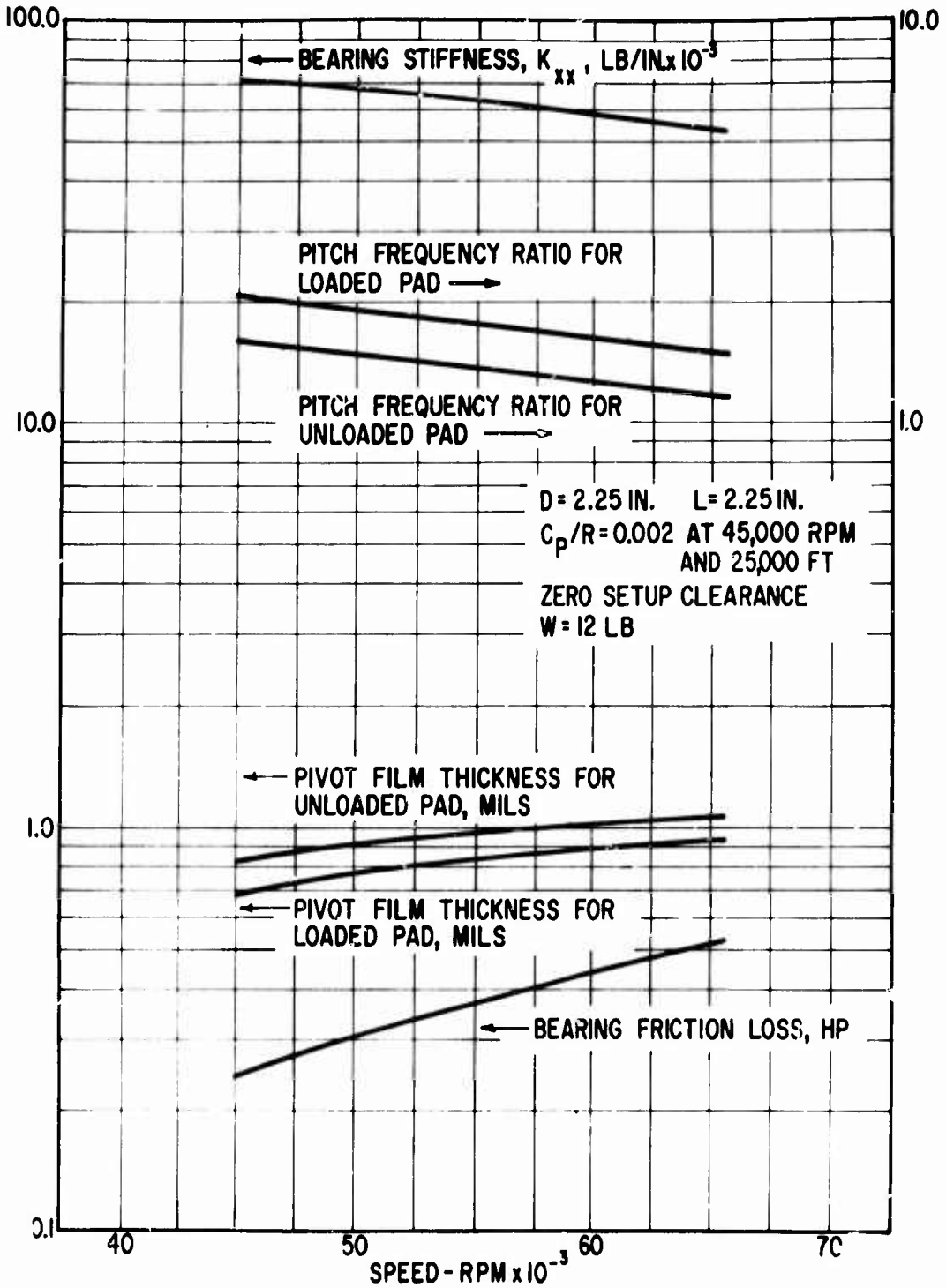


Figure 82. Performance of Compressor-End Pivoted-Pad Journal Bearing at Sea Level Under Isothermal Temperatures and Normal Load Conditions.



CALCULATED PERFORMANCE OF COMPRESSOR-END JOURNAL BEARING AT 25,000-FEET ALTITUDE AND NORMAL LOAD CONDITIONS (NONDISTORTED BEARING GEOMETRY)

Figure 83. Performance of Compressor-End Pivoted-Pad Journal Bearing 25,000 Feet Under Isothermal Temperatures and Normal Load Conditions.

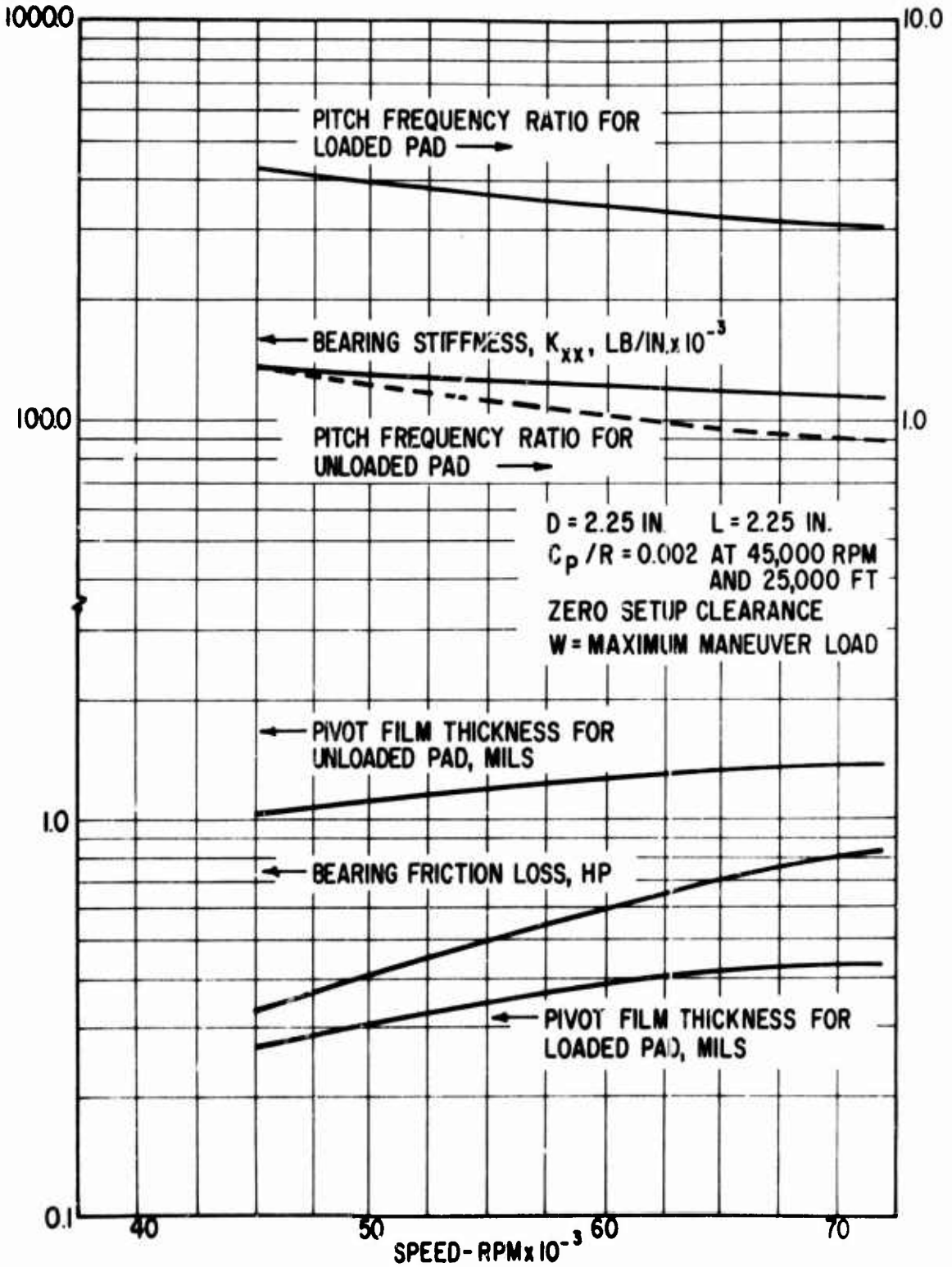
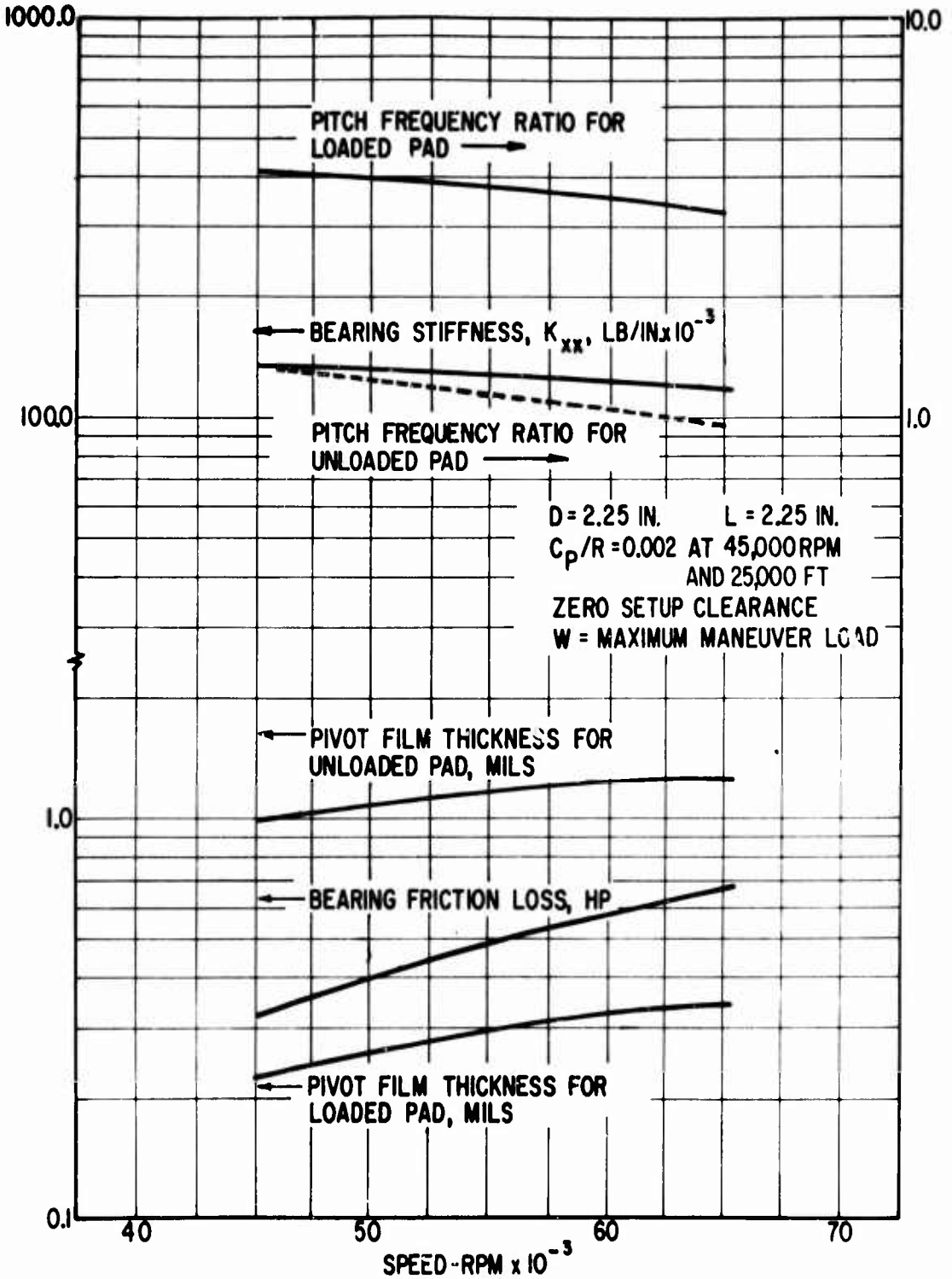


Figure 84. Performance of Compressor-End Pivoted-Pad Journal Bearing at Sea Level Under Isothermal Temperatures and Maximum Load Conditions.



CALCULATED PERFORMANCE OF COMPRESSOR-END JOURNAL BEARING AT 25,000-FEET ALTITUDE AND MAXIMUM LOAD CONDITIONS (NONDISTORTED BEARING GEOMETRY)

Figure 85. Performance of Compressor-End Pivoted-Pad Journal Bearing at 25,000 Feet Under Isothermal Temperatures and Maximum Load Conditions.

film thickness of the nondistorted loaded pad is smallest at engine idle and 25,000 feet altitude, the value being 0.25 mil. At higher speeds and reduced altitudes, the pivotal film thickness of the loaded pad increases above 0.3 mil.

The pitching frequency of the loaded pad in the maximum maneuver loading condition is well above the operating speed. Under the steady-state 12-pound load, the loaded-pad pitching frequency is at a minimum of 50 percent above the running speed up to a speed corresponding to 100-percent engine power output. This provides for some margin when non-isothermal operation will probably result in frequency ratios less than unity for the loaded pad. It is further apparent that under normal conditions of running speed, steady-state loading, and isothermal operation, the natural frequency of the unloaded pad in the pitching mode is above the running speed. However, any condition of either overspeed running, maximum maneuver loading on the loaded pad (relieving the preload on the unloaded pads), or non-isothermal operation could bring the unloaded pads into a resonant condition. Experience gained in MTI's turbomachinery developments to date have indicated that this condition, while not theoretically desirable, is a tolerable situation. Significant pad resonances have never been observed in those instances where operation has theoretically been coincident with the pad resonant frequency. These resonances can, in some respects, be likened to rigid-body rotor resonances where the energy is low and sufficient fluid film damping is available to attenuate the amplitude.

Compressor-End Bearing

In general, the comments made above for the turbine-end bearing also apply here.

Specifically, under all conditions of operation, the pivotal film thickness of the nondistorted, unloaded pad is larger than 0.8 mil. Under the 12-pound steady-state load, the pivotal film thickness of the loaded pad has its smallest value of 0.68 mil. As shown in Figures 12 and 13, this provides sufficient margin for non-isothermal operating effects. Under the maximum maneuver load condition, the pivotal film thickness of the nondistorted loaded pad is smallest at engine idle and 25,000 feet altitude, the value being 0.22 mil. At higher speeds and reduced altitudes, the pivotal film thickness increases above 0.3 mil.

The pitching frequency of the compressor-end loaded pad in the maximum maneuver loading condition is well above the operating speed. Under the steady-state 12-pound load, the loaded-pad pitching frequency is at a minimum of 60 percent above the running speed, up to a speed corresponding to 100-percent engine power output. This provides for some margin when non-isothermal operating conditions prevail. When running at 20-percent overspeed, with a load of 12 pounds, non-isothermal operation will probably result in frequency ratios less than unity for the loaded pad. As in the case of the turbine-end bearing, discussed above, under normal conditions of running speed, steady-state loading, and isothermal operation, the natural frequency of the unloaded pad in the pitching mode is above the running speed. For this bearing, a combination of overspeed running with

either non-isothermal operation or maximum maneuver loading could cause a resonant condition in the unloaded pads. As previously stated, this condition is not considered to be a problem.

JOURNAL BEARING THERMAL STUDIES

The success or failure of a particular method of bearing cooling is determined by three principal factors. First, the thermal gradients produced within a bearing must be such that they do not cause excessive distortion of the bearing surfaces. Second, the operating temperature level of the bearing must be compatible with the strength and corrosion capabilities of the bearing materials. Third, the temperature level of the bearing should be such as to minimize thermal stresses between the bearing and its adjacent components.

Compressor Bearing - Cooling Concepts and Design

Initially, consideration was given to cooling the bearing by passing the cooling air discharged from the thrust bearing heat exchanger through the bore of the compressor-end journal bearing. Cooling the bearing in this manner will cause the heat flow from the source (bearing gas film) to be predominantly in the radial direction, thereby keeping axial temperature gradients to a minimum.

To evaluate this method of cooling, an arbitrary heat transfer surface area was assigned to a computer model in a distributed pattern. By varying the heat transfer coefficient assigned to this surface, it is possible to generate a family of axial temperature profiles which can be evaluated for acceptability in terms of bearing performance. The results of this study are shown in Figure 86. It can be seen that even in the best case (h = 10,000 Btu/hr-ft^2-$^\circ$F), the axial temperature gradient at the right end of the bearing is rather steep. This gradient is caused by the presence of the compressor wheel heat sink which promotes an axial flow of heat out of the bearing. One way to eliminate this undesirable characteristic is to make axial heat flow more difficult than radial heat flow by use of a heat dam or similar construction.

Another method of cooling is to flow the heat radially inward through the journal and axially along a shunt of high thermal conductivity to the vicinity of the compressor wheel hub. By doing this, it is possible to make use of the natural heat sink provided by the cool intake air. Figure 87 shows the axial temperature profile obtained with a shunt of high conductivity material, such as beryllium, k = Btu/hr-ft-$^\circ$F.

A comparison of the heat exchanger and shunt methods of cooling shows that the shunt is superior to the heat exchanger in several respects. The shunt makes use of a heat sink at a temperature of 60°F, whereas the heat exchanger has a sink temperature of 610°F, this being the temperature of the air after cooling the thrust bearing. Also, the shunt uses a natural heat sink, whereas the heat exchanger must make use of parasitic cooling-air flow. Furthermore, the shunt design should be easier to translate into hardware than the heat exchanger design.

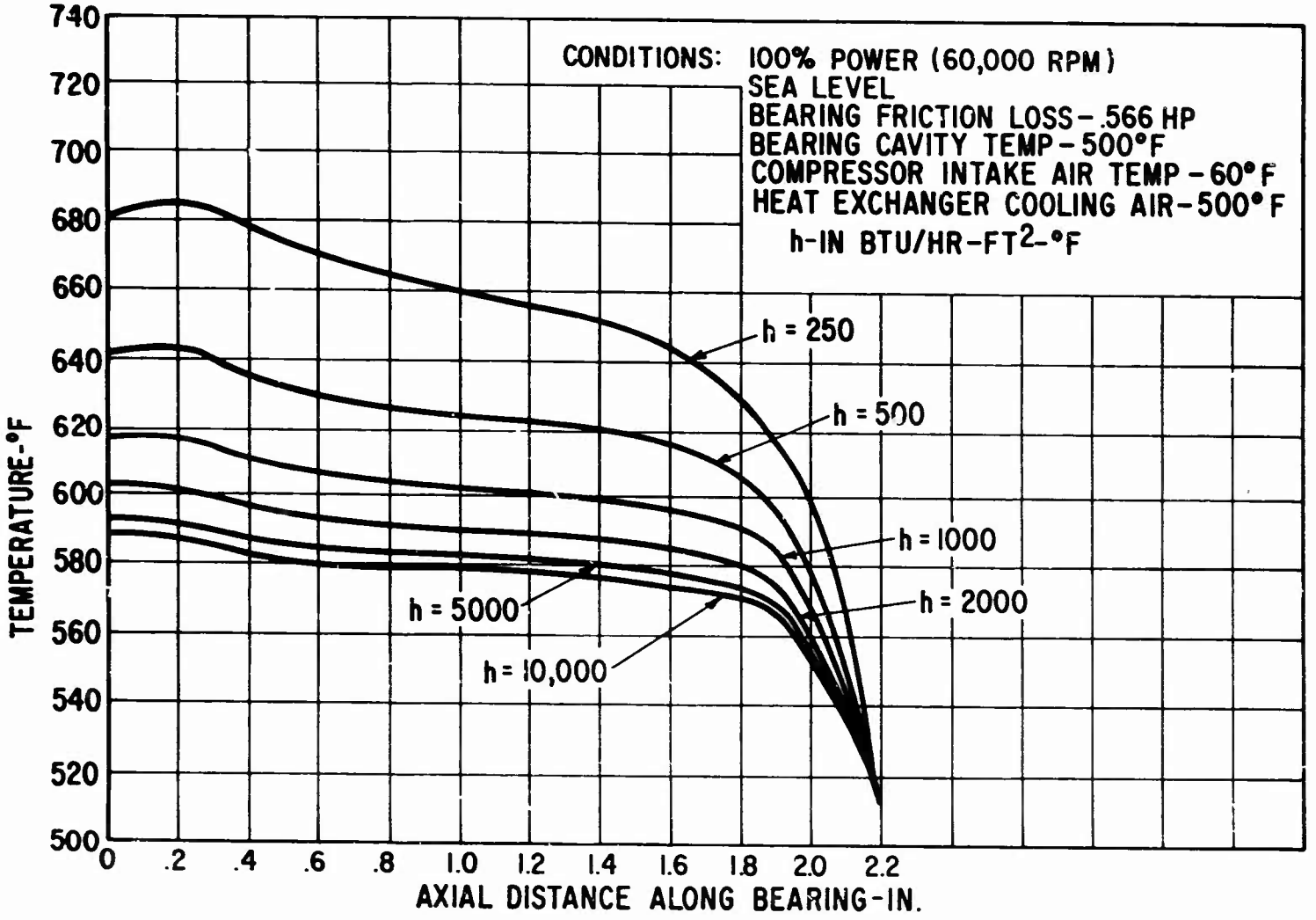


Figure 86. Variation of Axial Temperature Profile With Cooling Passage Heat Transfer Coefficient — Compressor-End Journal Bearing.

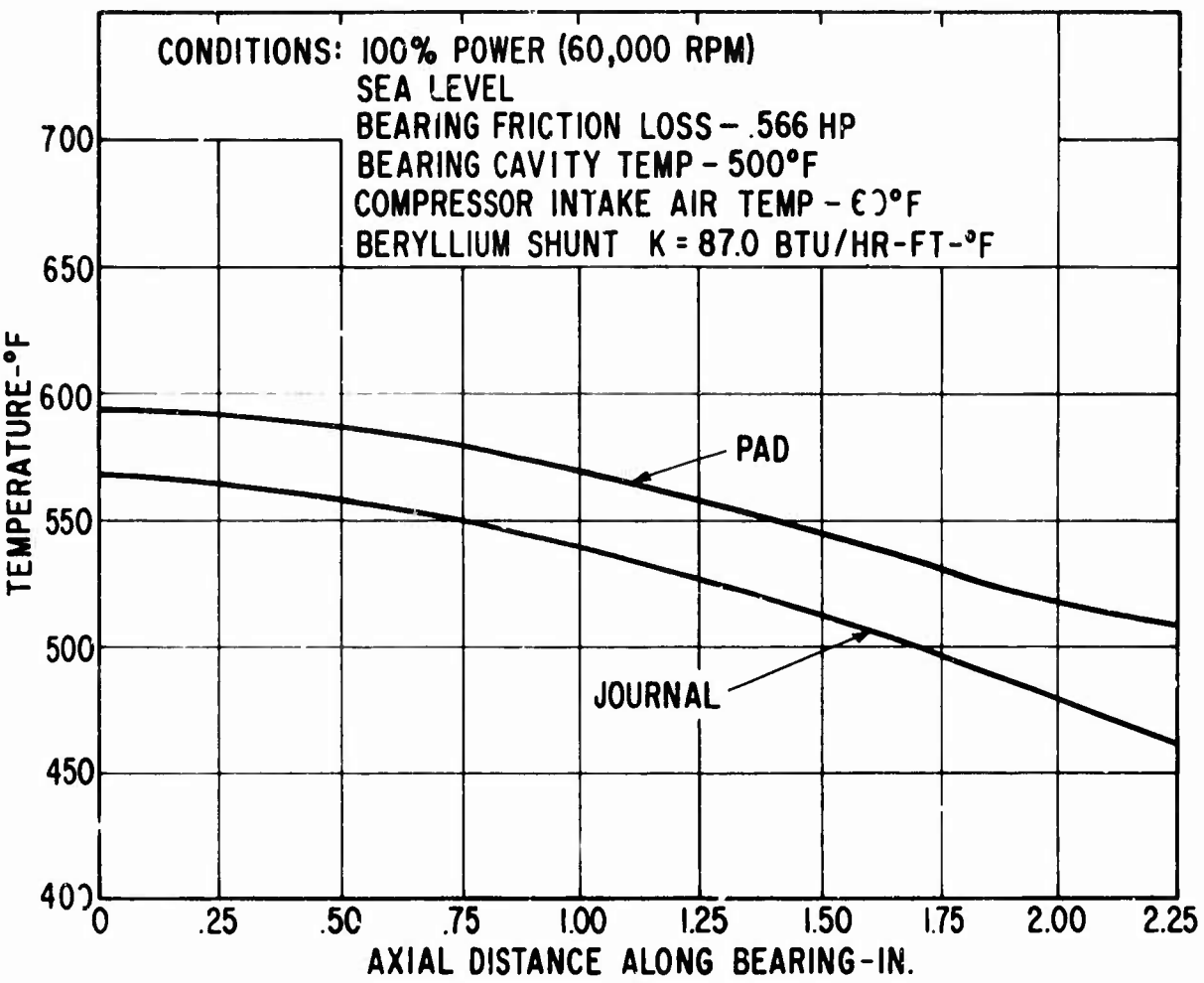


Figure 87. Axial Temperature Profile for Compressor-End Journal Bearing Using High-Conductivity Thermal Shunt to Compressor Wheel Hub.

A look at the heat-exchanger-produced temperature profile shows that the end gradients are very steep. This is caused by the large difference between the bearing mean temperature and the ambient temperature of the bearing cavity since the temperature of the exposed ends of the rotating shaft tend to follow the ambient temperature. The temperature profile achieved with the shunt is reasonably free of these end gradients because the mean bearing temperature is closer to that of the ambience. The lower operating temperature achieved with the shunt is more favorable from a standpoint of material strength and corrosion. Also, the temperature gradient between the bearing and the compressor wheel is less severe in the case of the shunt, thereby resulting in lower thermal stresses.

For these reasons, the shunt cooling method of the compressor end bearing was selected for further design evaluation.

Compressor-End Journal Thermal Model

The thermal model for the compressor-end journal bearing thermal study was chosen to include the bearing pads, the journal, the rotor tie-rod, and the first-stage compressor hub up to its juncture with the thrust bearing. Seventy-seven nodes were used to describe the model, which is shown in Figure 88. Of this total, 45 nodes were used to represent the pads and gas film. The remaining nodes were used to describe the cooling mechanism, the compressor hub and the interconnecting geometry.

The nodes representing the pads and the journal were constructed such that an accurate account of the bearing surface temperatures could be computed. Since the nodal temperature computed is the temperature at the node center, a thin layer of nodes was described for all bearing surfaces such that the computed temperatures would approach the surface temperatures.

The inner diameter of the model is considered to be insulated due to symmetry about the centerline. The pad outer surface transfers heat by natural convection to the ambience of the bearing cavity. This ambience is a constant temperature sink, which is assumed to be unaffected by the bearing heat load, and is supplied by cooled air from the second-stage compressor discharge in order to satisfy the ambient pressure level requirement of the bearing. All elements of the rotating shaft exposed to the bearing cavity ambience are considered to transfer journal bearing friction-generated heat by forced convection. The first-stage compressor wheel hub surface dissipates the journal bearing friction-generated heat to the engine-intake air by forced convection. The first-stage compressor wheel backface is washed by compressor leakage air, and heat transfer at this surface is also by forced convection. The interface between the first-stage compressor wheel hub and the thrust runner shaft is considered to be insulated.

Throughout this model, titanium, with a conductivity of 6.5 Btu/hr-ft-^{o}F, was taken to be the material from which bearing pads, journal, and first-stage compressor wheel would be fabricated.

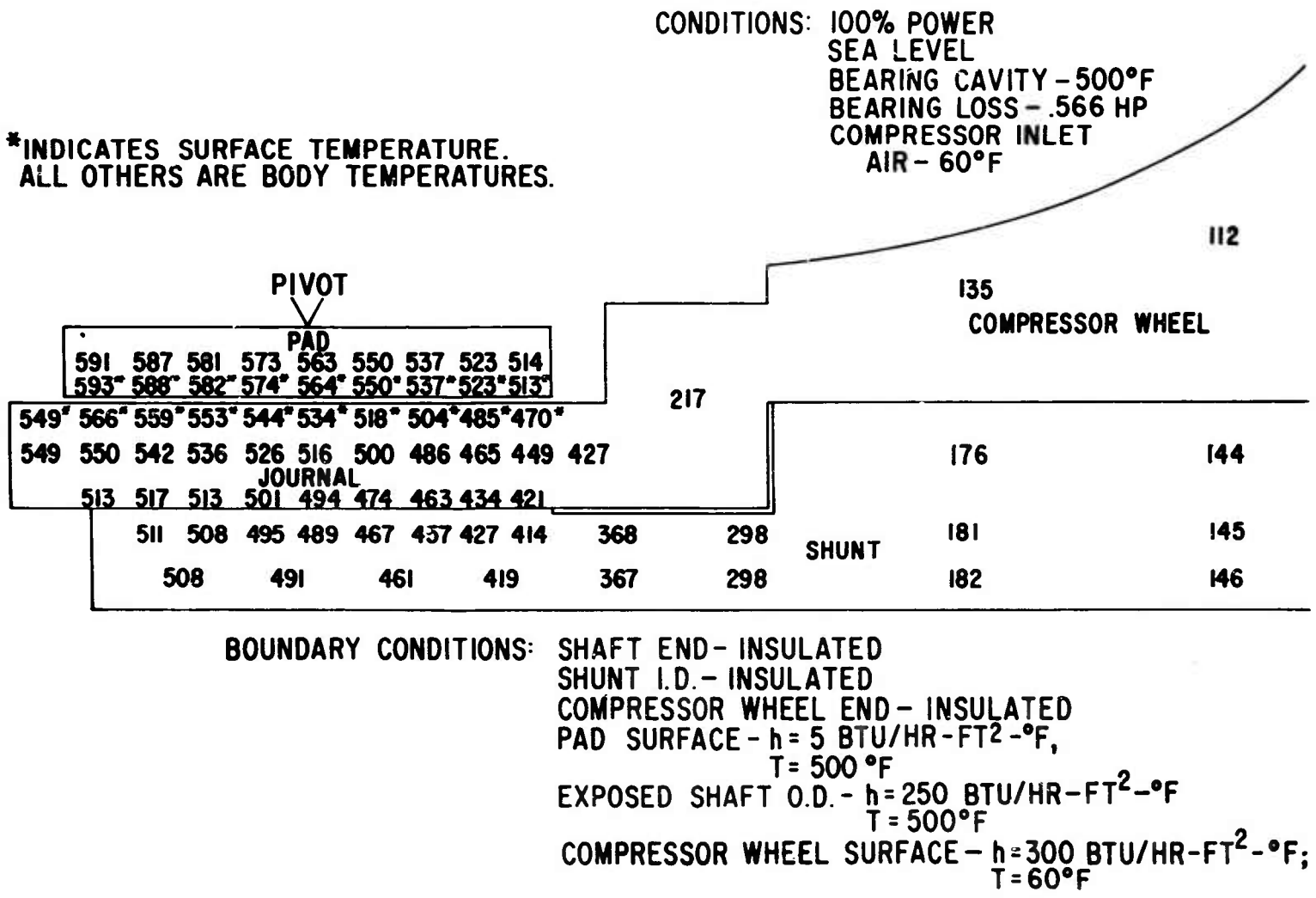


Figure 88. Thermal Model and Temperature Map (Sea Level, 100-Percent Power, and Maximum Maneuver Load) for the Compressor-End Journal Bearing.

Bearing Friction Losses

Calculations were made of bearing friction losses under maximum maneuver-load conditions for two limiting cases. The loss values used for the thermal calculations listed below are approximately equal for both the compressor- and turbine-end journal bearings.

Operating Condition	Friction Loss/Bearing - HP
Sea level - 100% power (60,000 rpm)	0.566
25,000 ft altitude - flight idle (45,000 rpm)	0.312

Calculated Results for a Shunt-Cooled Compressor-End Bearing

Temperatures for the shunt-cooled compressor-end bearing are shown in Figure 89. The engine operating conditions are sea-level flight at 100 percent power (60,000 rpm) under maximum maneuver bearing load. This figure also shows the corresponding bearing thermal distortion. Thermal input conditions for these calculations were as follows:

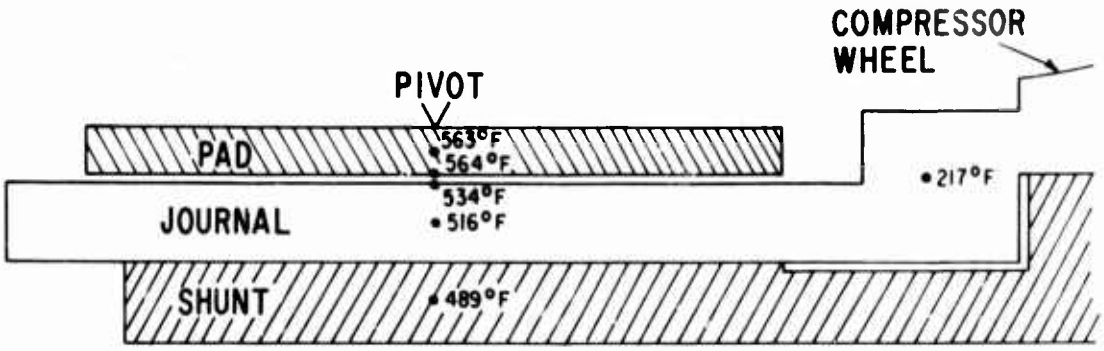
Bearing friction loss	0.566 hp
Boundary conditions for pad back	$h = 5$ Btu/hr-ft^2-$^\circ$F; $T = 500^\circ$F
Boundary conditions for exposed rotating parts	$h = 250$ Btu/hr-ft^2-$^\circ$F
Boundary condition for compressor wheel	$h = 360$ Btu/hr-ft^2-$^\circ$F
Shunt I.D.	insulated
Shaft left end	insulated
Compressor right end	insulated

Figure 90 shows the bearing thermal distortion for the condition at 25,000 feet altitude, flight idle (45,000 rpm) under maximum bearing load. The thermal input conditions for these calculations were as follows:

Bearing friction loss	0.312 hp
Boundary conditions for pad back	$h = 5$ Btu/hr-ft^2-$^\circ$F; $T = 250^\circ$F
Boundary conditions for exposed rotating elements	$h = 200$ Btu/hr-ft^2-$^\circ$F; $T = 250^\circ$F
Boundary conditions for compressor wheel	$h = 240$ Btu/hr-ft^2-$^\circ$F; $T = -30^\circ$F

CONDITIONS: 100% POWER (60,000 RPM)
SEA LEVEL
INTAKE AIR - 60°F
BEARING LOSS - .566 HP
CAVITY TEMP - 500°F

MATERIAL: PAD AND JOURNAL - TITANIUM
SHUNT - BERYLLIUM



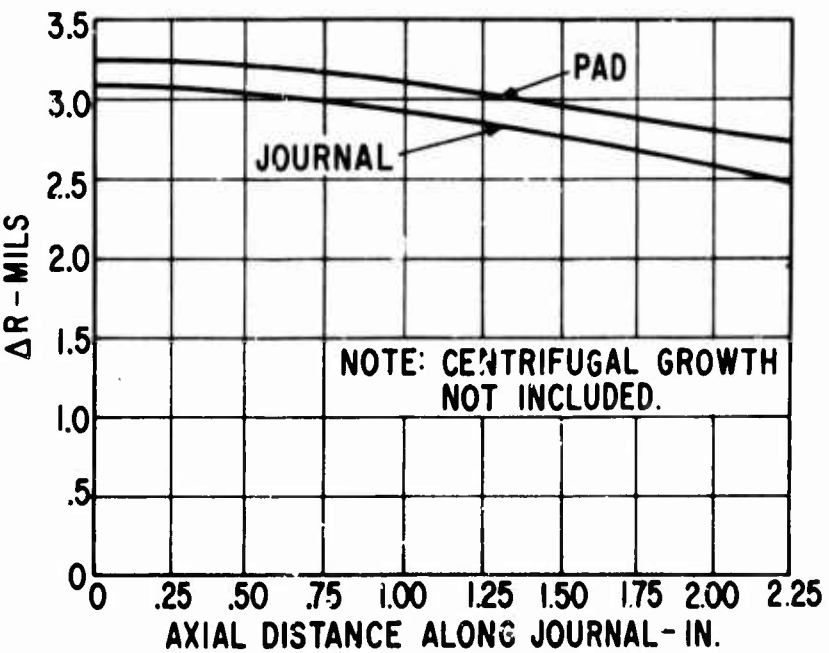
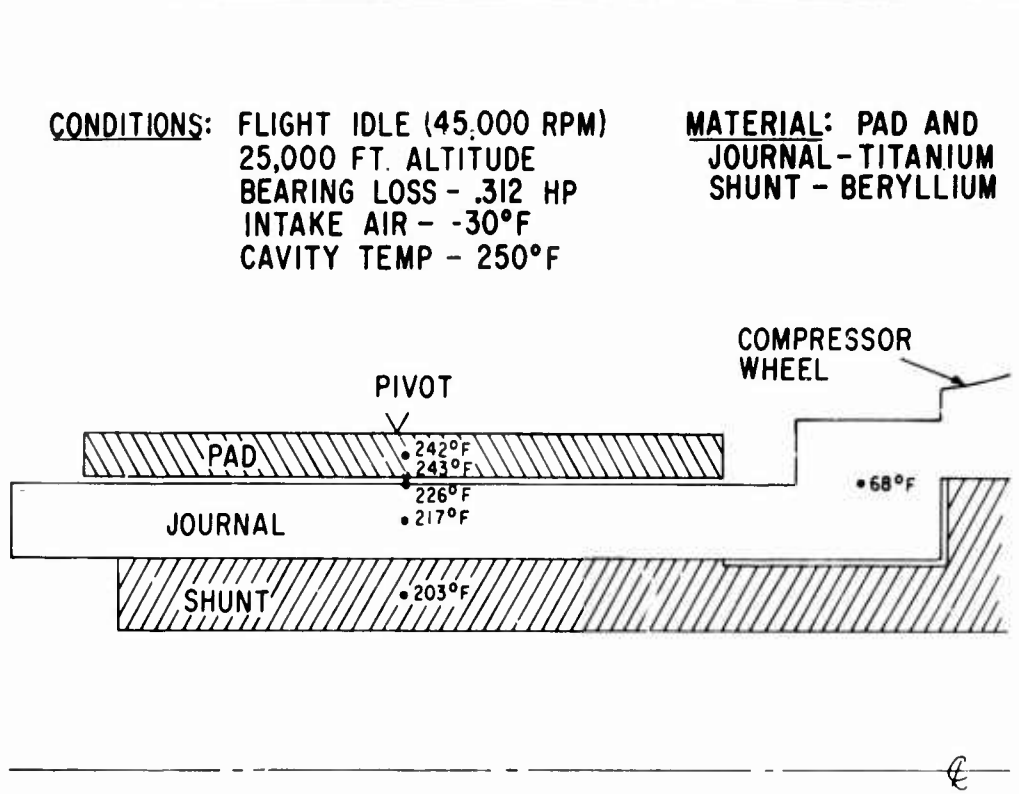
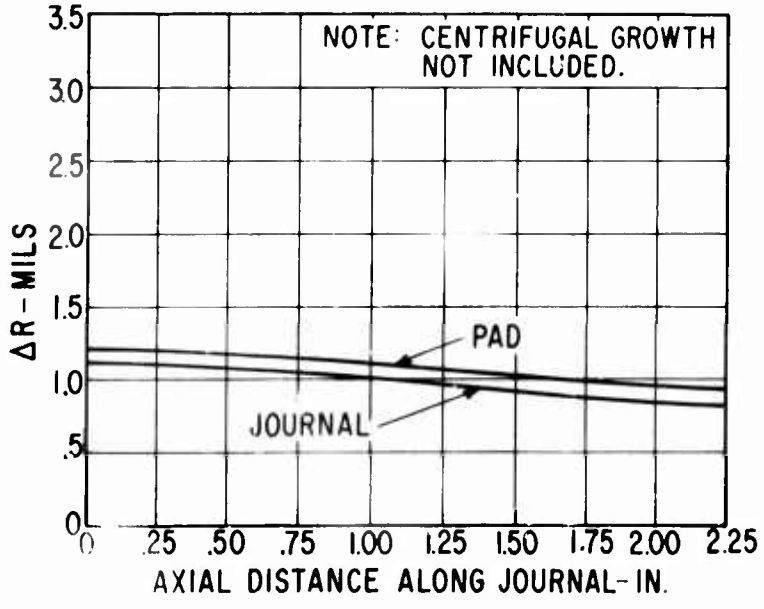


Figure 89. Thermal Distortion for the Compressor-End Journal Bearing at Sea Level, 100-Percent Power, and Maximum Maneuver Load Conditions.





PIVOT-PLANE TEMPERATURES AND THERMAL DISTORTION ALONG THE COMPRESSOR-END JOURNAL BEARING UNDER MAXIMUM MANEUVER LOAD CANDITIONS

Figure 90. Thermal Distortion for the Compressor-End Journal Bearing at 25,000 Feet Altitude, Flight Idle, and Maximum Maneuver Load Conditions.

Shunt I.D.	insulated
Shaft left end	insulated
Compressor right end	insulated

Since, under the maximum maneuver conditions, the film thickness is smallest, creating the maximum heat generation to be dissipated, these cases represent the extreme in bearing distortions.

The engine conditions of sea level at 100-percent power, and 25,000 feet altitude at flight idle are considered to result in the limiting steady-state thermal conditions. All other steady-state conditions are expected to give results (distortions and temperatures) bracketed by these limiting conditions. Examination of Figures 89 and 90 shows that the maximum crowning distortion (axial profile) will vary between approximately .1 mil and .05 mil. Both of these crowning distortion levels are less than the minimum bearing film thickness, which is in excess of .2 mil. More important, however, is the fact that in both cases the pad axial profile conforms very closely with the journal axial profile. Therefore, only minor effects on actual bearing film thickness are anticipated under conditions of distorted bearing operation.

Turbine Bearing-Cooling Concept and Design

Since no natural heat sink is available in the vicinity of the turbine-end journal bearing, the concept of a thermal shunt could not be used. The effort here, therefore, was to investigate the possibility of cooling by air and the design of an air heat exchanger. As before, the approach is to cool the bearing from the journal bore such that the heat flow is radially inward, thereby minimizing bearing distortion.

A heat exchanger of arbitrary surface area was initially described in a thermal model to determine the approximate magnitude of heat transfer coefficient necessary to cool the bearing. The coefficient assigned to the surface was varied over the range considered available.

Figure 91 shows the set of curves generated by varying the cooling flow heat transfer coefficient. The curves representing the higher cooling rates are concave upward, indicating too much cooling with respect to the other boundary conditions specified (in this case the turbine wheel to the left of the bearing). In particular, the exposed shaft ends tend to assume the temperature of the bearing cavity ambience, and any cooling of the bearing below the bearing cavity ambience produces a rather severe temperature gradient at the bearing ends. Therefore, either the bearing cavity ambience temperature should be lowered to a level compatible with the amount of cooling provided, or the amount of cooling should be lessened to provide internal bearing temperatures compatible with the bearing cavity ambience.

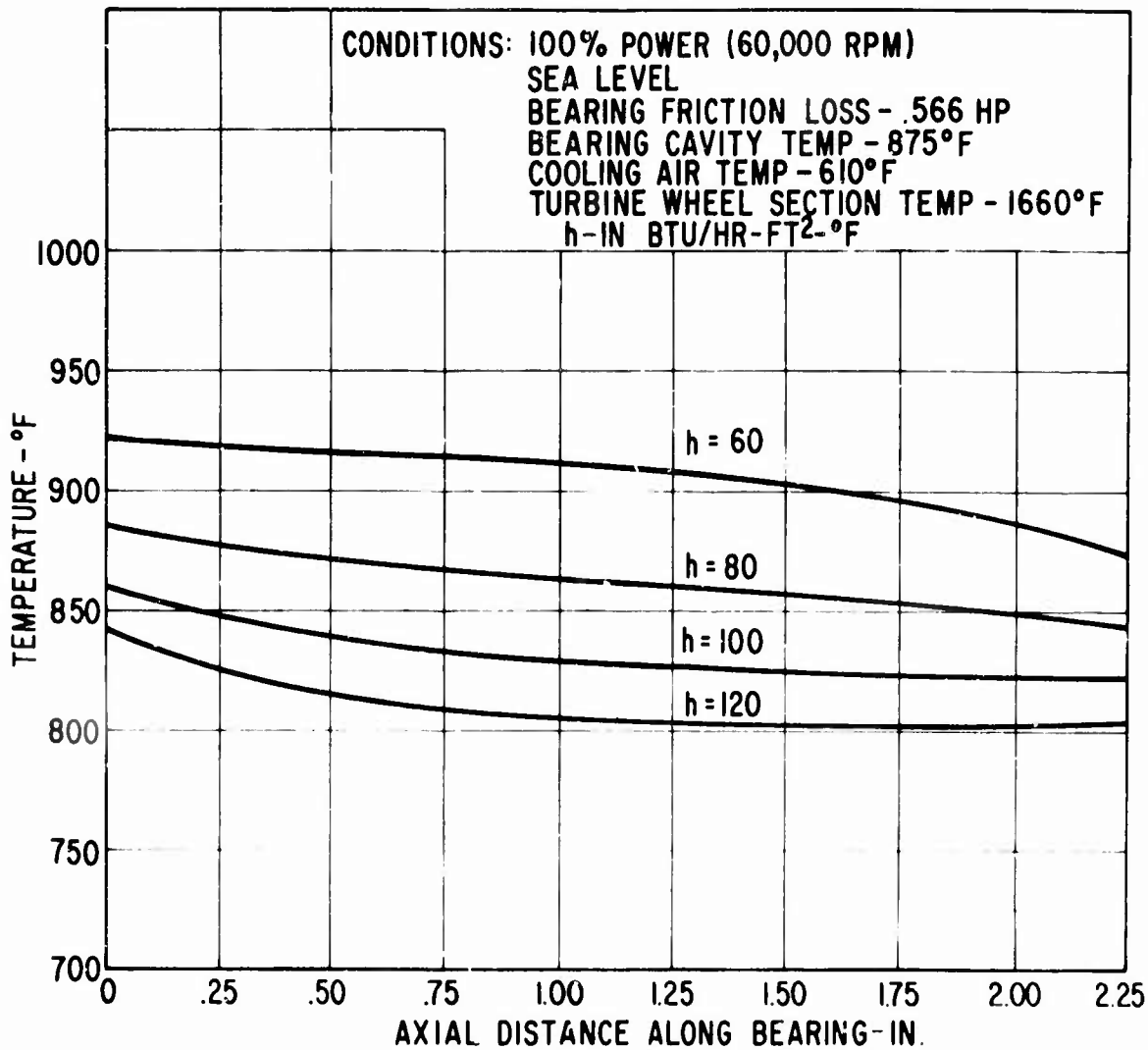


Figure 91. Variation of Axial Temperature Profile With Cooling Passage Heat Transfer Coefficient — Turbine-End Journal Bearing at Sea Level, 100-Percent Power, and Maximum Maneuver Load Conditions.

Lowering the bearing cavity ambient temperature has two disadvantages and one advantage. One disadvantage is that in order to lower the ambient temperature, the supply air must be cooled, which essentially means that an additional component is necessary. Another disadvantage is that by cooling the bearing to a lower temperature, the thermal stress between the bearing and the adjacent turbine wheel is increased. The advantage in this situation is that the temperature level of the bearing is lower.

Decreasing the amount of bearing cooling has two obvious advantages; i.e., the ambient air does not have to be cooled, and the thermal stresses between the bearing journal and adjacent components are reduced. The disadvantage then is, of course, higher operating temperatures. One additional advantage of significance here is that by doing less bearing cooling, the journal heat exchanger design needed to give a sufficient amount of heat transfer surface area can be significantly simplified. In fact, the amount of cooling necessary to make the bearing temperatures compatible with the ambience can be accomplished with a straight annular cooling passage.

Turbine-End Journal - Thermal Model

The thermal model for the turbine-end journal bearing was chosen to include the pads, the journal, the rotor tie-rod, and a portion of the radial inflow turbine wheel hub. Sixty-six nodes were used to describe the model (Figure 92), the journal pads and gas film being represented by 45 of these nodes. The remaining nodes were used to describe the cooling mechanism, the turbine wheel, and the interconnecting geometries.

The bearing nodes were constructed in the manner described for the compressor-end journal bearing model.

The radial inflow turbine wheel hub was included in the model to account for the large heat source represented by high-temperature gas washing over the turbine surfaces.

Bearing frictional losses were assumed to be identical to those of the compressor end journal bearing.

The I.D. surfaces of the model are considered to be insulated because of symmetry about the engine center line; i.e., there is no radial temperature gradient at the inside diameter surfaces. The section through the turbine wheel is considered to have a fixed temperature determined by the flow-path temperature at this station and by the effects of turbine cooling. The pad outer surfaces are assumed to have natural convection to the bearing cavity ambience. All rotating parts exposed to the bearing cavity ambience have a convective heat transfer coefficient based on their rotational speed. The cooling air supplied to the journal is assumed to be the air discharged from the thrust bearing heat exchangers (note that this air is initially taken from the first-stage compressor discharge). The boundary condition for the cooling mechanism was determined by the air mass flow and temperature, and the flow area.

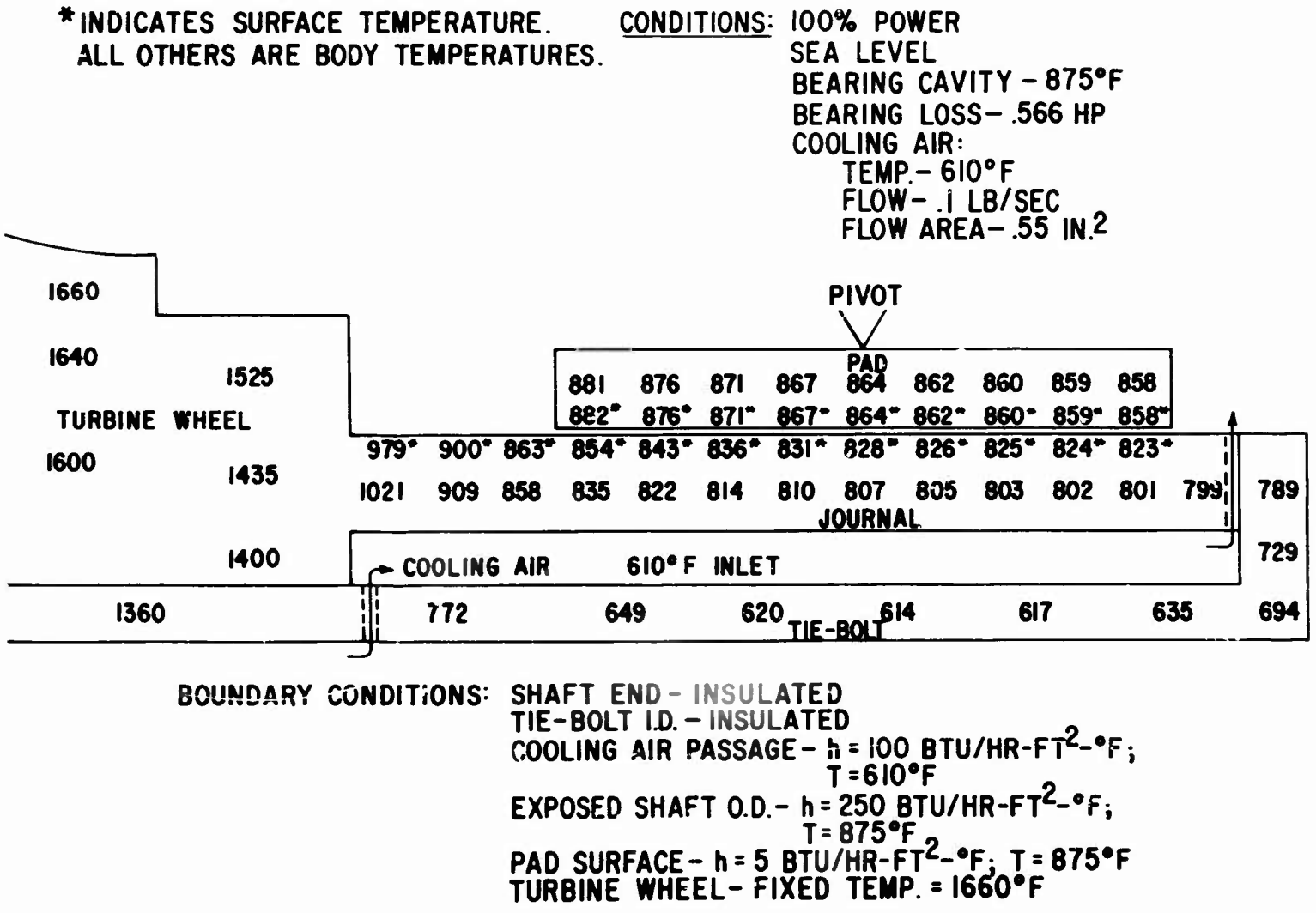


Figure 92. Thermal Model and Temperature Map (25,000 Feet Altitude, Flight Idle, and Maximum Maneuver Load) for the Turbine-End Journal Bearing.

Calculated Results of an Air-Cooled Turbine-End Bearing

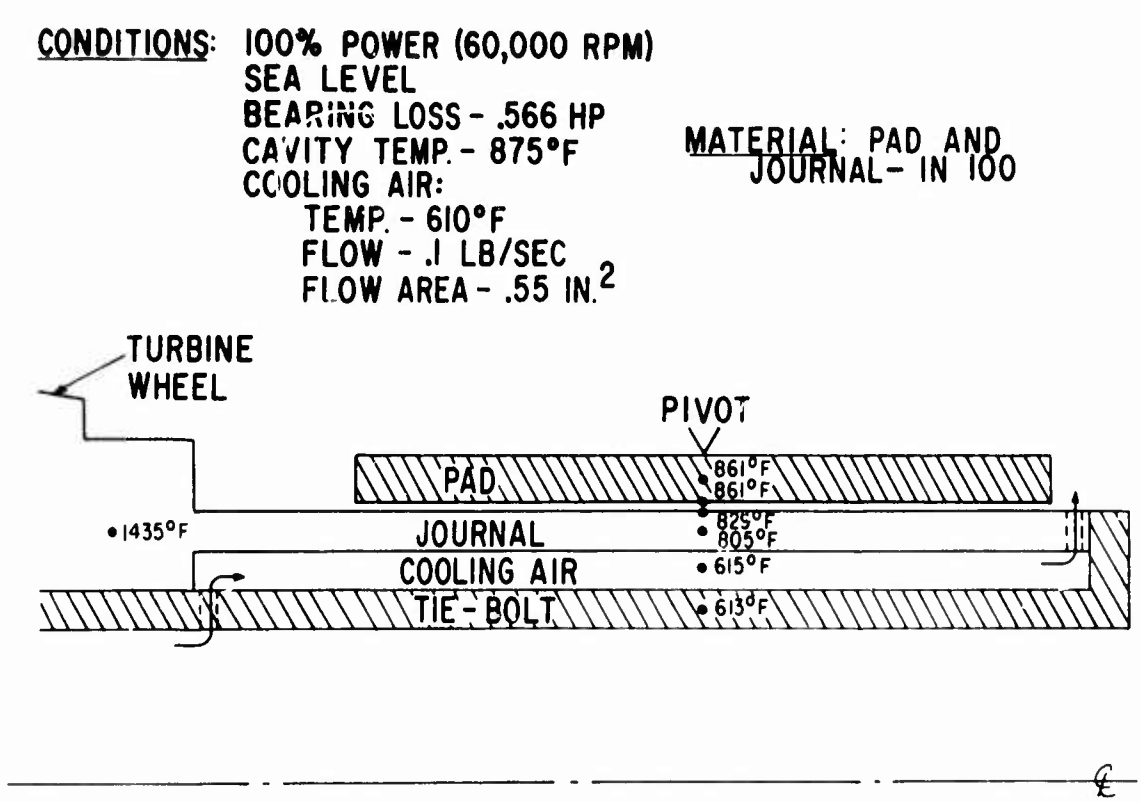
The geometry chosen for the heat exchanger model was as shown in Figure 92. The annular dimensions are 1.550 inches I.D., 1.8 inches O.D. and 3.25 inches length. Temperatures and corresponding bearing distortions for the air-cooled turbine-end bearing at sea-level flight at 100-percent power (60,000 rom) under maximum maneuver bearing loads are shown in Figure 93. Thermal input conditions for these calculations were:

Bearing friction loss	0.566 hp
Boundary condition for pad outer surface	$h = 5$ Btu/hr-ft^2-$^\circ$F; $T = 875^\circ$F
Boundary condition for exposed rotating elements	$h = 250$ Btu/hr-ft^2-$^\circ$F; $T = 875^\circ$F
Boundary condition for turbine wheel	fixed temperature - 1660°F
Shunt I.D.	insulated
Cooling passage	$h = 100$ Btu/hr-ft^2-$^\circ$F; $T = 610^\circ$F
Cooling air weight flow	$w = 0.1$ lb/sec

Figure 94 shows the bearing temperatures and thermal distortion for the condition at 25,000 feet altitude, flight idle (45,000 rpm) under maximum bearing load. The thermal input conditions for these calculations were:

Bearing friction loss	0.312 hp
Boundary condition for pad outer surface	$h = 5$ Btu/hr-ft^2-$^\circ$F; $T = 450^\circ$F
Boundary condition for exposed rotating elements	$h = 200$ Btu/hr-ft^2-$^\circ$F; $T = 450^\circ$F
Boundary conditions for turbine wheel	fixed temperature - 1375°F
Shunt I.D.	insulated
Cooling air weight flow	$w = .06$ lb/sec

Examination of Figures 93 and 94 shows that the crowning distortion (axial profile) in both cases is approximately .1 mil. This is less than the minimum bearing film thickness, which is in excess of .2 mil. In both cases, the pad axial profile conforms very closely with the journal axial profile. The consistency between the two thermal distortion curves is attributable to the judicious selection of cooling air weight flows. However, if the cooling air flow network is designed to allow 0.1 lb/sec of



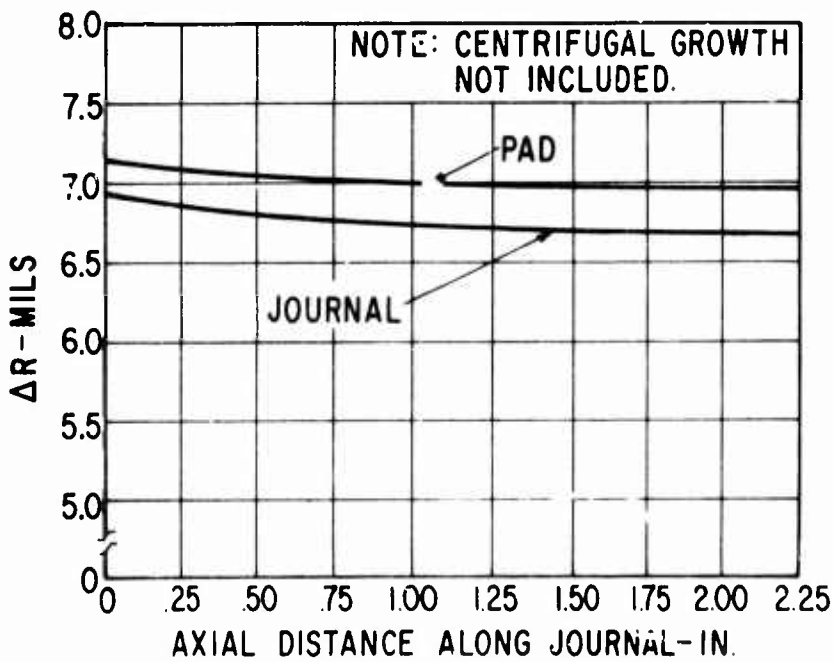
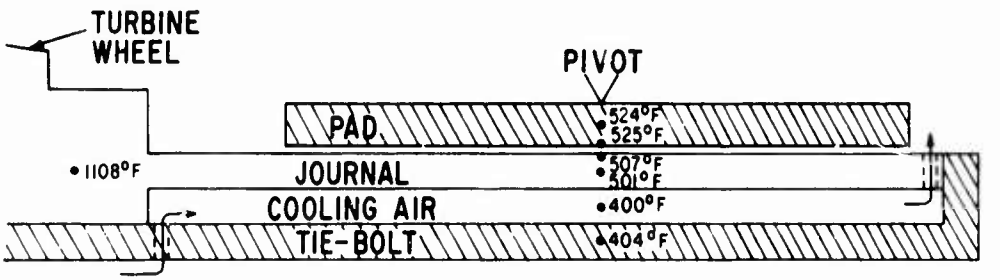


Figure 93. Thermal Model and Temperature Map (Sea Level, 100-Percent Power, and Maximum Maneuver Load) for the Turbine-End Journal Bearing.

CONDITIONS: FLIGHT IDLE (45,000 RPM)
25,000 FT ALTITUDE
BEARING LOSS - .312 HP
CAVITY TEMP. - 450°F
COOLING AIR:
TEMP. - 400°F
FLOW - .06 LB/SEC
FLOW AREA - .55 IN.^{2}

MATERIAL: PAD AND JOURNAL - IN 100



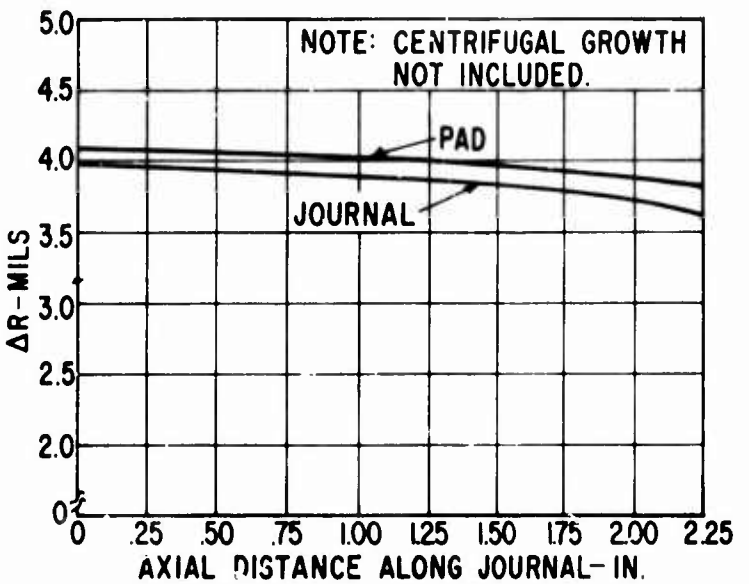


Figure 94. Thermal Distortion for the Turbine-End Journal Bearing at 25,000 Feet Altitude, Flight Idle, and Maximum Maneuver Load Conditions.

air for the sea-level 100-percent power condition, and if a static flow network is assumed, then the weight flow specified in Figure 94 will not be available for the 25,000 feet altitude, flight idle condition. The weight flow delivered at this latter condition will be approximately 0.013 lb/sec, and a thermal distortion profile corresponding to h = 20 in Figure 95 will result. Depending upon how well the bearing pad thermally follows the shaft, this may or may not be an acceptable situation.

The effect of cooling flow rate, or more accurately, heat transfer coefficient, on the turbine bearing distortion will be evaluated and quantified in terms of bearing performance during the simulator tests to be conducted during Phase II of the program. As will be discussed later, the engine simulator has provision for experimental evaluation of this potential problem area, and it is felt that experimental evaluation of this type of problem is much more meaningful and accurate than additional analytical investigation.

If the results of the experimental program indicate that higher heat transfer coefficients are necessary for the turbine bearing heat exchanger, they can readily be achieved by at least two different methods:

1. Incorporating flow control into the engine such that the required flow at 25,000 feet, flight idle would be delivered but, at conditions of higher engine power, the cooling flow would be restricted.

2. Revising the mechanism of achieving the heat transfer coefficient from that of forced through-flow to that of relative rotation of the heat exchanger components. For example, take advantage of the Taylor vortices produced by the different speeds of the gas generator and power turbine shafts to produce the required heat transfer coefficient. Such an approach has the advantage of significantly reducing the cooling flow requirement; thus there may be potential for reducing engine parasitic losses.

This latter approach is discussed in more detail in the section of this report dealing with the engine simulator design.

JOURNAL BEARING STRESS AND CENTRIFUGAL GROWTH

The use of air-lubricated bearings to support a high-speed rotor requires that the rotor be well balanced and that this standard of balance be retained. An accurately balanced, one-piece rotor would be the most suitable type of construction. However, in a complex machine such as a gas turbine, the rotor must be made from several parts, usually held together with such devices as curvic couplings and tie bolts. The standard of balance attained with a multipiece rotor, the assembly of which usually progresses as the engine assembly progresses, is largely dependent on the accuracy and repeatability of assembly of the curvic couplings or other similar joining and locating devices. From consideration of the standard of balance, it follows that the integrity of a rotor system is improved if the number of parts required to make up the rotor is kept to a minimum.

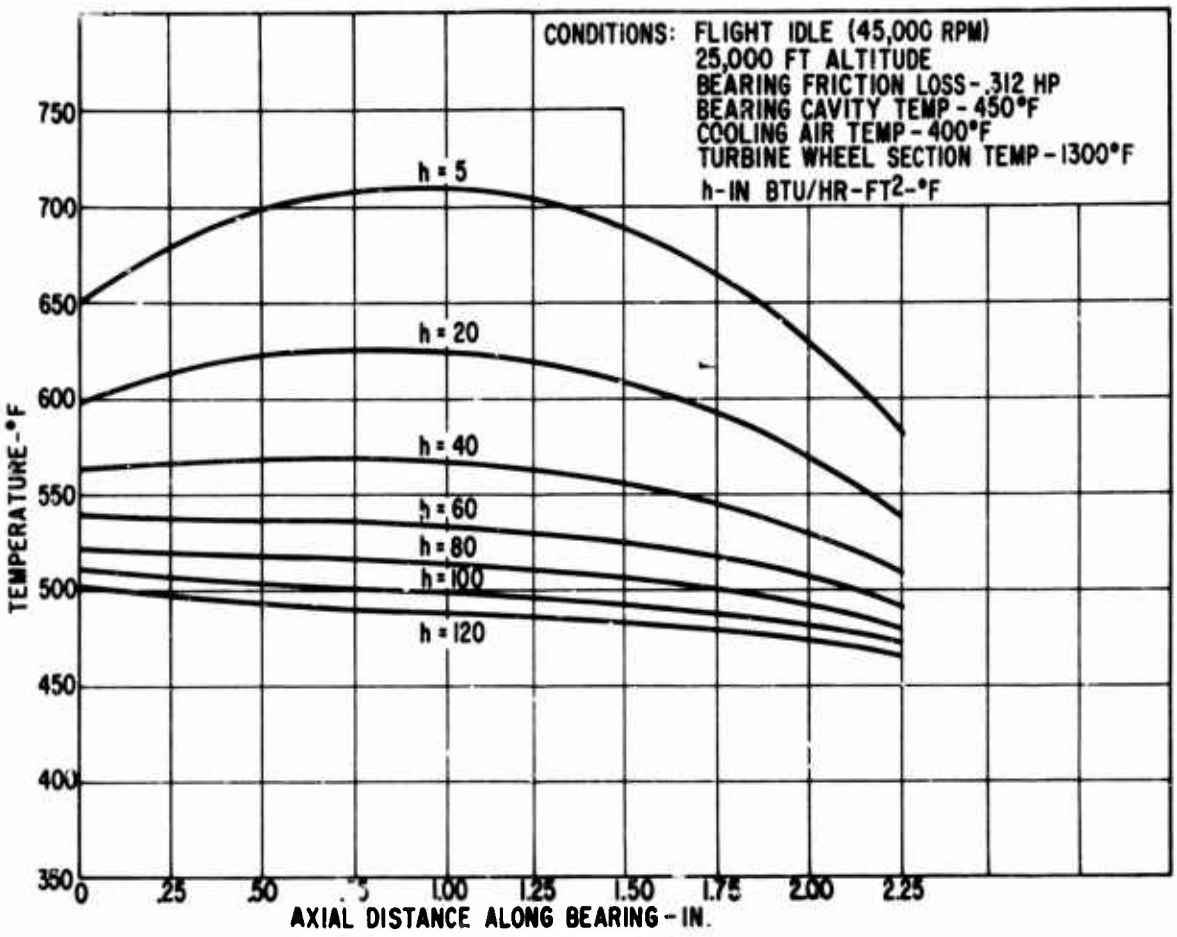


Figure 95. Variation of Axial Temperature Profile With Cooling Passage Heat Transfer Coefficient – Turbine-End Journal Bearing at 25,000 Feet Altitude, Flight Idle, and Maximum Maneuver Load Conditions.

For this reason, the journal sections of the engine rotor shown in Figure 68 are integral with the adjacent wheels. This, of course, means that the substrate material from which the journals are fabricated is the same as that of the wheels. In the case of the compressor-end journal, the material will be a titanium-based alloy, while IN-100, or perhaps IN-102, is proposed for use at the turbine end.

Values of the 0.2-percent yield stress and ultimate stress versus temperature are shown in Figures 96 and 97, respectively, for three candidate alloys. From these figures, it is seen that the maximum allowable stress levels for these alloys at the journal temperatures prevailing in the engine at 100-percent power conditions are as given in Table XVIII.

TABLE XVIII. PROPERTIES OF THREE CANDIDATE BEARING MATERIALS

	Compressor End Journal at 550°F	Turbine End Journal at 850°F	
	Ti-7Al-4Mo	IN-102	Alloy 901
0.2% Yield Stress (psi)	119,000	137,000	114,000
Ultimate Stress (psi)	120,000	190,000	152,000

The circumferential stress and radial centrifugal growth of the turbine end journal versus rotor speed is shown in Figure 98. From this figure, it is seen that the stress in the turbine end journal at 100-percent power is 21,000 psi. This is obviously a very low level of stress, considering the capability of the IN-102 material. This same figure shows the radial centrifugal growth to be 0.85 mil at 100-percent power. This radial growth is, of course, taken into consideration along with the growth resulting from thermal expansion, when calculating the performance of the journal bearings over the complete range of engine operation.

The circumferential stress and radial growth of the compressor-end journal is shown in Figures 99 and 100 respectively. To remove the friction-generated heat from the compressor-end journal bearing, a beryllium shunt is shrunk into the bore of the journal. To ensure that the joint efficiency of the beryllium-titanium interface remains high over the operating speed range, a fairly heavy shrink fit is required. Figures 99 and 100 show the effects of this shrink fit in the curves entitled 'composite'. From these curves the stress in the composite at 100-percent power (at an average journal temperature of 510°F) is seen to be 36,380 psi. Again, this may be considered to be a very safe stress level.

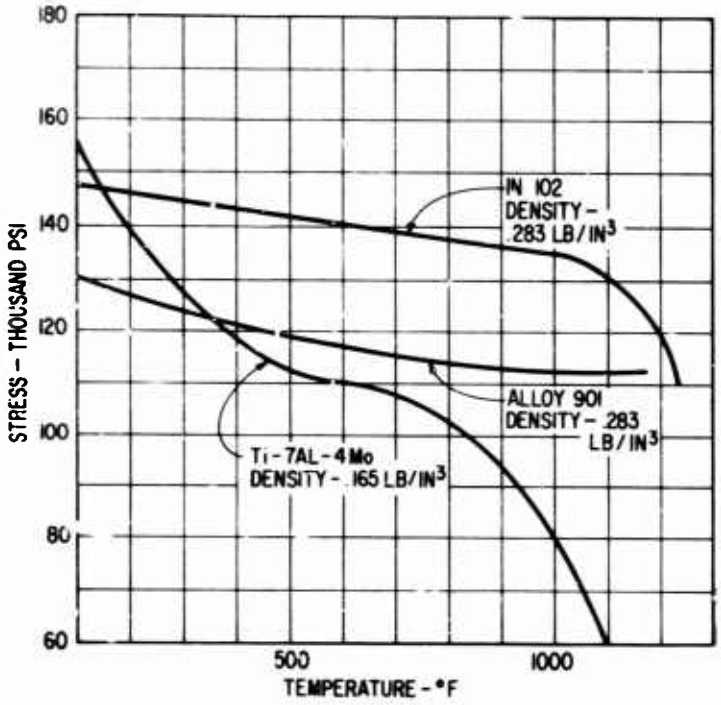


Figure 96. 0.2-Percent Yield Stress Versus Temperature for Three Candidate Bearing Materials.

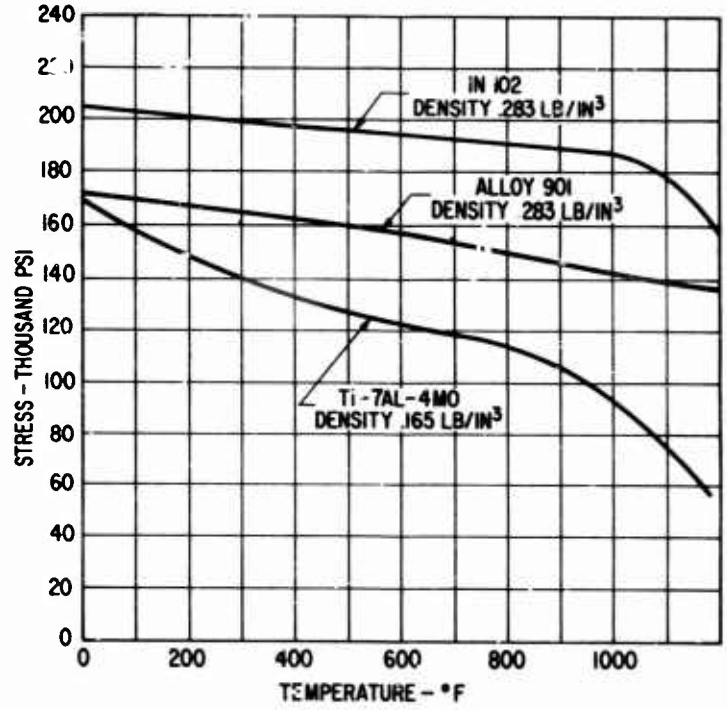


Figure 97. Ultimate Stress Versus Temperature for Three Candidate Bearing Materials.

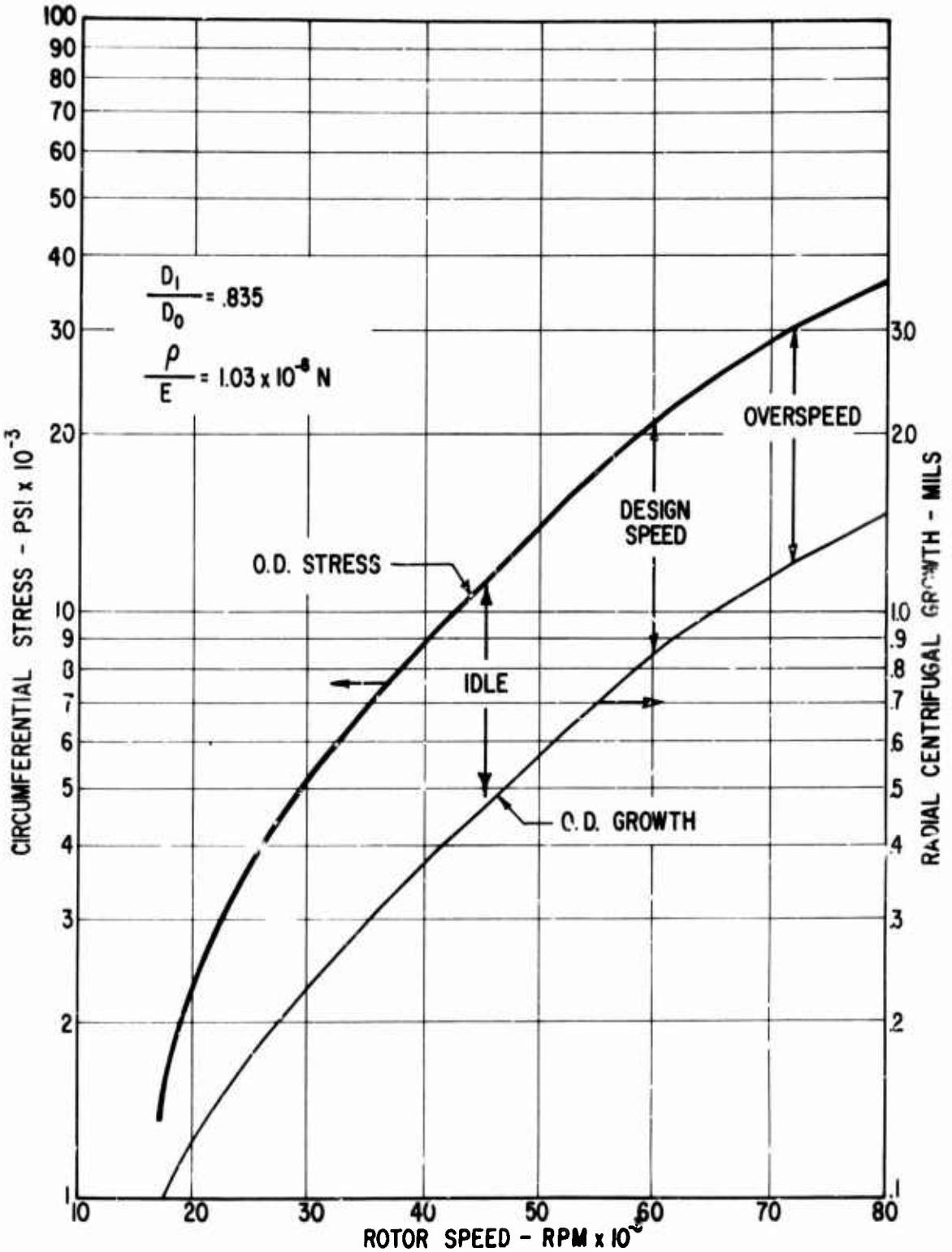


Figure 98. Effect of Speed on Stress and Centrifugal Growth of the Turbine Bearing Journal.

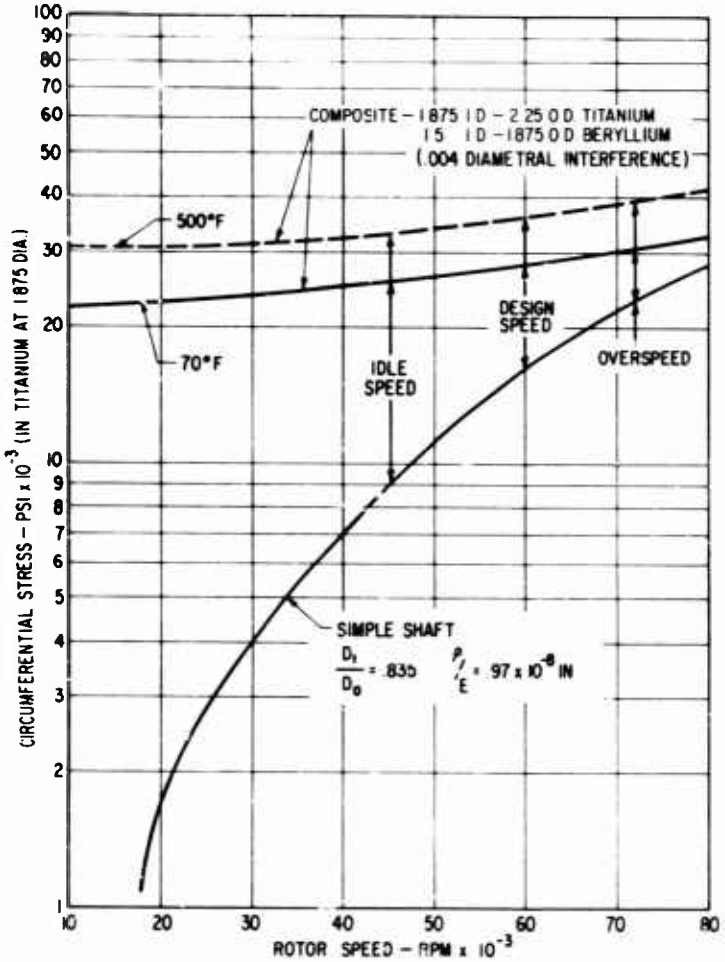


Figure 99. Effect of Speed on Stress of the Compressor Journal Bearing.

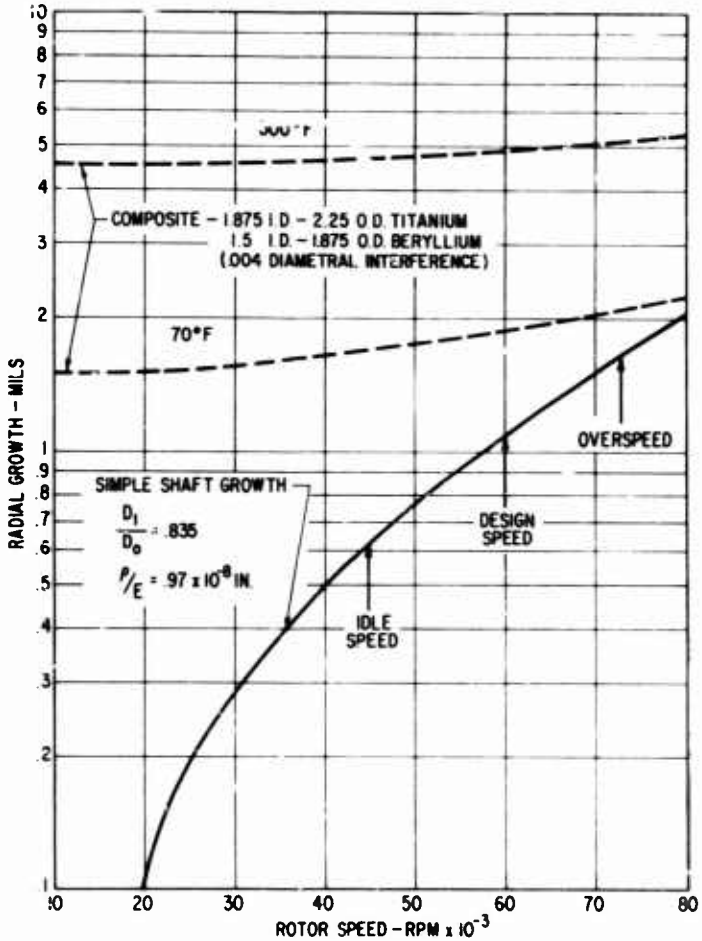


Figure 100. Effect of Speed on Centrifugal Growth of the Compressor Journal Bearing.

DESIGN OF THE DOUBLE-ACTING THRUST BEARING FOR THE ENGINE

Previous studies [1] have indicated that a hydrostatic air bearing design would be the most suitable for carrying the anticipated aerodynamic and maneuver-induced thrust loads in a gas-turbine application. It was further indicated in Reference 1 that a hydrodynamic (spiral-grooved) thrust bearing was thought to be inadequate; i.e., it was not capable of carrying the applied thrust load at a reasonable, practical film thickness. This conclusion, however, was reached because of the large aerodynamic thrust loads encountered in the engine design then under consideration. In the present program, the aerodynamic rotor thrust load has been considerably reduced by the use of shrouded centrifugal compressor wheels in conjunction with a radial inflow turbine. Calculations previously discussed have shown that the aerodynamic thrust loads to be supported by the air bearing in the present program are indicated in Table XIX.

TABLE XIX. AERODYNAMIC THRUST LOADS

Engine Power Level	1st Stage Compressor (lb)	2nd Stage Compressor (lb)	Turbine (lb)	Net Thrust On Rotor (lb)
100% Sea Level	+75.7	-96.5	+58.5	+37.7
Idle Sea Level	+28.7	-20.7	+28.6	+36.6
100% 25,000 Feet	+22.8	-28.7	+29.6	+23.5
Idle 25,000 Feet	+13.4	-14.74	+14.4	+13.56

+Denotes Forward Thrust
-Denotes Rearward Thrust

It is seen from the above values that the aerodynamic load to be supported by the thrust bearing is quite low. A more significant axial load, also to be supported by the thrust bearing, results from aircraft maneuver conditions. MIL-E-5007C specifies an acceleration of 10g, which results in an acceleration thrust load (presumably of short duration) for the present design of 240 lb. Both aerodynamic and maneuver loads are considered to be additive and to act in either direction. The thrust bearing design, therefore, is double acting, with a required load-carrying capacity of 277 pounds. Because the magnitude of this load is less than the load considered in [1], the possibility of using a hydrodynamic bearing with its inherent simplicity was reconsidered.

Additional thrust bearing studies were made for the 3.5 lb/sec flow-rate engine, which were concerned with the load versus film thickness characteristics of three different thrust bearings, and a combination of these two designs called the hybrid design. This third bearing concept employs the

usual spiral-grooved bearing design but, in addition, introduces a high-pressure air supply (taken from second-stage compressor discharge) through a circumferential row of orifices, located in the plain (seal) region of the bearing.

Thrust Bearing Geometry

The surface geometries of the three thrust bearing types are depicted in Figure 101. Figure 101a shows the pure hydrostatic type with centrally located feeding holes. Figure 101b shows the pure spiral-groove hydrodynamic ty, with groove geometric relationships typical of previous bearings of this type. Figure 101c is a combination of the first two, with the hydrostatic feeding holes located in the center of the bearing seal area.

For the comparative studies, each bearing was 5.74 inches OD x 3.10 inches I.D. The ambient pressure was assumed to be that of first-stage compressor discharge for the particular operating condition, and the supply pressure for the hydrostatic and hybrid versions was taken to be second-stage compressor discharge. Other significant dimensions for the three bearings were as indicated below.

	Hydrostatic	Hydrodynamic	Hybrid
Number of Feed Holes	20	NA	20
Size of Feed Holes (in.)	0.015	NA	0.014
Radius at Feed Holes (in.)	2.15	NA	1.755
Number of Spiral Grooves	NA	15	15
Radial Extent of Grooves (in.)	NA	0.92	0.92
Depth of Grooves (in.)	NA	0.0021	0.0021
Groove-to-Land Width Ratio	NA	1.6	1.6
Groove Angle (deg)	NA	161.9	161.9

Thrust Bearing Load Capacity

The load capacities of the three bearing types, assuming no distortion, are shown in Figures 102 through 104 as a function of speed at sea level and 25,000 feet altitude pressure conditions. Also indicated is the required operating load range.

The load-carrying capability of the hydrostatic thrust bearing as a function of engine speed and loaded bearing film thickness is shown in Figure 102 at both sea level and 25,000 feet altitude. At both of these altitudes, the bearing has adequate capacity to carry the thrust loads resulting from maximum maneuver conditions. At sea level and 45,000 rpm, the maximum load is carried with a minimum film thickness of 1.0 mil. At 25,000 feet altitude, the maximum load is carried at approximately 0.8 mil.

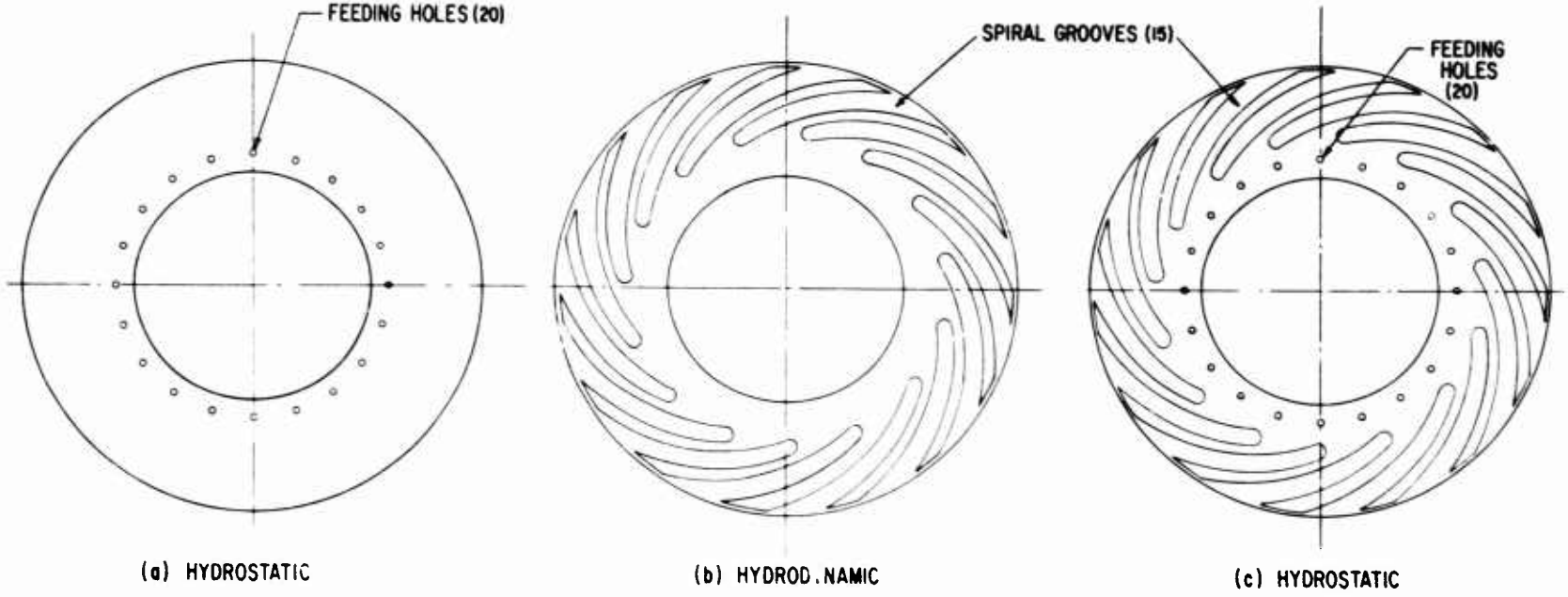


Figure 101. Thrust Bearing Types.

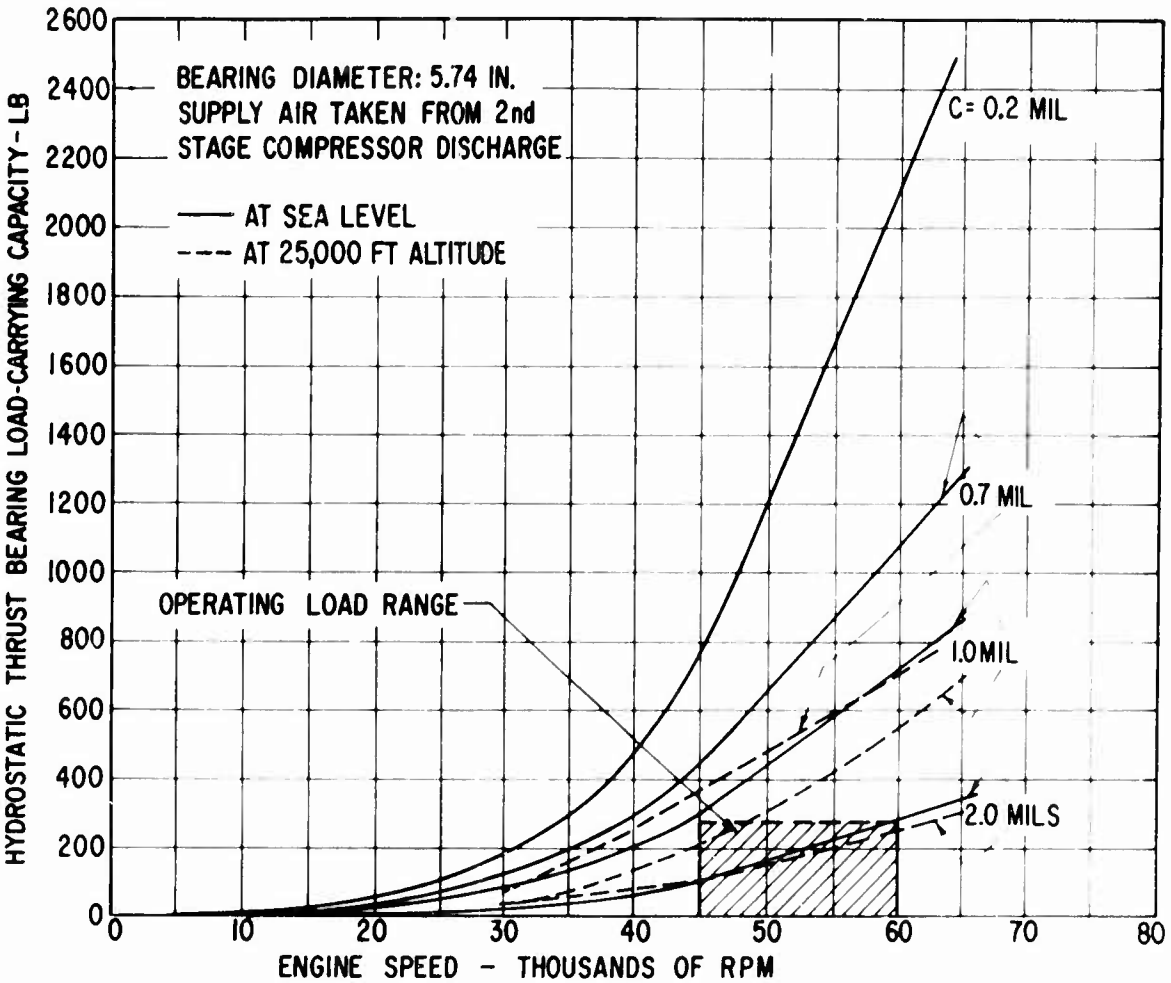


Figure 102. Performance of an Undistorted Hydrostatic Thrust Bearing.

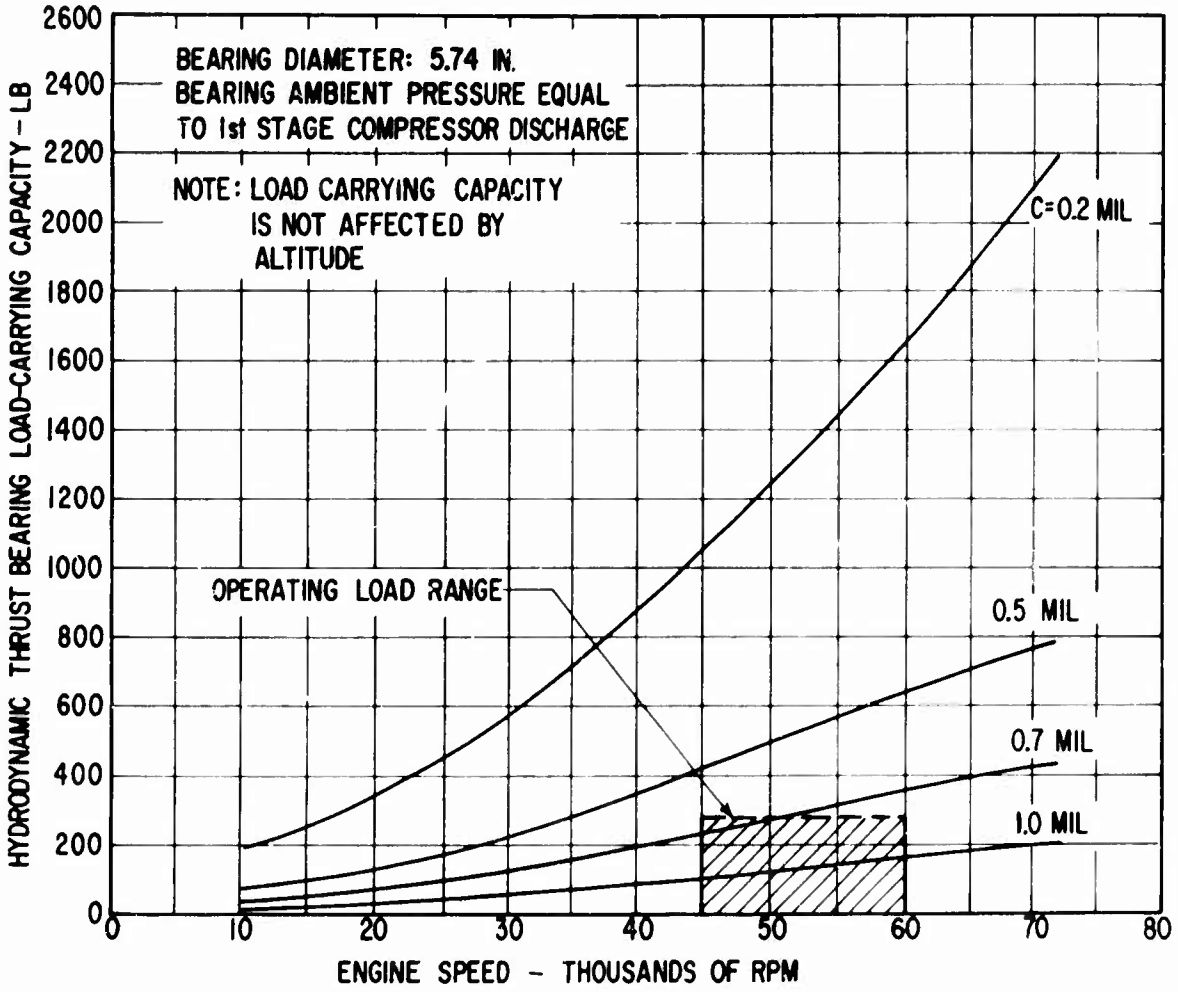


Figure 103. Performance of an Undistorted Hydrodynamic Thrust Bearing.

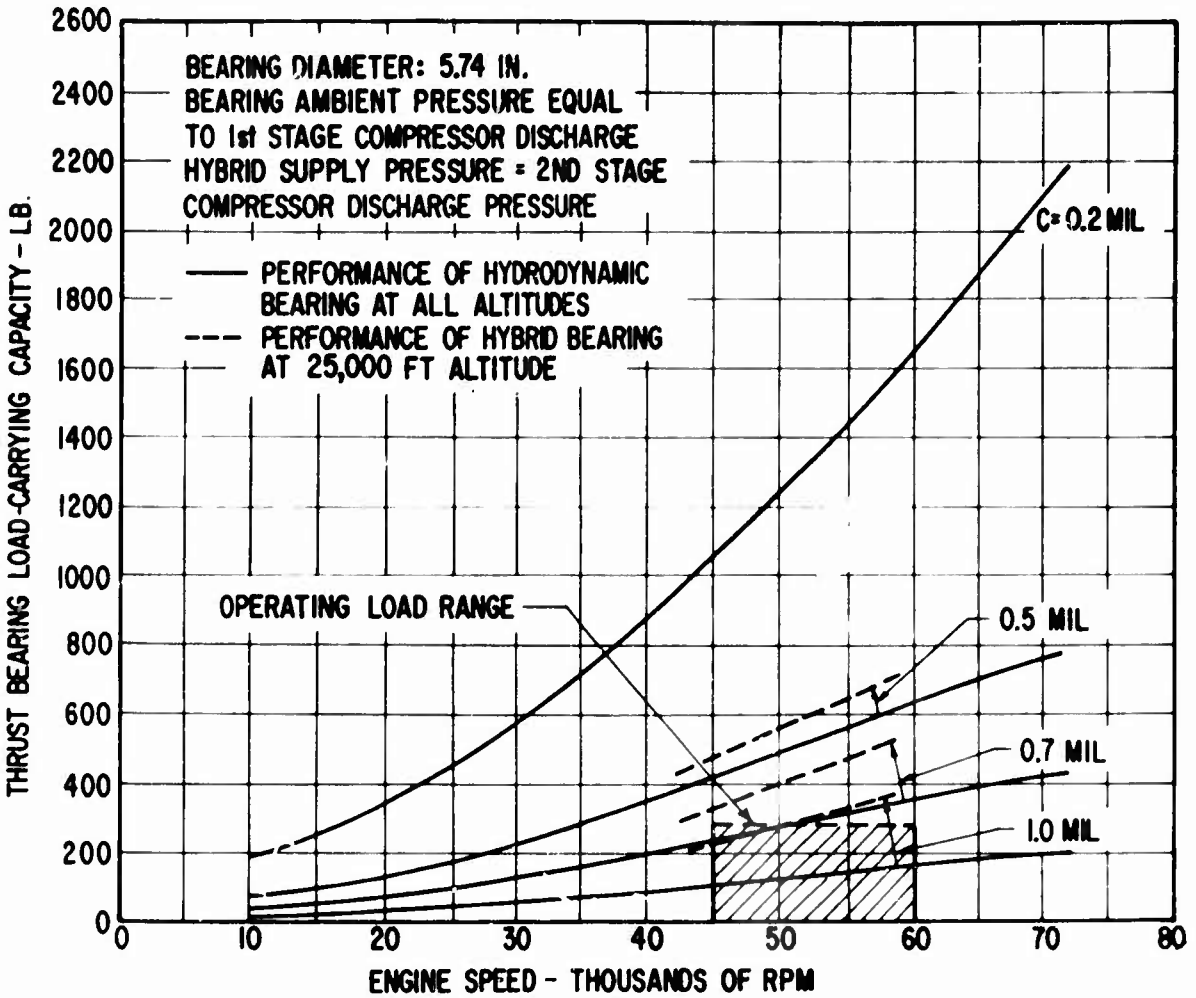


Figure 104. Performance of an Undistorted Hybrid Thrust Bearing.

The load-carrying capability of the spiral-grooved hydrodynamic thrust bearing, with a uniform film thickness, is shown in Figure 103 as a function of engine speed and loaded bearing film thickness. In general, this figure represents the hydrodynamic load versus film thickness relationship at all altitudes (the load-carrying capacity of the spiral groove thrust bearing is independent of ambient pressure). The operating load range superimposed on this chart shows that this bearing will be operating at a film thickness between 0.5 and 0.7 mil when at engine idle and under maximum maneuver loads.

The performance of the hybrid thrust bearing at 25,000 feet altitude with the engine at both idle and 100-percent power is shown and compared with the plain hydrodynamic bearing performance in Figure 104. The main point illustrated by these data is that the uniform-film, hybrid design can carry as much load at 1-mil film thickness as the hydrodynamic bearing design carries at 0.7 mil.

Based upon these results, further evaluation of the pure hydrostatic bearing was discontinued. Although it will carry the required load at 45,000 rpm at film thickness comparable to the other two types, the hybrid has two significant off-design advantages over the pure hydrostatic type.

As can be seen by comparing Figures 102 and 103, the hydrodynamic bearing (Figure 103) has greater overload capability (as seen by comparing the two C = 0.2 mil curves) and has higher load capacity at speeds below 45,000 rpm. Obviously, the higher overload capability gives the engine more tolerance to unforeseen events such as surge, momentary shocks in excess of 10g, etc. The low-speed load capability advantage is desirable from startup and shutdown considerations, in that positive fluid film separation of the bearing elements will occur at lower speeds.

The hybrid bearing, as indicated in Figure 104, has the same general characteristics as the hydrodynamic bearing, with an added load margin provided by the hydrostatic assist.

Because the hybrid design indicated the most favorable load capacity performance over the range of engine performance under consideration, further studies were made to include the effect of a nonuniform bearing gap (associated with thermal distortion of the thrust plates). Both the hydrodynamic and hybrid designs for the reasons stated previously were studied to determine what effect the maximum anticipated distorted film would have on the bearing load-carrying capability.

Distorted Film

Experience with high-speed thrust bearings has indicated that the temperature distribution resulting from bearing friction will distort the bearing surfaces such that the uniform film can only be considered as an ideal situation. However, the use of external cooling can minimize this distortion. Considerable effort was put into the thrust bearing external cooling design, the results of which are discussed in a later section of this report. It is the intent of this section to present the effects of

the maximum anticipated distortion on bearing load capacity. The distortion analysis considers the thermal distortion under both zero and 10g loading as steady-state problems. The results of these preliminary analyses indicated that at a 2-mil film thickness on both sides of the thrust runner (zero load), the film will vary about 0.2 mil across the annular surface, with the smallest film at the inner radius. With a 1-mil film thickness on the loaded side and a 3-mil film thickness on the unloaded side (approximating the case of a 10g load), the film varies across the annular surface by 0.8 mil, with the smallest film at the outer radius. Thus at the outer radius, the film thickness is 1 mil, at the inner radius, the film thickness is 1.8 mil. This amount of distortion under the 10g load, assuming that steady-state conditions have had time to become established, is the maximum anticipated distortion. For the purposes of analysis, this amount of film distortion was assumed to exist at other smaller bearing films (as measured at the bearing OD), and load capacity calculations based upon this distorted film shape were made.

Load versus film thickness performance for both the hydrodynamic and hybrid bearings is plotted in Figure 105. This shows the effects of the aforementioned maximum distortion on the load-carrying capability of both bearing types under conditions of 100-percent power at sea level, and engine idle at 25,000 feet altitude. On this figure, load is plotted versus minimum operating film thickness as measured at the outer radius of the thrust bearing. The main points that can be ascertained from Figure 105 are that at 45,000 rpm and 25,000 feet altitude operation, the hybrid thrust bearing will carry a 280-pound load at a minimum film thickness of from 0.55 to 0.8 mil, dependent on the amount of distortion. At 60,000 rpm and sea-level operation, the hybrid bearing will carry this same load at a minimum film thickness of from 0.9 to 1.2 mils. Also, the superior load-carrying capability of the hybrid bearing over the hydrodynamic bearing is clearly evident.

Hybrid Thrust Bearing Friction Loss

The hybrid thrust bearing friction loss (for one thrust face and for a nondistorted film) versus thrust load is plotted in Figure 106, for operating conditions of 45,000 rpm at 25,000 feet altitude and 50,000 rpm at sea level. For a 280-pound load, the loss is 1.15 horsepower at 45,000 rpm and 1.80 horsepower at 60,000 rpm.

Double-Acting Hybrid Thrust Bearing Flow Requirements

The hybrid thrust bearing will require a continuous supply of air from the second-stage compressor discharge. The flow requirements for this bearing operating with a 2-mil film thickness on either side of the thrust runner will vary from 0.009 lb/sec at 45,000 rpm and 25,000 feet altitude, to 0.036 lb/sec at 100-percent power, sea level conditions (approximately 1 percent of engine flow rate). Having left the thrust bearing, this flow joins the flow of air which has been used to cool the thrust bearings. The combined flow is then used to cool the turbine-end journal bearing and the power turbine before entering the gas generator exhaust (power turbine inlet).

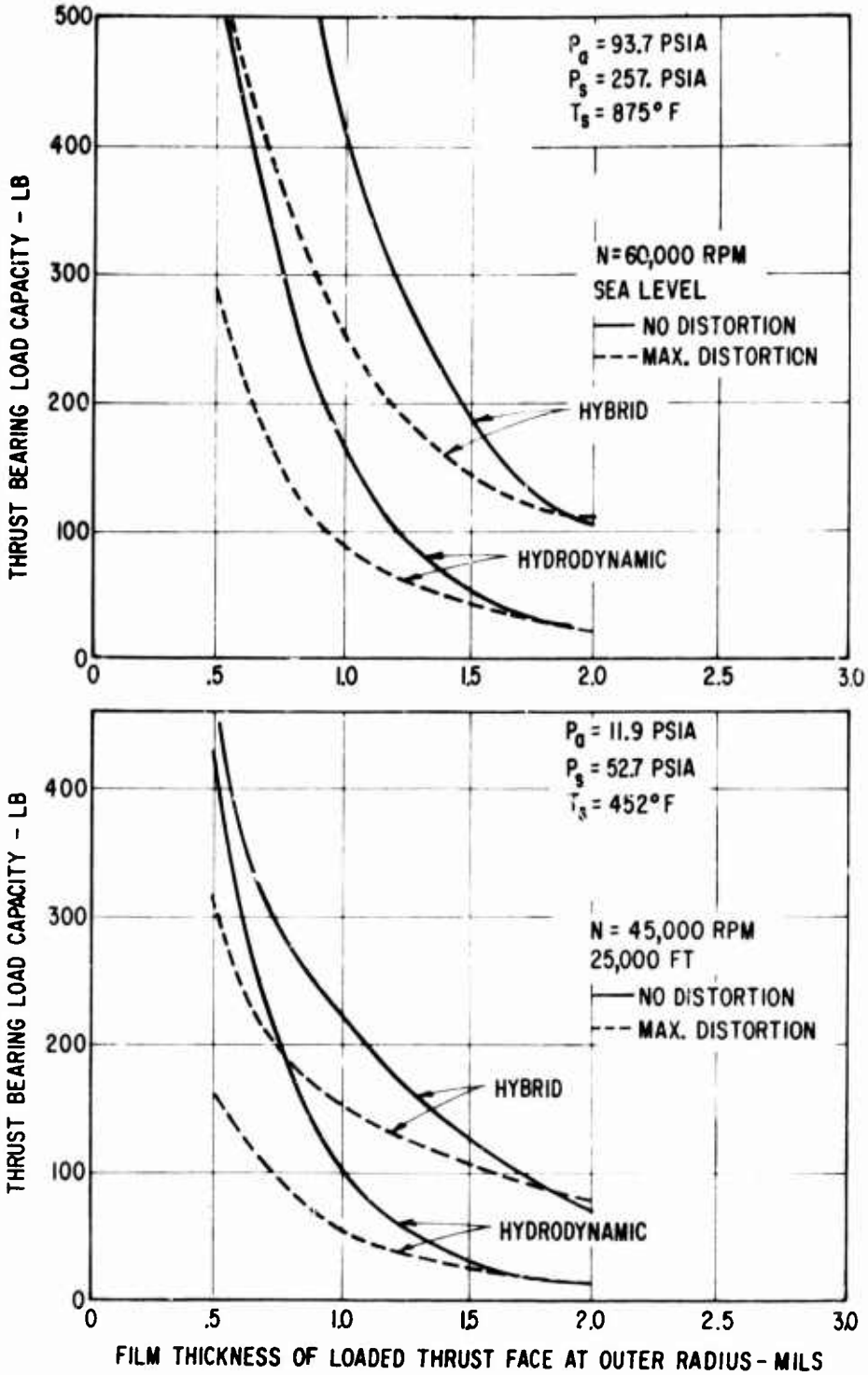


Figure 105. Comparison of Hybrid and Hydrodynamic Thrust Bearing Load Capacity With and Without Distorted Film.

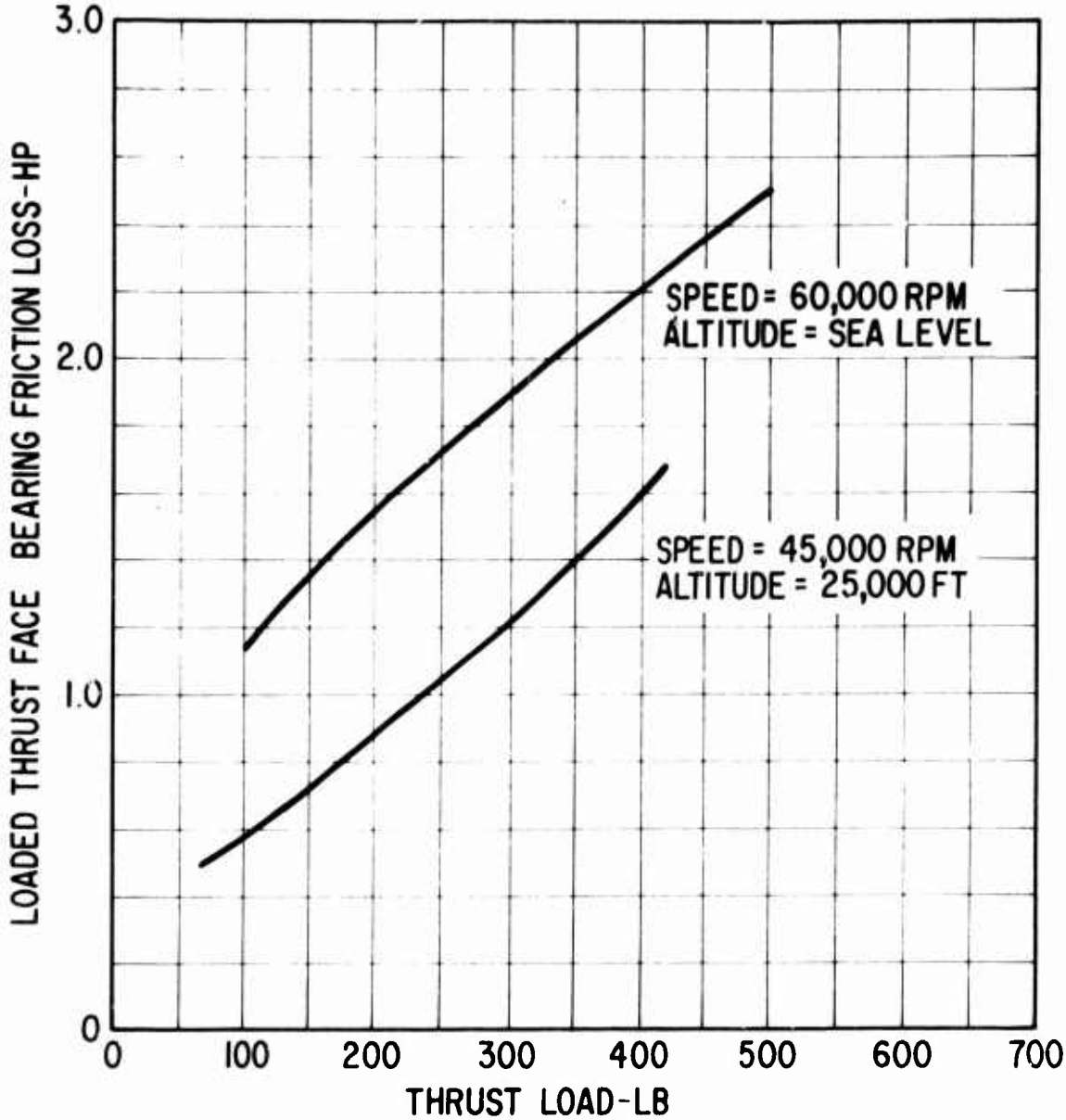


Figure 106. Hybrid Thrust Bearing Friction Loss (Nondistorted Film).

Thrust Bearing Thermal Design

Like the journal bearings, most high-speed air lubricated thrust bearings must be externally cooled, since the quantity of gas circulated through the clearance space is insufficient to remove the heat generated within the film by viscous shear. Thus the external cooling is required not only to limit the bearing operating temperature to within the capabilities of the bearing surface and structural materials, but also must be accomplished in such a manner that the bearing structural members remain as nearly isothermal as possible. This latter requirement is essential to minimize the bearing distortions caused by internal temperature gradients. Unless the bearing distortions as reflected in the bearing film thickness non-uniformity are limited to a fraction of the bearing operating clearance, the bearing load capacity will be all but lost.

Thus, considerable attention was paid to the thrust bearing cooling problem, and extensive design analyses were conducted to assure that the thrust bearing surface would remain flat and parallel to the extent required to carry the load at reasonable film thickness.

Cooling Concept

The thrust bearing is cooled by means of an air heat exchanger built into each of the bearing stator plates as shown in Figure 107.

The heat exchanger consists of three layers of slotted thin metal plates, each of which is 0.02 inch thick. On each plate, 20 equally spaced slots are generated along the involute of the base inner circle as illustrated in Figure 107. Each side of the double-acting thrust bearing, therefore, has 60 slots. The slotted construction was selected to achieve a high heat transfer coefficient and large effective area.

Consideration was given to both possible cooling flow directions, i.e., radial inward or radial outward.

Figure 108 shows an outflow cooling system. The cooling flow is taken from the second-stage compressor inlet, then enters the heat exchanger at the bearing inner radius, and is finally discharged into the power turbine inlet Because of the low resistance to air flow between the back of the thrust plates and the casings, two seals are needed in this design. These two seals ensure that sufficient pressure gradient is available for the required cooling air flow through the heat exchangers. The alternative inflow design is shown in Figure 109. Here the cooling fluid is bled from the first-stage diffuser outlet, is used to cool the thrust bearing, and, after passing into the rotor shaft, is then used to cool the turbine-end journal bearing. From the thrust bearing standpoint, the significant difference lies in the gas-temperature-rise characteristics of the two schemes. The coolant will pick up heat and increase in temperature as it proceeds along a heated surface. It is intuitive to take advantage of this effect with an inflow design to offset the nonuniform radius-dependent heat generation, which is significantly greater at the larger radii.

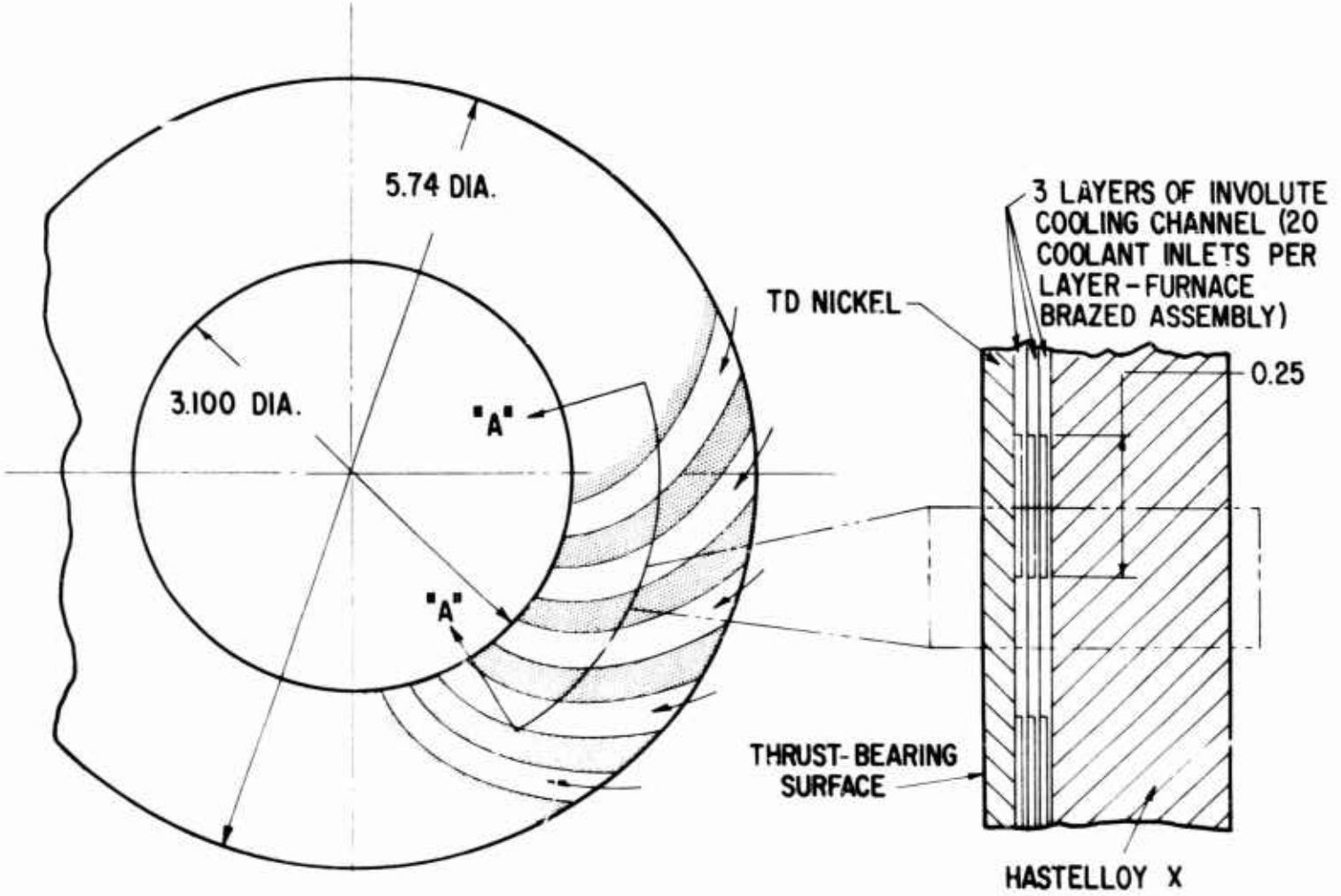


Figure 107. Geometry of the Thrust-Bearing Heat Exchanger Involute Cooling Pattern.

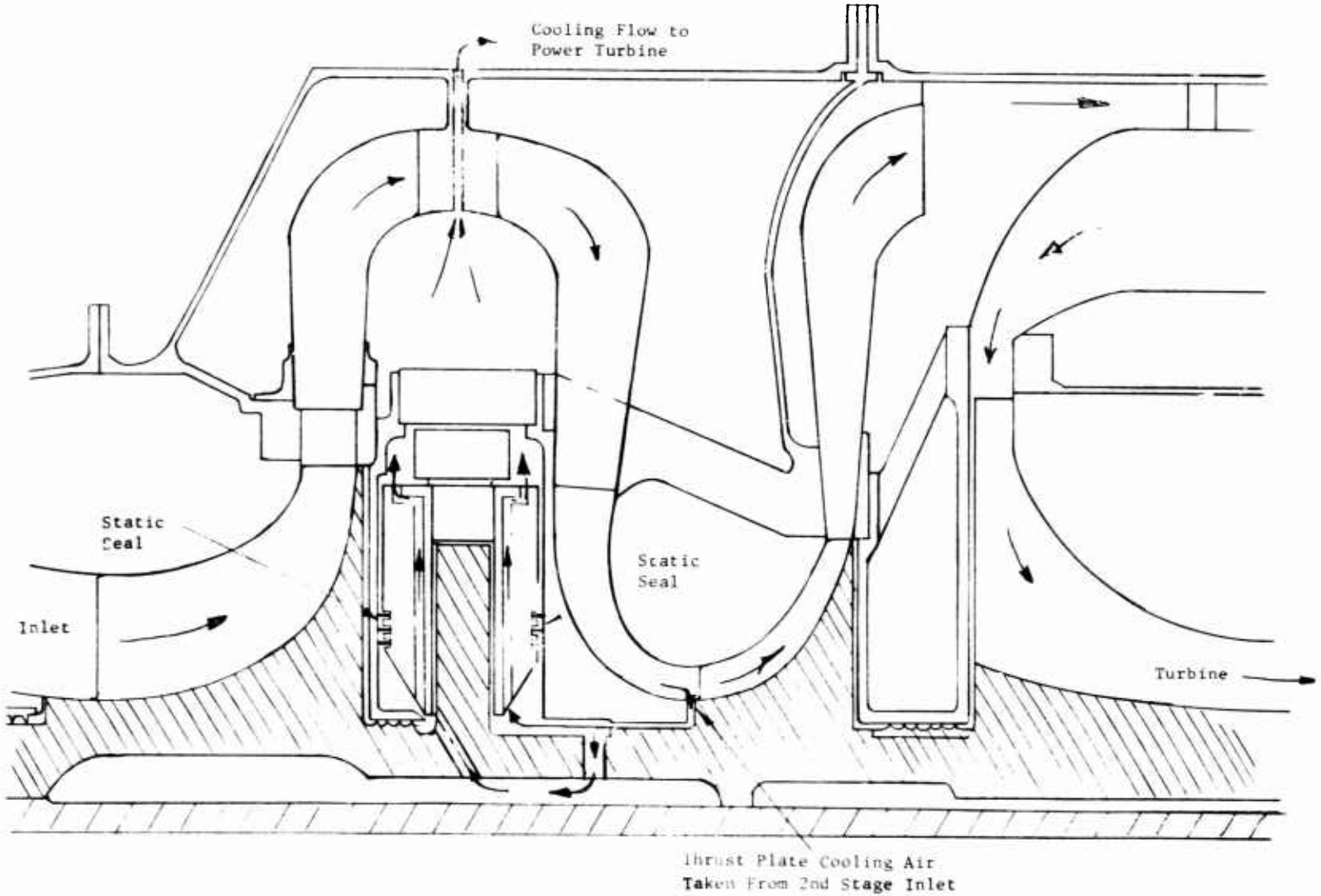


Figure 108. Thrust Bearing With Radial Outflow Cooling.

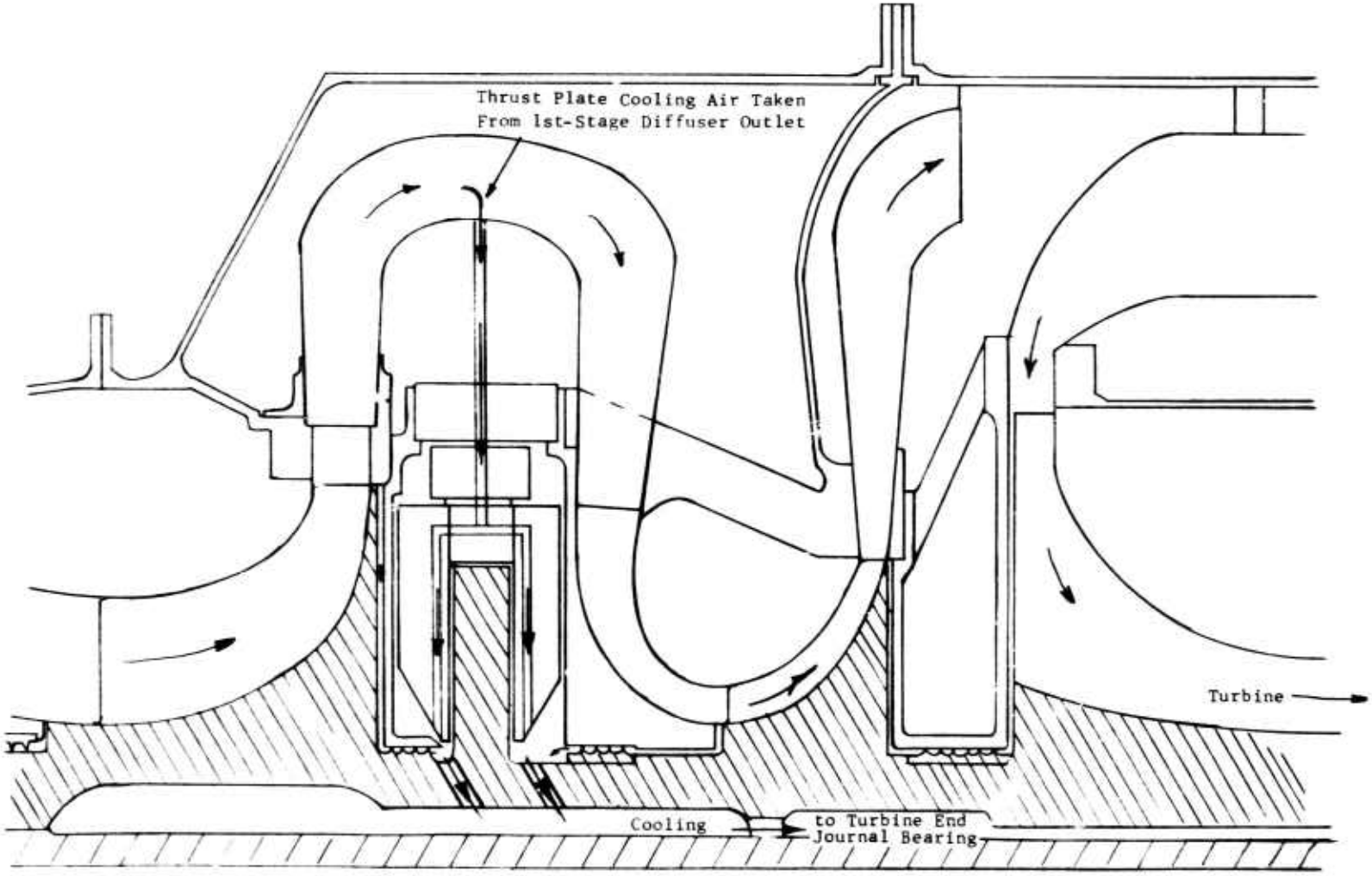


Figure 109. Thrust Bearing With Radial Inflow Cooling.

Results of temperature rise calculations along the flow path are shown in Figure 110 for 100-percent power operation at sea level. These reveal that the outflow design will give a flow-wise temperature rise of 120°F, while the inflow design will produce only 10°F in temperature rise. Obviously, the bearing radial temperature gradient is much larger using the outflow approach. Similar calculations were made over a range of bearing film thickness to show the effect of varying the thrust bearing load. The relative merit of employing an inflow design is clearly seen by the results shown in Figure 111. It is superior to the outflow design at all film clearances and markedly so at small film thicknesses (high load). Therefore, the inflow design was selected as the most suitable configuration for use in the engine.

Coolant Flow Rate

The choice of coolant flow rate is more sensitive in the present application than is usually found with conventional heat transfer designs. The normal requirements of a heat exchanger are all present (high effectiveness, low pressure drop, and small size) but, in addition, the surfaces of the thrust bearing must remain essentially parallel, preferably within fractions of a mil, under all conditions of engine operation. Overcooling or undercooling, if allowed to take place, could result in unacceptable bearing distortion.

Initially, a cooling flow rate of 0.1 lb/sec (0.05 lb/sec for each side of the thrust bearing) was selected for study. This flow rate coincides with the cooling flow requirements of the radial inflow turbine wheel, and it was hoped that engine parasitic losses could be minimized if the thrust bearing coolant could be further utilized to cool the turbine. Later studies, however, indicated that the sum of the pressure drops through the thrust bearing heat exchanger and the turbine wheel was in excess of the pressure drop available, the air being taken from first-stage compressor discharge. It was then proposed that the air used to cool the thrust bearing should be further used to cool the turbine-end journal bearing (which has a lower pressure drop than the turbine) before being discharged into the power turbine inlet. Cooling of the radial inflow turbine is accomplished by taking air from second-stage compressor tip static. Cooling of the compressor-end journal bearing is not affected, as a high-conductivity shunt is used to transfer the friction loss from this bearing to the first-stage compressor wheel, which uses the total engine air flow as a heat sink.

Temperature Distribution and Distortion

Steady-state temperature distribution and thermoelastic deformation of the thrust runner and thrust stators were both calculated for zero load and 10g maximum load at:

1. Sea level, 100-percent power (60,000 rpm) - 0.05 lb/sec coolant flow rate

2. Sea level, flight idle (45,000 rpm) - 0.025 lb/sec coolant flow rate

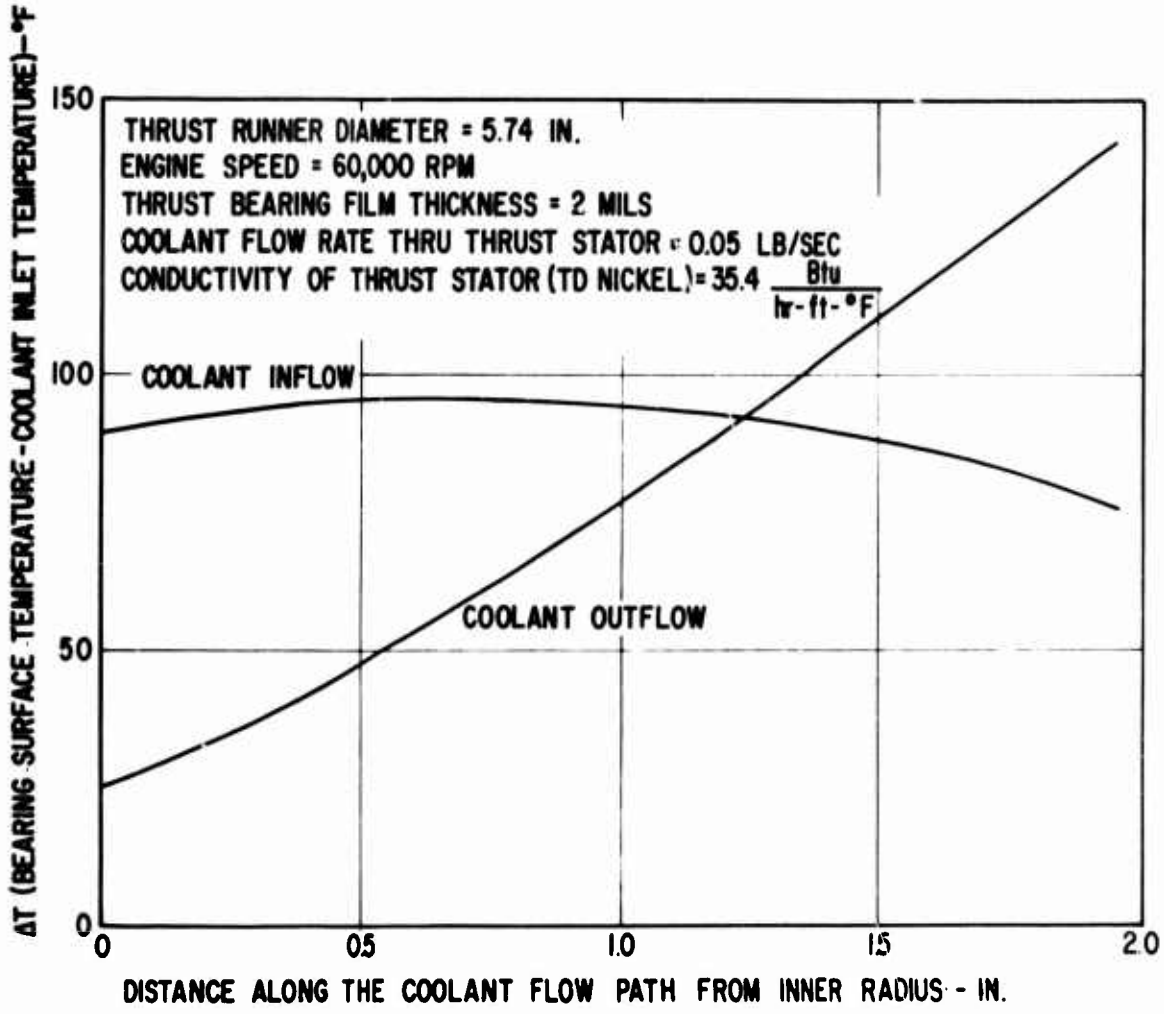


Figure 110. Effect of Flow Direction on Thrust Bearing Surface Temperature.

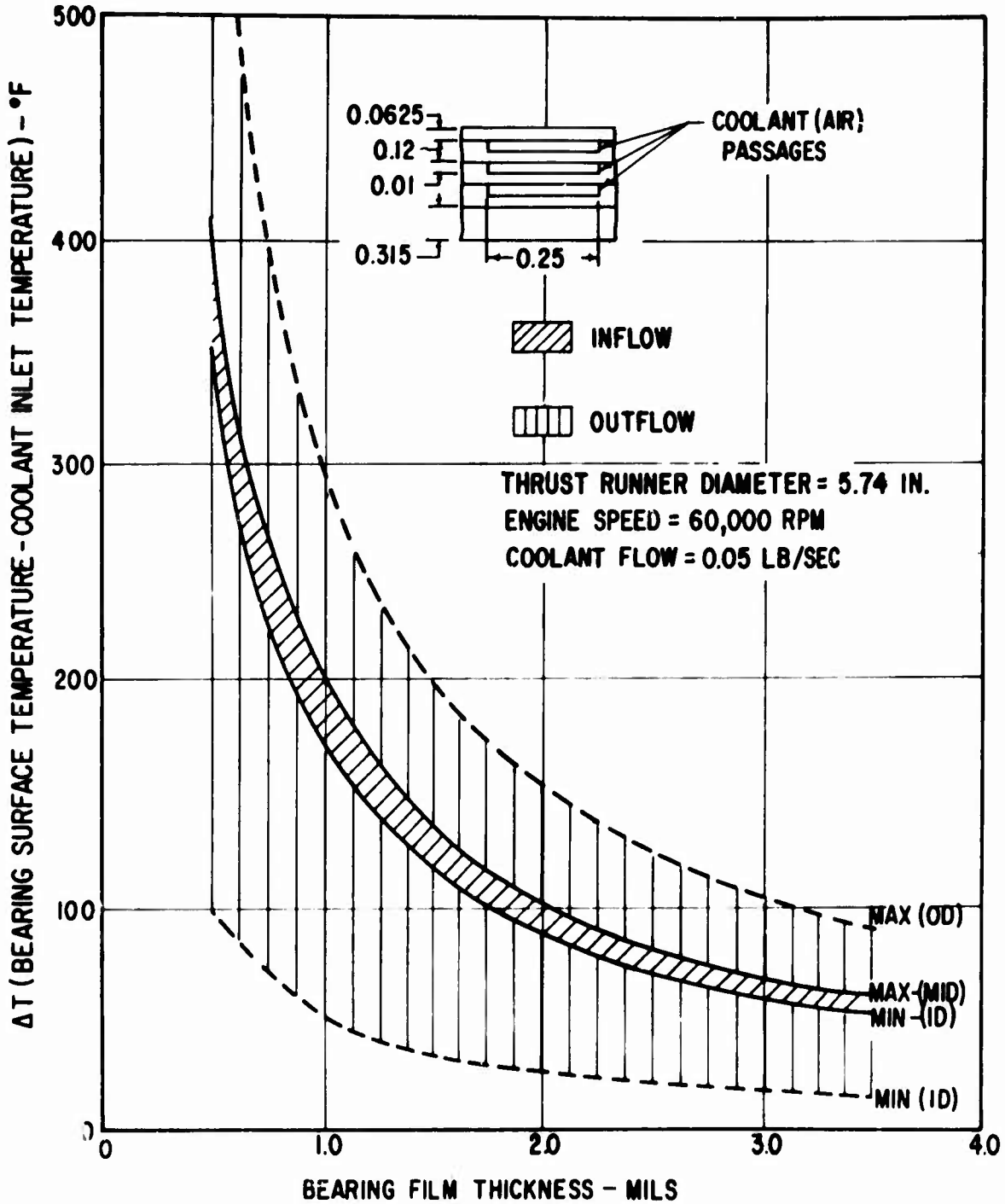


Figure 111. Effect of Bearing Film Thickness and Cooling Flow Direction on the Thrust Bearing Surface Temperature.

The reduction of cooling flow for the flight-idle condition was based on the physical limitation of available pressure gradient at this condition and also on the consideration that the heat generation rate reduces to 56 percent of that occurring at the 100-percent power condition of operation.

The temperature distribution and deformation results are plotted in pairs in Figures 112 through 119. It should be noted here that the scale in the thermal distortion map only shows the extent of distortion relative to the original flat surface. The spacing between stator and runner surface does not represent the true bearing gap. These results clearly indicate that at the 100-percent power and sea-level condition of operation, i.e., at zero load and 60,000 rpm, the two surfaces are essentially parallel to each other. Under a steadily applied 10g load, however, the facing surfaces become slightly convex, thus producing about 0.6 mil variation in the lubricant film thickness. Distortions at 45,000 rpm remain generally at the same level, with a 0.5-mil film thickness variation under zero-load condition and 0 6 mil at a 10g load.

The reader is reminded that these variations in film thickness are less than the maximum (0.8 mil) assumed for the distorted thrust bearing load capacity analysis discussed in the preceding section.

THRUST BEARING MOUNTING SYSTEM

The performance of air-lubricated bearings deteriorates quickly if the opposing surfaces do not remain parallel. An air thrust bearing for use in a gas turbine, which is basically a rather compliant structure subject to a wide range of temperature gradients and transients, must, therefore, be provided with self-aligning supports. The mounting of the stationary elements of the bearing (stators or thrust plates) enables the stators to self-align with the thrust runner. Basically, a self-aligning support accommodates static misalignment only, thereby allowing the thrust stators to remain essentially parallel to the thrust runner. No attempt is made to enable the stators to follow the once-per-rev (or more) run out of the runner. The essential features of a self-aligning support system for an air-lubricated thrust bearing are:

1. A support tilt stiffness significantly less than the tilt stiffness of the gas film. This ensures that misalignment (or change in alignment) between journal bearings is accommodated mainly by the support and not by the gas film.

2. A high axial stiffness. This ensures that changes in axial thrust load do not result in large axial movements of the rotor, thus avoiding wheel rubs or mismatch between compressor wheel and diffuser inlet.

3. An ability to accommodate the differential thermal expansions resulting from the radial temperature gradients encountered when operating over a wide range of engine performance conditions.

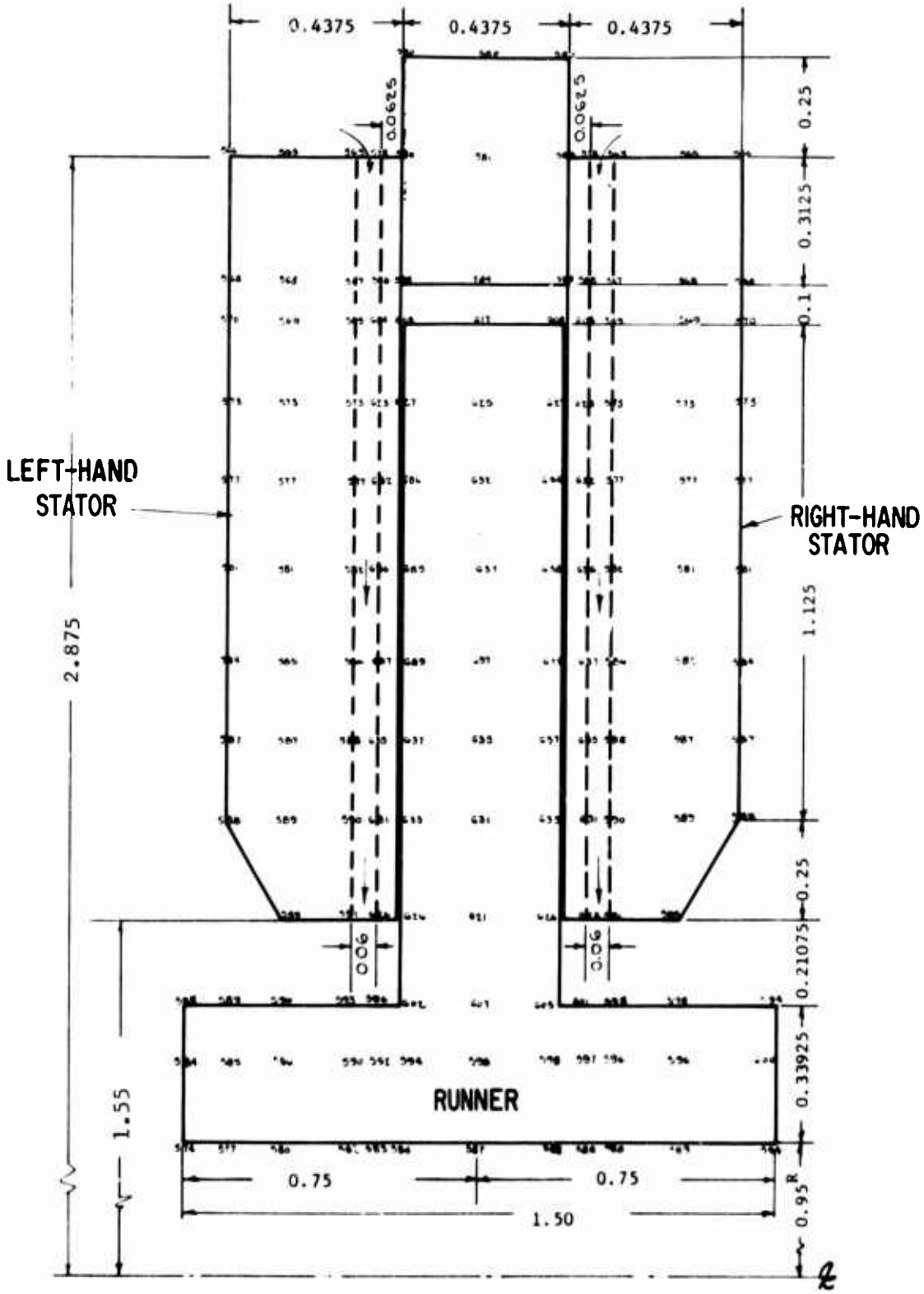


Figure 112. Temperature Distribution in Thrust Bearing at Zero Load (2-Mil Film Thickness); Speed 60,000 rpm; Cooling Flow 0.050 lb/sec Each Side.

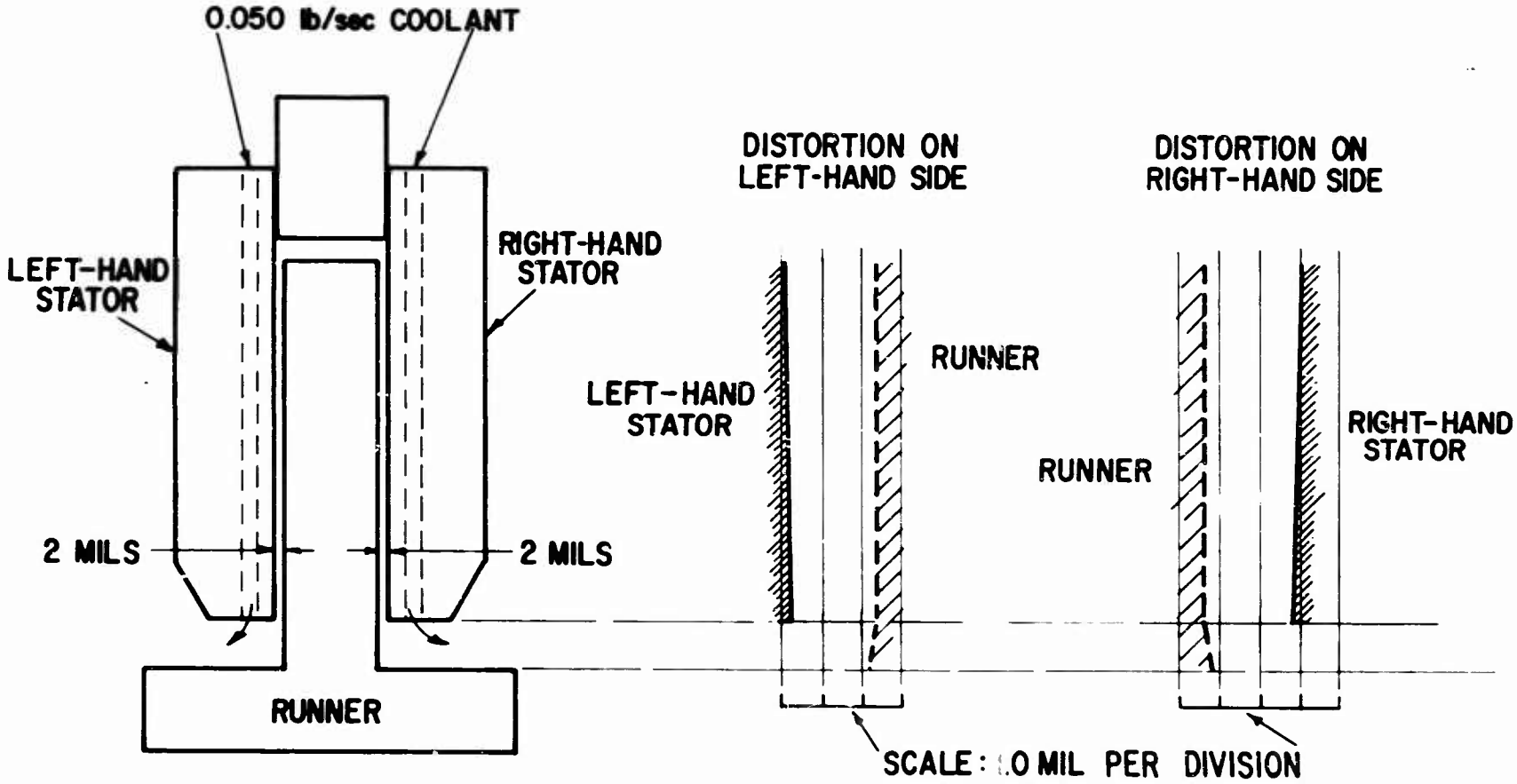


Figure 113. Thermal Distortion in Thrust Bearing at Zero Load (2-Mil Film Thickness): Speed 60,000 rpm; Cooling Flow 0.050 lb/sec Each Side.

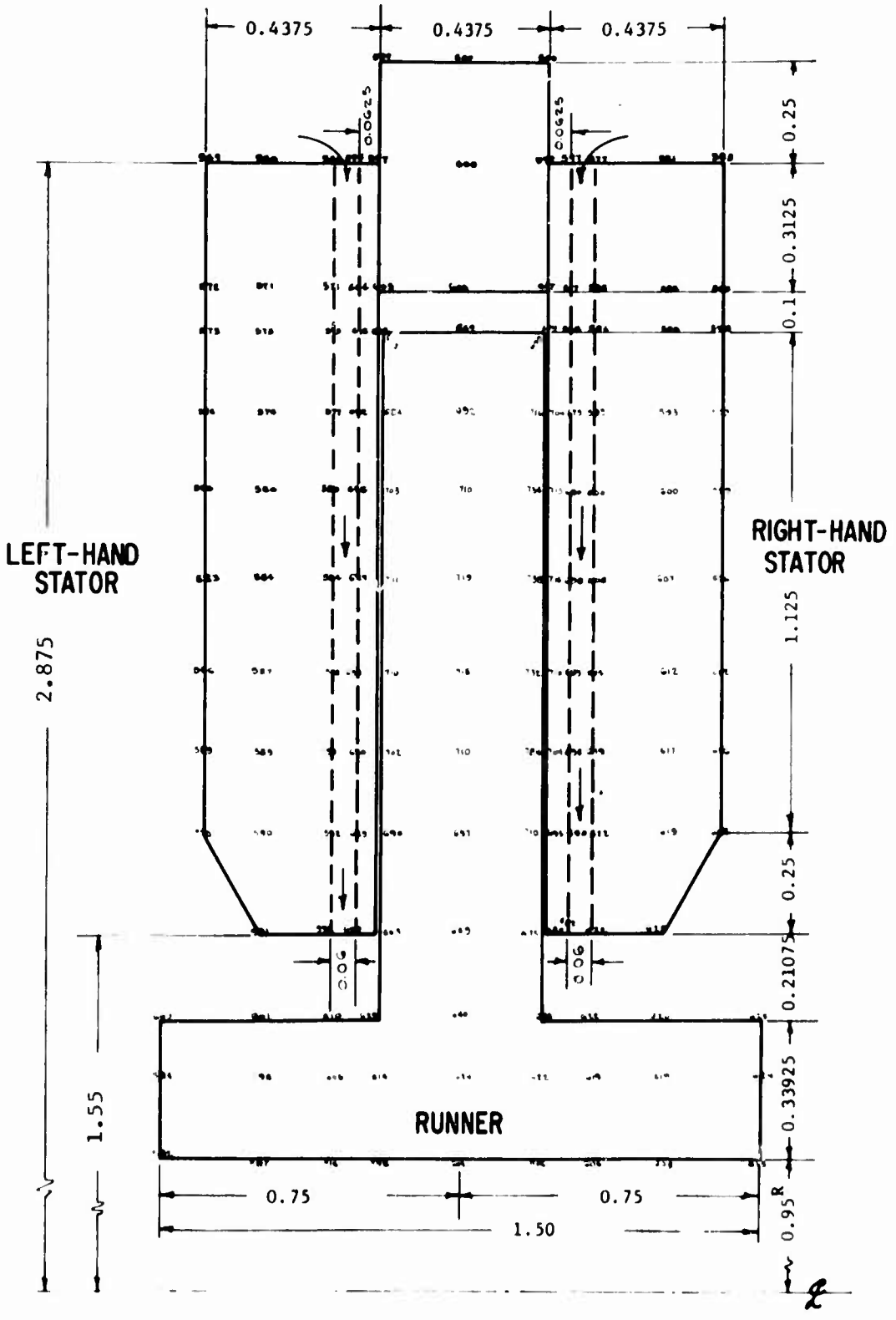


Figure 114. Temperature Distribution in Thrust Bearing at Continuous Maximum Load (10g – 1 Mil Film Thickness); Speed 60,000 rpm; Cooling Flow 0.050 lb/sec Each Side.

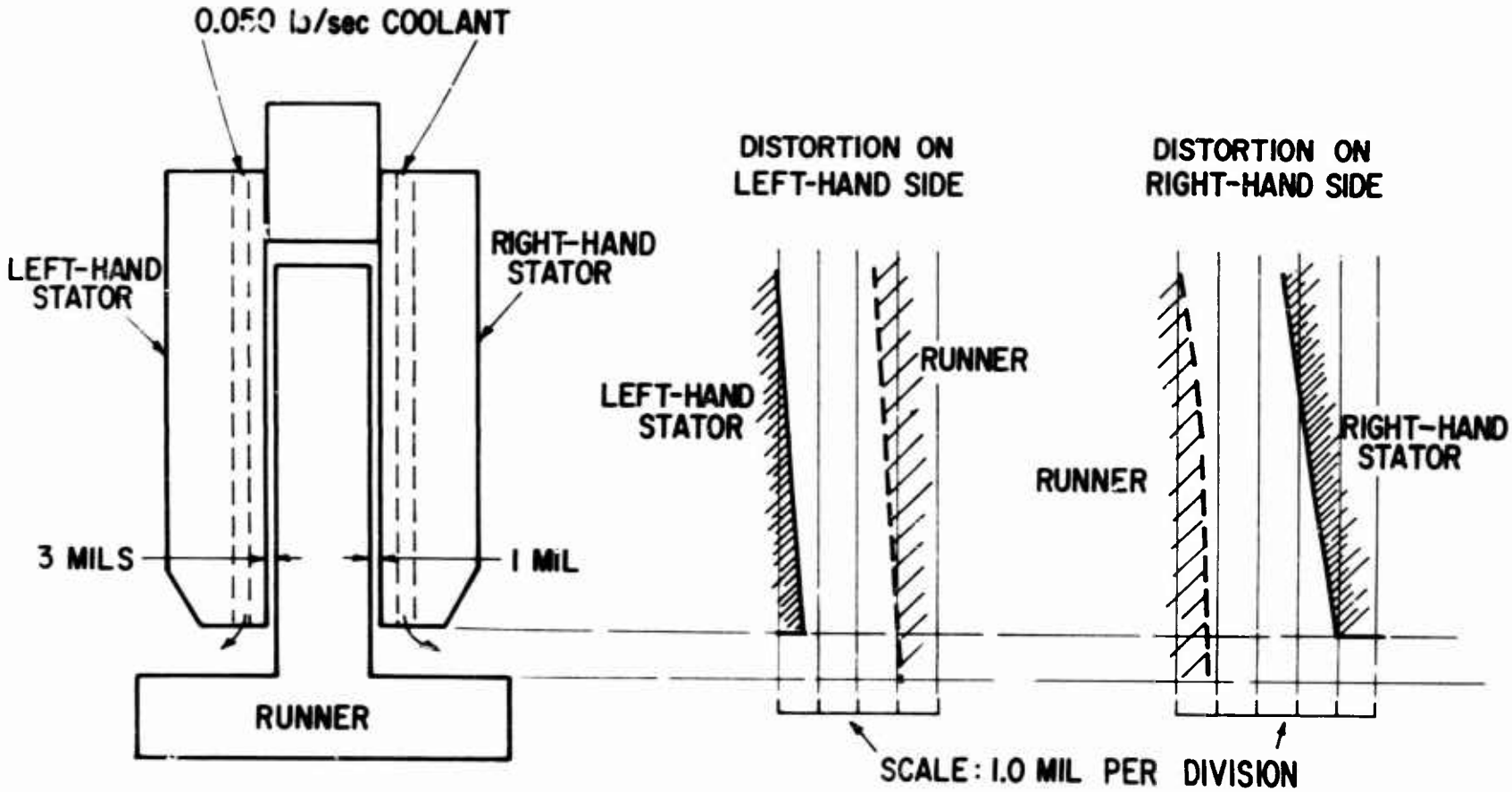


Figure 115. Thermal Distortion in Thrust Bearing at Continuous Maximum Load (10g — 1-Mil Film Thickness), Speed 60,000 rpm; Cooling Flow 0.050 lb/sec Each Side.

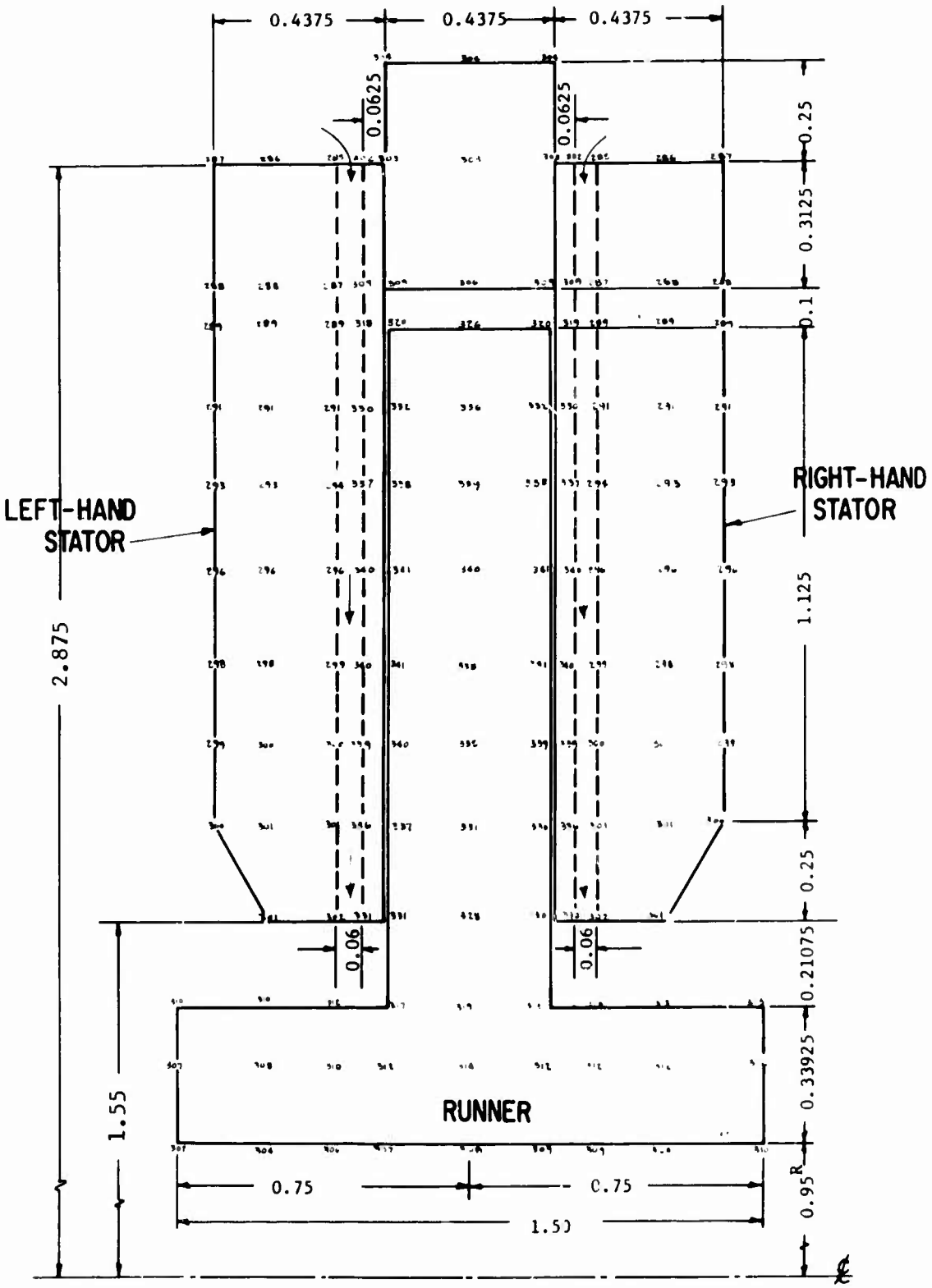


Figure 116. Temperature Distribution in Inrust Bearing at Zero Load (2-Mil Film Thickness); Speed 45,000 rpm; Cooling Flow 0.025 lb/sec Each Side.

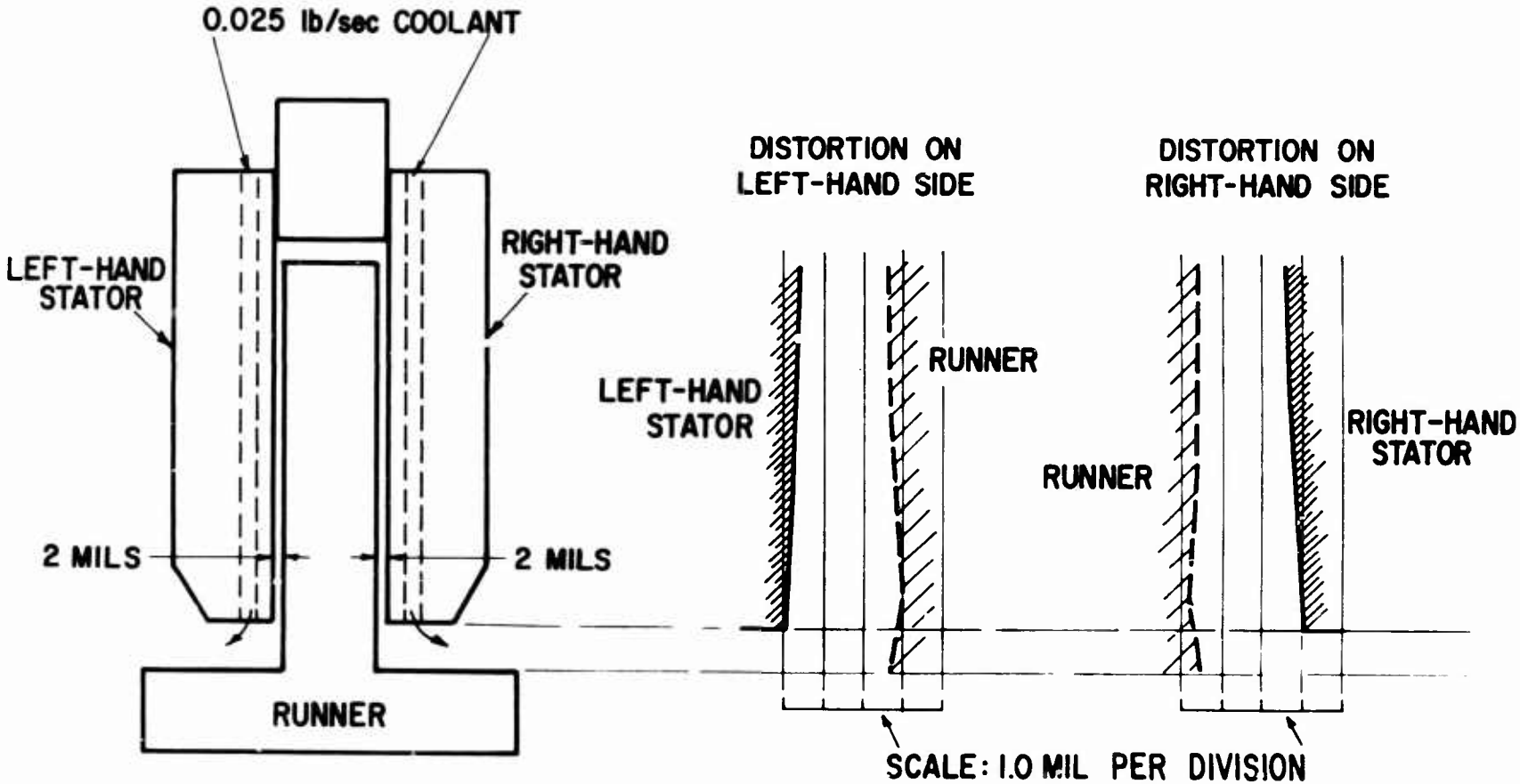


Figure 117. Thermal Distortion in Thrust Bearing at Zero Load (2-Mil Film Thickness); Speed 45,000 rpm; Cooling Flow 0.025 lb/sec Each Side.

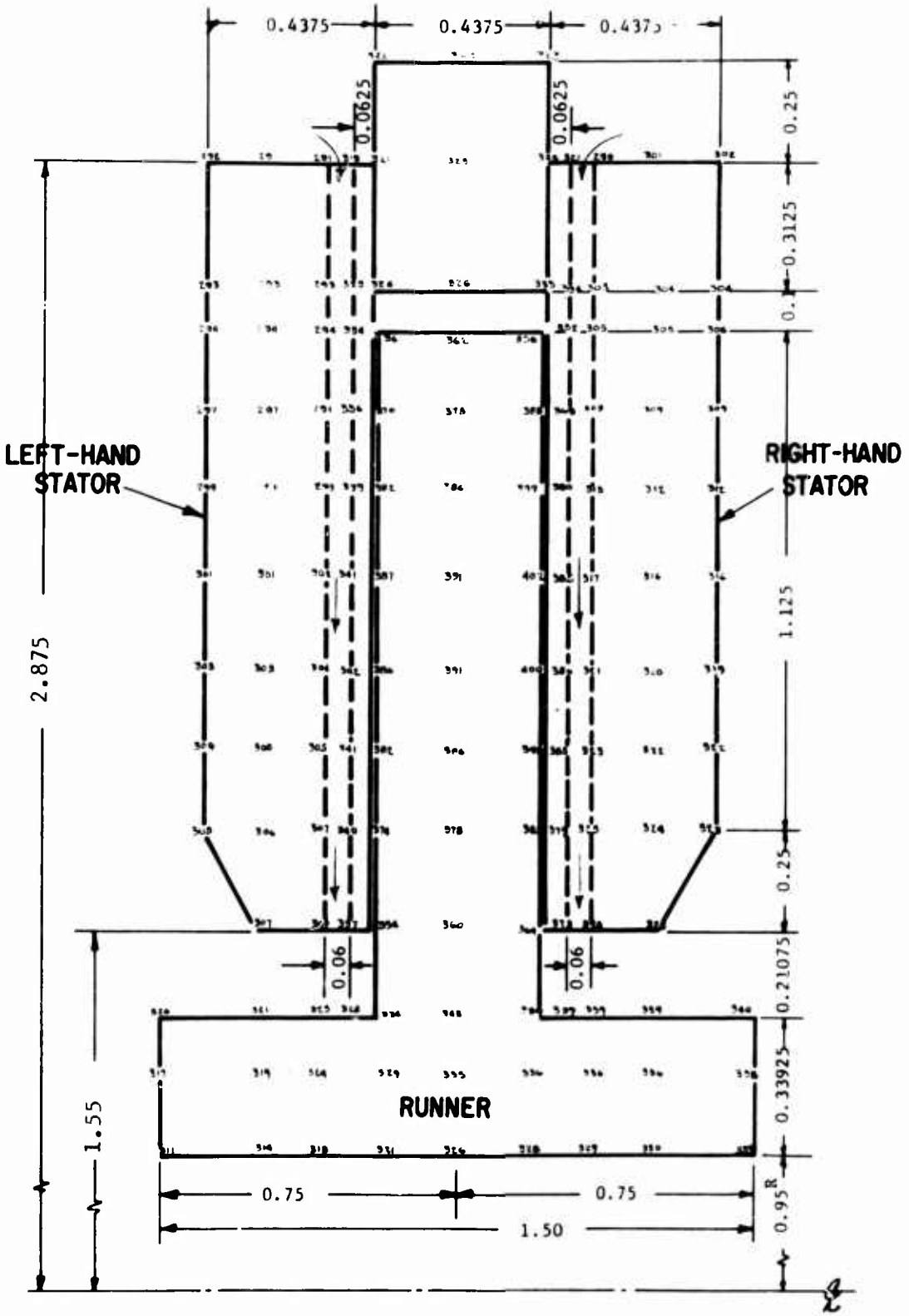


Figure 118. Temperature Distribution in Thrust Bearing at Continuous Maximum Load (10g — 1-Mil Film Thickness); Speed 45,000 rpm; Cooling Flow 0.025 lb/sec Each Side.

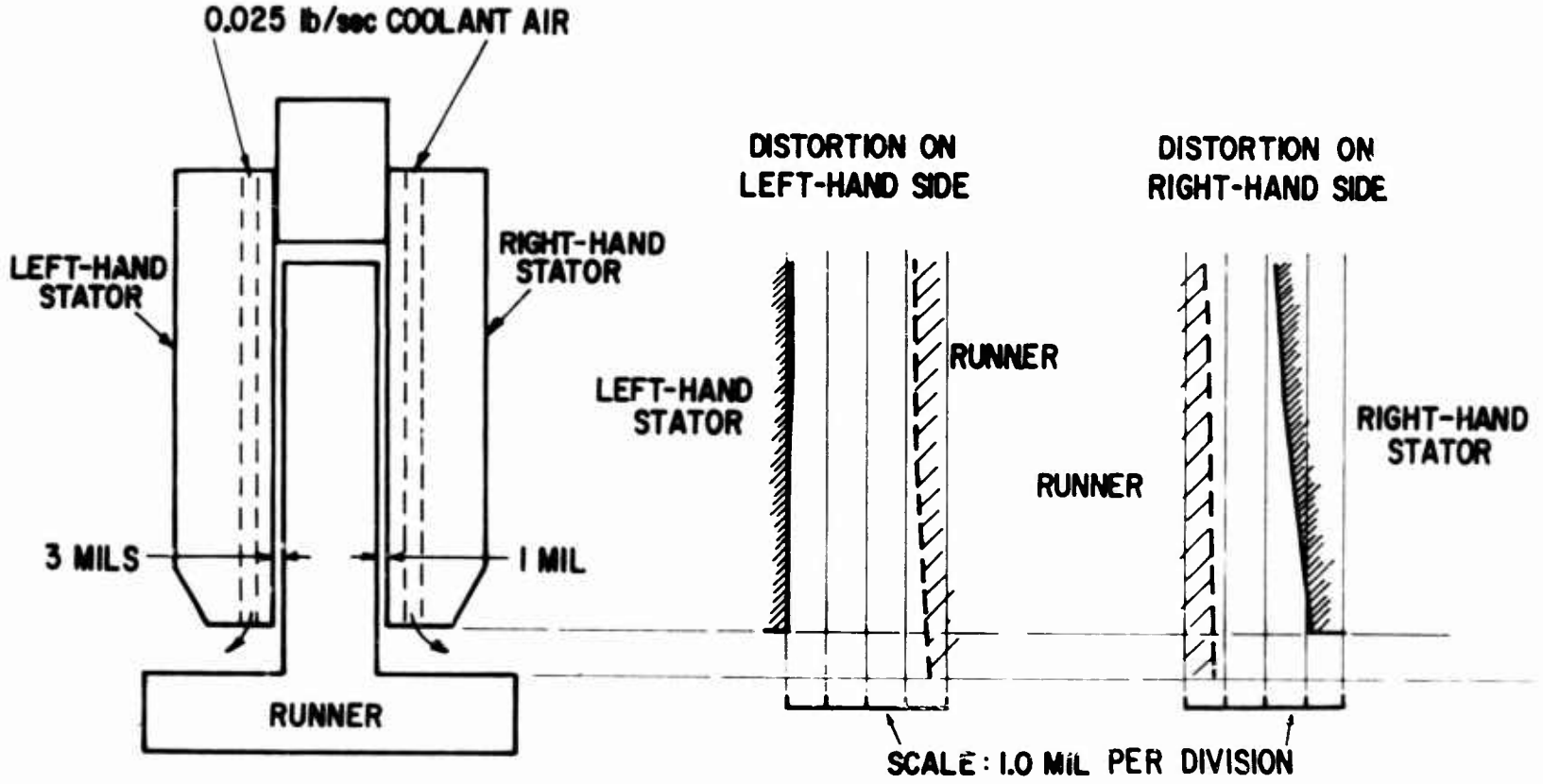


Figure 119. Thermal Distortion in Thrust Bearing at Concinuous Maximum Load (10g — 1-Mil Film Thickness); Speed 45,000 rpm; Cooling Flow 0.025 lb/sec Each Side.

4. The ability to operate in a stable manner, i.e., the dynamic behavior of the support system, when considered in conjunction with rotor-bearing performance, must not interfere with the proper operation of the air thrust bearing.

Over a number of years, several support systems have been developed which possess the essential features required for proper thrust bearing operation. These supports, which have been built and tested in a number of applications, fall into two categories; namely, radial supports and axial supports. In this application the lack of axial space, which results from the need to keep the rotor length to a minimum in order to satisfy the critical speed criterion, allows the use of radial supports only. One such support is shown in Figure 120. In this design, alignment is achieved as a result of bending of the four tangential spokes. Differential radial thermal expansion is accommodated by rotation of the inner ring relative to the outer ring. Unfortunately, suitable proportions of the spokes, to give the desired values of support tilt stiffness, cannot be achieved for the present application because of physical size and stress limitations.

An alternate arrangement for achieving alignment is the gimbal. This device, which, in various forms, has been in use for many years, usually has bearings or pivots on each axis. For air bearing applications, the use of flexures instead of bearings is considered to be more suitable. Several flexible pivot arrangements and concepts were evaluated, including "Free-Flex" flexural pivots, "T" flexures, and axial pin flexures.

A modified version of the "Free-Flex" flexural pivot was established as the most suitable. The details of the design of the thrust bearing mount are discussed in more detail later in the report where the engine simulator design is described.

THRUST BEARING STABILITY

A potential problem which exists for any high-speed rotating machine is bearing-excited rotor-bearing system instability. The problem of instability has been recognized for many years, primarily with respect to journal bearings. For example, the notorious fractional-frequency whirl of self-acting, gas-lubricated, plain journal bearings has limited application of these bearings to low-speed, horizontal rotors. By applying external pressurization to the plain journal bearing (i.e., hybrid operation), the instability threshold speed can be raised to approximately twice the first critical speed of the rotor. However, even this approach is insufficient for the subject air-bearing engine concept. Consequently, to gain the maximum potential for stable journal bearing operation, self-acting pivoted-pad bearings have been selected. The pivoted-pad journal bearing is the most stable of currently known, practical, gas bearing types.

Until very recently, MTI has been aware of only one instance of instability (aside from pneumatic hammer) of a gas-lubricated thrust bearing. This occurred during one of our early developments when a self-acting spiral-grooved thrust bearing was operated at abnormally low ambient pressures (approximately 2 psia). The thrust plate in this instance was supported

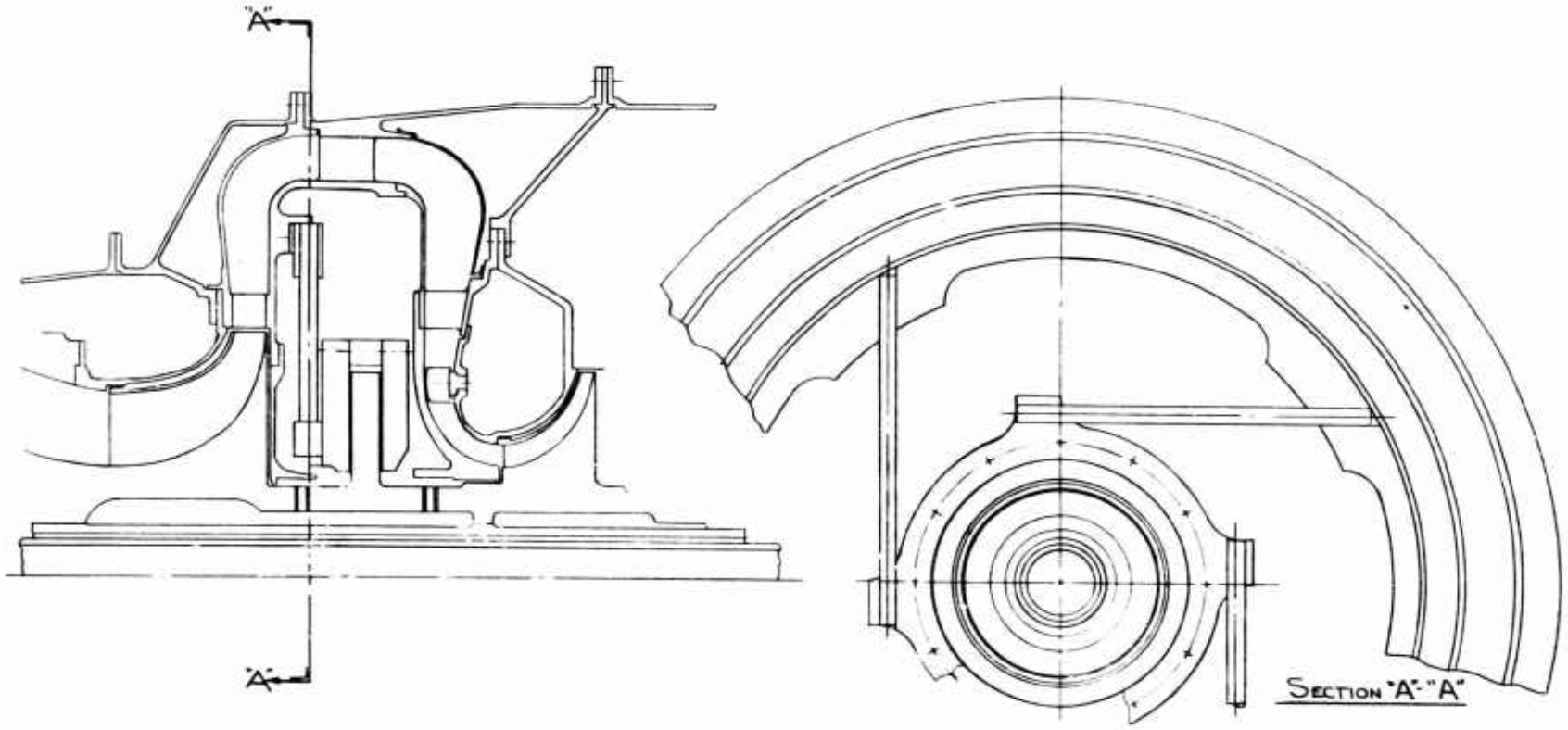


Figure 120. Thrust Bearing Support Flexure With Tangential Spokes.

by beam-type flexures to give the plate angular self-aligning capability. Since that time, MTI has built a number of self-aligning thrust bearing assemblies, using various designs of beam-type flexures, without any occurrence of bearing instability.

During the Task 4 design studies for the subject program, the use of self-aligning thrust bearing supports using beam-type flexures was investigated. It was found that beam-type flexure supports are not suitable for the 3.5 lb/sec $C_{o_o}T_o$ air-bearing engine concept because of excessive axial deflections with this type of mount. Consequently, a txo-axis gimbal-type thrust bearing support using flexure pivots was designed as discussed in the preceding section. These supports have the desired attributes of high axial stiffness, short axial length, and low angular stiffness. However, the use of a gimbal-type mount raised a question about thrust bearing stability, for reasons which had only recently come to our attention.

In November, 1969, a case of thrust bearing instability was encountered on the NASA-Lewis gas-lubricated Brayton Rotating Unit (BRU). The instability occurred in the thrust bearing mount and prevented design-point operation of the BRU.

NASA had the problem analyzed to establish that the instability could be predicted analytically and was resolvable by changes in design (Ref. 9).

The BRU thrust bearing is a self-acting Rayleigh-Step bearing supported by a two-axis self-aligning gimbal mount. The BRU analysis definitely identified the Rayleigh-Step gas film as the source of the instability excitation. The analysis also showed that proper selection of the gimbal-mount torsional sitffness and/or inertia could stabilize the thrust bearing.

Because of this recent experience of instability in a gimbal-mounted thrust bearing, and because of the relative ease with which a thrust bearing stability analysis could be accomplished, an analysis of the gimbal-mounted spiral groove bearing was undertaken late in Phase I of the program. Such an analysis was deemed prudent during the design phase for the following reasons:

1. The 3.5-lb/sec engine thrust bearing operates at considerably higher maximum speeds than the BRU (72,000 rpm versus 43,000 rpm). The possibility of encountering instability problems is inherently increased with higher speeds.

2. Should thrust bearing instability be a problem, but not be identified until the Phase II simulator test program, considerably more cost would be involved to correct the problem at that point than if identified and corrected during the Phase I design study. A stability problem identified during the simulator test program would require a stability analysis to be performed at that time. In addition, bearing parts would have to be redesigned, the new or modified parts then made, the simulator reassembled, and

additional testing performed. Besides the additional redesign, shop, assembly and testing costs, the Phase II test program would be subjected to considerable delay.

Technical Approach

To perform the stability analysis, the well-established frequency-domain stability analysis technique was employed. The major aspects of this technique are: (1) frequency-dependent dynamically perturbed bearing film forces and moments, and (2) a parametric search for the roots of the characteristic frequency equation resulting from the equations of motion for the thrust bearing gimbal mount. Digital computer programs are, of course, utilized for these calculations.

The computer program for calculating the frequency-dependent bearing film forces and moments for spiral-grooved thrust bearings was already available at MTI. Only minor input-output adaptations were required to implement the stability analysis. The characteristic matrix for the mathematical model of the two-axis gimbal mount (including the rigid thrust plate assembly) was derived and programmed for searching out the instability thresholds as a function of the thrust bearing design parameters and operating conditions. The details of this portion of the analysis are given in Appendix I.

From the computer solutions, stability maps to cover the appropraite ranges of fluid-film conditions, inertia parameters, and torsional stiffness values for the gimbal design were prepared.

Thrust Bearing Stability Maps

The thrust bearing design selected for the engine was described in the preceding section of this report. As discussed later in this report in the sections concerning the thrust bearing component tests, it was found that this thrust bearing design was unstable. This design was then modified by changing the spiral groove geometry. The stability analysis computer program which was nearing completion during the experimental phase was used to guide the redesign.

Experiments conducted on the modified thrust bearing indicated that it would be stable over the engine operating range provided proper thrust stator inertia properties were maintained. These results are discussed in the section entitled "Results of Modified Thrust Bearing Tests".

The differences between the engine and the bearing element test rig thrust bearing should be pointed out here. The bearing surface geometry, spiral-groove pattern and size of the test bearing were identical to those previously described for the engine. The method of mounting was, however, different. The test thrust bearing stator was mounted on an axial post which was flexible in its bending mode. This flexibility provided the bearing its angular self-aligning capability. The engine thrust bearing derives its self-aligning capability by means of a gimbal ring mount. As discussed later, the method of mounting is a significant factor affecting

thrust bearing stability. The aforementioned modified thrust bearing involved changes in both the spiral groove pattern and the test rig mount design.

The stability analysis for the gimbal-mounted thrust bearing was applied to the modified thrust bearing spiral-groove geometry to assess the stability characteristics of the engine bearing assembly.

Stability maps were prepared for the four conditions of engine operation which bracket the operating speed and bearing-pressure-level envelope. These conditions were:

1. Sea Level - Flight Idle
2. Sea Level - 100% Power
3. 25,000 ft - Flight Idle
4. 25,000 ft - 100% Power

Each condition was evaluated at zero and 277 pounds (maximum design condition) thrust load.

The stability maps for these conditions are shown in Figures 121-124. These maps are plots of the critical thrust bearing stator (I_T) and gimbal ring (I_G) inertias. The area generally below and to the right of each plot is the stable operating region. Thus the maps are created independently of the bearing and mount inertias. From the maps, the required inertias to achieve stability can be found.

The engine (and simulator) bearing design point in terms of stator (I_T) and gimbal ring (I_G) inertias is indicated on each map. As can be seen from the maps in Figures 121-124, the modified bearing design is well within the stable region under all of the engine operating conditions that were calculated.

ENGINE CRITICAL SPEEDS

Since air bearings have very low inherent damping capacity relative to oil-film bearings, a rotor with air-lubricated bearings is generally more prone to exhibit resonant unbalance response amplitudes at rotor critical speeds. Because of the absence of boundary lubrication in air bearings, any conditions which could result in repeated bearing contacts, whether induced by resonant unbalance response or by externally applied vibration and shock, must be avoided if at all possible. It follows that the rotor-bearing system should be designed to avoid operation at or near the rotor critical speeds. The avoidance of operation near the third critical speed is probably the most important; for this reason, a criterion for design acceptability has been established which requires that the third critical should not occur at a speed below 133 percent of engine overspeed (160 percent of design speed).

Based on the proportions shown in the conceptual layouts of the gas generator and the rotor given in Figure 68, a critical speed analysis was performed. This computer-solved analysis computes rotor-system undamped transverse

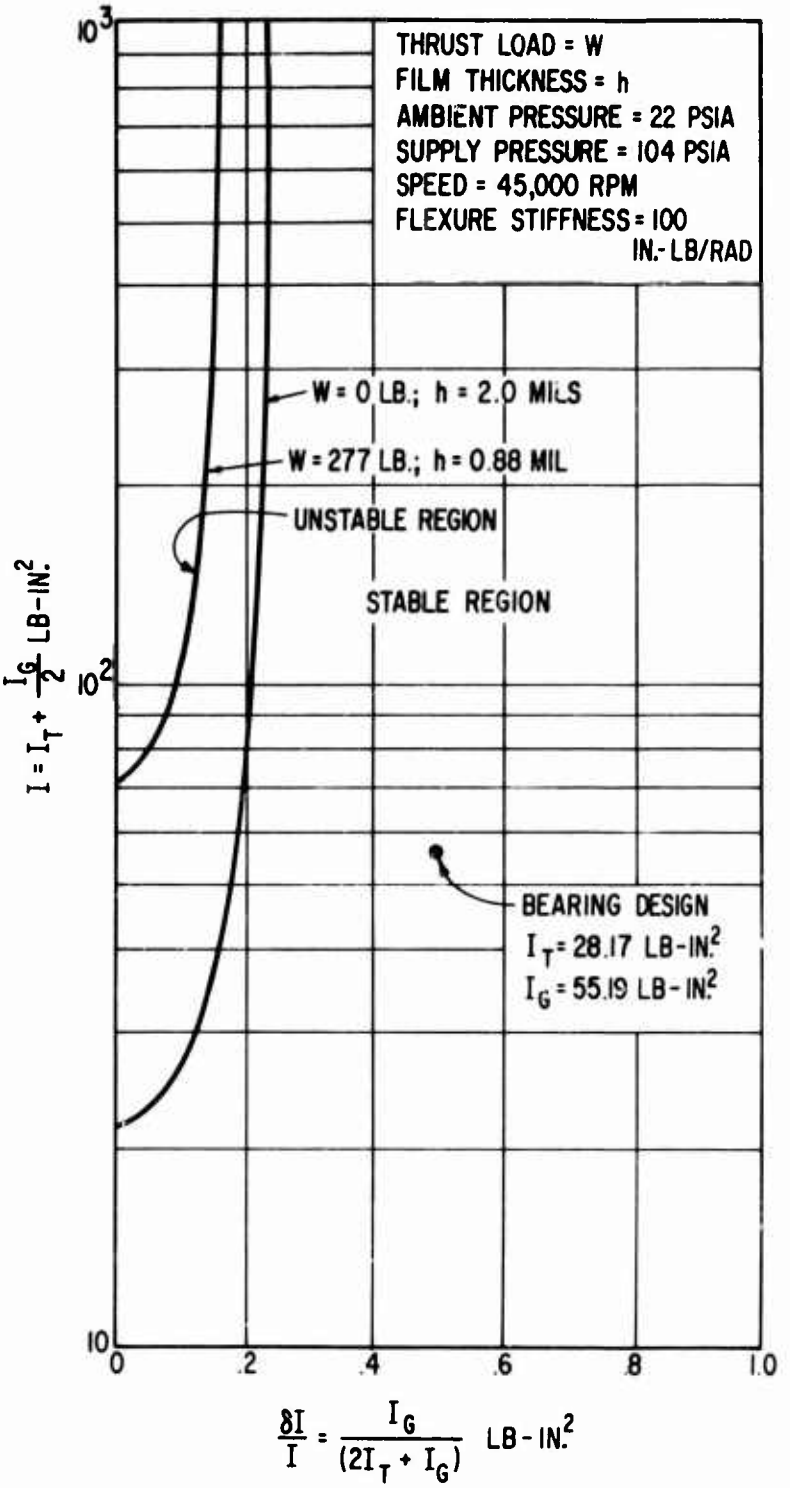


Figure 121. Thrust Bearing Stability Map for Sea-Level, Flight-Idle Condition.

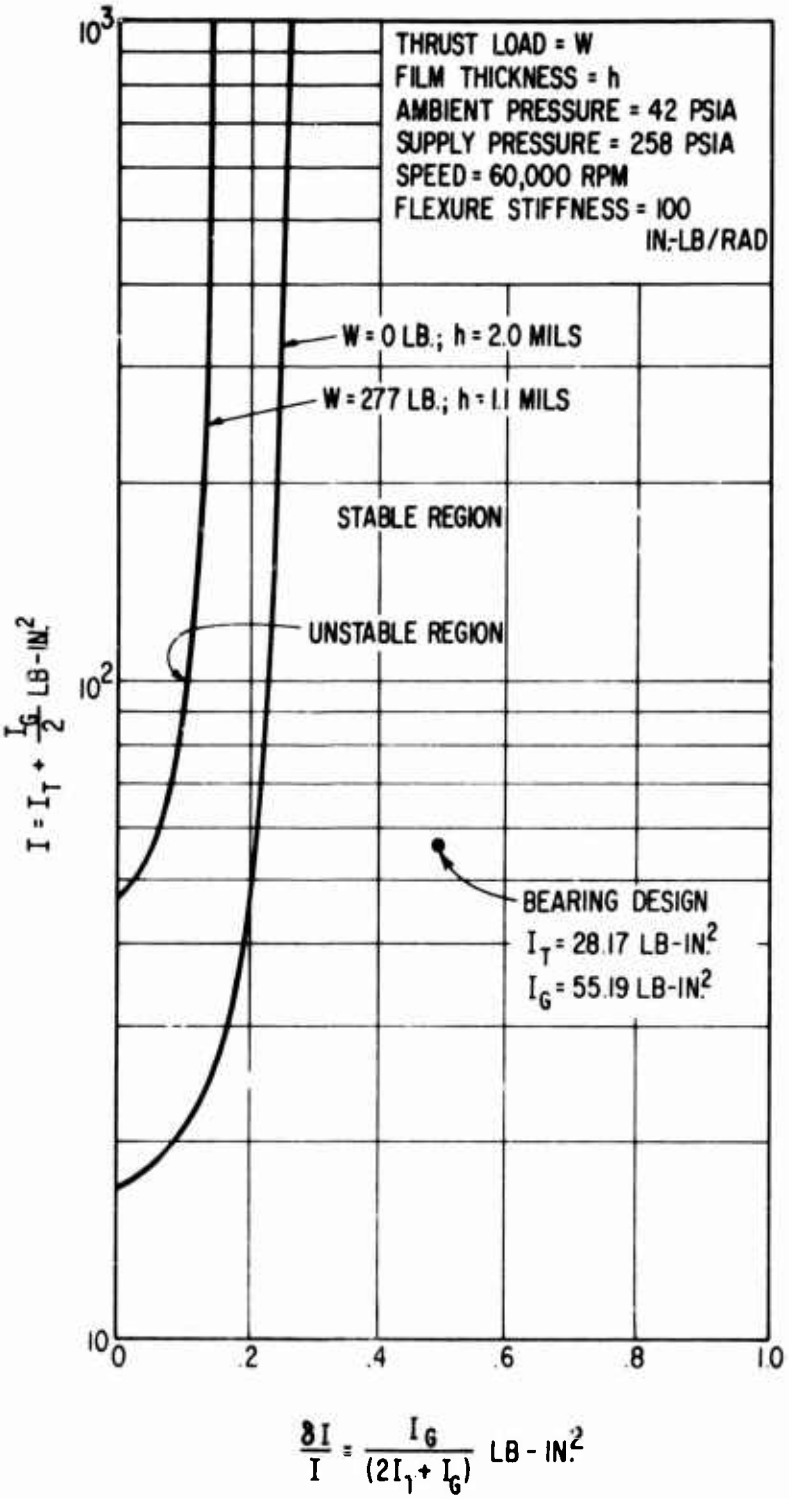


Figure 122. Thrust Bearing Stability Map for Sea-Level, 100-Percent Power Condition.

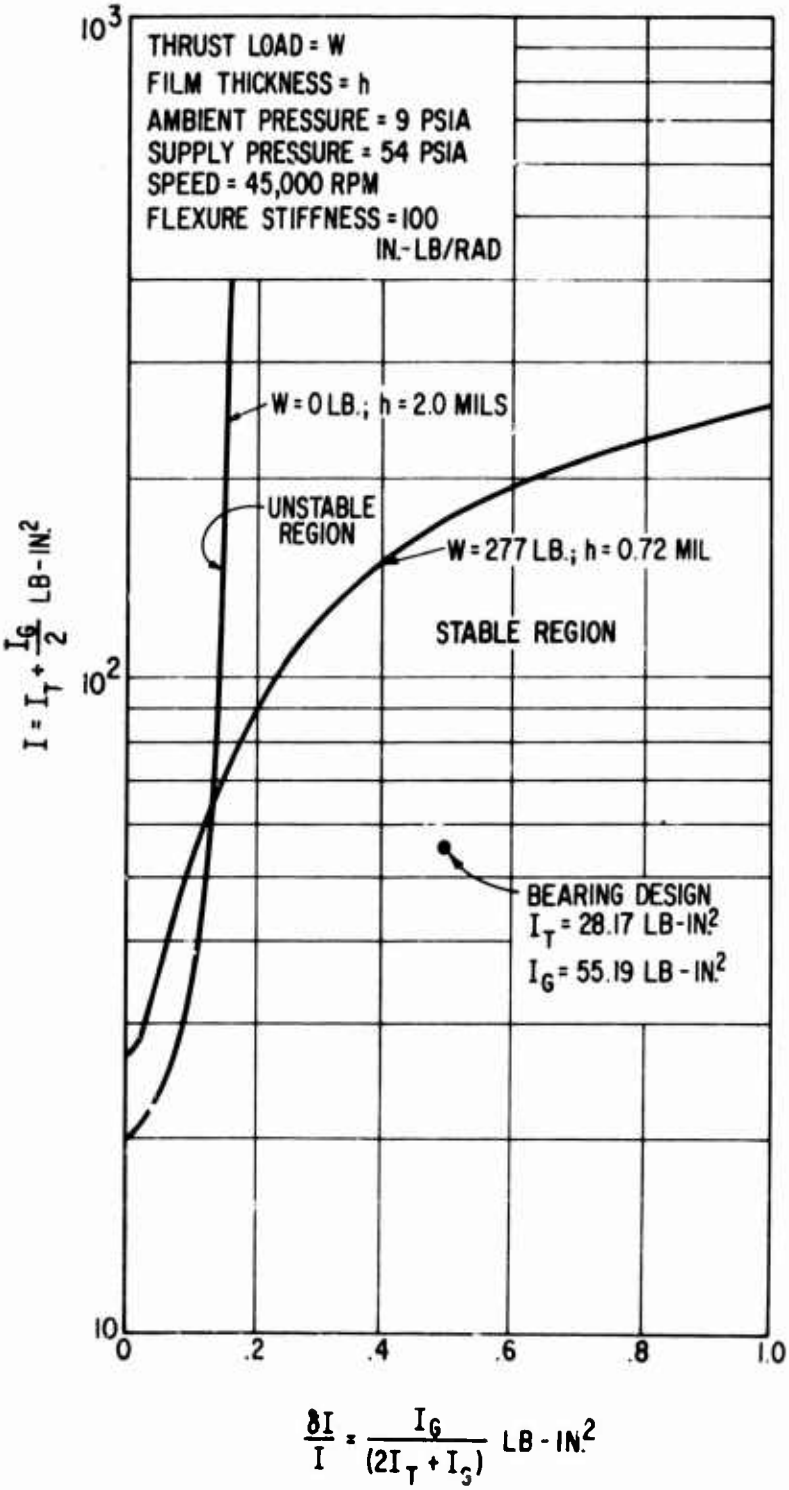


Figure 123. Thrust Bearing Stability Map for 25,000 Feet, Flight-Idle Condition.

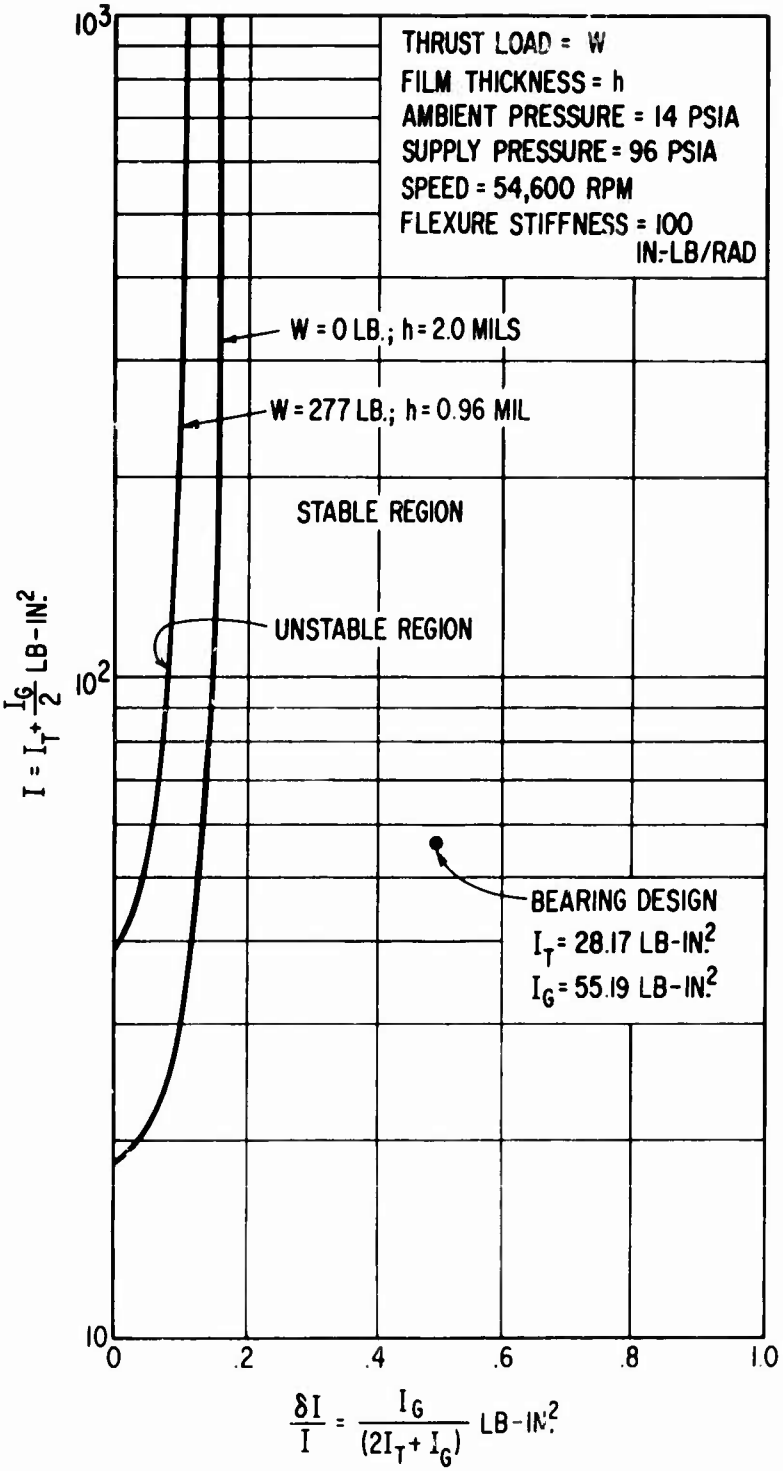


Figure 124. Thrust Bearing Stability Map for 25,000 Feet, 100-Percent Power Condition.

natural frequencies (critical speeds) and corresponding mode shapes, taking into account the stiffness and mass characteristics of both the rotor and the bearings. The results are plotted in Figure 125. Superimposed on the critical speed curves are two cross-hatched areas which show the range of bearing stiffness to be expected over the operating speed range. The two areas are used to show the effect on bearing stiffness of increasing the bearing load from the normal operating condition to the load resulting from maximum maneuver conditions.

Resonant amplitudes of vibration would be expected at any point where the bearing stiffness curve intersects the critical speed curve. Figure 125 clearly indicates that the gas generator operating speed range will not involve passing through any of the critical speeds. However, during engine startup and shutdown, the first and second critical speeds will be encountered. These two criticals are commonly referred to as rigid-body criticals because there is little or no bending of the shaft and the mode is that of the rigid (non-bent) shaft vibrating on the bearing fluid film. Since the shaft is rigid and the speeds low, rigid-body criticals possess little energy and the inherent damping properties of the bearings are sufficient to adequately attenuate the vibration amplitudes to within acceptable limits.

From Figure 125 it can be seen that the third critical speed, which is definitely a flexural critical, meets the criterion of being at least 133 percent above overspeed (96,000 rpm).

ROTOR-BEARING DYNAMIC SIMULATOR

As has been discussed previously in this report, a conceptual design of a 3.5-lb/sec engine was defined. A rotor-bearing simulator has, in turn, been designed which is based on the rotor-bearing system contained in the engine design. The simulator design objective is to obtain a rotor having the same properties of mass, mass distribution, moments of inertia and bearing span as those in the engine. When such a rotor is supported on the air bearings designed for the engine, tests can be conducted to determine bearing and rotor-bearing system performance. To accomplish this end without incurring the complexities, power levels, and temperatures of a yet undeveloped engine requires the use of unbladed wheels and a means of driving the rotor. The rotor-bearing simulator design shown in Figure 126 meets these requirements. In addition to meeting these requirements, the simulator will have the capability of changing test parameters independently, thereby allowing more flexibility during the test program than would be possible if the engine itself were being tested.

The ability to test the simulator over the full range of conditions expected in an aircraft gas turbine requires that substantial dynamic loads be applied to both journal and thrust bearings. In the simulator design, the required loads will be achieved by two means. Dynamic journal bearing loads will be applied (and sustained) by rotating the simulator on a turntable, the gyroscopic couple resulting from turntable rotation providing

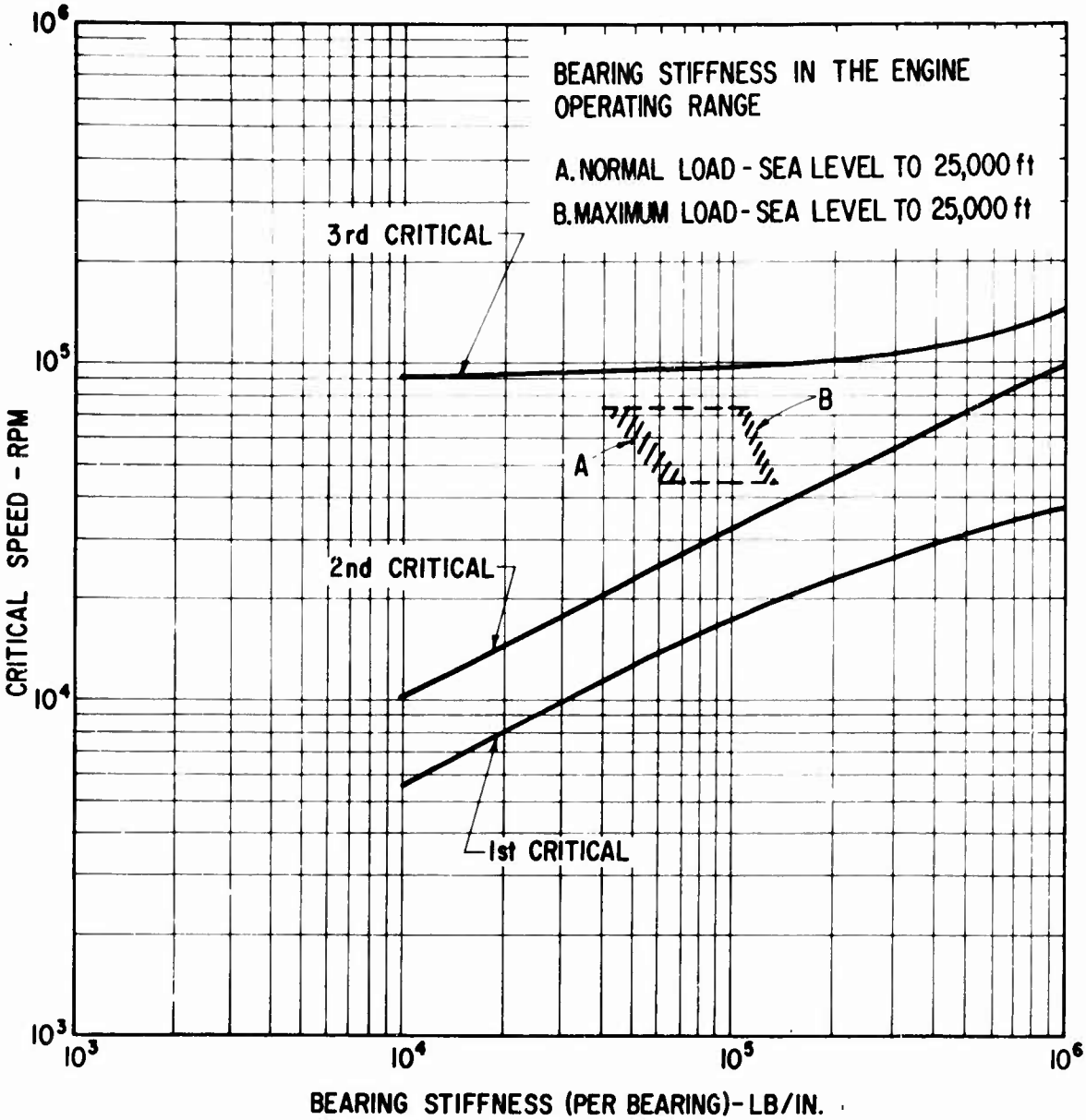


Figure 125. Critical Speeds of Gas Generator Rotor for a 3.5-lb/sec Flow-Rate Engine.

the journal bearing load.* Abrupt vertical and low-frequency sinusoidal motion of the turntable will be used to impose short-duration (shock) and large-amplitude vibration loads on the journal bearings. With the axis of the simulator turned 90 degrees, i.e., vertical rotor, simular loads can be applied to the thrust bearing. Steady-state loading of the thrust bearing, up to the maximum level (10g) resulting from maneuver conditions, is accomplished by means of pneumatic load pistons within the simulator.

Rotor-Bearing Arrangement

The rotor-bearing simulator design is shown in Figure 126. The rotor configuration is the same as the gas generator rotor-bearing system with minor exceptions. The rotor, like the engine rotor, is constructed of five components: a simulated titanium first-stage compressor wheel, a titanium thrust runner, a simulated titanium second-stage compressor wheel, a simulated Waspaloy turbine wheel, and a 4340-alloy-steel tie bolt. All simulator rotor materials are identical to the engine rotor materials except the simulated Waspaloy turbine wheel. In this case, Waspaloy was substituted for IN-100 nickel alloy to expedite material procurement and to reduce simulator costs. The pertinent mechanical properties of these materials are:

	Waspaloy	IN-100
Density ($lb/in.^3$)	0.296	0.280
Mean Coefficient of Thermal Expansion $70^{\circ}F$ to $800^{\circ}F$ ($in./in.^{\circ}F$)	7.6×10^{-6}	7.5×10^{-6}
Dynamic Modulus of Elasticity at $800^{\circ}F$ (psi)	27.6×10^{6}	28.1×10^{6}
Thermal Conductivity at $800^{\circ}F$ ($Btu/ft^2/hr/^{\circ}F/ft$)	9.1	9.8
Yield Strength at .2% Offset at $1000^{\circ}F$ (ksi)	105	128

As can be seen from the tabulated properties of the two materials, Waspaloy is ideally suited for this substitution. IN-100 is required for the turbine wheel in the engine because of its elevated-temperature strength properties Since the simulator test program will not require temperatures approaching turbine inlet, this substitution is possible. The four wheels and attendant bearing components are connected by curvic couplings and held together with a 4340-alloy-steel tie bolt. The weight of the engine

* The reader is reminded that the major portion of the design bearing load is a result of the gyroscopic forces as defined in MIL-E-5007C.

compressor and turbine vanes and shrouds have been added to the respective simulator wheels in such a way that the mass and inertia properties of the simulator wheels are nearly the same as the engine wheels. An impulse turbine has been added to the first-stage compressor wheel to provide a means of driving the rotor. The titanium thrust runner for the simulator is identical to that in the engine. However, the overall length of the simulator rotor is 0.6 inch longer than the engine rotor. This added length is required to provide space for one additional labyrinth seal on the compressor end of the rotor. This seal is used to seal a cavity at the end of the rotor which is used to supply a pressure on the rotor end to produce the load on the thrust bearing.

The calculated critical speeds and mode shapes of the 3.5-lb/sec C_8-T_8 engine and rotor bearing simulator are shown in Figures 127 and 128. ^{o}It is seen from these plots that the objective of duplicating the engine dynamic characteristics with the rotor bearing simulator has been closely achieved.

Overall Temperature Control

One major objective of the simulator test program is to achieve the same bearing temperature levels as are anticipated for the engine. This is necessary to demonstrate that the bearing mechanical and thermal design is capable of tolerating the bearing internal distortions caused not only by load and inertia forces but also by internal thermal gradients. However, before subjecting the simulator to elevated temperature tests, low-temperature testing will be accomplished to identify any yet unforeseen problems and to develop the necessary equipment operational experience. The rotor-bearing simulator has therefore been designed to test the gas-generator rotor-bearing system both at "low" temperatures and at the temperatures predicted for the engine.

There are inherently two major sources of heat within the simulator: (1) bearing friction heat and (2) windage losses of the simulated compressor and turbine wheels. The method of removing the heat produced by bearing friction in the simulator is identical to the method used in the engine.

The compressor-end journal bearing is "shunt" cooled. This concept uses a beryllium sleeve, held inside the journal with a shrink fit to conduct the heat to the first-stage compressor wheel, which acts as a heat sink. The first-stage compressor wheel in turn is cooled by the drive turbine exhaust. The simulator thrust bearing is air cooled exactly as the engine thrust bearing except that it has an independent air supply. Monitoring the temperature, pressure and flow of the thrust bearing cooling air along with distortion of the thrust plates due to thermal gradients will enable the simulator test to thoroughly evaluate the thrust bearing thermal design concept.

The turbine-end journal bearing, as in the engine, is air cooled. It will be remembered from the discussions regarding the engine that the turbine bearing cooling air flow is ducted from the thrust bearing cavity through an annular channel under the turbine to the turbine bearing heat exchanger.

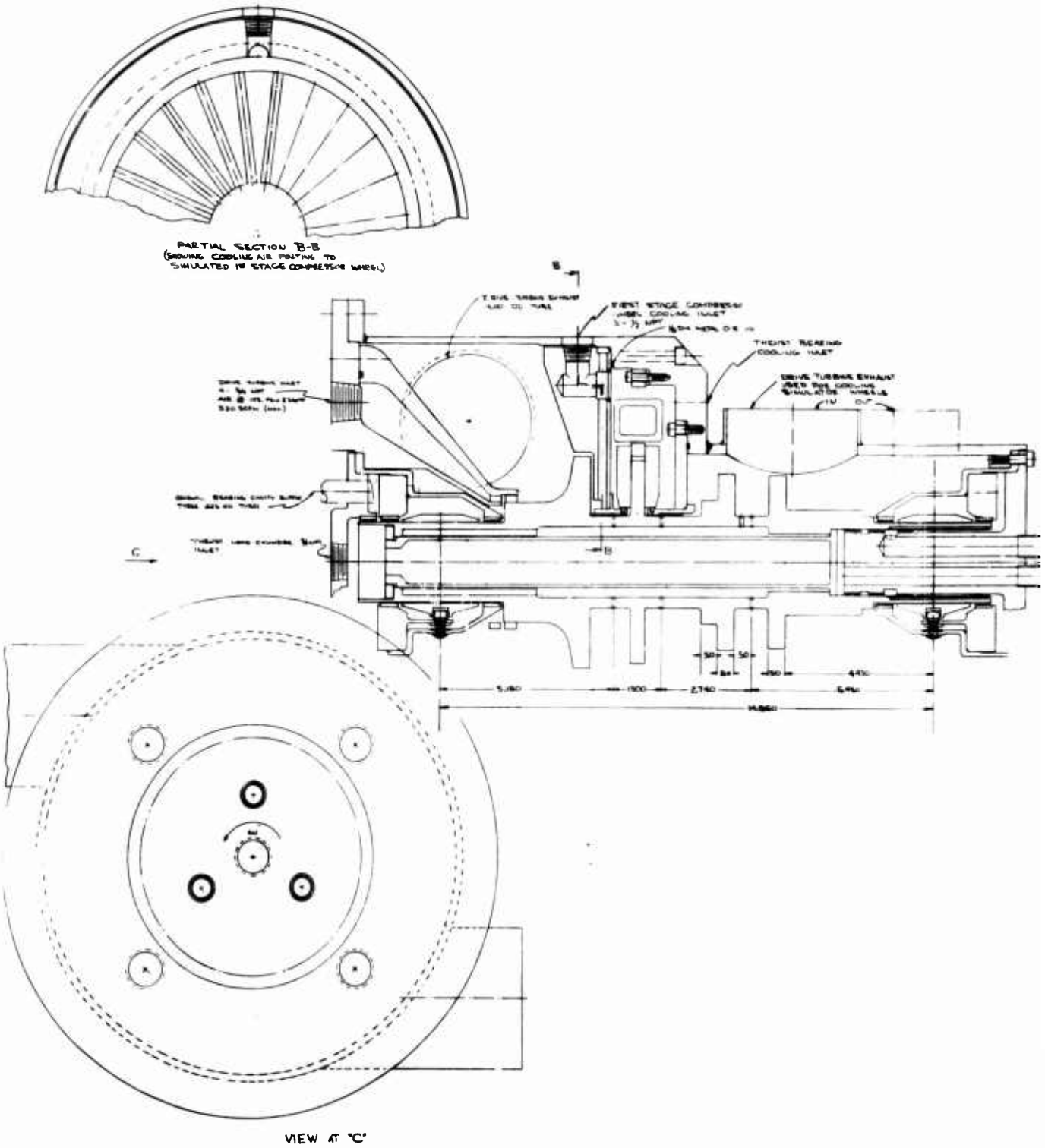
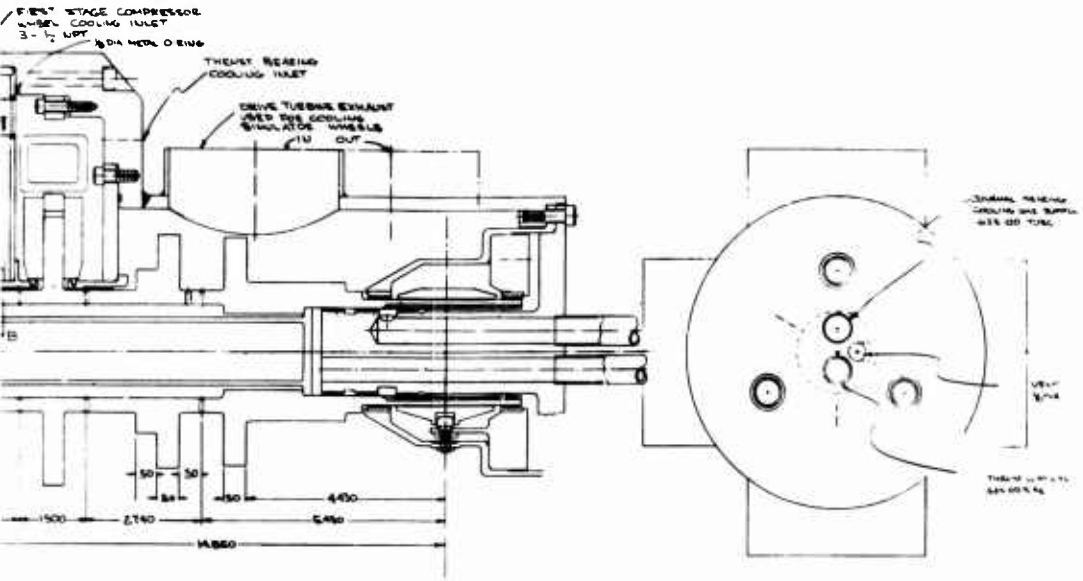


Figure 126. Rotor-Bearing Dynamic Simulator.


THRUST BEARING
COOLING INLET
DRIVE TURBINE EXHAUST
OUT
50
50
450
1500
2740
5490
14,850

mulator.

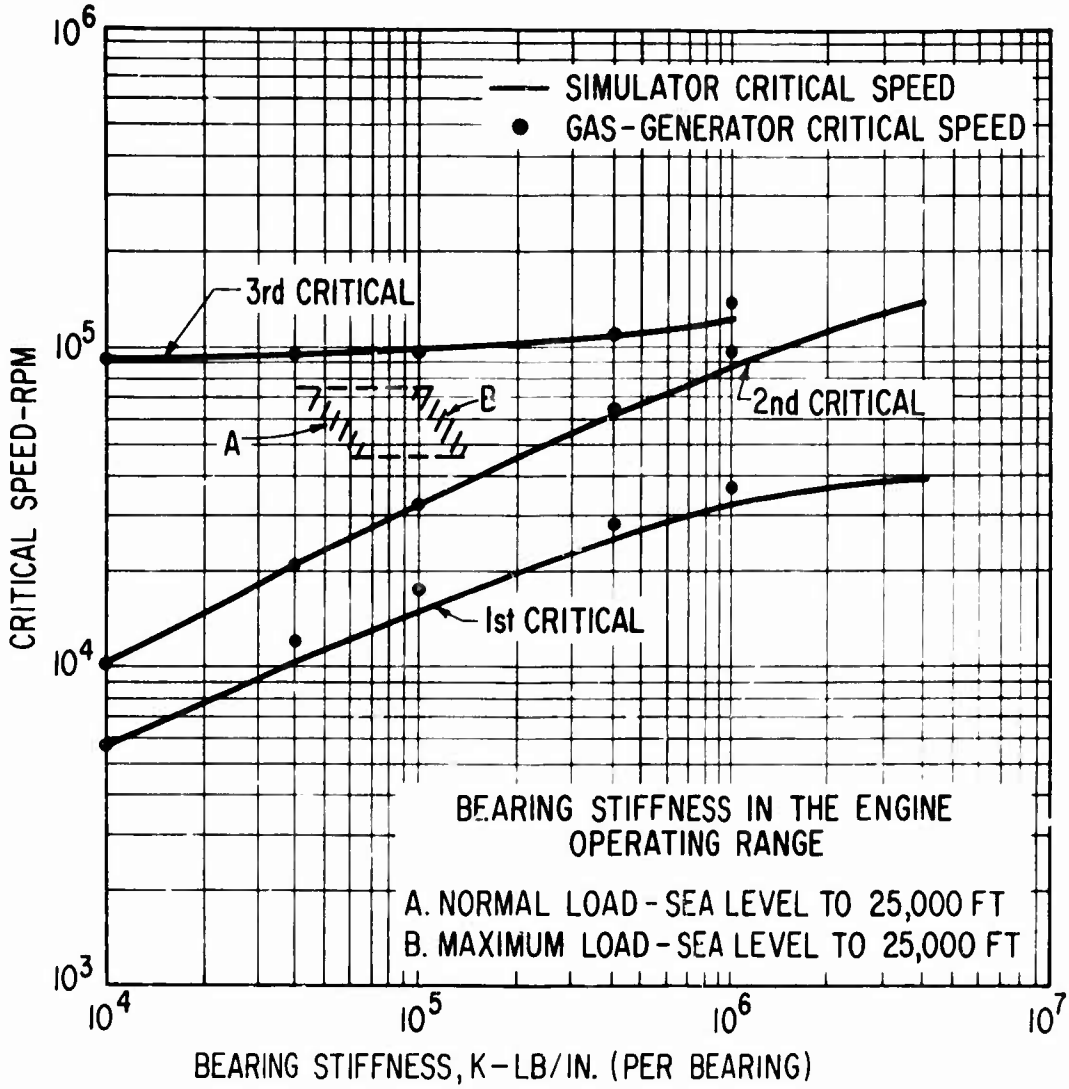


Figure 127. Undamped Critical Speed Map of the 3.5-lb/sec C_o-T_o Engine and Rotor Dynamic Simulator.

"PRECEDING PAGE BLANK-NOT FILMED."

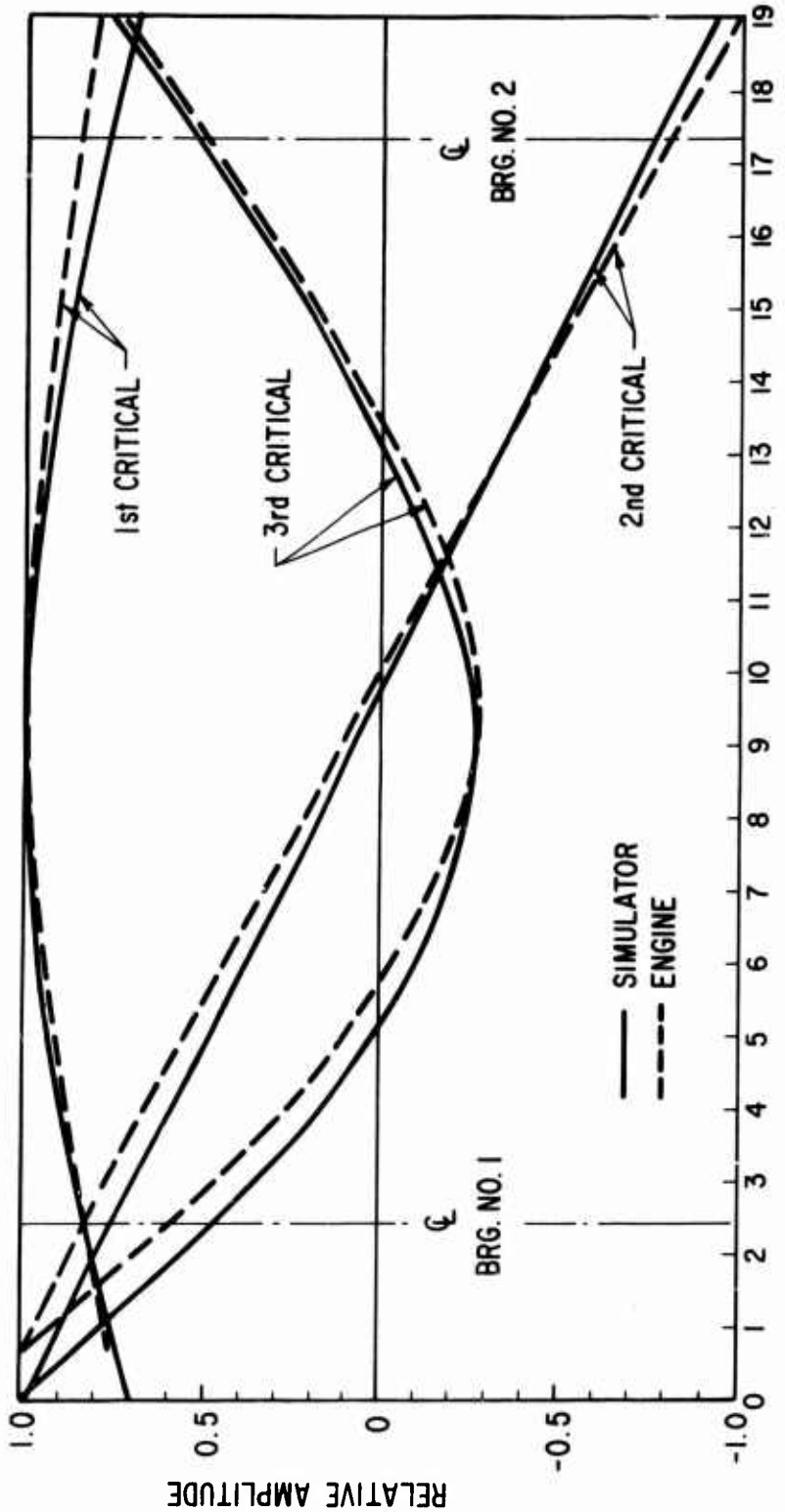


Figure 128. Undamped Critical Speed Mode Shapes of the 3.5-1b/sec C_o-T_o Engine and Rotor Dynamic Simulator.

In the simulator, the turbine bearing cooling air flow is independently supplied such that the thrust bearing and turbine bearing cooling flows can be controlled independently of one another. This arrangement increases the test flexibility and will allow experimentation over a broader range of parameters since the minimum requirements of one bearing will not limit experimentation of the other.

In the simulator, a stationary post inside the turbine bearing end of the shaft is provided. The cooling air is introduced within the post, where it is ducted into the rotating annular heat exchanger passage under the turbine bearing. Pretest calibrations of the supply passage labyrinth seal leakages will enable determination of actual cooling flow rates.

The stationary post has another advantage in that it permits easy evaluation of an alternative cooling approach. That is one that utilizes the rotational energy of the shaft to achieve the desired heat transfer coefficient. In the engine design shown in Figure 68, the turbine-bearing heat-exchanger heat transfer coefficient is achieved by the velocity of the fluid flowing through the annular heat exchanger. Thus, it is dependent upon cooling flow rate. The alternative approach is to eliminate the inner rotating sleeve and to pass the cooling flow directly between the rotating journal ID and a stationary sleeve. Here the heat transfer coefficient is dependent on shaft speed, not flow rate. Thus, a reduction in required cooling flow rate may be achievable which would be reflected in a savings in engine parasitic loss. It should be noted that this method of heat transfer is also applicable to the situation of a gas-generator and power-turbine-shaft combination since the stationary post simulates the power turbine shaft.

During the simulator test program, the minimum flow rates for the thrust bearing and the turbine journal bearing for both cooling schemes can be established. At that point, the best turbine bearing cooling approach from an engine performance standpoint will be identified.

At 72,000 rpm (the 120% engine overspeed condition), the simulator rotor windage losses are approximately 16 HP. This loss occurs in the form of heat, which must be removed in order to maintain the desired temperatures throughout the rotor bearing system. The wheel that simulates the first-stage compressor wheel is cooled by the drive turbine exhaust on the front face, while the back face is cooled by an independent air supply ducted to the area of the back face ID. The second-stage compressor wheel and the turbine wheel are cooled by a portion of the drive turbine exhaust gas which is ducted through the test housing. This design is inherently flexible from a temperature standpoint because the temperature of the drive turbine inlet air can be controlled and any portion of the drive turbine exhaust can be ducted to the simulator rotor cavity.

For high-temperature operation of the simulator, the only area that may require an external heat source is the turbine wheel. This will be accomplished by attaching electric radiant heaters around the turbine wheel as shown in Figure 126. The temperature of the other wheels will be controlled by removing more or less heat by ducted turbine exhaust cooling

air. For the high-temperature operation, the supply air to the journal and thrust bearing cavities will be heated with electric heaters in the supply lines.

Thrust Bearing Design

Like the engine concept previously described, the simulator thrust bearing stator is attached to the frame of the simulator through a gimbal ring arrangement. The gimbal ring mount provides the self-aligning capability to the thrust bearing.

The gimbal ring, which is shown in Figure 129, is attached to the bearing stator and simulator frame by flexural pivots instead of the more conventional sliding pins. The flexural pivots eliminate the friction and wear problems normally associated with sliding joints. The gimbal ring, in cross section, is a box structure with the flexure pivots located within the ring. This arrangement, as can be seen in Figure 129, results in a very compact structure. The flexural pivots are mechanically attached to the gimbal ring through an integral diaphragm mount which accommodates the radial differential thermal gradient between the stator plate and frame. A mechanical stop is provided to prevent overstressing the diaphragms under a 10g transverse load condition. The flexural pivots are rigidly attached to the thrust bearing stator plate and frame.

The flexural-pivot gimbal-ring appraoch results in a high overall mount axial stiffness (5.3×10^4 lb/in.) while still maintaining a low angular stiffness (100 in.-lb/rad). Under the design thrust load of 277 pounds, the maximum axial deflection of the mount system will be approximately 0.005 inch or about 25% of the turbine blade axial clearance (0.020 inch total). This is considered to be an acceptable deflection from an engine design standpoint. The angular stiffness of the mount is less than one-thousandth of the thrust bearing angular stiffness (which is between 10^5 and 10^6 in.-lb/rad depending upon the applied load). Thus, large mounts of static misalignment can be tolerated with practically no influence on the bearing film thickness.

Journal Bearing Mechanical Design

The mechanical design of the simulator journal bearings shown in Figure 130 is the same as that proposed for the engine. The pivoted pads are constructed from the same substrate material as the shaft journals, i.e., titanium for the compressor bearing and Waspaloy for the turbine bearing. The pivots and seats are constructed of hardened M-1 tool steel. The pads are positioned for proper film thickness by a ground spacer located between the pivot and its mount.

As was indicated in the section discussing the engine bearing design, the bearing pads are mounted on flexures to accommodate the differential radial thermal and centrifugal growth between the journal and housing. Two soft flexures and one stiff flexure supporting the three journal bearing pads were selected for the engine design. These flexures are cantilever beams projecting from the outboard end of the bearing cavity housing.

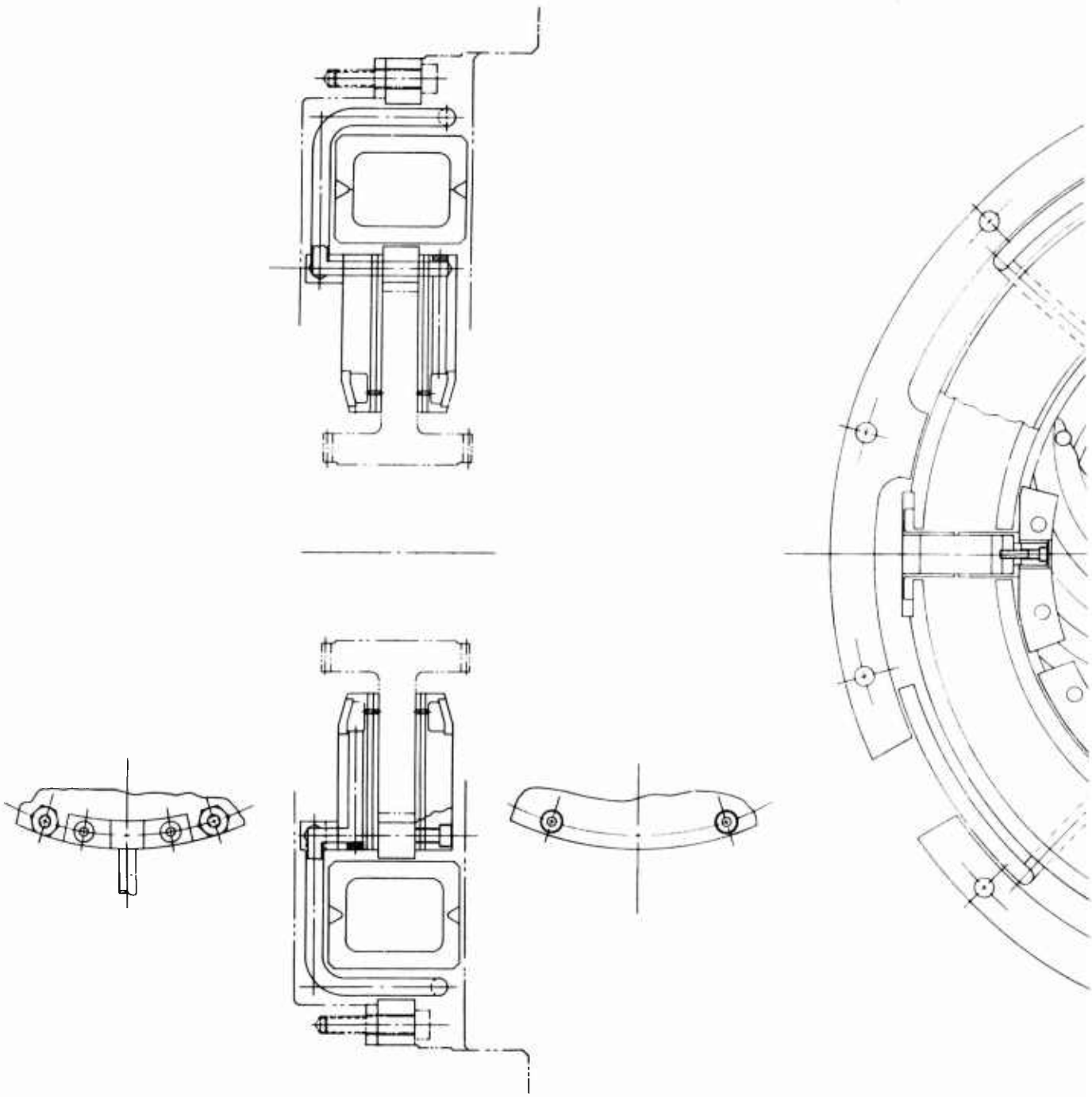
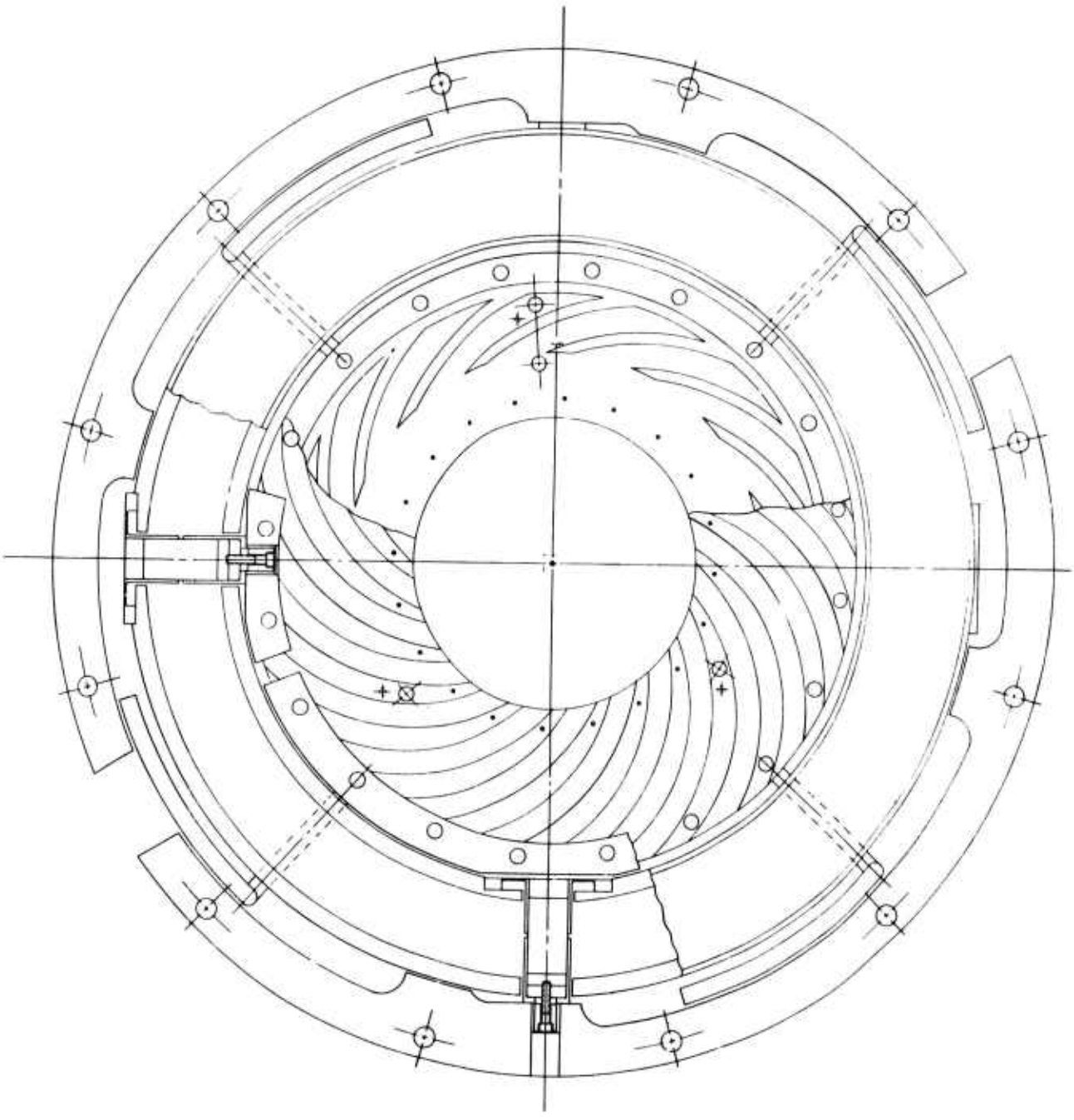
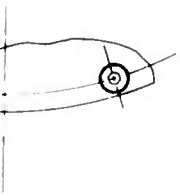


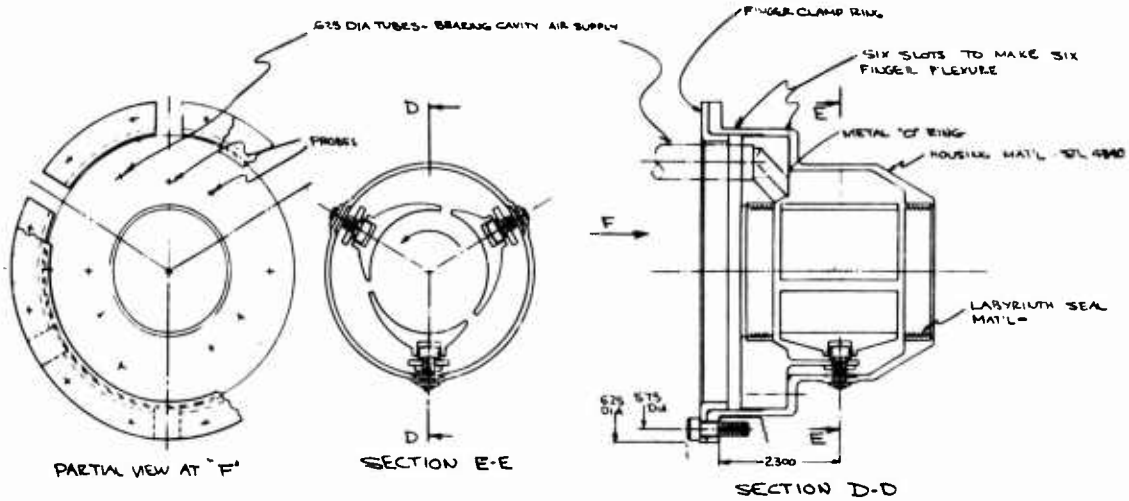
Figure 129. Thrust Bearing Layout Design.





sign.

JOURNAL BEARING MOUNTING DESIGN
FULL SCALE



— JOURNAL BEARING DETAIL DESIGN —
DOUBLE SCALE

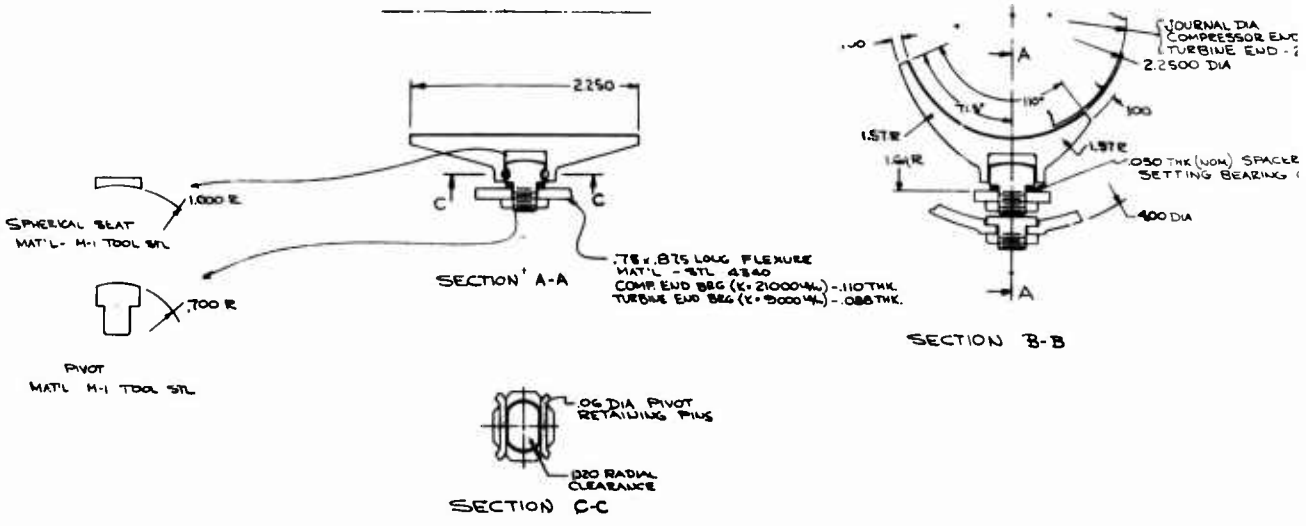


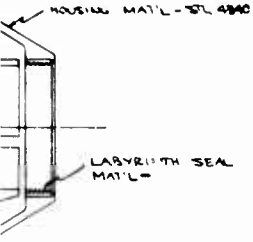
Figure 130. Journal Bearing Layout Design.

"PRECEDING PAGE BLANK-NOT FILMED."

SLOTS TO MAKE SIX
FLEXURE

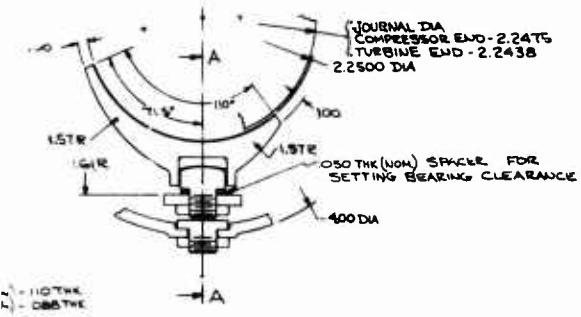
O RING

HOUSING MAT'L - SAE 4340



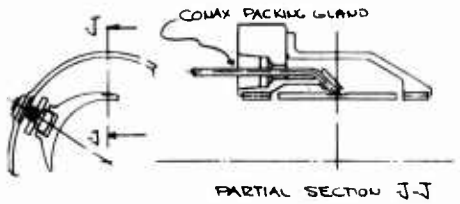
D

SIGN—



SECTION B-B

DESIGN OF CAPACITANCE PROBE MOUNTING
(PAD PROBES .000-.005 RANGE
.125 DIA PROBE



PARTIAL SECTION J-J

The design concept for the simulator differs from that of the engine in that the simulator has three soft flexures of the required stiffness supporting the pads. These flexure supports are backed up with an adjustable stop that is ground at assembly to limit pad motion. This allows the "hard" flexure to be realized by having the stop "short-out" the soft flexure, i.e., zero deflection of the soft flexure. This feature will enable the evaluation of different combinations of mount stiffness, such as two "stiff" and one "soft" flexures, during the test program.

The bearing cavity housing together with the cantilever flex mounts and two labyrinth seals are mounted to the housing with six fingers. These fingers can deflect to accommodate the relative radial motion caused by the relative differential thermal expansion of the bearing housing and frame, yet retain the centerline of the bearing assembly coincident with the machine centerline. In the radial direction the "finger" assembly is very stiff ($>10^6$ lb/in.). Thus, it will have negligible effect on the rotor dynamics of the system.

Air at high pressure is contained within the bearing cavity and is sealed by the two labyrinth seals which are attached to the bearing cavity. The diameters of the two labyrinth seals are different in the engine design (see Figure 68); however, they were made identical in the simulator. By making all bearing cavity labyrinth seals the same diameter as the journals in the simulator, a major advantage is realized: elimination of the effect of bearing cavity pressure on the thrust load.

"PRECEDING PAGE BLANK-NOT FILMED."

EVALUATION OF BEARING MATERIALS

It is becoming increasingly apparent that the most critical factor facing the successful application of air bearings to small aircraft gas-turbine engines is the durability of the bearing materials, particularly the surfacing materials. This fact was intuitively identified in Reference 1 and has been further confirmed by the results of the present Phase I design studies and test evaluations. The engine design studies have confirmed that air bearings can be integrated into viable engine configurations. Although several problem areas have been identified (and additional problems may appear during the Phase II simulator testing), it is felt that resolution of these problems will simply be a matter of normal design iteration and optimization, accompanied by a moderate development effort. Likewise, the Phase I bearing component tests (discussed in the next section) have shown that air bearings can carry the required loadings, and that load-capacity performance can be confidently predicted. Thus, by a process of elimination, durability of the bearing materials is now emerging as the key factor affecting overall feasibility of air bearings for small aircraft gas turbines.

During normal (i.e., design range) operation of an air bearing engine, wherein the rotating and stationary bearing members are separated by a film of air, bearing materials do not present any serious problems. Rather, the potential for problems arises from environmental shock and vibration, and from abnormal (i.e., unexpected or unintentional) situations, such as a labyrinth seal or shroud rub. It is well established that under these conditions, surface-to-surface contact may occur between the rotating and stationary bearing members. Unlike oil-lubricated bearings, air bearings have no boundary lubrication to fall back on during periods of surface-to-surface contact. For this reason, the air bearing surface material must fulfill some of the boundary lubricating functions inherent in conventional lubricants.

Previous developments of air- and gas-lubricated rotating machinery have been limited to applications where the journal surface velocities, the bearing temperatures, and the number of rotor start-stop cycles are considerably less than will be encountered in advanced aircraft engines of the type being considered in the current investigation. It was therefore necessary to extend the knowledge of previously successful bearing surface materials to the conditions of the aircraft engine application, and to establish other bearing surface material combinations that could extend the range of application, particularly to higher temperatures.

The primary objectives of the Phase I materials evaluation tasks (Tasks 7 through 12) were as follows:

1. To obtain data relative to the structural adequacy of the bearing and bearing coating materials at the temperatures and surface velocities anticipated for the engine.

2. To obtain data to assess the capability of the engine bearings to withstand 15,000 cycles of engine start-up and coast-down. (Fifteen thousand cycles results from the required three starts per hour over a 5,000-hr engine design life.)

The materials evaluation effort was accomplished in three basic steps:

1. Preliminary Selection of Materials (Task 7)

2. Preliminary Test Evaluation (Tasks 8 and 9)

3. Final Selection and Test Evaluation (Tasks 10, 11, and 12)

PRELIMINARY SELECTION OF BEARING COATING MATERIALS

During Task 1 of the program, when the effects of engine size and rotor configuration on the performance of air bearings were being studied, it became apparent that the journal bearings would probably be located at the rotor extremities, with the thrust bearing located between the first- and second-stage compressor wheels. Thus, the temperature environment for each of the bearings was preliminarily established as given in Table XX.

TABLE XX. TEMPERATURE OF BEARING REGIONS

Bearing Description	Temperature of Bearing Region
Compressor-End Journal	Compressor inlet temperature, increased by bearing friction loss and temperature of air used to pressurize the bearing cavity (400 - 600°F).
Thrust Bearing	First-stage compressor discharge temperature, increased by bearing friction loss and bearing supply air (600 - 800°F).
Turbine-End Journal	Turbine exhaust temperature, reduced by bearing cooling and by temperature of air used to pressurize the bearing cavity (800 - 1000°F).

Initial Bearing Material Selections

A comprehensive summary of material technology for high-temperature gas bearings is given in Appendix II of Reference 1; the reader is referred to this appendix for a discussion of the requirements and problems relative to gas-bearing materials, and the progress which has been made over the past 10 years. At the present time, the most successful approach toward

achieving the desired material characteristics has been to fabricate the bearing parts from metals or metal-alloys, selected on the basis of structural strength and other mechanical requirements, and to then apply a plasma-sprayed ceramic coating to obtain the best possible surface properties. This same basic approach was used for the Phase I materials evaluations.

From considerations of rotor integrity and retention of a high standard of rotor balance, it was desirable to minimize the number of joints in the rotor. This was accomplished by making the compressor-end and turbine-end journal bearings an integral part of the first-stage compressor and the turbine, respectively, the thrust runner remaining as a separate component. Mechanical design requirements dictated the use of a titanium alloy for the first- and second-stage compressor wheels and a nickel-based alloy for the turbine wheel. Therefore, titanium-based alloys and nickel-based alloys were the primary candidates for the bearing substrate (structural) materials.

Based upon past gas-bearing machinery experience and other factors discussed below, six coatings were selected for initial evaluations:

1. Chrome Oxide (Normal Density)

2. Chrome Oxide (High Density)

3. Nickel-Chrome-Bonded Chrome Carbide (NiCr-Bonded Cr_3C_2)

4. 25% Nickel-Chrome + 75% Chrome Oxide (25% NiCr + 75% Cr_2O_3)

5. 50% Nickel-Chrome-Bonded Chrome Carbide + 50% Chrome Oxide (50% NiCr-Bonded Cr_3C_2 + 50% Cr_2O_3)

6. 40% Chrome + 60% Chrome Oxide (40% Cr + 60% Cr_2O_3)

Discussion of Initial Coating Selections

The above list consists of two basic coating materials - Cr_2O_3 and NiCr-bonded Cr_3C_2 - and various mixtures of these two basic materials.

From the standpoint of wear resistance, chrome oxide coatings have been the most successful in gas-bearing applications to date. In fact, the wear track in Cr_2O_3 bearing components is usually smoother than the unworn portion, indicating a light polishing action of the Cr_2O_3. However, it was known that at temperatures in excess of 900°F, the friction and wear rate of Cr_2O_3 greatly increases above that experienced at lower temperatures; and spalling of Cr_2O_3 coatings occurs at temperatures in excess of 1000°F. Since temperatures of the order of 900°F and above had to be considered for the turbine-end bearing, additional evaluation of Cr_2O_3 in this range was required. Furthermore, the need for improved high-temperature-capability materials was apparent.

Nickel-chrome-bonded chrome carbide has been successfully used at temperatures up to 1400°F. However, its coefficient of sliding friction, wear

rate, and surface damage characteristics are significantly poorer than those of chrome oxide.

For the high-temperature turbine-end journal bearing, the following three coating material mixtures were selected in an attempt to retain the good wear and low friction properties of Cr_2O_3, while extending the high-temperature integrity (bond strength) of the coating to that of NiCr-bonded Cr_3C_2:

1. 25% NiCr + 75% Cr_2O_3
2. 50% NiCr-bonded Cr_3C_2 + 50% Cr_2O_3
3. 40% Cr + 60% Cr_2O_3.

It was hoped that the addition of metallic binders would allow the Cr_2O_3 to expand during high-temperature thermal cycles without reduction in bond strength.

The six coatings were subjected to a series of initial screening tests in order to:

1. Better establish the spalling limits of the chrome oxides and the NiCr-bonded Cr_3C_2 on the candidate substrates
2. Verify the high-temperature bond strength capability of the NiCr-bonded Cr_3C_2 on the candidate substrates
3. Evaluate the improvement, if any, in the spalling limits and wear characteristics of the various mixtures containing Cr_2O_3

Two types of screening tests were performed: thermal cycle tests and sliding tests. Both were performed using washer-type specimens where the test coating was applied to a 1.0-inch OD x 0.5-inch ID x 0.25-inch thick washer of the desired substrate material.

Sliding Tests

The sliding tests were conducted on an MTI model MT-6 thrust washer test machine, similar to the one shown in Figure 131, that had been modified to obtain higher loads than are achievable with the standard tester. In this test rig, two washer specimens (one rotating and one stationary) are loaded against one another by means of a deadweight loader. The test conditions and results of the sliding tests are summarized in Table XXI.

The results of these tests indicated that the straight Cr_2O_3 coatings were the best from both a friction and a damage viewpoint. There was little difference between the normal-density and the high-density Cr_2O_3. The NiCr-bonded Cr_3C_2, on the other hand, produced high friction at the 3.5-psi stress level and seized at the 5.4-psi stress level. The surfaces were badly abraded. This surface damage started to occur at the 3.5-psi stress level and became severe at the 5.4-psi stress level. From the results of

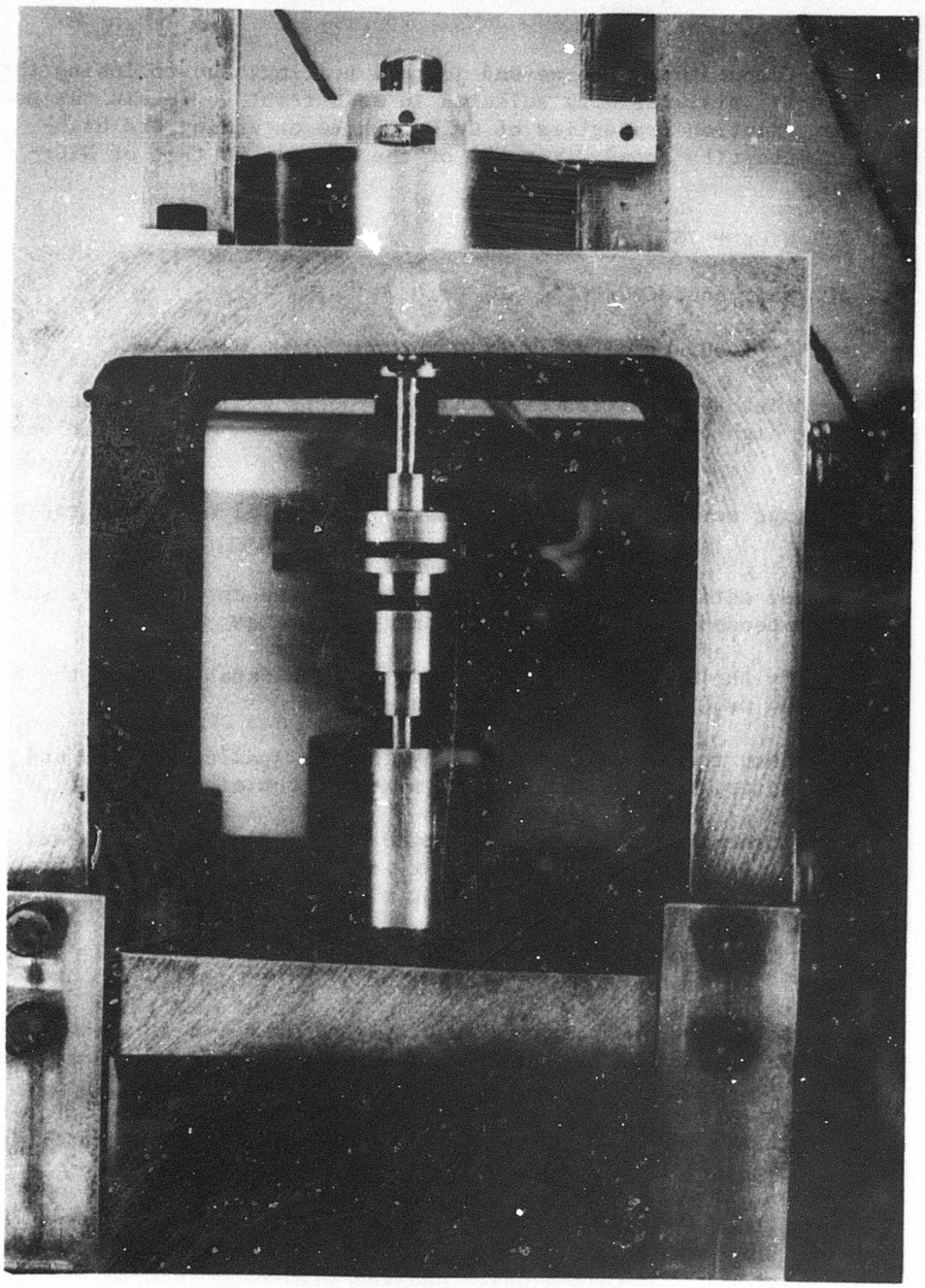


Figure 131. MT-6 Thrust Washer Test Machine.

TABLE XXI. EFFECTS OF STRESS ON FRICTION AND SURFACE DAMAGE CHARACTERISTICS OF VARIOUS COATING COMBINATIONS

Dry Air Tests - 75°F
Mean Sliding Velocity - 118 Feet/Minute
Test Time - 15 Minutes at Each Stress Level

Coating Material	Coefficient of Friction						
	(1) Cr_2O_3 Normal Density	(2) Cr_2O_3 High Density	(3) NiCr Bonded Cr_3C_2	(6) 25% NiCr + 75% Cr_2O_3	(7) 50% NiCr Bonded Cr_3C_2 + 50% Cr_2O_3	(8) 40% Cr + 60% Cr_2O_3	(9) Si_3N_4
Stress* Level							
2 psi	.30-.35	.34-.4	.40-.40	.45-.35	.46-.90-.46	.25-.30	.06-.12
3.5 psi	.45-.35	.44-.3	.43-1.0	.3-.22-.48	.48-.48	.27-.50-.30	.23-.55-.23
5.4 psi	.29-.32	.34-.3	seized	.39-.39	.7 → seizing	.3 → seizing	.35-.55
Final Appearance	No Damage	No Damage	Badly Abraded	No Damage	One Heavily Scored Area	Heavy Scratches	A Few Very Light Scratches

*Stress level, as defined in this table, is obtained by dividing the bearing load by the projected bearing area.

this test, it appears that the NiCr-bonded Cr_3C_2 should be limited to applications where the bearing stress levels are below 3.5 psi.

Of the coatings containing Cr_2O_3 and other Cr binders, the 25% NiCr + 75% Cr_2O_3 ranked best, with a coefficient of friction similar or slightly higher than the Cr_2O_3 and no evidence of damage. Both the 50% NiCr-bonded Cr_3C_2 + 50% Cr_2O_3 and the 40% Cr + 60% Cr_2O_3 behaved erratically at the lower stress levels and eventually seized at the 5.4-psi stress level.

The last material shown on Table XXI is silicon nitride. This material, which is produced in England by Dalton Industries, came to our attention late in the program and appeared to have potential for high-temperature air-bearing applications. A silicon nitride washer specimen was obtained in solid form and subjected to the same frictional tests for direct comparison to the coatings that were tested at an earlier date.

At the 2-psi stress level, the coefficient of friction of the Si_3N_4 was very low (0.06 - 0.12). At the higher stress levels, the friction coefficient increased gradually until it reached 0.55. At the conclusion of the test, a few light scratches were noted which appeared to be originating at the OD of the specimen. This is not uncommon since the edges of the ceramic are the most likely places for chipping to occur. It should be noted, however, that at the 5.4-psi stress level, the coefficient of friction and surface damage of the Cr_2O_3 is slightly superior to that observed with silicon nitride.

Spalling Tests

These tests were designed to evaluate the coating's ability to remain bonded to the substrate at elevated temperatures and after thermal cycling. The test specimens were prepared by coating washers of Ti-6Al-4V and Waspaloy with the six plasma-spray coatings under consideration. These washers were then thermal cycled at various temperatures until a predetermined maximum temperature was reached or until the coating spalled off the surface of the substrate. The silicon nitride test specimens, being in solid form, were not subjected to this test. However, one specimen was heated to 1800°F without any apparent damage or significant oxidation.

The test procedure was as follows:

(a) The coating was plasma-sprayed on the surface of the washer.

(b) The coating was ground back to a thickness of approximately 0.003 inch.

(c) The surface was lapped and micropolished.

(d) The surface was examined, and photomicrographs and photomacrographs were taken.

(e) The specimen was placed in a furnace and heated to the desired temperature. The furnace was controlled by a timer which cycled on and off five times at each temperature.

(f) At the end of the fifth cycle, the specimen was removed, examined, and rephotographed.

(g) The specimen was put back in the furnace and recycled at the next higher temperature.

(h) Steps f and g were repeated. This continued until the predetermined maximum test temperature was reached.

The time taken for each series of five cycles at a given temperature was 12 hours; that is, 4 hours on and 8 hours off.

The test temperatures were 400°, 600°, 800°, 1000°, 1200°, and 1400°F. The titanium specimens were removed from the test at 1200°F. Two specimens of each substrate material and coating combination were used to determine consistency in the test results.

At the end of the spalling tests, the specimens which still had the coating remaining were repolished, and photomicrographs and macrographs were taken. The results of the spalling tests are summarized on Table XXII.

Surprisingly, none of the coatings spalled off of the titanium substrate, even though the specimens had become severely oxidized. Photomicrographs of a typical cross section of the coated face and uncoated face of the titanium specimen are shown in Figure 132. The gray area is the chrome oxide. The white area in the lower portion of the photographs is the typical structure of the titanium alloy in the annealed condition. A secondary white phase exists at the interface, which contains particles of the chrome oxide boundary. This phase appeared to have formed in the system after the specimen had been heated to 1200°F. To achieve a better understanding of the nature of this interface, the specimen was subjected to an electron probe microanalysis.

The results of this analysis revealed a phase present at the boundary interface, which was rich in chrome and aluminum. The exact stoichiometry could not be obtained without increased observation using a more precise point count analysis technique. The aluminum-chromium area could also be a mixed oxide, but further examination would be needed to establish this. The important point is that the aluminum could have come only from the titanium alloy (6AL-4V) and the chromium could have come only from the coating (Cr_2O_3). These two elements formed an intermediate phase between the coating and the substrate which allowed the coating to remain bonded to the substrate surface at higher temperatures than would normally be expected.

It should be noted that although the coating did not spall, it was severely warped on the substrate surface and could not be used as a bearing surface. This warpage was not evident until the specimen had been exposed to the

TABLE XXII. THERMAL CYCLE TEST RESULTS (IN AIR)

Nonrotating Thrust Washer Specimen						
Coating and Substrate Materials	70°F to 400°F	70°F to 600°F	70°F to 800°F	70°F to 1000°F	70°F to 1200°F	70°F to 1400°F
1) Normal-Density Cr_2O_3						
Ti6Al-4V	OK	OK	OK*	**	**	-
Waspaloy	OK	OK	OK	OK	Completely Spalled Off	-
2) High-Density Cr_2O_3						
Ti6Al-4V	OK	OK	OK*	**	**	-
Waspaloy	OK	OK	Partially Spalled	Completely Spalled Off	-	-
3) NiCr Bonded Cr_3C_2						
Ti6Al-4V	OK	OK	OK*	**	**	-
Waspaloy	OK	OK	OK	OK	OK	OK
6) 25% NiCr + 75% Cr_2O_3						
Ti6Al-4V	OK	OK	OK*	**	**	-
Waspaloy	OK	OK	OK	OK	Partially Spalled Off	Partially Spalled Off
7) 50% NiCr Bonded Cr_3C_2 + 50% Cr_2O_3						
Ti6Al-4V	OK	OK	OK*	**	**	-
Waspaloy	OK	OK	OK	OK	OK	OK
8) 40% Cr + 60% Cr_2O_3						
Ti6Al-4V	OK	OK	OK*	**	**	-
Waspaloy	OK	OK	OK	OK	OK	OK

* Coating OK. Substrate material has started to oxidize.

** Substrate material severely oxidized at bond interface, causing coating to bulge.

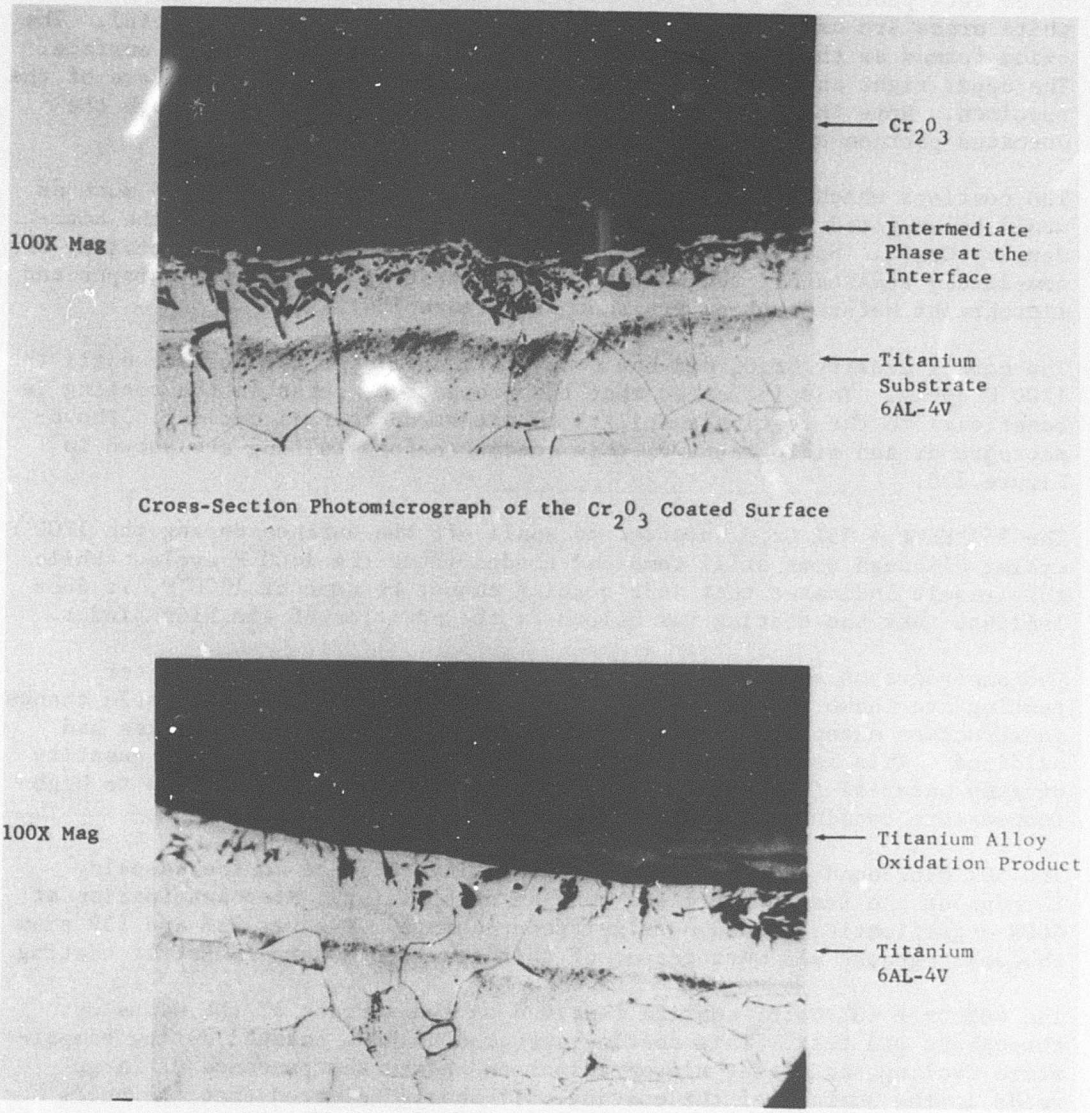


Figure 132. Cross-Section Photomicrograph of Cr_2O_3 Coated Titanium Specimens.

1000°F thermal cycle. At temperatures below 800°F, all of the coatings appeared to be well bonded with no significant change in their appearance.

Photographs of the titanium-coated specimen are shown in Figure 133. The upper left photograph shows the uncoated face of the washer. The gray-white areas are oxides of the alloy and the dark areas are the metal. The oxide formed as thin sheets which could be easily peeled off the surface. The upper right and center photographs show the Cr_2O_3 coated surface of the specimen. Note that the Cr_2O_3 coating is still intact, even though the uncoated portion of the specimen is severely oxidized.

The coatings which were applied to the Waspaloy substrate behaved much as would be expected. The first one to show signs of spalling was the high-density Cr_2O_3. Spalling started at 800°F, and after 1000°F the coating was completely spalled off the surface of the substrate. Photomacrographs and micrographs before testing are shown in Figure 134.

The normal-density Cr_2O_3 did not completely spall off the surface until the 1200°F cycle. This indicated that the presence of pores in the coating is beneficial to the coating's ability to withstand thermal cycling. Photomacrographs and micrographs of this coating before testing are shown in Figure 135.

The 25% NiCr + 75% Cr_2O_3 started to spall off the surface during the 1200°F cycle, although some still remained bonded after the 1400°F cycle. While this result indicates that this coating cannot be used at 1200°F, it does indicate that the coating was helped by the addition of the NiCr binder.

Photomacrographs and micrographs of these specimens before and after testing are shown in Figures 136 and 137. These figures show little change in structure except that the surface of some of the metal particles had oxidized. This is evident from these photomicrographs since the quantity of gray material (oxidized material) has increased after exposure to high-temperature cycling.

The 50% NiCr-bonded Cr_3O_2 + 50% Cr_2O_3 coating remained on the Waspaloy throughout the test. There was no sign of spalling. Microexamination at 400X magnification showed no significant change. Figures 138 and 139 show photomicrographs and macrographs of this specimen before and after testing.

The 40% Cr + 60% Cr_2O_3 coating remained on the surface of the Waspaloy throughout the test. This coating appeared to have changed during temperature cycling, and later microexamination showed the presence of large voids in the surface of the coating. It should be noted that the voids present in the Cr_2O_3 normal-density coating were there before testing, while the voids present in this coating occurred during testing. The fact that the coating changed during thermal cycling could present problems in a bearing application as a result of the possibility of debris being introduced into the clearance space. Photomicrographs and macrographs before and after testing are shown in Figures 140 and 141.

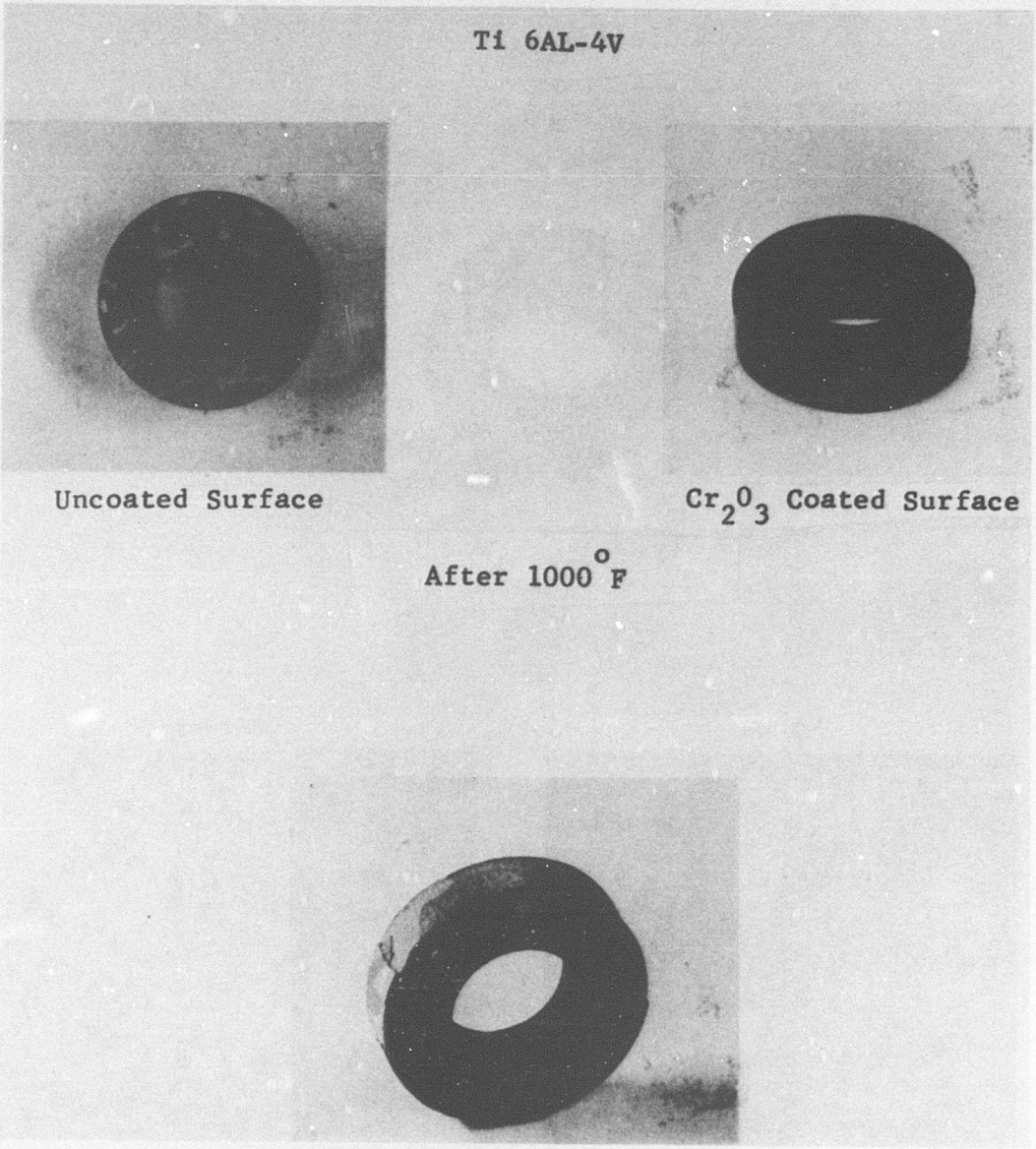


Figure 133. Photographs of the Titanium Alloy Specimen Coated With Cr_2O_3.

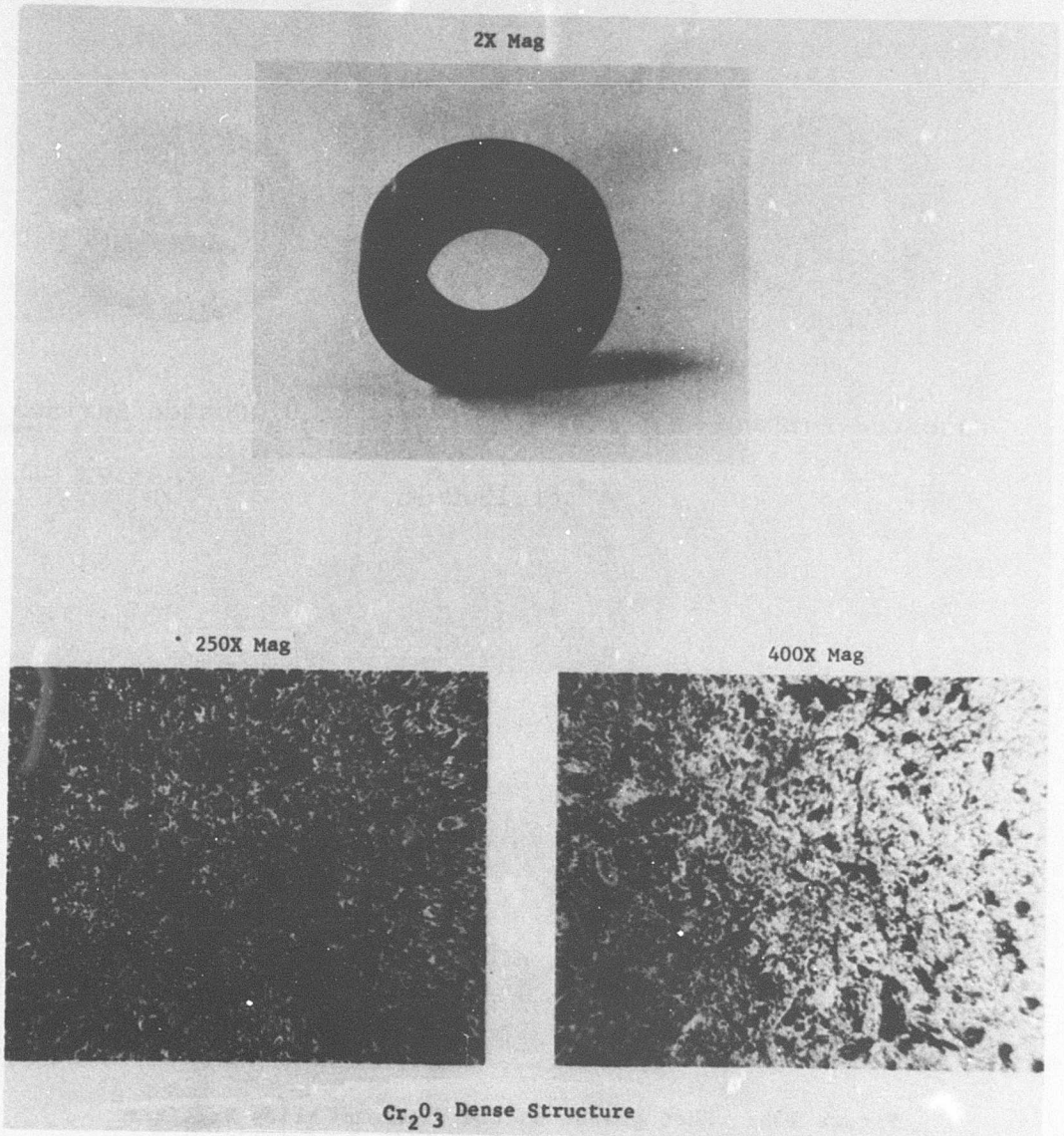


Figure 134. Typical Surface Structure of Dense Cr_2O_3 Coating Before Testing.

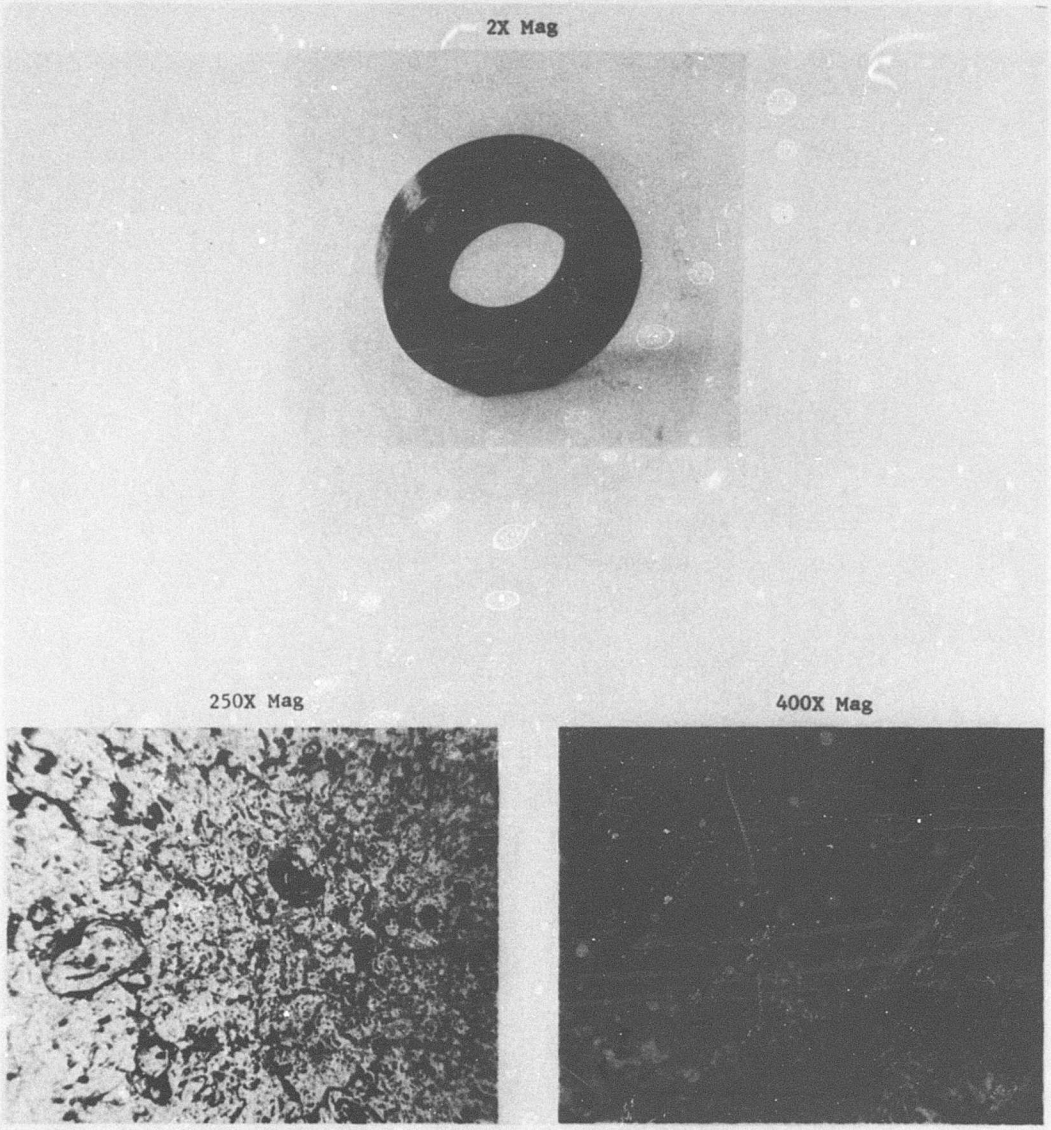


Figure 135. Typical Surface Structure of Normal Density Cr_2O_3 Coating Before Testing.

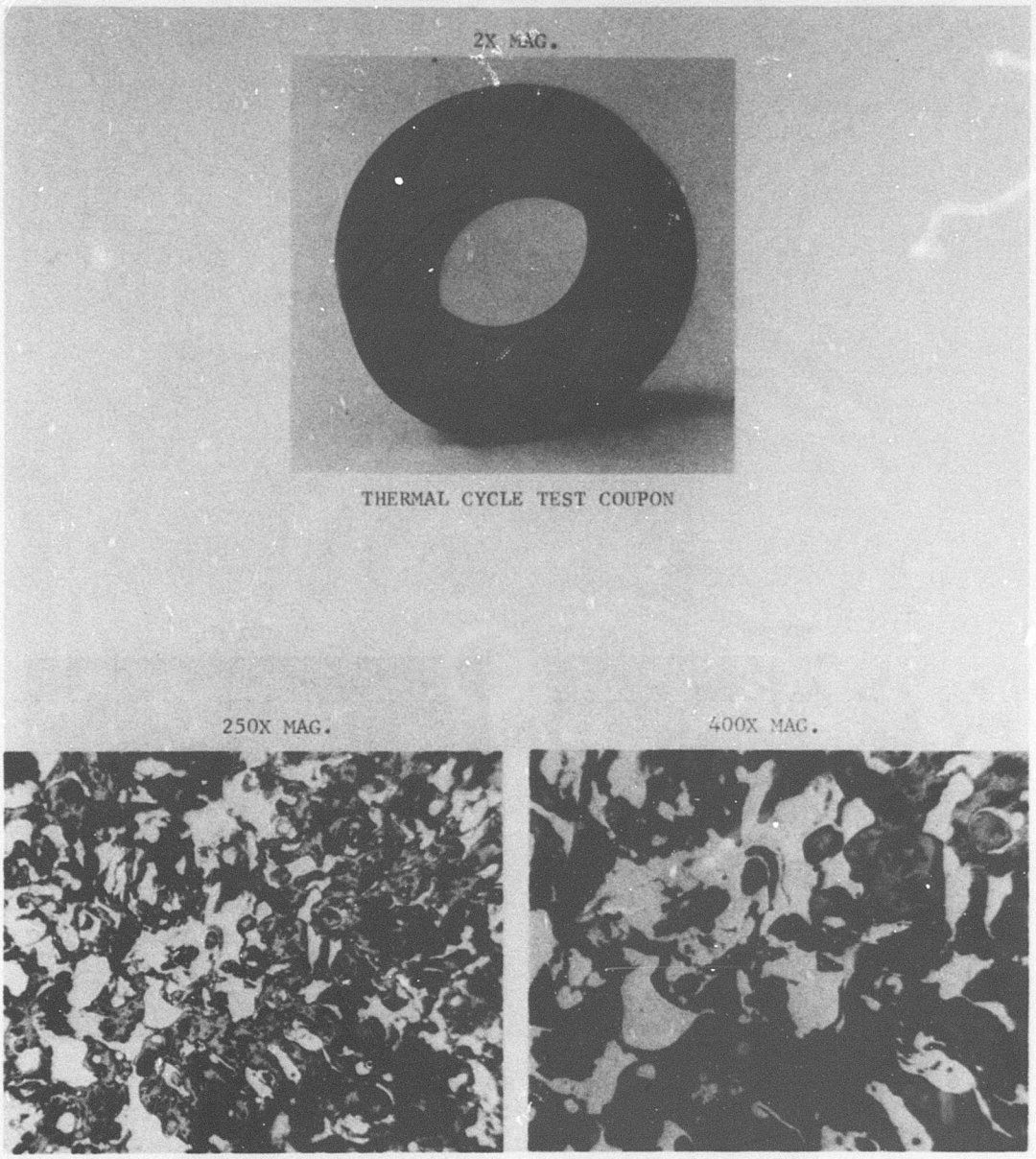


Figure 136. Typical Surface Structure of 25-Percent Nickel-Chrome and 75-Percent Chrome-Oxide Coating Before Test.

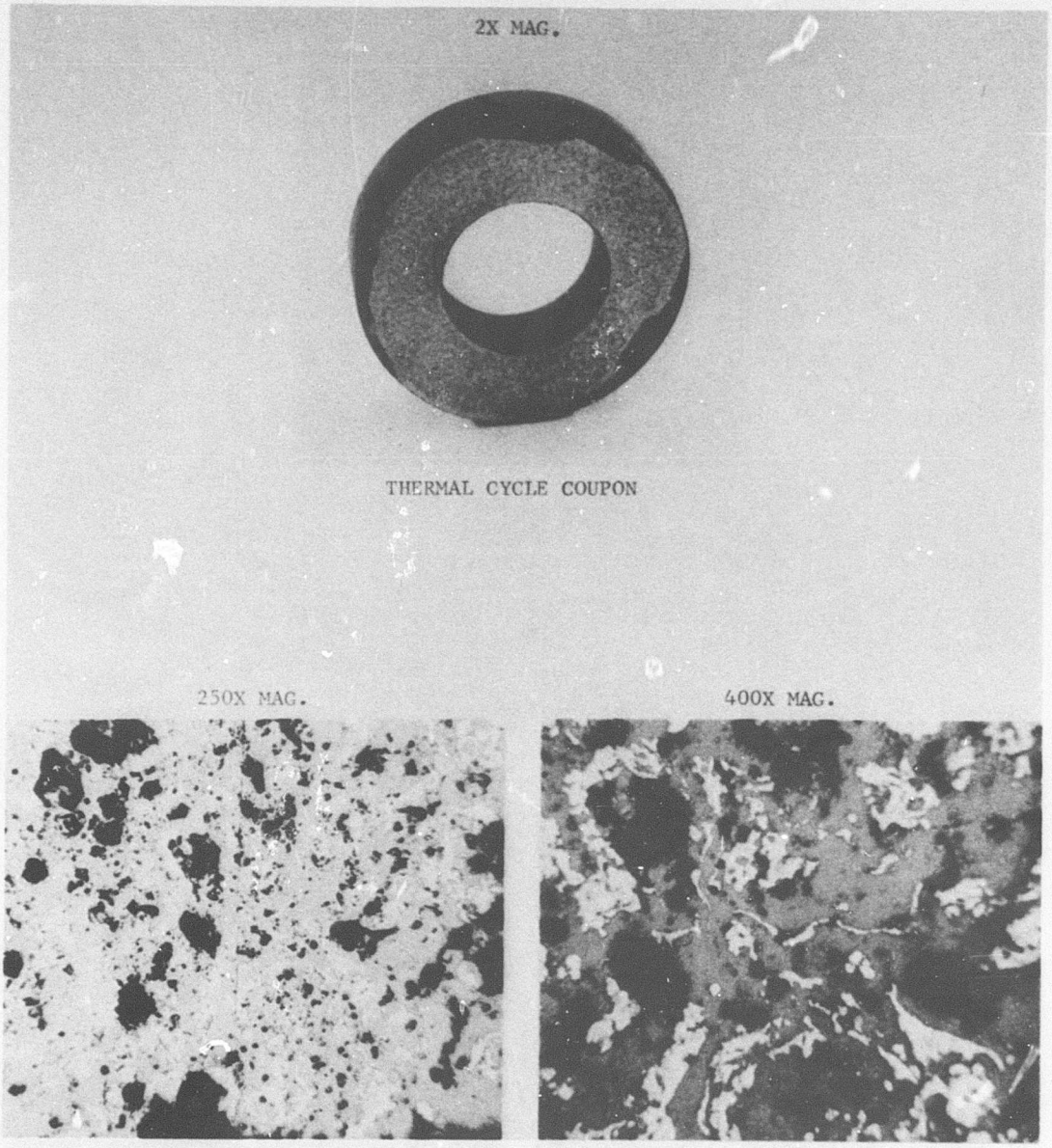


Figure 137. Typical Surface Structure of 25-Percent Nickel-Chrome and 75-Percent Chrome-Oxide Coating After Test.

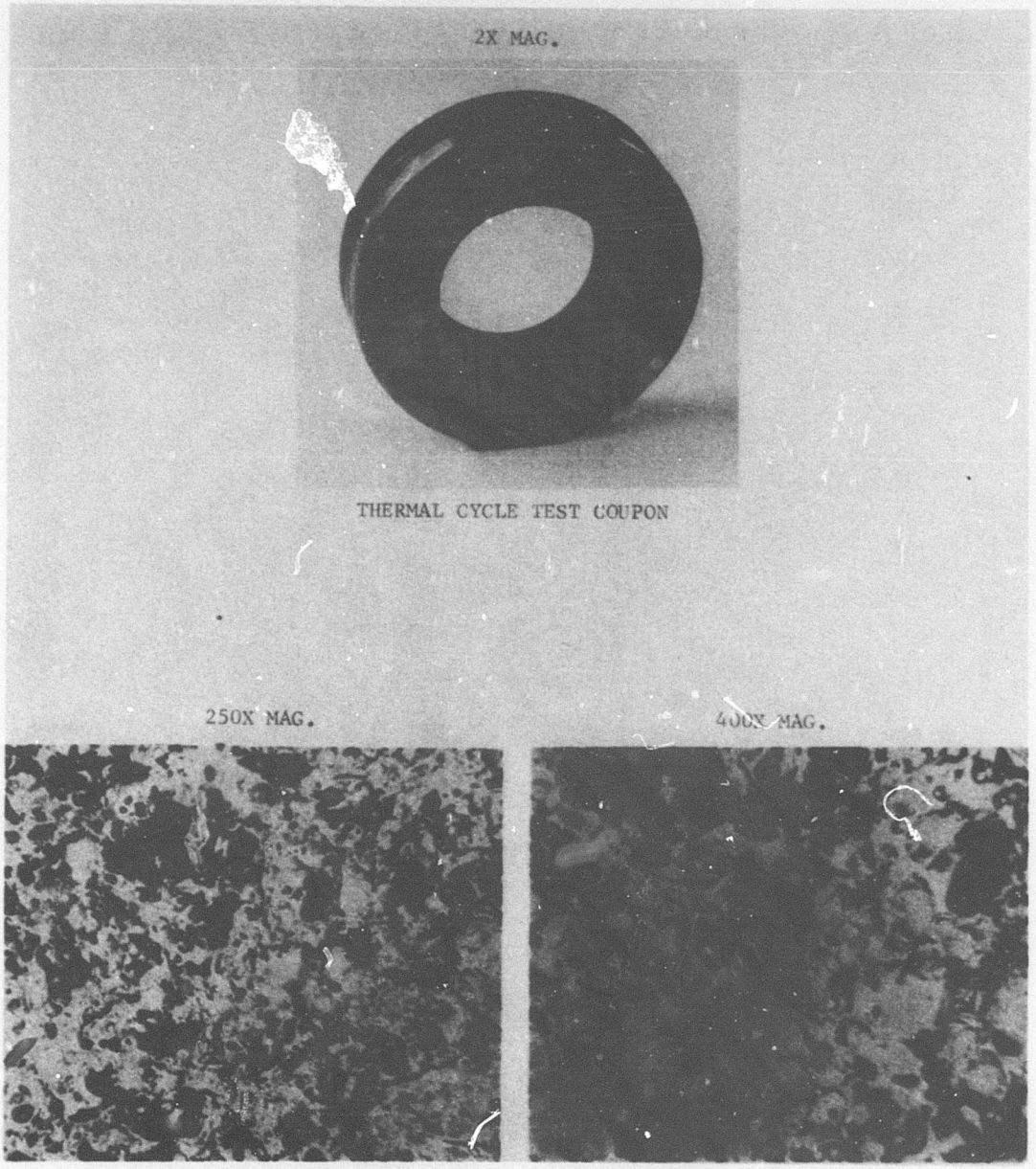


Figure 138. Typical Surface Structure of 50-Percent NiCr Bonded Cr_3C_2 + 50-Percent Cr_2O_3 Before Test.

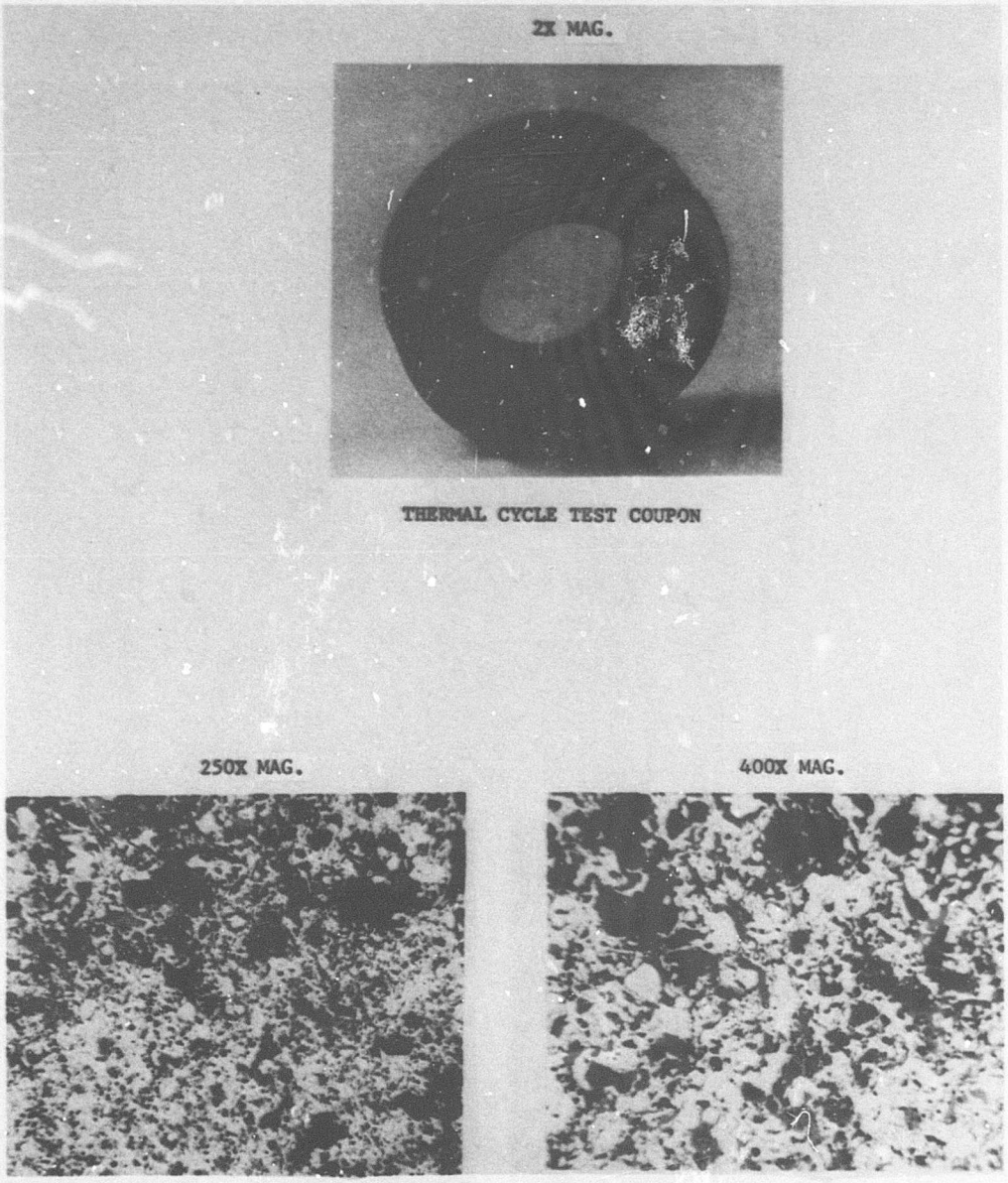


Figure 139. Typical Surface Structure of 50-Percent NiCr Bonded Cr_3C_2 + 50-Percent Cr_2O_3 After Test.

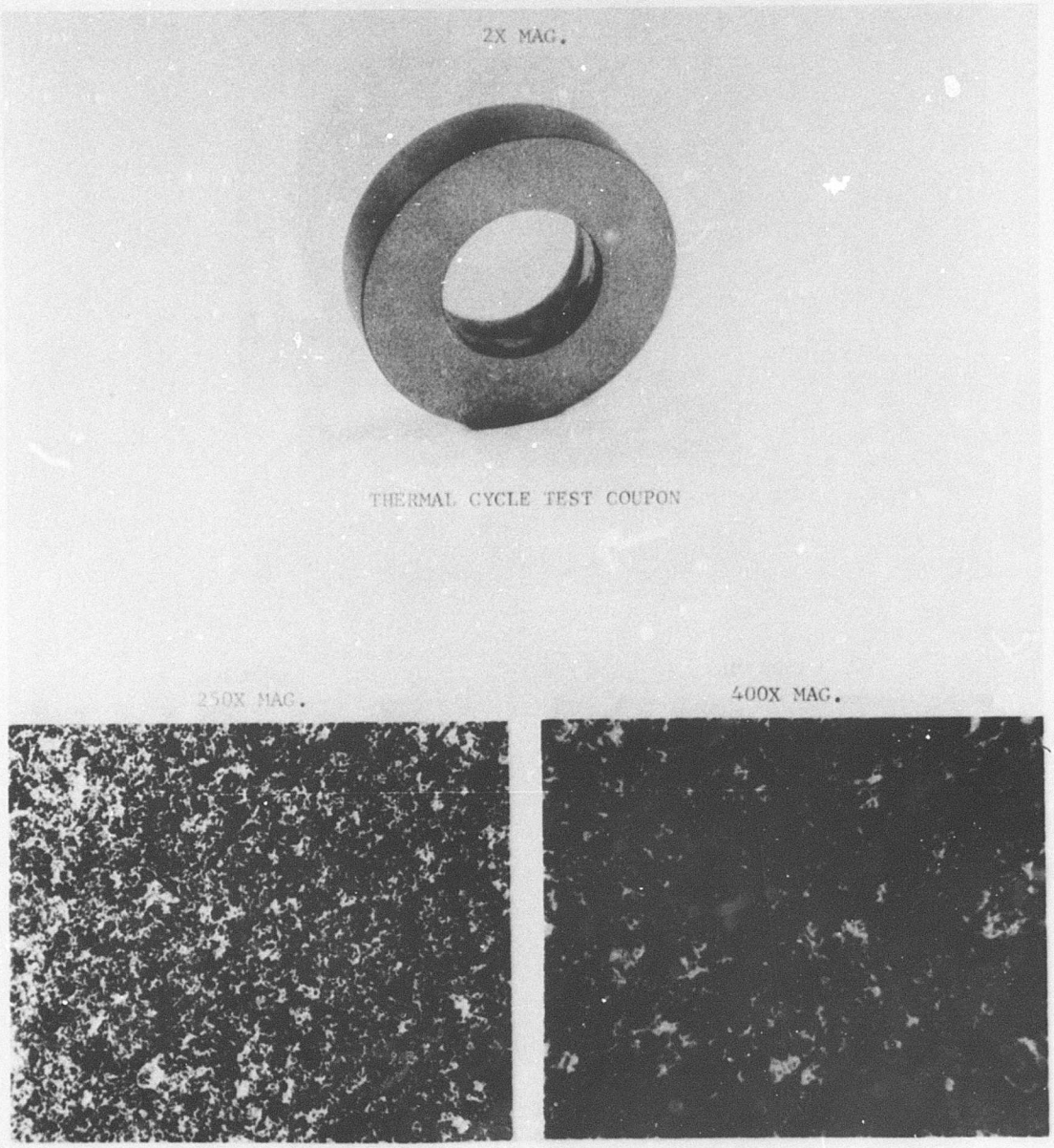


Figure 140. Typical Surface Structure of 40-Percent Chrome and 60-Percent Cr_2O_3 Before Test.

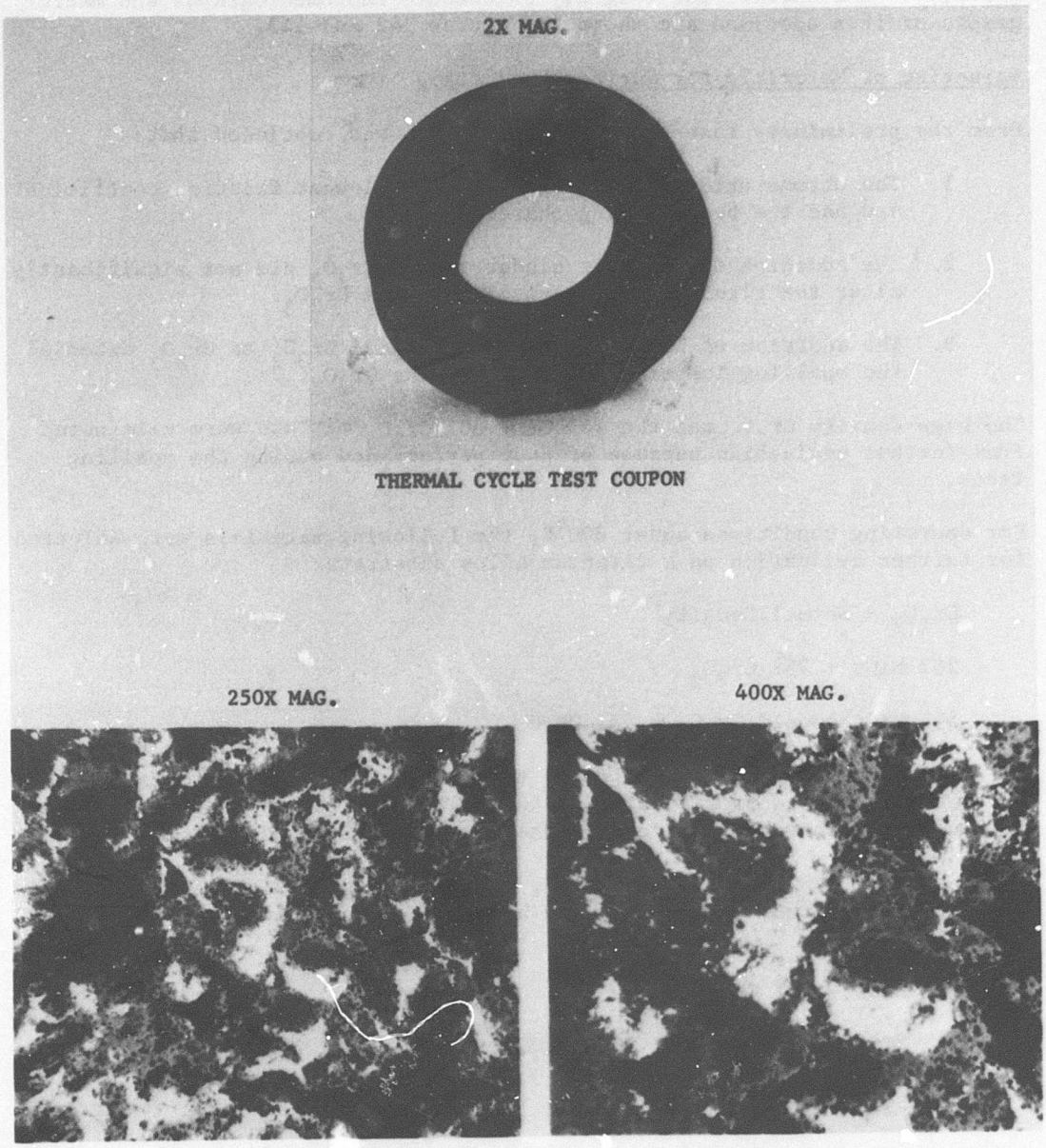


Figure 141. Typical Surface Structure of 40-Percent Chrome and 60-Percent Cr_2O_3 After Test.

The NiCr-bonded Cr_3C_2 coating also remained on the surface throughout the test. There was little change in the microstructure and no increase in porosity. The surface was slightly oxidized. Photomicrographs and macrographs of this specimen are shown in Figures 142 and 143.

Selection of Materials for Further Evaluation

From the preliminary tests described above, it was concluded that:

1. The chrome oxide coatings produced the lowest friction coefficient and had the best sliding characteristics.

2. The addition of 25% NiCr binder to the Cr_2O_3 did not significantly alter the sliding characteristics of the Cr_2O_3.

3. The addition of NiCr, Cr, and NiCr-bonded Cr_3C_2 to Cr_2O_3 extended the spalling temperature limits of the Cr_2O_3.

The high-density Cr_2O_3 and the 40% Cr + 60% Cr_2O_3 mixture were eliminated from further evaluation because of poor performance during the spalling tests.

For operating conditions under 800°F, the following materials were selected for further evaluation on a titanium alloy substrate:

Cr_2O_3 - Normal Density

25% NiCr + 75% Cr_2O_3

50% NiCr-bonded Cr_3C_2 + 50% Cr_2O_3

The first two of these had performed the best in the sliding tests, while the last one showed promise of high-temperature spalling resistance and improved wear characteristics over the straight NiCr-bonded chrome carbide.

For operating conditions above 800°F, the following coating materials were selected for further evaluation on a high-temperature nickel-based alloy substrate:

25% NiCr + 75% Cr_2O_3

50% NiCr-bonded Cr_2C_2 + 50% Cr_2O_3

NiCr-bonded Cr_3C_2

Although the Cr_2O_3 did not spall off the Waspaloy substrate until after temperatures in excess of 1000°F had been reached, previous experience with this coating at temperatures in excess of 900°F indicated that spalling and high friction could be a problem at 1000°F. For this reason, it was not considered for any application where the temperature might approach 1000°F.

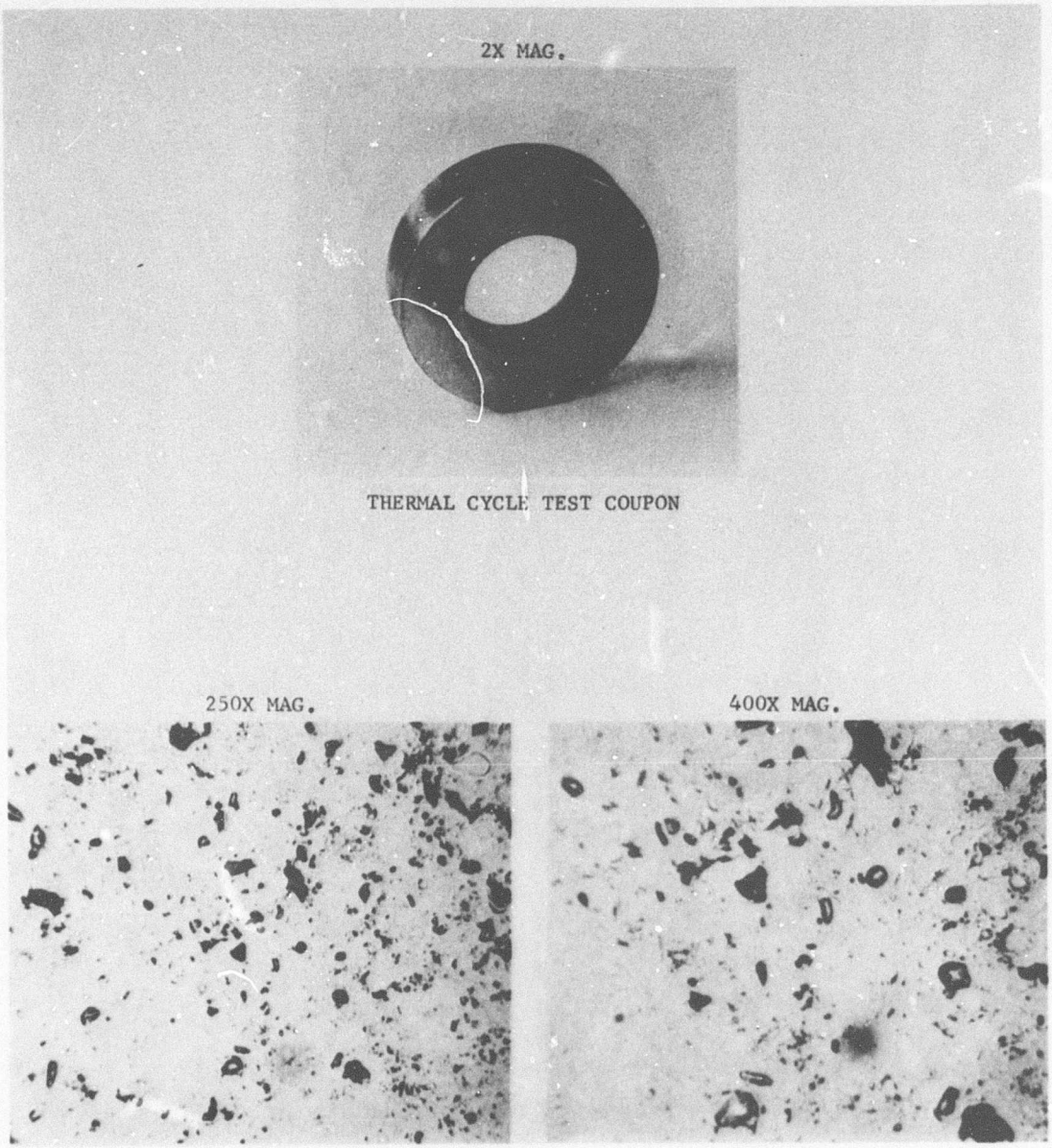


Figure 142. Typical Surface Structure of NiCr Bonded Cr_3C_2 Before Test.

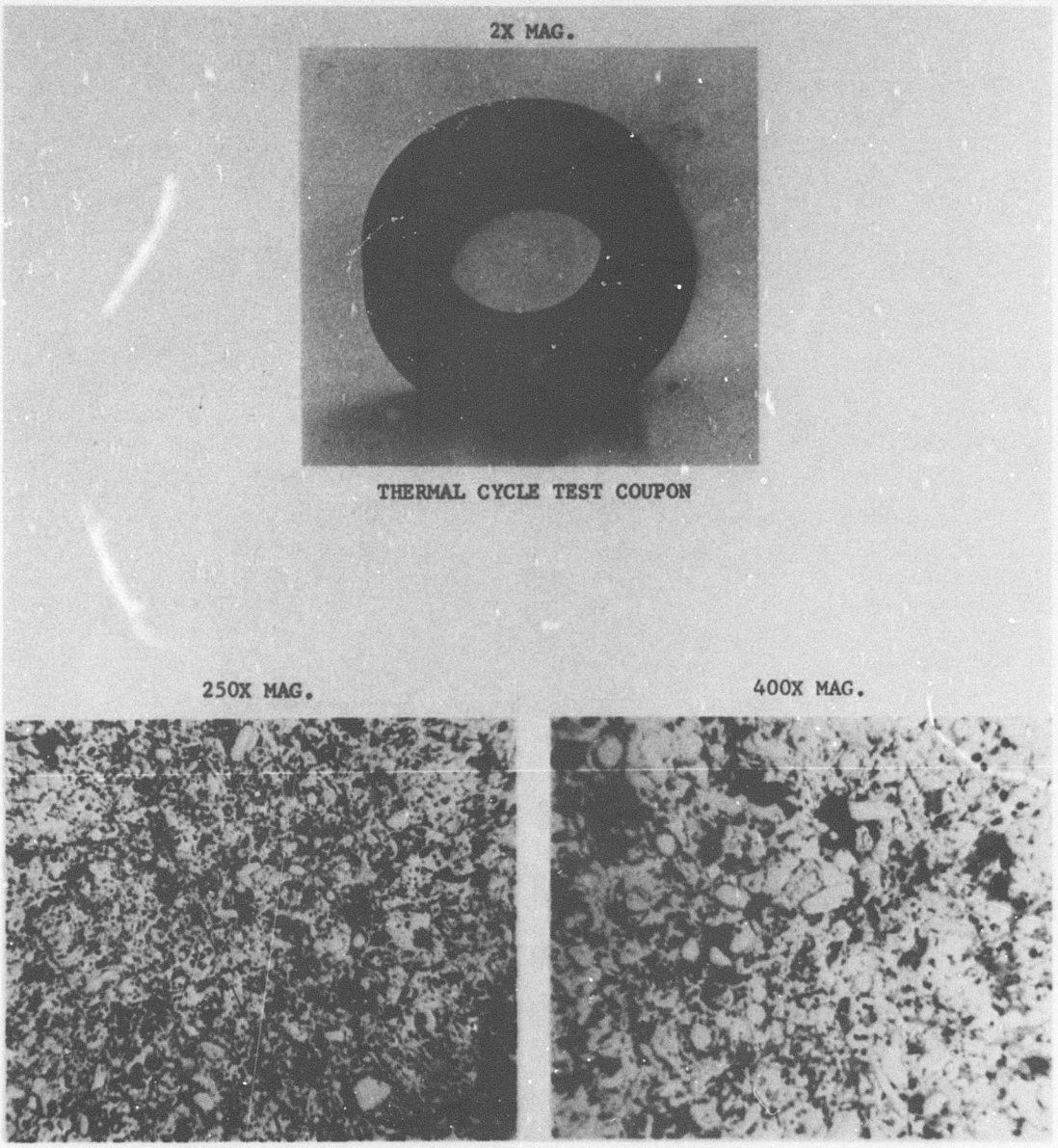


Figure 143. Typical Surface Structure of NiCr Bonded Cr_3C_2 After Test.

PRELIMINARY TEST EVALUATION

The selected coatings were subjected to preliminary test evaluations to determine their potential for surviving the start-stop sliding and stress conditions that would be imposed by the engine. These preliminary tests consisted of start-stop sliding tests in which the coatings were subjected to 1000 start-stop cycles (500 at room temperature and 500 at 800°F), and rotating bond-strength tests in which the coatings were applied to test journals and spin-tested to near the yield strength of the substrate.

Start-Stop Sliding Tests

Since the engine bearings are hydrodynamic, there is no bearing surface contact under normal engine operating conditions. However, during engine startup, the bearings are in contact until a sufficient speed is attained to form a hydrodynamic gas film.

The start-stop tests discussed here were run in such a manner as to simulate the sliding conditions in an actual journal bearing under the speed and load conditions that would be encountered in the engine during startup and shutdown.

The test specimens consisted of partial-arc pads loaded against a rotating cylinder, both of these being coated with the test material. In like manner to a tilting-pad journal bearing, the radius of curvature of the pad was larger than the cylinder (journal) and the pad was able to produce a hydrodynamic film. Thus, the type of contact (initially line) and the lift-off speed that would occur in the engine bearing could be duplicated with the subject test specimens by proper selection of load and area parameters.

The test rig used to perform these tests is shown in Figure 144. The test specimens consisted of a shaft and a partial-arc pad. These items were coated with the various coatings under consideration, and were ground and lapped to the diameters required to operate as an air bearing. The shaft is supported on ball bearings which are mounted in a water-cooled housing. The test journal is held onto the support shaft by means of an interference fit. The test shaft protrudes through the housing and supports the test bearing pad, which is coated with the same coating as the shaft. The pad is loaded by means of dead weight through a load arm and an Al_2O_3 ball pivot which allows the pad freedom to self-align. The test specimens are then heated to the desired temperature by means of a clam-shell type furnace with quartz infrared heating tubes. The temperature is monitored by means of a shielded thermocouple which is approximately 1/8 inch away from the end of the shaft. The furnace is controlled by means of a second thermocouple which is also mounted approximately 1/8 inch away from the test specimens. The shaft is driven by a 3450-rpm electric motor mounted on the opposite end of the test rig. The drive motor is connected to a timer which starts and stops the test rig as desired.

The diameters of the test shafts and test pads were 1.4984 inches and 1.5001 inches respectively, resulting in a clearance ratio (C/R) of $1/13 \times 10^{-3}$. The length of the pads was 0.75 inch, giving a length-to-diameter ratio of 0.5.

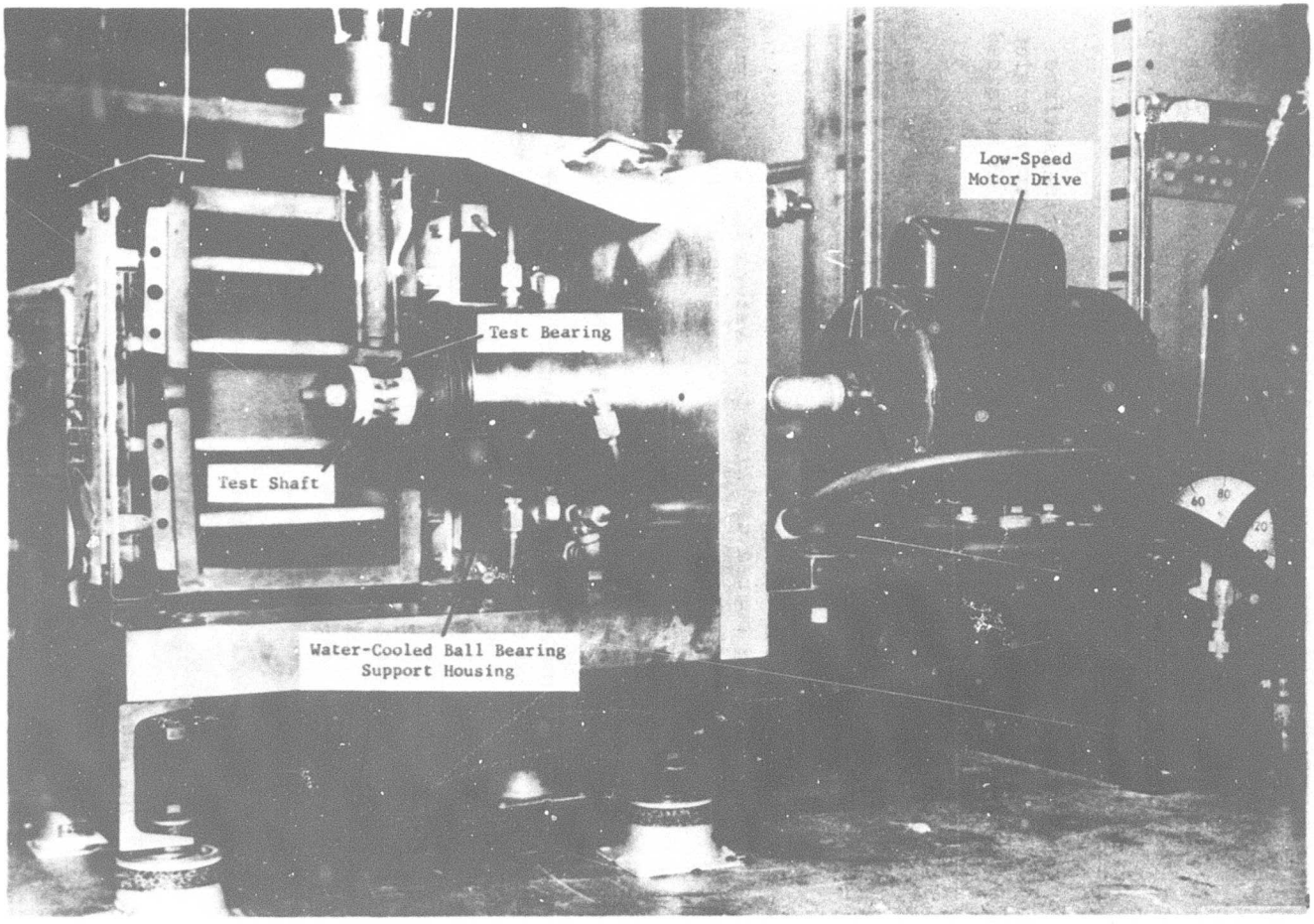


Figure 144. Test Rig Setup for Start-Stop Tests to Demonstrate Coating Sliding Compatibility.

The test conditions were as follows:

Temperature - 500 cycles, room temperature
500 cycles, 800°F

Speed - 3450 rpm

Cycle Time - 30 seconds (15 seconds on - 15 seconds off)

Atmosphere - air at 14.7 psia

Load - 4.5 pounds

Coating Thickness - shaft, 0.003 inch
pad, 0.003 inch

The procedure for the start-stop sliding tests was as follows:

1. Photographs of the test specimens were taken.
2. Talysurf traces of the surfaces of the test specimens were taken.
3. The specimens were assembled in the test rig and cleaned with reagent grade alcohol to eliminate any contamination of the specimens during assembly.
4. 500 start-stop cycles were run at room temperature for each specimen.
5. The test specimens were removed and examined.
6. Talysurf traces and photographs were again taken.
7. The specimens were recleaned and reassembled.
8. The clamshell furnace was assembled around the test specimens and heated to 800°F.
9. 500 start-stop cycles were run.
10. The test rig was cooled and disassembled.
11. Talysurf traces and photographs were again taken.

The results of these tests are shown in Tables XXIII and XXIV. These tables give the Center Line Average (CLA) surface finish of the pad and shaft at the start of the test, after 500 cycles at room temperature, and after another 500 cycles at 800°F.

The CLA is a method of measuring surface roughness in microinches, where a stylus is traversed across the surface to measure the surface asperities, recording them at preset distance intervals. These readings are averaged

and indicated on the instrument at the end of the traverse cycle. Several readings were taken to ensure repeatability. The traverse distance was 1/2 inch.

It will be noted in Tables XXIII and XXIV that the starting finish of the pad is smoother (lower CLA) than the shaft. This is a result of the lapping process which is normally employed on the pad (an ID surface) to bring it to final size. Shaft size is readily obtained by normal OD grinding techniques, and the finish produced is adequate for gas-bearing applications.

As can be seen from Table XXIII and Figures 145 and 146, the Cr_2O_3 and 25% NiCr + 75% Cr_2O_3 coatings showed no significant change in surface roughness; in fact, the lapping action which can be noted in Figures 145 and 146 is reflected in the reduced shaft CLA readings after 500 and 1000 start-stop cycles.

The test specimens coated with 50% Cr_3C_2 + 50% Cr_2O_3, as can be seen from Table XXIII and Figure 147, showed a marked change in surface characteristics during the test portion at 800°F. It was in fact noted during the test run at 800°F that the test pad had difficulty in lifting after about the three-hundredth cycle. This decreased hydrodynamic bearing performance was attributed to the character of the damaged surfaces.

The results of the start-stop sliding tests of the material coatings applied to the nickel-based alloy (Waspaloy) substrate are summarized in Table XXIV and Figures 148 to 150. As in the tests using the titanium substrate, the 25% NiCr + 75% Cr_2O_3 showed little change in surface characteristics. The other two, which were straight Cr_3C_2 and a 50% mixture of Cr_3C_2 and Cr_2O_3, both showed, by comparison, a large deterioration in surface finish.

Although the change in surface finish as indicated by the CLA values was larger for the 50% Cr_3C_2 + 50% Cr_2O_3 on the Waspaloy substrate tests than for the titanium substrate tests, the former did not show the degradation in hydrodynamic performance that the latter did. This would indicate that average surface finish per se is not the only criterion for judging the adequacy of surface for a bearing application.

Bond Strength Tests

In addition to the preliminary start-stop sliding tests on the aforementioned initially selected coating materials, the coatings were also subjected to high-temperature bond strength tests to evaluate their structural characteristics under conditions anticipated in the engine. High-speed spin testing was selected as the evaluation technique because it produced the combination of surface strain and centrifugal forces that would be encountered in the actual application.

The same three coatings on each substrate material as in the preliminary start-stop sliding tests were applied to a journal test specimen which measured 2.18 inches ID x 2.50 inches OD x 2.75 inches long. These dimensions approximated the actual engine journal dimensions. The three

TABLE XXIII. RESULTS OF SCREENING START-STOP SLIDING TESTS (TITANIUM SUBSTRATE)

4 psi loading
0 to 3450 rpm
2 cycles/min

Titanium Substrate (6Al-4V)		CLA Pad* (μ in.)	CLA Shaft* (μ in.)	Surface Condition for Continued Gas Bearing Operation
Cr_2O_3	Start	13	22	good
	A	24	22	good
	B	20	16	good
25% NiCr + 75% Cr_2O_3	Start	5	24	good
	A	6	22	good
	B	19	15	good
50% Cr_3C_2 + 50% Cr_2O_3	Start	6	18	good
	A	6	22	good
	B	43	43	poor

A - After 500 cycles at room temperature

B - After 500 cycles at room temperature + 500 Cycles 800°F

* - Centerline average readings (obtained from Talysurf at 0.1 in. cutoff distance)

TABLE XXIV. RESULTS OF SCREENING START-STOP SLIDING TESTS (WASPALOY SUBSTRATE)

4 psi loading
0 to 3450 rpm
2 cycles/min

Waspaloy Substrate		CLA Pad* (μ in.)	CLA Shaft* (μ in.)	Surface Condition for Continued Gas Bearing Operation
Cr_3C_2	Start	12	23	good
	A	12	19	good
	B	85	70	poor
25% NiCr + 75% Cr_2O_3	Start	1	20	good
	A	4	26	good
	B	18	25	good
50% Cr_3C_2 + 50% Cr_2O_3	Start	14	20	good
	A	18	16	good
	B	190	240	poor

A - After 500 cycles at room temperature

B - After 500 cycles at room temperature + 500 cycles at 800°F

* - Centerline average readings (obtained from Talysurf at 0.1 in. cutoff distance)

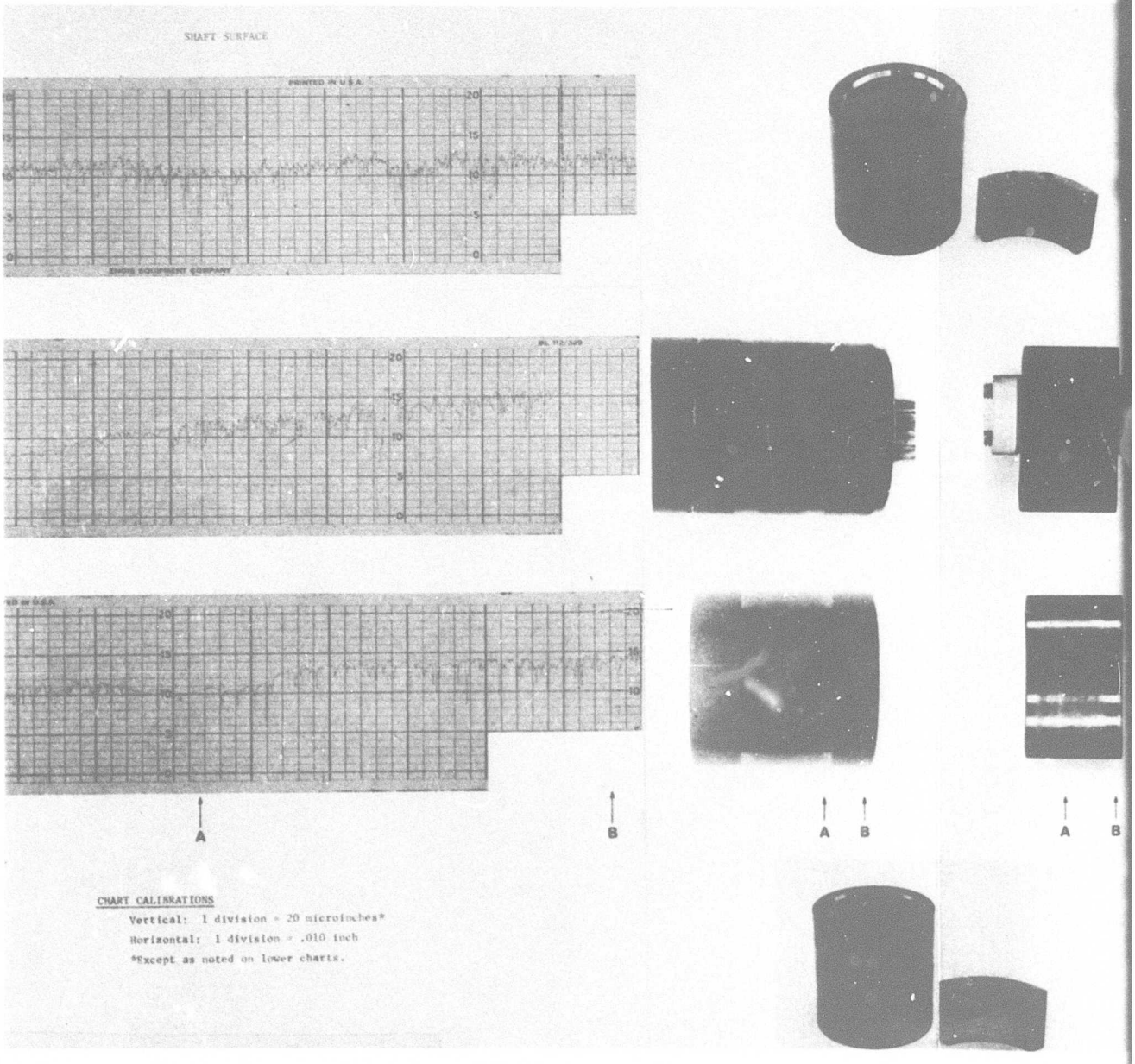
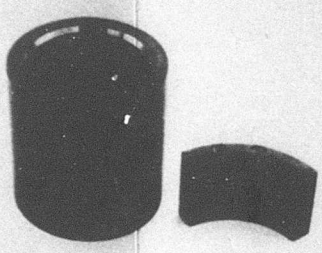
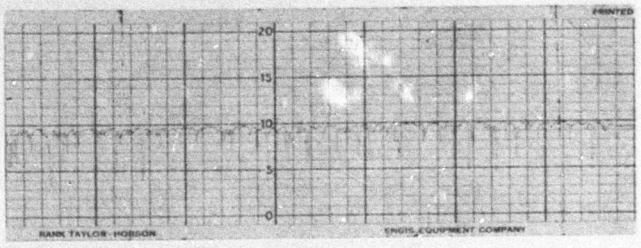


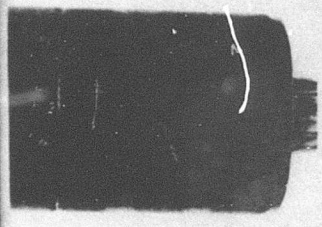
Figure 145. Results of Preliminary Start-Stop Sliding Tests for Cr_2O_3 Plasma Sprayed on Titanium Substrate at 4-psi Loading.

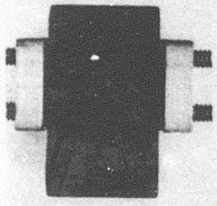
PAD SURFACE



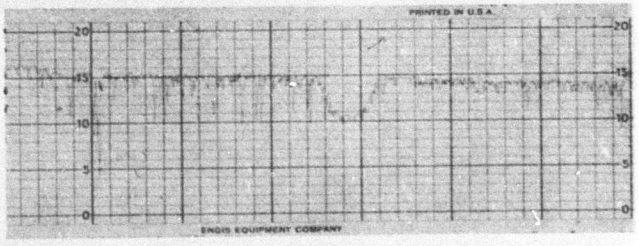
BEFORE TEST

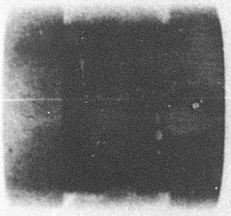


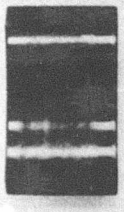




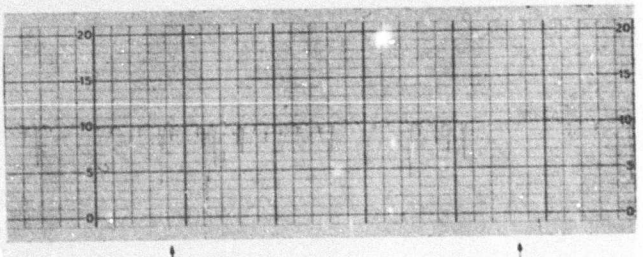
AFTER 500 CYCLES- ROOM TEMP.



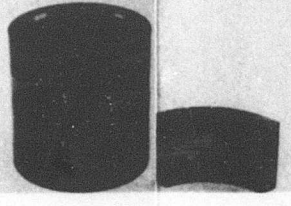




AFTER 500 CYCLES- ROOM TEMP. + 500 CYCLES AT 800°F



A B A B A B



AFTER TEST

liding Tests
Substrate

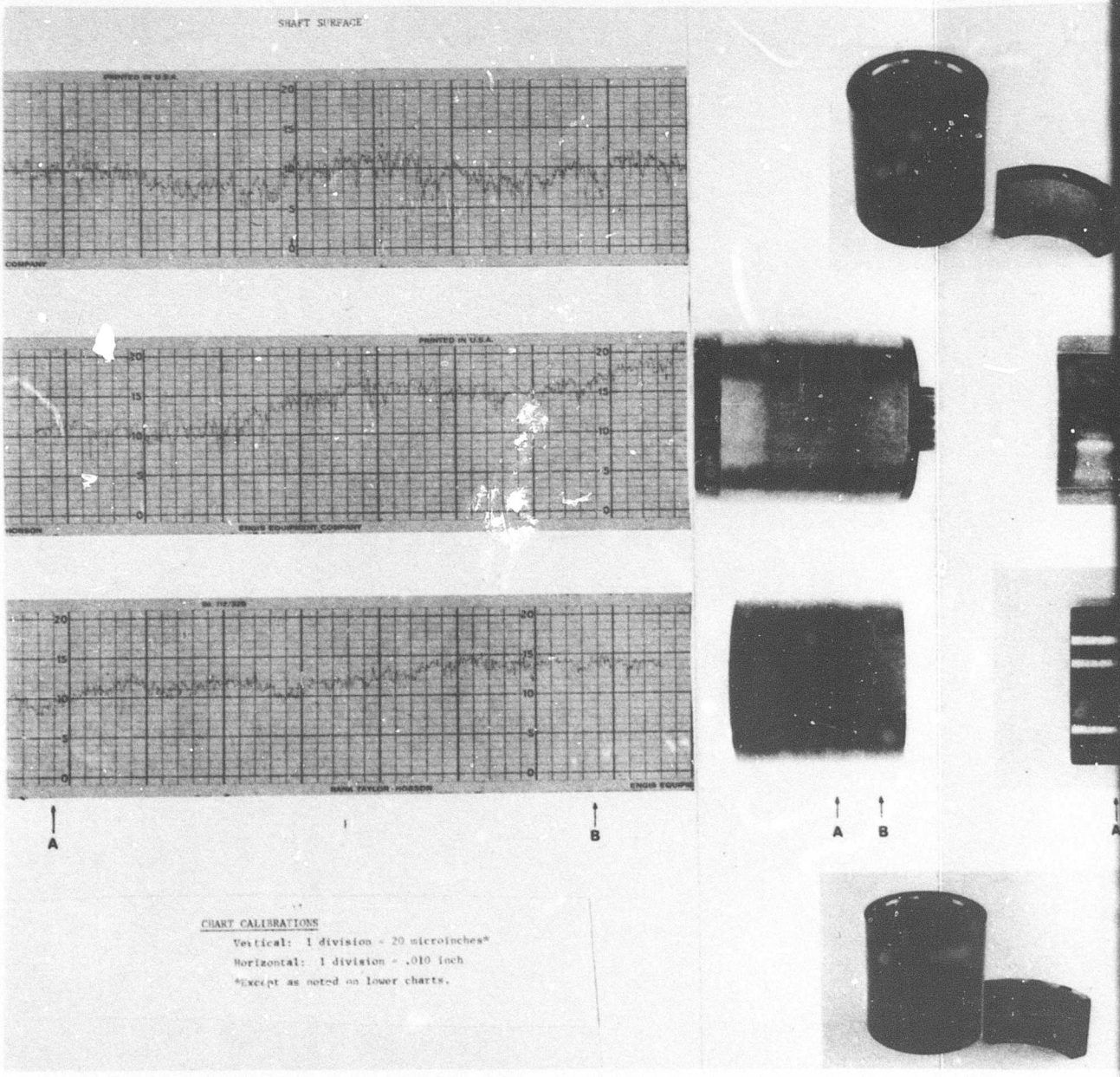
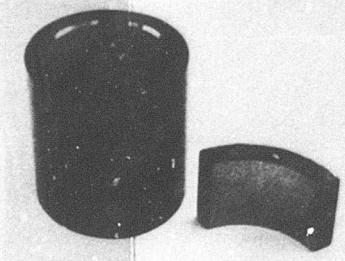


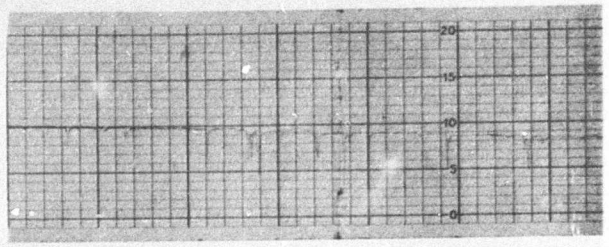
Figure 146. Results of Preliminary Start-Stop Sliding Tests for 25-Percent NiCr + 75-Percent Cr_2O_3 Plasma Sprayed on Titanium Substrate at 4-psi Loading.

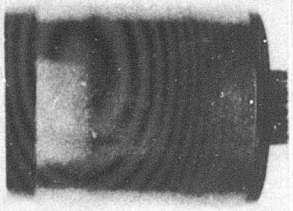
"PRECEDING PAGE BLANK-NOT FILMED."

PAD SURFACE



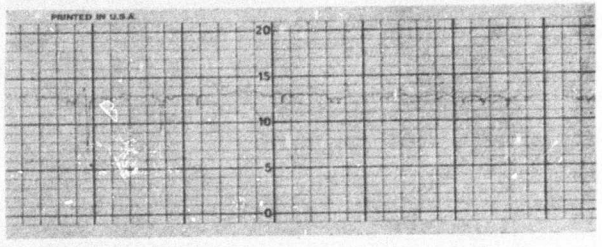
BEFORE TEST

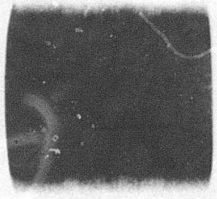


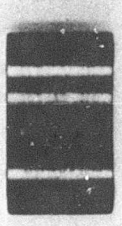




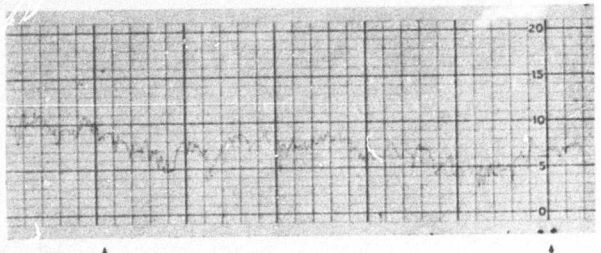
AFTER 500 CYCLES- ROOM TEMP.



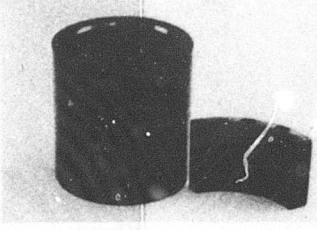




AFTER 500 CYCLES- ROOM TEMP. + 500 CYCLES AT 800°F



A B A B A B



AFTER TEST

liding Tests
$_2O_3$ Plasma
si Loading.

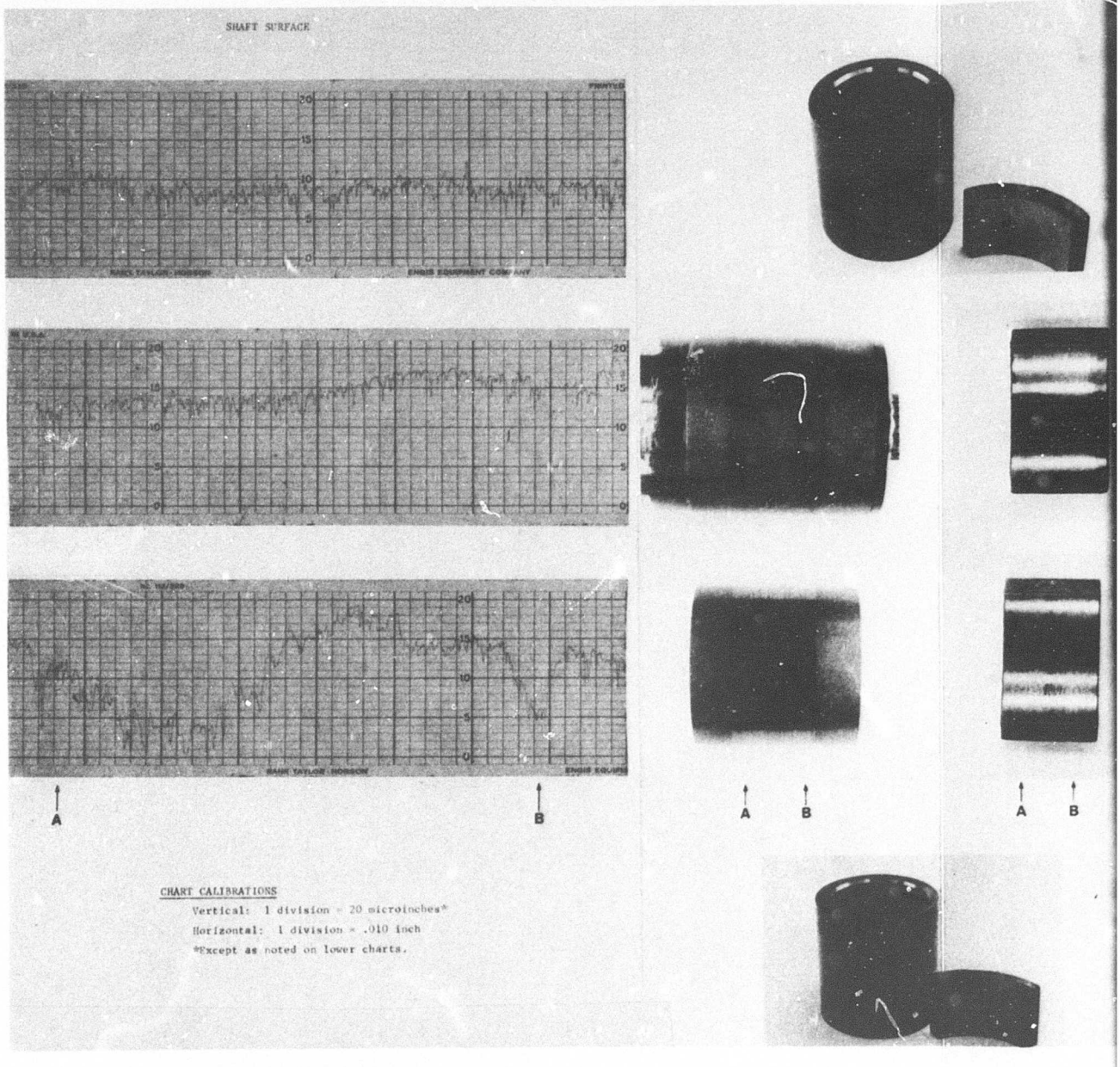
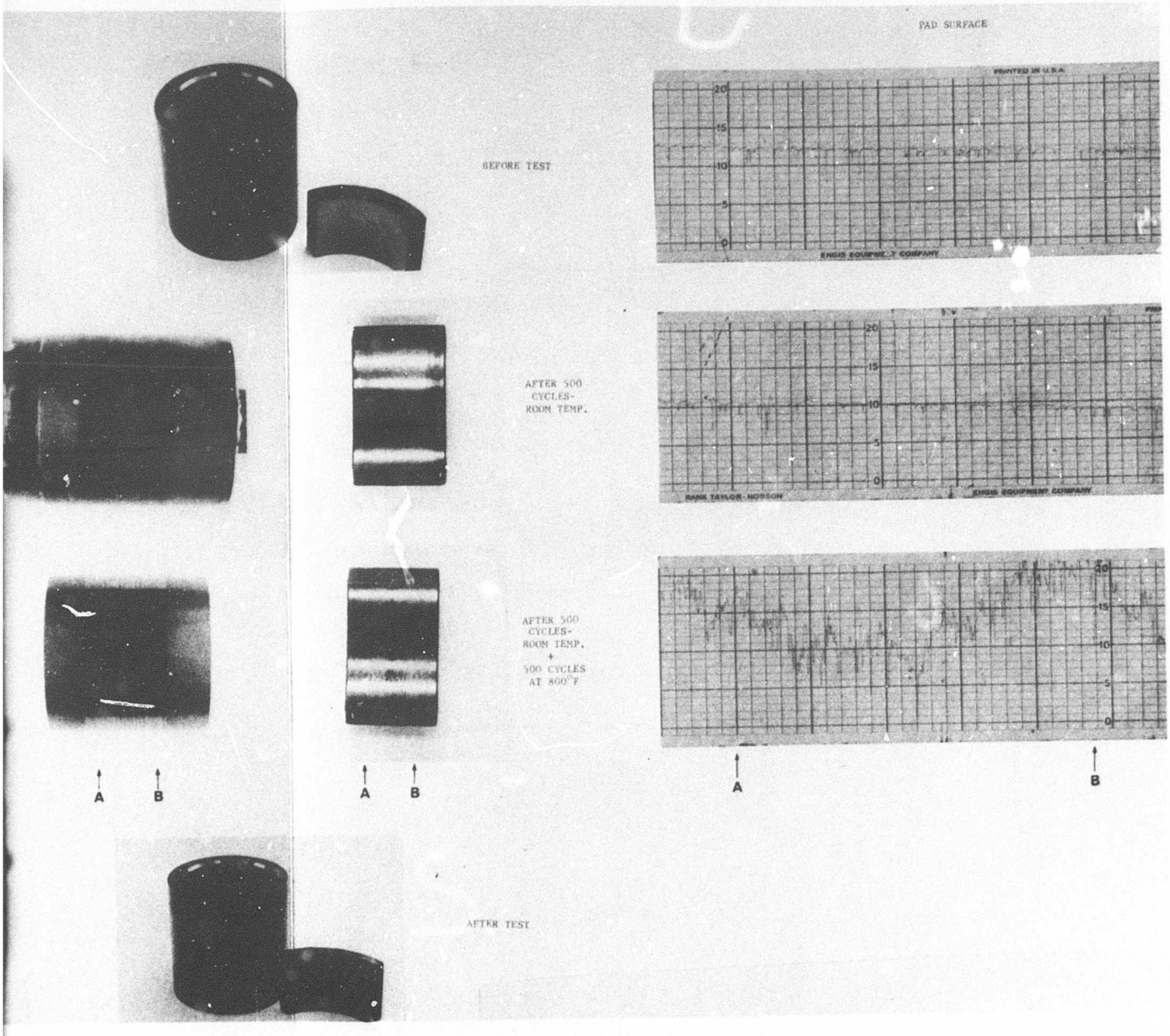


Figure 147. Results of Preliminary Start-Stop Sliding Tests for 50-Percent NiCr Bonded Cr_3C_2 + 50-Percent Cr_2O_3 Plasma Sprayed on Titanium Substrate at 4-psi Loading.

"PRECEDING PAGE BLANK-NOT FILMED."



liding Tests
50-Percent
bstrate at

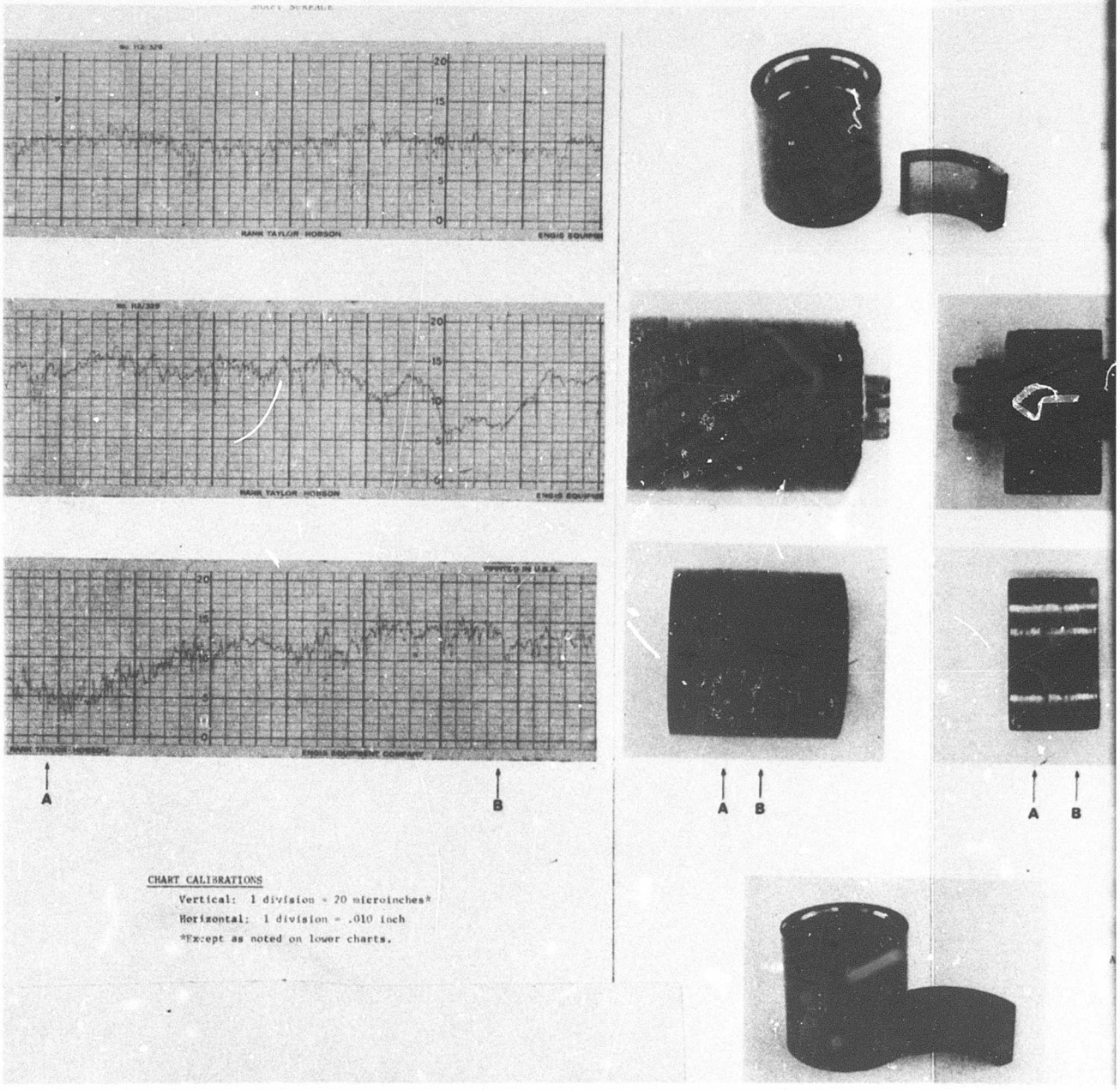
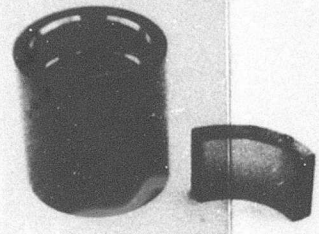


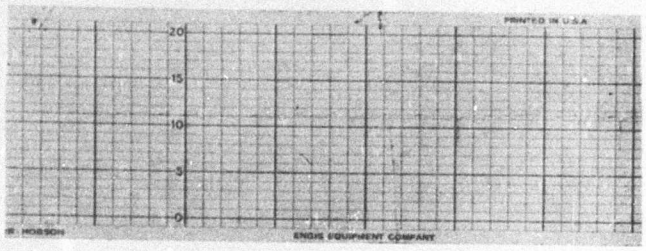
Figure 148. Results of Preliminary Start-Stop Sliding Tests for 25-Percent NiCr + 75-Percent Cr_2O_3 Plasma Sprayed on Waspaloy Substrate at 4-psi Loading.

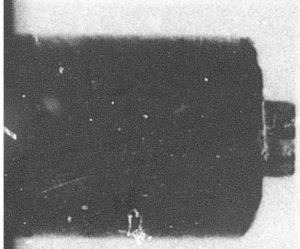
"PRECEDING PAGE BLANK-NOT FILMED."

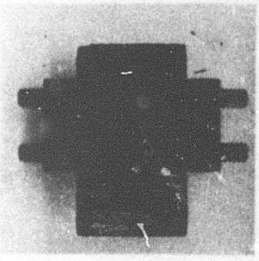
PAD SURFACE



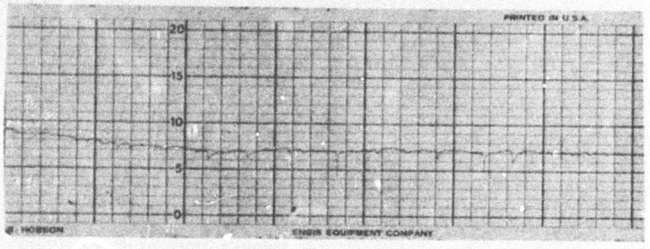
BEFORE TEST

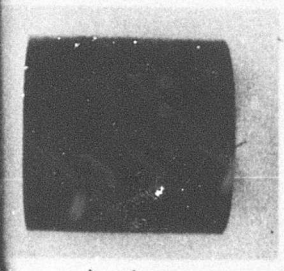


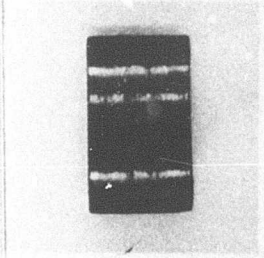




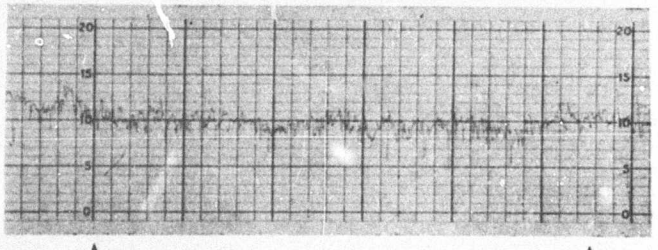
AFTER 500 CYCLES- ROOM TEMP.



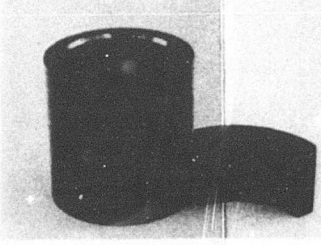




AFTER 500 CYCLES- ROOM TEMP. + 500 CYCLES AT 800°F



A B A B A B



AFTER TEST

ng Tests
Plasma
Loading.

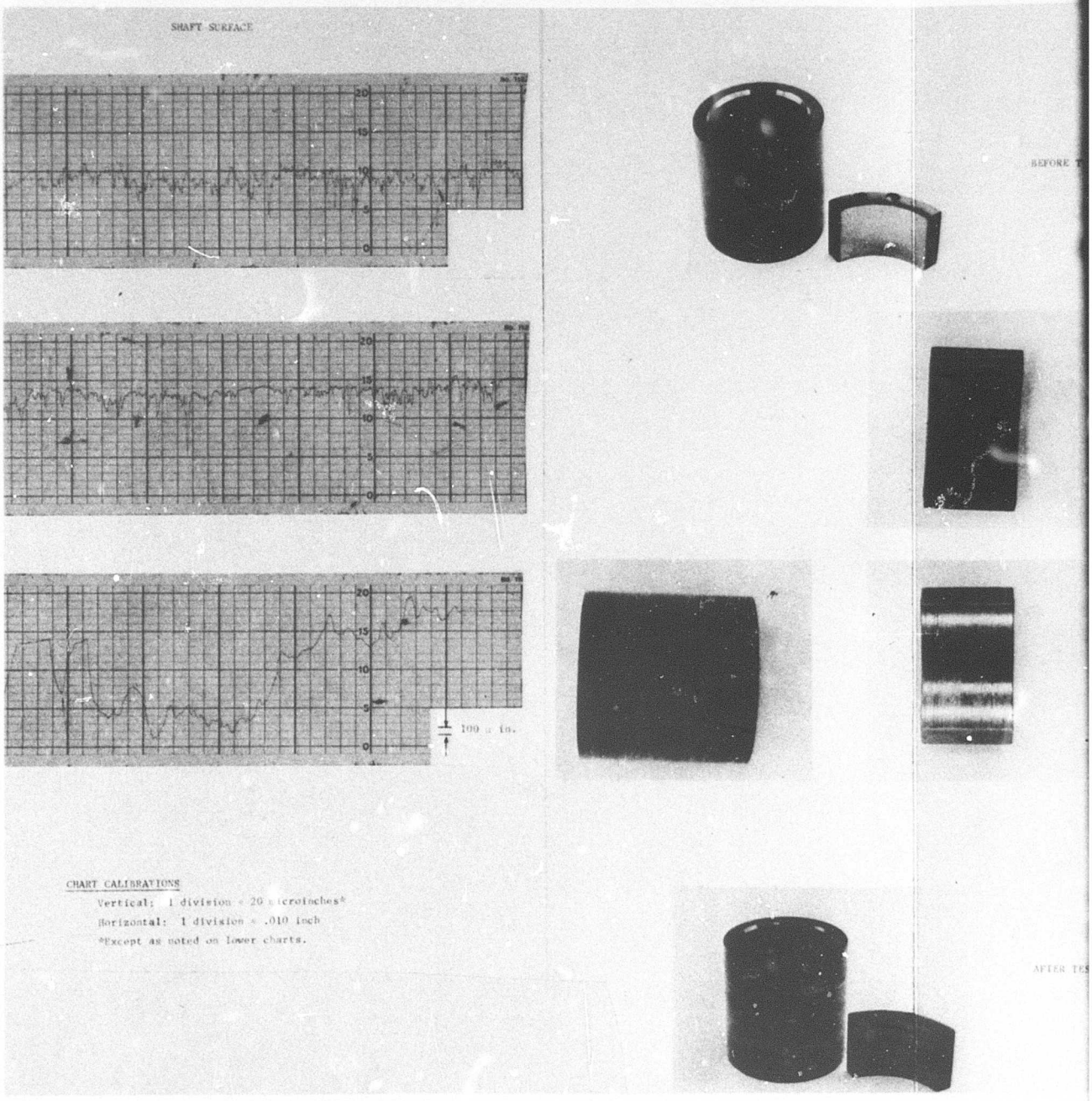
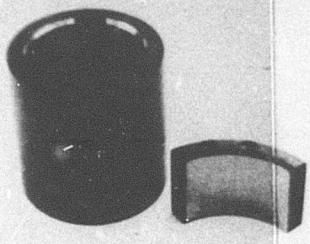


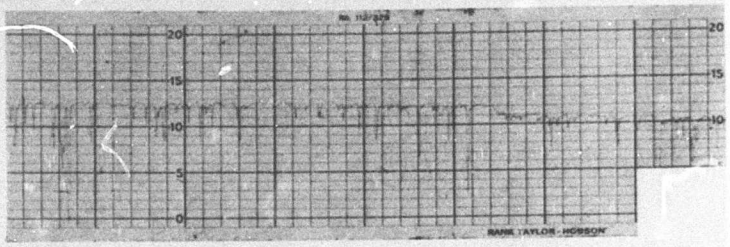
Figure 149. Results of Preliminary Start-Stop Sliding Tests for 50-Percent NiCr Bonded Cr_3C_2 + 50-Percent Cr_2O_3 Plasma Sprayed on Waspaloy Substrate at 4-psi Loading.

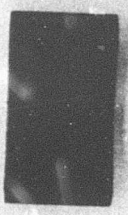
"PRECEDING PAGE BLANK-NOT FILMED."

PAD SURFACE

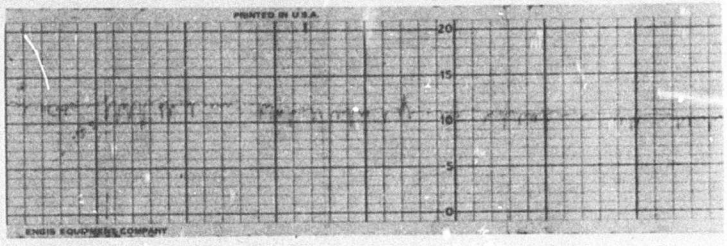


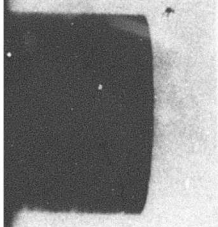
BEFORE TEST

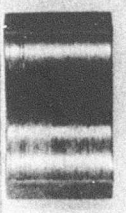




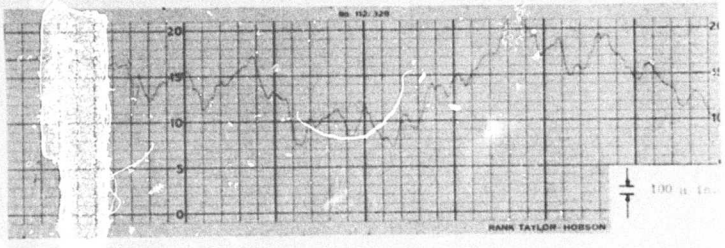
AFTER 500 CYCLES- ROOM TEMP.

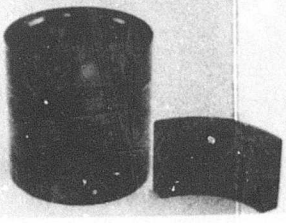






AFTER 500 CYCLES- ROOM TEMP. + 500 CYCLES AT 800°F





AFTER TEST

liding Tests
0-Percent
strate at

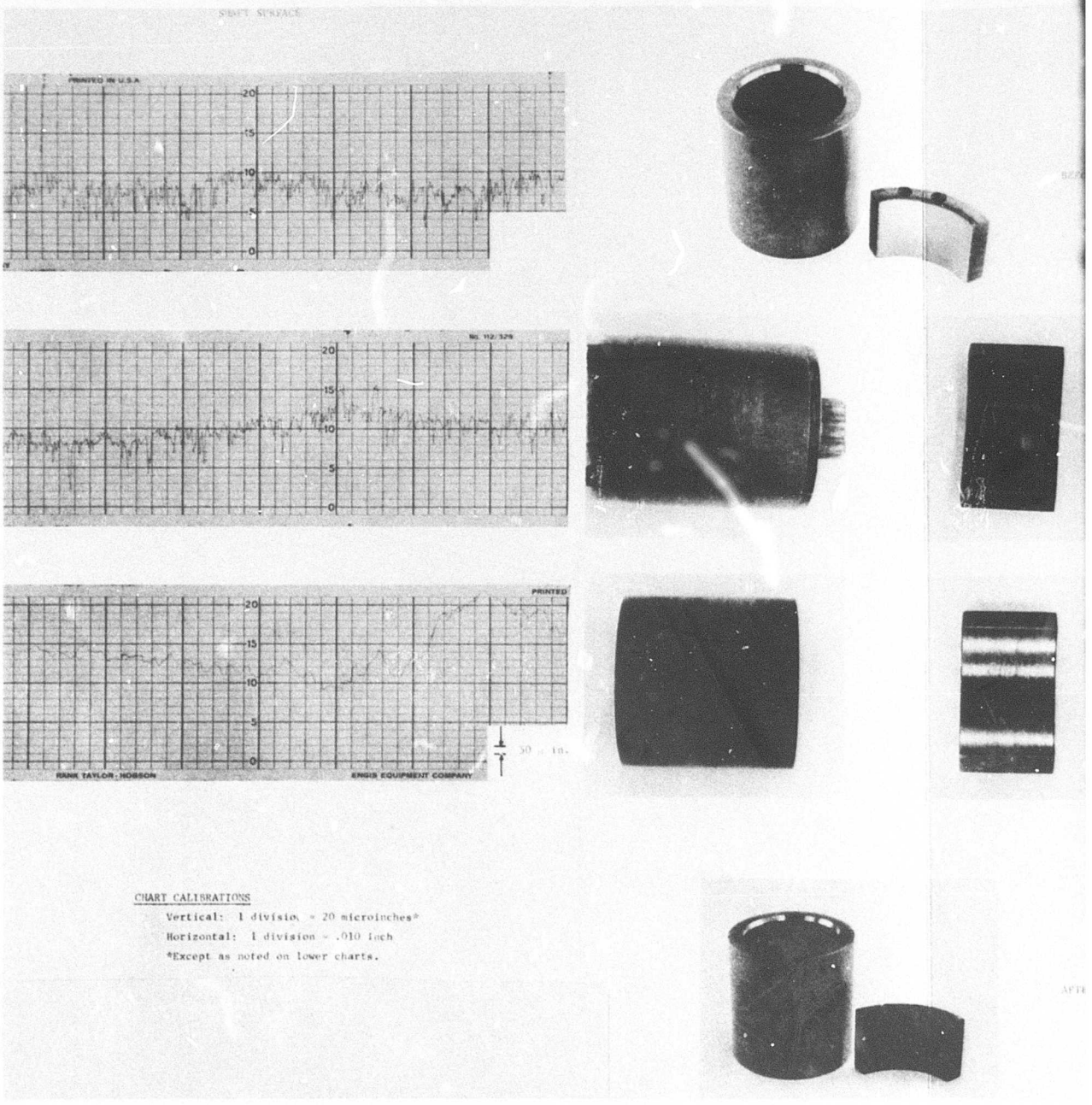
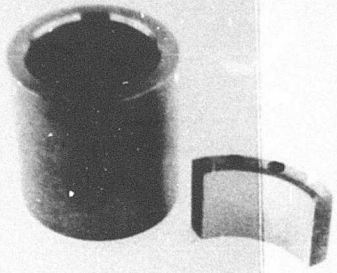


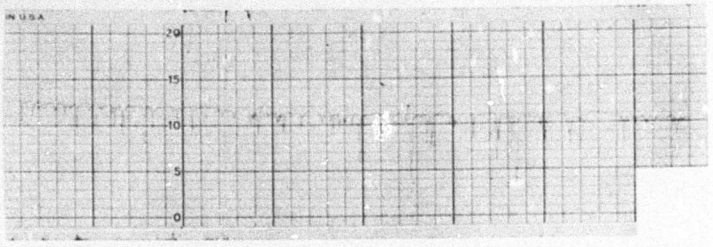
Figure 150. Results of Preliminary Start-Stop Sliding Tests for NiCr Bonded Cr_3C_2 Plasma Sprayed on Waspaloy Substrate at 4-psi Loading.

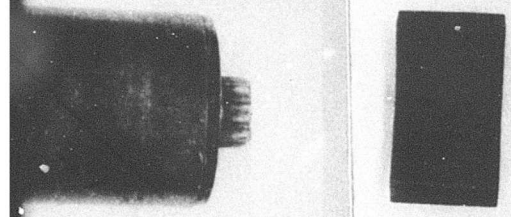
"PRECEDING PAGE BLANK-NOT FILMED."

PAD SURFACE

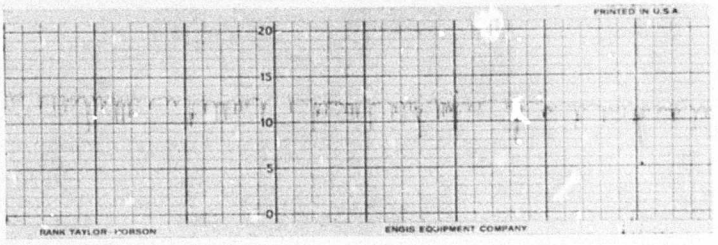


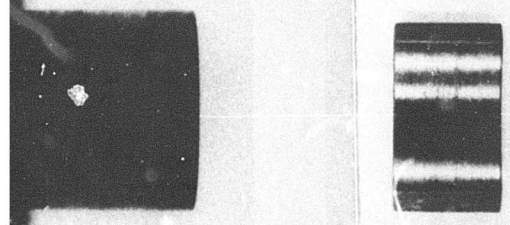
BEFORE TEST



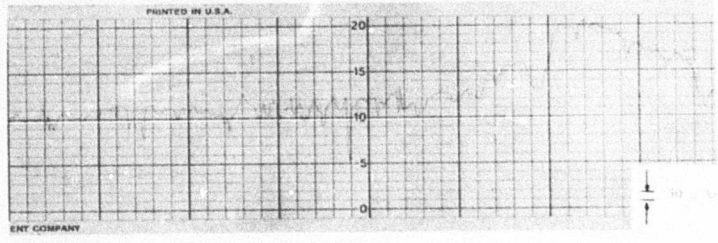


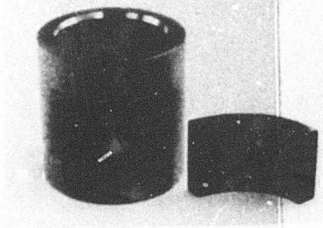
AFTER 500 CYCLES- ROOM TEMP.





AFTER 500 CYCLES- ROOM TEMP. + 500 CYCLES AT 800°F





AFTER TEST

Sliding Tests
ed on Waspaloy

selected coatings for each substrate were applied to a single test specimen so that data on all three coatings could be obtained from a single test.

The closed spin-pit is shown in Figure 151. The spin-pit facility consists of an armored pit, a drive turbine with a maximum speed of 150,000 rpm, a resistance heating coil, and a console for speed and temperature control. Nitrogen jets were used to seal the drive spindle and to aid in maintaining a uniform temperature along the test specimen. Nitrogen was used to insure a relatively inert atmosphere in the pit in case of lubricating oil leakage. The pit was not evacuated during the tests, and air was also present since the pit base was vented. A journal test specimen, with the spin-pit drive arbor, is shown in Figures 152 and 153.

Specimen temperature was determined in the tests by calibrating nearby non-rotating thermocouples against a thermocouple on the specimen surface before the tests were started. The spin-pit temperatures were allowed to stabilize until they were consistent with the required specimen temperature prior to starting each test.

The titanium specimen was tested first at 800°F using the following test sequence:

1. Set desired specimen temperature $\pm$ 25°F and allow to stabilize for approximately one hour.

2. Run five speed cycles from 0 to 65,000 rpm.

3. Remove specimen and inspect coatings visually and dimensionally.

4. Reinstall specimen.

5. Repeat steps 1 through 4, incrementally increasing maximum cyclic speed to 70,000, 75,000, 80,000, and 85,000 rpm.

The Waspaloy specimen was tested in the same manner as the titanium except that its test temperature was 1000°F.

The starting point of 65,000 rpm was selected to subject the coating/substrate interface to the strain levels predicted for the 3.5-lb/sec engine rotating journal at 120% of design speed. However, the temperatures were in excess of the engine values at 120% design power. The tests were terminated at 85,000 rpm because the stress level in the specimen at that speed was near the 0.2% yield strength of titanium.

Some question was present after the first set of tests as to the influence of the relatively inert atmosphere on the test results. The limited amount of oxygen may have resulted in reduced oxidation of the titanium, thereby affecting the test results. Therefore, a second titanium specimen was prepared and tested. This specimen was baked in an air-filled furnace for 16 hours at 800°F before it was spin tested. The test sequence was the same as for the first specimen except that the specimen was not removed for inspection between speed levels.

PRECEDING PAGE BLANK-NOT FILMED.

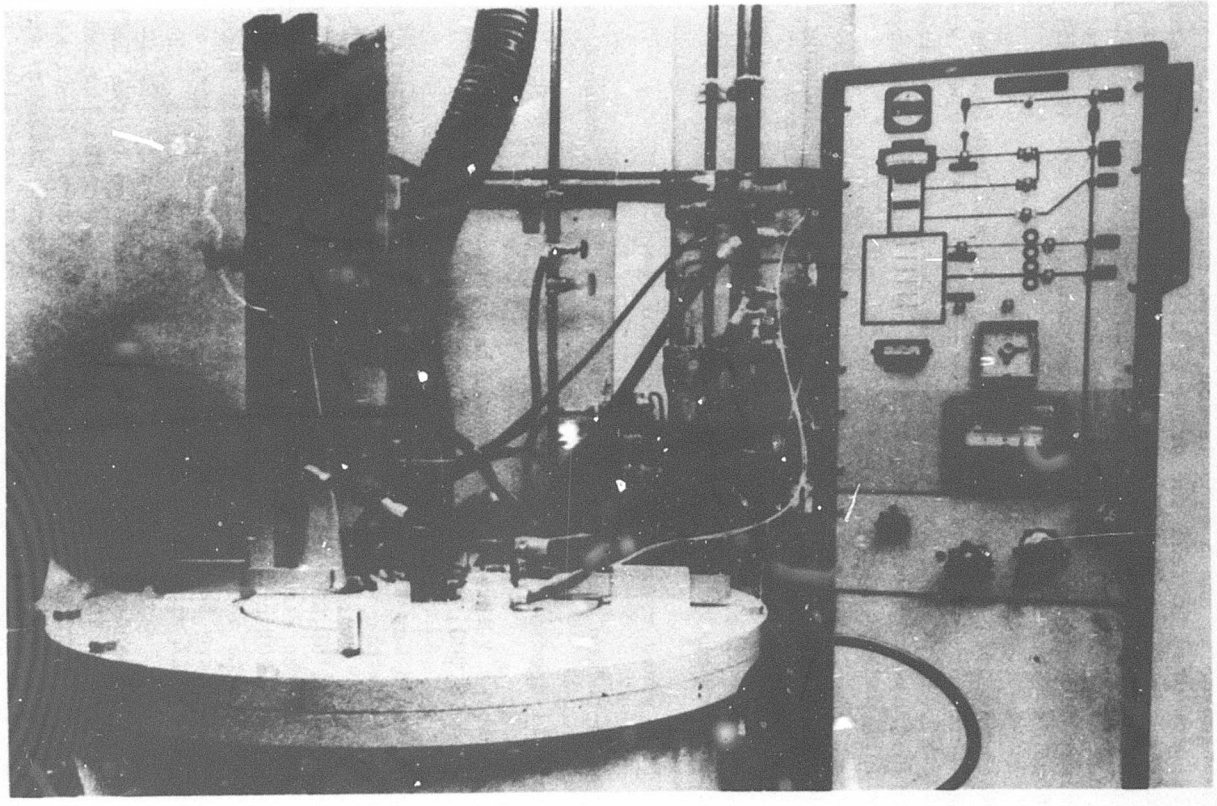


Figure 151. HSD Elevated Temperature Spin Test Facility (Pit Closed).

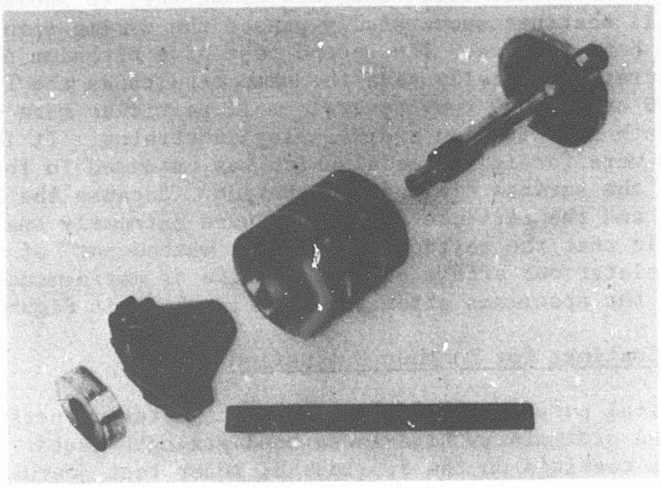


Figure 152. Spin Test Components — Arbor and Test Cylinder.

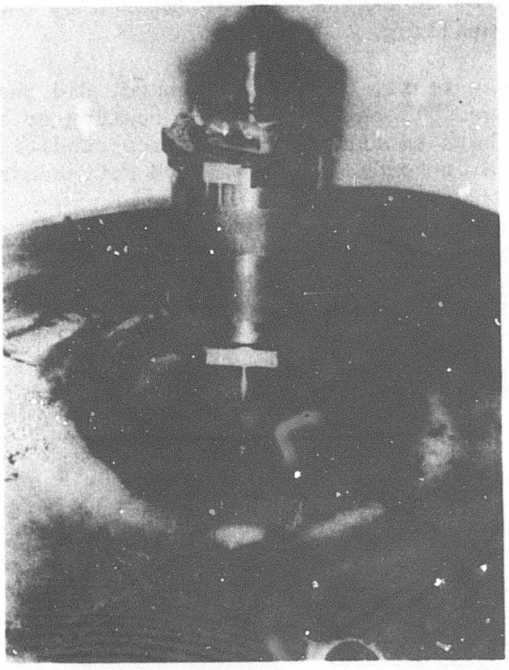


Figure 153. Cylinder-Arbor Assembly Mounted for Test.

The results of the cyclic spin tests are summarized in Tables XXV, XXVI, and XVII. All coatings successfully passed the cyclic spin tests without indication of bond failure. The second test of a titanium specimen, with oxidized substrate, generally gave the same results as the first test. Between 70,000 and 75,000 rpm, several small particles were shed from the coatings on both the titanium and Waspaloy substrates. It is believed that the particles were foreign material which was embedded in the surface, possibly from the surface finishing operation. Because the bearing pads are segmented and the particles dislodged were extremely small, it is highly probable that the particles would be "washed out" of the bearing without any deleterious effect on bearing life or performance. The general appearance of the specimens after the test is shown in Figures 154 and 155.

Selection of Coatings for Further Evaluation

For all practical purposes, each of the coatings tested performed equally well during the preliminary high-speed bond strength tests. At the 85,000-rpm speed, the coatings on the 2.5-inch-diameter test journals were subjected to surface strains in excess of 170% of those that would be experienced by the 2.25-inch-diameter journals in the 3.5-lb/sec engine at the 120% overspeed condition (72,000 rpm). Furthermore, with the possible exception of the 50% NiCr-bonded Cr_3C_2 + 50% Cr_2O_3, temperature cycling to temperatures in excess of that imposed by the engine did not produce evidence of spalling.

The start-stop sliding tests, on the other hand, did show a wider variation in coating performance. The straight Cr_2O_3 coating on titanium and the 25% NiCr + 75% Cr_2O_3 on both substrates had surface conditions after 1000 cycles far superior to the NiCr-bonded Cr_3C_2 and 50% NiCr-bonded Cr_3C_2 + 50% Cr_2O_3.

Therefore, primarily because of their superior sliding characteristics, the following coating materials were selected for the engine and were subjected to further testing to verify that they would satisfy the endurance requirements under engine operating conditions:

1. Cr_2O_3 on a titanium substrate for the compressor-end bearings where surface temperatures would be below 800°F.

2. 25% NiCr + 75% Cr_2O_3 on a nickel-based alloy substrate where surface temperatures would be between 800°F and 1000°F.

ENDURANCE TEST EVALUATIONS

Two types of endurance evaluations were performed on the two selected coating/substrate combinations. These were start-stop sliding and high-speed spin testing similar to that which had been performed during the preliminary evaluation tasks.

The conditions imposed upon the test specimens were derived from the specified engine life and duty cycle, and from the environmental conditions calculated for the 3.5-lb/sec selected engine concept.

TABLE XXV. HIGH-SPEED COATING BOND STRENGTH TESTS INSPECTION LOG

Rotor No. T_1 (8-1-1) Titanium 800°F

Coatings: (1) Cr_2O_3 (Chrome Oxide)

(6) 25% NiCr (Nickel Chrome) + 75% Cr_2O_3

(7) 50% NiCr Bonded Cr_3C_2 (Chr. Carb.) + 50% Cr_2O_3

Speed (rpm)	Cycles	Remarks
65,000	5	No discernible change in surface appearance. No dimensional change.
70,000	5	Coating (1) (Cr_2O_3) shows slight pit flaking - pits appear to be associated with embedded grit particles - possibly from grinding wheel. No dimensional change.
75,000	5	Coatings (1) and (7) now show pitting. No dimensional change.
80,000	5	Same as 75,000 rpm.
85,000	5	Coating (6) now showing small pitting; coatings (1) and (7) now showing flaking. No dimensional change.

TABLE XXVI. HIGH-SPEED COATING BOND STRENGTH TESTS INSPECTION LOG

Rotor No. W_1 (WASPALOY) 1000°F

Coatings: (3) NiCr Bonded Cr_3C_2

(7) 50% NiCr Bonded Cr_3C_2 + 50% Cr_2O_3

(6) 25% NiCr + 75% Cr_2O_3

Speed (rpm)	Cycles	Remarks
65,000	5	No change in surface appearance. No dimensional change.
70,000	5	Coating (6) showing pitting, all over surface. Coating (7) flaking along edges. (This had a ragged edge when received.)
75,000	5	Pitting on (6), flaking on (7) (3) unchanged.
80,000	5	Same as 75,000. No dimensional change.
85,000	5	(6) - More pitting and small edge flaking - More flaking on (7) - (3) still good.

Note: (3) coating had pits initially. It appears that low spots are not hit by grinding. No change in this band throughout spin test.

TABLE XXVII. HIGH-SPEED COATING BOND STRENGTH TESTS INSPECTION LOG

Rotor No. T_2 (8-1-1) Titanium 800°F

Coatings: (1) Cr_2O_3 (Chrome Oxide)

(7) 50% NiCr Bonded Cr_3C_2 + 50% Cr_2O_3

(6) 25% NiCr + 75% Cr_2O_3

Note: This specimen was spun 5 cycles at 65,000, 70,000, 75,000 80,000 and 85,000 rpm without removing from pit (800°F). Examination of surface shows coating (7) (50% CiCr bonded Cr_3C_2 + 50% Cr_2O_3) having experienced no evidence of damage from test.

(7) and (6) show very little change.

(7) and (1) (Chrome Oxide) flaking at boundary.

Note: Coating (6) was not too well deposited initially. Feathering edge effect noticed before spin. Very little change after spin.

Spalling on all surfaces - minimal.

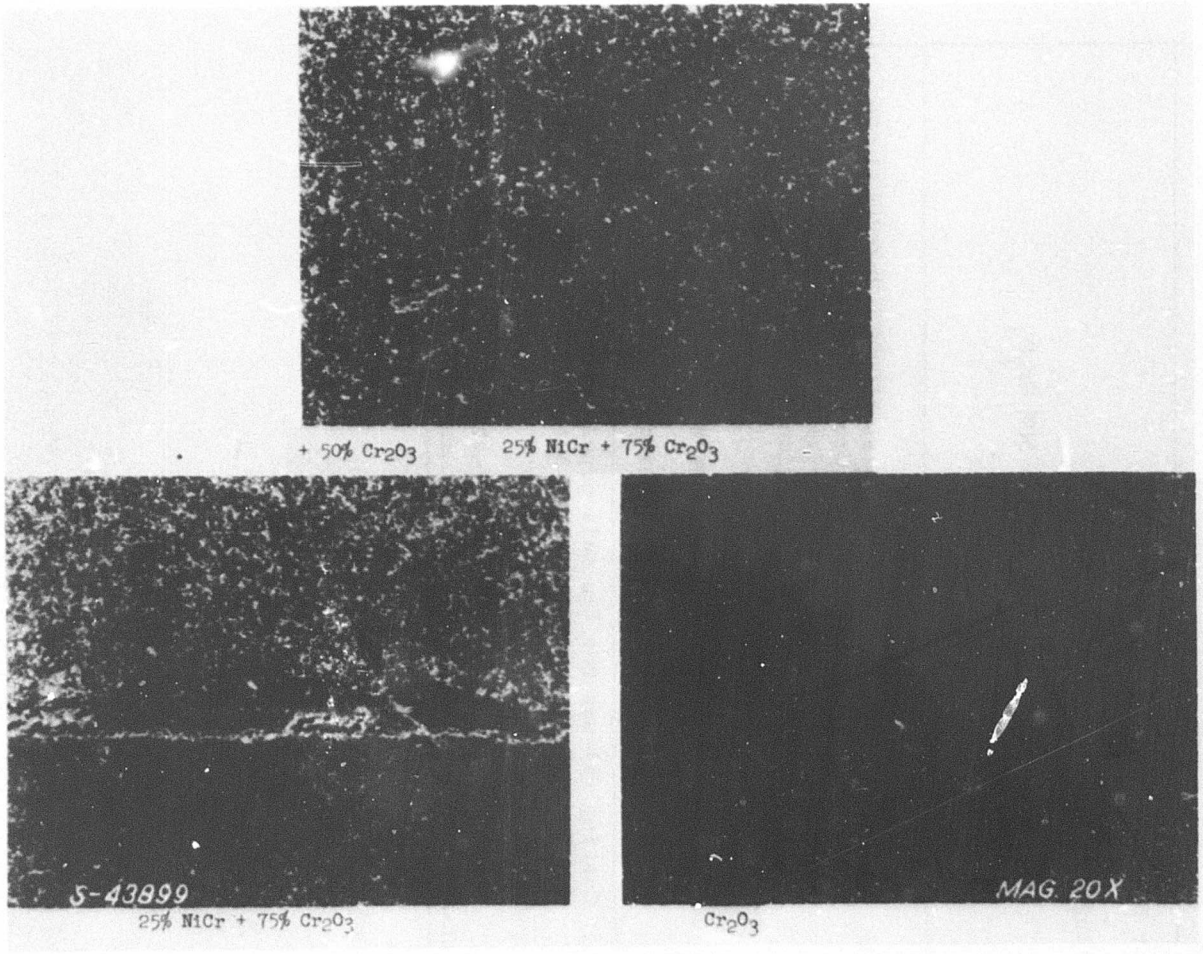


Figure 154. General Appearance of Coatings at End of Test-Cylinder No. 1.

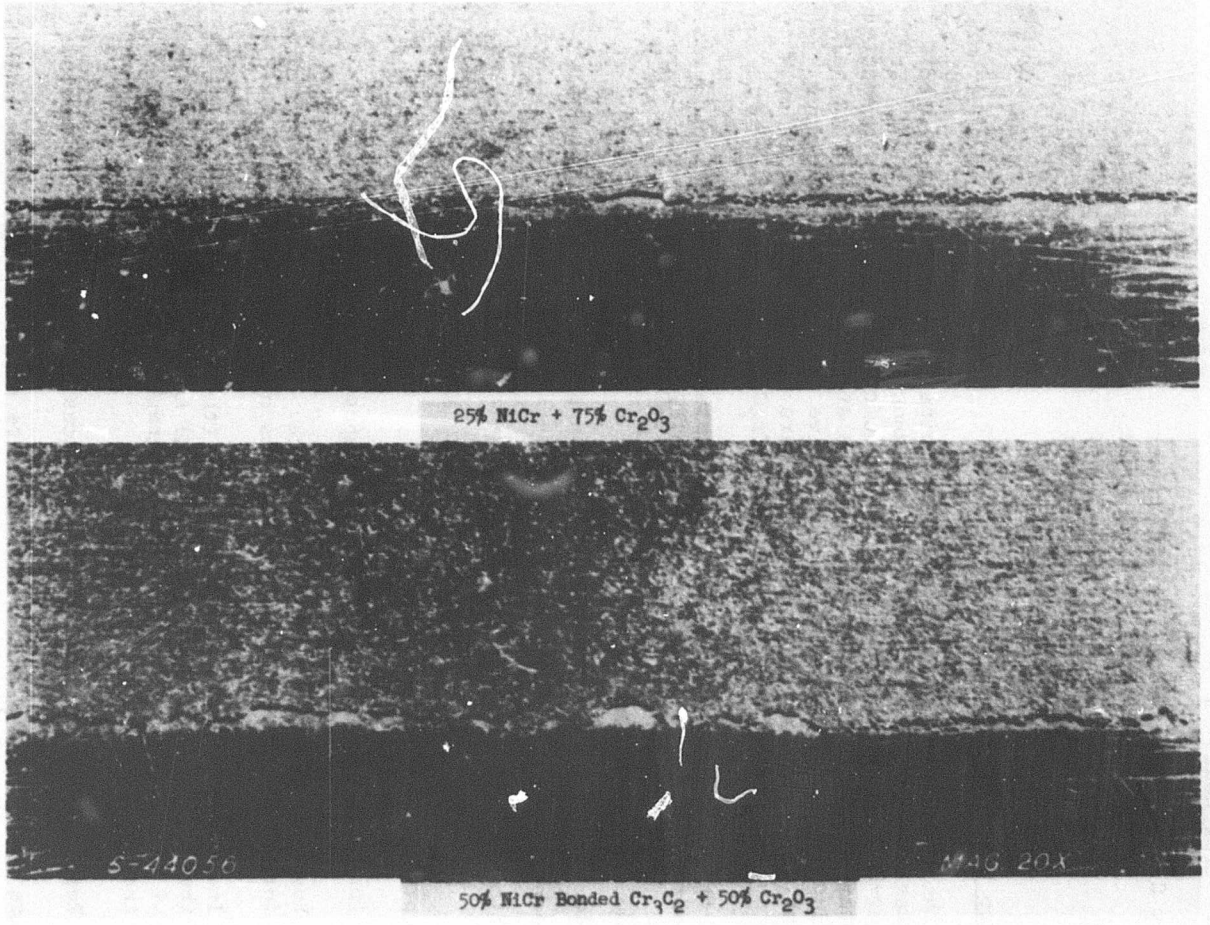


Figure 155. Appearance of Coating Edges After Test-Cylinder No. 2.

The significant engine specification requirements that set the test conditions were as follows:

Design Life: 5000 hours

Starts Per Hour: 3

Duty Cycle:
750 hr at 100% power
2250 hr at 75% power
1250 hr at 55% power
500 hr at 35% power
250 hr at idle

Start-Stop Endurance Tests

Both of the selected coating/substrate combinations were subjected to 15,000 start-stop cycles to duplicate the specification design life and starts-per-hour criteria. One half of these cycles (7500) were conducted at room temperature to simulate cold engine starting, and the other half were conducted at temperatures representative of hot engine shutdown conditions. These elevated temperatures were 550°F for the Cr_2O_3 on titanium and 700°F for the 25% NiCr + 75% Cr_2O_3.

The load imposed was 4 pounds, which duplicated the engine bearing Hertzian contact stress at start-up. The other significant test conditions were:

Speed - 0 to 3450 rpm

Cycle Time - 30 seconds, i.e., 15 seconds on and 15 seconds off

Atmosphere - air at 14.7 psia

Coating Thickness - Shaft, .003 inch
Pad, .003 inch

The test procedure was as follows:

1. Photograph and talysurf the test specimens before test.

2. Run 7500 cycles at room temperature. Stop at 1000-cycle intervals for photographs and talysurf traces of the test pad.

3. Increase the temperature to 550°F (the estimated temperature of the compressor-end journal bearing) and run 7500 cycles. Stop at 1000-cycle intervals for photographs and talysurf traces of the test pad.

4. Rephotograph and take talysurf traces at the end of the tests.

The results of the Cr_2O_3 on titanium test are shown in Figures 156 and 157. The centerline average (surface roughness) is plotted as a function of the number of cycles in Figure 156, where the circles show the surface roughness of the pad at 1000-cycle intervals. The squares show the surface

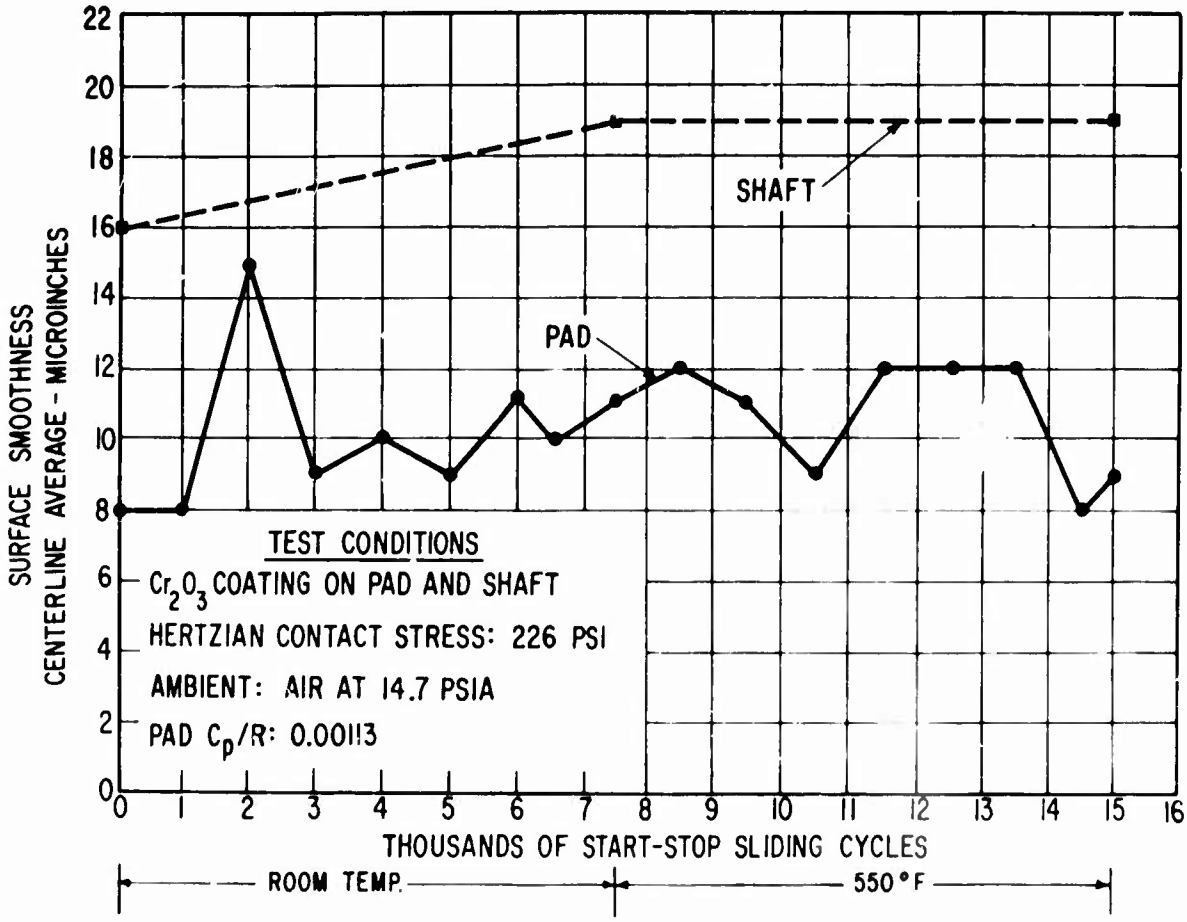


Figure 156. Surface Finish of Cr_2O_3 Coating During 15,000-Cycle Start-Stop Test.

roughness of the shaft at the start of the test, after 7500 cycles at room temperature, and after 7500 cycles at 550°F. The surface roughness measurements were taken at three places across the wear track, and the averages were plotted in Figure 156. The actual CLA readings did not vary more than 1 microinch on any of the three readings. The centerline average of the pad was 8 microinches at the start of the test and 9 microinches at the end. At one point, however, it had increased to 15 microinches but decreased during the next thousand cycles and remained between 8 and 12 microinches to the completion of the test. The shaft centerline average increased from 16 to 17 microinches over the entire 15,000-cycle test. Since the shaft surface finish was measured only three times during the course of the test, any changes similar to that encountered with the pad were not identified. The photographs shown in Figure 157 indicate a worn area, but there is no damage. In fact, the wear area appears more as a lapped surface. The diameter of the pad and shaft was measured to 5 decimal places before and after the test. There was no change in diameter; that is, the wear was not measurable to within 5 decimal places.

The results of the 25% NiCr + 75% Cr_2O_3 on Waspaloy tests are similarly shown in Figures 158 and 159. This test ran at room temperature with little difficulty. The roughness varied between 5 and 10 microinches except at 6000 cycles, when it increased to 15 microinches, but returned to 10 microinches by the end of 7000 cycles. During the 7500 cycles at 700°F, the surface roughness varied between 5 and 15 microinches until a total of 13,500 cycles had been completed.

The test was continued for another 1500 cycles, at which point the final roughness had increased to 32 microinches. The shaft roughenss had also increased from 15 to 20 microinches.

Although the surface smoothness of the 25% NiCr + 75% Cr_2O_3 coated pad and journal tested at 700°F deteriorated more than the straight Cr_2O_3 tested at 550°F, it must be emphasized that the test pad was still operating hydrodynamically, although with poorer performance, at the end of the 15,000-cycle test.

Because of the very promising test results at 700°F, a second 25% NiCr + 75% Cr_2O_3 specimen was prepared and tested at 1000°F for 1000 cycles. This test condition was established to simulate a start-up condition following a hot shutdown with turbine temperature soak-back.

The procedure for this test was as follows:

1. Talysurf and photograph the pad and shaft.
2. Assemble the test rig and heat to 1000°F.
3. Run 120 cycles.
4. Allow the test rig to cool.
5. Disassemble the test rig.
6. Talysurf and rephotograph.

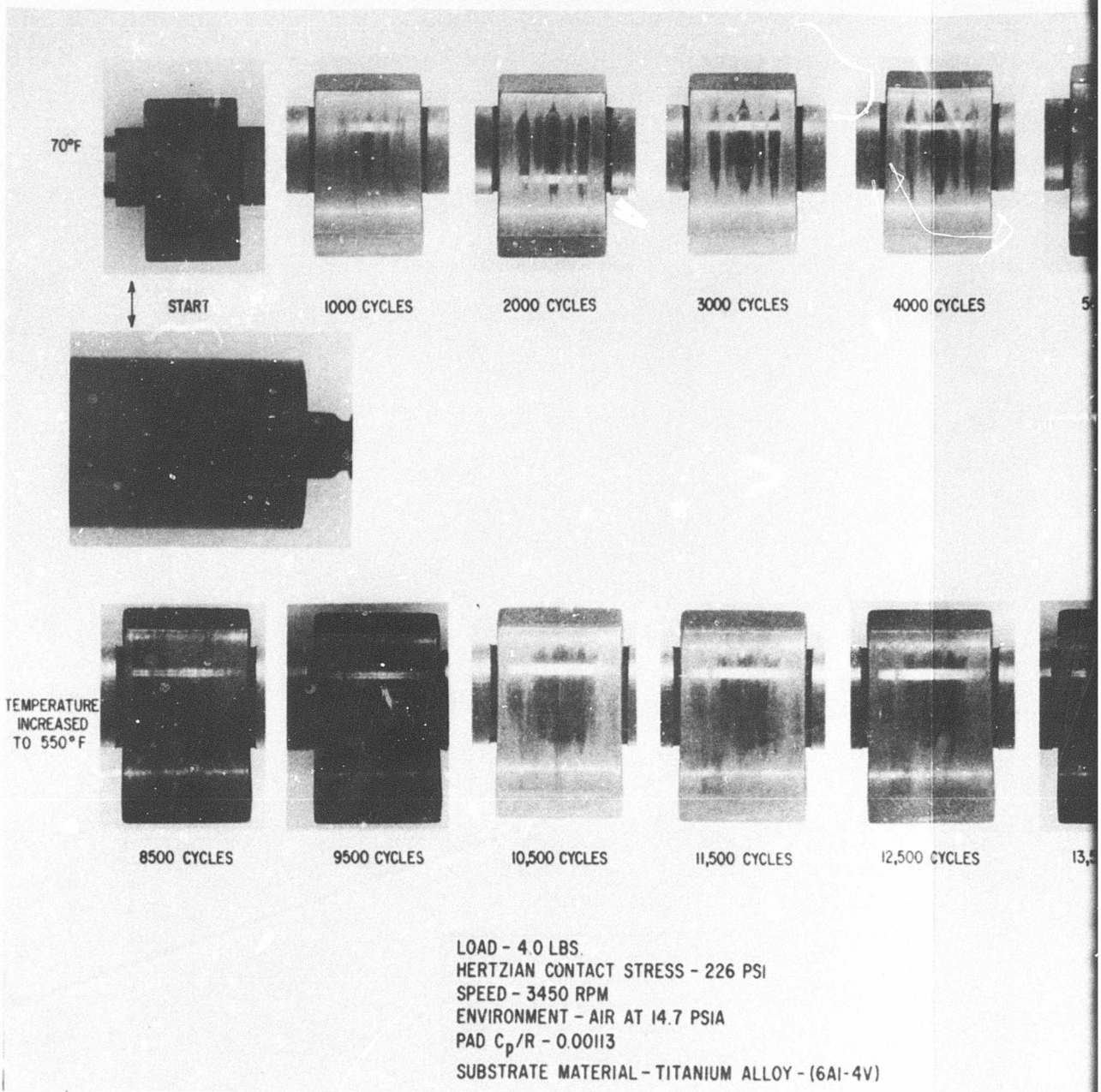
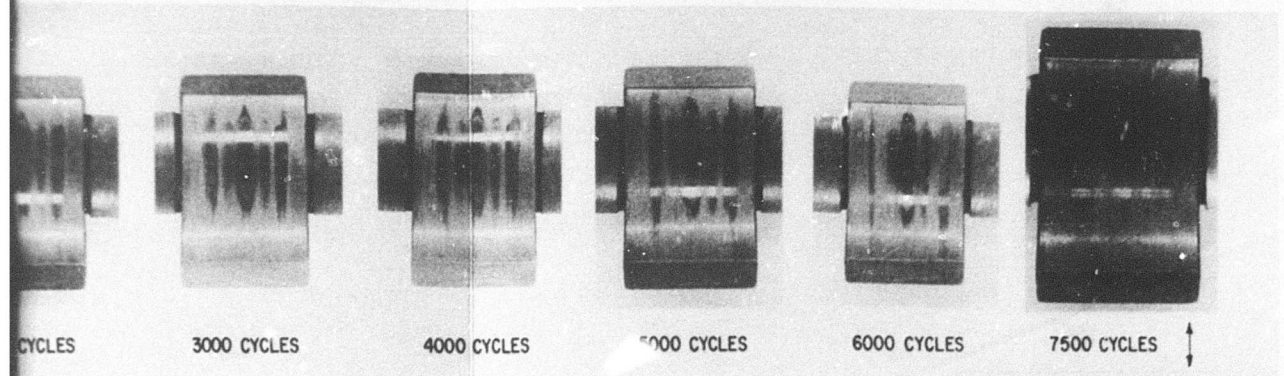
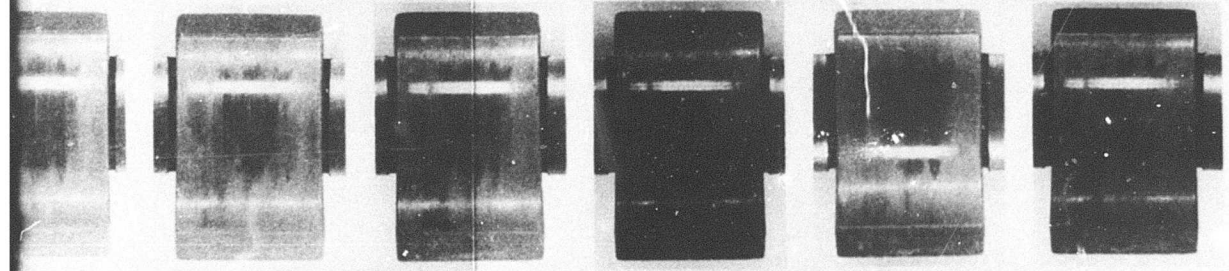


Figure 157. Surface Appearance of Cr_2O_3 Coating During 15,000-Cycle Start-Stop Test.

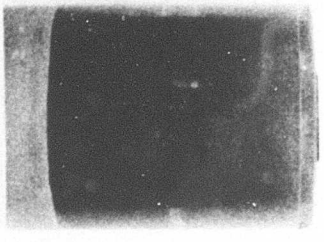


CYCLES | 3000 CYCLES | 4000 CYCLES | 5000 CYCLES | 6000 CYCLES | 7500 CYCLES





0 CYCLES | 11,500 CYCLES | 12,500 CYCLES | 13,500 CYCLES | 14,500 CYCLES | 15,000 CYCLES



LBS.
CONTACT STRESS - 226 PSI
50 RPM
NT - AIR AT 14.7 PSIA
- 0.00113
E MATERIAL - TITANIUM ALLOY - (6Al-4V)

O_3 Coating During
Test.

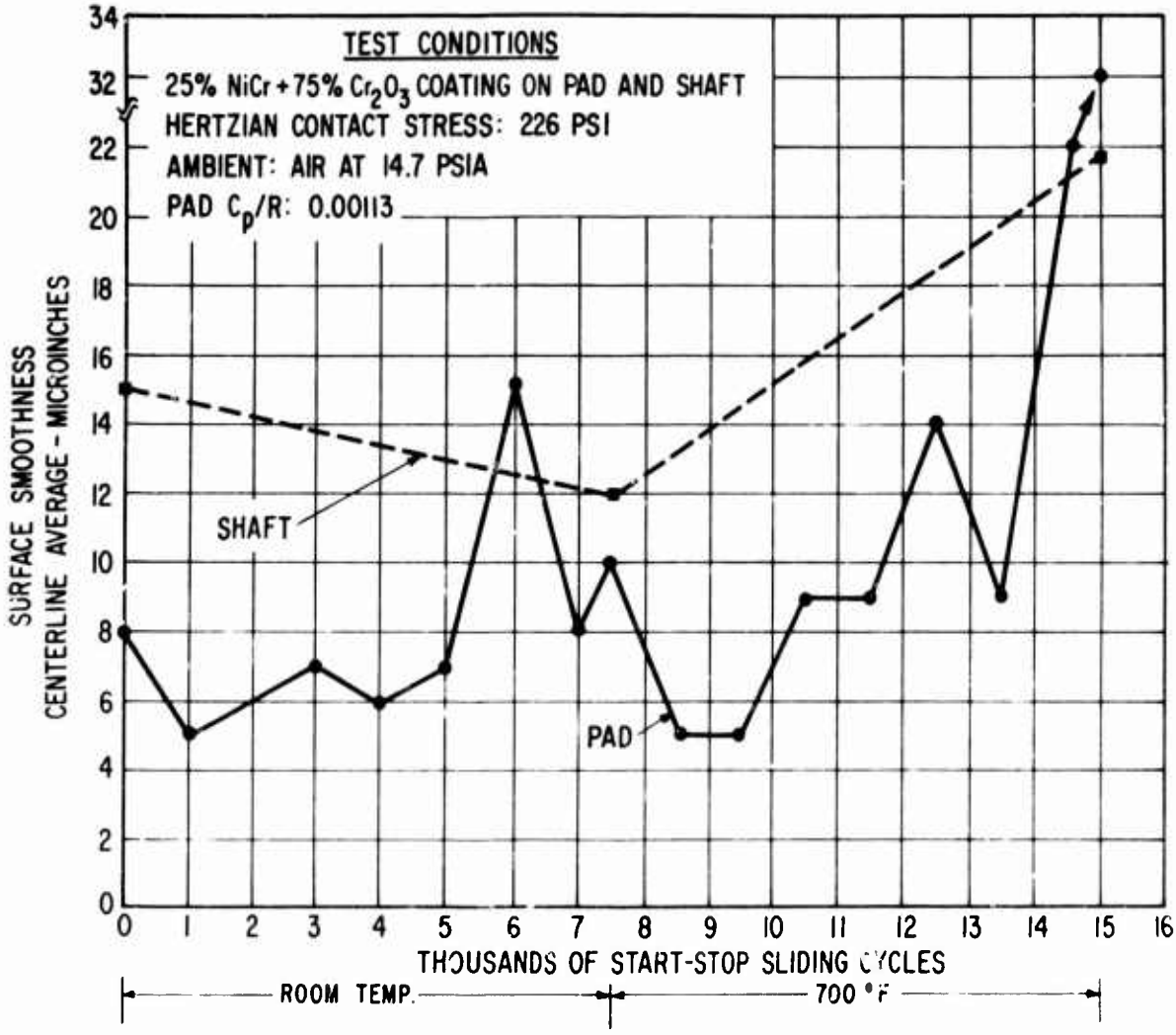


Figure 158. Surface Finish of 25-Percent NiCr + 75-Percent Cr_2O_3 Coating During 15,000-Cycle Start-Stop Test.

"PRECEDING PAGE BLANK-NOT FILMED."

This was repeated four times for a total of 480 cycles. The test was then assembled and 520 uninterrupted cycles were run at 1000°F, giving a total of 1000 cycles at 1000°F. As can be seen in Figure 160, the surface roughness of the pad increased from 11 to 24 microinches during the first 120 cycles and then dropped to 20 microinches at 480 cycles. During the next 520 cycles, the surface roughness increased to 32 microinches. At this point the test was discontinued because of a drop in efficiency of the bearing which had first been noted as a decrease in coastdown time at the end of approximately 850 cycles. The pad did, however, continue to perform hydrodynamically throughout the test. The total diametral wear measured on the shaft at the end of the test was 0.0002 inch.

Figure 161 shows the photographs of the pad and shaft taken at the beginning of the test, at the shutdown interval, and at the end of testing.

750-Hour High-Temperature Spin Test

A 750-hour high-temperature endurance test was conducted in the Hamilton Standard spin pit to demonstrate the life potential of the selected bearing coatings. The spin pit facility was the same as described previously. The turbine-end journal has the most severe operating environment and the smallest operating safety margin, so its environmental condition was selected for evaluation and simulation. A Waspaloy sleeve test specimen was used, again because of the scarcity of the more desirable IN-100. The test specimen was identical in size to the ones previously tested. The two candidate coatings selected were 25% NiCr + 75% Cr_2O_3 and NiCr-bonded Cr_3C_2.

The 25% NiCr + 75% Cr_2O_3 coating was selected based upon the preliminary start-stop sliding tests discussed above. The NiCr-bonded Cr_3C_2 was also selected for endurance evaluation, as this would have been the second choice for the turbine-end bearing application should the endurance test reveal any unforeseen mechanical difficulties with the 25% NiCr + 75% Cr_2O_3.

The specimen was baked in an air atmosphere for 750 hours at 800°F and for 75 hours at 1000°F to permit any high-temperature oxidation to take place. This was done to ensure that the relatively inert spin-pit atmosphere did not affect test results. The test procedure was as follows:

1. Statically calibrate specimen temperature against spin-pit ambient thermocouples.

2. Heat spin pit; allow to stabilize until the calibrated specimen temperature is 850 ± 20°F.

3. Set speed at 55,000 ± 300 rpm.

4. Operate under these conditions for 750 hours, interrupting at convenient intervals for coating inspection.

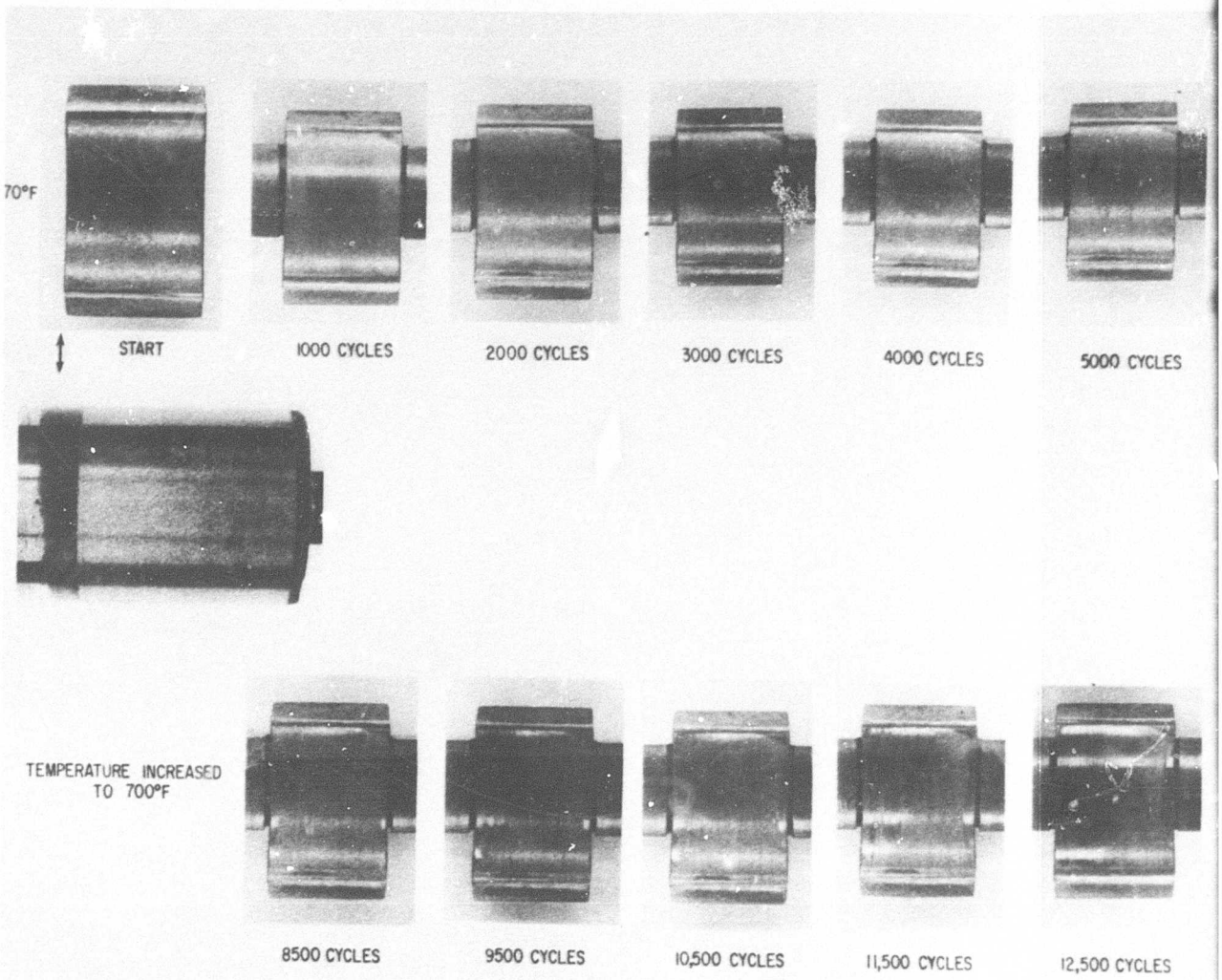
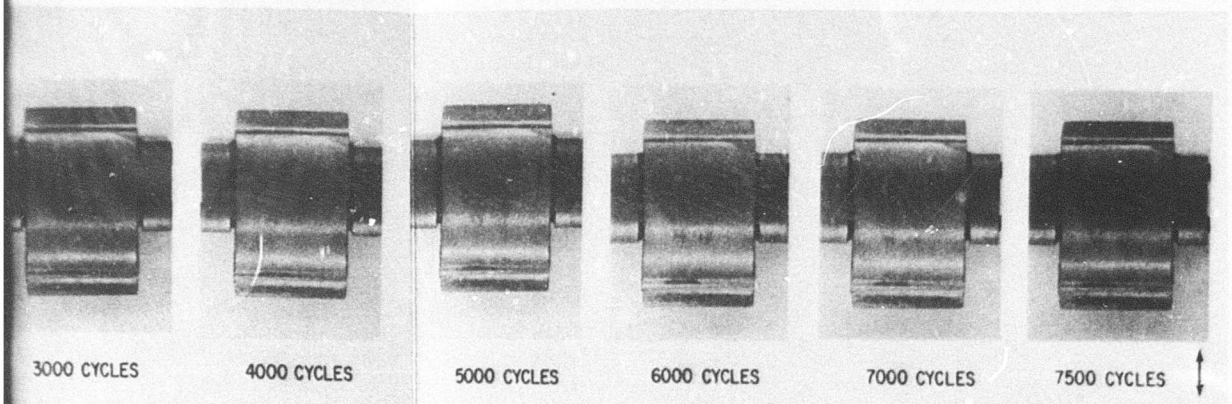
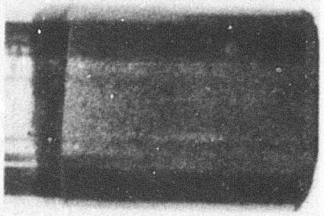
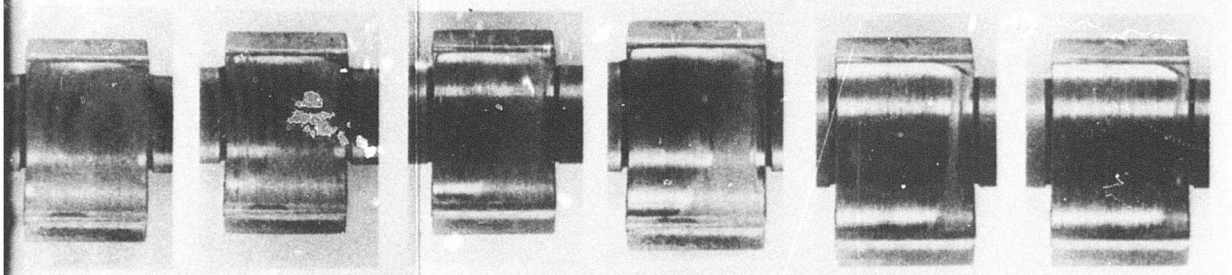


Figure 159. Surface Appearance of 25-Percent NiCr + 75-Percent Cr_2O_3 Coating During 15,000-Cycle Start-Stop Test at 1000°F.

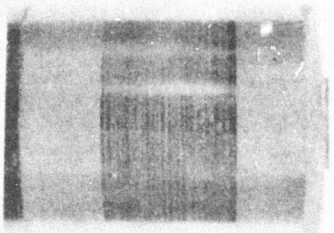


3000 CYCLES 4000 CYCLES 5000 CYCLES 6000 CYCLES 7000 CYCLES 7500 CYCLES





10,500 CYCLES 11,500 CYCLES 12,500 CYCLES 13,500 CYCLES 14,500 CYCLES 15,000 CYCLES



LBS.
CONTACT STRESS - 226 PSI
TO 3450 RPM
NT - AIR AT 14.7 PSIA
0.00113
MATERIAL - WASPALOY

ent NiCr + 75-Percent
ycle Start-Stop Test

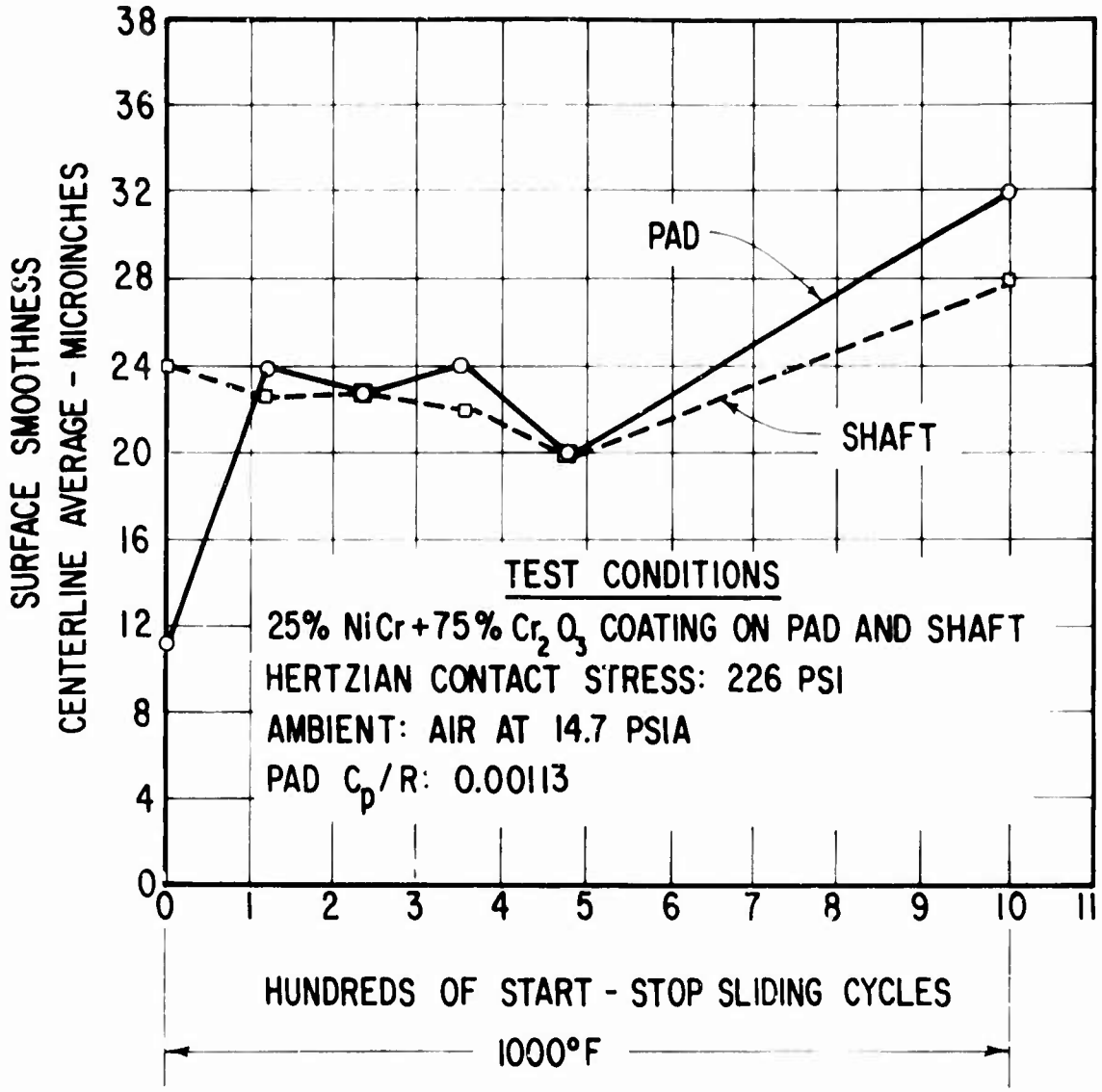


Figure 160. Surface Finish of 25-Percent NiCr + 75-Percent Cr_2O_3 Coating During 1000-Cycle Start-Stop Test at 1000°F.

"PRECEDING PAGE BLANK-NOT FILMED."

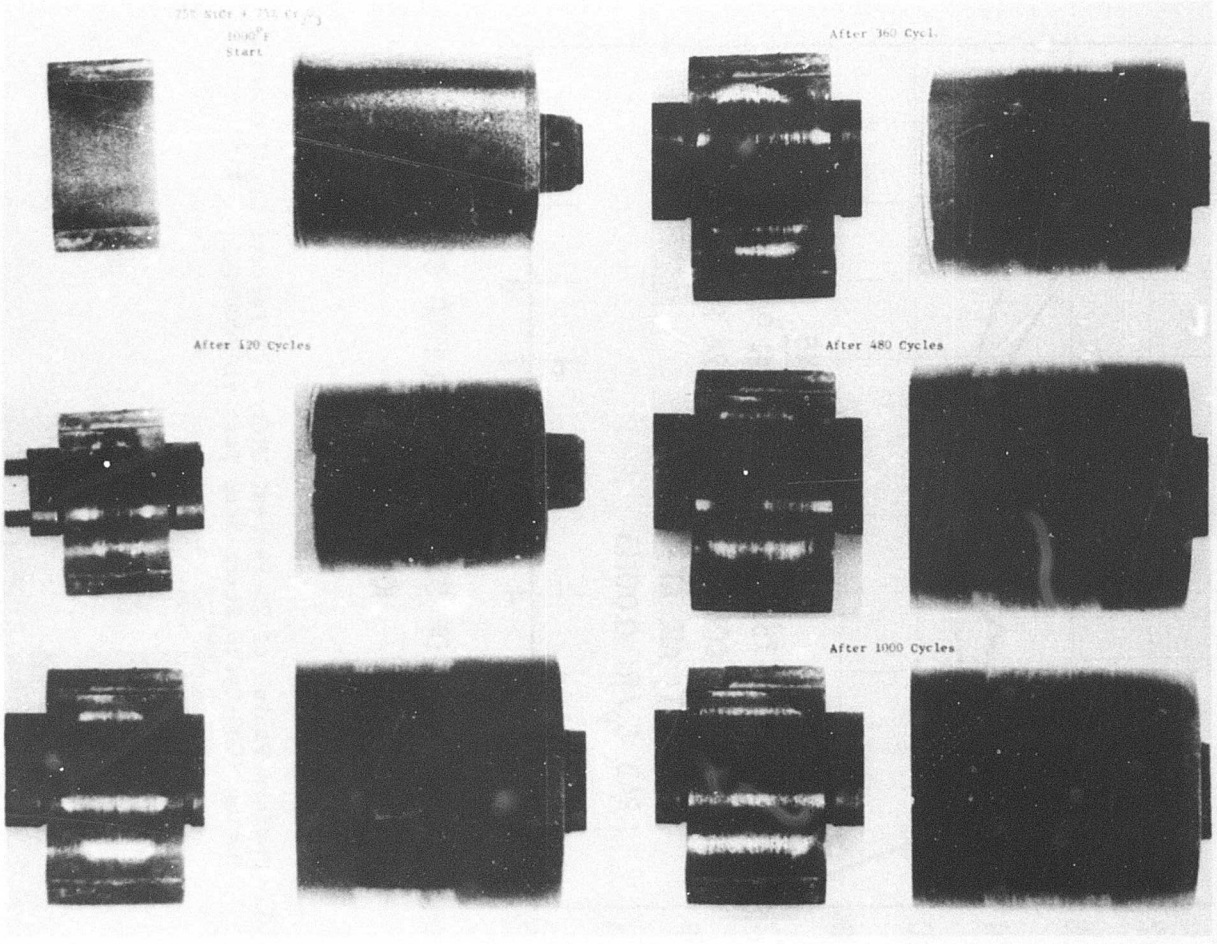


Figure 161. Surface Appearance of 25-Percent NiCr + 75-Percent Cr_2O_3 Coating During 1000-Cycle Start-Stop Test at 1000°F.

The above temperature condition is representative of the maximum turbine bearing temperature at 100%-power sea-level conditions - the maximum bearing temperature condition. The speed conditions are representative of the 75%-power conditions - the condition of maximum duty-cycle operation.

A total of 751 hours of testing was completed. The results of inspections taken during the test are summarized in Table XXVIII. The 25% NiCr + 75% Cr_2O_3 coating showed a small amount of pitting, and the NiCr-bonded Cr_3C_2 coating experienced continued flaking along one edge. The same edge was irregular prior to the test, however, and initially appeared poorly bonded. The condition of the coatings at the start, at 249 hours, and at 751 hours is shown in Figures 162, 163 and 164 respectively.

The coatings were in an acceptable condition at the end of the endurance test, and either of them would be expected to perform well in an engine application. The small amount of pitting noted from the 25% NiCr + 75% Cr_2O_3 coating would not affect bearing performance and should easily "wash" out of the bearing clearance space. The edge flaking of the NiCr-bonded Cr_3C_2 coating was also slight and should not affect bearing operation.

CONCLUSIONS FROM MATERIALS EVALUATION TESTS

As a result of the work performed to evaluate candidate air-bearing materials for small aircraft gas turbines, the following observations and conclusions can be made:

Selection of Materials for Simulator Tests

The Phase I materials tests and engine design studies performed to date have shown that a plasma-sprayed Cr_2O_3 coating on a titanium alloy substrate is the best candidate material combination for the compressor-end journal bearing and for the thrust bearing. This material combination can be used for operating temperatures up to 800°F. From the standpoint of surface wear characteristics, Cr_2O_3 is the best coating material thus far identified for air-bearing applications at temperatures below 800°F.

The materials tests and engine design studies performed to date have shown that a plasma-sprayed 25% NiCr + 75% Cr_2O_3 coating on a high-temperature nickel-based alloy (such as IN-100) is the best candidate material combination for the turbine-end journal bearing. This material combination can be used for operating temperatures up to 1000°F, and possibly 1100°F.

The above identified coating and substrate materials are suitable for use at the predicted temperature levels of the small aircraft engine application and have been selected for the Phase II simulator tests.

Start-Stop Sliding Capability

The Phase I materials tests have demonstrated that the selected air-bearing coating materials can satisfactorily sustain 15,000 hydrodynamic start-stop sliding cycles at Hertzian contact stresses (226 psi) and temperature levels representative of small aircraft-engine operating conditions. The

TABLE XXVIII. 750-HR ENDURANCE TEST INSPECTION LOG

Coating No. 1: 25% NiCr + 75% Cr_2O_3

No. 2: NiCr Bonded Cr_3C_2

Inspection Interval (hr)	(6) 25% NiCr + 75% Cr_2O_3	(3) NiCr Bonded Cr_3C_2	Remarks
0	-	One irregular boundary	Using Teflon spindle seal
26	No change	No change	Replaced turbine parts - new spindle - same seal
56	No change	No change	Replaced spindle
121	Slight pitting	Slight flaking at boundary and slight pitting	Replaced spindle and bushings - replaced Teflon with Neoprene seal - rebalanced assembly
153	No change	Same	Replaced bearings and spindle
249	No change	Increased flaking and pitting	Replaced turbine parts - photographed specimen
321	No change	Same	Replaced line filters
409	No change	Same	Replaced turbine parts, spindle and line filters
530	No change	Same	Replaced turbine parts
657	No change	Same	Overhauled all equipment
710	No change	Same	Changed line filters
751	Increased pitting	Flaking and pitting	End-of-test photographs

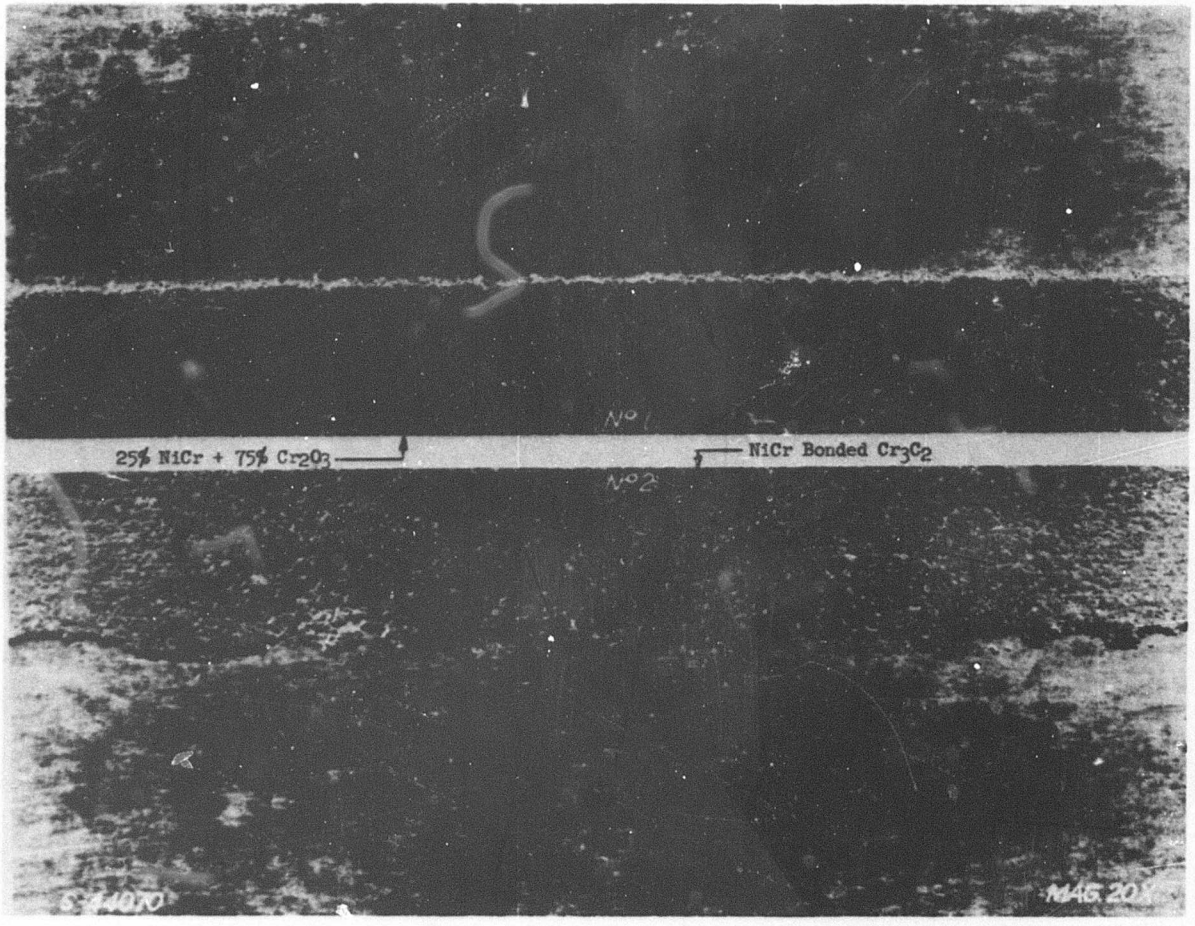


Figure 162. Coating Boundary and Surface Appearance at Start of Endurance Spin Test.

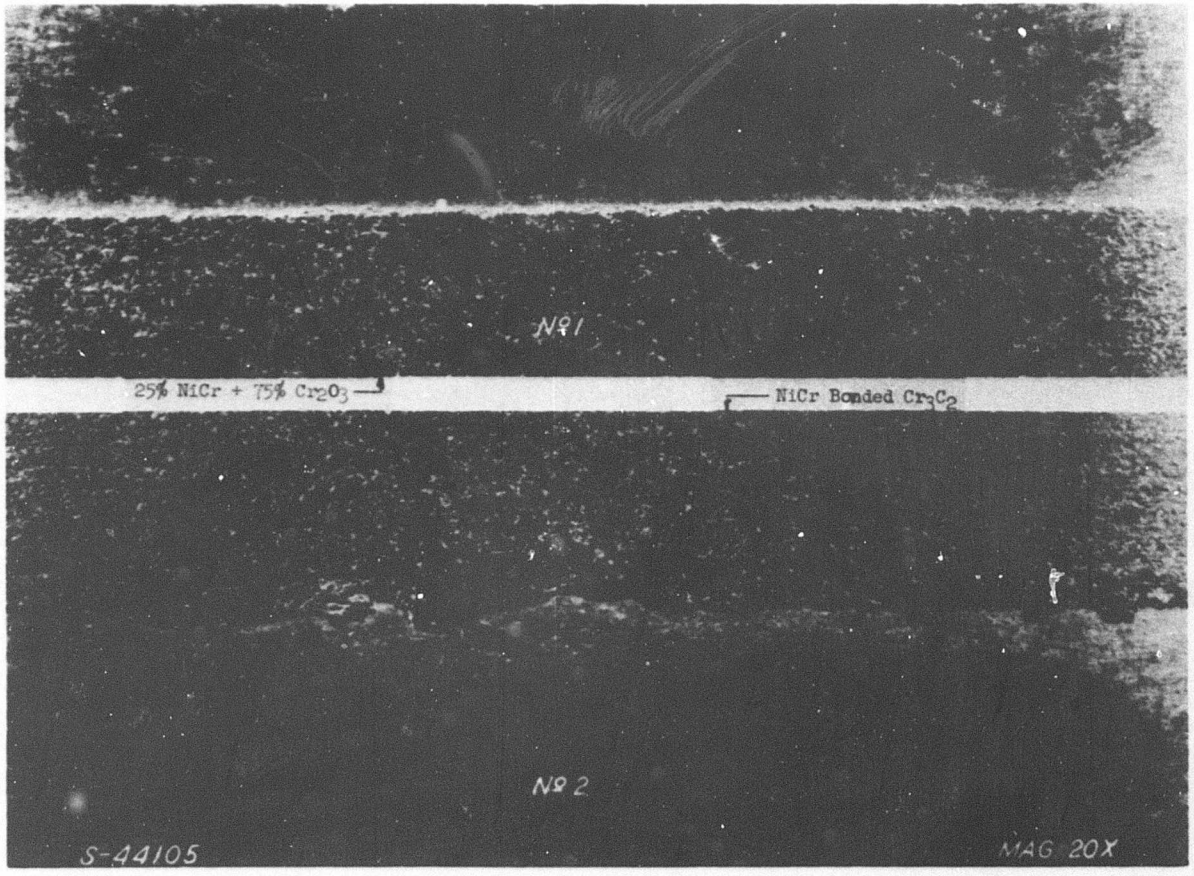


Figure 163. Coating Boundary and Surface Appearance After 249 Hours of Endurance Spin Test.

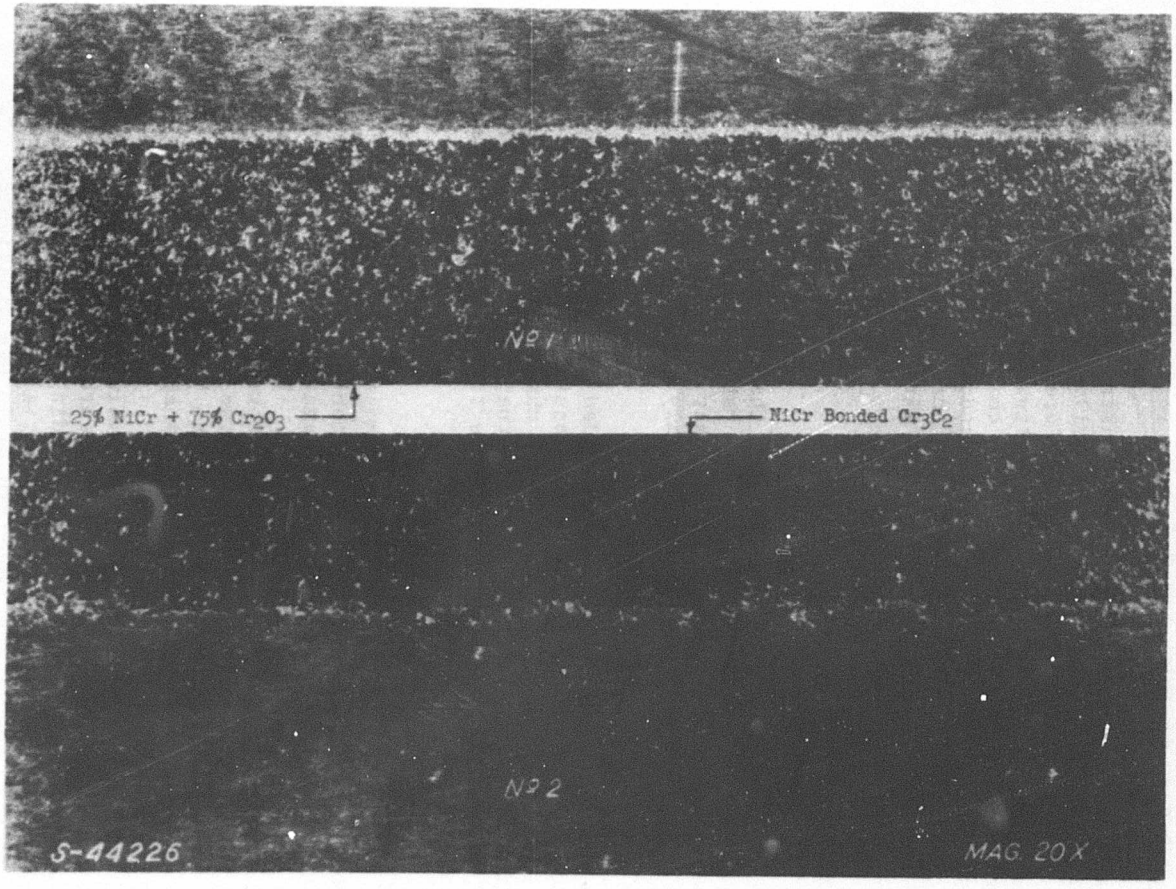


Figure 164. Coating Boundary and Surface Appearance After 751 Hours of Endurance Spin Test.

elevated-temperature tests for the Cr_2O_3 coating consisted of 7500 start-stop cycles at 550°F. The elevated-temperature tests for the 25% NiCr + 75% Cr_2O_3 coating consisted of 7500 start-stop cycles at 700°F, plus 1000 cycles at 1000°F.

Rotating Journal Bond-Strength and Endurance Tests

The Phase I rotating journal tests have demonstrated that the selected air-bearing material combinations can satisfactorily sustain the mechanical strains, the centrifugal forces, and the differential thermal expansions which will occur in the rotating journal sections of a small aircraft gas-turbine engine. No problems relative to the coating/substrate bond strength were identified. The results of a 751-hour endurance test at speed and temperature conditions representative of the turbine-end journal at 75% engine power likewise identified no problems with either the coating or the substrate materials.

Addition of Metallic Binders to Cr_2O_3

The Phase I material tests have demonstrated that the addition of metallic binders to Cr_2O_3 does extend the temperature range of the coating before spalling occurs. However, the sliding and wear characteristics of the modified Cr_2O_3 coatings appear to be inversely related to the temperature range capability.

That is, the addition of either 50% NiCr-bonded Cr_3C_2 or 40% Cr to the Cr_2O_3 extended the temperature range to at least 1400°F (the maximum test temperature). However, the sliding and wear characteristics of these modified coatings were significantly poorer than the 25% NiCr modified Cr_2O_3. This latter coating, however, appears to have a maximum temperature limit somewhere between 1000° and 1200°F.

Effects of Sustained High-Speed Sliding

A limited number of shock-induced momentary-contact tests were conducted on a single test pad at 45,000 rpm using the bearing component test rig described in the next section of this report. These tests fully confirmed the quite extensive tests which had been performed on prior contracts - namely, that Cr_2O_3 coatings can survive a large number of high-speed momentary contacts (contact duration less than 10 milliseconds) without damage or degradation of air-bearing performance.

Although not part of the planned materials evaluation tests, two opportunities did arise during the bearing components testing to observe the effects of sustained high-speed sliding (sliding duration greater than 100 milliseconds) on Cr_2O_3 coatings. During initial assembly of the bearing components test rig, one of the labyrinth seals was misaligned. This misalignment caused the labyrinth seal to thermally expand into the test shaft the first time the test rig was brought up to test temperature and speed. The resulting seal rub caused the shaft to come into sliding contact with the two "fixed" pads of the shaft support bearings (which were pivoted-pad

air bearings). The sustained sliding contact caused a sudden deceleration of the shaft - from 50,000 rpm to 0 rpm in less than a second. Figure 165 shows the appearance of the test shaft and the bearing pads after this first seizure.

The second bearing seizure resulted from a thrust bearing hydrodynamic instability condition which was encountered during the initial thrust bearing load-capacity tests. This instability condition also produced sustained sliding between the shaft and support bearings, and resulted in deceleration of the shaft from 45,000 rpm to 0 rpm in about 4 seconds.

Both shaft seizures resulted from a rapid build-up of Cr_2O_3 debris in the air-bearing clearances. There was no significant damage or welding of any of the test rig parts. Subsequent to the first seizure, the pads were simply relapped. The shaft, however, was recoated due to the presence of small surface-crazing (thermal stress) cracks in the coating. The nature of these cracks can be seen in the photomicrograph of Figure 166, which was taken after the second seizure. After the second seizure, the pads were again relapped and the shaft reground; the shaft was not recoated. The refurbished pads and shaft were used throughout the remainder of the bearing component test program without any problems.

The two test rig seizures described above occurred as a result of unexpected and unintentional conditions - conditions which should not occur in a developed engine. Except for start-stop sliding and momentary shock-induced contacts, an air-bearing engine must be designed to maintain full air-film lubrication under all possible conditions of engine and aircraft operation. Nonetheless, it would be folly to assume that a sustained high-speed sliding condition will never arise; that is, that unexpected or unintentional events will never occur during the operating life of an aircraft engine. Accordingly, it is obvious from the above effects of sustained sliding that increased emphasis must now be placed on improving the high-speed sustained-sliding capabilities of air-bearing materials. A meaningful and reasonable objective of future materials development and evaluation testing should be the ability to survive 5 seconds of sustained high-speed sliding without bearing failure or serious degradation of performance. Several steps to achieve this goal are suggested in the Conclusions and Recommendations section of this report.

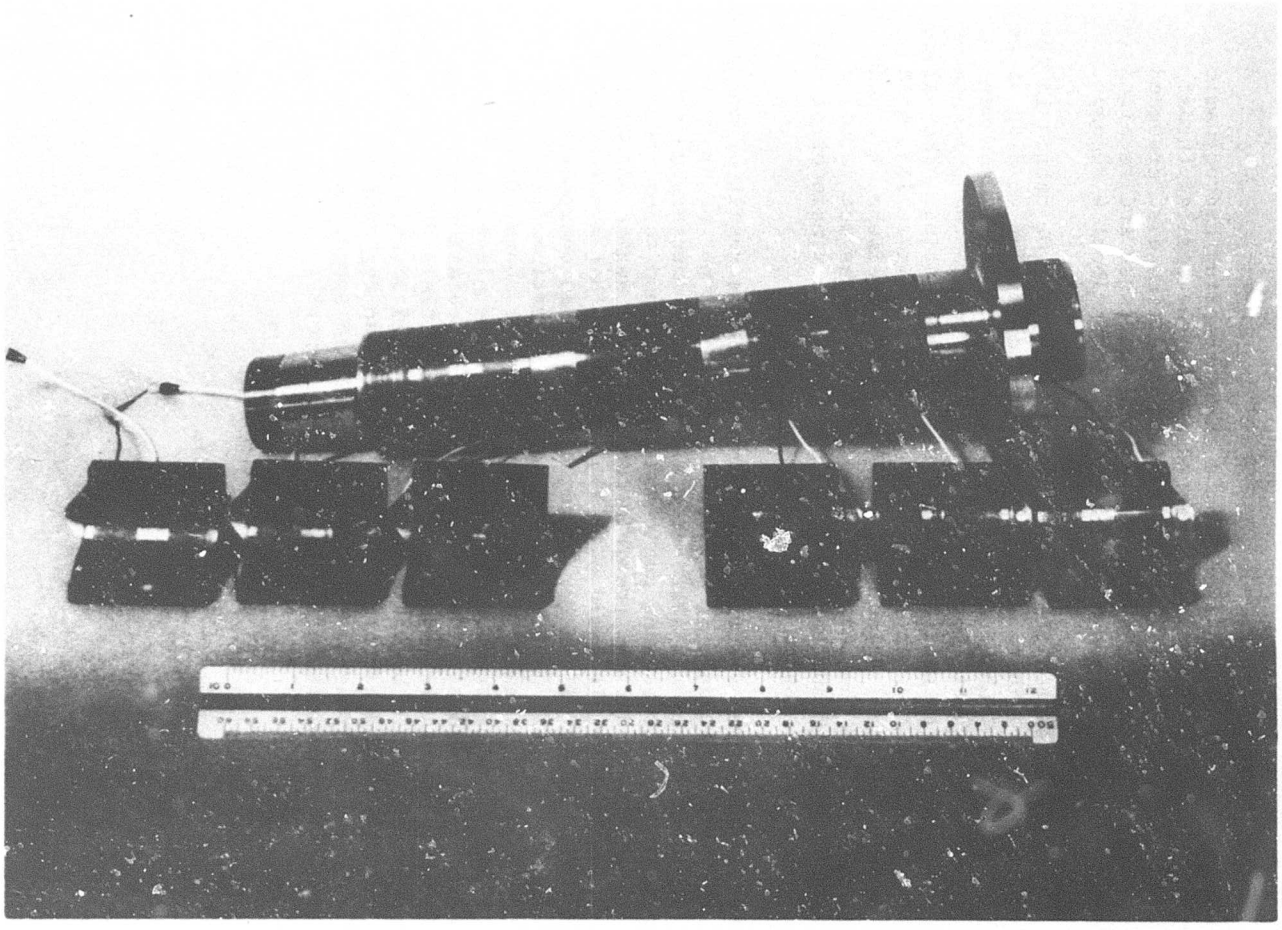


Figure 165. Test Rig Shaft and Pads After Sustained Sliding Seizure at 50,000 rpm.

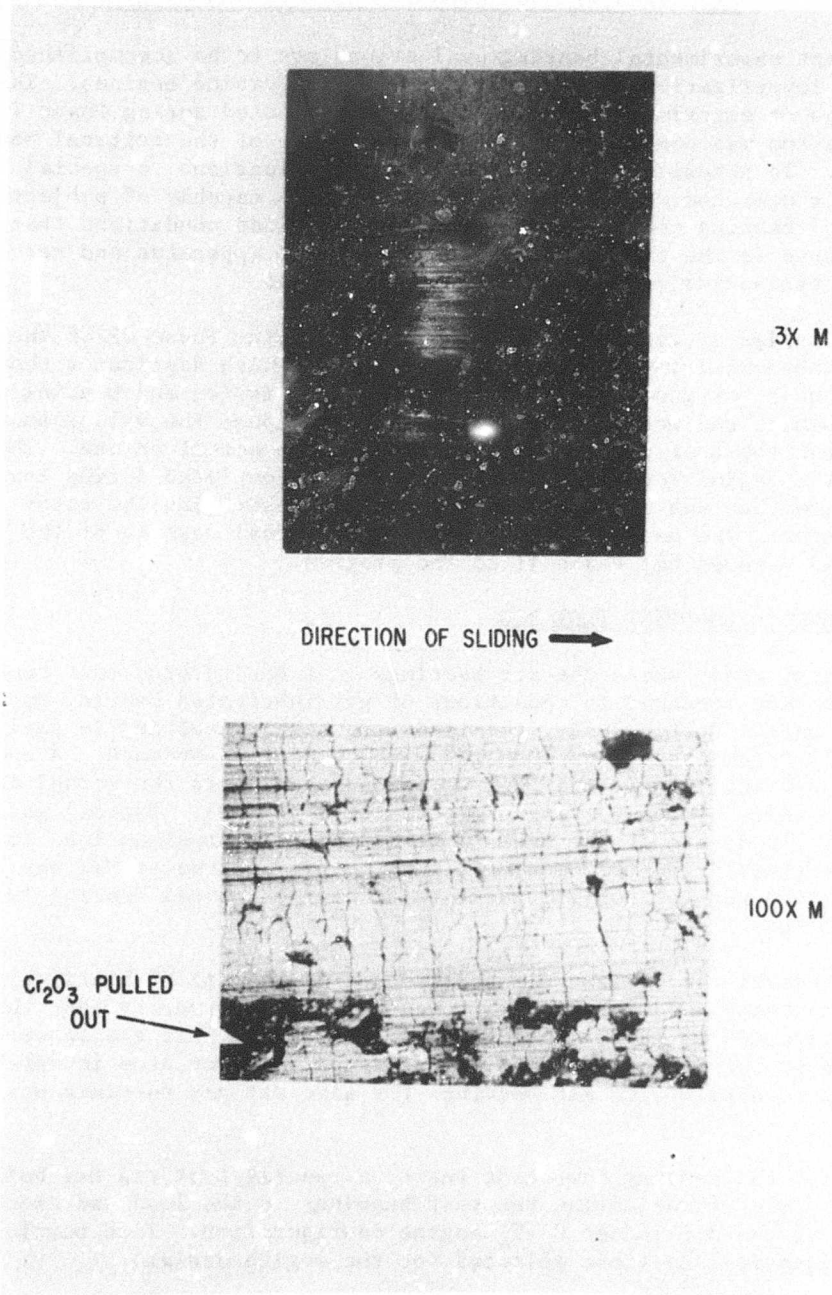


Figure 166. Cr_2O_3 Coated Pad Surface After Thrust Bearing Instability Induced Shaft Seizure at 45,000 rpm.

EXPERIMENTAL EVALUATION OF BEARING COMPONENTS

Two different experimental bearing evaluations are to be accomplished during the investigation of air bearings for gas-turbine engines. The first series of experimental evaluations was conducted during Phase I of the program and was concerned with the performance of the critical bearing components. To accomplish these experimental evaluations, a special bearing test rig was designed and built. This test rig is capable of subjecting the critical bearing components to the speed and load conditions that would be encountered in the 3.5-lb/sec engine. The test apparatus and results of the first test series are discussed in this section.

The second series of tests are to be conducted during Phase II of the program. These will involve a dynamic simulator which duplicates the 3.5-lb/sec engine rotor geometry and inertia characteristics and bearing cooling schemes, and which will also be able to impose the values and types of loads upon the bearings as would be seen in the actual engine. The design of the engine rotor-bearing simulator was completed during Phase I of the program and was discussed in the section describing the rotor bearing system. The manufacture, assembly and actual testing of the simulator is planned for Phase II of the program.

BEARING ELEMENT COMPONENT TEST RIG

The conditions under which the air bearings in a gas turbine must operate are extreme when compared to conditions of gas-lubricated bearing applications to date. Particularly, the loads are high, resulting in small bearing film thicknesses when compared with current experience. A common measure of bearing load is the "per unit load", which is the actual load in pounds divided by the bearing projected area (L x D). Typical gas bearing unit loads are of the order 5 to 10 psi. The maximum load applied to a gas-lubricated journal bearing prior to this program at MTI was 15 psi. The design load for the subject gas turbine engine journal bearing is in excess of 35 psi.

Primarily because the design film thicknesses of the engine bearings are small (approximately 0.0002 inch), it was necessary to verify that the load capacity predicted by theory could indeed be achieved. If the theoretical predictions at thin films could be demonstrated, a major step in establishing the feasibility of air bearings for aircraft gas turbines would be achieved.

To accomplish the bearing component tests, a special test rig was built which is capable of subjecting the test bearings to the load and speed conditions of the 3.5-lb/sec C_o-T_o engine configuration. Test bearing sizes are identical to those selected for the engine design:

Journal Bearing = 2.25-inch dia. x 2.25-inch length
Thrust Bearing = 5.74-inch O.D. x 3.10-inch I.D.

A cross-sectional drawing of the test rig is shown in Figure 167. The single-piece rotor is supported on two three-pad tilting-pad journal bearings. Each journal, as in the engine, has one flexibly mounted pad to accommodate journal centrifugal growth and radial thermal gradients. A single test pad is located midway between the support journals. The test thrust bearing is overhung at the end of the rotor. The thrust bearing, which can be either single or double acting, is mounted on an axial flexure which is soft in the angular direction but axially stiff. This flexure provides for the self-alignment of the test thrust bearing. The rotor is driven by means of an air turbine mounted directly to the shaft end opposite the test thrust bearing.

Labyrinth seals are provided to isolate the journal bearing and thrust bearing cavities such that the desired control of bearing ambient pressures can be achieved. The journal bearings are cooled by means of an air passage through the center of the shaft. The thrust bearing is cooled by means of a water heat exchanger built into the test thrust bearing.

Loading of the test thrust bearing is achieved by means of a pneumatic loading chamber at the turbine end of the shaft. The single journal test pad is also loaded pneumatically by a loading device rigidly attached to the test rig frame. The shaft connecting the load piston to the test pad is radially supported by a hydrostatic gas bearing to eliminate any friction in the mechanism.

The test rig was designed to permit the critical air bearing elements to be tested over the following range of conditions

Speed (rpm)	3000 - 72,000
Journal bearing load (lb)	0 - 250
Journal bearing ambient pressure (psia)	14.7 - 250
Thrust bearing load (lb)	0 - 300
Thrust bearing ambient pressure (psia)	14.7 - 120
Thrust bearing supply pressure (psia)	14.7 - 300

These conditions bracket the bearing environmental conditions that will be imposed by the 3.5-lb/sec C_o-T_o engine.

The most significant data that can be obtained during a test on air bearings is first a measurement of film thickness and next a measurement of rotor dynamic performance. Therefore, the test rig bearings and the bearings under test are equipped with capacitance probes: one in each pad of the test rig journal bearings, three in the journal-bearing pad under test, and five in the loaded side of the double-acting thrust bearing being tested. Rotor dynamic performance is measured with four probes: two in the plane of the journal pad under test and two in the plane of the thrust bearing. The temperature of each of the journal bearing pads and the thrust bearing is obtained from thermocouples and recorded on multi-channel chart recorders. Schematic layouts of the bearing element test

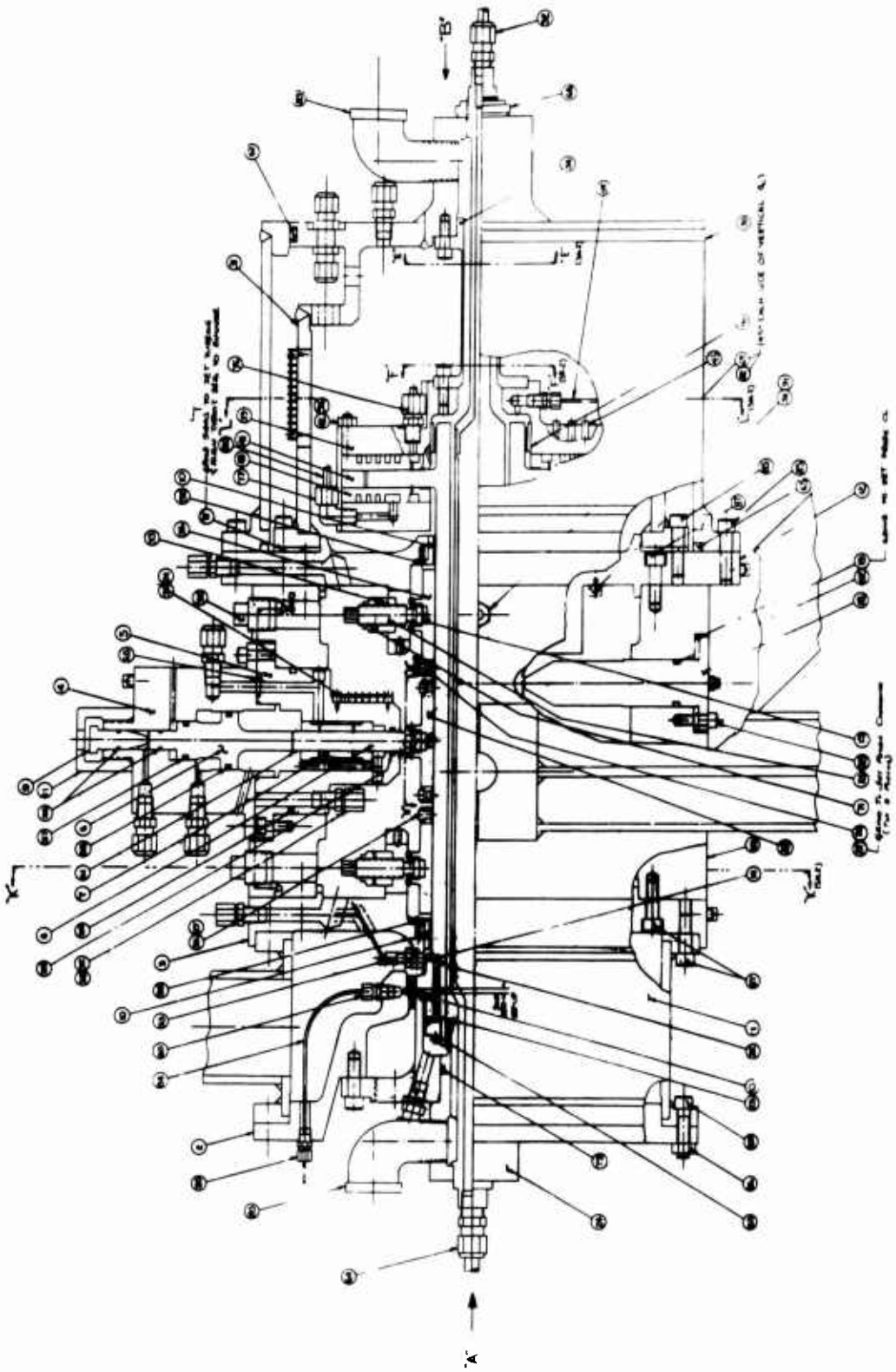


Figure 167. Assembly of Bearing Element Test Rig.

rig supply control system and instrumentation system are shown in Figures 168 and 169 respectively.

Photographs of the bearing test rig, components, and installation are shown in Figures 170 through 175.

RESULTS OF JOURNAL BEARING SINGLE-PAD TESTS

The primary emphasis during the journal tests was on the single test pad located midway between the test rig rotor support journals. The rotor support journal pads were instrumented with proximity probes and thermocouples such that operational data and experience could be gained on the composite bearing which is similar in design to the engine bearings.

The single test pad, which is shown in Figures 176 and 177, was instrumented with three capacitance probes. One probe was located directly under the pivot, and the other two were located beyond the bearing edges in line with the pivot. Thus, the pivot line film thickness could be directly measured at three points along the bearing length.

The pertinent geometric parameters of the pivoted test pad are summarized below.

Pad length	2.25 inches
Pad diameter	2.25 inches
Machined radial clearance	0.00393 inch
Pad average radial thickness	5/16 inch
Pad circumferential length	110 degrees
Pivot position ratio	0.65

Typical results of the journal bearing pad tests are shown on Figures 178 through 180 for ambient pressures equivalent to the engine 25,000 feet flight condition, which represents the most severe bearing operating condition. Figures 178 through 180 show the bearing pad film thickness as a function of applied load for engine conditions representative of 75-percent power (52,000 rpm), 50-percent power (50,000 rpm), and flight idle (45,000 rpm). The upper plot on each figure is a direct comparison of the experimental results with the theoretical prediction at each operating condition. From an examination of these experimental results, the following observations and conclusions have been made:

1. At low values of load (large operating film thickness), the measured film thickness is larger than that predicted by theory. A large part of this increased load capacity can be explained by the fact that, at large values of film thickness, the bearing gas film tends to be turbulent, giving a significant increase in load capacity. Calculations made using turbulent lubrication theory indicate that a pad operating at the 50-percent engine power conditions shown in Figure 179 and at a 1.0-mil film thickness

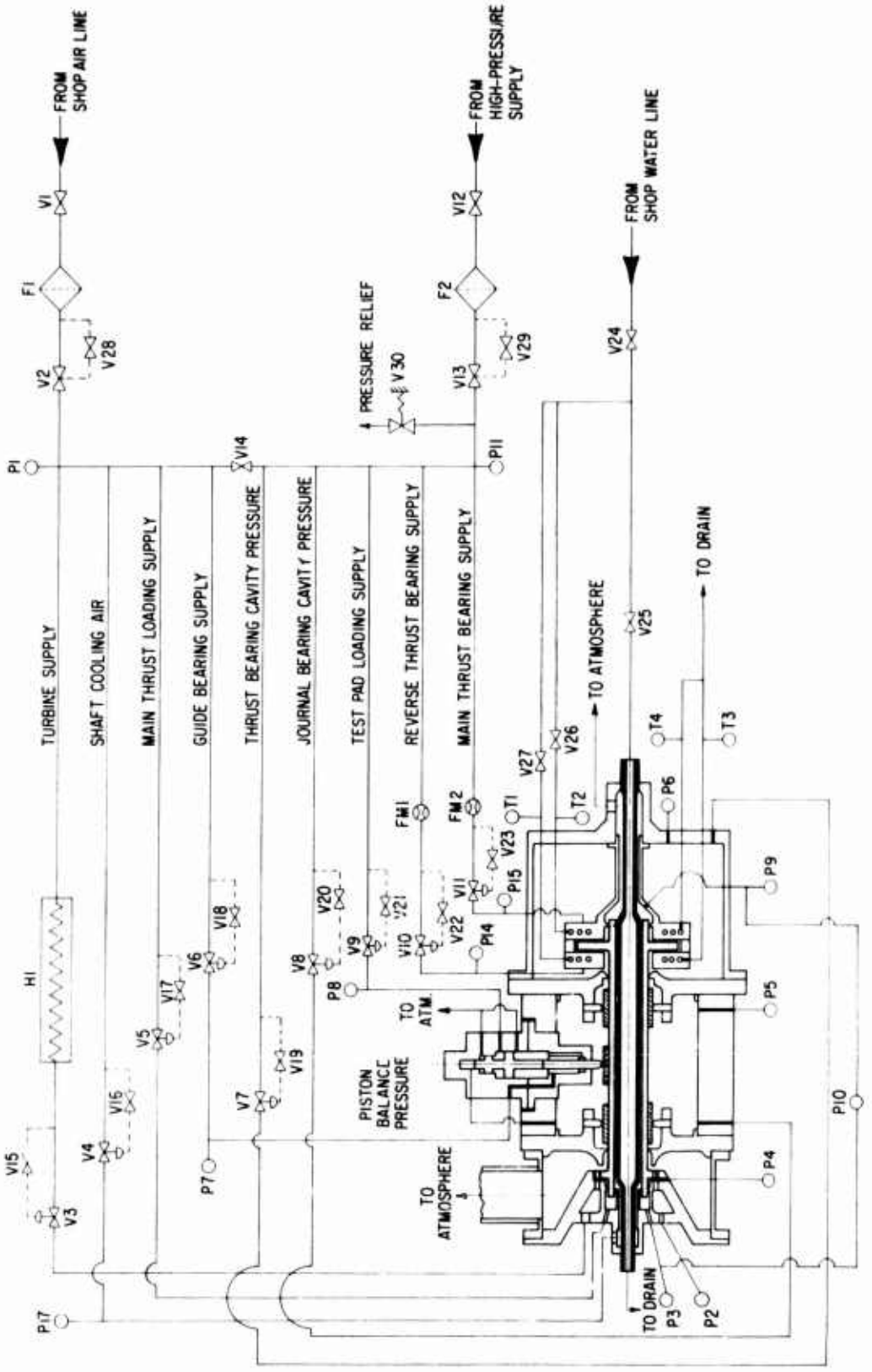


Figure 168. Bearing Element Test Rig (Schematic of Rig Supply System).

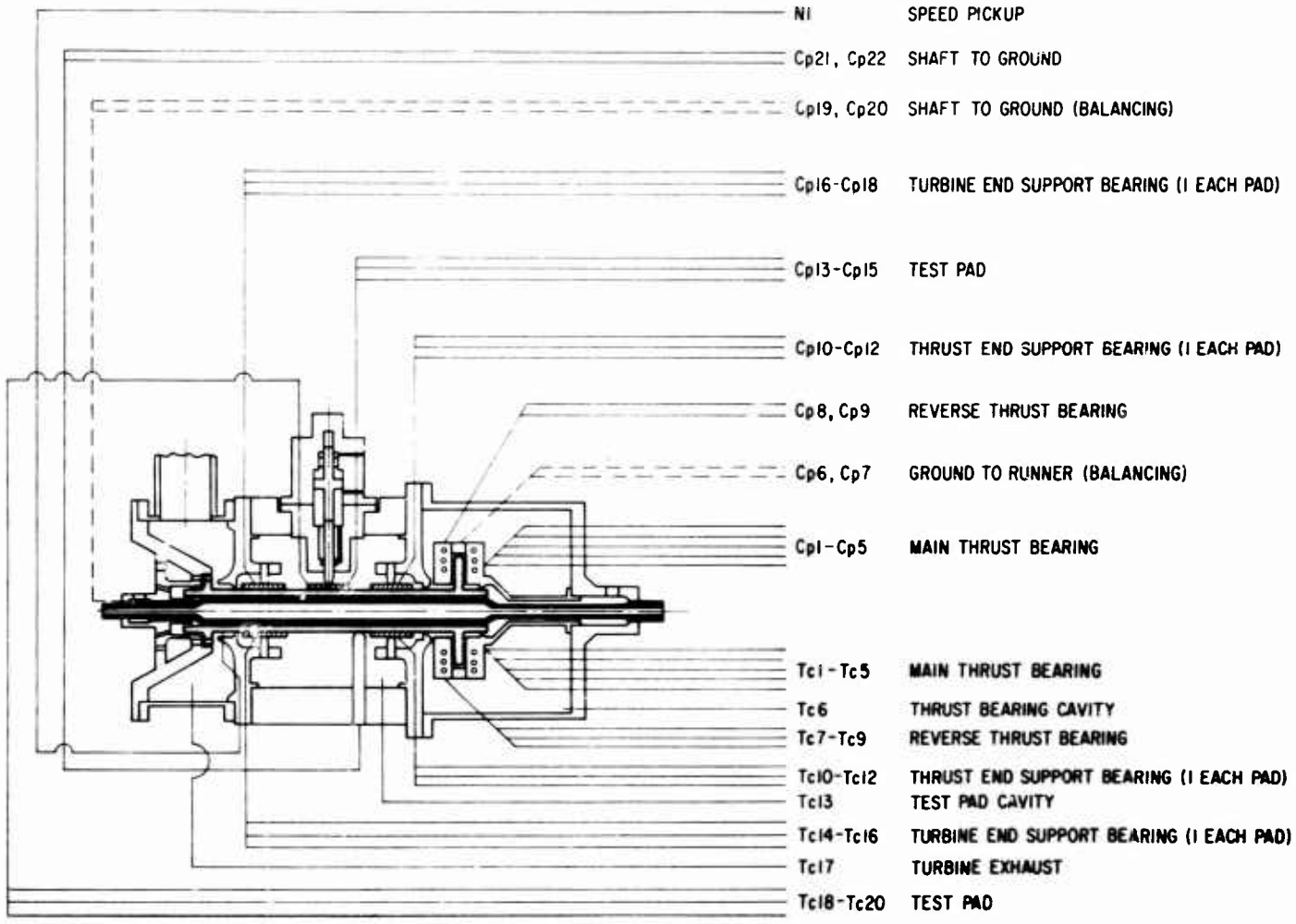


Figure 169. Bearing Element Test Rig
(Schematic of Instrument Locations).

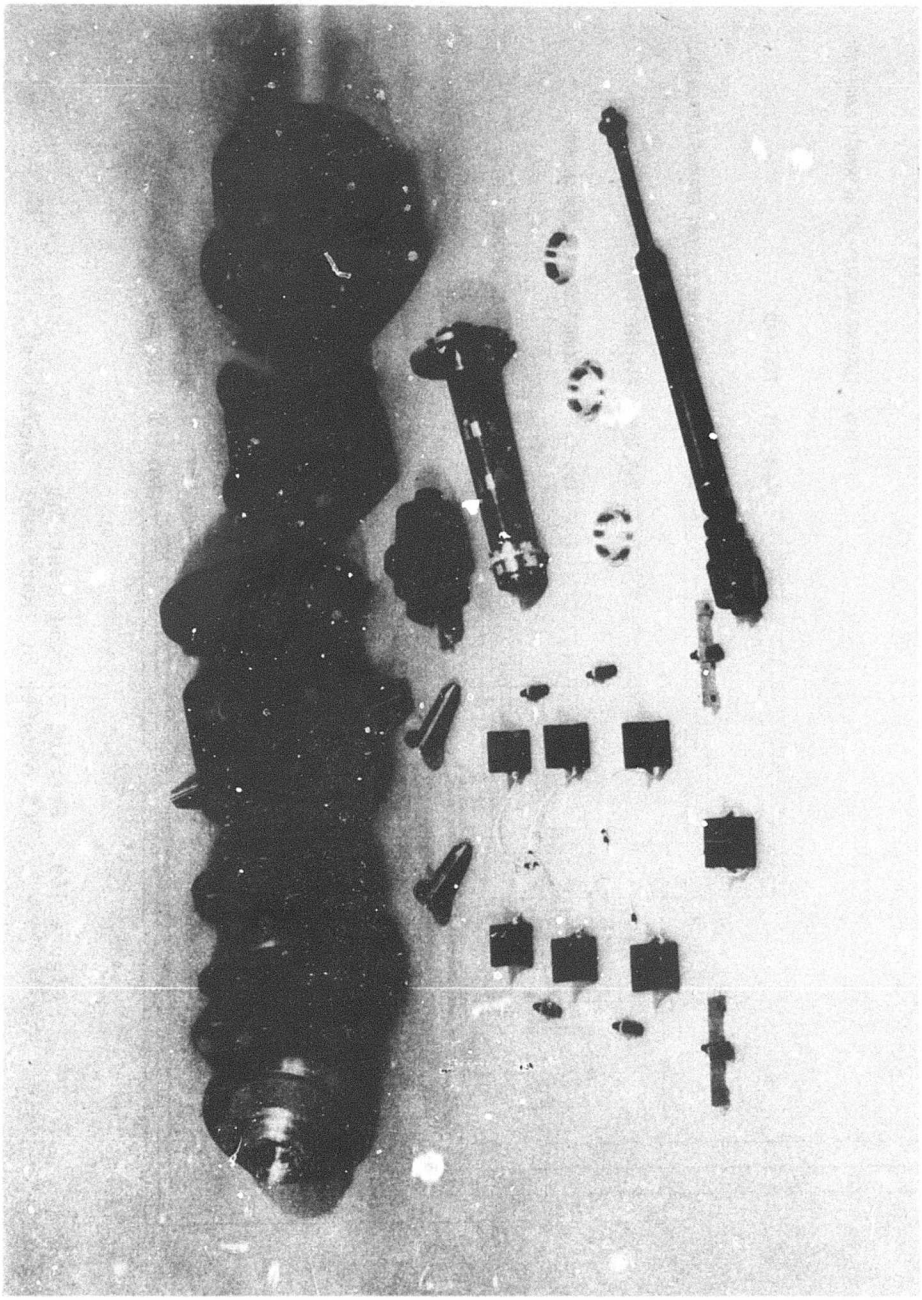


Figure 170. Components for Bearing Element Test Rig.

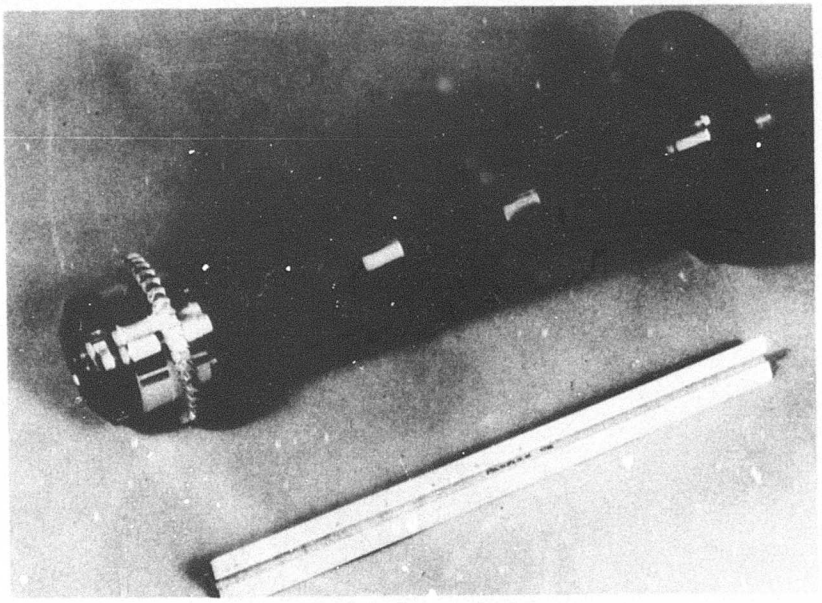


Figure 171. Rotor and Turbine Wheel for Bearing Element Test Rig.

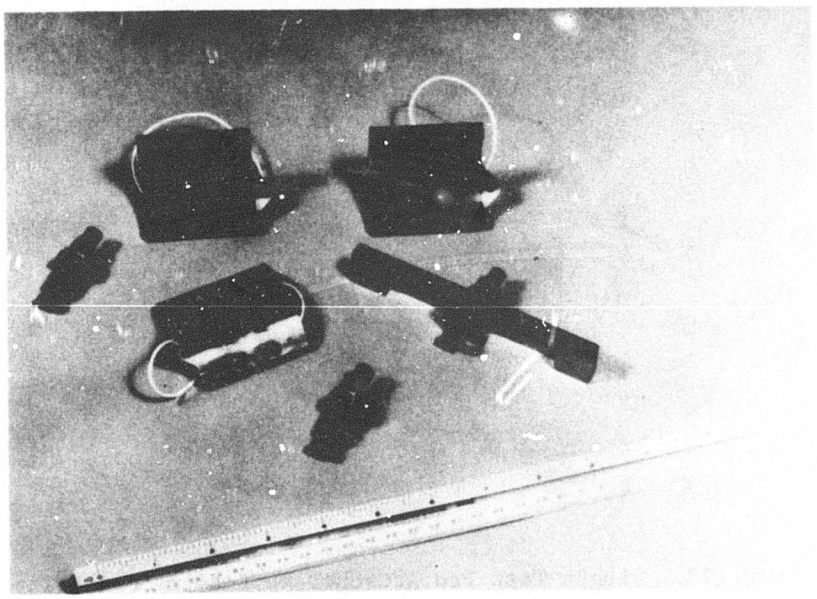


Figure 172. Three-Pad Air Bearing for Bearing Element Test Rig.

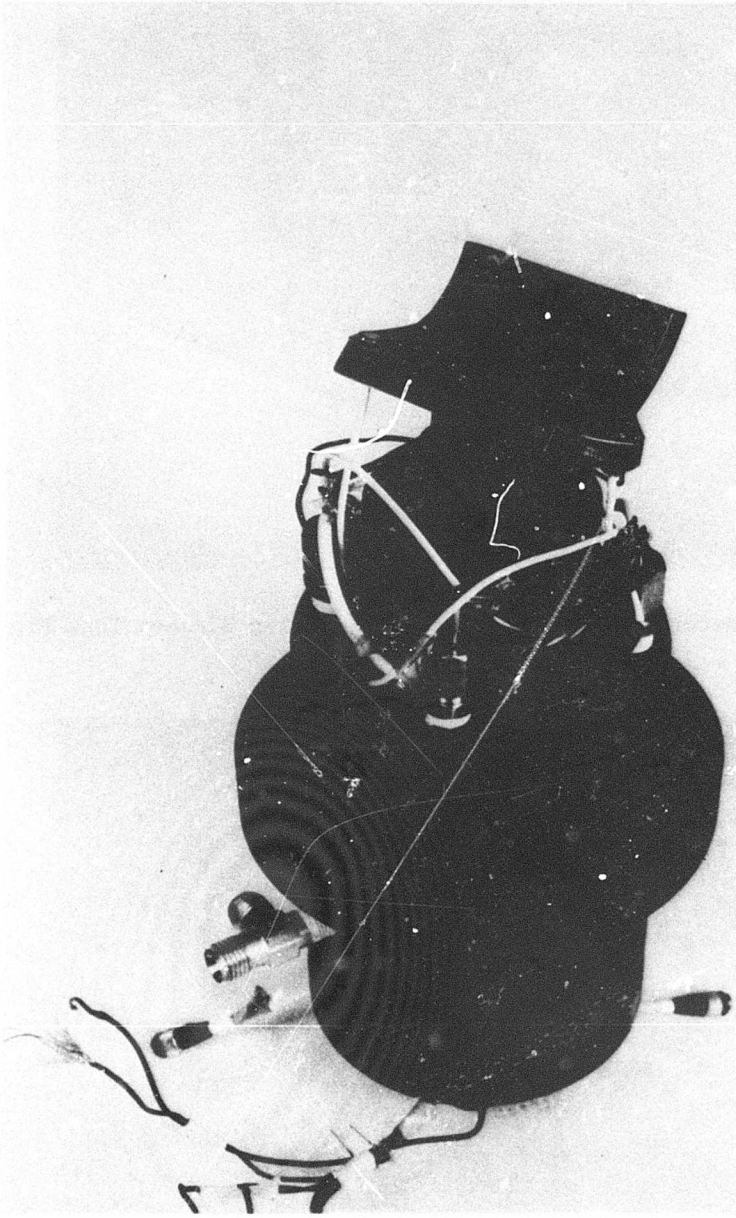


Figure 173. Single Test Pad Attached to Loading Mechanism.

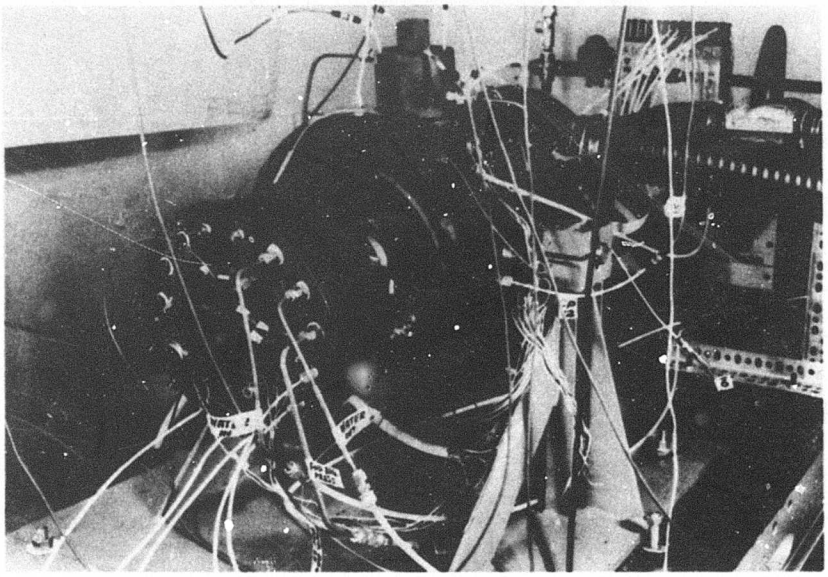


Figure 174. Assembled Test Rig.

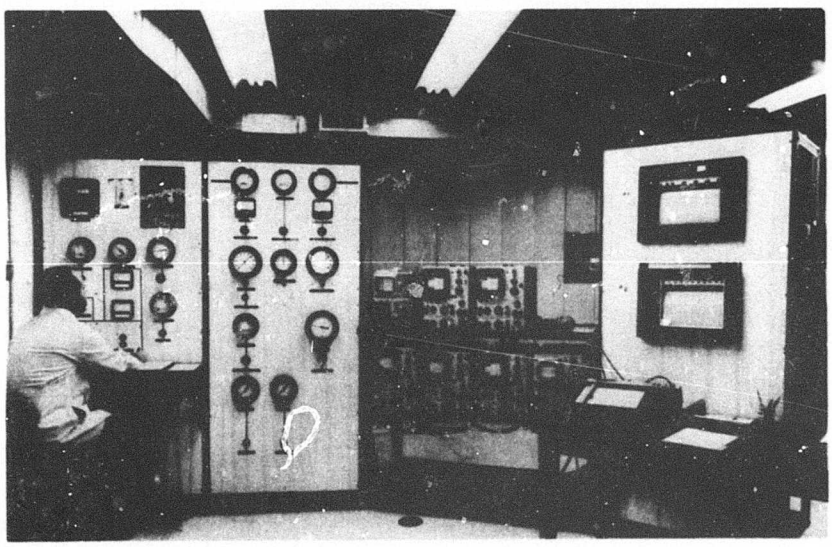


Figure 175. Control Panel and Instrumentation for Bearing Element Test Rig.

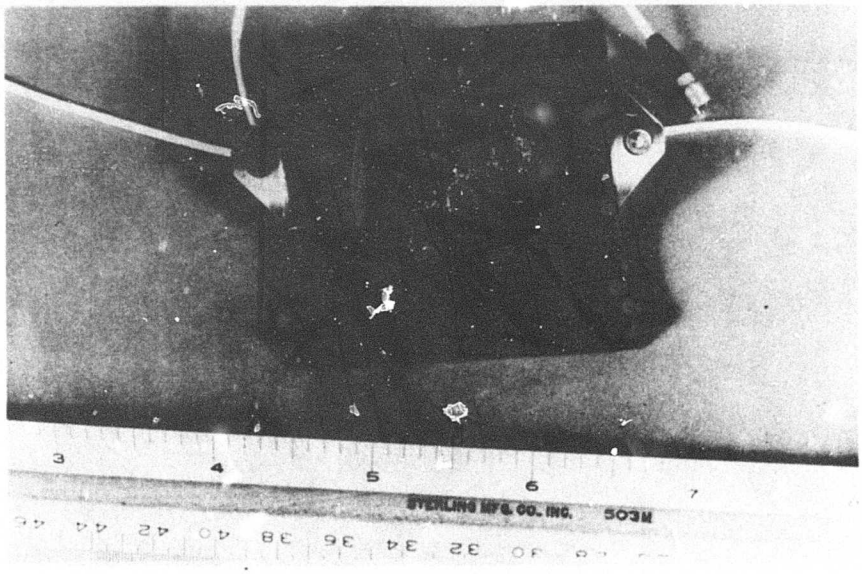


Figure 176. Surface of Journal Bearing Pad Showing Instrumentation for Measurement of Film Thickness.

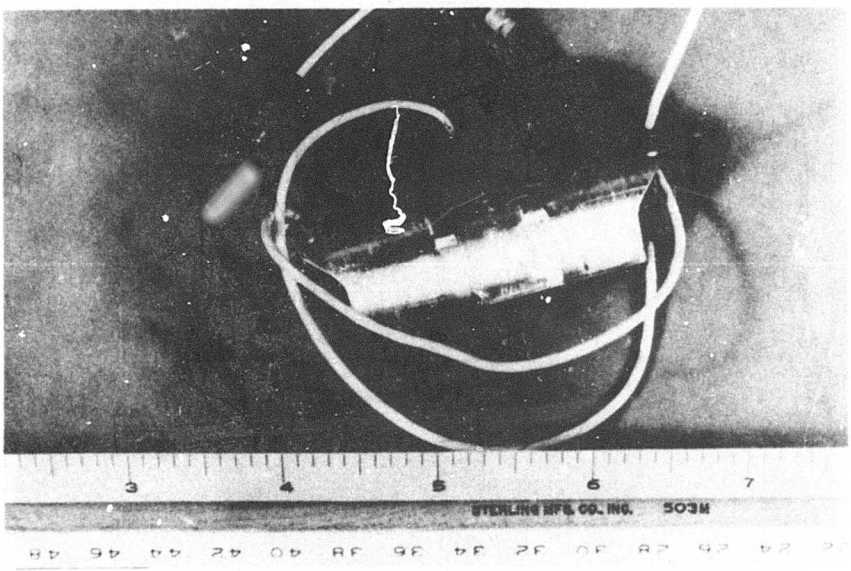
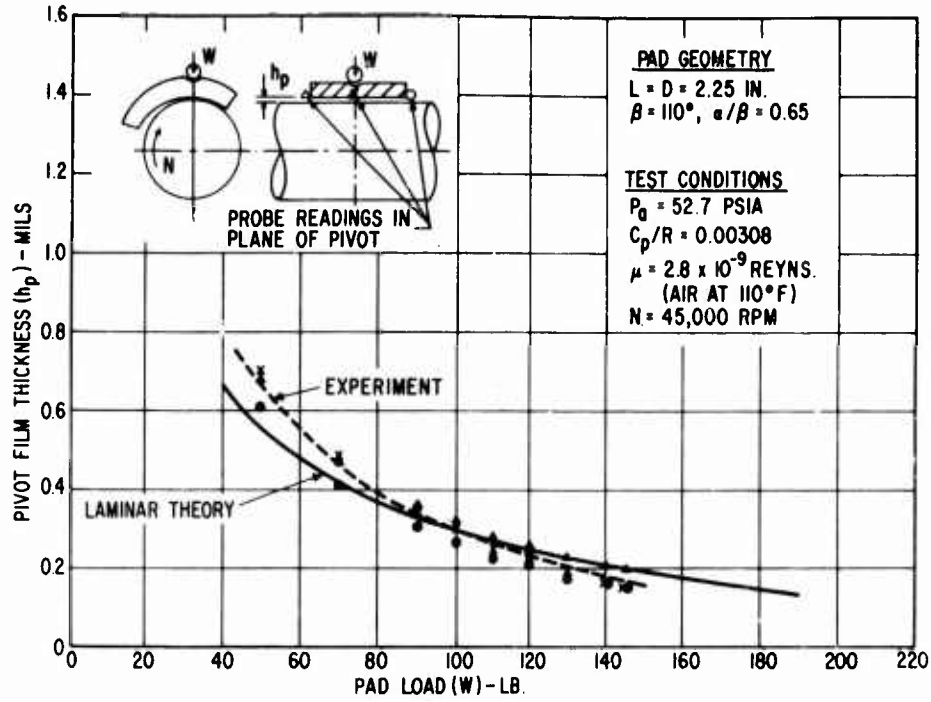
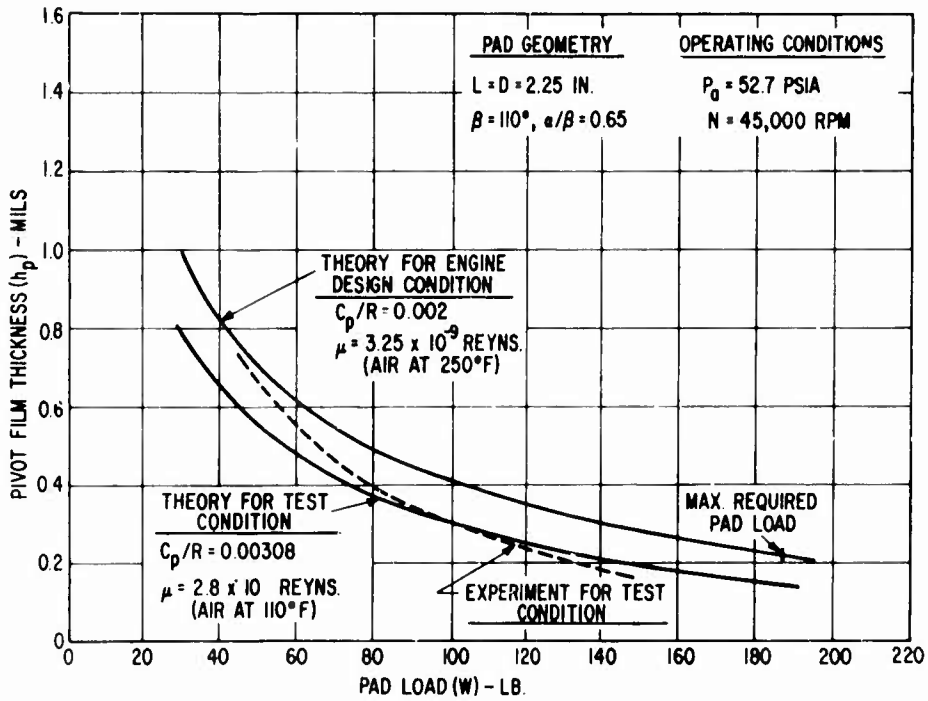


Figure 177. Pivot Seat and Reverse Side of Journal Bearing Pad.

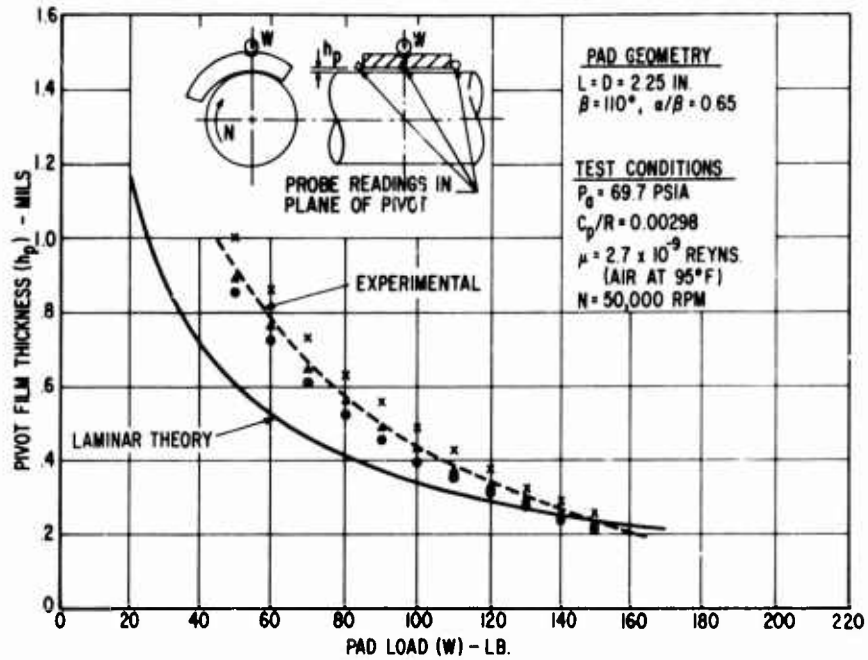


SINGLE-PAD LOAD CAPACITY DATA (SPEED AND PRESSURE REPRESENTATIVE OF ENGINE IDLE AT 25,000 FEET ALTITUDE)

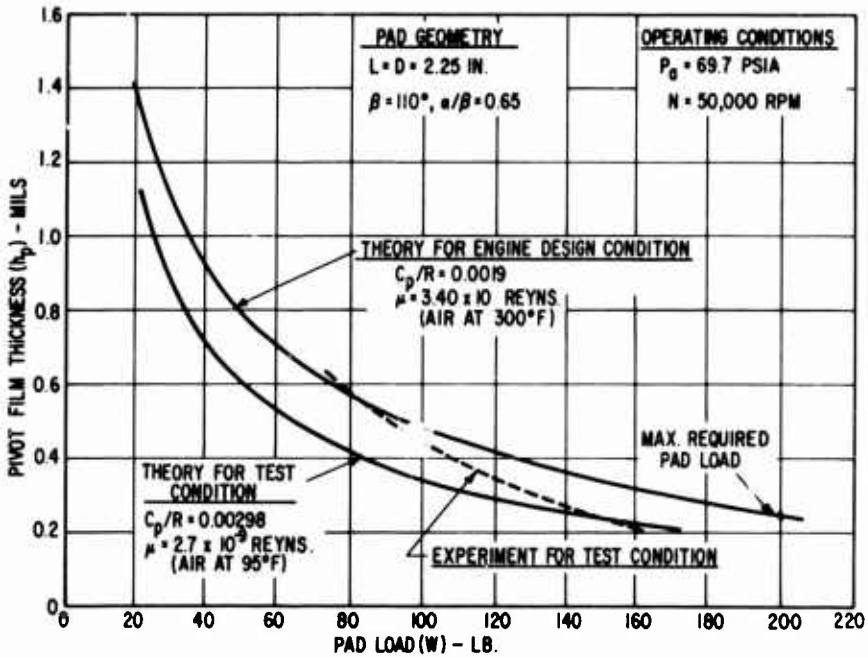


COMPARISON OF SINGLE-PAD DATA FOR TEST CONDITION AND ENGINE DESIGN CONDITION (SPEED AND PRESSURE REPRESENTATIVE OF ENGINE IDLE AT 25,000 FEET ALTITUDE)

Figure 178. Single Journal Pad Test Results at 25,000 Feet, Flight-Idle Conditions.

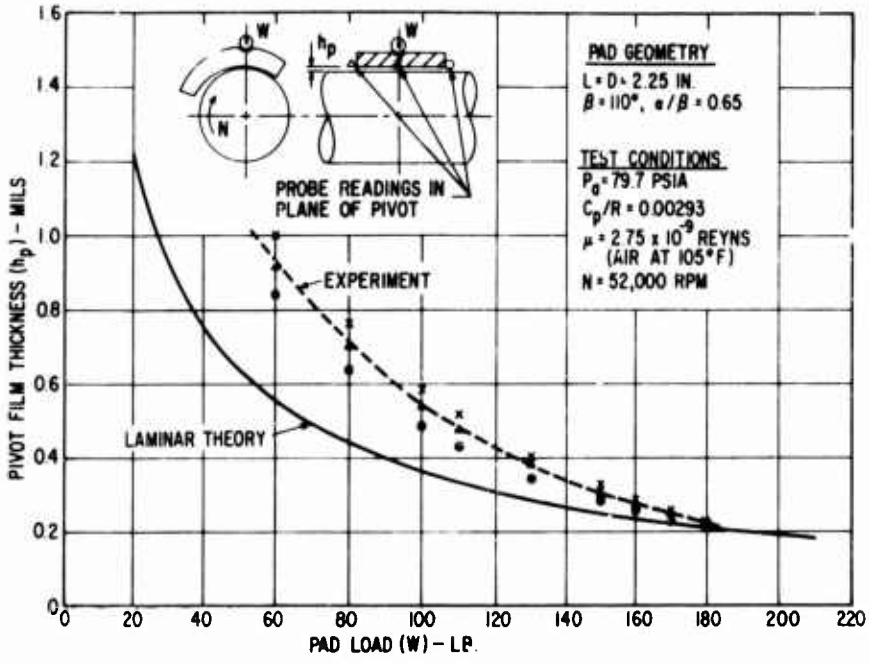


SINGLE-PAD LOAD CAPACITY DATA (SPEED AND PRESSURE REPRESENTATIVE OF 50-PERCENT ENGINE POWER AT 25,000 FEET ALTITUDE)

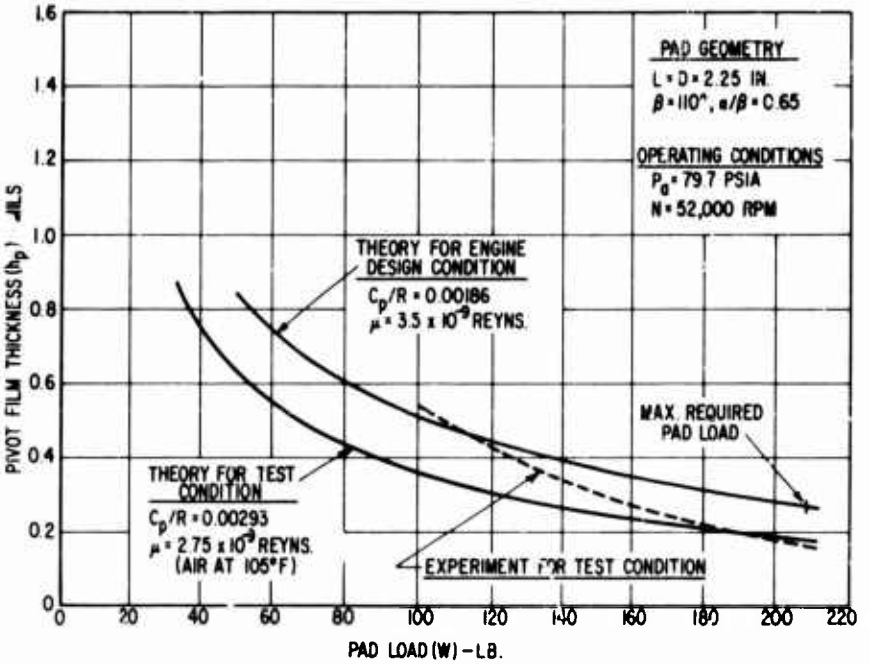


COMPARISON OF SINGLE-PAD DATA FOR TEST CONDITION AND ENGINE DESIGN CONDITION (SPEED AND PRESSURE REPRESENTATIVE OF 50-PERCENT ENGINE POWER AT 25,000 FEET ALTITUDE)

Figure 179. Single Journal Pad Test Results at 25,000 Feet, 50-Percent Power Conditions.



SINGLE-PAD LOAD CAPACITY DATA (SPEED AND PRESSURE REPRESENTATIVE OF 75-PERCENT ENGINE POWER AT 25,000 FEET ALTITUDE)



COMPARISON OF SINGLE-PAD DATA FOR TEST CONDITION AND ENGINE DESIGN CONDITION (SPEED AND PRESSURE REPRESENTATIVE OF 75-PERCENT ENGINE POWER AT 25,000 FEET ALTITUDE)

Figure 180. Single Journal Pad Test Results at 25,000 Feet, 75-Percent Power Conditions.

would have approximately 50 percent more load capacity than predicted by the laminar film theory. As the film thickness, ambient pressure, and/or speed is decreased, the Reynolds number also decreases and the deviation from laminar theory also decreases. This trend is clearly seen in Figures 178 through 180.

2. At high values of load (small operating film thickness), the measured film thickness closely approaches or becomes slightly less than that predicted by theory. The experimental deviations from theory when the pad is operating in the 0.2-mil range are small and can be explained by thermal and load distortion effects, which can easily be of the order of 50 microinches - a significant percentage of the measured film thickness.

The lower plots shown in Figures 178 through 180 compare the theoretical film thickness predictions for the engine operating condition with the theoretical predictions for the test condition. The differences between the test and the actual engine operating conditions are twofold. First, the engine operates at a higher ambient temperature than the test condition, yielding a higher lubricant (air) viscosity which results in increased load capacity. Secondly, the test pad was machined to a larger clearance ratio than that selected for the engine design. This off-optimum geometry reduces the test-pad load capacity.

The experimental results are also superimposed on the lower plots. By extrapolating the experimental curve to the engine design conditions (by simply raising the experimental curve such that it intersects the engine theory curve at the same film thickness value), it appears that the predicted film thickness under maximum pad load conditions will equal or exceed 0.2 mil for the 50- and 75-percent power conditions (Figures 179 and 180). At flight idle (Figure 178), however, the predicted film thickness would approach 0.18 mil, which is below the design criterion (0.2 mil) set for the journal bearings.

Although the film thickness fell short of our criterion objective, the magnitude of the deviation was only 20 microinches. Thus, the objective of verifying the adequacy of the design theory and the adequacy of the basic bearing design to carry the required bearing loads was achieved.

Methods of Improving Journal Bearing Performance at High Loads

To meet the 0.2-mil minimum film thickness criterion under conditions of maximum load at flight-idle engine operation, an increase in film thickness of approximately 11 percent is required.

To achieve such an increase in film thickness, the effect of minor bearing geometry changes was evaluated. These changes and the attendant performance improvement are summarized in Table XXIX. The effect of increasing the bearing diameter, increasing bearing length, increasing the distance of the pivot position from the leading edge, and various combinations of these individual changes was calculated. As can be seen from Table XXIX, all of the considered modifications, which are relatively minor, result in a

TABLE XXIX. EFFECT OF JOURNAL BEARING DESIGN CHANGES ON PAD FILM THICKNESS AT ENGINE IDLE, 25,000 FEET ALTITUDE, AND MAXIMUM MANEUVER LOAD CONDITIONS

N = 45,000 rpm | C_p/R = 0.002

μ = 3.25×10^{-9} lb-sec/in.^{2} | Λ = 0.436

P_a = 52.7 psia | W = 187 lb

Design Change	θ/β	D (in.)	L (in.)	Pivot Film Thickness (mils)	Increase in Film Thickness
Present design	0.65	2.25	2.25	0.222	——
15.4% increase in pivot location ratio (θ/β)	0.75	2.25	2.25	0.244	9.9%
5.55% increase in diameter and length	0.65	2.375	2.375	0.259	16.7%
15.4% increase in θ/β plus a 10% increase in bearing length	0.75	2.25	2.475	0.265	19.4%
15.4% increase in θ/β plus a 5.55% increase in diameter and length	0.75	2.375	2.375	0.285	28.4%

considerable percentage increase in bearing film thickness. All except the first one (increasing pivot location ratio) achieves the desired 11-percent film thickness increase.

No changes in the bearing geometry for either the 3.5-lb/sec C_o-T_o engine or the rotor dynamic simulator are suggested at this time. Provisions have been made, however, in the simulator design to accept a longer bearing (2.475 inches) with the larger pivot location ratio (0.75). Such a bearing modification could be incorporated into the simulator at a later date should the simulator bearing test results demonstrate the need for film thickness improvement over that measured in the component test rig.

RESULTS OF THRUST BEARING TESTS

The thrust bearing having the same spiral-groove surface geometry as described in the section entitled DESIGN AND ANALYSIS OF ROTOR BEARING SYSTEM was subjected to experimental evaluation in the bearing element component test rig. A photograph of this bearing is shown in Figure 181.

Testing of this bearing was not successfully completed because of a hydrodynamic instability that manifested itself in a subsynchronous precession of the thrust stator. This phenomenon occurred generally at speeds in excess of 20,000 rpm and at film thicknesses of less than 1 mil.

An example of a typical instability experienced during the tests is shown in Figure 182. Shown are photographs of oscilloscope traces which display the bearing film thickness as measured by the three capacitance probes (CP-3 through CP-5) located near the ID of the bearing. These probes can be seen in the photograph shown in Figure 181. The upper photo in Figure 182 shows a typical trace of a stable bearing. The only disturbance is a slight once-per-revolution (synchronous) ripple caused by runner run-out. The second two photos show a large-amplitude nonsynchronous vibration typical of bounded unstable operation. Precession of the thrust stator is indicated by the out-of-phase relationship of the three film thickness measurements. The frequency of the instability is that of the lowest system resonance. This resonance is, as shown in the lower photo in Figure 182, that of the thrust stator on its self-aligning mount.

The thrust bearing design was subjected to a stability analysis to establish the modifications required to stabilize the bearing. Based upon the results of this analysis, the bearing design was modified and successfully tested. The following sections describe the results of the analysis, the design modifications, and the final test results.

Thrust Bearing Stability Analysis

As a first step, existing tools for the prediction of hybrid thrust bearing performance were extended to provide specific stability information relating

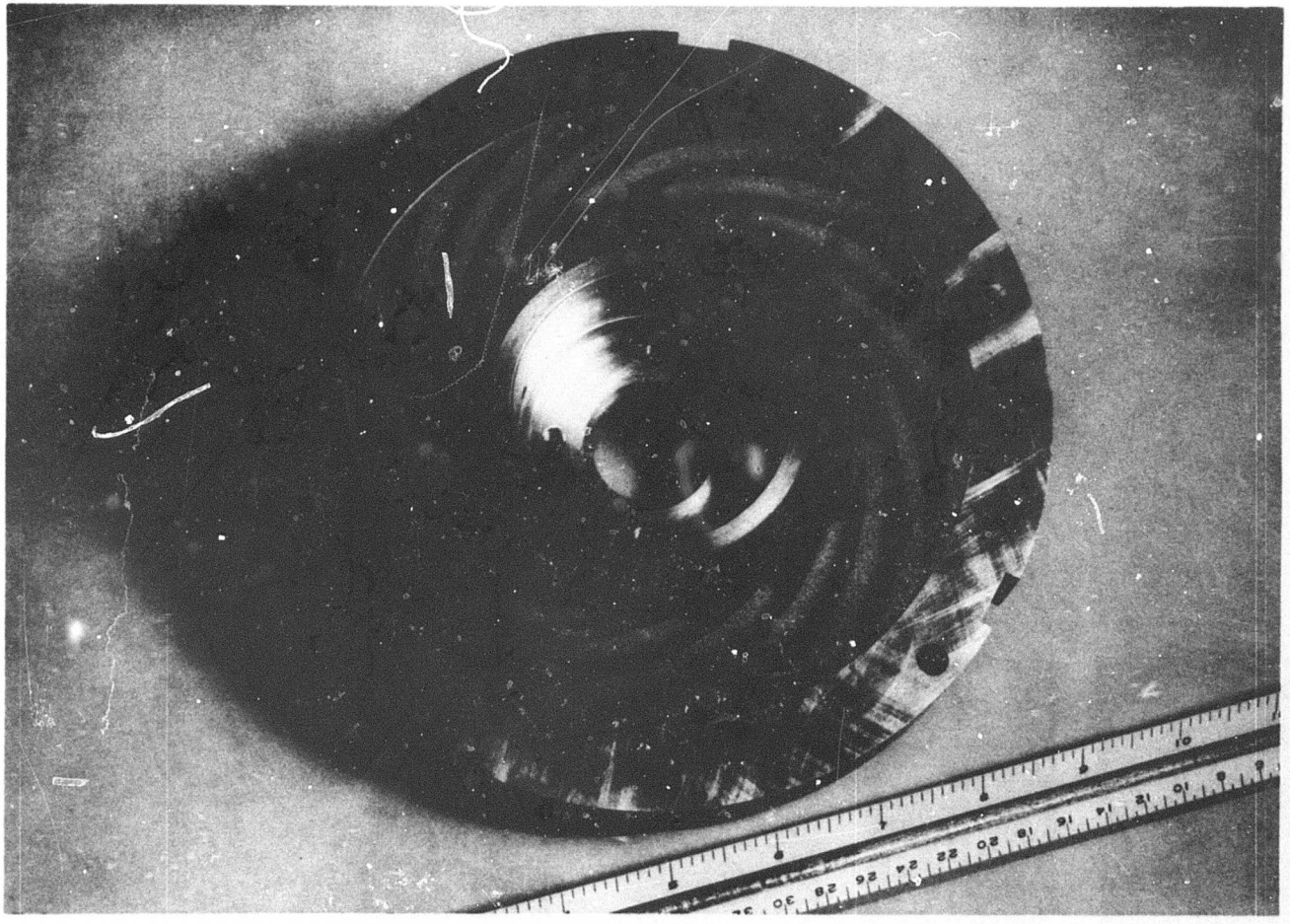


Figure 181. Surface of Hybrid Thrust Bearing Showing Instrumentation for the Measurement of Film Thickness.

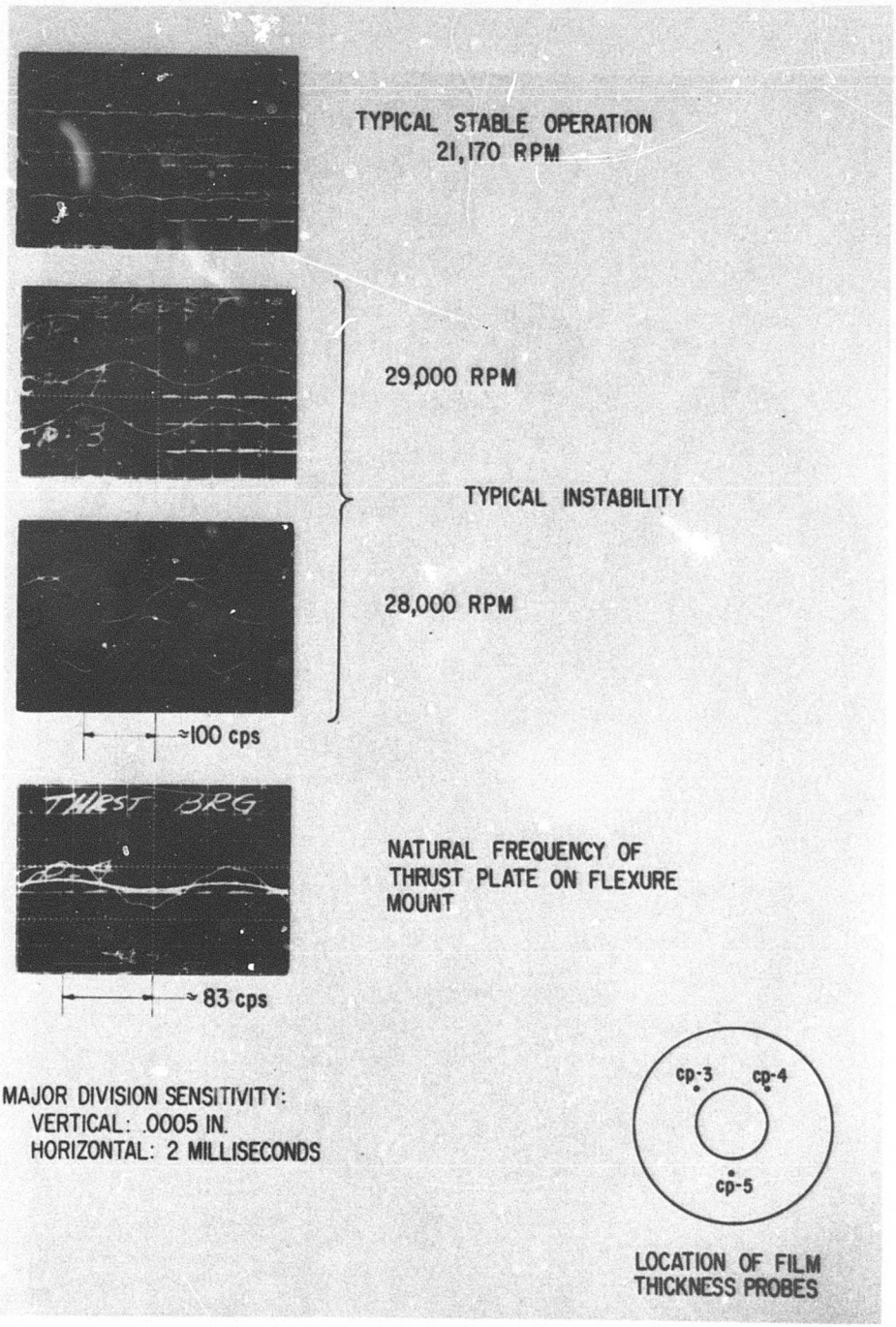


Figure 182. Examples of Hydrodynamic Thrust Bearing Instability.

to the rig.* The theoretical procedure incorporated is described below.

Secondly, efforts were made to correlate stability performance data for the existing rig design with the theoretical predictions. The objective of this correlation was to gain confidence in the theoretical data and to determine its limitations.

Finally, a redesign was undertaken, the objective of which was to improve stability characteristics by all means possible, while minimizing any sacrifice in the predicted axial load capacity.

Theoretical Procedure

The model used for stability analysis is shown schematically in Figure 183. The thrust plate is mounted on a cantilevered flexible beam (flexure), whose inertia is neglected. The connection at both ends of the flexure is assumed to be rigid. Between the stator and the rotor thrust plate, the bearing film acts as an angular spring and dashpot. Both flexure and film provide angular restraint about the x and y axes of Figure 183, but only the gas film provides damping. The rotor thrust plate is assumed to be rigid with respect to angular motion for the purpose of this analysis.

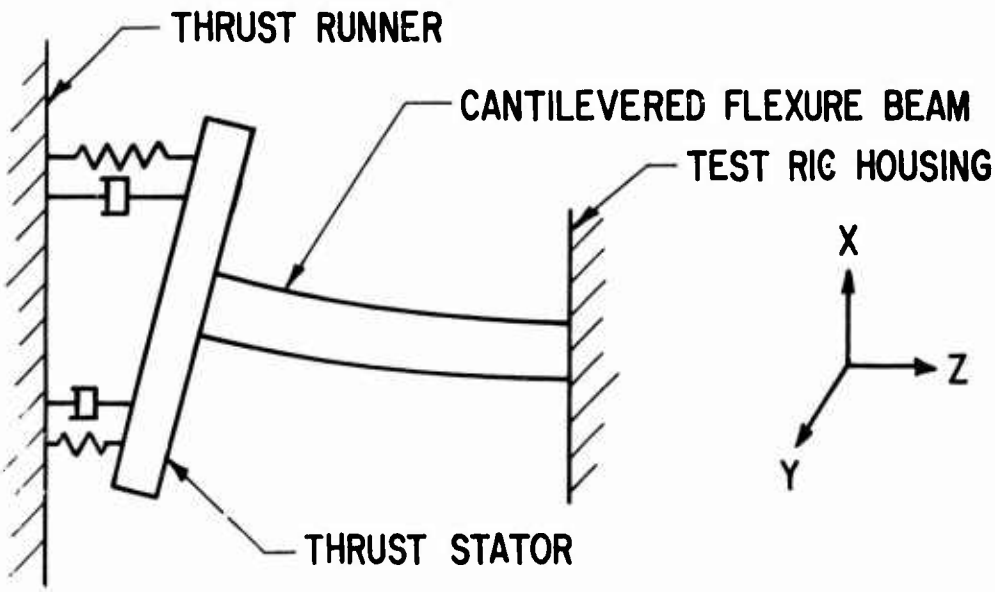


Figure 183. Schematic of Stability Analysis Model.

*This stability analysis is different from the gimbaled thrust bearing stability analysis made under this contract. The stability analysis used for the test bearing was a simpler one, in that provision for a gimbal ring is not included.

The gas film is analyzed, accounting for the presence of both the inward pumping spiral grooves and the hydrostatic feeding holes. The conventional compressible laminar lubrication theory is applied to yield linearized angular stiffness and damping for angular vibration of the stator about an initially aligned condition.

Self-excited vibration occurs in an elastic system when the damping force acts to drive the vibration rather than restrain it. In the stability analysis, angular whirl motion (precession) of the stator is postulated at a series of vibration frequencies, and for each frequency, bearing film response is calculated. If the damping direction corresponds with the direction of motion, thereby compounding the vibration, the system is potentially unstable. Actual instability would occur at this frequency if it were the same as the system natural frequency ("the system" implies stator mounted on flexure and film in parallel). By scanning a range of frequencies, the stability algorithm seeks to establish the threshold frequencies at which the direction of film damping changes sign with respect to the imposed motion. At each change of sign, a quantity "the critical inertia" is calculated. The "critical inertia" is the stator inertia for which the threshold frequency and system natural frequency coincide. In addition, by scanning the slope of the damping versus frequency curve, it is established whether larger or smaller inertias than critical would cause the system to operate in a region of instability.

The procedure described is used to set up a "stability map" for the design in question. A stability map is a plot of critical inertia versus either film thickness or axial load (see Figure 184, for example). For correlation purposes, the line representing actual system inertia is compared with the critical inertia line to establish regions of instability and stability. For design purposes, the relative position of both lines should be adjusted to maximize the regions of stability.

Correlation

Examination of oscilloscope traces indicated that the mode of instability was a forward whirl (precession) of the thrust bearing stator (Figure 182). Initial theoretical predictions indicated that there was indeed a potential for forward whirl corresponding to the observed instability.

The trends predicted by the analysis for the forward whirl mode were:

1. Larger inertias than the critical inertia induce instability.
2. Critical inertia falls with increasing speed.
3. Critical inertia increases with supply pressure.

These trends corresponded to the experimental observations, which showed both increased tendency for instability at higher speeds and a significant stabilizing influence of increased supply pressure.

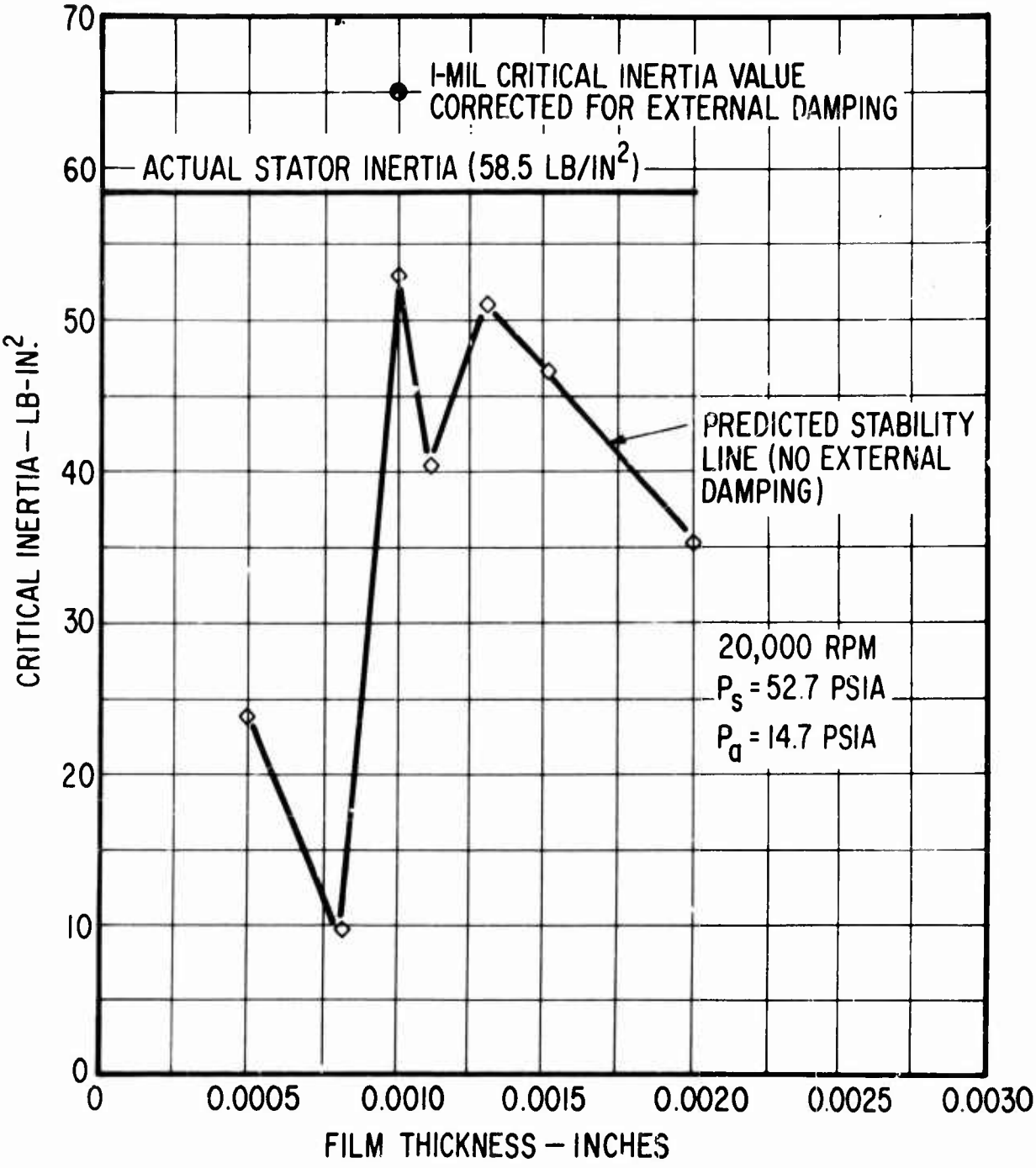


Figure 184. Calculated Thrust Bearing Stability Map – Original Test-Rig Configuration.

Figure 184 shows a typical critical inertia map for the test rig bearing at 20,000 rpm with a supply pressure of 52.7 psia, an ambient pressure of 14.7 psia, and the rig flexure stiffness of 5×10^4 lb in./radian. The predicted stable side of the critical inertia line is below the line. The predicted unstable side of the line is above it. The effective stator inertia of the original test configuration is represented by the horizontal line.

Clearly, this critical inertia map shows a complicated variation with film thickness, and the line has not been pinned down in detail. However, it is sufficient to indicate that the rig is predicted to be unstable over all of the film thickness range. Observations of stability trends for the rig were available under two similar conditions, both at 20,000 rpm with 14.7 psia ambient pressures:

1. At a supply pressure of 45 psia, the configuration was predominately stable, with a region of instability at about 0.75 mil gap (the point of lowest critical inertia on Figure 184).

2. At a supply pressure of 25 psia, the configuration was predominately unstable, with regions of stability at about 1 mil (the point of highest critical inertia on Figure 184.

Thus, the theoretical predictions are somewhat conservative in this case. However, there is clearly some correspondence; and if it is considered that no effect of external damping was included in the analysis, some reason for the conservative predictions is obtained. On Figure 184, at 1 mil, an approximately corrected value of critical inertia is shown based on the effect of measured external damping. Similar corrections over the full map would be found to bring the predictions and observations into close agreement.

It was concluded from this correlation that the analysis was capable of predicting stability trends satisfactorily and that numerical predictions of instability neglecting external damping would probably be somewhat conservative.

Redesign of the Thrust Bearing Stator

As discussed, in designing to avoid instability, the range of film thickness for which the actual inertia line is on the stable side of the critical inertia line should be maximized. Thus, to suppress the observed mode of instability, the critical inertia line should be raised and the actual inertia line should be lowered.

Although the correlation was carried out at 20,000 rpm, a more severe case was selected for the initial design studies: 45,000 rpm, with a supply pressure of 52.7 psia and an ambient pressure of 14.7 psia. This condition corresponds very closely with the 25,000 feet, flight idle condition. Under this condition, the predicted critical inertia of the test rig at a 1-mil film thickness is 0.478 lb-in.^{2}, far below the actual inertia value of 58.5 lb-in.^{2}.

Prior experience suggested that the critical inertia line could be raised by reducing the volume of the spiral grooves. Table XXX shows the influence on the critical inertia of reductions in length, depth, and width ratio of the grooves. At this stage in the redesign, the same 5 x 10^4 lb-in./radian flexure stiffness was maintained.

TABLE XXX. INFLUENCE OF GROOVING ON CRITICAL INERTIA

45,000 rpm
52.7 psia Supply
14.7 psia Ambient
1-mil Film Thickness

Condition	Groove Width Ratio	Groove Depth (in.)	Groove External (in.)	Critical Inertia ($lb\text{-}in.^2$)
1	0.615*	0.002*	0.92*	0.478*
2	0.615	<u>0.001</u>	0.92	14.8
3	<u>0.4</u>**	0.002	0.92	4.4
4	0.615	0.002	<u>0.61</u>	2.15
5	<u>0.4</u>	<u>0.001</u>	<u>0.61</u>	37.8

*Original test rig configuration

**Underlining indicates parameter changed from original

Figure 185 shows the variation of axial load with film thickness for these various configurations, and it may be seen that the most stable design of Table XXX (Condition 5) also has the highest predicted load capacity at small film thicknesses. At larger film thicknesses, the predicted load capacity for this design is very similar to that of the original configuration.

Based on these predictions, Condition 5 of Table XXX was adopted as an intermediate improved design, and more detailed stability data was obtained for this configuration.

The stability map for the intermediate design is shown in Figure 186, in this case as a function of load (film thickness values are shown in parenthesis). It was found to be possible, as described later, to reduce the effective stator inertia to 30 $lb\text{-}in.^2$ from the original value of 58.5 $lb\text{-}in.^2$. This lower inertia line is shown on the stability map.

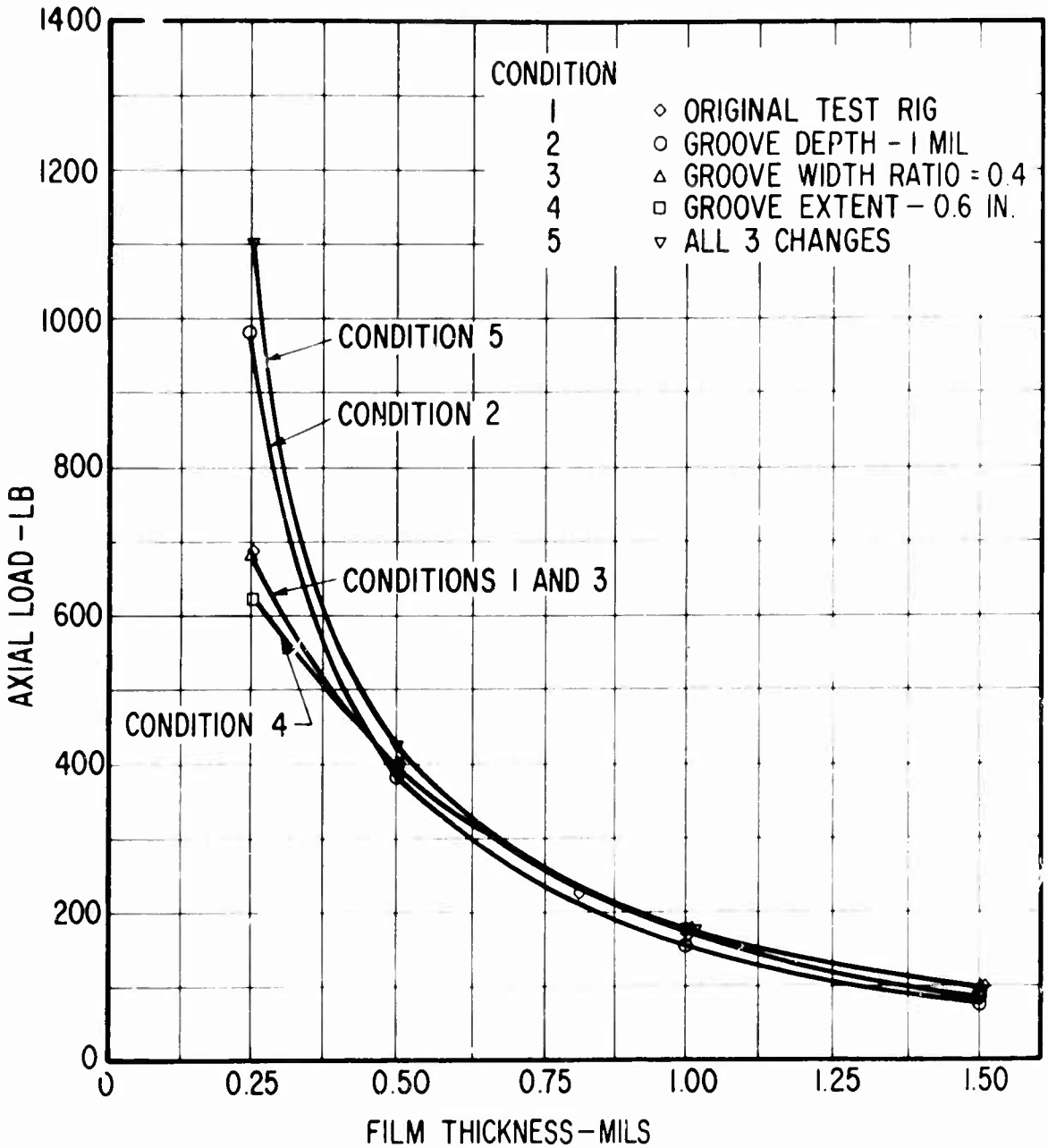


Figure 185. Calculated Load Capacity of Various Thrust Bearing Groove Geometries.

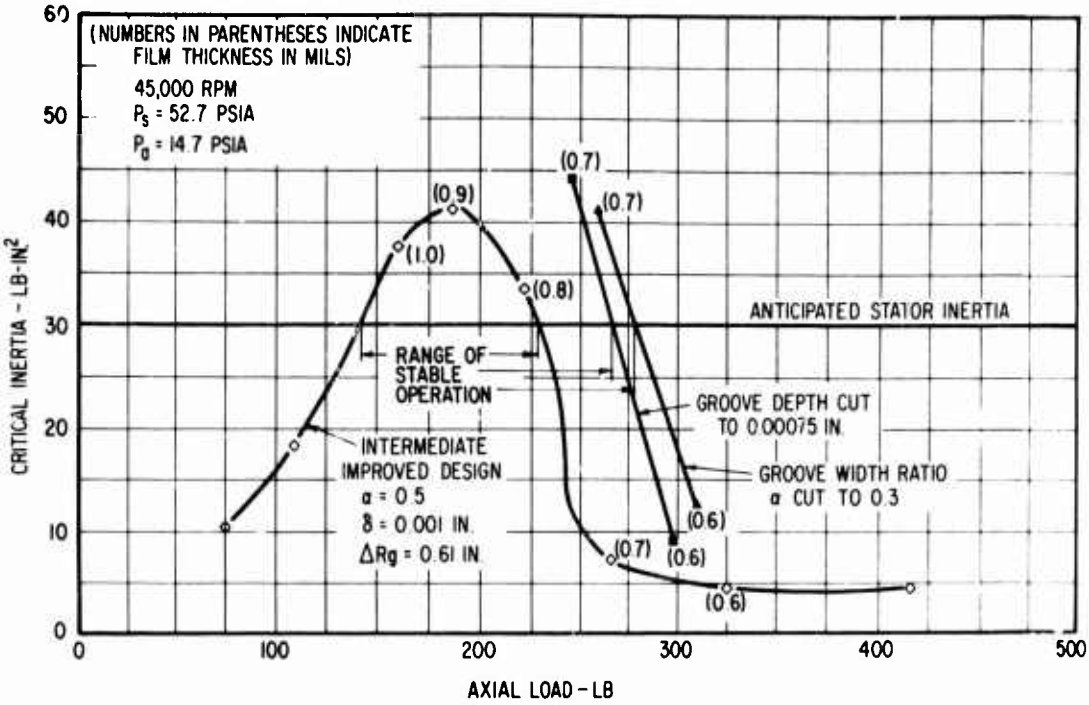


Figure 186. Calculated Thrust Bearing Stability Map Showing Effect of Groove Geometry on Range of Stable Operation.

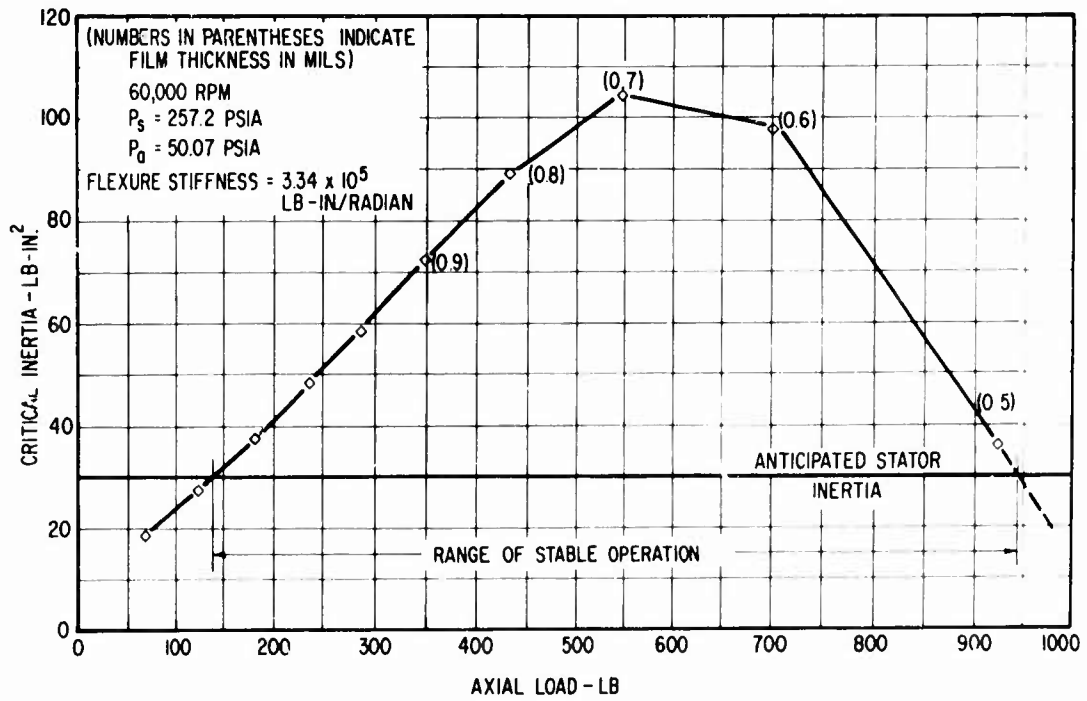


Figure 187. Calculated Thrust Bearing Stability Map for Final Modified Thrust Stator at Sea Level, 100-Percent Power Conditions.

Even with the above improvements, it was predicted that the design load of 277 pounds could not be met without inducing instability. Further improvement in stability under high loading was therefore sought. Alternatives of cutting groove depth and groove width were studied, and two stability lines, around the maximum loading condition, are shown for a groove width ratio of 0.3 and a groove depth of 0.75 mil, respectively, with conditions otherwise as for the full line. Both of these lines appear to satisfy the maximum loading condition without inducing instability. The line for a groove width ratio of 0.3 indicates a slightly larger margin of safety.

It was clear from the stability map for the intermediate design that there remained a potential instability problem at high film thicknesses. To overcome this problem, the decision was made to sacrifice aligning flexibility of the stator mounting and to raise the critical inertia above 30 lb-in.^{2} by stiffening the cantilever angular stiffness of the mount. For this film height, the threshold frequency was calculated to be 376 Hz and the film stiffness was about 105,000 lb-in./radian.

To push the critical inertia above 30 lb-in.^{2}, it is necessary, therefore, that the total stiffness K_{tot} (formed as the sum of film and flexure stiffness) be given by

$$376 \text{ cps} = \frac{1}{2\pi}\sqrt{\frac{K_{tot}g}{30}}$$

Therefore, $K_{tot} = 434{,}000$ lb-in./rad

The necessary flexure stiffness, K_{flex}, to achieve this condition is

$$K_{flex} = (4.34 - 1.05) \times 10^5 \text{ lb-in./rad}$$

$$K_{flex} = 3.29 \times 10^5 \text{ lb-in./rad}$$

Since the film stiffness increases with decreasing film thickness, and the stability map is smooth in this case, no stability problem is anticipated between a film thickness of 2.0 mils and one of about 0.65 mil.

The configuration selected for the redesigned thrust bearing stator is specified in Table XXXI.

TABLE XXXI. FINAL MODIFIED THRUST STATOR DESIGN	
Groove Depth, δ	$0.001 \pm \begin{matrix} .0001 \\ .0003 \end{matrix}$ inch
Groove Width Ratio (groove width/ groove + land width)	0.3
Groove Radial Extent	0.61 inch
Flexure Stiffness	334,000 lb/in.
Stator Inertia	30 lb-in.^{2}

This design was anticipated to give stable operation between 2.0 mils and 0.65 mil film thickness. Above 2.0 mils, the energy available in the negative film damping should not be sufficient to overcome external damping. Below 0.65 mil, instability problems were to be anticipated.

Figure 187 shows the stability map for the configuration of Table XXXI at the sea-level, 100-percent power condition (60,000 rpm, Ps = 257 psia, Pa = 50.07 psia). Based on this figure, no stability problems were anticipated at this condition.

Modification of Thrust Bearing Mount

As was discussed above, it was necessary to reduce the thrust plate inertia and to increase the mounting angular stiffness to achieve the improved stability limits. These two objectives were met by modifying the bearing mount flexure as shown in Figure 188.

The inertia of the thrust stator is

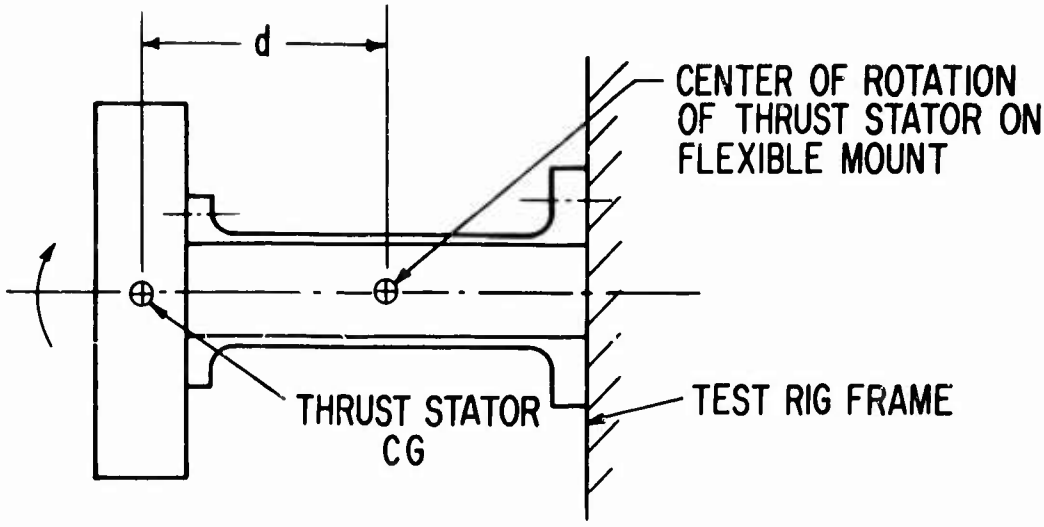
$$I = I_{CG} + md^2$$

where I = thrust stator total inertia - lb-in.^{2}

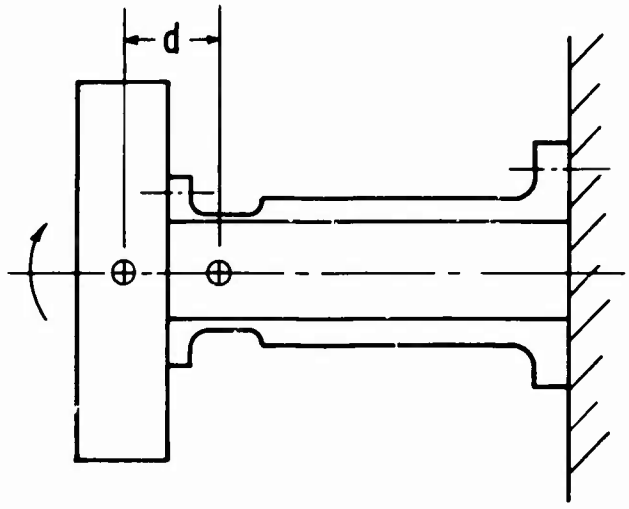
I_{CG} = thrust stator transverse inertia about center of gravity

m = thrust stator mass - lb-sec^2/in.

d = distance from CG to center of rotation - in.



ORIGINAL MOUNTING FLEXURE



MODIFIED MOUNTING FLEXURE

Figure 188. Test Rig Thrust Bearing Flexible Mount.

Reduction in the thrust stator inertia was achieved in the modified flexure by reducing the distance (d) from the stator center of gravity to the center of rotation. This was accomplished by reducing the length of the flexible portion of the tubular beam and placing the flexure portion as close as possible to the thrust stator (see Figure 188). The increased flexure stiffness was achieved by appropriate selection of the tube thickness in the flexible section.

Modified Thrust Bearing Test Results

Steady-state load-capacity tests were successfully conducted on the modified thrust bearing (which is shown in Figure 189) at the following conditions:

Speed (rpm)	Supply Pressure (psia)
0	59.7 to 79.7
40,000	59.7 to 69.7
45,000	69.7 to 79.7
48,200	73.7

All tests were run with the bearing ambient pressure equal to atmospheric. Except at the lower supply pressures at zero and 40,000 rpm, loads in excess of the 277-pound design load were imposed on the test bearing. In addition, the thrust bearing was operated with no sign of instability to 52,000 rpm with an imposed load of 235 pounds. Higher loads and speeds were not attainable because of the capacity limitations of the laboratory air supply which was used to drive the test rig turbine and to supply the thrust-load-chamber pressurization.

Load-capacity tests were conducted at zero speed at three different supply pressures (59.7, 69.7, and 79.7 psia) to gain a calibration of the hydrostatic portion of the hybrid thrust bearing. The lower pressure (59.7 psia) corresponds to the engine 25,000 feet, flight idle condition, where the difference between supply and ambient pressure is 45 psi.

The results of these tests are shown on Figure 190. Two test points are shown at each load for each supply pressure. The circle (o) is the average of the three proximity probe readings that are located 120 degrees apart near the inner radius of the bearing. The triangle (Δ) is the single probe reading located near the outer radius of the bearing. The difference between the two represents the net distortion of the air lubricant film due to nonflatness of the runner and stator. It will be noted that at the higher loads, these two points tend to converge because the pressure on the runner causes it to flatten.

The load performance of the bearing at zero speed is typical of a hydrostatic bearing; i.e., higher load capacity with higher supply pressures, and a limitation in maximum load capacity due to collapse of the film. This latter characteristic is commonly called "lock-up" because, as the

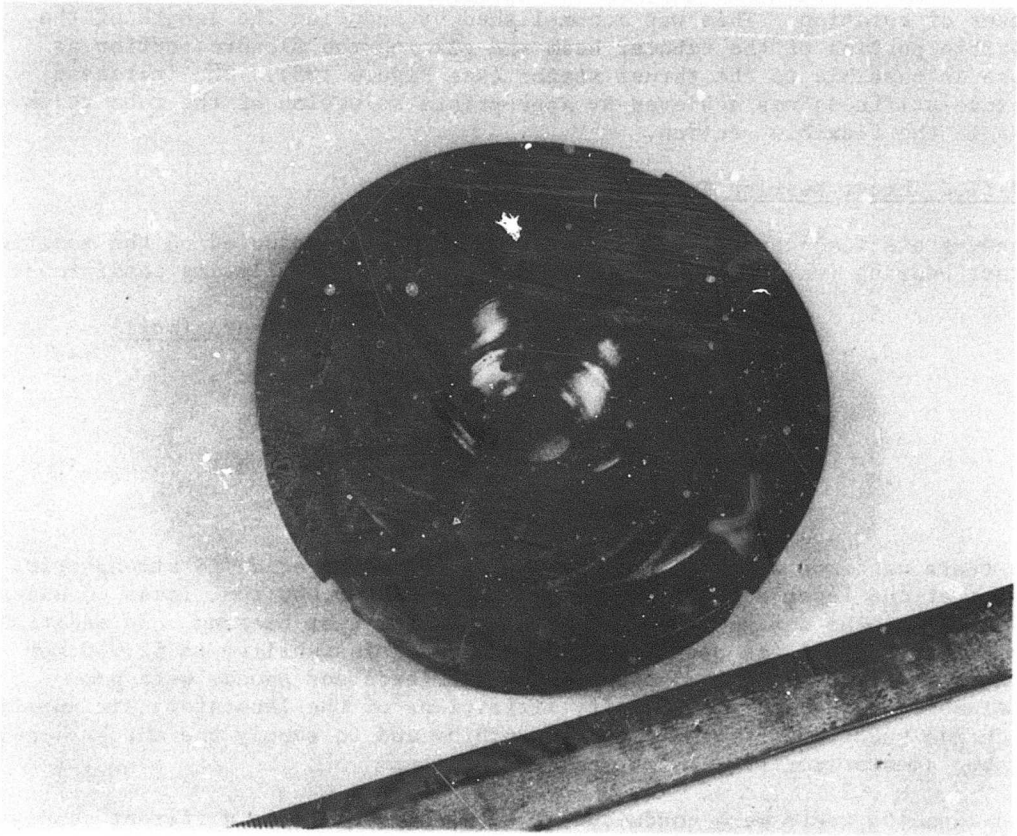


Figure 189. Surface of Modified Thrust Bearing.

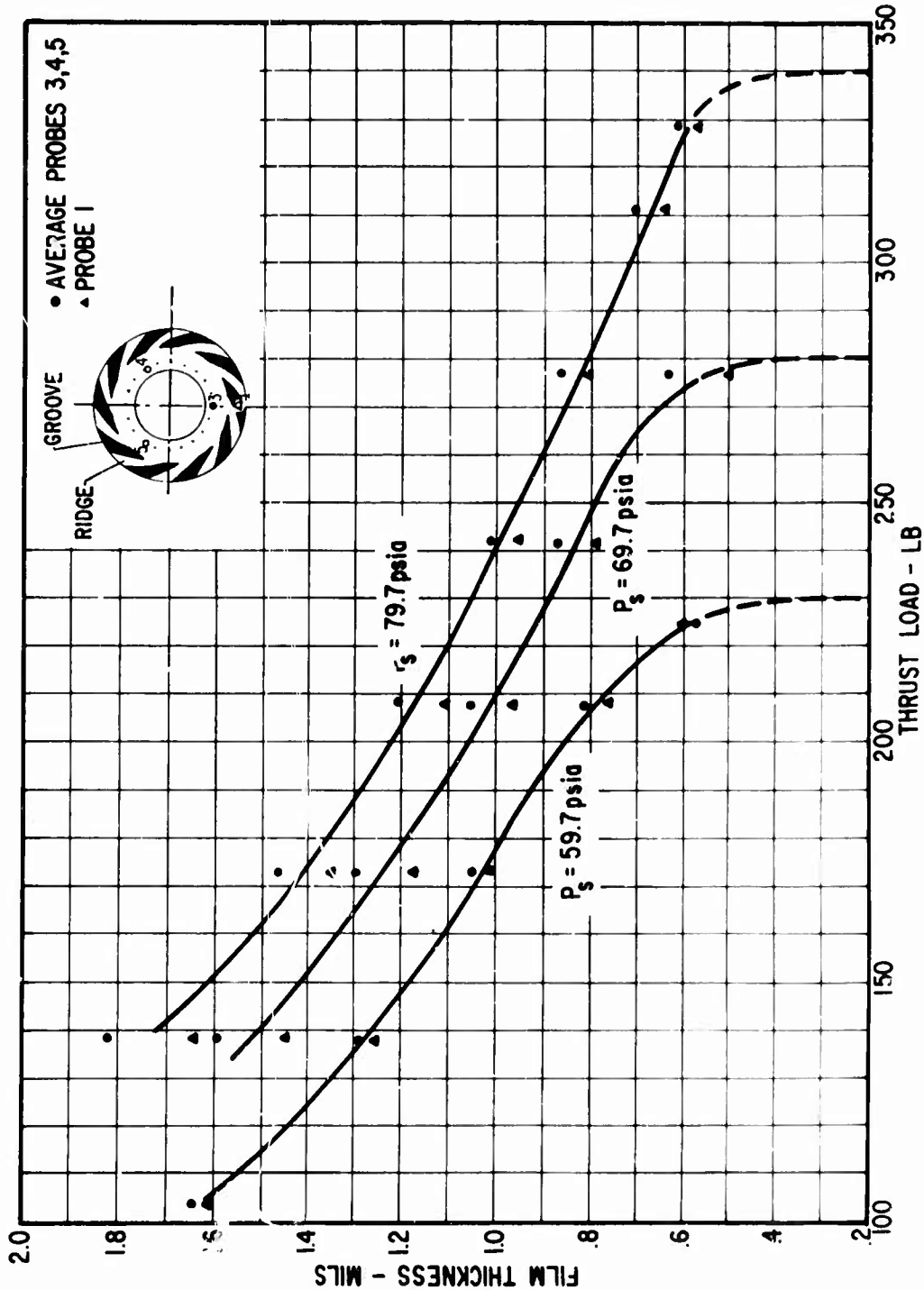


Figure 190. Thrust Bearing Load Capacity at Zero Speed.

load is increased, the film thickness decreases until some finite value is reached, at which point the film collapses completely. This is clearly evident in Figure 190.

The test results at 40,000, 45,000 and 48,200 rpm are shown on Figures 191 through 195. Figures 191 and 192 show a large load-capacity dependence on supply pressure, indicating that the bearing is strongly hydrostatic in the lower speed ranges. However, hydrodynamic action is evident by the reduced tendency of the load curve to drop off at the higher loads, as was typical of zero-speed operation (see Figure 190). Note that at 45,000 rpm and 48,200 rpm (Figures 192 and 193), there appears to be little tendency for the curve to drop, whereas at 40,000 rpm (Figure 191), the tendency is pronounced.

This pronounced hydrodynamic effect is more clearly shown in Figure 194, where the appropriate zero speed, 40,000 rpm, and 45,000 rpm experimental curves have been replotted. The speed, or hydrodynamic, effect on increasing load capacity and increasing the load at which lock-up occurs is clearly evident.

The experimental results at 45,000 rpm and 69.7-psia supply along with theoretical predictions are shown in Figure 195. Three theoretical curves are shown: two assuming that the air lubricant film is laminar, and one based upon turbulent lubrication theory. One of the laminar calculations assumes nondistorted bearing geometry, while the other is based upon a distorted film shape where the film is 0.2 mil smaller at the outer radius than at the inner radius.

There is generally good agreement between experiment and theory. At film thicknesses greater than about 0.8 mil, the measured load capacity is greater than that predicted by the laminar theory; at smaller film thicknesses, it is smaller than that predicted by the laminar theory. At large film thicknesses, most of the discrepancy between theory and experiment can be explained by the effects of turbulence and distortion. At small film thicknesses, these effects are small, and it is postulated that the reduced load capacity is partially attributable to the load curve drop-off characteristic of a hydrostatic bearing previously discussed (most clearly shown in Figure 191). It is currently not possible to theoretically predict when this effect sets in.

From the standpoint of engine operation, the most severe conditions for the thrust bearing are the lower power ranges at 25,000 feet. At these conditions, the available supply pressure (second-stage discharge) is low and the speed is low - these affecting both the hydrostatic and hydrodynamic functions of the bearing. Under all conditions of engine operation, the design thrust load has been set at 277 pounds, of which 240 pounds is a result of the 10g acceleration specified in MIL-E-5007C. The remaining 37 pounds is the total variation in aerodynamic thrust over the entire engine operating range.

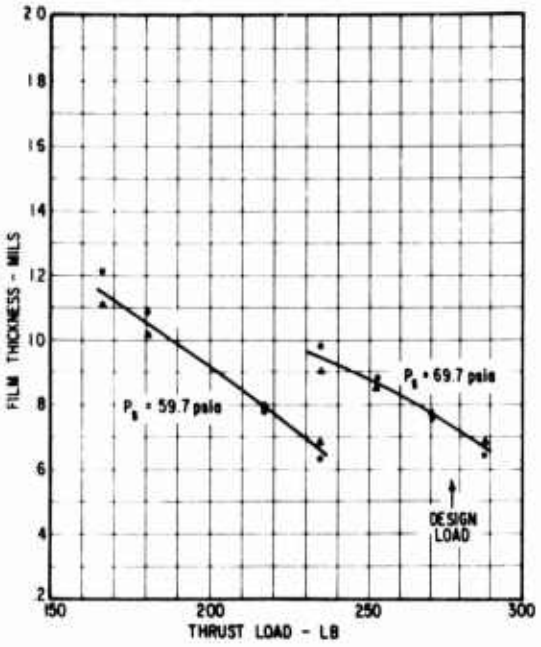


Figure 191. Thrust Bearing Load Capacity at 40,000 rpm.

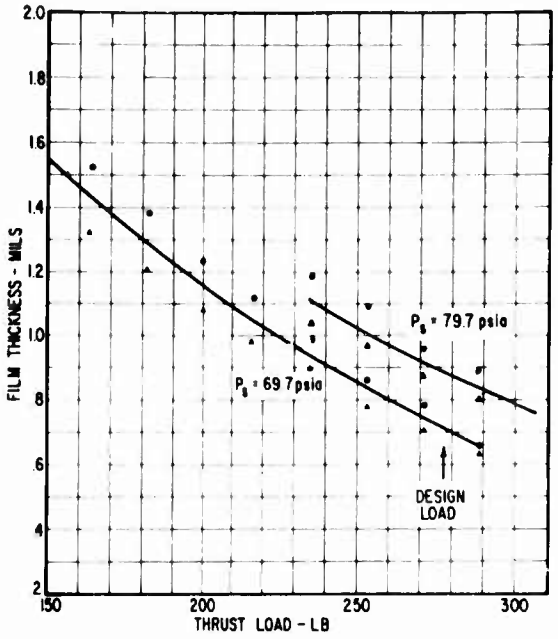


Figure 192. Thrust Bearing Load Capacity at 45,000 rpm.

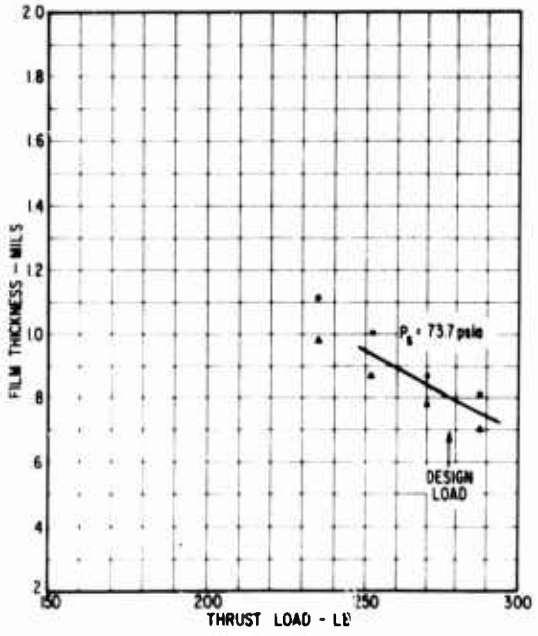
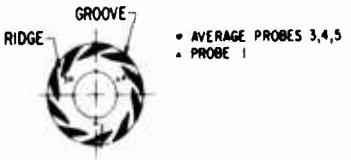


Figure 193. Thrust Bearing Load Capacity at 48,200 rpm.



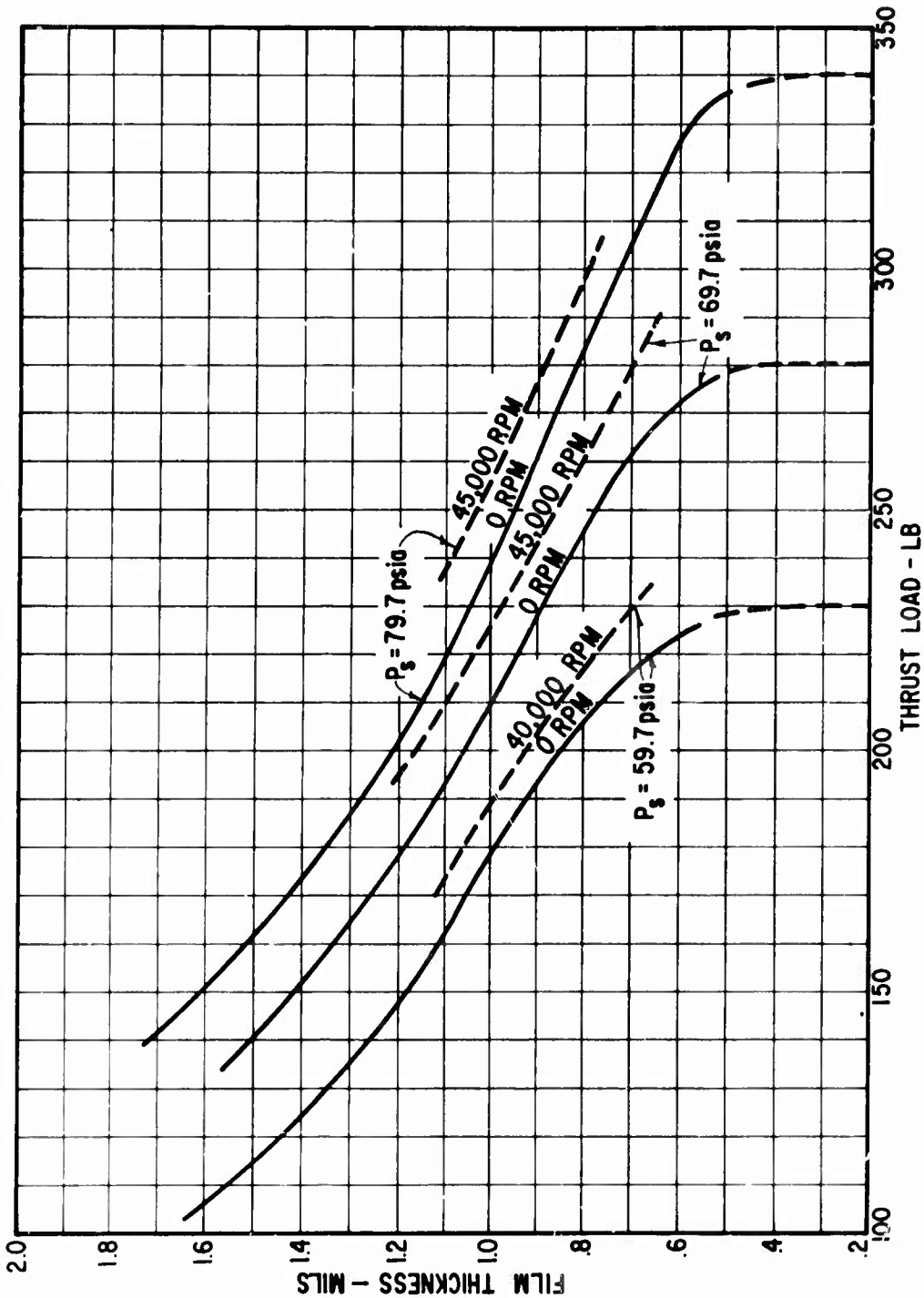


Figure 194. Effect of Speed on Bearing Load Capacity.

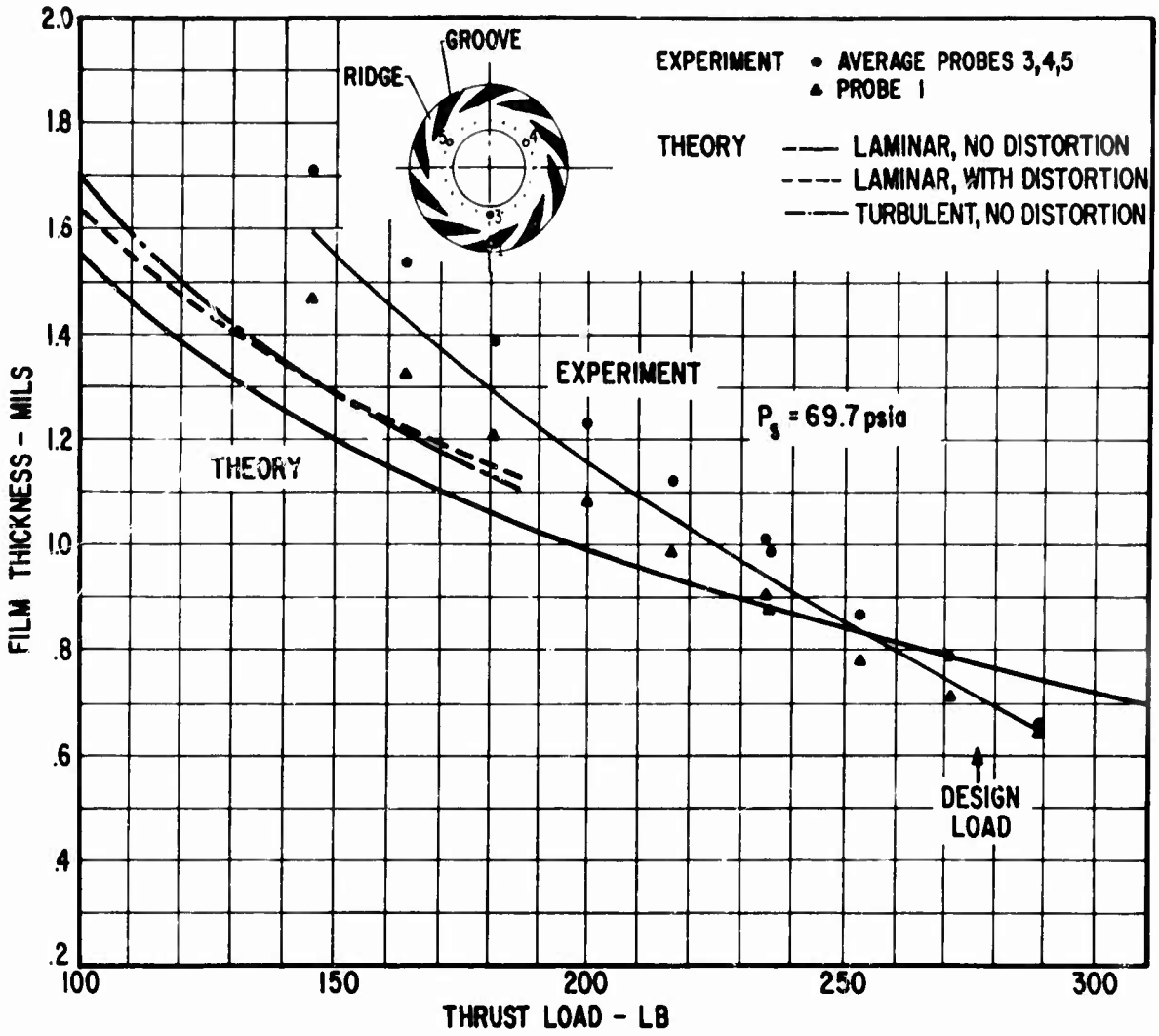


Figure 195. Thrust Bearing Load Capacity at 45,000 rpm.

Because of the lower thrust bearing load capacity characteristics at low speed and low pressure, the test conditions imposed were concentrated near the speed and pressure conditions corresponding to the 25,000 feet altitude condition at power levels from flight idle to 50 percent. Also, emphasis was placed on high-load small-film-thickness data.

The results presented in Figures 193 and 195 most closely duplicate low-power - 25,000 feet altitude engine operating conditions. The conditions in Figure 193 duplicate the speed and pressure differential conditions of the 25,000 feet 50-percent power condition. As can be seen, the 277-pound design load was comfortably supported at a film thickness of 0.8 mil. The conditions in Figure 195 duplicate the 25,000 feet flight-idle speed. However, the pressure differential across the bearing (55 psi) is 10-psi higher than is available from the engine. At 45,000 rpm and with pressure differentials across the bearing lower than 55 psi, the bearing was not inherently stable at the design load condition.

The diagram in Figure 196 shows the envelope of the available pressure difference across the engine thrust bearing. The numbers in parentheses at each corner of the envelope are the calculated critical inertia values for the engine thrust bearing stator, assuming no gimbal inertia. These values were taken from Figures 121 through 124, where the value of $\delta I/I = 0$ and the load equals 277 pounds. For high load conditions, the critical inertias of the test thrust bearing and the engine thrust bearing without a gimbal are very close to each other. This is because, at high loads, the unloaded side of the double-acting engine thrust bearing has little influence on its overall performance. The values of critical inertia indicate the effect of speed and pressure on stability*, and it is clearly seen that the low power conditions at altitude present the most difficult stability situation.

The cross-hatched area shown in Figure 196 is the area of the pressure-speed envelope where stable operation could not be achieved in the component thrust bearing tests. This area is, however, seen to be a very small part of the total operating envelope.

The results of the stability analysis that had been previously conducted on the modified thrust bearing indicated that it should have been stable at the conditions corresponding to flight idle at 25,000 feet. The lack of inherent stability of the test thrust bearing has been attributed to the flexibility of the self-aligning bearing mount in the test rig, which caused the center of rotation of the stator to be farther displaced from the bearing center of gravity than is indicated in Figure 188. This caused the actual thrust stator inertia to be larger than the calculated value indicated in Figure 186, thus lowering the magnitude of the applied load under which stable operation could be assured. (As can be seen in Figure 186, a small increase in inertia would result in unstable operation at high loads.) This conclusion is based upon tests of the natural frequency

*It will be remembered from preceding sections that the higher the critical inertia, the more stable the bearing.

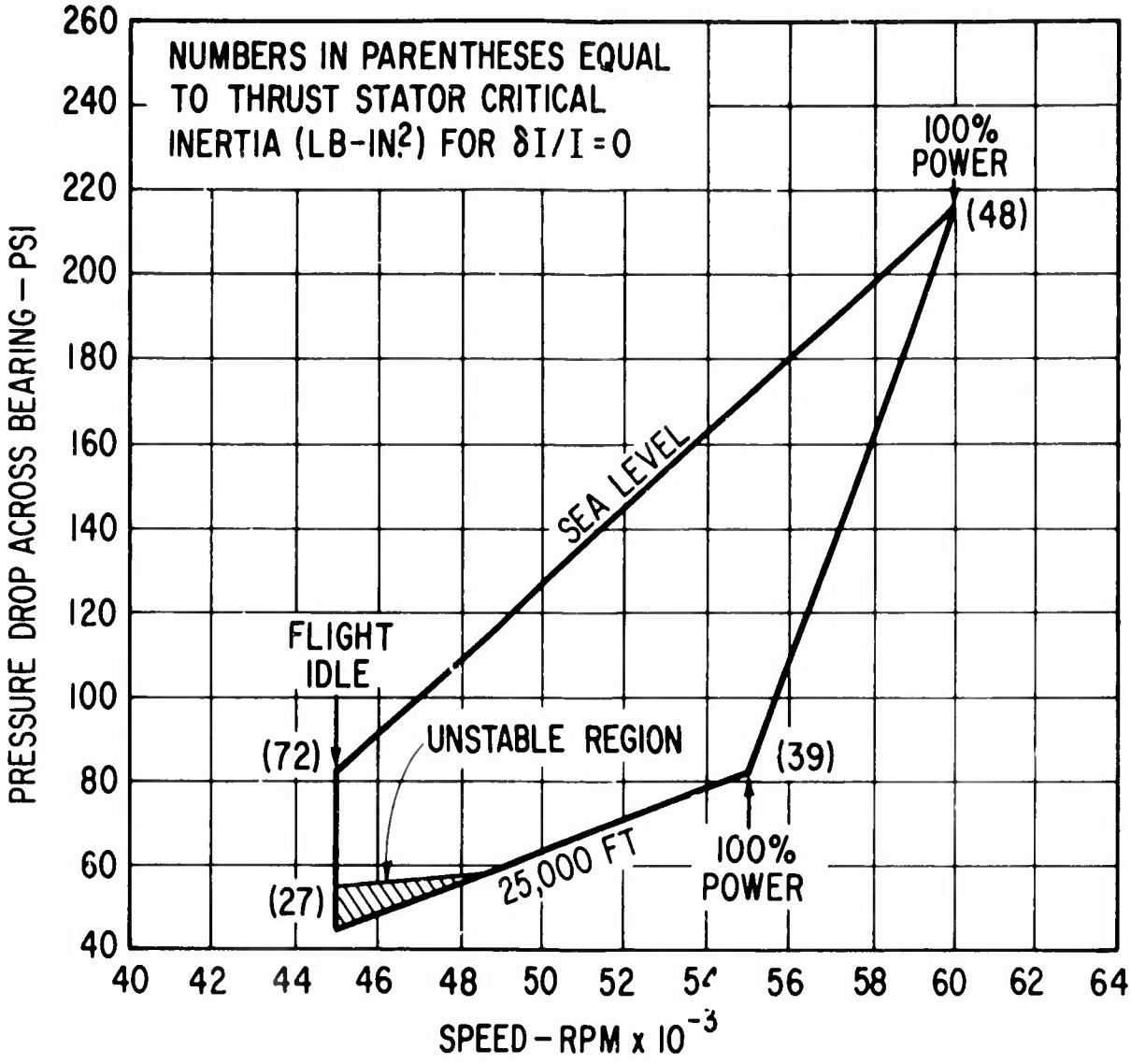


Figure 196. Thrust Bearing Fressure – Speed Envelope.

of the thrust bearing mount system. The results of these tests indicated that the natural frequency was approximately one-half of the value that would be achieved using the same inertia and mount stiffness values that were used in the stability analysis. Since the mass of the stator plate is known, the difference must lie in the overall flexibility of the mount.

The most probable location of this previously overlooked additional flexibility is at the ends of the tubular beam. The ends consist of relatively small flanges which are secured to the mating members by four 1/4-inch-diameter cap screws. In calculating the mount flexibility, the ends of the tubular beam were assumed to be fixed (slope equal to zero), whereas in reality, there is some bending of the flanges and stretch in the bolts which results in a finite slope at the ends and reduced overall stiffness.

Such compliance would not only soften the mount system, but also increase the transverse inertia of the thrust plate. The latter effect is a result of shifting to the right (as viewed in Figure 188) of the actual center of thrust stator rotation because of the angular displacement (slope) of the post at the test rig frame. Both of these effects would cause a reduction in the natural frequency of the system. As previously mentioned, the increased transverse inertia would lower the thrust bearing stability limit.

Because of the difference in the method of mounting the test rig and engine thrust bearings, a similar difficulty is not anticipated in the engine or engine simulator. The engine and simulator thrust bearings are gimbal mounted in such a way that the center of plate and gimbal ring rotations are accurately known; thus, the inertia is accurately predicted.

Conclusions From Modified Thrust Bearing Tests

From the results of the thrust bearing tests, the following conclusions have been drawn:

1. The correlation between the experimental load-capacity data and the laminar theory is sufficiently close at high loads to give confidence to the adequacy thrust bearing design calculations.

2. Correlation of experiment and theory at low loads is not as good. The apparent discrepancy is reduced by considering contributions of film turbulence and film distortions. The discrepancy which exists between theory and experiment at low loads is a favorable one, in that the measured film thicknesses are greater than predicted.

3. As anticipated, hydrostatic lockup will occur at zero-speed, high-load conditions. Under hybrid conditions (hydrostatic plus hydrodynamic) over the engine speed range, the lockup effect does not occur. Consequently, lockup will not be a problem for the operating range of the engine thrust bearing.

4. The pressure differential across the thrust bearing varies between 45 psi and 216 psi over the conditions from flight idle at 25,000 feet to full power at sea level. Tests were conducted on the thrust bearing with loads equal to or in excess of the 277-pound design load with pressure differences as low as 55 psi without difficulty. The measured load-capacity data indicates that the thrust bearing will carry the design thrust load at the minimum required pressure in the engine.

5. Although the modified thrust bearing was significantly more stable than the original design, it did not achieve the magnitude of stability anticipated. At 45,000 rpm, the bearing was not inherently stable at the lowest pressure conditions. The lack of inherent stability was not a reflection on the stability analysis used to design the bearing, but was a result of an overlooked compliance of the flexure mounting flange which prevented realization of the intended mounting stiffness. This problem is peculiar to the test rig and will not be a problem in the gimbal mount selected for the engine design.

6. In summary, the thrust bearing test results demonstrate that the modified thrust bearing will carry the anticipated engine thrust loads and that, when mounted on the engine gimbal arrangement, no stability problems should be anticipated.

CONCLUSIONS AND RECOMMENDATIONS

CONCLUSIONS

As was indicated in the introduction of this report, the Phase I program was subdivided into three major parts. Although the tasks were necessarily interrelated, each part had its own major objectives. The results and conclusions drawn from each of the three program parts are summarized below.

Rotor System Arrangements and Bearing System Design

The major objectives of this part of the Phase I investigation were as follows:

1. To determine the effect of engine size (over the range of 2 to 5 lb/sec) on the feasibility of air bearings

2. To establish the best arrangement and types of aerodynamic components for an air-bearing gas-turbine engine

3. To establish the air-bearing design parameters and operating environment for use in subsequent bearing design and experimental evaluation tasks

4. To identify any problem areas peculiar to applying air bearings to advanced high-performance gas-turbine engines

From the results of this part of the study, the following conclusions have been drawn:

1. Engine flow rate per se, over the range of 2 to 5 lb/sec, has no significant effect on the feasibility of air-lubricated bearings. The larger engine sizes tend to have more lightly loaded bearings because proportionately larger bearings can be utilized. On the other hand, the smaller engine sizes tend to have higher third-critical-speed margins because of their proportionately lower rotor weight and shorter bearing span. However, the study results indicate that air bearings are feasible over the entire flow range of interest.

2. Based on combined consideration of engine performance, weight, durability, cost, and thrust balance, the following five rotor arrangements were rated the best of the nine arrangements studied (listed in descending order of attractiveness):

Compressor	Turbine	Designation
2-stage centrifugal	single-stage radial	C_o-T_o
1-stage axial, 1-stage centrifugal	single-stage radial	C_1-T_o
2-stage axial, 1-stage centrifugal	single-stage radial	C_2-T_o
2-stage centrifugal	single-stage axial	C_o-T_1
1-stage axial, 1-stage centrifugal	single-stage axial	C_1-T_1

3. The best rotor arrangements from the standpoints of rotor critical speeds and application of air bearings are the C_o-T_o and C_o-T_1 arrangements. With these arrangements, the first flexural critical speed can be maintained at 33 percent above the 20-percent overspeed condition. For rotors with axial compressor stages, such a margin can not be maintained.

4. Both the C_o-T_o and C_o-T_1 arrangements require special attention to aerodynamic thrust balancing. For the C_o-T_o rotor, shrouded compressor wheels are required to minimize aerodynamic thrust. For the C_o-T_1 rotor, a thrust-balancing piston is required to minimize these loads. In this case, close clearance (floating) seals would be required to prevent excessive performance loss due to seal leakage. The thrust balance problem may not be unique to air bearings, inasmuch as there is little, if any, experience with heavily loaded high-speed rolling-element bearings. To achieve a reasonable fatigue life with ball bearings, it may be necessary to greatly reduce thrust loads or rotor speed with a corresponding reduction in performance.

5. Self-acting tilting pad journal bearings and a hybrid spiral-grooved double-acting thrust bearing have been selected for the air-bearing engine. Bearing designs have been evolved which can carry the maximum applied loads under all specified conditions of engine operation. However, particular attention must be paid to minimizing bearing film distortions under high loads such that bearing load capacity is not adversely reduced.

6. Means of self cooling the bearings have been established which should achieve the required control of thermally-induced film distortions. Shunt cooling using a high conductivity material (beryllium) was selected as the means of transferring heat from the compressor-end journal bearing. Compressor bleed flow is used to cool the turbine-end journal and thrust bearings.

7. From the standpoint of engine performance, the principal interaction of air bearings is a reduction in available shaft horsepower (and a corresponding increase in specific fuel consumption) due to bleed-air flows associated with pressurization of the two journal bearing cavities and with cooling of the thrust and turbine-end journal bearings. At the present state of design evolution, the calculated rated-power performance characteristics of the 3.5-lb/sec engine are 658 hp and 0.448 lb/hp-hr sfc. Assuming no bleed flow for bearing purposes, the engine could develop approximately 785 hp with an sfc of about 0.414. For direct comparison to a rolling-element bearing supported rotor, bearing, seal, and lube system losses, along with any required bleed flow losses, would have to be deducted from the aforementioned output power. While this level of performance of the air bearing engine is quite satisfactory, significant improvements in performance do appear reasonably possible. For example, by providing pressure limiting (or regulating) control for the journal bearing cavities, it appears that the shp can be increased to 705 and the sfc reduced to 0.435. Still further improvements in shp and sfc are believed to be possible by design optimization of the cooling techniques for the thrust and turbine end-journal bearings.

8. The area of accessory drives and engine starting originally appeared to be a major problem, but several attractive potential solutions have evolved from the limited accessory study conducted as part of this program. However, considerable effort will be required to develop and evaluate these advanced accessory system concepts.

Test Rig Evaluation of Bearing Components

The primary objectives of the Phase I bearing component tests were as follows:

1. To verify the theoretical load-capacity predictions for the key bearing components under the most severe loading conditions which will exist in the engine

2. To identify any problem areas relative to the key bearing components

From the results of the bearing components test program, the following conclusions have been drawn:

1. The theory used to predict the load capacity of both the thrust and journal bearings is adequate for the design of highly loaded air bearings. At all except the highest loading conditions, the laminar theory gave conservative results; that is, predicted film thicknesses were smaller than measured values. This conservative discrepancy between theory and experiment is believed to be due primarily to fluid-film turbulence effects.

2. The test data have demonstrated the capability of the key bearing components to carry the maximum maneuver loads specified in MIL-C-5007 under the most severe conditions of bearing operation; namely, engine idle at 25,000 feet altitude.

3. A problem of broad-range hydrodynamic instability was identified, both experimentally and analytically, for the initial design of the hybrid spiral-grooved thrust bearing. The instability caused the bearing to fall far short of its required load-capacity rating.

   The thrust bearing design was modified on the basis of an analytical parametric stability analysis. Subsequent testing of the modified bearing demonstrated stable operation up to the maximum thrust load requirements. A very small region of instability did remain, however, at the most severe bearing operating condition; namely, in the vicinity of engine idle at 25,000 feet altitude. The reason for this small region of instability in the test rig bearing was identified.

   A thorough stability analysis was performed for the gimbal-mounted thrust bearing design selected for the actual engine design and for the Phase II simulator test program. Based on the results of the stability analysis and the Phase I testing, the gimbal-mounted bearing design is expected to be completely stable under all possible operating conditions.

Test Evaluation of Bearing Materials

The major objectives of this part of the Phase I program were as follows:

1. To select the best available bearing coating and substrate materials for the bearing environmental conditions within the engine

2. To establish the durability of the selected bearing materials by subjecting them to endurance testing at the environmental and operating conditions which will exist in small aircraft gas-turbine engines

Based upon the results obtained from the test evaluations of bearing materials, the following conclusions have been drawn:

1. A plasma-sprayed chrome oxide (Cr_2O_3) coating on a titanium-alloy substrate is the best candidate material combination for the compressor-end journal bearing and for the thrust bearing. This material combination can be used for operating temperatures up to 800°F. From the standpoint of surface wear characteristics, Cr_2O_3 is the best coating material thus far evaluated for air-bearing applications at temperatures below 800°F.

2. A plasma-sprayed nickel-chrome-bonded chrome oxide coating (25% NiCr + 75% Cr_2O_3) on a high-temperature nickel-based alloy (such as IN-100) is the best candidate material combination for the turbine-end journal bearing. This material combination can be used for operating temperatures up to 1000°F, and possibly 1100°F.

3. The above identified material combinations can satisfactorily sustain the specified 15,000 start-stop cycles over the range of temperatures anticipated during engine startup and shutdown. Additionally, the selected material combinations can satisfactorily sustain the mechanical strains, the centrifugal forces, and the differential thermal expansions which will occur in the rotating journal sections of a small aircraft gas-turbine engine.

4. Although not a planned part of the experimental program, two unexpected and unintentional situations arose during the bearing components test program which induced sustained high-speed sliding contact between the rotating and stationary Cr_2O_3-coated bearing surfaces. The sustained sliding (of the order of a few seconds) caused a rapid buildup of Cr_2O_3 debris in the air-bearing clearances which resulted in seizure of the test shaft. The rapid buildup of Cr_2O_3 debris appears to be the result of surface crazing and spalling of the Cr_2O_3 coating due to severe thermal stresses.

   Except for start-stop sliding and momentary (less than 10 milliseconds) shock-induced contacts, an air-bearing engine must be designed to maintain full air-film lubrication under all possible conditions of engine and aircraft operation. Nonetheless, it must also be anticipated that a sustained high-speed sliding condition may arise sometime during the operating life of the engine, perhaps from a labyrinth seal or shroud rub. Consequently, it is concluded that increased emphasis must now be placed on improving the high-speed sustained sliding capabilities of air-bearing materials. Recommendations to this end are presented in the next section.

RECOMMENDATIONS

The results and conclusions drawn from the Phase I program have been gratifying, in that generally positive answers have been obtained to all the questions of air-bearing feasibility to which the Phase I effort was specifically directed. In a very real sense, a significant advance has been made in the overall demonstration of feasibility of air bearings for small aircraft gas-turbine engines. It is therefore recommended that the Phase II full-scale simulator program now be initiated as originally planned, so that the additional important feasibility areas relative to stability, cooling effectiveness, and dynamic load capacity of the complete engine rotor-bearing system can be experimentally assessed.

As briefly mentioned in the preceding conclusions, and as discussed in more detail in the Evaluation of Bearing Materials section of this report, an unplanned adjunct of the Phase I effort was identification of the

limited ability of the Cr_2O_3 bearing surfacing material to withstand sustained sliding at high speeds. This same result is undoubtedly true for the 25% NiCr + 75% Cr_2O_3 coating material. Methods of improving the high-speed sustained sliding characteristics of the bearing materials need to be developed at the earliest possible date to be certain that air-bearing engines can survive unforeseen or unintentional circumstances which could cause sustained high-speed bearing sliding.

Achievement of the total desired spectrum of air-bearing materials capabilities will ultimately require a comprehensive program of materials and methods development. To this end, MTI recommends that a major air-bearing materials technology program be initiated by the U. S. Government. A multi-agency coordinated program is suggested since there are several government agencies which are actively engaged in gas-bearing turbomachinery programs (Army, Air Force, NASA). All of these agencies would definitely benefit from a well-oriented, well-directed materials technology effort.

On a shorter-term basis, there are two approaches to alleviating the sustained high-speed sliding problem which could perhaps have a high payoff. One approach is to apply a very thin film of solid, high-temperature lubricant on the surface of the plasma-sprayed coating. The hoped-for effect of the solid-film lubricant would be a significant reduction in the presently high coefficient of friction of the straight Cr_2O_3 coating. This would, of course, directly reduce the heat generation rate during the interval of sliding, and hence alleviate the thermal stress problem in the coating.

Several candidate solid-film lubricants are available for normal operating temperatures up to 1200°F. It is recommended that these solid-film lubricants be subjected to preliminary screening tests to determine their potential for improving the coating sliding behavior. Washer and pad type specimen tests similar to those conducted on the coatings in Phase I of this program would give an early and inexpensive insight into the value of pursuing the solid-film lubricant approach. If such evaluations were authorized at the beginning of the Phase II effort, it would be possible to incorporate any materials improvements into the simulator bearing hardware.

A possible second approach which has recently come to our attention is the use of special processing techniques to achieve strengthening of the surface coatings by compressive surface stresses. These techniques have been developed for, and are currently being used by, the ceramic materials industry. Strengthening by surface compressive stresses should permit a significant increase in thermal-stress levels to be imposed on the coatings before thermal crazing begins. The use of surface-compressive-stress strengthening, in conjunction with solid, thin-film lubricants, may provide a compound increase in the ability of coatings to survive sustained sliding. The possible use of surface-compressive-stress strengthening will be studied further before a definite recommendation is made.

LITERATURE CITED

1. Curwen, P. W., FEASIBILITY OF GAS BEARINGS FOR SMALL HIGH-PERFORMANCE AIRCRAFT GAS TURBINES, Mechanical Technology, Inc., USAAVLABS Technical Report 68-87, U.S. Army Aviation Materiel Laboratories, Fort Eustis, Virginia, March 1969, AD 684956.

2. Morris, R. E., and Kenny, D. P., HIGH PRESSURE RATIO CENTRIFUGAL COMPRESSORS FOR SMALL GAS TURBINE ENGINES, 31st Meeting of Propulsion and Energetic Panel of AGARD, Helicopter Propulsion System, Ottawa, June 1968.

3. ELEMENT DESIGN AND DEVELOPMENT OF SMALL CENTRIFUGAL COMPRESSORS [redacted] The Boeing Co., USAAVLABS Technical Report 67-30, U.S. Army Aviation Materiel Laboratories, Fort Eustis, Virginia, August 1967, Vol I - AD 384923L, Vol II - AD 384924L.

4. Muller, C.H., and Sabatiuk, A., THE DEVELOPMENT OF SUPERSONIC AXIAL COMPRESSOR BOOST STAGES FOR SMALL GAS TURBINES, ASME Paper 69-GT-44, March 1969.

5. Calvert, G., and Okapuu, V., DESIGN AND EVALUATION OF A HIGH-TEMPERATURE RADIAL TURBINE, Phase I Final Report AD688164, January 1969.

6. Balje, O.E., A STUDY ON DESIGN CRITERIA AND MATCHING OF TURBOMACHINES, Part A - SIMILARITY RELATIONS AND DESIGN CRITERIA OF TURBINES, Journal of Engineering for Power, January 1962.

7. Thompson, V.W., and Marman, H.V., TURBOACCELERATOR COMPONENT EVALUATION PROGRAM, AF APL-TR-69-61, August 1969.

8. Benstein and Wood, APPLICATIONS AND PERFORMANCE LEVELS OF RADIAL INFLOW TURBINE, SAE Trans. Vol 72, 1964.

9. Shapiro, W., and Colsher, R., IMPLEMENTATION OF TIME-TRANSIENT AND STEP JUMP DYNAMIC ANALYSES OF GAS-LUBRICATED BEARINGS, ASME Paper 69-WA/Lub-5, presented at the Winter Annual Meeting, Los Angeles, California, November 16-20, 1969.

APPENDIX I
STABILITY ANALYSIS OF GIMBALED THRUST BEARING SYSTEM

GIMBALED THRUST BEARING SYSTEM DESCRIPTION

The typical gimbaled thrust bearing is shown in Figure 129. The thrust plate is subjected to fluid-film forces, and is connected to a gimbal ring through a pair of torsional springs characterized by their stiffness K_{TY}. The gimbal is connected to a rigid housing by another pair of springs of torsional strength K_{GX}. The two degrees of freedom of the system may be described by the angular motion of the gimbal relative to the housing θ and the angular motion of the thrust plate relative to the gimbal ϕ.

The dynamic equations governing a rotational system are

$$\frac{d\vec{H}}{dt} + \vec{\omega} \times \vec{H} = \vec{M} \tag{1}$$

where $\vec{\omega}$ is the angular velocity of a rotating body, $\vec{H}$ its angular momentum measured in the body coordinate frame about its mass center, and $\vec{M}$ the external moment acting on the body.

When Equation (1) is applied to the gimbaled thrust bearing system, the linearized version of the equations of motion in terms of the above-mentioned two degrees of freedom (θ,ϕ) is as follows:

$$[I_{GT}]\ddot{\vec{\phi}} + [D_{GT}]\dot{\vec{\phi}} + [K_{GT}]\vec{\phi} = \vec{M}_F \tag{2}$$

where upper dot denotes time derivative. Further,

$$[I_{GT}] = \begin{bmatrix} I_{GT} + I_{TX} & 0 \\ 0 & I_{TY} \end{bmatrix}$$

$$[D_{GT}] = \begin{bmatrix} D_{GX} & 0 \\ 0 & D_{TY} \end{bmatrix} \tag{3}$$

$$[K_{GT}] = \begin{bmatrix} K_{GX} & 0 \\ 0 & K_{TY} \end{bmatrix}$$

and

$$\vec{\phi} = \begin{bmatrix} \theta \\ \varphi \end{bmatrix}$$

where I_{GX} = inertia of gimbal about x-axis

I_{TX} = inertia of thrust plate about x-axis

I_{TY} = inertia of thrust plate about y-axis

D_{GX} = gimbal pivot damping

D_{TY} = thrust plate pivot damping

The fluid-film moment $\vec{M}_F$ can be expressed in terms of the angular displacements:

$$\vec{M}_F = -\begin{bmatrix} Z_{//} & \underline{Z_{/}} \\ -\underline{Z_{/}} & Z_{//} \end{bmatrix} \vec{\phi} \tag{4}$$

where $Z_{//}$ and $\underline{Z_{/}}$ are fluid-film stiffnesses, and in general are complex quantities [11]:

$$\begin{aligned} Z_{//} &= U_{//} + i\, V_{//} \\ \underline{Z_{/}} &= \underline{U_{/}} + i\, \underline{V_{/}} \end{aligned} \tag{5}$$

The dynamic stability problem of the gimbaled thrust bearing system will be treated based on Equation (2), in a general manner, in the next section. The following notations are defined for later reference:

$$\Delta K = \frac{1}{2}(K_{GX} - K_{TY})$$

$$\Delta D = \frac{1}{2}(D_{GX} - D_{TY})$$

$$K = \frac{1}{2}(K_{GX} + K_{TY})$$

$$D = \frac{1}{2}(D_{GX} + D_{TY})$$

$$
\begin{aligned}
I &= \frac{1}{2}\,(I_{GX} + I_{TX} + I_{TY}) \\
\Delta I &= \frac{1}{2}\,(I_{GX} + I_{TX} - I_{TY}) \\
I_g &= I - \frac{K}{\nu^2} \\
\Delta I_g &= \Delta I - \frac{\Delta K}{\nu^2} \\
\tilde{U}_{//} &= U_{//} + K \\
\tilde{V}_{//} &= V_{//} + \nu D
\end{aligned}
\tag{6}
$$

In the above notations, ν is the characteristic frequency of vibration.

GENERAL METHOD OF SOLUTION

The characteristic equations of the thrust bearing system are:

$$
\begin{bmatrix} Z_x - z_x & \underline{Z_/} \\ -\underline{Z_/} & Z_y - z_y \end{bmatrix} \begin{bmatrix} 0 \\ \varphi \end{bmatrix} = 0 \tag{7}
$$

The fluid-film behavior is assumed to be isotropic, representing, for instance, a rotationally symmetric, spiral-grooved thrust bearing. Asymmetry in the mechanical arrangement may appear in terms of gimbal inertia as well as pivot axis constraints. To isolate the asymmetric effects, the following are defined:

$$
\begin{aligned}
z &= \frac{1}{2}\,(z_x + z_y) \\
\Delta z &= \frac{1}{2}\,(z_x - z_y) \\
\tilde{Z}_{//} &= \frac{1}{2}\,(Z_x + Z_y) \\
\Delta\tilde{Z}_{//} &= \frac{1}{2}\,(Z_x - Z_y)
\end{aligned}
\tag{8}
$$

$\tilde{Z}_{//}$ includes both fluid film and pivot axis constraints. $\underline{Z}_{/}$ is exclusively fluid-film related since usual mechanical arrangements do not introduce cross-coupling effects. $\Delta\tilde{Z}_{//}$ represents asymmetry in pivot axis constraints, while Δz is related to gimbal inertia. For simple harmonic motion, using the complex notation $e^{i\nu t}$:

$$\begin{aligned} z &= I\nu^2 \\ \Delta z &= \Delta I \nu^2 \\ \tilde{Z}_{//} &= \tilde{U}_{//} + i\,\tilde{V}_{//} \\ \Delta\tilde{Z}_{//} &= \Delta K + i\nu\Delta D \end{aligned} \tag{9}$$

A self-sustained motion requires the vanishing of the characteristic determinant:

$$\begin{bmatrix} \tilde{Z}_{//} + \Delta\tilde{Z}_{//} - (z + \Delta z) & \underline{Z}_{/} \\ -\underline{Z}_{/} & \tilde{Z}_{//} - \Delta\tilde{Z}_{//} - (z - \Delta z) \end{bmatrix} = 0 \tag{10}$$

or

$$(\tilde{Z}_{//} - z)^2 - (\Delta\tilde{Z}_{//} - \Delta z)^2 + \underline{Z}_{/}^2 = 0 \tag{11}$$

If the self-sustained motion is simple harmonic, the relations given by Equations (9) can be substituted into Equation (11):

$$W = (\tilde{U}_{//} - I\nu^2 + i\tilde{V}_{//})^2 - (\Delta K - \Delta I\nu^2 + i\nu\Delta D)^2 + (\underline{U}_{/} + i\underline{V}_{/})^2 = 0 \tag{12}$$

Regrouping real and imaginary parts and introducing the definitions of I_g and ΔT_g from Equation (6)

$$\begin{aligned} W &= \mathrm{Re} + i\,\mathrm{Im} \\ &= [\,(U_{//} - I_g\nu^2)^2 - \tilde{V}_{//}^2 - (\Delta I_g\nu^2)^2 + \nu^2(\Delta D)^2 + \underline{U}_{/}^2 - \underline{V}_{/}^2\,] \\ &\quad + 2i\,[\tilde{V}_{//}(U_{//} - I_g\nu^2) + \nu\Delta D(\Delta I_g\nu^2) + \underline{U}_{/}\,\underline{V}_{/}\,] = 0 \end{aligned} \tag{13}$$

The real and imaginary parts must equal zero separately. Thus, from the imaginary part,

$$I_g\nu^2 - U_{//} = \frac{1}{\tilde{V}_{//}} \left[\nu\Delta D(\Delta I_g\nu^2) + \underline{U}_{/}\,\underline{V}_{/}\right] \tag{14}$$

and from the real part,

$$(I_g\nu^2 - U_{//})^2 - \tilde{V}_{//}^2 - (\Delta I_g\nu^2)^2 + \nu^2(\Delta D)^2 + \underline{U}_{/}^2 - \underline{V}_{/}^2 = 0 \tag{15}$$

Eliminating $(I_g\nu^2 - U_{//})$ between the above equations yields

$$(\Delta I_g\nu^2)^2 \left[1 - \left(\frac{\nu\Delta D}{\tilde{V}_{//}}\right)^2\right] - 2\,\frac{\nu\Delta D}{\tilde{V}_{//}}\,\frac{\underline{U}_{/}\,\underline{V}_{/}}{\tilde{V}_{//}}\,(\Delta T_g\nu^2)$$

$$+ \left[\frac{(\tilde{V}_{//}^2 + \underline{V}_{/}^2)(\tilde{V}_{//}^2 - \underline{U}_{/}^2)}{\tilde{V}_{//}^2} - (\nu\Delta D)^2\right] = 0 \tag{16}$$

which is a quadratic equation of $\Delta I_g\nu^2$ and can readily be solved:

$$\Delta I_g\nu^2 = \tilde{V}_{//}F \tag{17}$$

where

$$F = \frac{\frac{\nu\Delta D}{\tilde{V}_{//}}\,\frac{\underline{U}_{/}\,\underline{V}_{/}}{\tilde{V}_{//}^2}}{1-\left(\frac{\nu\Delta D}{\tilde{V}_{//}}\right)^2} \pm \left\{\frac{\left[1 + \left(\frac{\underline{V}_{/}}{\tilde{V}_{//}}\right)^2\right]\left[\left(\frac{\underline{U}_{/}}{\tilde{V}_{//}}\right)^2 - 1\right]}{1 - \left(\frac{\nu\Delta D}{\tilde{V}_{//}}\right)} + \right.$$

$$\left. \frac{\left(\frac{\nu\Delta D}{\tilde{V}_{//}}\right)^2\left[\left(\frac{\underline{U}_{/}\,\underline{V}_{/}}{\tilde{V}_{//}^2}\right) + 1 - \left(\frac{\nu\Delta D}{\tilde{V}_{//}}\right)^2\right]}{\left[1 - \left(\frac{\nu\Delta D}{\tilde{V}_{//}}\right)^2\right]^2}\right\}^{1/2} \tag{18}$$

Substituting into Equation (14):

$$I_g \nu^2 = U_{//} + \frac{U_{/} V_{/}}{\tilde{V}_{//}} + \nu \Delta DF \tag{19}$$

Equations (17) and (19) define the state of neutral stability in terms of the eigenvalue system (ν, I_g, ΔI_g, D, ΔD) for a prescribed set of fluid-film stiffnesses. Among the five parameters, three may be specified. For computational convenience, (ν, D, ΔD) may be specified and Equation (17) would be solved to determine a possible ΔT_g. Subsequently, Equation (19) would be solved to determine the corresponding I_g.

The eigenvalues of the neutrally stable state determine the boundary separating stable and unstable domains. However, it remains to be established which side of the boundary is the unstable domain. Consider a variation from the neutrally stable state such that the eigenvalue system now is given by

$$\begin{aligned} &\nu + \frac{1}{i} \delta\lambda + \delta\nu \\ &I_g + \delta I_g \\ &\Delta I_g + \delta \Delta I_g \\ &D + \delta D \\ &\Delta D + \delta \Delta D \end{aligned} \tag{20}$$

The characteristic equation is accordingly treated with a corresponding variational technique. For notational brevity, the following is defined:

$$\xi_i \ (i = 1,2,3,4) \ = (I_g, \Delta I_g, D, \Delta D) \tag{21}$$

Then the variational characteristic equation, derived from Equation (13), can be written in the following form:

$$\frac{\partial W}{\partial \nu} \left(\frac{1}{i} \delta \lambda + \delta \nu\right) = - \frac{\partial W}{\partial \xi_i} \delta \xi_i \tag{22}$$

Separating out the imaginary part,

$$\delta\lambda = \mathrm{Im}\left\{\left(\frac{\partial W}{\partial \nu}\right)^{-1} \frac{\partial W}{\partial \xi_i}\ \delta\ \xi_i\right\}$$

$$= \left(\frac{\partial W}{\partial \nu}\right)^{-2} \left(\frac{\partial \mathrm{Re}}{\partial \nu}\ \frac{\partial \mathrm{Im}}{\partial \xi_i} - \frac{\partial \mathrm{Im}}{\partial \nu}\ \frac{\partial \mathrm{Re}}{\partial \xi_i}\right) \delta\ \xi_i \qquad (23)$$

The stability criterion is that if $\frac{\delta\lambda}{\delta\xi_i} > 0$, the system becomes unstable (exponential growth of amplitude) for increasing ξ_i relative to the neutrally stable state, and stable (exponential decay of amplitude) for decreasing ξ_i. If $\frac{\delta\lambda}{\delta\xi_i} < 0$, the converse is true.

The influence of each of the four parameters I_g, ΔI_g, D, ΔD at the neutrally stable state may be considered separately by letting i vary from 1 to 4.

The real and imaginary parts of $\frac{\partial W}{\partial \xi_i}$, i.e., $\frac{\partial\ \mathrm{Re}}{\partial \xi_i}$ and $\frac{\partial\ \mathrm{Im}}{\partial \xi_i}$ are as follows:

i	ξ_i	$\frac{\partial\ \mathrm{Re}}{\partial \xi_i}$	$\frac{\partial\ \mathrm{Im}}{\partial \xi_i}$
1	I_g	$2\nu^2 (I_g \nu^2 - U_{//})$	$-2\nu^2 \tilde{V}_{//}$
2	ΔI_g	$-2\Delta I_g \nu^4$	$2\nu^3 \Delta D$
3	D	$-2\nu \tilde{V}_{//}$	$2(U_{//} - I_g \nu^2)\nu$
4	ΔD	$2\nu^2 \Delta D$	$2\Delta I_g \nu^3$

(24)

$\frac{\partial W}{\partial \nu}$ can be numerically computed directly from Equation (13); i.e.,

$$\mathrm{Re}\left(\frac{\partial W}{\partial \nu}\right) = \frac{\partial\ \mathrm{Re}}{\partial \nu}$$

$$\mathrm{Im}\left(\frac{\partial W}{\partial \nu}\right) = \frac{\partial\ \mathrm{Im}}{\partial \nu} \qquad (25)$$

where

$$Re = (I_g \nu^2 - U_{//})^2 - \tilde{V}_{//}^2 (\Delta I_g \nu^2)^2 + \nu^2 (\Delta D)^2 + \underline{U}_{/}^2 - \underline{V}_{/}^2$$

$$Im = 2 [\tilde{V}_{//} (U_{//} - I_g \nu^2) + \nu \Delta D (\Delta I_g \nu^2) + \underline{U}_{/} \underline{V}_{/}] \qquad (26)$$

In summary, the eigenvalue system (ν, I_g, ΔI_g, D, ΔD) governed by Equations (17) and (19) determines the states of neutral stability. The domains of stability and instability in terms of the influence of each of the parameters I_g, ΔI_g, D, ΔD can be determined by the variational technique described by Equation (23).

It is important and interesting to note that the mechanical stiffnesses (K, ΔK) and the system inertias (I, ΔI) are grouped as a single pair of variables (I_g, ΔI_g) defined by Equation (6). Regarding system stability, an excessive I (an increase in gimbal and/or thrust plate inertias) is equivalent to a deficient K (a decrease in pivot torsional stiffnesses), while an excessive ΔI (an increase in gimbal inertia) is equivalent to a deficient ΔK (an increase in thrust plate pivot stiffness or a decrease in gimbal pivot stiffness), and vice versa. These relationships are shown mathematically as follows:

$$\frac{\delta \lambda}{\delta I_g} = \frac{\delta \lambda}{\delta I} = -\nu^2 \frac{\delta \lambda}{\delta K}$$

$$\frac{\delta \lambda}{\delta \Delta I_g} = \frac{\delta \lambda}{\delta \Delta I} = -\nu^2 \frac{\delta \lambda}{\delta \Delta K} \qquad (27)$$

PROCEDURES FOR NUMERICAL COMPUTATIONS

Stability maps for gimbaled thrust-bearing systems may be presented in terms of the generalized inertias (I_g, ΔI_g). The procedure for numerical construction of these stability maps is as follows:

1. Prescribe the system dampings (D, ΔD).

2. Determine the fluid-film stiffness ($U_{//}$, $V_{//}$, $\underline{U}_{/}$, $\underline{V}_{/}$) as functions of vibrational frequency ν, based on lubrication theory.

3. Determine all possible ΔI_g from Equation (17) for a series of input frequencies covering a sufficiently wide range. Then compute all the corresponding I_g from Equation (19). The stability map is thus constructed in terms of (I_g, ΔI_g, ν) for a given physical system.

4. Determine the domains of instability (and stability) from Equation (23), and study the influence of other physical parameters (D, ΔD) on the system stability from the same equation.

The stability maps obtained from the above procedure apply to all values of mechanical stiffnesses (K, ΔK). For a specified set of (K, ΔK), the characteristic system inertias (I, ΔI) can be computed from (I_g, ΔI_g, ν) via Equation (6).

Stability maps in terms of (I, ΔI) may thus be generated for that set of (K, ΔK). Lines of neutrally-stable states (sets of points of (I, ΔI)) shift as the values of (K, ΔK) change. But the relative position of the domains of instability and stability remains the same as that of the general stability map (I_g, ΔI_g, ν) because of Equation (27).

It should be noted that when the stability map is constructed in terms of (I, ΔI), the characteristic frequency ν is no longer a directly relevant physical parameter but the values of (K, ΔK) have to be specified.

APPENDIX II
COMPUTER PROGRAM FOR STABILITY ANALYSIS OF GIMBALED THRUST BEARINGS

INTRODUCTION

The analysis presented in Appendix I has been incorporated in a computer program which will produce stability maps for a gimbaled thrust bearing in angular motion. This program is named "DSGIML", and will be referred to by this name in the following description.

As angular instability is induced by the particular angular stiffness and damping characteristics of the fluid film thrust bearing, an essential component of a stability analysis is the calculation of these fluid film characteristics. In the computer program description herein, the fluid film characteristics are calculated by a user-supplied subroutine entitled STIFF, whose specific function is detailed below. This subroutine is called where needed by the stability program (DSGIML).

To allow maximum flexibility, the stability program (DSGIML) itself has been written as a subroutine. Two forms of usage are possible. The subroutine may be added to any existing computer program for calculating fluid film characteristics. Alternatively, a short main program may be written to call the subroutine, so forming a stand-alone unit. An example of the latter usage is presented herein. The short main program is referred to as "STABMAP", and the subroutine STIFF is written to calculate fluid film characteristics by interpolation from a table. The program "DSGIML" produces data from which a stability map of critical values of thrust plate inertia (parameter I) as a function of gimbal inertia (parameter ΔI) can be plotted (Appendix I, Equation 6).

PROGRAM DESCRIPTION

The structure of the demonstration program is illustrated in Figure 197.

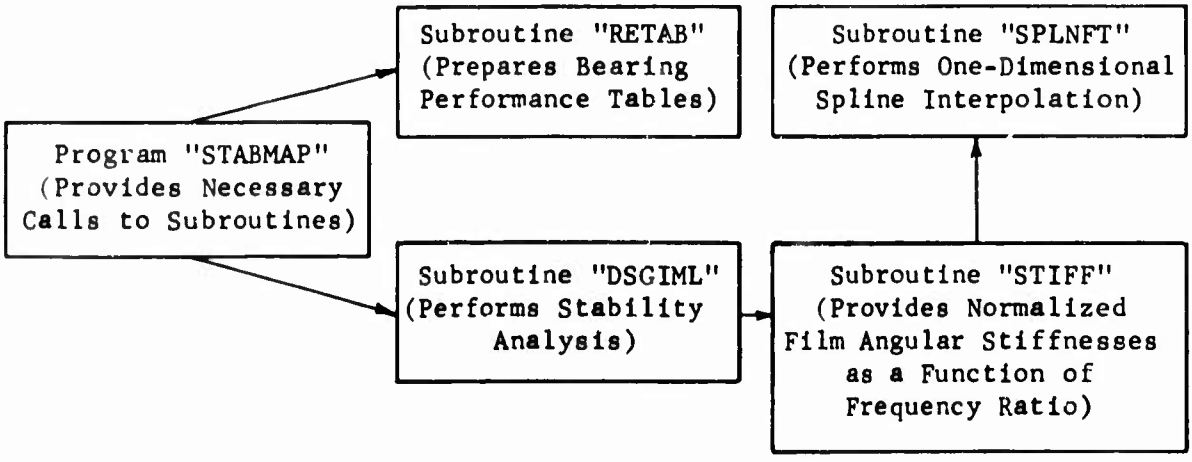


Figure 197. Program Structure

The subroutines shown in Figure 197 are described and defined below:

STABMAP

This is a short main program. Its sole function is to call the subroutines RETAB and DSGIML, in which all input, output and calculation are performed.

DSGIML (NBRG, ET, HR, C, PA, RO, OMEG3)

This is the basic stability analysis program which performs the analysis presented in Appendix I.

Inputs to DSGIML include the torsional stiffnesses and damping values of the thrust-gimbal and gimbal-ground connections, and the frequency range of interest. In addition, it is necessary for the user to insure that the variables C, PA, RO, and OMEG3 are set before the call to DSGIML. (In the present example, this function is performed by subroutine RETAB.) These variables enable DSGIML to convert the dimensionless data from subroutine STIFF to dimensional quantities, and are defined as follows:

C	Thrust bearing clearance, inches
PA	Ambient pressure, psia
RO	Reference radius, inches
OMEG3	Angular speed of thrust plate, rpm

RETAB

This subroutine reads tables of dimensionless fluid film characteristics as a function of frequency ratio, recombines the variables into the form required by subroutine STIFF (see below), and places the resultant tables in COMMON storage. For each frequency, the variables read by subroutine RETAB are:

AMR(1), AMT(1), AMR(2), AMT(2) (See input description for definition)

The recombination performed by subroutine RETAB is to set up tables of the quantities UPAR, UPER, VPAR, and VPER as follows:

$$UPAR = \frac{1}{2} (AMR(2) + AMR(1))$$

$$UPER = \frac{1}{2} (AMT(2) + AMT(1))$$

$$VPAR = \frac{1}{2} (AMT(2) - AMT(1))$$

$$VPER = \frac{1}{2} (AMR(2) - AMR(1))$$

In addition, the subroutine RETAB reads the COMMON variables C, PA, RO, and OMEG3, which are required by subroutine DSGIML to convert dimensionless stiffness and damping data to dimensional information.

STIFF (IAFTER, IMIS, NBRG, ET, ANU, HR, UPAR, UPERP, VPAR, VPERP)

This subroutine calculates normalized values of stiffness as a function of frequency ratio. The argument list is defined as follows:

IAFTER Set = 1 for first call to STIFF, zero thereafter.

IMIS, NBRG, ET, HR: These variables are a number of dummy arguments which provide flexibility if an alternative user supplied subroutine STIFF is to be used. In the present example they were not used.

ANU Ratio between vibration frequency and rotational frequency. This is the controlling input parameter to the subroutine.

UPAR Normalized in-phase, direct angular stiffness ($\bar{K}_{xx}$).

UPERP Normalized in-phase, cross-coupling angular stiffness ($\bar{K}_{xy}$).

VPAR Normalized, out of phase, direct angular stiffness ($\bar{B}_{xx}$).

VPERP Normalized, out of phase, cross-coupling stiffness ($\bar{B}_{xy}$).

The last four variables form the output from subroutine STIFF. They are computed by interpolating values from the tables set up by subroutine RETAB.

Normalization

$$\bar{K} = \frac{KC}{\pi p_a R_o^4}$$

$$\bar{B} = \frac{2\pi BC\nu}{\pi p_a R_o^4}$$

where K is angular stiffness in lb in./rad

B is angular damping in lb sec in./rad

C is the clearance, in.

P_a is the ambient pressure, in. lb/in.^{2}

R_o is the reference radius of the bearing surface

ν is the vibration frequency, cps

Note that isotropic film characteristics are assumed ($K_{yy} = K_{xx}$; $K_{yx} = K_{xy}$).

SPLNFT (N, X, Y, F2, KENN, IDER, M, T, F)

This subroutine performs spline interpolation in one dimension.

N is the number of points in the table

X is the independent table

Y is the dependent table

F2 is the table of the second derivatives

KENN = 0, Subroutine returns dependent values and stores the table of second derivatives

= 1, Subroutine returns dependent values using previously stored second derivatives

IDER = 0, Only values are returned in F(1→M)

= 1, Values and first derivatives are returned in F(1→M) and F(M+1→2M) respectively

M is the number of points to be interpolated

T is the table of points at which interpolation is required

F is the table of results

INPUT DESCRIPTION FOR SUBROUTINE RETAB

Card 1	Control, 1 card, FORMAT(I5), containing
NFREQ	No. of frequency values to be read
Card 2a	Backward whirl data, FORMAT(5E15.8), containing
TFR(I)	Frequency ratio
"BLANK"	Redundant field
AMR(I,1)	Normalized backward whirl in-line angular stiffness
"BLANK"	Redundant field
AMT(I,1)	Normalized backward whirl perpendicular stiffness

Card 2a	Forward whirl data, FORMAT(5E15.8), containing
TFR(I)	Frequency ratio
"BLANK"	Redundant field
AMR(I,2)	Normalized forward whirl in-line stiffness
"BLANK"	Redundant field
AMT (I,2)	Normalized forward whirl perpendicular stiffness

Note: NFREQ pairs of cards 2a and 2b are read.

The normalization factor for all angular stiffnesses is

$$\frac{C}{\pi p_a R_o^4}$$

Forward whirl angular stiffness is the ratio of film moment to angular displacement of a steady vibration in the direction of rotation.

Backward whirl angular stiffness is the ratio of film moment to angular displacement of a steady vibration in the direction opposite to rotation.

For parallel stiffness, the film moment vector parallel to the displacement vector is taken.

For perpendicular stiffness, the film moment vector perpendicular to the displacement vector is taken.

INPUT DESCRIPTION FOR SUBROUTINE DSGIML

Card 1	Title, FORMAT(100H), 1 card, containing any alphanumeric title.
Card 2	Search control card, FORMAT(E10.3), 1 card, containing
TEST	Search control. Set = 1
Card 3	First parameter card, FORMAT(8E10.3), 1 card, containing
"BLANK" "BLANK" "BLANK"	Three redundant variables. Leave blank
KTY	Torsional stiffness of thrust plate - gimbal connection. lb in./rad
KTX	Torsional stiffness of gimbal - ground connection. lb in./rad
AMUI	Initial frequency of range, cpm
AMUF	Final frequency of range, cpm
DAM	Frequency increment, cpm
Card 4	Second parameter card, FORMAT(8E10.3), 1 card, containing
"BLANK" "BLANK" "BLANK"	Three redundant variables, leave blank.
DGX	Torsional damping of gimbal - ground connection. lb sec in./rad
DGY	Torsional damping of thrust plate - gimbal connection. lb sec in./rad

SAMPLE CASE

An example is presented of a stability analysis for a gimbal mounted double-acting spiral grooved thrust plate with the following operating conditions.

TABLE XXXII. OPERATING CONDITIONS FOR SAMPLE CASE	
Outer Diameter	5.74 inches
Inner Diameter	3.10 inches
Clearance	0.002 inch
Speed	54000 rpm
Ambient Pressure	14.00 psia
Supply Pressure	96.00 psia

The surface pattern for this bearing is shown in Table XXXIII.

TABLE XXXIII. SURFACE PATTERN	
Groove Depth	0.001 inch
Spiral Groove Angle	18.1°
Groove Width Ratio	0.3
Groove Radial Extent	0.63 inch
Orifice Diameter	0.041 inch
No. of Orifices	20.
Radius of Orifice Line	1.755 inches

Table XXXIV gives the complete program input. The first 36 lines are the input to subroutine RETAB, and the next 4 lines are the input to subroutine DSGIML.

The first number of the input, 17, is the number of frequency values to be read. The next 34 lines are the pairs of forward and backward whirl stiffness values as a function of frequency ratio. The 36th line contains the values of reference radius, ambient pressure, clearance and speed, completing the input to subroutine RETAB. The following line contains the title for the case. On the next line the value of TEST has been set = 1 as required. On the next line the torsional stiffnesses of the thrust-plate to gimbal and gimbal to ground connections have been set to 100 lb in./rad, and the frequency range of interest is set as 22,000 to 28,000 cpm in increments of 1000 cpm. On the last card the damping values have been set to zero.

Tables XXXV and XXXVI give the output from the program. Table XXXV and the first 7 lines of Table XXXVI simply repeat the input. The next 2 lines print out the factor needed to convert the dimensionless angular stiffness data to dimensional information. This factor is equal to $\pi p_a R^4/c$. The remaining data is output from the program. The following columns of information are printed:

FREQ(RPM)	This is the frequency in cpm.
UPAR UPERD VPAR VPERD	These are the normalized values of the stiffness components obtained at the particular frequency.
I(LB-IN**2)	Critical values of the thrust plate inertia parameter, $I(=(I_{gx} + I_{tx} - I_{ty})/2)$. (See Equation 6)
DI(LB-IN**2)	Critical values of the gimbal inertia parameter, $DI(=I_{gx} + I_{tx} - I_{ty})/2)$. (See Equation 6)
DI/I	Ratio of DI to I.

It will be noted that pairs of values of I, DI, and DI/I are printed, which in the case of DI and DI/I are arithmetically equal, but of opposite sign. Now DI is defined as the sum of the gimbal transverse moment of inertia added to the difference between the x and y transverse moments of inertia of the thrust plate. Thus a negative value of DI implies that the difference between the x and y transverse moments of inertia of the thrust plate is greater than the gimbal transverse moment of inertia. Whether DI is negative or positive, the corresponding critical value of I is the same.

The results typified in Table XXXVI should be used to plot maps of critical values of I as a function of the parameter DI/I, such as Figures 121 through 124 of this report. It will be noted that each line of data in Table XXXVI is followed by a message indicating whether instability is

TABLE XXXIV. COMPLETE PROGRAM INPUT

```
   17
     1.0989E-02  0.          3.1536E+00  0.          4.6565E-01
     1.0989E-02  0.          3.1466E+00  0.          4.4698E-01
     4.3956E-02  0.          3.1645E+00  0.          4.9333E-01
     4.3956E-02  0.          3.1367E+00  0.          4.1868E-01
     7.6923E-02  0.          3.1760E+00  0.          5.2063E-01
     7.6923E-02  0.          3.1273E+00  0.          3.9005E-01
     1.0989E-01  0.          3.1881E+00  0.          5.4753E-01
     1.0989E-01  0.          3.1187E+00  0.          3.6109E-01
     4.3956E-01  0.          3.3352E+00  0.          7.9113E-01
     4.3956E-01  0.          3.0695E+00  0.          5.9093E-02
     7.6923E-01  0.          3.5158E+00  0.          9.8321E-01
     7.6923E-01  0.          3.0929E+00  0.         -2.4759E-01
     1.0989E+00  0.          3.7106E+00  0.          1.1230E+00
     1.0989E+00  0.          3.1847E+00  0.         -5.3331E-01
     4.3956E+00  0.          4.9829E+00  0.          1.1641E+00
     4.3956E+00  0.          4.7463E+00  0.         -1.2460E+00
     7.6923E+00  0.          5.3589E+00  0.          9.1752E-01
     7.6923E+00  0.          5.2789E+00  0.         -9.7403E-01
     1.0989E+01  0.          5.5198E+00  0.          7.7724E-01
     1.0989E+01  0.          5.4778E+00  0.         -8.0809E-01
     4.3956E+01  0.          5.9485E+00  0.          4.4156E-01
     4.3956E+01  0.          5.9410E+00  0.         -4.4515E-01
     7.6923E+01  0.          6.0688E+00  0.          3.4745E-01
     7.6923E+01  0.          6.0652E+00  0.         -3.4919E-01
     1.0989E+02  0.          6.1308E+00  0.          2.4675E-01
     1.0989E+02  0.          6.1285E+00  0.         -2.9782E-01
     1.4286E+02  0.          6.1702E+00  0.          2.6381E-01
     1.4286E+02  0.          6.1686E+00  0.         -2.6455E-01
     1.7582E+02  0.          6.1982E+00  0.          2.4016E-01
     1.7582E+02  0.          6.1969E+00  0.         -2.4071E-01
     2.0879E+02  0.          6.2193E+00  0.          2.2206E-01
     2.0879E+02  0.          6.2183E+00  0.         -2.2250E-01
     2.4176E+02  0.          6.2361E+00  0.          2.0761E-01
     2.4176E+02  0.          6.2353E+00  0.         -2.0796E-01
     1.5500E+00     1.4000E+01     2.0000E-03     5.4600E+04
1  DOUBLE ACTING THRUST BEARING STABILITY 25K FT
1.
0.        0.        0.       100.      100.     22000.    28000.      1000.
0.          0.        0.        0.        0.        0.
```

TABLE XXXV. INPUT BEARING FILM CHARACTERISTICS

INPUT BEARING FILM CHARACTERISTICS

17 FREQUENCY VALUES

FREQUENCY	RR	AMR	RT	AMT
1.0989E-02	0.	3.1536E+00	0.	4.6565E-01
1.0989E-02	0.	3.1466E+00	0.	4.4698E-01
4.3956E-02	0.	3.1645E+00	0.	4.9333E-01
4.3956E-02	0.	3.1367E+00	0.	4.1868E-01
7.6923E-02	0.	3.1760E+00	0.	5.2063E-01
7.6923E-02	0.	3.1273E+00	0.	3.9005E-01
1.0989E-01	0.	3.1881E+00	0.	5.4753E-01
1.0989E-01	0.	3.1187E+00	0.	3.6109E-01
4.3956E-01	0.	3.3352E+00	0.	7.9113E-01
4.3956E-01	0.	3.0695E+00	0.	5.9093E-02
7.6923E-01	0.	3.5158E+00	0.	9.8321E-01
7.6923E-01	0.	3.0929E+00	0.	-2.4759E-01
1.0989E+00	0.	3.7106E+00	0.	1.1230E+00
1.0989E+00	0.	3.1847E+00	0.	-5.3331E-01
4.3956E+00	0.	4.9829E+00	0.	1.1641E+00
4.3956E+00	0.	4.7463E+00	0.	-1.2460E+00
7.6923E+00	0.	5.3589E+00	0.	9.1752E-01
7.6923E+00	0.	5.2789E+00	0.	-9.7403E-01
1.0989E+01	0.	5.5198E+00	0.	7.7724E-01
1.0989E+01	0.	5.4778E+00	0.	-8.0809E-01
4.3956E+01	0.	5.9485E+00	0.	4.4156E-01
4.3956E+01	0.	5.9410E+00	0.	-4.4515E-01
7.6923E+01	0.	6.0688E+00	0.	3.4745E-01
7.6923E+01	0.	6.0652E+00	0.	-3.4919E-01
1.0989E+02	0.	6.1308E+00	0.	2.9675E-01
1.0989E+02	0.	6.1285E+00	0.	-2.9782E-01
1.4286E+02	0.	6.1702E+00	0.	2.6381E-01
1.4286E+02	0.	6.1686E+00	0.	-2.6455E-01
1.7582E+02	0.	6.1982E+00	0.	2.4016E-01
1.7582E+02	0.	6.1969E+00	0.	-2.4071E-01
2.0879E+02	0.	6.2193E+00	0.	2.2206E-01
2.0879E+02	0.	6.2183E+00	0.	-2.2250E-01
2.4176E+02	0.	6.2361E+00	0.	2.0761E-01
2.4176E+02	0.	6.2353E+00	0.	-2.0796E-01

RO	PA	C	OMEG3
1.5500E+00	1.4000E+01	2.0000E-03	5.4600E+04

TABLE XXXVI. DYNAMIC STABILITY ANALYSIS RESULTS

DOUBLE ACTING THRUST BEARING STABILITY 25K FI

DYNAMIC STABILITY ANALYSIS

GIMBAL-HOUSING STIFFNESS(LB-IN/RAD)= 1.0000E+02

PLATE-GIMBAL STIFFNESS(LB-IN/RAD)= 1.0000E+02

GIMBAL DAMPING(LB-IN-SEC)= 0.

THRUST PLATE DAMPING(LB-IN-SEC)= 0.

FREQUENCY RANGE(RPM)= 2.2000E+04 2.8000E+04 1.0000E+03

BEARING STIFFNESS AND CRITICAL INERTIALS
STIFFNESS NORMALIZED BY 1.2693E+05 LB-IN

REQ.(RPM)	UPAR	UPERD	VPAR	VPERD	I(LB-IN**2)		DI(LB-IN**2)		DI/I	
2.2000E+04	3.1942E+00	4.2991E-01	3.3658E-01	-1.2267E-01	2.8105E+01	2.8105E+01	2.6333E+00	-2.6333E+00	9.3694E-02	-9.3694E-02
FOR ABOVE LINE OF DATA INERTIAS GREATER THAN I INDUCE INSTABILITY										
2.3000E+04	3.1982E+00	4.2755E-01	3.5134E-01	-1.2779E-01	2.5758E+01	2.5758E+01	2.1943E+00	-2.1943E+00	8.5188E-02	-8.5188E-02
FOR ABOVE LINE OF DATA INERTIAS GREATER THAN I INDUCE INSTABILITY										
2.4000E+04	3.2024E+00	4.2511E-01	3.6602E-01	-1.3285E-01	2.3698E+01	2.3698E+01	1.7879E+00	-1.7879E+00	7.5445E-02	-7.5445E-02
FOR ABOVE LINE OF DATA INERTIAS GREATER THAN I INDUCE INSTABILITY										
2.5000E+04	3.2067E+00	4.2258E-01	3.8063E-01	-1.3785E-01	2.1880E+01	2.1880E+01	1.3986E+00	-1.3986E+00	6.3920E-02	-6.3920E-02
FOR ABOVE LINE OF DATA INERTIAS GREATER THAN I INDUCE INSTABILITY										
2.6000E+04	3.2112E+00	4.1997E-01	3.9516E-01	-1.4278E-01	2.0267E+01	2.0267E+01	1.0014E+00	-1.0014E+00	4.9408E-02	-4.9408E-02
FOR ABOVE LINE OF DATA INERTIAS GREATER THAN I INDUCE INSTABILITY										
2.7000E+04	3.2158E+00	4.1727E-01	4.0961E-01	-1.4765E-01	1.8831E+01	1.8831E+01	5.1940E-01	-5.1940E-01	2.7582E-02	-2.7582E-02
FOR ABOVE LINE OF DATA INERTIAS GREATER THAN I INDUCE INSTABILITY										
2.8000E+04	3.2206E+00	4.1449E-01	4.2394E-01	-1.5245E-01	1.8831E+01	1.8831E+01	5.1940E-01	-5.1940E-01	9.9990E+03	9.9990E+03
FOR ABOVE LINE OF DATA INERTIAS GREATER THAN I INDUCE INSTABILITY										

induced by greater or smaller inertias than the critical value I (in this Sample Case it is greater inertias). The latter information enables the stable and unstable regions of the stability map to be identified.

PROGRAM LISTING

```
RUN VERSION 2.3 --LEVEL 265--

                PROGRAM STARMAP(INPUT,OUTPUT,DATA,TAPE5=INPUT,TAPE6=OUTPUT,
               1 TAPE8=DATA)
000003          COMMON/RVAR/ RO,PA,C,OMEG3,IMIS
000003          COMMON/DIM/NDIM
000003          DIMENSION RR(40,2),AMR(40,2),RT(40,2),AMT(40,2),HR(100)
000003          CALL RETAB(RR,AMR,RT,AMT,IOP)
000007          CALL DSGIML(NBRG,ET,HR,C ,PA,RO,OMEG3)
000016          CALL EXIT
000017          END
```

```
RUN VERSION 2.3 --LEVEL 265--

                SUBROUTINE RETAB(RR,AMR,RT,AMT,IOP)
000010          DIMENSION RR(40,1),AMR(40,1),RT(40,1),AMT(40,1),ER
000010          COMMON /UVTAB/UPATAB(40),UPETAB(40),VPATAB(40),VPET    40),TFR(40),
               1 NFREQ
000010          COMMON/RVAR/ RO,PA,C,OMEG3,IMIS
000010          COMMON/DIM/NDIM
000010          DATA IN,IO/5,6/
000010          NDIM=1
000011          IMIS=1
000012          IREAD=5
000013          READ(IREAD,100) NFREQ
000020          WRITE(IO,102) NFREQ
000026          DO 10 I=1,NFREQ
000033          DO 10 J=1,2
000034          READ(IREAD,101)   TFR(I),RR(I,J),AMR(I,J),RT(I,J),AMT(I,J)
000076          WRITE(IO,103)     TFR(I),RR(I,J),AMR(I,J),RT(I,J),AMT(I,J)
000142       10 CONTINUE
000152          IF (IOP.EQ.3)  IREAD=5
000155          READ(IREAD,101) RO,PA,C,OMEG3
000171          IF(NDIM.EQ.0) GO TO 150
000175          WRITE(IO,105) RO,PA,C,OMEG3
000211      150 CONTINUE
000211          IF(IMIS.EQ.1)  GO TO 40
000216          DO 30 J=1,NFREQ
000220          UPATAB(J)=0.5*(RR(J,1)+RR(J,2))
000224          UPETAB(J)=0.5*(RT(J,1)+RT(J,2))
000230          VPATAB(J)=-.5*(RT(J,2)-RT(J,1))
000234          VPETAB(J)=.5*(RR(J,2)-RR(J,1))
000240       30 CONTINUE
000242       40 CONTINUE
000242          DO 50 J=1,NFREQ
000244          UPATAB(J)=0.5*(AMR(J,1)+AMR(J,2))
000250          UPETAB(J)=0.5*(AMT(J,1)+AMT(J,2))
000254          VPATAB(J)=-.5*(AMT(J,2)-AMT(J,1))
000260          VPETAB(J)=.5*(AMR(J,2)-AMR(J,1))
000264       50 CONTINUE
000266          WRITE(IO,107)
000272          RETURN
000273      100 FORMAT(I5)
000273      101 FORMAT(5E15.8)
000273      102 FORMAT(1H1,5X,40H***INPUT BEARING FILM CHARACTERISTICS*** /
                  A10X,I5,20H FREQUENCY VALUES          /
                  1 5X,  55HFREQUENCY          RR           AMR           RT           AMT )
000273      103 FORMAT(5X,5E12.4)
000273      105 FORMAT(/1H0,5X,45H      RO           PA           C            OMEG3  /
                 1 5X,4E12.4)
000273      106 FORMAT(//5X,5E12.4)
000273      107 FORMAT(/1H1)
000273          END
```

```
RUN VERSION 2.3 --LEVEL 265--

                SUBROUTINE STABLE2(EI,DI,KGX,KTY,DGX,DTY,AMU)
000012          COMMON/RVAR/RO,PA,C,OMEG3,IMIS
          C     INPUT DESCRIPTION
          C     FREQUENCIES IN RPM (AMU,AMU1,AMU2)
          C     INERTIALS IN LB-IN**2 (EI,DI)
          C     STIFFNESSES IN LB-IN (KTY,KGX)
          C     DAMPINGS IN LB-IN-SEC (DGX,DTY)
          C     FILM STIFFNESSES NORMALIZED BY 3.1416*PA*RO**4/CR (UPAR,ETC.)
          C     PA=LB/IN**2
          C     RO=IN
          C     CR=IN
          C     AMU-AMU1=AMU2-AMU
000012          REAL ITX,ITY,IGX,KTY,KGX
000012          CR=C
000013          ANU=AMU/OMEG3
000015          ANU2=1.0001*ANU
000016          ANU1=.9999*ANU
000020          AMU1=ANU1*OMEG3
000021          AMU2=ANU2*OMEG3
000023          CALL STIFF(0.1,NBRG,ET,ANU,HR,UPAR,UPERD,VPAR,VPERD)
000035          CALL STIFF(0.1,NBRG,ET,ANU1,HR,UPAR1,UPERD1,VPAR1,VPERD1)
000047          CALL STIFF(0.1,NBRG,ET,ANU2,HR,UPAR2,UPERD2,VPAR2,VPERD2)
000061          AA=3.1416*PA*RO**4/CR
000065          F=AMU*6.2832/60.
000067          F1=AMU1*6.2832/60.
000071          F2=AMU2*6.2832/60.
000073          AAA=AA*32.2*12.
          C     NORMALIZATION
000075          KTY=KTY/AA
000102          KGX=KGX/AA
000103          DGX=DGX/AA
000104          DTY=DTY/AA
000105          EI=EI/AAA
000107          DI=DI/AAA
000110          RRDD=DI/EI
000111          DK=(KGX-KTY)/2.
000113          DD=(DGX-DTY)/2.
000115          EK=(KGX+KTY)/2.
000117          ED=(DGX+DTY)/2.
000121          SUPAR=UPAR+EK
000123          SUPAR1=UPAR1+EK
000124          SUPAR2=UPAR2+EK
000126          SVPAR=VPAR+ED*F
000131          SVPAR1=VPAR1+ED*F1
000134          SVPAR2=VPAR2+ED*F2
000137          FSQ=F**2
000140          AIR=2.*FSQ*(EI*FSQ-SUPAR)
000144          AII=-2.*FSQ*SVPAR
000147          ADIR=2.*FSQ*(DK-DI*FSQ)
000153          ADII=2.*FSQ*F*DD
000156          ADKR=2.*(DI*FSQ-DK)
000161          ADKI=-2.*DD*F
000164          ADDR=2.*FSQ*DD
000165          ADDI=2.*F*(DI*FSQ-DK)
```

```
000171          AKR=-2.*(EI*FSQ-SUPAR)
000174          AKI=2.*SVPAR
000176          ADR=-2.*F*SVPAR
000200          ADI=2.*F*(SUPAR-EI*FSQ)
000203          F1Q=F1**2
000205          F2Q=F2**2
000206          G1=(EI*F1Q-SUPAR1)**2-SVPAR1**2-(DK-DI*F1Q)**2+F1Q*DD**2+UPERD1**2
               1-VPERD)**2
000232          G2=(EI*F2Q-SUPAR2)**2-SVPAR2**2-(DK-DI*F2Q)**2+F2Q*DD**2+UPERD2**2
               1-VPERD2)**2
000255          H1=  (SVPAR1*(SUPAR1- EI*F1Q)+UPERD1*VPERD1+F1*DD*(DI*F1Q-DK))*2.
000271          H2=2.*(SVPAR2*(SUPAR2-EI*F2Q)+UPERD2*VPERD2+F2*DD*(DI*F2Q-DK))
000305          AFR=(G2-G1)/(F2-F1)
000310          AFI=(H2-H1)/(F2-F1)
000314          AFM=AFR**2+AFI**2
000316          SNI=AFR*AII-AFI*AIR
000321          SNDI=AFR*ADII-AFI*ADIR
000325          SNDK=AFR*ADKI-AFI*ADKR
000330          SNDD=AFR*ADDI-AFI*ADDR
000333          SNK=AFR*AKI-AFI*AKR
000336          SND=AFR*ADI-AFI*ADR
000341          DDI=SNI/AFM
000343          DDDI=SNDI/AFM
000344          DDDK=SNDK/AFM
000346          DDDD=SNDD/AFM
000347          DDK=SNK/AFM
000351          DDD=SND/AFM
000353          IF(DDI)20,30,40
000355       20 WRITE(6,210)
000361          GO TO 30
000365       40 WRITE(6,200)
000371       30 CONTINUE
000371          KTY=KTY*AA
000376          KGX=KGX*AA
000377          DGX=DGX*AA
000400          DTY=DTY*AA
000400          EI=EI*AAA
000402          DI=DI*AAA
000403      210 FORMAT(1H+,1X,67H FOR ABOVE LINE OF DATA INERTIAS SMALLER THAN I I
              1NDUCE INSTABILITY /)
000403      200 FORMAT(1H+,1X,67H FOR ABOVE LINE OF DATA INERTIAS GREATER THAN I I
              1NDUCE INSTABILITY /)
000403          RETURN
000403          END
```

```
RUN VERSION 2.3 --LEVEL 265--

                SUBROUTINE DSGIML(NBRG,ET,HR,CR    ,P          G3)
          C     NDYN MUST BE SET ZERO
          C     CR IN IN
          C     PA IN LB/IN**2
          C     RO IN IN
000012            DIMENSION ROOTS(10),CM(10),IGX(10),  (10),DI1(10),DI2(10),CINET(10)
                 1,R1(10),R2(10) ,CDI(10)
000012            COMMON/THIRTY/ITX,ITY,IGX,KTY,KGX,UPAR,VPAR,UPERD,VPERD
                 1,OMEG33,IAFTER,NNB,EETT,HHRR(100),ED
000012            COMMON/EIGHT/N
000012            COMMON/ACCURY/ERR
000012            COMMON/TTEST/EII,TEST
000012            COMMON/DIM/NDIM
000012            EXTERNAL FF
000012            REAL ITX,ITY,IGX,KTY,KGX
000012            REAL III
000012          1 FORMAT(100H
                 1
000012            NDIM=1
000013            READ(5,1)
000016            WRITE(6,1)
000022            WRITE(6,120)
000026            READ(5,5) TEST
000034            RTD1=RTD2=9999.
000037            DO 900 I=1,10
000044          900 DI1(I)=DI2(I)=9999.
000052            READ(5,5) GGX,ITX,ITY,KTY,KGX,AMUI,AMUF,DAM
000075            READ(5,5) ERR,TD,TMASS,DGX,DTY
000113          120 FORMAT(//// 33H ***DYNAMIC STABILITY ANALYSIS***)
000113            IF(NDIM.EQ.0) GO TO 1000
000120            WRITE(6,121) KGX
000125          121 FORMAT(/ 37H GIMBAL-HOUSING STIFFNESS(LB-IN/RAD)=,E12.4)
000125            WRITE(6,122) KTY
000133          122 FORMAT(/ 35H PLATE-GIMBAL STIFFNESS(LB-IN/RAD)=,E12.4)
000133            WRITE(6,130) DGX
000141            WRITE(6,131) DTY
000147          130 FORMAT(/ 27H GIMBAL DAMPING(LB-IN-SEC)=,E12.4)
000147          131 FORMAT(/ 33H THRUST PLATE DAMPING(LB-IN-SEC)=,E12.4)
000147            IF(TD.EQ.0.) GO TO 126
000154            WRITE(6,125)TD
000161          125 FORMAT(/ 36H DISTANCE OF PLATE TO PIVOT PT.(IN)=,E12.4)
000161            WRITE(6,128) TMASS
000167          128 FORMAT(/ 19H PLATE MASS(LB)  M=,E12.4)
000167          126 WRITE(6,127) AMUI,AMUF,DAM
000201          127 FORMAT(/ 22H FREQUENCY RANGE(RPM)=,3E12.4 //)
000201            GO TO 501
000205         1000 WRITE(6,1001) KGX
000213            WRITE(6,1002) KTY
000221            WRITE(6,1003) DGX
000227            WRITE(6,1004) DTY
000235         1001 FORMAT(/ 37H NORMALIZED GIMBAL-HOUSING STIFFNESS=,E12.4)
000235         1002 FORMAT(/ 35H NORMALIZED PLATE-GIMBAL STIFFNESS=,E12.4)
000235         1003 FORMAT(/ 27H NORMALIZED GIMBAL DAMPING=,E12.4)
000235         1004 FORMAT(/ 33H NORMALIZED THRUST PLATE DAMPING=,E12.4)
```

```
000235          WRITE(6,1005) AMUI,AMUF,DAM
000247     1005 FORMAT(/ 28H NORMALIZED FREQUENCY RANGE=,3E12.4 /
000247        5 FORMAT(8E10.3)
           C      AMUI,AMUF=FREQUENCY RANGE,RPM
           C      DAM=INCREMENT IN FREQUENCY,RPM
           C      KTY,KGX=STIFFNESS LB-IN/RAD
000247      501 IAFTER=1
000250          OMEG33=OMEG3
000251          NNB=NBRG
000256          EETT=E1
000257          DO 70 K=1,N
000261       70 . ;R(K)=HR(K)
000266          IF(NDIM.EQ.0) GO TO 1006
000267          AA=3.1416*PA RO**4/CR
000271          ITX=(ITX+TMASS*TD**2)/(32.2*12.*AA)
000277          ITY=(ITY+TMASS*TD**2)/(32.2*12.*AA)
000305          GGX=GGX/(32.2*12.*AA)
000310          EII=(GGX+ITX+ITY)/2.
000313          DI=(GGX+ITX-ITY)/2.
000315          EEII=EII*32.2*12.*AA
000320          DDI=DI*32.2*12.*AA
000322          RRDD=DDI/EEII
           C      ITX,ITY IN SEC**2
000323          KTY=KTY/AA
000325          KGX=KGX/AA
000326          DGX=DGX/AA
000327          DTY=DTY/AA
000330          AMUI=AMUI*6.28/60.
000332          AMUF=AMUF*6.28/60.
000333          DAM=DAM*6.28/60.
000335     1006 CONTINUE
000335          DK=(KGX-KTY)/2.
000340          EK=(KGX+KTY)/2.
000342          ED=(DGX+DTY)/2.
000345          DD=(DGX-DTY)/2.
000347          IF (TEST.NE.1.) GO TO 803
000351          WRITE(6,804)AA
000357          WRITE(6,805)
000363          ANUU=AMUI
000365      800 ANUU2=ANUU**2
000366          IF(NDIM.EQ.0) GO TO 1007
000373          AMUU=ANUU*60./6.28/ OMEG33
000375          AMT=AMUU*OMEG33
000378          GO TO 1008
000377     1007 AMUU=ANUU
000400          AMT=ANUU
000402     1008 CONTINUE
000402          CALL STIFF(IAFTER,1,NNB,EETT,AMUU,HHRR,UPAR,UPERD,VPAR,VPERD)
000414          SUPAR=UPAR+EK
000416          SVPAR=VPAR+ED*ANUU
000421          DFV=ANUU*DD/SVPAR
000423          DFV2=DFV**2
000424          DFVD=1.-DFV2
000426          UPV2=(UPERD/SVPAR)**2
000430          VPV2=(VPERD/SVPAR)**2
```

```
000432          TTT=(1.+VPV2)*(UPV2-1.)/DFVD+DFV2*(UPV2*VPV2+DFVD)/DFVD**2
000446          IF(TTT.LT.0) GO TO 810
000454          FFD1 =DFV*SQRT(VPV2*UPV2)/DFVD+SQRT(TTT)
000465          FFD2=FFD1-2.*SQRT(TTT)
000472          DTT1=(SVPAR*FFD1+DK)/ANUU2
000475          DTT2=(SVPAR*FFD2+DK)/ANUU2
000500          EI1=SUPAR+UPERD*VPERD/SVPAR+DD*ANUU*FFD1
000507          EI2=SUPAR+UPERD*VPERD/SVPAR+DD*ANUU*FFD2
000516          IF(NDIM.EQ.0) GO TO 1010
000523          TI1=EI1*32.2*12.*AA/ANUU2
000526          TI2=EI2*32.2*12.*AA/ANUU2
000530          TD1=DTT1*32.2*12.*AA
000532          TD2=DTT2*32.2*12.*AA
000535          GO TO 1011
000535     1010 TI1=(EI1-EK)/ANUU2
000540          TI2=(EI2-EK)/ANUU2
000542          TD1=DTT1-DK/ANUU2
000545          TD2=DTT2-DK/ANUU2
000550     1011 RTD1=TD1/TI1
000552          RTD2=TD2/TI2
000554      810 WRITE(6,806)AMT,UPAR,UPERD,VPAR,VPERD,TI1,TI2,TD1,TD2,RTD1,RTD2
000606          CALL STABLE2(TI1,TD1,KGX,KTY,DGX,DTY,AMT)
000615          RTD1=RTD2=9999.
000620      801 ANUU=ANUU+DAM
000622          IF(ANUU.LE.AMUF) GO TO 800
000630      804 FORMAT(// 43H *BEARING STIFFNESS AND CRITICAL INERTIALS* /  25H *S
               1TIFFNESS NORMALIZED BY,E12.4,7H LB-IN* //)
000630      805 FORMAT(1X,10HFREQ.(RPM),4X,4HUPAR,8X,5HUPERD,7X,4HVPAR,8X,5HVPERD,
               111X,11HI(LB-IN**2),13X,12HDI(LB-IN**2),15X,4HDI/I   /)
000630      806 FORMAT(11E12.4 /)
000630          GO TO 105
000631      803 WRITE(6,807)AA
000637      807 FORMAT(// 43H *BEARING STIFFNESS AND CHARACT. FUNCTION * /  25H *S
               1TIFFNESS NORMALIZED BY,E12.4,7H LB-IN* //)
000637          WRITE(6,808)
000643      808 FORMAT(1X,10HFREQ.(RPM),4X,4HUPAR,8X,5HUPERD,7X,4HVPAR,8X,5HVPERD,
               17X,5HF(MU),7X,6HVPAR*D /)
000643          CALL GROOT(AMUI,AMUF,DAM,FF,NROOT,ROOTS)
000647          IF(NROOT.LT.1) GO TO 100
000655          DO 50 M=1,NROOT
000657          CM(M)=ROOTS(M)*60./6.28
000661          ANU=   CM(M)/OMEGJJ
000663          IF(NDIM.EQ.0) ANU=ROOTS(M)
000666          IF(NDIM.EQ.0) CM(M)=ROOTS(M)
000671          CALL STIFF(IAFTER,1,NBRG,ET,ANU,HR,UPAR,UPERD,VPAR,VPERD)
000704          IF(TEST.EQ.2.)GO TO 505
000712          IF(TEST.EQ.4.)GO TO 601
000714          GX=(2.*UPERD*VPERD+(-ITY*ROOTS(M)**2+KTY+UPAR)*VPAR+(-ITX*ROOTS(M)
               1**2+KGX+UPAR)*VPAR)/(ROOTS(M)**2*VPAR)
000735          IGX(M)=GX*AA*32.2*12.
000741          GO TO 50
000742     505  RTS=ROOTS(M)**2
000744          VPAR2=VPAR**2
000745          VPERD2=VPERD**2
000747          UPERD2=UPERD**2
```

```
000750          CCCC=((VPAR2+VPERD2)*(VPAR2-UPERD2)+VPAR2*(KGX-KTY)**2/4.)/VPAR2
000760          TTT=(KTY-KGX)**2/4.-CCCC
000764          IF(TTT.LT.0.) GO TO 50
000766          DI1(M)=((KGX-KTY)/2.+SQRT(TTT))/RIS  *32.2*12.*AA
000776          DI2(M)=((KGX-KTY)/2.-SQRT(TTT))/RTS  *32.2*12.*AA
001007          R1(M)=DI1(M)/EEII
001012          R2(M)=DI2(M)/EEII
001014          GO TO 50
001020      601 SVPA=VPAR+ED*ROOTS(M)
001024          CINET(M)=(              UPAR+UPERD*VPERD/SVPA)/(ROOTS(M)**2)
001034          IF(NDIM.NE.0) CINET(M )=(CINET(M)+EK/ROOTS(M)**2)*(32.2*12.*AA)
001045          CDI(M)=0.
001047          IF(NDIM.NE.0) CDI(M)=(CDI(M)+DK/ROOTS(M)**2)*(32.2*12.*AA)
001057       50 CONTINUE
001062          WRITE(6,15)(CM(I),I=1,NROOT)
001074          IF(TEST.EQ.2.)GO TO 560
001102          IF(TEST.EQ.4.) GO TO 610
001104          WRITE(6,16)(IGX(I),I=1,NROOT)
001116       15 FORMAT(///31H CRITICAL FREQUENCIES (RPM)    = ,10E13.4)
001116       16 FORMAT(/ 31H CRIT. GIMBAL INERT.(LB-IN**2)= ,10E13.4)
001116          GO TO 105
001122      100 WRITE(6,10)
001126       10 FORMAT(/// 41H NO ROOT IN THE FREQUENCY RANGE SPECIFIED )
001126          GO TO 105
001132      560 WRITE(6,561) (DI1(I),I=1,NROOT)
001145      561 FORMAT(/ 15H DI(LB-IN**2)= ,10E13.4)
001145          WRITE(6,562) (DI2(I),I=1,NROOT)
001160      562 FORMAT(15X,10E13.4)
001160          WRITE(6,902) EEII
001166      902 FORMAT(14H I(LB-IN**2)= ,E13.4)
001166          WRITE(6,911) (R1(I),I=1,NROOT)
001201      911 FORMAT(7H DI/I= ,10E13.4)
001201          WRITE(6,912) (R2(I),I=1,NROOT)
001214      912 FORMAT(7X,10E13.4)
001214          GO TO 105
001220      610 WRITE(6,611) (CINET(I),I=1,NROOT)
001233          WRITE(6,903) (CDI(I),I=1,NROOT)
001246      611 FORMAT(/ 26H CRIT. INERTIAL(LB-IN**2)=,10E13.4)
001246      903 FORMAT(14H DI(LB-IN**2)=,10E13.4)
001246          WRITE(6,904)
001252      904 FORMAT(/ 17H FOR DTY=DGX ONLY)
001252      105 CONTINUE
001252          RETURN
001253          END
```

```
RUN VERSION 2.3 --LEVEL 265--

                SUBROUTINE SPLNFT(N,X,Y,F2,KENN,IDER,M,T,F)
          C     N=NUMBER OF POINTS IN TABLE. MUST BE AT LEAST 3
          C     X=INDEPENDENT TABLE
          C     Y= DEPENDENT TABLE
          C     F2= TABLE OF SECOND DERIVATIVES, CALCULATED BY SPLNFT
          C     KENN=0 RETURNS DEPENDENT VALUE(S), STORES F2
          C     IDER=1 RETURNS DERIVATIVES IN F(M+1),...
          C     M= COUNT OF POINTS TO INTERPOLATE
          C     T= TABLE OF POINTS TO INTERPOLATE
          C     F= RETURNED VALUE TABLE (ANSWERS)
000014            DIMENSION H(100),DY(100),S(100),E(100),X(1),Y(1),F2(1),T(1
000014            DIMENSION F(1)
000014            IF(N.LT.3) GO TO 100
000016            N1=N-1
000017            N2=N-2
000021            INC1=0
000021            INC2=0
000023            DO 70 I=1,N1
000024            XDIFF=X(I+1)-X(I)
000027            IF(XDIFF.EQ.0.) GO TO 75
000030            IF(XDIFF.GT.0.) INC1=1
000033            IF(XDIFF.LT.0.) INC2=1
000036            IF(INC1.EQ.1.AND.INC2.EQ.1) GO TO 75
000045         70 CONTINUE
000047            DO 10 I=1,N1
000051            H(I)=X(I+1)-X(I)
000054            DY(I)=(Y(I+1)-Y(I))/H(I)
000061         10 CONTINUE
000064            IF(KENN.GT.0) GO TO 200
000066            F2(1)=0.
000066            F2(N)=0.
000070            I=1
000071         20 I=I+1
000073            F2(I)=6.0*(DY(I)-DY(I-1))
000100            IF(I.LT.N1) GO TO 20
000102            Z=0.5/(H(1)+H(2))
000105            S(1)=-H(2)*Z
000106            E(1)=F2(2)*Z
000110            K=1
000111            DO 30 I=2,N2
000113            J=I+1
000114            Z=1.0/(2.0*(H(I)+H(J))+H(I)*S(K))
000123            S(I)=-H(J)*Z
000127            E(I)=(F2(J)-H(I)*E(K))*Z
000136            K=I
000137         30 CONTINUE
000141            F2(N1)=E(N2)
000144            I=N2
000145         40 K=I-1
000147            F2(I)=S(K)*F2(I+1)+E(K)
000154            I=I-1
000155            IF(I.GT.1) GO TO 40
000160            IF(KENN.LT.0) GO TO 300
000161        200 CONTINUE
```

```
000161          DO 50 I=1,N1
000163          S(I)=(F2(I+1)-F2(I))/H(I)
000170       50 CONTINUE
000173          DO 60 J=1,M
000174          IF(INC1.EQ.1.AND.(T(J).LT.X(1).OR.T(J).GT.X(N))) GO TO 125
000211          IF(INC2.EQ.1.AND.(T(J).LT.X(N).OR.T(J).GT.X(1))) GO TO 150
000226          I=2
000226          K=1
000230       61 IF(T(J).LE.X(I).AND.INC1.EQ.1) GO TO 62
000245          IF(T(J).GE.X(I).AND.INC2.EQ.1) GO TO 62
000260          K=I
000260          I=I+1
000262          IF(I.GT.N) GO TO 80
000265          GO TO 61
000265       62 H1=T(J)-X(K)
000272          H2=T(J)-X(I)
000276          H3=H1*H2
000277          H4=F2(K)+H1*S(K)
000304          Z=(F2(I)+F2(K)+H4)/6.0
000311          F(J)=Y(K)+H1*DY(K)+H3*Z
000321          MJ=M+J
000323          IF(IDER.EQ.1) F(MJ)=DY(K)+Z*(H1+H2)+H3*S(K)/6.0
000341          GO TO 60
000342      125 IF(T(J).GT.X(1)) GO TO 130
000347          F(J)=Y(1)+DY(1)*(T(J)-X(1))
000357          GO TO 60
000357      130 IF(T(J).LT.X(N)) GO TO 80
000364          F(J)=Y(N)+DY(N1)*(T(J)-X(N))
000377          GO TO 60
000377      150 IF(T(J).LT.X(1)) GO TO 170
000403          F(J)=Y(1)+DY(1)*(T(J)-X(1))
000413      170 IF(T(J).GT.X(N)) GO TO 80
000421          F(J)=X(N)+DY(N)*(T(J)-X(N))
000430       60 CONTINUE
000433          GO TO 300
000433      100 WRITE(6,1000)
000437          GO TO 300
000443       75 WRITE(6,1001)
000447          GO TO 300
000453       80 WRITE(6,1002)
000457     1000 FORMAT(3X,16HN IS LESS THAN 3)
000457     1001 FORMAT(3X,33H INDEPENDENT TABLE IS NOT ORDERED)
000457     1002 FORMAT(3X,54H INDEPENDENT VALUE IS NOT FOUND WRT. INDEPENDENT TABL
                1E)
000457      300 CONTINUE
000457          RETURN
000460          END
```

```
RUN VERSION 2.3 --LEVEL 265--

                SUBROUTINE STIFF(IAFTER,IMIS,NBRG,ET,ANU,HR,UPAR,UPERP,VPAR,VPERP)
000015          DIMENSION F21(40),F22(40),F23(40),F24(40),HR(100),FRR(15)
000015          COMMON /UVTAB/UPATAB(40),UPETAB(40),VPATAB(40),VPETAB(40),TFR(40),
               1 NFREQ
000015          COMMON/ELEVEN/KOUNT
000015          COMMON/SEVEN/DQC(100,3),CCOM(100),PNU(100)
000015          COMMON/EIGHT/ N
000015          COMMON/NOSTIC/KDIAG
000015          COMPLEX DQC,CCOM,PNU
000015          NAMELIST/DAG6/IAFTER,IMIS,N,NBRG,ET,ANU,HR,DQC,CCOM,PNU
000015          NAMELIST/DAGEM/ANU,UPAR,UPERP,VPAR,VPERP,NFREQ,TFR,UPATAB,F21,KENN
               1,FRR
000015          IF(KDIAG.EQ.6)  WRITE(6,DAG6)
000025          FRR(1)=ANU
000026          KENN=0
000027          IF(IAFTER.NE.1) KENN=1
000032          CALL SPLNFT(NFREQ,TFR,UPATAB,F21,KENN,0,1,FRR,UPAR)
000043          CALL SPLNFT(NFREQ,TFR,UPETAB,F22,KENN,0,1,FRR,UPERP)
000054          CALL SPLNFT(NFREQ,TFR,VPATAB,F23,KENN,0,1,FRR,VPAR)
000065          CALL SPLNFT(NFREQ,TFR,VPETAB,F24,KENN,0,1,FRR,VPERP)
000076          RETURN
000077          END
```

Distribution
not shot

Unclassified
Security Classification

DOCUMENT CONTROL DATA - R & D

(Security classification of title, body of abstract and indexing annotation must be entered when the overall report is classified)

1. ORIGINATING ACTIVITY *(Corporate author)*
Mechanical Technology Incorporated
968 Albany-Shaker Road
Latham, New York 12110

2a. REPORT SECURITY CLASSIFICATION
Unclassified

2b. GROUP
N/A

3. REPORT TITLE
(6) AN INVESTIGATION OF AIR BEARINGS FOR GAS TURBINE ENGINES.

4. DESCRIPTIVE NOTES *(Type of report and inclusive dates)*
(9) Phase I Summary Report on Phase I,

5. AUTHOR(S) *(First name, middle initial, last name)*
(10) Warren D. Waldron,
William E. Young
Peter W. Curwen

6. REPORT DATE
(11) December 1971

7a. TOTAL NO. OF PAGES
(12) 393 pp.

7b. NO. OF REFS
9

8a. CONTRACT OR GRANT NO.
(15) DAAJ02-69-C-0062

8b. PROJECT NO.
(17)
c. Task 1G162203D14413
d. (16) DA-1-G-162203-D-144

9a. ORIGINATOR'S REPORT NUMBER(S)
USAAMRDL Technical Report 71-59

9b. OTHER REPORT NO(S) *(Any other numbers that may be assigned this report)*

10. DISTRIBUTION STATEMENT
[redacted]

11. SUPPLEMENTARY NOTES

12. SPONSORING MILITARY ACTIVITY
Eustis Directorate USAAMRDL,
Fort Eustis, Virginia

13. ABSTRACT

Due to ascending performance conditions and accompanying high rotational speeds, increasingly severe operating requirements will be imposed on main engine bearings and seals. Conventional oil lubrication techniques may not be adaptable to the next generation of small engines. This report presents a summary of the results of work performed during Phase I of an investigation of air bearings for gas turbine engines.

Results of a study of the significant effects of engine size on the design feasibility of air bearings show that the engine size over a range of from 2 to 5 lb/sec design-point air flow is not a significant factor with respect to air-bearing feasibility. However, the types of compressor and turbine components selected as well as their arrangement will influence the feasibility.

Two experimental efforts undertaken during Phase I are discussed - one involving evaluation tests of candidate air-bearing material combinations (substrate and coatings). The best material combination for the compressor-end journal and thrust bearings was determined to be a plasma-sprayed Cr_2O_3 coating on a titanium-alloy substrate; for the turbine-end journal bearing the best combination is a plasma-sprayed coating of 25% NiCr + 75% Cr_2O_3 on a high-temperature nickel-based alloy. The second series of tests involved experimental verification of the load carrying capability of the key journal and thrust bearing components. The test demonstrated that the components can carry the required high operating loads under the most severe conditions of bearing operation; namely, engine idle at 25,000 feet altitude.

DD FORM 1 NOV 68 1473 REPLACES DD FORM 1473, 1 JAN 64, WHICH IS OBSOLETE FOR ARMY USE.

Unclassified
Security Classification

MH (224550)

14 KEY WORDS	LINK A		LINK B		LINK C	
	ROLE	WT	ROLE	WT	ROLE	WT
Gas Turbines						
Bearing Systems						
Gas Bearings						
Lubrication Systems						
Gas Bearing Materials						
Bearing Stability						